Crystallography Reports, Vol. 49, No. 5, 2004, pp. 705–712. Translated from Kristallografiya, Vol. 49, No. 5, 2004, pp. 791–798.
Original Russian Text Copyright © 2004 by Smirnova.

THEORY OF CRYSTAL STRUCTURES

Radii of Ions and Frequency of Their Occurrence

N. L. Smirnova
Moscow State University, Vorob'evy gory, Moscow, 119992 Russia
e-mail: snl194@mail.ru

Received March 13, 2003

Abstract—Positive and negative ions are considered, and their absolute and effective radii are systematized. The frequency of occurrence of ions is analyzed as a function of the charge, the radius, and the type (*s*, *f*, *d*, *p*). A scheme of continuously isomorphic pairs of cations and anions is proposed. *© 2004 MAIK "Nauka/Interperiodica".*

The atomic and ionic radii are the most important characteristics of chemical elements, and knowledge of these characteristics is required for modern research. Data on the atomic and ionic radii can be found in many textbooks [1–4]; numerous monographs on crystallography, crystal chemistry, mineralogy, and chemistry; reference books; etc. (see, for example, [5–8]). It should be noted that the radii of atoms and ions are not constants and depend on the valence, coordination number, temperature, pressure, chemical composition, local environment, etc. At present, there are several systems of radii.

The Kepler–Shubnikov nets [9] are the ABC of the system of crystal structures. The ratio between the atomic (ionic) radii and the unit cell parameters predetermines the set of Kepler–Shubnikov nets and, consequently, the series of structures composed of a small number of structural minals (modules) [10–13]. In this respect, the analysis of the system of atomic (ionic) radii is of particular interest.

Table 1. Absolute ionic radius

Charge	Absolute ionic radius	Σ
1+	0, 1: H, D, 8: Li, Cu, 9: Pd, 10: Ag, 12: Na, 14: Pb, Hg, 15: Au, 16: K, 17: Tl, 18: Rb, Cs, 22: Fr	11–15
1–	8: F, 12: Cl, Br, 14: H, D, 15: I	4–6
2+	2: C, 4: Be, 6: Fe *ls*, 7: Mg, V, Nb, Cu, Mn *ls*, Co *ls*, Ni, 8: Cr *ls*, Fe *hs*, Co *hs*, Zn, Ge, 9: Ti, Ta, Cr *hs*, Mn *hs*, Pt, Pd, 10: Zr, Ag, 11: Ca, Cd, 12: Tm, Dy, Yb, Pa, U, Pu, Y, Hg, Pb, 13: Sm, Np, Am, No, Sn, 14: Sr, Nd, Eu, 15: Ba, 16: Ra	13–44 (40)
2–	8: O, 12: S, 14: Se, 15: Te	4–6
3+	0: N, 3: B, 4: P, 5: Co *ls*, Cu, Al, 6: Mn *ls*, Fe *ls*, Fe *hs*, Co *hs*, Ni *ls*, Ni *hs*, As, 7: Ti, Y, Cr, Ru, Rh, Ir, Ga, 8: Sc, Nb, Ta, Mo, Mn *hs*, Ag, Br, 9: Pd, In, Sb, 10: Ho, Er, Tm, Yb, Lu, Y, Au, Tl, 11: Sm, Eu, Gd, Tb, Dy, Bk, Cf, 12: La, Pr, Nd, Pm, U, Np, Pu, Am, Cm, Bi, 13: Ce, Pa, 14: Ac	13–58 (54)
3–	9: N	1–1
4+	1: C, 2: N, 4: Si, S, 5: Ni *ls*, Se, 6: V, Cr, Mn, Co *hs*, Ge, 7: Ti, Re, Fe, Ru, Rh, Pd, Os, Ir, Pt, 8: Zr, Nb, Ta, Mo, W, Tc, Sn, 9: Tb, Hf, Pb, 10: Bk, Cf, 11: Ce, Pr, U, Np, Pu, Am, Cm, 12: Th, Pa, Te, 13: Po	12–43
5+	1: N, 3: P, 4: Cl, 6: V, Cr, Mn, As, Br, 7: Mo, Re, Ru, Rh, Os, Ir, Pt, Au, 8: Nb, Ta, W, Tc, Sb, 10: Pa, Np, Pu, Bi, 11: U, 13: I	9–27
6+	3: S, 5: Cr, Mn, Fe, Se, 7: Mo, W, Re, 8: Os, Te, 10: Np, Pu, Po, 11: U	6–14
7+	0: F, 3: Cl, 5: Mn, Br, 7: Tc, Re, Ru, 8: Os, I, 10: At, 11: Np	7–11
8+	7: Ru, Os, 8: Xe	2–3
Σ		82–226 (218)

Note: The numbers ahead of the ion symbols correspond to the ionic radii. In the last column, the total numbers of different radii and different ions (for example, 2–3) are presented for each charge. The total number of different ions without regard for spin states is given in parentheses. Zero denotes that the ionic radius is less than 0.05 Å.

Table 2. Dependence of the effective ionic radius on the ion charge

Charge	Effective ionic radius	Σ
1+	1: D2, 4: H1, 6: **Li**4, Pd2, 8: **Cu**, 10: Na, (Pb), 11: *Cd, ***Ga**, 12: **Ag**, Hg, 13: ***In**, 14: Au, **K**, 15: !**NH**$_4$, 16: **Tl**8, **Rb**8, 17: **Cs**, *Kr, 18: Er, 19: *Xe	14–20 (1)
1–	13: **F**, 14: *H, *D, **OH**, 18: **Cl**, !HS, !**CN**, 19: !HSe, 20: **Br**, 21: !BF_4, 22: **I**, NO_3, !ClO_4, 23: *At, 24: !PF_6	9–15 (8)
2+	(C), 3: **Be**4, 6: **Fe** *ls*, 7: **Mg**, *Nb, Cr *ls*, **Mn** ls, **Co** *hs*, **Co** *ls*, **Ni**, **Cu**, **Zn**, Ge, 8: V, Cr *hs*, **Mn** *hs*, **Fe** *hs*, Pt, 9: Ti, (Ta), *Mo, **Pd**, *Rh, *Os, *Ir, Ag, 10: Tm, *Tc, **Cd**, 11: **Ca**8, Yb8, Np, *Md, No, *Lr, *Zr, **Hg**8, 12: **Eu**, Dy8, (Pa, U, Pu), *Cm, *Bk, *Es, *Fm, (Y), **Pb**, **Sn**8, 13: **Sr**8, Nd8, Sm8, Am8, 14: **Ba**, 15: Ra8	11–49
2–	14: **O**, 18: **S**, 20: Se, 22: Te, 23: *Po, 25: *Sb, 26: CO_3, 30: SO_4	8–8 (2)
3+	1: **B**4, 2: **N**, 4: P, 5: **Co** *ls*, Cu, **Al**, 6: **V**, **Cr**, **Mn** *hs*, **Mn** *ls*, **Fe** *ls*, **Fe** *hs*, **Co** *hs*, **Ni** *ls*, **Ni** *hs*, **Ga**, **As**, Br4, 7: **Sc**, **Ti**, Nb, Ta, Mo, Ru, **Rh**, Ir, 8: Ag, Pd, *Os, **In**, Tl4, **Sb**, 9: Dy, **Er**, **Tm**, **Yb**, **Y**, *Lr, Au, 10: **Ce**, **Nd**, Pm, **Tb**8, Ho8, **Lu**8, *Th, Pa, **U**, Np, **Pu**, Am, Cm, Bk, Cf, *Es, *Fm, *Md, *No, 11: **Sm**8, **Eu**8, **Gd**8, **Pr**8, Ac, 12: **La**8, **Bi**8	11–65
3–	15: N4, 19: P, As, *21*: Sb, Bi, 27: BO_3, 29: VO_4, 30: PO_4, AsO_4	6–9 (4)
4+	1: **C**, (N), 3: **Si**, 4: S, 5: Ni *ls*, **Se**, **Mn**, Co *hs*, **Ge**, 6: **V**, Cr, **Ti**, **Re**, Fe, **Ru**, Rh, Pd, Os, **Ir**, Pt, 7: **Zr**, Hf, **Nb**, Ta, Mo, W, **Tc**, **Sn**, 8: Tb, Bk, *Fm, *Md, *No, *Lr, **Pb**, 9: Ce, *Tm, Pa, Np, Pu, Am, Cm, Cf8, *Es, 10: Pr8, **U**8, **Te**, 11: **Th**9, Po8	10–48
4–	26: C3, 27: *Ge, *Si4, 29: SiO_4	3–4 (1)
5+	1: **N**3, **Cl**3, 2: **P**4, 3: Mn4, Br3, 4: **V**4, 5: Cr, **As**, 6: **Nb**, **Ta**, Mo, W, Tc, Re, Ru, Rh, Os, Ir, Pt, Au, Sb, *At, 7: Pu, 8: Np, Bi, U, 9: Pa8, *Am, 10: I	10–29
6+	1: **S**4, 3: **Cr**4, **Mn**4, Fe4, Se4, 4: **W**4, 5: Os, 6: **Mo**, Re, Te, 7: **U**, Np, **Pu**, Po, 8: *Am	6–15
7+	1: F, 3: Mn4, **Cl**4: Tc4, Re4, Ru4, Br, I4, 5: Os, 6: At, 7 : Np	6–11
8+	4: **Ru**4, Os4, Xe4	2–3
Σ	36 anions, 240 cations, 232 cations without regard for spin states, 16 polyatomic ions	96–276

Note: The numbers ahead of the ion symbols correspond to the ionic radii. Numerals to the right of the symbols of monoatomic ions indicate the coordination number (unless this number is equal to six). The symbols of cations for which the absolute radii without effective radii are presented in [14] are given in parentheses. The Goldschmidt anionic radii are italicized. The ions whose radii are taken from [15, 16] are indicated by exclamation points. Asterisks signify ions with radii taken from [7] for which data on the coordination numbers are not available. Coordination numbers of complex ions are not given. Ions of completely (continuously) isomorphic pairs are marked with bold type. The total numbers of different radii and different ions are presented in the last column. The total number of different polyatomic ions is given in parentheses.

The purposes of the present work were as follows: (i) to analyze the frequency of occurrence of different ions on the basis of the theoretical data taken from [4, 8, 14], namely, the data on the absolute radii of ions with a noble-gas shell and the Shannon–Prewitt effective radii; (ii) to determine the frequency of their occurrence as a function of the charge, the radius, and the type (*s*, *f*, *d*, *p*); and (iii) to construct a scheme of continuously isomorphic pairs of cations and anions. The continuously isomorphic pairs of cations and anions involve ions that can substitute for each other upon the formation of a continuous solid solution. The ionic radii taken from [2, 4, 6–8, 14] were compared. Most of these data are based on the set of Shannon–Prewitt effective radii. However, different authors present sets of radii with omissions. For this reason, the set of effective ionic radii was complemented. Within the model of hard spheres, polyatomic ions are represented as spheres (see, for example, [2]). The radii of these spherical ions were also included in the analysis, especially as there exists a specific type of polymorphism associated with the rotation of molecules. In nature, isomorphism of monoatomic and polyatomic ions is well known. The radii are given accurate to within 0.01 nm (0.1 Å) and are designated by integral numbers. For example, 1 corresponds to 0.01 nm. This approach makes it possible, at a first approximation, to analyze more conveniently the possibility of interchanging ions and different dependences.

The valences (charges) and the absolute radii of ions are presented in Table 1. Four cations with a valence of +2 (Cr, Mn, Fe, Co) and four cations with a valence of +3 (Mn, Fe, Co, Ni) can exist in low-spin (*ls*) and high-spin (*hs*) states. A total of 226 ions are included. A total of 218 ions are included without regard for the spin states, of which 11 are anions and 207 are cations.

The effective radii and valences of ions are listed in Table 2. For a number of cations, the absolute radii are given in [14]; however, their effective radii are not determined. In this case, the symbols of cations are

Table 3. Frequency of occurrence of charges with the absolute and effective radii of cations and anions

Charge	1 +	1 –	1 +	1 –	2 +	2 –	2 +	2 –	3 +	3 –	3 +	3 –	4 +	4 +	4 –	5 +	5 +	6 +	6 +	7 +	7 +	8 +	8 +	Σ +	Σ –	Σ +	Σ –
r	a	a	e	e	a	a	e	e	a	a	e	e	a	a	e	a	e	a	e	a	e	a	e	a	a	e	e
0	2								1															3			
1			1								1		1	1		1	2		1	1	1			3		7	
2					1						1		1				1							2		2	
3							1		1					1		1	2	1	4	1	2			4		10	
4			1		1				1		1		2	1		1	1		1		5		3	5		13	
5									3		3		2	5			2		1	2	1			7		12	
6			2		1		1		7		12		5	11		5	14	4	3		1	2		24		44	
7					6		10		7		8		9	8		8	1	3	4	3	1	1		37		32	
8	2	1	1		6	1	5		7		6		7	7		5	3	2	1	1				30	2	23	
9	1				6		7		3	1	7		3	9			2	3		2				18	1	25	
10	1		1		2		3		8		19		2	3		4	1			1				18		27	
11			2		2		8		7		5		7	2		1		1						18		17	
12	1	1	2		9	1	8		10		2		3											23	2	12	
13			1	1	5		4		2				1			1								9		5	1
14	2	1	2	3	3	1	1	1	1															6	2	3	4
15	1	1	1		1	1	1					1												2	2	2	1
16	1		2		1																			2		2	
17	1		2																					1		2	
18	2		1	3				1																2		1	4
19			1	1								2														1	3
20				1				1																			2
21				1								2															3
22	1			3				1																1			4
23				1				1																			2
24				1																							1
25								1																			1
26								1							1												2
27												1			2												3
28																											
29												1			1												2
30								1				2															3
31																											
Σ	15	4	20	15	44	4	49	8	58	1	65	9	43	48	4	27	9	14	15	11	11	3	3	215	9	240	36

Note: a—absolute radius, e—effective radius, and *r*—radius.

Table 4. Valences of ions

Ion (i)/charge (c)	1	2	3	4	5	6	7	8	Σa^0	Σi	$\Sigma c+$	$\Sigma c-$	$\Sigma i \times c$	$\Sigma a^0 + i \times c$
He, Ne, Ar, Rn									4					4
Li, Na, K, Rb, Cs, Fr, Kr, NH_4	+								7	8	1		8	15
OH, CN, HS, HSe, BF_4, NO_3, ClO_4, PF_6	–									8		1	8	8
H, D	±								2	2	1	1	4	6
Be, Mg, Ca, Sr, Ba, Ra, Zn		+							7	7	1		7	14
O, CO_3, SO_4		–							1	3		1	3	4
Cd, Hg	+	+							2	2	2		4	6
La, Pm, Gd, Ho, Er, Ac, Sc, Y, Lu, B, Al			+						11	11	1		11	22
VO_4, BO_3, PO_4, AsO_4			–							4		1	4	4
Ga, In, Tl	+		+						3	3	2		6	9
Nd, Sm, Eu, Dy, Yb		+	+						5	5	2		10	15
Cu, Ag	+	+	+						2	2	3		6	8
Hf				+					1	1	1		1	2
SiO_4				–						1		1	1	1
C, Si				±					2	2	1	1	4	6
Ge		+		±					1	1	2	1	3	4
Zr, Sn, Pb		+		+					3	3	2		6	9
Ce, Pr, Tb, Th, Cf			+	+					5	5	2		10	15
Ti, Co, Ni, Tm, Cm, Bk, Es, Fm, Md, No, Lr		+	+	+					11	11	3		33	44
Pd	+	+	+	+					1	1	4		4	5
N, P, As, Bi			±		+				4	4	2	1	12	16
Sb		–	±		+				1	1	2	2	4	5
Au	+		+		+				1	1	3		3	4
Pt		+		+	+				1	1	3		3	4
Pa, Ta			+	+	+				2	2	3		6	8
V, Nb, Ir, Rh		+	+	+	+				4	4	4		16	20
S, Se, Te, Po		–		+		+			4	4	2	1	12	16
Fe		+	+	+		+			1	1	4		4	5
W				+	+	+			1	1	3		3	4
U, Pu			+	+	+	+			2	2	4		8	10
Cr, Mo, Am		+	+	+	+	+			3	3	5		15	18
F	–						+		1	1	1	1	2	3
Cl, I, At	–				+		+		3	3	2	1	9	12
Br	–		+		+		+		1	1	3	1	4	5
Tc		+		+	+		+		1	1	4		4	5
Re				+	+	+	+		1	1	4		4	5
Mn, Np		+	+	+	+	+	+		2	2	6		12	14
Xe	+							+	1	1	2		2	3
Ru			+	+	+		+	+	1	1	5		5	6
Os		+	+	+	+	+	+	+	1	1	7		7	8
Σ 40 combinations; 120 atoms + ions, 16 polyatomic ions	13	18	22	23	16	8	8	3	104	116	97	14	268	372

Note: The valences are given for the atoms and ions whose effective radii are available in the data array under consideration. Designations: a^0—atoms, + —cations; – —anions; and Σ—sum. The total number of charges is 111 (97 + 14). The total number of different ions is equal to 268 (232 cations, 36 anions).

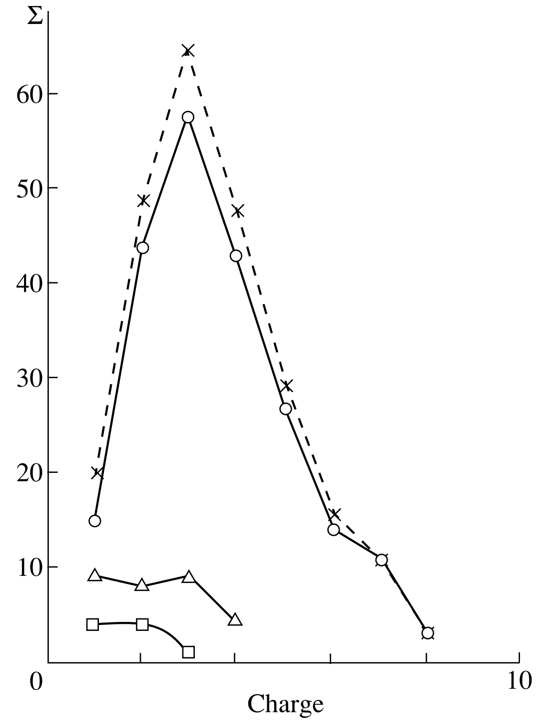

Fig. 1. Dependences of the frequency of occurrence Σ of cations with absolute (circles) and effective (crosses) radii and anions (squares, triangles) on the charge.

given in parentheses. The number of these ions is equal to eight. Table 2 also presents the Goldschmidt anionic radii, which are italicized. Moreover, the effective radii of polyatomic anions and one complex cation [15, 16] indicated by exclamation points are included in the table. The effective radii of cations marked by asterisks are taken from [7]. The total number of different ions is 276, including 16 polyatomic ions, 36 anions, and 240 cations. Four cations with a valence of +2 (Cr, Mn, Fe, Co) and four cations with a valence of +3 (Mn, Fe, Co, Ni) can be in low-spin and high-spin states. Therefore, the total number of different ions without regard for the spin states is 268, including 232 cations.

The radii of ions as a function of the ion charge (valence) and the frequency of occurrence of ions with a particular charge and a particular radius are given in Table 3. The data presented in this table enable us to compare the absolute and effective radii of cations and anions and also the frequency of their occurrence.

An ion can have one or several valence states. The combinations of ion valences are presented in Table 4. The total number of different atoms and ions is 372, of which the number of different atoms (with zero charge) is 104 and the total number of different cations and anions is 268. There are 40 different combinations of valences, even though more than one hundred combinations can be obtained from eight different charges. Four elements have only a zero charge. Elements with valences of 1, 2, 3, and 4 can have a solo nonzero charge. For example, hafnium ions can be only tetravalent. If the valence of ions lies in the range from 5 to 8, the corresponding elements should have at least one more valence. In particular, the valence of xenon can be equal to +1 or +8. For ions with a sole charge, there exist nine combinations of charges: 0, +1, +2, +3, +4, –1, –2, –3, and –4. For ions with two possible charges, there exist the following nine combinations of charges: +1 and +2, +1 and +3, +2 and +3, +2 and +4, +3 and +4, +1 and +8, +1 and –1, +4 and –4, and –1 and +7. For ions that can have three different charges, there are ten combinations of charges: +1, +2, and +3; +2, +3, and +3; +2, +3, and +4; +2, +4, and +4; +3, +3, and +5; +1, +3, and +5; +3, +4, and +5; +4, +5, and +6; –2, +4, and +6; and –1, +5, and +7. Eight combinations of charges are found for ions with four possible charges: +1, +2, +3, and +4; +2, +3, +4, and +5; +2, +3, +4, and +6; +3, +4, +5, and +6; +2, +4, +5, and +7; +4, +5, +6, and +7; –1, +3, +5, and +7; and –2, –3, +3, and +5. For ions with five possible charges, there are two combinations of charges: +2, +3, +4, +5, and +6; and +3, +4, +5, +7, and +8. There exists only one combination of charges (from +2 to +7) for ions that can have six different charges. For ions with seven different charges (osmium), there exists also only one combination (from +2 to +8). All the possible combinations are realized for positive charges of 1–3. Among the possible combinations with a charge of +4, many combinations are not realized. The sets 1234 and 2 345 678 involve virtually all possible combinations of cations. Among the 40 different combinations of valences, only four combinations include five or six different valences. Therefore, the number of like or unlike cations with different charges in the chemical compound obeys the law of small numbers; i.e., it can rarely be larger than four.

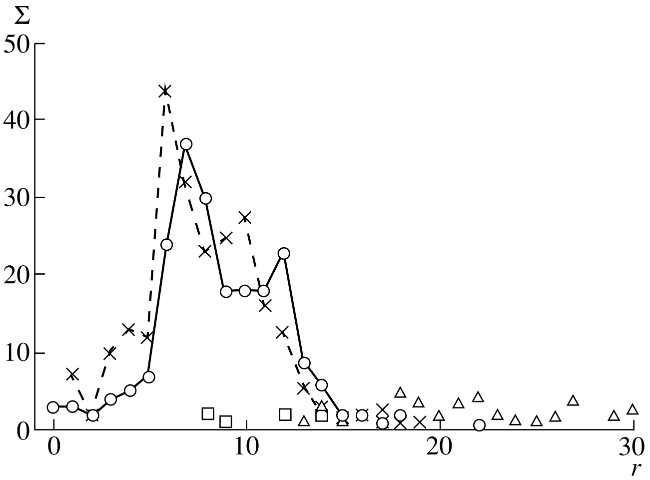

Fig. 2. Dependences of the frequency of occurrence of cations with absolute (circles) and effective (crosses) radii and anions (squares, triangles) on the radius.

The system of combinations is prognostic (because it is based on the periodic table of elements) and pre-

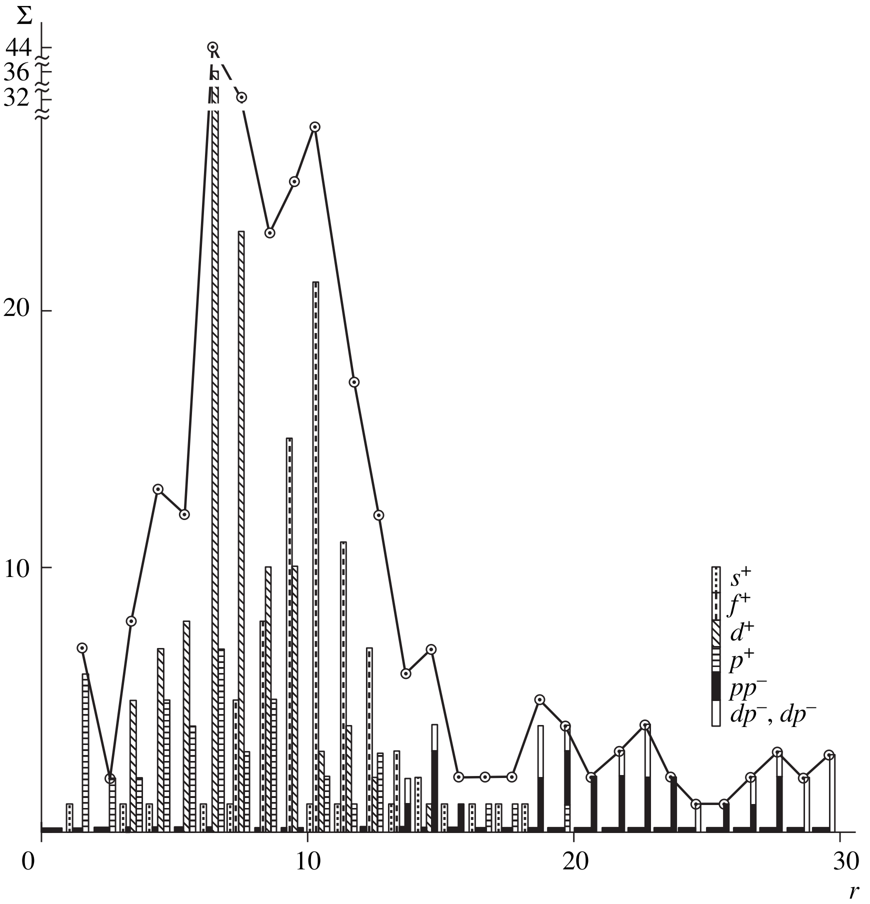

Fig. 3. Dependences of the frequency of occurrence of *s*, *f*, *d*, and *p* cations and *p* anions on the effective radius. Circles indicate the total dependence for ions of all types.

dicts all the possible sets of valences. However, not only copper from the first subgroup but also elements of other subgroups (for example, Ce^{4+}) can have valences of 2 and 3. Furthermore, the question as to the realization of particular sets and their constituent elements remains open. The systems of valences can be complemented by elements with new valences. Therefore, elements can be transferred from one row to another row.

The dependences of the frequency of occurrence of ions on their charge are depicted in Fig. 1. The difference between the dependences obtained for ions with absolute and effective radii is insignificant and can be associated with a small amount of data. The dependence exhibits a maximum at a valence of +3 in the range from +2 to +5. The total dependence of the frequency of occurrence of ions on their radius is plotted in Fig. 2. In this case, the difference between the dependences for the absolute and effective radii is substantially larger. The maximum of the dependence is observed at radii of 6–7 in the range 5–13. For comparison, the dependences of the frequency of occurrence of *s*, *f*, *d*, and *p* ions on the effective radius are shown in Fig. 3. Note that ionic radii in the range 5–13 occur most frequently. At the same time, the dependence exhibits two maxima at 5–6 and 10. This means that we obtain a bimodal distribution of ionic radii.

In our earlier works [17–19], we established the tolerance space for perfect isomorphs of cations and anions. The perfect isomorphs are considered to be a pair of atoms or ions that continuously substitute for each other and enter into the composition of at least one pair of compounds forming a continuous solid solution. In the scheme of the tolerance space, ions of such a pair are connected by a line (Fig. 4). The tolerance space is divided into two sets: anions and cations. The set of anions is separated into two subsets containing anions with charges of –1 and –2. The set of cations has five subsets that involve cations with charges of +1, +2, +3, +4, and (+5, +6, +7, +8). The differently charged cations and anions with the above properties are also joined by the lines. The effective radius is written ahead of each ion. These ions in the table of the effective radii are marked with bold type. In the scheme, each ion has first and second surroundings that consist of the nearest ions connected to it. If the ion under consideration is a species-forming ion in a mineral (i.e., it has the highest content at the position among the isomorphic ions), the

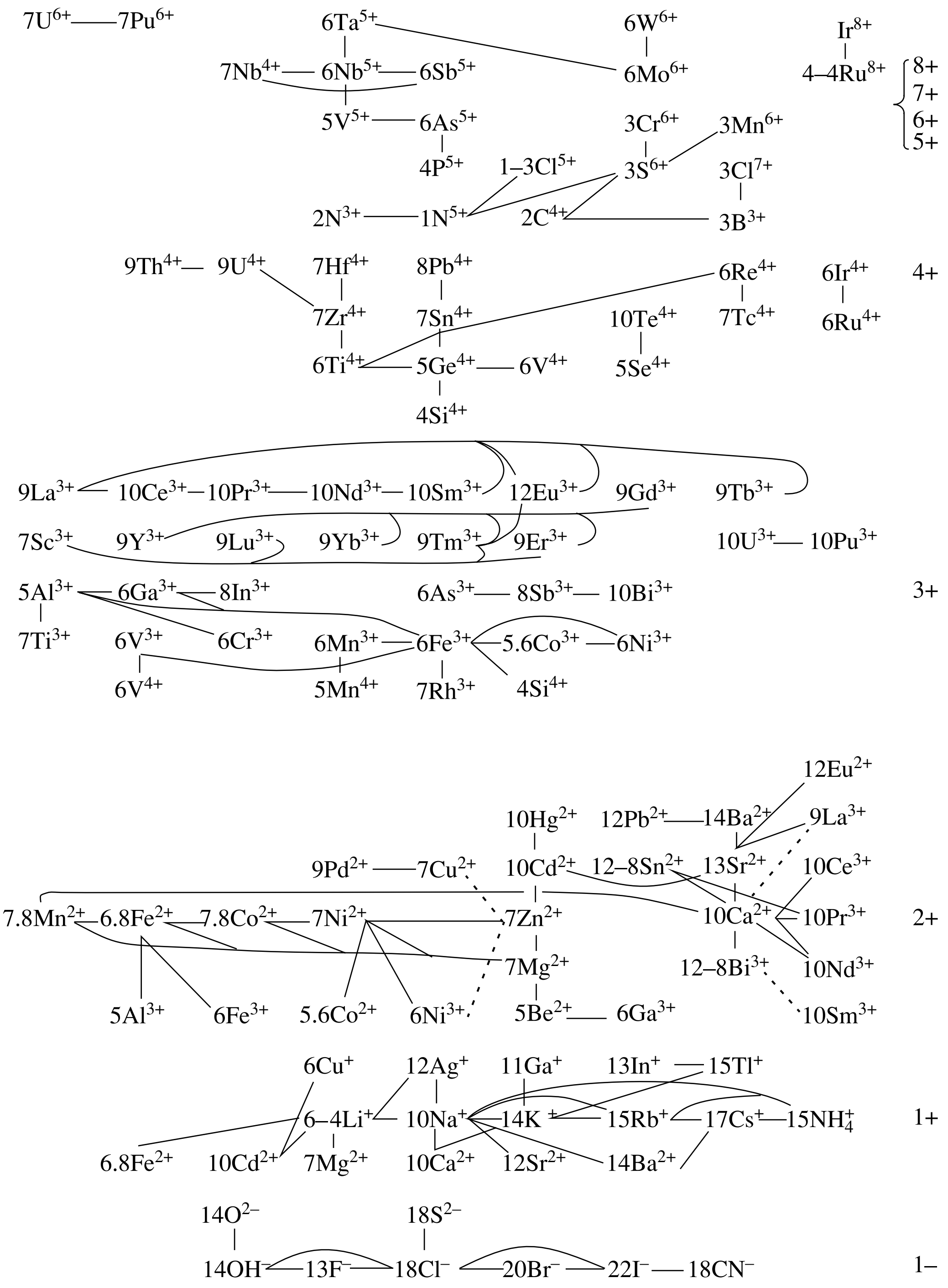

Fig. 4. Tolerance space for pairs of completely isomorphic cations and anions. The valences and effective radii are given for each ion. Two different radii are separated by a point. Values of a radius and a coordination number are separated by a dash.

ions from its surroundings in the scheme most likely will be next in content at the position. The system of perfect isomorphs is open and can be complemented. This system is useful for experimental and theoretical investigations.

A similar analysis can be performed for other systems of ionic radii. It can be expected that the results of this analysis will be somewhat different. However, this should not substantially affect the inferences made in the present work.

REFERENCES

1. V. F. Barabanov, *Geochemistry* (Nedra, Leningrad, 1985) [in Russian].
2. G. B. Bokiĭ, *Crystal Chemistry* (Nauka, Moscow, 1971) [in Russian].
3. A. G. Bulakh, *General Mineralogy* (S.-Peterb. Gos. Univ., St. Petersburg, 1999) [in Russian].
4. V. S. Urusov, *Theoretical Crystal Chemistry* (Mosk. Gos. Univ., Moscow, 1987) [in Russian].
5. A. Wells, *Structural Inorganic Chemistry* (Clarendon, Oxford, 1984; Mir, Moscow, 1987), Vols. 1–3.
6. S. S. Batsanov, *Structural Chemistry: Facts and Dependences* (Dialog MGU, Moscow, 2000) [in Russian].
7. J. Emsley, *The Elements* (Clarendon, Oxford, 1989; Mir, Moscow, 1993).
8. *Modern Crystallography*, Ed. by B. K. Vaĭnshteĭn *et al.* (Nauka, Moscow, 1978–1981; Springer, Berlin, 1981–1988), Vols. 1–4.
9. A. V. Shubnikov, Izv. Akad. Nauk SSSR, Ser. 6 **16**, 515 (1922).
10. N. L. Smirnova and L. S. Mezhueva, Zh. Strukt. Khim. **7** (4), 566 (1966).
11. N. L. Smirnova and R. E. Chigar'kova, Zh. Strukt. Khim. **10** (6), 1076 (1969).
12. N. L. Smirnova and N. S. Utochkina, Kristallografiya **22** (4), 759 (1977) [Sov. Phys. Crystallogr. **22**, 436 (1977)].
13. N. L. Smirnova and V. S. Urusov, *Crystal Chemical Classification of Minerals*, Ed. by V. S. Urusov (Mosk. Gos. Univ., Moscow, 1985), p. 5.
14. J. Ziolkowski, New J. Solid State Chem. **57**, 269 (1985).
15. A. G. Ryabukhin, Izv. Chelyab. Nauchn. Tsentra, No. 1, 24 (1998).
16. A. G. Ryabukhin and A. V. Sterligova, Izv. Chelyab. Nauchn. Tsentra, No. 1, 27 (1998).
17. N. L. Smirnova, *System Approach in Geology* (MING, Moscow, 1986), p. 78.
18. N. L. Smirnova and Yu. K. Egorov-Tismenko, *Crystal Chemistry and X-ray Diffraction of Minerals* (Nauka, Leningrad, 1987), p. 75 [in Russian].
19. N. L. Smirnova and N. V. Belov, Kristallografiya **26** (6), 1240 (1981) [Sov. Phys. Crystallogr. **26**, 705 (1981)].

Translated by O. Borovik-Romanova

Crystallography Reports, Vol. 49, No. 5, 2004, pp. 713–718. Translated from Kristallografiya, Vol. 49, No. 5, 2004, pp. 799–805.
Original Russian Text Copyright © 2004 by Nikitina, Prokhorskiĭ, Tunichenko, Fofanov.

Computer Simulation of the Structure of Small Tungsten Oxide Clusters

E. A. Nikitina, M. E. Prokhorskiĭ, L. V. Tunichenko, and A. D. Fofanov

Petrozavodsk State University, Petrozavodsk, Russia
e-mail: Nikitina@mainpgu.karelia.ru

Received April 3, 2002

Abstract—The structure of tungsten oxide clusters was simulated by constructing a random 3D grid either disregarding or taking into account the energy of Coulomb interaction between cluster particles and an attached ion. The obtained clusters are subjected to relaxation by the molecular dynamics method. It is shown that the relaxation of clusters modeled with or without using periodic boundary conditions leads to the formation of different atomic structures. *© 2004 MAIK "Nauka/Interperiodica".*

INTRODUCTION

At present, small clusters of atoms are attracting increasing interest in view of various problems in obtaining new materials for nanoelectronics. It is well known that many physical properties of microscopic (a few nanometers in size) volumes of materials significantly differ from the corresponding characteristics of bulk materials. At the same time, many properties of materials substantially depend on their atomic structure. In this study, we performed simulation of microvolumes of tungsten oxide WO_3 by constructing a three-dimensional (3D) random grid with the use of two algorithms, one of which disregards and the other of which takes into account the Coulomb interaction between oxide ions. The clusters formed as a result of both computer experiments were brought to equilibrium in the course of a molecular-dynamics experiment. Previously, a similar computer experiment was carried out for amorphous aluminum oxide [1, 2]. However, the Coulomb interaction between atoms was taken into account in constructing 3D random grids for the first time.

AN ALGORITHM FOR FORMING A 3D RANDOM GRID WITH REGARD TO COULOMB INTERACTION BETWEEN IONS

It is well known that experimental diffraction data on non-single-crystal objects yield information only on the one-dimensional correlation in the mutual positions of atoms. The algorithm for constructing a 3D random grid, which has been described in detail in [1], makes it possible to reconstruct 3D positions of atoms only on the basis of experimentally determined structural characteristics (the radii of coordination spheres and their dispersions) without making additional assumptions of the character of interatomic interaction. In particular, for diatomic compounds, the five shortest interatomic distances and their dispersions serve as initial data for constructing a grid [1].

The algorithm for constructing a 3D random grid with regard to the energy of Coulomb interaction between ions is almost the same as the algorithm described in [1]. The modification of this algorithm is as follows: when each subsequent atom is attached to a cluster, an increment in the energy of Coulomb interaction between the attached atom and all the cluster particles is calculated and, of all possible attachment variants, only those are implemented that lead to a decrease in the total cluster energy.

Analysis of the structure of 60-atom clusters formed using two variants of the algorithm for constructing a 3D random grid showed that the chemical composition of clusters depends on the choice of algorithm variant. In the first variant (disregarding Coulomb interaction), the chemical composition of a cluster differs significantly from stoichiometric (WO_3): there are 50 oxygen atoms per 10 tungsten atoms (WO_5). In the second variant (with regard to the Coulomb interaction), the composition is similar to stoichiometric: we have 46 oxygen atoms per 14 tungsten atoms ($WO_{3.3}$). Thus, the account of the Coulomb interaction energy makes it possible to construct a cluster with a chemical composition that is closer to that typical of bulk material.

As can be seen from Fig. 1, when the algorithm for constructing a 3D random grid disregarding the Coulomb interaction between cluster particles is used (curve *1*), the total Coulomb energy changes nonmonotonically with an increase in the number of atoms. Pronounced jumps are observed that are related to significant deviations from stoichiometry and, hence, electroneutrality. When a cluster is constructed with regard to the energy of Coulomb interaction between its particles and an attached ion, no such jumps are observed (curve *2*). Therefore, a more favorable energetic configuration is constructed in the latter case, because the

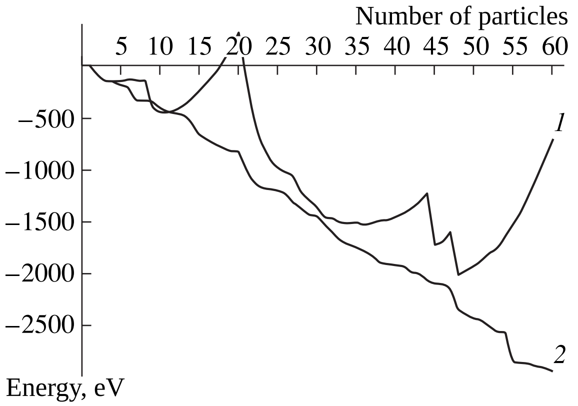

Fig. 1. Dependence of the Coulomb energy of a cluster on the number of particles, calculated for clusters constructed (*1*) disregarding the energy of interaction between ions and (*2*) taking into account the interaction energy.

attachment of atoms is accompanied by a monotonic decrease in the cluster energy.

CLUSTER-RELAXATION TECHNIQUE

The clusters formed using the aforementioned algorithms are loose nonequilibrium fractal-like systems with a large number of incomplete oxygen octahedra around tungsten atoms. In order to obtain equilibrium atomic configurations, the clusters were made to relax to a minimum-energy state by the molecular-dynamics method. Here, relaxation means maintaining a model system of atoms under constant conditions (specified temperature, fixed interatomic-interaction potentials, and so on) for a sufficiently long time. In this case, the potential energy of a system should decrease to the equilibrium value and remain, on average, constant for a long time.

In order to describe interatomic interactions in the molecular-dynamics experiment, we used the Born–Mayer–Higgins potential:

$$V_{ij}(r) = -\frac{e^2 q_i q_j}{4\pi\varepsilon_0 r_{ij}} - A\exp(-r_{ij}/R_{0ij}) + \frac{C}{r_{ij}^6}, \qquad (1)$$

where the coefficients for W–O and O–O pairs were taken from [3]. The interaction of W^{6+} ions with each other was assumed to be Coulomb-like.

The clusters to be relaxed were placed at the center of a model volume in the form of a cube with side L = 50 Å. Since the clusters under consideration were composed of a small number of particles and, thus, were fairly small, the periodic boundary conditions were invalid and the cluster surface was assumed to be free, i.e., it could take an energetically more favorable form. In all the model experiments, the potential cutoff radius was assumed to be 16 Å, which, in fact, made it possible to take into account the Coulomb interaction of each ion with all other ions in calculating the interaction forces. The temperature of the system was 300 K. The time step in the molecular-dynamics experiment was 10^{-15} s. During the experiment, we fixed the potential and kinetic energies of a cluster, as well as its state (the atom coordinates and velocities), for subsequent analysis of the structural state of the model cluster.

METHOD OF ANALYSIS OF CLUSTERS AND COMPARISON WITH EXPERIMENTAL DATA

In the final stage of the computer simulation, the scattering intensity of a cluster was calculated and the result compared with the experimental X-ray diffraction data for amorphous tungsten oxide formed by deposition [4].

The intensity distribution of the X-rays scattered from a cluster was calculated by the Debye formula [5]. The scattering intensities were transformed into the pair correlation function $D(r)$ [5]. The one-dimensional pair correlation function $D(r)$, which was calculated along the entire curve of scattering intensity distribution, including the small-angle peak, contains information on the configuration, size, and form of a cluster, especially when the latter is small and the fraction of surface atoms is significant [6]. The function $D(r)$ was used to calculate the curves of radial distribution of the probability density $W(r) = D(r)/D_0(r)$, where $D_0(r)$ is a pair function for a cluster, calculated from the small-angle scattering intensity peak alone.

EXPERIMENTAL RESULTS. ANALYSIS OF CLUSTERS FORMED DISREGARDING AND WITH REGARD TO THE COULOMB INTERACTION ENERGY

When constructing clusters of amorphous oxide WO_3 from 64, 128, and 256 atoms within the model of a 3D random grid, disregarding the Coulomb interaction energy, we used the interatomic distances R_{ij} and their dispersions σ_{ij} from [4], which were obtained for deposited tungsten trioxide (see table). A model was proposed in [4] to describe the structure of deposited tungsten oxide. According to this model, oxygen octahedra with W atoms inside share vertices and form W–O–W bonds with an angle close to 180° (Fig. 2). Then, using the value of the shortest W–O distance, one can calculate other interatomic distances (see table). It can be seen that, in terms of the proposed model, the W–W distance should be 0.04 Å larger and the W–O(2) distance should be much larger (by 0.24 Å). Since the W–W distance is determined quite reliably from the distribution curve for pair functions, we can suggest that the W–O–W-bond angle is smaller than 180°.

Analysis of the obtained clusters showed that, in all cases, their chemical composition differs from that of an infinite medium and ranges from $WO_{2.6}$ to $WO_{3.6}$. With an increase in the number of atoms in clusters, the average coordination number for the first coordination sphere of tungsten atoms increases from 2.78 (64-atom cluster) to 5.26 (256-atom cluster).

However, even the structure of a fairly large 256-atom cluster is loose and fractal-like. In its structure, there are only three complete oxygen octahedra around a tungsten atom. Complete and incomplete oxygen octahedra share vertices; in this case, the W–O–W-bond angle ranges widely. Fragments of oxygen octahedra with shared edges are observed in clusters, which is inconsistent with the tungsten oxide structure of the ReO_3 type.

Similar 64-, 128-, and 256-atom clusters were constructed using the algorithm for forming a 3D random grid with regard to the minimization of the Coulomb interaction energy as a result of the attachment of an ion. In order to construct an amorphous oxide WO_3 cluster within this model, we used the same interatomic distances R_{ij} and their dispersions σ_{ij} (see table).

Comparison of the microstructure of clusters of different sizes, which were formed using the two noted variants of the algorithm for constructing a 3D random grid, showed that the modified variant, which takes into account the minimization of Coulomb interaction energy when an ion is attached, is to be preferred over the unmodified variant. First, the variant with the energy minimization makes it possible to obtain clusters of different sizes with almost stoichiometric composition, although, even in this case, we obtain a fairly loose structure, in which incomplete and complete octahedra are linked in the same way as in clusters that were constructed disregarding the interaction energy. Second, the analysis of the sequence of the cluster growth under the condition of Coulomb interaction energy minimization shows that, specifically due to the requirement that the cluster energy be decreased, the octahedral environment of oxygen atoms around a tungsten atom is not formed immediately in the early stage: only fragments of three to five oxygen atoms are formed in the first coordination sphere. At large interatomic-distance dispersion values, which were used in the computer experiments, the constructed atomic configuration is strongly distorted; i.e., the octahedral fragments are randomly shifted and rotated with respect to each other. The vertices of octahedra unoccupied by oxygen atoms are screened by other fragments and become inaccessible for occupation by oxygen atoms during the model cluster growth. It is noteworthy that these shifts of octahedral fragments increase with an increase in the distance from the center of a cluster to its periphery and with increasing the interatomic-distance dispersion used in the algorithm.

Initial data for constructing a tungsten oxide cluster within the model of a 3D random grid

Type of sphere	R_{ij}, Å	R_{ij}, Å (Calculation)	σ_{ij}, Å
W–O(1)	1.88	1.88	0.12
O–O(1)	2.65	2.65	0.1
W–W(1)	3.72	3.76	0.28
W–O(2)	3.94	4.20	0.35
O–O(2)	3.72	3.75	0.28

RELAXATION OF CLUSTERS BY THE MOLECULAR-DYNAMICS METHOD

The clusters constructed by formation of a 3D random grid were subjected to relaxation using the molecular-dynamics method.

Analysis of the clusters obtained both disregarding and taking into account the Coulomb interaction between ions, which was carried out after the molecular-dynamics experiment, showed that the structure of such clusters becomes denser and the number of complete oxygen octahedra increases, due to which the first coordination number of a tungsten atom becomes greater as well. For example, after the molecular-dynamics experiment, a full 17 complete oxygen octahedra with a tungsten atom at the center were observed in a 256-atom cluster. However, tungsten atoms arose that had seven or even eight oxygen atoms around them in a spherical layer with a radius from 1.4 to 2.0 Å. It was also found that, after carrying out the molecular-dynamics experiment, the microstructure of clusters, the initial state of which was formed with regard to the

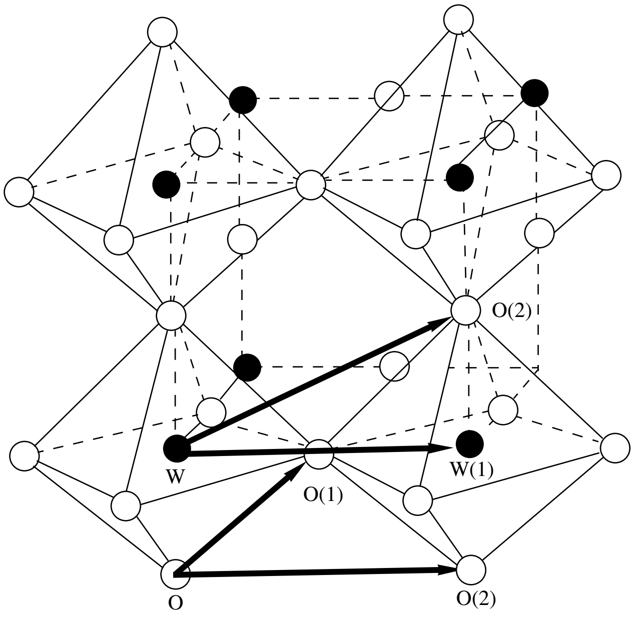

Fig. 2. Tungsten–oxygen octahedra sharing vertices.

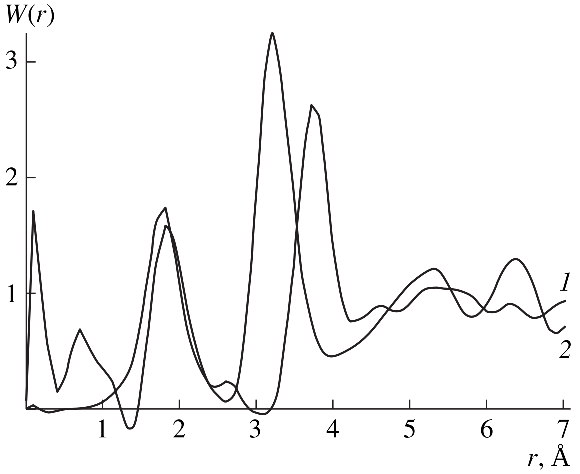

Fig. 3. Radial distribution curves $W(r)$: (*1*) X-ray radiography experiment and (*2*) calculation for a 128-atom cluster constructed with regard to the interaction energy after 10 000 steps of the molecular-dynamics experiment.

minimization of Coulomb interaction energy upon the attachment of an ion, differs from the structural state of clusters constructed when energy minimization is disregarded. The reason for this is the difference in the stoichiometry of clusters constructed within different algorithmic variants.

Much more unexpected was a significant change in the structural state of a stoichiometric cluster due to the molecular-dynamics experiment in comparison with the initial state. Indeed, the radial distribution of the probability density $W(r)$ for a cluster in the initial state is qualitatively (by the positions of peaks) similar to that obtained by X-ray radiography. At the same time, after the molecular-dynamics experiment, the second peak (related mainly to W–W(1) pairs) shifts significantly to smaller distances ($R \sim 3.2$ Å) (Fig. 3). In crystalline modifications of WO_3 with an ReO_3 structure [6], this distance comes to 3.7–3.92 Å. The distance may be equal to 3.2 Å only when oxygen octahedra around tungsten atoms—or their fragments in the case of sharing vertices via a common oxygen atom—are rotated by a large angle with respect to each other and when the W–O–W-bond angle is about 117°.

It appears that the repulsive Coulomb forces acting between the W^{6+} ions and negatively charged oxygen shells surrounding each tungsten ion in the model of pair-interaction potentials are, obviously, insufficient for increasing the distance between tungsten atoms to 3.76 Å and render the W–O–W-bond angle close to 180°.

RELAXATION OF A CUBIC-PHASE WO_3 NANOCRYSTALLITE

Since sharing of both vertices and edges of oxygen octahedra was observed initially in the clusters formed by constructing a 3D random grid, we constructed a cluster in which the octahedra share only vertices. This cluster was subjected to relaxation by the molecular-dynamics method and constructed for cubic tungsten oxide from 256 atoms (64 tungsten and 192 oxygen atoms). The coordinates of the atoms in the unit cell were W(0,0,0), O(1/2,0,0), O(0,1/2,0), and O(0,0,1/2). The lattice period was taken to be 3.755 Å. This cell was translated in all three crystallographic directions to obtain a cluster 4 × 4 × 4 unit cells in size. The cluster under study was placed at the center of a model volume in the form of a cube with an edge of 50 Å. Within this volume, the cluster surface remained free.

It can be seen from Fig. 4 that, during the molecular-dynamics experiment, the curves $W(r)$ vary in the same way as in the case of relaxation of 3D random grids constructed for WO_3 (Fig. 3). The peak corresponding to W–W(1) pairs on model curves *3–5* (Fig. 4) shifts to smaller distances ($R_{W-W(1)} = 3.2$ Å) in comparison with the X-ray radiography data ($R_{W-W(1)} \sim 3.72$ Å). Hence, carrying out the molecular-dynamics experiment with an initially regular structure leads to the same decrease in the W–W(1) distance, as in the case of the formation of a cluster by the algorithm for constructing a 3D random grid. Analysis of the positions of atoms in this cluster has shown that its structure is fairly dense. The cluster is formed of irregular octahedra, many of which are incomplete. The incomplete and complete octahedra share vertices, but they are rotated at an angle smaller than 180°. As well as in the case of clusters of 3D random grids, elements composed of seven or eight oxygen atoms are formed around tungsten atoms.

Such a transformation of the microstructure of clusters in a molecular-dynamics experiment that does not impose periodic boundary conditions is quite reasonable. In an initial cluster formed by 64 unit cells of the cubic phase WO_3, 37 tungsten atoms do not have a complete environment of 6 oxygen atoms (1 atom has 3 neighbors, 9 atoms have 4 neighbors, and 27 atoms have 5 neighbors). Therefore, in the beginning of the molecular-dynamics experiment, these ions are pulled by Coulomb forces into the cluster volume, the real temperature increases to 4000 K, and the whole system becomes substantially disordered. Then, as the temperature of the system is reduced to a specified value (300 K), the atomic configuration passes into a state similar to that observed upon the relaxation of 3D grids.

Relaxation of a similar cluster was performed with imposed periodic boundary conditions that imitated its environment in a crystal medium. The cluster under investigation was placed at the center of the model volume in the form of a cube, the side of which (15.02 Å) corresponded to the cluster size. During the experiment, the potential cutoff radius was 7.5 Å. Under such boundary conditions, an atom located near one of the cube faces will interact with the atoms located near the opposite face.

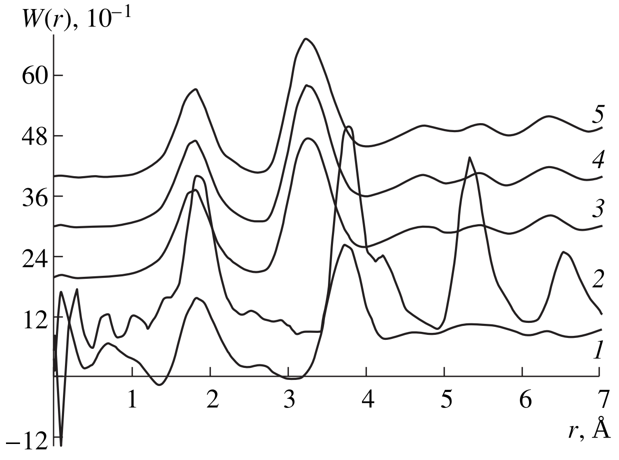

Fig. 4. Molecular-dynamics experiment without periodic boundary conditions. Radial distribution curves of the probability density $W(r)$ for (*1*) X-ray radiography experiment; (*2*) an initial cluster composed of 64 unit cells of cubic WO_3; and the same cluster after (*3*) 10 000, (*4*) 15 000, and (*5*) 20 000 steps of the molecular-dynamics experiment. The curves are shifted along the ordinate axis by (*2*) 1, (*3*) 2, (*4*) 3, and (*5*) 4.

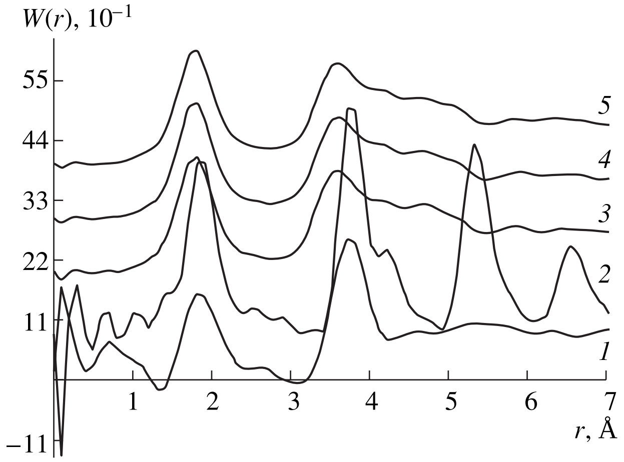

Fig. 5. Molecular-dynamics experiment with periodic boundary conditions. Radial distribution curves of the probability density $W(r)$ for (*1*) X-ray radiography experiment; (*2*) an initial cluster composed of 64 unit cells of cubic WO_3; and the same cluster after (*3*) 10 000, (*4*) 15 000, and (*5*) 20 000 steps of the molecular-dynamics experiment. The curves are shifted along the ordinate axis by (*2*) 1, (*3*) 2, (*4*) 3, and (*5*) 4.

It can be seen from Fig. 5 that the peak corresponding to W–W(1) pairs somewhat shifts to smaller distances ($R \sim 3.6$ Å) in comparison with the X-ray radiography data ($R = 3.72$ Å). At the same time, this shift is significantly smaller than in the experiment performed without periodic boundary conditions (Fig. 4). The general form of the curves $W(r)$ indicates that the degree of distortion of the cluster microstructure is fairly high in the model system and that the spread of coordination spheres exceeds that observed in the X-ray radiography experiment.

Analysis of the atomic positions in the cluster showed that, in the case under consideration, no more than six oxygen atoms are observed in the first coordination sphere of a tungsten atom. Both incomplete and complete octahedra share only vertices.

The reason for the high degree of order violation in the cluster may be the following. Tungsten trioxide belongs to the structural type ReO_3 with the perovskite-like structure ABX_3. A decrease in the size of ion A in perovskite increases the instability of a cubic structure. This instability reaches its maximum in WO_3, where ion A is absent; i.e., the cubic phase WO_3 is unstable in principle. Deformation phase transitions between five different phases, which are stable in certain temperature ranges and can reversibly change into each other, are typical of tungsten oxide. Near 300 K, tungsten oxide WO_3 exists in triclinic (from 230 to 287 K) and monoclinic (from 287 to 315 K) modifications [7]. The cubic modification was found experimentally only in films thinner than 100 Å and deposited on carbon substrates at 670 K [8]. In other words, the cubic phase of tungsten oxide is unstable at the temperatures at which the molecular-dynamics experiment is carried out, which was confirmed by the results of this experiment.

ESTIMATION OF THE INTERATOMIC INTERACTION FORCES IN TUNGSTEN OXIDE CLUSTERS

Thus, the clusters constructed in the model experiments contain incomplete octahedra, even after relaxation by the molecular-dynamics method. In order to find the reasons for this, we calculated the forces acting on an oxygen ion from other particles forming a octahedron (one tungsten atom and five oxygen atoms) (Fig. 6).

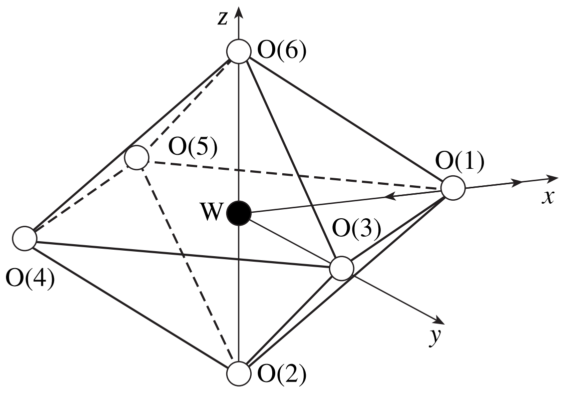

Fig. 6. Schematic illustrating the calculations of the force of interaction of the oxygen ion O(1) with the W^{6+} ion and other oxygen ions, forming an incomplete octahedron.

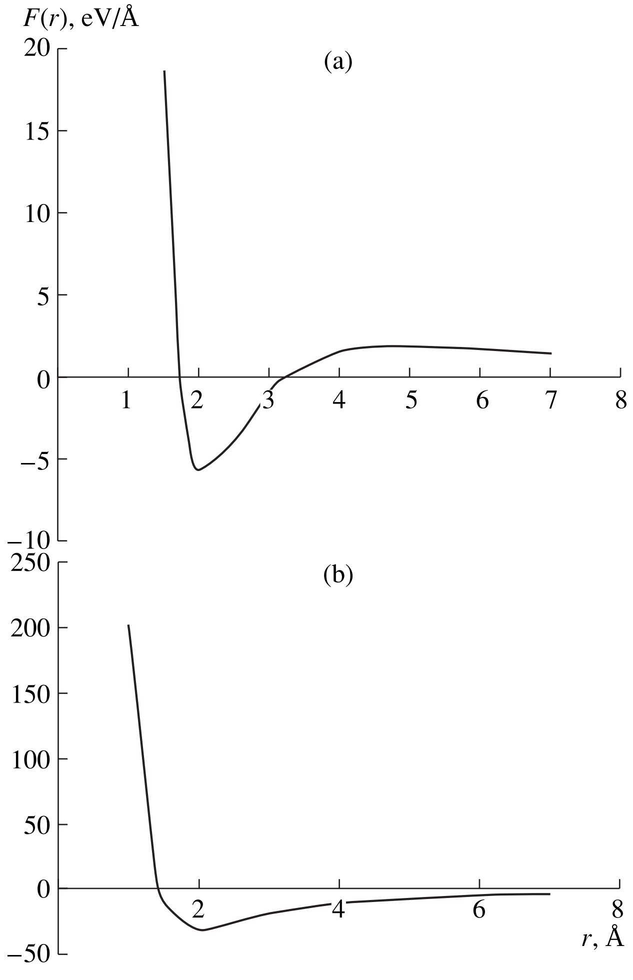

Fig. 7. Dependence of the force $F(r)$ acting on the oxygen ion from (a) the incomplete octahedron WO_5 and (b) the tungsten ion.

Figure 7a shows the x component of the force acting on an atom O(1) as a function of the W–O(1) distance. It can be seen that, at distances shorter than 1.73 Å, a repulsive force (the x component of the force being positive) acts on an oxygen ion from the other particles in this system. In the distance range from 1.73 to 3.3 Å, an attractive force (the x force component being negative) acts on the O(1) ion from the other particles. With a further increase in the interatomic distance ($r > 3.3$ Å), the force acting on the oxygen ion from the other particles again becomes repulsive. Therefore, if the O(1) ion is located at a distance exceeding 3.3 Å, it will be repelled by the system composed of one W^{6+} ion and five O^{2-} ions (incomplete octahedron) and, thus, will not be able to complete the octahedron. The octahedron can be completed only if an attached atom is in the range of action of the attractive forces, i.e., at a distance in the range 1.73–3.3 Å. This result is somewhat unexpected, although the calculation was not precise (just to obtain an estimation), since the oxygen ion was shifted only along the x axis and the incomplete octahedron was assumed to be regular.

For comparison, the force acting on one oxygen ion from a tungsten ion alone was calculated on the basis of pair potential (1). The calculations showed (Fig. 7b) that, for the W^{6+}–O^{2-} pair, the oxygen ion is in equilibrium with the tungsten ion at $r \sim 1.43$ Å. This value significantly differs from the equilibrium interatomic distance $R_{W–O} = 1.88$ Å for tungsten oxide [4]. Since the equilibrium position for the O^{2-} ion interacting with a group of ions is obtained at $r \sim 1.73$ Å rather than 1.43 Å, it is obvious that the shift of the equilibrium position by 0.3 Å is due to the repulsive Coulomb forces acting between like charges of oxygen ions. Moreover, if we take into account that, in real tungsten oxide WO_3, the O(1) ion must interact with other groups of ions, which will pull it away from the center of the incomplete octahedron, it is quite possible that the equilibrium distance will increase from 1.73 to 1.88 Å.

Thus, in condensed media with a sufficiently strong long-range Coulomb interaction, the values of equilibrium interatomic distances are determined by many-body interactions between large groups of particles rather than pair interactions between particular atoms.

REFERENCES

1. A. D. Fofanov, M. E. Prokhorskiĭ, and E. A. Nikitina, Available from VINITI, No. 3127-V97 (1997).
2. A. D. Fofanov, M. E. Prokhorskiĭ, and E. A. Nikitina, Available from VINITI, No. 3543-V97 (1997).
3. D. K. Belashchenko, Neorg. Mater. **30** (7), 948 (1994).
4. L. A. Aleshina, A. D. Fofanov, and O. N. Shivrin, Dokl. Akad. Nauk SSSR **267** (3), 596 (1982) [Sov. Phys. Dokl. **27**, 945 (1982)].
5. L. A. Aleshina and A. D. Fofanov, *X-ray Analysis of Amorphous Materials* (Petrozavod. Gos. Univ., Petrozavodsk, 1987).
6. A. D. Fofanov, Doctoral Dissertation in Physics and Mathematics (Moscow, 1998).
7. M. Kawaminami and T. Hirose, Sci. Rep. Kagoshima Univ., No. 27, 77 (1978).
8. L. S. Palatnik, O. A. Obol'yaninova, and M. N. Naboka, Izv. Akad. Nauk SSSR, Neorg. Mater., No. 5, 801 (1973).

Translated by Yu. Sin'kov

Crystallography Reports, Vol. 49, No. 5, 2004, pp. 719–723. Translated from Kristallografiya, Vol. 49, No. 5, 2004, pp. 806–810.
Original Russian Text Copyright © 2004 by Isupov.

CRYSTAL CHEMISTRY

Problems in Crystal Chemistry of Ferroelectric and Antiferroelectric Perovskites $\mathrm{Pb}B'_{0.5}B''_{0.5}\mathrm{O}_3$

V. A. Isupov

Ioffe Physicotechnical Institute, Russian Academy of Sciences,
Politekhnicheskaya ul. 26, St. Petersburg, 194021 Russia

Received February 13, 2003

Abstract—The most interesting problems in the crystal chemistry of ferroelectric and antiferroelectric perovskites $\mathrm{Pb}B'_{0.5}B''_{0.5}\mathrm{O}_3$ are considered. The properties and specific features of perovskites (such as the smearing of ferroelectric phase transitions, relaxor state, ferroelectric–antiferroelectric transformations, and spontaneous phase transitions to a macrodomain state) depend on the distribution of B' and B'' ions over octahedral positions of the crystal lattice, i.e., on the order and disorder of these ions. *© 2004 MAIK “Nauka/Interperiodica”.*

INTRODUCTION

Although $\mathrm{Pb}B'_{0.5}B''_{0.5}\mathrm{O}_3$ perovskites exhibit ferroelectric and antiferroelectric properties, these materials cannot be considered usual ferroelectrics or antiferroelectrics. The point is that the octahedral positions in the crystal structure of $\mathrm{Pb}B'_{0.5}B''_{0.5}\mathrm{O}_3$ perovskites are occupied by ions of two types (namely, B' and B'') in a 1 : 1 ratio, and, consequently, these ions either can be arranged in staggered order or can be disordered. In the latter case, the B' and B'' ions occupy octahedral positions in a random manner. The disordering of ions substantially affects the Curie temperature T_C, enhances the smearing of the ferroelectric phase transition, and initiates manifestation of relaxor properties [1–4]. On the other hand, the ordering of ions can induce a transformation from the ferroelectric state into the antiferroelectric state [5, 6]. The spontaneous phase transition to a macrodomain state is observed only in disordered crystals [7–9].

The degree of long-range ionic ordering *s*, which can be determined from the intensities of lines in the X-ray diffraction pattern of the studied compound according to the relationship [10],

$$s^2 = (I_{311}/I_{222})_{\mathrm{exp}}/(I_{311}/I_{222})_{\mathrm{theor}},$$

varies from zero for a completely disordered state to unity for a completely ordered state. For a number of perovskites, as the degree of ionic ordering *s* increases above a critical value s_{cr}, the ferroelectric state transforms into the antiferroelectric state [5, 6]. The thermodynamic calculations performed by Bokov *et al.* [11, 12] demonstrated that, for perovskites undergoing a ferroelectric–antiferroelectric phase transition, an increase in the parameter *s* to the critical value s_{cr} is accompanied first by a decrease in the Curie temperature T_C and then (in the antiferroelectric phase) by an increase in this temperature. For materials without phase transformations, the Curie temperature T_C can either decrease or increase depending on the sign of the coefficients in the expansion of the free energy.

Upon variation in the degree of ionic ordering *s*, the phase transition from the paraelectric phase to the ferroelectric phase can change in character: the abrupt transition in an ordered perovskite becomes smeared due to disordering (with a decrease in the parameter *s*). As a result, the material exhibits relaxor properties. In this case, the temperature T_m, which corresponds to a maximum in the curve $\varepsilon(T)$, becomes frequency dependent. At temperatures $T < T_m$, there can occur a spontaneous phase transition to a macrodomain state due to the orientation and coalescence of polar regions (for greater detail, see [13, 14]).

The smeared ferroelectric phase transition involves a large number of local phase transitions occurring in regions of nanometer size [15], which are characterized by different local Curie temperatures $T_{\mathrm{C, loc}}$ due to fluctuations of concentrations of the components (in our case, these are the local concentrations of B' and B'' ions). The width of the smearing region of the ferroelectric phase transition is described by the quantity σ, which can be determined from the temperature dependence of the permittivity at temperatures above T_m:

$$1/\varepsilon = 1/\varepsilon_m + (T - T_m)^2/(2\varepsilon_m\sigma^2),$$

where $\varepsilon_m = \varepsilon$ at the temperature T_m. This dependence is observed in the experiment and can be derived from the Gaussian distribution of local Curie temperatures $T_{\mathrm{C, loc}}$ in the aforementioned nanoregions [16, 17].

In the range of the smeared ferroelectric phase transition, polar regions appear in increasing numbers upon cooling and gradually occupy the entire volume of the crystal. If the polar regions could coalesce freely together, there would occur a conventional percolation (but ferroelectric) phase transition. However, the polar regions with identical direction of spontaneous polarization are separated by distorted paraelectric interlayers that hinder the coalescence of these regions into a single macrodomain [13, 14]. The polar regions can coalesce by overcoming an energy barrier to breakdown of the interlayers. Therefore, the formation of a macrodomain state, whether it be spontaneous or induced (by an electric field), is a relaxation process proceeding over a period of time. Similar time dependences were observed experimentally in [18, 19].

It should be emphasized that both the polar and ion-ordered regions are formed without disturbing the coherence of atomic planes in the crystal [20]. This ensures a high mobility of the boundaries of these regions. In the real perovskites $\mathrm{Pb}B'_{0.5}B''_{0.5}\mathrm{O}_3$, the ordered and disordered regions can coexist. Moreover, in crystals, there can coexist paraelectric, ferroelectric, and antiferroelectric regions, which also undergo transformations under the action of external factors or even only with time. These specific features distinguish the perovskites under consideration from ferroelectric and antiferroelectric materials with a simple perovskite structure.

However, the behavior of ferroelectric and antiferroelectric perovskites $\mathrm{Pb}B'_{0.5}B''_{0.5}\mathrm{O}_3$ is not completely understood. In particular, there exist a number of crystal chemical problems, which will be considered in this paper.

ORDERING OF IONS AND ITS ORIGIN

It is obvious that the B' and B'' ions are ordered under the action of electrostatic forces, which are caused by the difference between the ion charges, and elastic forces arising from the difference between the ion sizes (see, for example, [21]). The energy of electrostatic interaction responsible for the ordering of ions in different niobates and tantalates $\mathrm{Pb}B^{3+}_{0.5}B^{5+}_{0.5}\mathrm{O}_3$ only slightly varies in the series of these compounds because of the insignificant difference between the parameters of the crystal lattices. A different situation occurs with ion sizes. For the $\mathrm{PbFe_{0.5}Nb_{0.5}O_3}$ and $\mathrm{PbFe_{0.5}Ta_{0.5}O_3}$ perovskites, in which, according to all the available data (see, for example, [21, 22]), the long-range order is absent, the radius of the ion $B' = \mathrm{Fe}^{3+}$ (0.54 Å [23]) and the ratio between the sizes of the B' and B'' ions ($p = 0.84$) are relatively small. On the other hand, in the case of the $\mathrm{PbSc_{0.5}Nb_{0.5}O_3}$ and $\mathrm{PbSc_{0.5}Ta_{0.5}O_3}$ compounds containing the ions $B' = \mathrm{Sc}^{3+}$ with a radius of 0.73 Å and ratio $p = 1.14$, both the ordered and disordered states can easily be obtained through annealing at different temperatures [1–4]. For the $\mathrm{PbIn_{0.5}Nb_{0.5}O_3}$ and $\mathrm{PbIn_{0.5}Ta_{0.5}O_3}$ perovskites in which the ordered state can be achieved more readily [24, 25], the radius of the ion $B' = \mathrm{In}^{3+}$ is equal to 0.79 Å and $p = 1.23$. In the $\mathrm{PbYb_{0.5}Nb_{0.5}O_3}$ compound, ions can be disordered only by introducing special additives [26]. For the last compound, the radius of the B' ion is equal to 0.858 Å and $p = 1.34$. It can be seen that, as the radius of the B' ion and the ratio p increase, the tendency toward ordering of ions becomes more pronounced. Therefore, the inference can be made that the size factor plays an important role. This inference is confirmed by the ionic ordering observed in all the $\mathrm{Pb}B'_{0.5}\mathrm{Sb}^{5+}_{0.5}\mathrm{O}_3$ perovskites [27] in which the radius of the Sb^{5+} ion (0.61 Å) is smaller than that of the niobium ion and, correspondingly, the ratio p is larger.

However, quite a different situation is observed in the case of $\mathrm{Pb}B^{2+}_{0.5}\mathrm{W}_{0.5}\mathrm{O}_3$ tungstates. In these compounds, the radius of the ion $B'' = \mathrm{W}^{6+}$ is equal to 0.58 Å and the difference between the charges is two times larger than that for niobates and tantalates. Seemingly, the tendency toward ordering of ions should be much more pronounced. In actual fact, the X-ray diffraction patterns of all these perovskites always contain superstructure lines, which are treated as evidence for the doubling of the spacing of the pseudocubic lattice. This gives grounds to believe that all these tungstates are completely ordered. However, the author has his doubts.

Let us analyze the available data for the $\mathrm{PbCo_{0.5}W_{0.5}O_3}$ tungstate. According to Bokov and Kizhaev [28, 29], the antiferroelectric phase exists in the range from 32 to –206°C and, at the latter temperature, transforms into the ferroelectric phase. In our previous work [30], it was found that this compound is characterized by the Curie temperature $T_C = 38°\mathrm{C}$ and undergoes the antiferroelectric–antiferroelectric phase transition at –20°C. According to Brixel [31] and Buehrer [32], the paraelectric phase *I* exists at temperatures above 25°C, the incommensurate monoclinic antiferroelectric phase *II* is observed below this temperature, the ferroelectric phase *III* is formed at temperatures lower than –53°C, and the transition to the antiferromagnetic phase occurs at 9 K. Phases *II* and *III* coexist in the temperature range from –53 to –173°C. It should be noted that there are other variants of phase sequences for the $\mathrm{PbCo_{0.5}W_{0.5}O_3}$ tungstate. Thus, it can be seen that different researchers have revealed different features and different phase sequences in the $\mathrm{PbCo_{0.5}W_{0.5}O_3}$ perovskite.

All these contradictory results can easily be explained by assuming that cobalt and tungsten ions are disordered, regions with different degrees of ordering coexist in the same crystal, and the specific features of their coexistence depend on the crystal prehistory. Therefore, all the above contradictions stem from the fact that different researchers studied the $\mathrm{PbCo_{0.5}W_{0.5}O_3}$ tungstate in different states.

A similar situation arises with the $\mathrm{PbCo_{0.5}W_{0.5}O_3}$ tungstate [33]. In our earlier works [34, 35], we observed a small but sharp step in the dependence $\varepsilon(T)$

at a temperature of 400°C and a flattened maximum in the temperature range 130–240°C. (Note that, among these features, only the flattened maximum is characterized by a dispersion at frequencies up to 37 GHz.) However, Fesenko [33] revealed only an intense maximum in the vicinity of 400°C in the dependence $\varepsilon(T)$ and did not observe a flattened maximum.

These experimental findings can be interpreted under the assumption that cadmium and tungsten ions are partially disordered. Consequently, the anomaly observed in the curve $\varepsilon(T)$ at temperatures close to 400°C can be assigned to the ordered phase, whereas the flattened maximum in the range 130–240°C can be attributed to the set of regions with different degrees of ordering.

The situation is complicated by the following factors: (i) the electrostatic energy of ionic ordering for tungstates is four times higher than that for niobates, and (ii) the ratio between the radii of the B' and B'' ions is relatively large (in particular, $p = 1.12$ for the $PbCo_{0.5}W_{0.5}O_3$ tungstate and $p > 1.5$ for the $PbCd_{0.5}W_{0.5}O_3$ tungstate). This should predetermine the higher tendency toward ordering of ions. However, the assumption that tungstates are partially disordered also cannot be abandoned. In this respect, the problem calls for further investigation.

SMEARING OF THE FERROELECTRIC PHASE TRANSITION AND FRUSTRATION

The majority of ferroelectric perovskites $PbB'_{0.5}B''_{0.5}O_3$ undergo a phase transition to the antiferroelectric state [36] when the degree of ionic ordering reaches a critical value, i.e., at $s = s_{cr}$. It is worth noting that, with an increase in the parameter s, the Curie temperature T_C decreases in the region of existence of the ferroelectric phase ($s < s_{cr}$) and increases in the region of existence of the antiferroelectric phase ($s > s_{cr}$). For $s = s_{cr}$, i.e., at the lowest Curie temperature T_C, the ferroelectric and antiferroelectric phase transitions are smeared to the greatest extent.

According to the concept proposed in my earlier work [15] regarding the role played by the composition fluctuations in the smearing of the ferroelectric phase transition, the degree of smearing is proportional to dT_C/dx (where x is the concentration of components in the solid solution). In our case, the degree of smearing is proportional to dT_C/ds. However, the derivative dT_C/ds at the minimum of the dependence $T_C(s)$ becomes zero, and, seemingly, no smearing of the ferroelectric (antiferroelectric) phase transition should occur. In order to elucidate the situation, we invoke the frustration phenomenon, which, in magnetism, is observed at the boundary between the ferromagnetic and antiferromagnetic states. However, the mechanism of the influence of frustration on the ferroelectric or antiferroelectric phase transition is rather difficult to perceive. It seems likely that this problem also calls for an extended discussion.

NONRELAXOR BEHAVIOR OF $PbFe_{0.5}Nb_{0.5}O_3$ AND $PbFe_{0.5}Ta_{0.5}O_3$ PEROVSKITES

Almost all disordered ferroelectrics $PbB'_{0.5}B''_{0.5}O_3$ are ferroelectric relaxors, and their temperature T_m shifts with an increase in the frequency of the measuring field. However, this does not hold for the $PbFe_{0.5}Nb_{0.5}O_3$ and $PbFe_{0.5}Ta_{0.5}O_3$ compounds, even though a consensus exists among all researchers that these perovskites have no long-range ionic order. The $PbFe_{0.5}Nb_{0.5}O_3$ and $PbFe_{0.5}Ta_{0.5}O_3$ perovskites do not exhibit relaxor properties. Moreover, the ferroelectric phase transition in these compounds is not smeared. These specific features can be explained under the assumption that the polarizability of BO_6 octahedra is determined by the displacement polarizability of the B ion. This is in complete agreement with the terminology proposed by Yu.N. Venevtsev, according to which the B ion is loosely (or not loosely) located in an octahedron [37].

Let us now compare the disordered perovskite $PbSc_{0.5}Nb_{0.5}O_3$ (ferroelectric relaxor) with the perovskite $PbFe_{0.5}Nb_{0.5}O_3$. The $PbSc_{0.5}Nb_{0.5}O_3$ compound is characterized by the following parameters: the lattice parameter $a \simeq 4.08$ Å, the radius of the scandium ion $r_{Sc} = 0.73$ Å, and the radius of the niobium ion $r_{Nb} = 0.64$ Å. For the $PbFe_{0.5}Nb_{0.5}O_3$ perovskite, the parameters are as follows: the lattice parameter $a \approx 4.00$ Å and the radius of the iron ion $r_{Fe} = 0.55$ Å. It is evident that the displacement polarizability of the Sc^{3+} ion in an octahedron is considerably less than the polarizability of the Nb^{5+} ion. Consequently, the $Nb^{5+}O_6$ octahedra have a large dipole moment and a high polarizability, whereas these quantities for the $Sc^{3+}O_6$ octahedra are small. As a result, owing to composition fluctuations, the regions enriched in niobium are characterized by a high local Curie temperature $T_{C,\,loc}$ and the regions depleted in niobium have a low local Curie temperature. The phase transition is strongly smeared, and the crystal possesses relaxor properties. For the $PbFe_{0.5}Nb_{0.5}O_3$ perovskite, the displacement of the small-sized Fe^{3+} ion is greater than that of the Nb^{5+} ion, which is rather bulky for the $PbFe_{0.5}Nb_{0.5}O_3$ crystal lattice. As a consequence, the dipole moments of the $Fe^{3+}O_6$ and $Nb^{5+}O_6$ octahedra can be approximately equal to each other. In this case, the composition fluctuations, even if they occur, result neither in a smearing of the ferroelectric phase transition nor in a manifestation of the relaxor properties.

Needless to say, much more research must be done to either validate or disprove the proposed hypothesis.

THE CURIE TEMPERATURES OF NIOBATES AND TANTALATES

The Curie temperature of the ordered perovskite $PbSc_{0.5}Nb_{0.5}O_3$ ($T_C \sim 77°C$) is lower than that of the disordered perovskite $PbSc_{0.5}Nb_{0.5}O_3$ ($T_C \sim 105°C$). By contrast, the Curie temperature of the ordered perovskite $PbSc_{0.5}Ta_{0.5}O_3$ ($T_C \sim 26°C$) is higher than that of the disordered perovskite $PbSc_{0.5}Ta_{0.5}O_3$ ($T_C \sim 2°C$) [36]. It is unlikely that, at present, someone can explain these unexpected results (not by the change in sign of the coefficients in the expansion of the free energy, but in terms of the nature of the acting forces). Moreover, it is necessary to elucidate whether or not other niobates and tantalates of this type exhibit a similar contradictory behavior.

There exists one more related problem. The $PbYb_{0.5}Nb_{0.5}O_3$, $PbYb_{0.5}Ta_{0.5}O_3$, $PbLu_{0.5}Nb_{0.5}O_3$, and $PbLu_{0.5}Ta_{0.5}O_3$ perovskites have very close Curie temperatures $T_C \sim 300°C$ [38]. As a rule, among the ferroelectric and antiferroelectric materials with different crystal structures, the tantalates have a considerably lower Curie temperature than the corresponding niobates. However, in our case, this is not true. The origin of the very close Curie temperatures has defied explanation and calls for further investigation. However, first of all, it is necessary to elucidate whether this phenomenon can be associated with the ordering–disordering of ions.

THE INFLUENCE OF HYDROSTATIC PRESSURE

The disordered perovskite $PbIn_{0.5}Nb_{0.5}O_3$, as a rule, possesses relaxor properties. However, under hydrostatic pressure, the ferroelectric phase transitions become less smeared and the antiferroelectric–ferroelectric phase transition occurs at $P = 0.4$ GPa [39–41]. The ferroelectric state is restored after the pressure release. It is characteristic that the pressure does not initiate any ordering of ions.

Under an external pressure, the Curie temperature T_C of the antiferroelectric perovskite $PbMg_{0.5}W_{0.5}O_3$ decreases ($dT_C/dp = -38$ K/GPa), whereas the extrapolated Curie temperature θ increases ($d\theta/dp = +14$ K/GPa) [42, 43]. Owing to the decrease in the difference $T_C - \theta$, the height of the maximum in the curve $\varepsilon(T)$ increases, so that, at some pressure, the permittivity ε at the maximum should tend to infinity and the phase transition should become ferroelectric. According to the calculations performed by Yasuda *et al.* [43], this crossover should be observed at a pressure of 1.08 GPa.

The influence of hydrostatic pressure on the perovskites under consideration is still not clearly understood. However, this problem is of particular interest for the physics of ferroelectricity.

ORDERING OF IONS IN SOLID SOLUTIONS

From the foregoing, it is evident that the smearing of the ferroelectric phase transition and the relaxor properties can be affected not only by annealing at different temperatures, which leads to a change in the degree of ionic ordering, but also by a compression under hydrostatic pressure, which does not change the degree of ordering. One more way of affecting the ferroelectric phase transition and the relaxor properties is to use solid solutions in which a variation in the concentration of components brings about a change in the degree or character of ordering. In some cases, this method can be useful as well. However, it should be remembered that the prehistory of the studied samples must always be taken into account.

CONCLUSIONS

Thus, we considered a number of problems in the crystal chemistry of ferroelectric and antiferroelectric perovskites $PbB'_{0.5}B''_{0.5}O_3$. These compounds exhibit unique properties that are absent in the usual ferroelectric and antiferroelectric perovskites. The specific features of the $PbB'_{0.5}B''_{0.5}O_3$ perovskites are explained by the fact that the octahedral positions in the crystal lattice of these compounds are occupied by ions of two types. These ions can be either ordered or disordered. In the latter case, regions with different degrees of ordering can coexist in the same crystal. When studying a particular sample, it is necessary to take into account its prehistory, to examine the specific features of the coexistence of the ordered and disordered phases, and to elucidate the nature of the coexisting paraelectric, ferroelectric, and antiferroelectric phases. This will provide a good basis for the interpretation of the results of the investigation into physical (in particular, ferroelectric) properties.

REFERENCES

1. C. G. F. Stenger, F. L. Sholten, and A. J. Burggraaf, Solid State Commun. **32** (11), 989 (1980).
2. C. G. F. Stenger and A. J. Burggraaf, Phys. Status Solidi A **61**, 275 (1980).
3. C. G. F. Stenger and A. J. Burggraaf, Phys. Status Solidi A **61**, 653 (1980).
4. N. Setter and L. E. Cross, J. Appl. Phys. **51**, 4356 (1980).
5. A. A. Bokov and I. P. Rayevsky, Ferroelectrics **54**, 241 (1984).
6. A. A. Bokov, I. P. Raevskiĭ, and V. G. Smotrakov, Fiz. Tverd. Tela (Leningrad) **26** (9), 2824 (1984) [Sov. Phys. Solid State **26**, 1708 (1984)].
7. F. Chu, N. Setter, and A. K. Tagantsev, J. Appl. Phys. **74** (8), 5129 (1993).
8. F. Chu, I. M. Reaney, and N. Setter, Ferroelectrics **151**, 343 (1994).

9. F. Chu, I. M. Reaney, and N. Setter, J. Appl. Phys. **77** (4), 1671 (1995).
10. V. V. Eremkin, V. G. Smotrakov, E. S. Gagarina, *et al.*, Kristallografiya **44** (5), 878 (1999) [Crystallogr. Rep. **44**, 818 (1999)].
11. A. A. Bokov, Ferroelectrics **90**, 155 (1989).
12. A. A. Bokov, I. P. Raevskiĭ, and V. G. Smotrakov, Fiz. Tverd. Tela (Leningrad) **25** (7), 2025 (1983) [Sov. Phys. Solid State **25**, 1168 (1983)].
13. V. A. Isupov, Fiz. Tverd. Tela (St. Petersburg) **38** (5), 1326 (1996) [Phys. Solid State **38**, 734 (1996)].
14. V. A. Isupov, Phys. Status Solidi B **213**, 211 (1999).
15. V. A. Isupov, Zh. Tekh. Fiz. **26** (9), 1912 (1956).
16. V. V. Kirillov and V. A. Isupov, Izv. Akad. Nauk SSSR, Ser. Fiz. **35** (12), 2602 (1971).
17. V. V. Kirillov and V. A. Isupov, Ferroelectrics **5**, 3 (1973).
18. S. B. Vakhrushev, J.-M. Kiat, and B. Dkhil, Solid State Commun. **103** (8), 477 (1997).
19. E. V. Colla, E. A. Koroleva, N. M. Okuneva, and S. B. Vakhrushev, Phys. Rev. Lett. **74** (9), 1681 (1995).
20. H. M. Ghan, M. P. Harmer, A. Bhalla, and L. E. Cross, J. Appl. Phys. (Suppl. 1.2) **24**, 550 (1985).
21. V. M. Yudin, Izv. Akad. Nauk SSSR, Ser. Fiz. **31** (11), 1788 (1967).
22. G. A. Smolenskiĭ and V. M. Yudin, Fiz. Tverd. Tela (Leningrad) **6** (12), 3668 (1967) [Sov. Phys. Solid State **6**, 2937 (1967)].
23. R. D. Shannon and C. T. Prewitt, Acta Crystallogr., Sect. B: Struct. Crystallogr. Cryst. Chem. **25** (5), 925 (1969).
24. A. V. Turik, Fiz. Tverd. Tela (Leningrad) **27** (9), 2802 (1985) [Sov. Phys. Solid State **27**, 1686 (1985)].
25. N. Yasuda, Jpn. J. Appl. Phys. B **40** (9), 1920 (2001).
26. V. Yu. Shonov and I. P. Raevskiĭ, Zh. Tekh. Fiz. **69** (3), 24 (1999) [Tech. Phys. **44**, 285 (1999)].
27. I. N. Danilenko, Neorg. Mater. **23** (5), 825 (1981).
28. V. A. Bokov and S. A. Kizhaev, Fiz. Tverd. Tela (Leningrad) **6** (10), 3038 (1964) [Sov. Phys. Solid State **6**, 2419 (1964)].
29. V. A. Bokov and S. A. Kizhaev, Izv. Akad. Nauk SSSR, Ser. Fiz. **29** (6), 929 (1965).
30. V. A. Isupov and L. V. Belous, Kristallografiya **16** (1), 164 (1971) [Sov. Phys. Crystallogr. **16**, 129 (1971)].
31. W. Brixel, Jpn. J. Appl. Phys. Suppl. 2 **24**, 242 (1985).
32. W. Buehrer, Physica B (Amsterdam) **156–157**, 10 (1989).
33. E. G. Fesenko, Fiz. Tverd. Tela (Leningrad) **11** (11), 3362 (1969) [Sov. Phys. Solid State **11**, 2729 (1969)].
34. V. A. Isupov and L. T. Emel’yanova, Kristallografiya **11** (5), 776 (1966) [Sov. Phys. Crystallogr. **11**, 659 (1966)].
35. Yu. M. Poplavko, V. G. Tsykalov, V. I. Molchanov, and V. A. Isupov, Fiz. Tverd. Tela (Leningrad) **10** (5), 1542 (1968) [Sov. Phys. Solid State **10**, 1217 (1968)].
36. A. A. Bokov, Doctoral Dissertation in Chemistry (Rostov State Univ., Rostov-on-Don, 1995).
37. Yu. N. Venevtsev, E. D. Politova, and S. A. Ivanov, *Ferroelectrics and Antiferroelectrics in the Family of Barium Titanate* (Khimiya, Moscow, 1985) [in Russian].
38. V. A. Isupov and N. N. Kraĭnik, Fiz. Tverd. Tela (Leningrad) **6** (12), 3713 (1964) [Sov. Phys. Solid State **6**, 2975 (1964)].
39. N. Yasuda, J. Phys. Soc. Jpn. **66** (7), 1920 (1997).
40. S. Nomura, J. Phys. Soc. Jpn. **68** (3), 866 (1999).
41. S. Nomura, J. Phys. Soc. Jpn. **68** (1), 39 (1999).
42. N. Yasuda, S. Fujimoto, and T. Yoshimura, Jpn. J. Appl. Phys., Suppl. 2 **24**, 245 (1985).
43. N. Yasuda, S. Fujimoto, and T. Yoshimura, J. Phys. C **19** (7), 1055 (1986).

Translated by O. Borovik-Romanova

Crystallography Reports, Vol. 49, No. 5, 2004, pp. 724–732. Translated from Kristallografiya, Vol. 49, No. 5, 2004, pp. 811–819.
Original Russian Text Copyright © 2004 by Orlova, Koryttseva.

STRUCTURE OF INORGANIC COMPOUNDS

Phosphates of Pentavalent Elements: Structure and Properties

A. I. Orlova and A. K. Koryttseva
Nizhni Novgorod State University, pr. Gagarina 23, Nizhni Novgorod, 603950 Russia
e-mail: oai@uic.nnov.ru

Received August 22, 2003

Abstract—Possible formula types of orthophosphate octahedron–tetrahedron frameworks $\{[T_2(PO_4)_3]^{n-}\}_{3\infty}$ (where T_2 are elements in identical or different oxidation states +1, +2, +3, +4, and +5) have been calculated and described. The data on the structure and properties of well-known phosphates with mixed frameworks of such a type containing elements in the oxidation state +5 are systematized. Most are crystallized in the structure type $NaZr_2(PO_4)_3$ (NZP). For these phosphates, the relative differences in the radii of framework-forming cations do not exceed 0.6. It is shown that NZP-like compounds with the expected structure and specified properties can be modeled by phosphates with electrically neutral frameworks. The model predictions were justified by synthesis and crystallographic investigations of niobium phosphates with bi- and trivalent elements. *© 2004 MAIK “Nauka/Interperiodica”.*

The mixed framework $\{[T_2(XO_4)_3]^{n-}\}_{3\infty}$ [1] plays a particular role in the crystal chemistry of compounds with tetrahedral anions. This three-dimensional framework, in which all the oxygen atoms are shared between XO_4 tetrahedra and TO_6 octahedra, is formed for atoms of different elements T (in the oxidation states +1, +2, +3, +4, and +5, denoted hereinafter as T^{I}, T^{II}, T^{III}, T^{IV}, and T^{V}, respectively) and X (X = Si, P, As, S, Mo, W). Since octahedra and tetrahedra can be occupied by T and X cations in many different ways, a large number of compounds with different compositions exist. Isovalent and heterovalent elements of the same or different types can also be incorporated into octahedrically coordinated framework positions. According to the Goldschmidt rule, the difference in the ionic radii of cations that can isomorphously substitute for each other in the L position of a mixed framework should not exceed 15% of the smaller radius. At present, most of the well-studied phosphates are those with cations of the same type in the frameworks $2T = T_2^{\mathrm{IV}}$ = Ti_2, Zr_2, Hf_2, Ge_2, Sn_2; $2T = T_2^{\mathrm{III}}$ = Al_2, Sc_2, Cr_2, Fe_2, Y_2, In_2, and Ln_2. The possibility of co-occupation of a framework by cations of different types in the same or different oxidation states was implemented for several combinations of T cations in the framework $2T = T^{\mathrm{IV}}(T')^{\mathrm{IV}}$, $T^{\mathrm{III}}(T')^{\mathrm{III}}$, $T^{\mathrm{IV}}T^{\mathrm{I}}$, $T^{\mathrm{IV}}T^{\mathrm{II}}$, $T^{\mathrm{IV}}T^{\mathrm{III}}$, $T^{\mathrm{IV}}T^{\mathrm{V}}$, and some other more complex compositions [2].

FORMULA TYPES

The theoretically predicted formulas of an octahedron–tetrahedron mixed framework of the $[T_2(PO_4)_3]^{n-}$ type for n = 0, 1, 2, 3, and 4 are presented by the compositions listed in Table 1. The principles of their formation are based on the following assumptions:

(i) two framework positions can be occupied by either isovalent atoms (TT) in the ratio 1 : 1 or heterovalent atoms (aT' bT'') in different ratios $a : b$; in this case, $a + b = 2$;

(ii) framework charge n can take values from 0 to 4, which follows from the assuming TO_6 and PO_4 polyhedra to be isolated and linked by sharing oxygen atoms in their vertices [1]; and

(iii) framework charge n depends on the composition of its cationic part $T'T''$ as follows: $n = aT' + bT''$.

Negative framework charge n is compensated by the charges of various cations, which can be located in

Table 1. Possible formula types of $\{[T_2(PO_4)_3]^{n-}\}_{3\infty}$ frameworks (T^{I}, T^{II}, T^{III}, T^{IV}, and T^{V} are elements in the oxidation states +1, +2, +3, +4, and +5, respectively)

2T				
$n = 0$	$n = 1$	$n = 2$	$n = 3$	$n = 4$
$T^{\mathrm{V}}T^{\mathrm{IV}}$	$T^{\mathrm{V}}T^{\mathrm{III}}$	$T^{\mathrm{V}}_{1/2}\ T^{\mathrm{III}}_{3/2}$	$T^{\mathrm{V}}_{2/3}\ T^{\mathrm{II}}_{4/3}$	$T^{\mathrm{V}}_{1/3}\ T^{\mathrm{II}}_{5/3}$
$T^{\mathrm{V}}_{3/2}\ T^{\mathrm{III}}_{1/2}$	$T^{\mathrm{V}}_{4/3}\ T^{\mathrm{II}}_{2/3}$	$T^{\mathrm{V}}T^{\mathrm{II}}$	$T^{\mathrm{V}}T^{\mathrm{I}}$	$T^{\mathrm{V}}_{3/4}\ T^{\mathrm{I}}_{5/4}$
$T^{\mathrm{V}}_{5/3}\ T^{\mathrm{II}}_{1/3}$	$T^{\mathrm{V}}_{3/2}\ T^{\mathrm{I}}_{1/2}$	$T^{\mathrm{V}}_{5/4}\ T^{\mathrm{I}}_{3/4}$	$T^{\mathrm{IV}}T^{\mathrm{II}}$	$T^{\mathrm{IV}}_{1/2}\ T^{\mathrm{II}}_{3/2}$
$T^{\mathrm{V}}_{7/4}\ T^{\mathrm{I}}_{1/4}$	$T^{\mathrm{IV}}T^{\mathrm{IV}}$	$T^{\mathrm{IV}}T^{\mathrm{III}}$	$T^{\mathrm{IV}}_{4/3}\ T^{\mathrm{I}}_{2/3}$	$T^{\mathrm{IV}}T^{\mathrm{I}}$
		$T^{\mathrm{IV}}_{3/2}\ T^{\mathrm{II}}_{1/2}$	$T^{\mathrm{III}}T^{\mathrm{III}}$	$T^{\mathrm{III}}T^{\mathrm{II}}$
		$T^{\mathrm{IV}}_{5/3}\ T^{\mathrm{I}}_{1/3}$		

1063-7745/04/4905-0724$26.00 © 2004 MAIK “Nauka/Interperiodica”

framework cages—in the positions of the $M1$ and $M2$ types. The general (with regard to the number of M positions) crystal–chemical formula of the compounds under study is $[M1][M2]_3L_2(PO_4)_3$. M positions in interframework cages can be occupied in different ways. Obviously, with an increase in n from 0 to 4, the number of occupied M positions increases: for $n = 0$, they are completely unoccupied, while, for $n = 4$, all the M positions can be occupied.

It can be seen from Table 1 that, of all the possible formula types of orthorhombic frameworks, the most numerous ones are those that contain elements in the +5 oxidation state (separated by a bold line in the upper part of the table). The rest (under the line) contain elements in the oxidation state +4, in most cases.

Phosphates and other compounds of tetravalent elements with tetrahedral XO_4 anions, having a framework structure of the $\{[T_2(XO_4)_3]^{n-}\}_{3\infty}$ type, have been investigated intensively over the last two decades. The number of such publications stands at several hundred and increases every year, although the formula types have not been investigated equally thoroughly. Another situation is observed for phosphates containing pentavalent elements. Although they are represented by a significantly larger number of theoretically possible formula types, the number of investigated objects is substantially smaller. It is noteworthy that some of these phosphates are absent in the list of known ones because either their formation is impossible due to steric hindrances or the synthesis methods used do not make it possible to overcome kinetic hindrances.

The purpose of this study was to generalize the available data on the phosphates of pentavalent elements with the $\{[T_2(PO_4)_3]^{n-}\}_{3\infty}$ motif, perform a comparative analysis of their crystal–chemical properties, and, based on the results of this analysis for known phosphates, "build" phosphates of a new composition with an expected structure and properties. A search for new materials with properties of practical importance (superconducting, catalytic, semiconducting, luminescent, and so on), specifically in the "structure–property–composition" context, makes it possible to avoid uncertainties typical of empirical synthesis by carrying out this synthesis purposefully.

CRYSTAL–CHEMICAL PROPERTIES

The composition and structural data for the known phosphates containing pentavalent elements are listed in Table 2.

Among the phosphates with electrically neutral frameworks ($n = 0$), the compounds $T^{V}T^{IV}(PO_4)_3$ (T^{V} = Nb, Sb, Ta; T^{IV} = Nb, Zr, Ti, V, Ge [4–12] and $T^{V}_{3/2}T^{III}_{1/2}(PO_4)_3$ (T^{III} = Cr, Sb, Nd, Eu, Bi; T^{V} = Nb, Sb, Ta) are being studied [13–16]. When a polyhedral framework is charged ($n > 0$), compensating cations are present in interframework cages. Among the phosphates with such frameworks, the best-studied compounds are those with frameworks of the $[T^{V}T^{III}(PO_4)_3]^-$ ($n = 1$) type (T^{V} = Sb, Nb, and Ta; T^{III} = Fe, Al, Ga, In, Cr, V, Ti, and Sc) [5, 12, 17–31]. Their negative framework charge is compensated by cations of either alkali elements A^{I} = Li, Na, and H in the $A^{I}[T^{V}T^{III}(PO_4)_3]$ phosphates (T^{III} = Fe, Al, Ga, In, Cr, V, Ti, Sc) [12, 17, 19–22, 24, 25, 28, 29] or divalent elements A^{II} = Ca, Ba, Pb, Sr, Cd, and Cu in the $A^{II}_{1/2}[NbT^{III}(PO_4)_3]$ phosphates (T^{III} = Fe and Al) [17, 18, 30, 31]. Study of electrochemical and chemical intercalation processes involving compounds with electrically neutral frameworks ($NbTi(PO_4)_3$, $Cr_{1/2}Nb_{3/2}(PO_4)_3$) has shown that these processes make it possible to deliberately increase the framework charge from 0 to 1, which gives rise to phases of the following types: $MeNbTi(PO_4)_3$ (Me = Li, Na, $Sn_{0.5}$, $Fe_{0.33}$) [5, 22, 24] and $Li_xCr_{1/2}Nb_{3/2}(PO_4)_3$ [13]. For frameworks with higher charges ($n > 1$), $Li_2Nb_{1/2}In_{3/2}(PO_4)_3$ [32] and $Na_3NbNa(PO_4)_3$ [33] compounds are known.

The data in Table 2 indicate that, of all the possible formula types of frameworks containing pentavalent elements (Table 1), only five have been implemented to date; i.e., wide ranges of compositions remain unstudied. The available data on the known phosphates allow us to make some generalizations concerning their crystal–chemical properties.

Although the compounds studied have various cationic compositions, only three structure types have been implemented: $NaZr_2(PO_4)_3$ (NZP or NASICON) (I), $Sc_2(WO_4)_3$ (SW) (II), and $Bi_{1/2}Sb_{3/2}(PO_4)_3$ (BiSb) (III).

Most studied phosphates have a type-I structure, including those with different values of n: from 0 to 1. Space groups with rhombohedral symmetry $R\bar{3}c$ and $R\bar{3}$ are typical of them. In these phosphates, the relative differences in the sizes of framework-forming cations do not exceed 0.2 Å, and their charges differ from each other by no more than a factor of two (Table 2). These data confirm the conception of wide isomorphism of phases of rhombohedral type—structural analogs of $NaZr_2(PO_4)_3$ (which has been experimentally established previously [2, 34]), supplementing the known isomorphous series with phosphates of pentavalent elements: niobium, antimony, and tantalum.

Some antimony and niobium phosphates (n = 0 or 2) (Table 2) are crystallized in the structure type of scandium tungstate (type II) of orthorhombic (sp. gr. *Pbcn*) and monoclinic (sp. gr. $P2_1/n$) modifications. A lower (in comparison with rhombohedral) structural symmetry was also noted for zirconium phosphates and their chemical analogs in the case of the incorporation of small cations (for example, Li^+, Mg^{2+}, or ions of d elements) into interframework cages [35]. Differences Δr

Table 2. Crystal–chemical properties of phosphates with $\{[T'_aT''_b(\mathrm{PO_4})_3]^{n-}\}_{3\infty}$ frameworks

n	Cations in the $T'_aT''_b$ framework		Cations in cages	Structure		Ionic radii of T cations, Å [3]			References
				type	space group	$T' \equiv T^{\mathrm{V}''}$	T''	$\Delta r/r_{\mathrm{min}}$	
0	$T^{\mathrm{V}}T^{\mathrm{IV}}$	NbTi		NZP	$R\bar{3}c$	0.64	0.61	0.05	[4, 5]
		$\mathrm{NbV^{IV}}$		NZP	*	0.64	0.58	0.10	[6]
		NbGe		NZP	*	0.64	0.53	0.21	[4, 6]
		NbZr		NZP	*	0.64	0.72	0.13	[7–9]
		$\mathrm{Nb^{V}Nb^{IV}}$		NZP	$R\bar{3}c$	0.64	0.68	0.06	[10, 11]
		$\mathrm{Sb^{V}Ti^{IV}}$		NZP	*	0.60	0.61	0.17	[4, 6]
		$\mathrm{Sb^{V}V^{IV}}$		NZP	*	0.60	0.58	0.03	[6]
		$\mathrm{TaTi^{IV}}$		NZP	*	0.64	0.61	0.05	[4]
		$\mathrm{TaV^{IV}}$		NZP	*	0.64	0.58	0.10	[12]
	$T^{\mathrm{V}}_{3/2}T^{\mathrm{III}}_{1/2}$	$\mathrm{Nb_{3/2}Cr_{1/2}}$		NZP	*	0.64	0.62	0.03	[13]
		$\mathrm{Nb^{V}_{3/2}Sb^{III}_{1/2}}$		SW	$Pbcn$	0.64	0.76	0.19	[14]
		$\mathrm{Nb_{3/2}Nd_{1/2}}$		SW	*	0.64	0.98	0.53	[14]
		$\mathrm{Sb^{V}_{3/2}Sb^{III}_{1/2}}$		SW	$P2_1/n$	0.60	0.76	0.27	[15]
		$\mathrm{Sb_{3/2}Nd_{1/2}}$		BiSb	$R\bar{3}$	0.60	0.98	0.63	[14]
		$\mathrm{Sb_{3/2}Eu_{1/2}}$		BiSb	$R\bar{3}$	0.60	0.95	0.58	[14]
		$\mathrm{Sb_{3/2}Bi_{1/2}}$		BiSb	$R\bar{3}$	0.60	1.03	0.72	[16]
		$\mathrm{Ta_{3/2}Sb_{1/2}}$		NZP	$R\bar{3}c$	0.64	0.76	0.25	[14]
1	$T^{\mathrm{V}}T^{\mathrm{III}}$	NbAl	H, Li, Na, Ca, Cu	NZP	$R\bar{3}c$	0.64	0.53	0.21	[12, 17, 18]
		TaAl	Li, Na	NZP	$R\bar{3}c$	0.64	0.53	0.21	[12, 19]
		NbSc	Na	NZP	$R\bar{3}c$	0.64	0.75	0.17	[20]
		$\mathrm{NbTi^{III}}$	Na	NZP	$R\bar{3}c$	0.64	0.67	0.05	[12]
		$[(\mathrm{Nb^{V}/Nb^{IV}})(\mathrm{Ti^{III}/Ti^{IV}})]$	Li, Na, Cu, Fe, Sn	NZP	$R\bar{3}c$	0.64	0.67	0.05	[5, 21–27]
		$\mathrm{NbV^{III}}$	Na	NZP	$R\bar{3}c$	0.64	0.64	0	[12]
			Li	SW	$P2_1/n$				[12]
		$\mathrm{TaV^{III}}$	Na	NZP	$R\bar{3}c$	0.64	0.64	0	[12]
			Li	SW	$P2_1/n$				[12]
		NbCr	Li, Na	NZP	$R\bar{3}c$	0.64	0.62	0.03	[28, 12, 19, 29]
		SbCr	Na	NZP	*	0.60	0.62	0.03	[28]
		TaCr	Li, Na	NZP	$R\bar{3}c$	0.64	0.62	0.03	[28, 12, 19]
		NbFe	Li, Na, Ca, Sr, Cd, Ba, Pb	NZP	$R\bar{3}c$	0.64	0.55	0.16	[28, 19, 18, 30, 31]
		SbFe	Na	NZP	*	0.60	0.55	0.09	[28]
		TaFe	Li, Na	NZP	$R\bar{3}c$	0.64	0.55	0.16	[28, 12, 19]
		NbGa	Na, Ca	NZP	*	0.64	0.62	0.03	[28, 18]
		SbGa	Na	NZP	*	0.60	0.62	0.03	[28]
		TaGa	Na	NZP	*	0.64	0.62	0.03	[28]
		NbIn	Na, Ca	NZP	*	0.64	0.80	0.02	[28, 18]
		SbIn	Na	NZP	*	0.60	0.80	0.29	[28]
		TaIn	Na	NZP	*	0.64	0.80	0.02	[28]
2	$T^{\mathrm{V}}_{1/2}T^{\mathrm{III}}_{3/2}$	$\mathrm{Nb_{1/2}In_{3/2}}$	Li	SW	$P2_1/n$	0.64	0.80	0.25	[32]
3	$T^{\mathrm{V}}T^{\mathrm{I}}$	NbNa	Na	NZP	*	0.64	1.02	0.59	[33]

* Space group is not given.

in the radii of cations in frameworks of type II are of the same order of magnitude as in NZP structures (Table 2).

Bismuth and antimony phosphates (type III) are characterized by an intrinsic-type structure with a rhombohedral cell and the sp. gr. $R\bar{3}$. By date, only several double phosphates of such a structure are known. They contain pentavalent niobium and tantalum cations and trivalent neodymium, europium, and bismuth cations (first and second types, respectively); i.e., the framework-forming cations are characterized by a rather large difference in radii: from 0.35 to 0.43 Å (Table 2).

One of the main factors determining the formation of a particular structural modification (from among those under consideration) is stereochemical. Such a correlation between the type of phosphate structure and the relative difference in the ionic radii of framework-forming cations is shown in Fig. 1. The NZP and SW structures are implemented if $0 \leq \Delta r/r_{\min} \leq 0.59$ and, in this case, T' and T'' cations are statistically distributed over equivalent framework positions L. When the difference in the radii of T' and T'' cations is in the range from 0.58 to 0.72, a structural modification of type III is formed that is characterized by a differentiated occupation of two framework positions of different structure types. On the basis of the above comparative analysis of the crystal–chemical data on the phases studied, one can predict implementation of a particular structure for other (yet to be implemented) compounds with other combinations of cations in the +5 oxidation state with cations in other oxidation states, estimating the relative differences in the radii of these cations.

It can be seen from Table 2 that two types of structures—NZP and SW—are implemented most often in phosphates with frameworks of the $\{[T_2(PO_4)_3]^{n-}\}_{3\infty}$ type. The similarity of the NZP and SW structure types has been noted in the literature [16]. It is often difficult to distinguish their monoclinically distorted modifications on the basis of powder X-ray diffraction patterns [36]. The geometrical basis of the NZP structure type (I) is the structure of iron sulphate $Fe_2(SO_4)_3$ with a rhombohedral modification (Fig. 2a), whereas the basis of the SW structure type (II) is the orthorhombic modification $Fe_2(SO_4)_3$ (Fig. 2b). Comparing them (Fig. 2) shows that, in the rhombohedral phase, the building units (two octahedra linked with three tetrahedra by shared oxygen atoms at vertices) are located strictly parallel to the hexagonal axis c, whereas, in the monoclinic phase, they are rotated with respect to each other.

The $Bi_{1/2}Sb_{3/2}(PO_4)_3$ (III) structure is characterized by another framework of the $\{[T_2(PO_4)_3]^{n-}\}_{3\infty}$ type (Fig. 3). Octahedrically coordinated T cations are located in chains of two types oriented parallel to the c axis. One of these chains corresponds to the threefold axis (i.e., is similar to the NZP structure), while the other passes through the center of the hexagonal cell or equivalent positions. Thus, the number of second-type

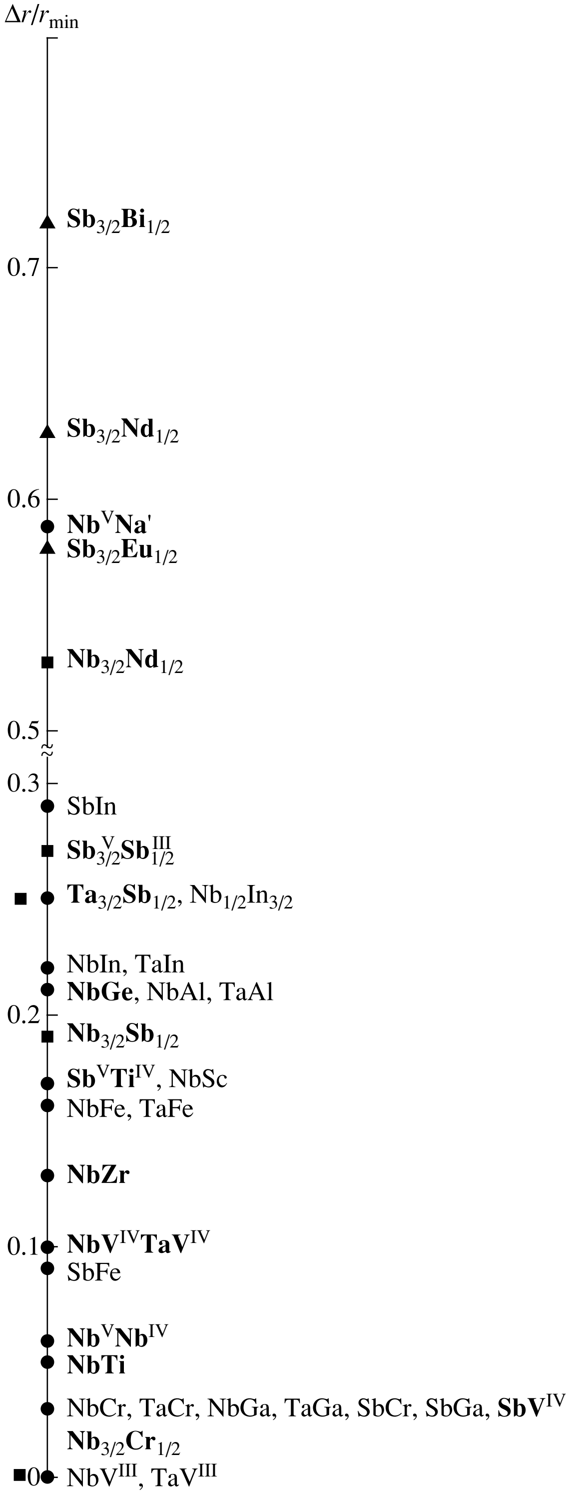

Fig. 1. Dependence of the mixed-framework structure on the relative difference in the radii of framework-forming cations ($\Delta r/r_{\min}$) for the structure types (▲) $Bi_{1/2}Sb_{3/2}(PO_4)_3$ (BiSb), (●) $NaZr_2(PO_4)_3$ (NZP), and (■) $Sc_2(WO_4)_3$ (SW); **NbTi**, SbFe, $Nb_{1/2}In_{3/2}$, and $\mathbf{Nb^{V}Na}$ denote the phosphates with framework charge n = 0, 1 and 2, 3, respectively.

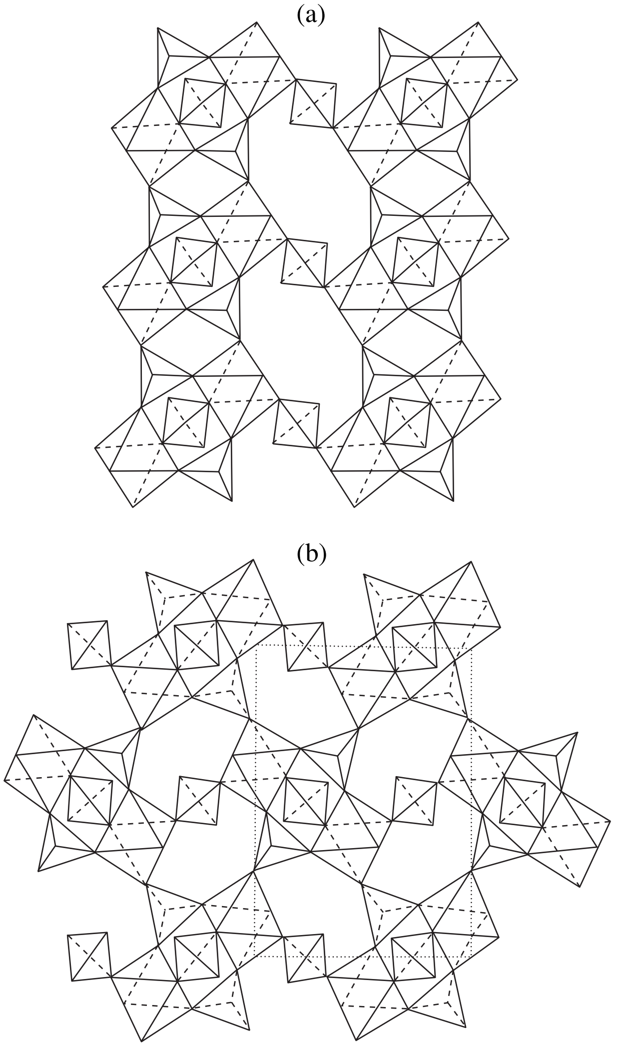

Fig. 2. (a) Rhombohedral and (b) monoclinic frameworks of iron sulphate (III) $Fe_2(SO_4)_3$ [36].

chains exceeds that of first-type chains by a factor of two (Fig. 3a). In the $\{[T_2(PO_4)_3]^{n-}\}_{3\infty}$ structure, the location of framework-forming T cations, as well as TO_6 octahedra, is pseudocubic-centered [16]. Comparison of the NASICON and scandium tungstate (types I, II) with the structures of bismuth phosphate and antimony phosphate (type III) [16] showed that, among the structures of the first two types, only one has the structure of an elementary cube (or pseudocube), the vertices of which are linked with neighboring octahedra by O–O bonds. In $Bi_{1/2}Sb_{3/2}(PO_4)_3$, there are six types of such cubes (Fig. 3b). They are centered with respect to six independent positions occupied by T cations (Bi(1), Bi(2), and Sb(1)–Sb(4)).

In generalizing the results of the above crystal–chemical analysis, we should note that, despite the differences in the process of structure formation, all the implemented structures of phosphates with pentavalent elements (see Table 2) are either symmetrically similar ($R\bar{3}c$, $R\bar{3}$), have similar structural motifs (NZP, SW), or have fragments of the same type $T_2(PO_4)_3$ in building units. This circumstance suggests manifestation of isomorphism and formation of solid solutions in systems with more complex cationic compositions, as well as polymorphism of the phases of this type.

The phosphates listed in Table 2 are being studied in view of their possible applications as functional materials.

COMPOSITION–STRUCTURE–PROPERTIES

It is well known that many properties of compounds are determined by the features of their structure and depend on the nature of the cations they contain. This is especially important for elements of Group V of the periodic system, in view of the large variety of their oxidation states and various manifestations of these states in an octahedral environment. The characteristic properties of these phosphates are thermal stability, low and controllable thermal expansion [7, 8], catalytic activity and selectivity [6], luminescence properties [13], ability to participate in intercalation processes [5, 13, 22, 24], and conductivity of ionic and mixed ionic–electronic types [19, 20, 22]. The role of structural factors in the implementation of the above properties is as follows.

(i) A framework built of multiply charged T cations rigidly bound in TO_6 polyhedra is only insignificantly distorted upon heating. This framework rigidity is responsible for the high thermal stability and low thermal expansion of the phosphates under consideration.

(ii) The $T_2(PO_4)_3$ framework is of mixed cation–anion type: TO_6 octahedra and PO_4 tetrahedra that share vertices are differently aligned in space, depending on the structure type in which the compound is crystallized. However, TO_6 octahedra are isolated from each other in space. This structural feature is of importance for applications of such materials as catalysts, because the possibility of structural isolation of catalytically active fragments from each other (octahedra with catalytically active cations alternate with catalytically inert tetrahedral groups) enhances the selectivity of catalysts [6]. The isolation of TO_6 polyhedra, and, hence, the sufficiently large T–T distance in the $T_2(PO_4)_3$ structure are also important for laser materials, since compounds of this type have a relation between the main characteristics of phosphors (the lifetime of an excited state and the quantum yield) that is optimal for practical use [37].

(iii) The degree of occupation of interframework positions M_1 and M_2 affects ionic conductivity and thermal expansion.

The fact that frameworks of the $\{[T_2(PO_4)_3]^{n-}\}_{3\infty}$ type contain channels of a certain size and cations of a similar size that are capable of moving through them determines the transport properties of the compounds under consideration. Their optimal characteristics

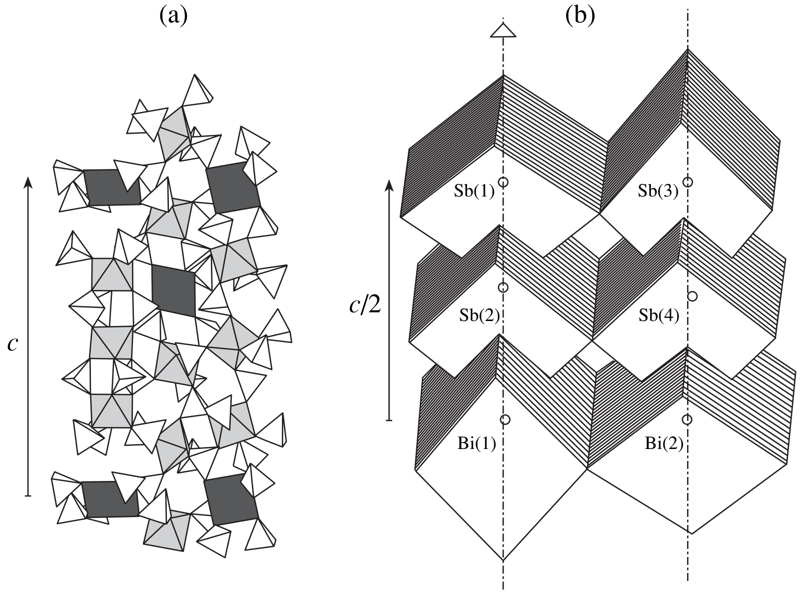

Fig. 3. Fragment of the $Bi_{1/2}Sb_{3/2}(PO_4)_3$ structure (a) projected onto the [120] plane and (b) shown in perspective to demonstrate the pseudocubic orientation of Bi and Sb atoms (each pseudocube vertex belongs to either a Bi or Sb atom) [16].

depend also on the ratio of occupied and unoccupied *M* positions. The presence of unoccupied positions and the possibility of some cations or molecules occupying them with changing the chemical composition of the initial matrix (conserving the structure at the same time) is important for applications of these materials in intercalation processes. If a cation with several possible oxidation states is a framework-forming one, a change in its oxidation state leads to mobile cations that are located in interframework positions contributing, along with ionic conductivity, to electronic conductivity. Such materials with mixed ionic–electronic conductivity can be used as reversible cathodes in electrochemical generators [13].

The presence and number of vacancies play an important role in predicting the thermomechanical properties of the aforementioned compounds. It is well known that, with an increase in the number of interframework vacancies to the maximum value $n = 4$, the axial strains in a rhombohedral structure are reduced. For example, phosphates with frameworks of the $T^{V}T^{IV}(PO_4)_3$ type are known to have low expansion ($\alpha_{av} < 2 \times 10^{-6}$ K^{-1}) upon heating (all the 4*M* positions are unoccupied) [8].

CRYSTAL–CHEMICAL PREDICTIONS AND EMPIRICAL INVESTIGATIONS

In the first part of this study, based on the general crystal–chemical formula of the compounds with the structural motif $T_2(PO_4)_3$, all the theoretically possible formula compositions were calculated, and that some of them are implemented in practice was confirmed by the data in the literature. This part of the study expands and supplements the experience in crystal–chemical prediction of the composition, structure, and properties of phosphates of pentavalent elements obtained to date.

Among the aforementioned variety of formula types of frameworks (Table 1), there is a particular group of materials with electrically neutral frameworks, which do not call for cations to compensate the framework charge. As can be seen from Table 1, they form the series

$$T^{IV}T^{V}(PO_4)_3 \longrightarrow T^{III}_{1/2}T^{V}_{3/2}(PO_4)_3$$

$$\longrightarrow T^{II}_{1/3}T^{V}_{5/3}(PO_4)_3 \longrightarrow T^{I}_{1/4}T^{V}_{7/4}(PO_4)_3.$$

Cations in the oxidation state +5 (T^{V}) are involved in the formation of each framework of this type. At present, the formula compositions from the above series are only represented by compounds with some $T^{IV}T^{V}$ and $T^{III}T^{V}$ cations (Table 2). Their structure is characterized by a rhombohedral unit cell, provided that the relative difference ($\Delta r/r_{min}$) in the radii of the T^{IV}–T^{V} and T^{III}–T^{V} cations does not exceed 0.6; at larger differences, these materials are crystallized in the structure type of bismuth and antimony phosphates (Fig. 1). Thus, we may suggest the existence of phosphates of T^{II}–T^{V} and T^{I}–T^{V} elements and, if the empirically found relation $0 \le \Delta r/r_{min} \le 0.6$ Å is satisfied, we can predict that they will have a rhombohedral structure of the NZP type.

In order to justify this prediction, we investigated the phosphates of the $T^{II}_{1/3}T^{V}_{5/3}(PO_4)_3$ [38, 39] and $T^{III}_{1/2}T^{V}_{3/2}(PO_4)_3$ types (T^{II} = Mg, Mn, Co, Ni; T^{III} = Al, Cr, Fe; T^{V} = Nb). The phosphates were synthesized

Table 3. Crystallographic properties of new niobium phosphates (structure type $NaZr_2(PO_4)_3$, sp. gr. $R\bar{3}c$)

Phosphate	Radii of cations, Å				a, Å	c, Å	V, Å^3
	$r(T^{II})$	$r(T^{III})$	r(Nb)	$\Delta r/r_{min}$			
$Mg_{1/3}Nb_{5/3}(PO_4)_3$ [38]	0.72		0.64	0.13	8.642	22.11	1430
$Mn_{1/3}Nb_{5/3}(PO_4)_3$ [39]	0.83		0.64	0.30	8.649(1)	22.126(3)	1433.3(4)
$Co_{1/3}Nb_{5/3}(PO_4)_3$ [38]	0.75		0.64	0.17	8.642	22.09	1429
$Ni_{1/3}Nb_{5/3}(PO_4)_3$ [38]	0.69		0.64	0.08	8.637	22.08	1429
$Al_{1/2}Nb_{3/2}(PO_4)_3$		0.53	0.64	0.21	8.577(5)	21.98(2)	1397(2)
$Cr_{1/2}Nb_{3/2}(PO_4)_3$		0.62	0.64	0.03	8.592(5)	22.03(2)	1408(2)
$Fe_{1/2}Nb_{3/2}(PO_4)_3$ [40]		0.55	0.64	0.16	8.6317(6)	22.125(1)	1427.6

Table 4. Thermal-expansion parameters of niobium phosphates with divalent and trivalent elements

Phosphate	Coefficients of thermal expansion;			Anisotropy of thermal expansion $\Delta\alpha \times 10^6$ K^{-1}
	$\alpha_a \times 10^6$ K^{-1}	$\alpha_c \times 10^6$ K^{-1}	$\alpha_{av} \times 10^6$ K^{-1}	
$Mg_{1/3}Nb_{5/3}(PO_4)_3$	–2.3	3.4	−0.39	5.7
$Co_{1/3}Nb_{5/3}(PO_4)_3$	–1.5	4.4	0.45	5.9
$Ni_{1/3}Nb_{5/3}(PO_4)_3$	–2.2	3.0	−1.53	5.2
$Al_{1/2}Nb_{3/2}(PO_4)_3$	–1.1	0	<0	–1.1
$Cr_{1/2}Nb_{3/2}(PO_4)_3$	–2.3	1.4	−1.05	3.7
$Fe_{1/2}Nb_{3/2}(PO_4)_3$	–2.6	1.3	−1.31	3.9

using a technique based on sintering of corresponding oxides upon their heating to 900°C [38]. X-ray diffraction analysis showed that these phosphates belong to the $NaZr_2(PO_4)_3$ structure type. $TiNb(PO_4)_3$ (sp. gr. $R\bar{3}c$) was used as an analog for purposes of identification [5]. Rietveld refinement of the $Fe_{1/2}Nb_{3/2}(PO_4)_3$ structure was performed using neutron powder diffraction analysis [40]. It was shown that Fe and Nb cations occupy L positions of mixed cation–anion framework in the structure of this phosphate, whereas interframework positions M_1 and M_2 remain unoccupied.

The investigations of the $Mg_{1/3}Nb_{5/3}(PO_4)_3$, $Mn_{1/3}Nb_{5/3}(PO_4)_3$, $Co_{1/3}Nb_{5/3}(PO_4)_3$, $Ni_{1/3}Nb_{5/3}(PO_4)_3$, $Al_{1/2}Nb_{3/2}(PO_4)_3$, $Cr_{1/2}Nb_{3/2}(PO_4)_3$, and $Fe_{1/2}Nb_{3/2}(PO_4)_3$ phosphates that we performed and described in [38, 39] showed that all these compounds are synthesized in a single phase and crystallized in the NZP structure type (sp. gr. $R\bar{3}c$).

The unit-cell parameters a and c are listed in Table 3, along with differences in the radii $\Delta r/r_{min}$ ($\Delta r = |r(T^{II}) - r(T^{V})|$ or $|r(T^{III}) - r(T^{V})|$) for framework-forming cations. The values of the differences in the radii are in agreement with the established range of implementation of the NZP structure type (Fig. 1).

It is well known that the properties of compounds with an expected composition and structure can also be predicted in accordance with the basic principle of materials science: composition–structure–property.

One property of practical importance that is generally typical of NZP phosphates is their low thermal expansion in a wide temperature range. Small deformations of the NZP structure upon heating are due to the presence of rigidly bound TO_6 and XO_4 polyhedra in its framework and depend on the number of unoccupied M cages. With an increase in the number of unoccupied positions, temperature-induced deformations tend to decrease [41]. The known phosphates with a very low thermal expansion—$Na_{0.5}Zr_{0.125}Zr_2(PO_4)_3$ [42], $Sr_{0.5}Zr_2(PO_4)_3$ [43, 44], $T^{III}_{0.33}Zr_2(PO_4)_3$ (T^{III} = La, Gd) [45], $Sr_{0.25}Nb_{0.5}Zr_{1.5}(PO_4)_3$ [44], and $ZrNb(PO_4)_3$ [7, 8, 46]—have partially occupied or completely unoccupied M positions. Therefore, very little thermal expansion should also be expected for NZP-type phosphates with a formula composition corresponding to an electrically neutral framework; i.e., when $n = 0$ and all the M positions are unoccupied.

Compounds of the $T^{II}_{1/3}T^{V}_{5/3}(PO_4)_3$ and $T^{III}_{1/2}T^{V}_{3/2}(PO_4)_3$ types obtained according to the above prediction for their composition and structure were studied by high-temperature X-ray diffraction in the temperature range $20 \leq t \leq 800$°C. The measuring technique was described in [38]. The thermal-expansion parameters (Table 4) indicate that all the phosphates have an anisotropy of axial thermal expansion ($\alpha_a < 0$, $\alpha_c > 0$) and average expansion α_{av} close to zero. Such behavior upon heating is characteristic of compounds with an NZP structure [47]. It should be noted that some of the phosphates obtained ($Al_{1/2}Nb_{3/2}(PO_4)_3$, $Fe_{1/2}Nb_{3/2}(PO_4)_3$) have, simultaneously, close to zero expansion and very small thermal-expansion anisotropy ($\Delta\alpha = -1.1 \times 10^{-6}$ 1/K and 3.9×10^{-6} 1/K, respectively).

Thus, the results obtained justify the crystal–chemical predictions concerning not only the composition and structure but, also, the properties of niobium phosphates and extend the possibilities of developing new materials.

CONCLUSIONS

In this study, we calculated and reported theoretically possible formula compositions of frameworks of the $\{[T_2(PO_4)_3]^{n-}\}_{3\infty}$ type. It is shown that most of them (containing elements in the oxidation state +5) have not been studied, while most of the known ones have been investigated in the last decade.

That phosphates of tetravalent and pentavalent elements have a similar structure was revealed: structure type $NaZr_2(PO_4)_3$ is most common for both.

On the basis of analysis of available data and the results of our experiments, a correlation between the structure type of phosphates and the relative difference in the ionic radii of framework-forming cations is established. For NZP-like phosphates, this parameter should not exceed 0.6.

The possibility of modeling compounds with expected structures and specified properties is shown and verified by an example of niobium phosphates.

New niobium phosphates with electrically neutral frameworks of the $T^{II}_{1/3}Nb_{5/3}(PO_4)_3$ and $T^{III}_{1/2}Nb_{3/2}(PO_4)_3$ types (T^{II} = Mg, Mn, Co, Ni; T^{III} = Al, Cr, Fe) were synthesized, and their crystallographic properties and thermal-expansion parameters were determined.

The results obtained confirm the predictions for composition, structure, and properties that were made for the compounds under consideration and expand possibilities of developing materials with expected and controlled properties on the basis of crystal–chemical data.

ACKNOWLEDGMENTS

This study was supported by the Russian Foundation for Basic Research, project no. 01-03-33013.

REFERENCES

1. R. G. Sizova, V. A. Blinov, A. A. Voronkov, *et al.*, Kristallografiya **26** (2), 293 (1981) [Sov. Phys. Crystallogr. **26**, 165 (1981)].
2. A. I. Orlova, Radiokhimiya **44** (5), 385 (2002).
3. R. D. Shannon, Acta Crystallogr., Sect. A: Cryst. Phys., Diffr., Theor. Gen. Crystallogr. **32**, 751 (1976).
4. R. Masse, A. Durif, J. C. Guitel, and I. Tordjman, Bull. Soc. Fr. Mineral. Cristallogr. **95** (1), 47 (1972).
5. F. J. Berry, C. Greaves, and J. F. Marco, J. Solid State Chem. 408 (1992).
6. P. A. Agaskar, R. K. Grasselli, D. J. Buttrey, and B. White, Stud. Surf. Sci. Catal. **110**, 219 (1997).
7. D. Taylor, Br. Ceram. Trans. J. **90** (2), 64 (1991).
8. K. V. Govindan Kutty, R. Asuvathraman, S. K. Mathews, and U. V. Varadaraju, Mater. Res. Bull. **29** (10), 1009 (1994).
9. A. D. Naramudayan and C. P. Kashinath, J. Mater. Chem. **5** (9), 1463 (1995).
10. A. Leclaire, M.-M. Borel, A. Grandin, and B. Raveau, Acta Crystallogr., Sect. C: Cryst. Struct. Commun. **45** (5), 699 (1989).
11. D. A. Stratiĭchuk, V. V. Lesnyak, M. S. Slobodyanik, and N. V. Stus', Zh. Neorg. Khim. **46** (9), 1449 (2001).
12. K. Kasthuri Rangan and J. Gopalakrishnan, Inorg. Chem. **34** (7), 1969 (1995).
13. M. Manickam, J. Power Sources **113**, 179 (2003).
14. A. Jouanneaux, A. N. Fitch, S. Oyetola, *et al.*, Eur. J. Solid State Inorg. Chem. **30** (1–2), 125 (1993).
15. A. Jouanneaux, A. Verbaere, D. Guyomard, *et al.*, Eur. J. Solid State Inorg. Chem. **28**, 755 (1991).
16. S. Oyetola, A. Verbaere, D. Guyomard, and Y. Piffard, J. Solid State Chem. **77**, 102 (1988).
17. M. Vithal, B. Srinivasulu, K. K. Rao, and Ch. M. Rao, Mater. Lett. **45**, 58 (2000).
18. B. Srinivasulu and M. Vithal, J. Mater. Sci. Lett. **18**, 1771 (1999).
19. V. Thangadurai, A. K. Shukla, and J. Gopalakrishnan, J. Mater. Chem. **9**, 739 (1999).
20. L. Znaidi, S. Launay, and M. Quarton, Solid State Ionics **93** (3–4), 273 (1997).
21. A. K. Padhi, K. S. Nanjundaswamy, C. Masquelier, and J. B. Goodenough, J. Electrochem. Soc. **144** (8), 2581 (1997).
22. O. Tillement, J. S. Couturier, J. Angenault, and M. Quarton, Solid State Ionics **48**, 249 (1991).
23. L. Bennouna, S. Arsalane, R. Brochu, *et al.*, J. Solid State Chem. **114** (1), 224 (1995).
24. U. V. Varadaraju, K. A. Thomas, B. Savasankar, and J. V. Subba Rao, Izv. Sib. Otd. Akad. Nauk SSSR, Ser. Khim. Nauk, No. 19/6, 10 (1987).
25. S. N. Nemnonov, V. V. Shumilov, V. M. Cherkashenko, and É. Z. Kurmaev, Zh. Strukt. Khim. **32** (1), 161 (1991).
26. A. El Jazouli, A. Serghini, R. Brochu, *et al.*, C. R. Acad. Sci., Ser. II **300** (11), 493 (1985).
27. J. F. Marco, J. R. Gancedo, and F. J. Berry, Polyhedron **16** (17), 2957 (1997).
28. L. Bennouna, M.-R. Lee, R. Brochu, and M. Quarton, C. R. Acad. Sci., Ser. II **310** (6), 727 (1990).

29. S. Aoustin, O. Tillement, and M. Quarton, Mater. Res. Bull. **27**, 1015 (1992).
30. A. El Jazouli, A. El Bouari, H. Fakrane, *et al.*, J. Alloys Compd. **262–263**, 49 (1997).
31. A. Housni, I. Mansouri, A. El Jazouli, *et al.*, Ann. Chim. Sci. Mater. **23**, 73 (1998).
32. X. Cieren, S. Jaulmes, J. Angenault, *et al.*, Acta Crystallogr., Sect. C: Cryst. Struct. Commun. **39**, 2967 (1996).
33. A. El Jazouli, C. Parent, J. M. Dance, and G. Le Flem, C. R. Acad. Sci., Ser. II **303** (11), 1005 (1986).
34. J. Alamo, Solid State Ionics **63–65**, 547 (1993).
35. F. Sedrau, D. Petit, and J. P. Boilot, J. Solid State Chem. **83**, 78 (1989).
36. A. Jouanneaux, A. Verbaere, Y. Piffard, *et al.*, J. Solid State Chem. **71**, 121 (1987).
37. B. I. Lazoryak, Usp. Khim. **65** (4), 307 (1996).
38. A. I. Orlova, V. I. Pet'kov, M. V. Zharinova, *et al.*, Zh. Prikl. Khim. (St. Petersburg) **76** (1), 14 (2003).
39. V. I. Pet'kov, A. I. Orlova, M. V. Sukhanov, *et al.*, J. Mater. Sci. Lett. **21**, 513 (2002).
40. I. G. Trubach, A. I. Orlova, A. I. Beskrovnyĭ, *et al.*, Kristallografiya **49** (3), 445 (2004).
41. A. I. Orlova, D. V. Kemenov, V. I. Pet'kov, *et al.*, High Temp. High Press. **34** (3), 315 (2002).
42. A. I. Orlova, D. V. Kemenov, S. G. Samoĭlov, *et al.*, Neorg. Mater. **36** (8), 995 (2000).
43. K. V. Govindan Kutty, R. Asuvathraman, and R. Sridharan, J. Mater. Sci. **33**, 4007 (1998).
44. T. Ota, P. Jin, and I. Yamai, J. Mater. Sci. **24**, 4239 (1989).
45. J. M. Heintz, L. Rabardel, M. Al Qaraoui, *et al.*, J. Alloys Compd. **250**, 515 (1997).
46. T. Oota and I. Yamai, J. Am. Ceram. Soc. **69** (1), 1 (1986).
47. A. W. Sleight, Endeavour **19** (2), 64 (1995).

Translated by Yu. Sin'kov

Crystallography Reports, Vol. 49, No. 5, 2004, pp. 733–740. Translated from Kristallografiya, Vol. 49, No. 5, 2004, pp. 820–828.
Original Russian Text Copyright © 2004 by Olekhnovich.

STRUCTURE
OF INORGANIC COMPOUNDS

Unstrained Bond Lengths and Corresponding Cation Radii in Crystals with Perovskite Structure

N. M. Olekhnovich

Institute of Solid-State and Semiconductor Physics, National Academy of Sciences of Belarus,
ul. Brovki 17, Minsk, 220072 Belarus
e-mail: olekhnov@ifttp.bas-net.by

Received September 1, 2002

Abstract—A method for determining average lengths of unstrained bands *A*–*X* (l_{0AX}) and *B*–*X* (l_{0BX}) and the ratio of the rigidity constants of these bonds for ABX_3 compounds with perovskite structure is proposed. The values of l_{0AX} and l_{0BX} correspond to the minimum energies of cation–anion interaction of the crystal sublattices. Values of l_{0AX} and l_{0BX} are obtained for several groups of halide and oxide compounds: $A^+B^{2+}F_3$, $Cs^+B^{2+}Cl_3$, $A^+B^{5+}O_3$, $A^{2+}B^{4+}O_3$, and $A^{3+}B^{3+}O_3$. It is ascertained that, for most compounds studied, the values of l_{0AX} and l_{0BX} are equal or close to the interatomic distances in crystals of binary compounds. The values of l_{0AX} and l_{0BX} are compared with the sums of the radii of the corresponding cations (R_A, R_B) and anions (${}^{\mathrm{VI}}R_{\mathrm{O}^{2-}}$, ${}^{\mathrm{VI}}R_{\mathrm{F}^-}$, ${}^{\mathrm{VI}}R_{\mathrm{Cl}^-}$). It is found that the differences $l_{0\mathrm{AO}} - {}^{\mathrm{VI}}R_{\mathrm{O}^{2-}}$ ($L_{0\mathrm{AF}} - {}^{\mathrm{VI}}R_{\mathrm{F}^-}$) and $l_{0\mathrm{BO}} - {}^{\mathrm{VI}}R_{\mathrm{O}^{2-}}$ ($l_{0\mathrm{BF}} - {}^{\mathrm{VI}}R_{\mathrm{F}^-}$), regarded as the radii of the *A* and *B* cations in unstrained bonds, are close to the Shannon radii for a coordination number of six. It is shown that the rigidity constant for *A*–*X* bonds is several times smaller than that for *B*–*X* bonds. © *2004 MAIK "Nauka/Interperiodica".*

INTRODUCTION

Among binary and more complex oxides and halides, a large class of compounds is known that have an ideal (cubic) or distorted (of lower symmetry) perovskite structure. In the ideal cubic structure of ABX_3 compounds, cations are located at the centers of BX_6 octahedra and AX_{12} dodecahedra. The distances between the nearest ions *A*–*X* (bond lengths l_{0AX}) and *B*–*X* (bond lengths l_{0BX}) in this structure are determined by the sum of their effective radii and satisfy the condition $l_{0AX}/\sqrt{2}l_{0BX} = t = 1$ (*t* is the tolerance factor) [1, 2]. They correspond to the minima of the potential energy of interaction between ions in the sublattices, i.e., U_{0A} and U_{0B}. This circumstance means that the bonds are unstrained and l_{0AX} and l_{0BX} are the unstrained-bond lengths.

Most compounds of this family have a distorted structure, and the ratio of the effective ion radii for these compounds differs from the one for the ideal structure (the tolerance factor $t \neq 1$). Due to the difference in the ion sizes, the lengths of the *A*–*X* and *B*–*X* bonds differ from l_{0AX} and l_{0BX}. At these bond lengths, the potential energies of the sublattices do not reach minima corresponding to the ideal structure. As a result, the bonds become strained. In this case, the total energy of the system and its components U_A and U_B increase. The energy of bond strengthening ($\Delta U_s = (U_A + U_B) - (U_{0A} + U_{0B})$) is an important factor for understanding the structural features and physical properties of compounds with perovskite structure. This energy is the driving force responsible for the occurrence of ordered structural distortions, which reduce ΔU_s at a transition of a system to a more stable state. The character of these distortions depends on the nature of the atoms forming ABX_3 compounds and temperature. However, the question of bond strengthening in crystals with perovskite structure has not been adequately studied [1–3].

To estimate quantitatively the energy of strained bonds and the character of its dependence on the distortion parameters and to estimate the distortion parameters themselves, one has to know the lengths of unstrained bonds or the corresponding values of effective ionic radii. The possibility of using the most complete system of effective ionic radii [4] for the above purposes and the limits of its applicability require special analysis.

In this study, on the basis of the structural data reported in [1, 2, 5], we determined the average unstrained bond lengths l_{0AX} and l_{0BX} for binary halides and oxides ($A^+B^{2+}F_3$, $Cs^+B^{2+}Cl_3$, $A^+B^{5+}O_3$, $A^{2+}B^{4+}O_3$, and $A^{3+}B^{3+}O_3$) with perovskite structure. The found values of l_{0AX} and l_{0BX} are compared with the sums of the radii of the corresponding cations (R_A, R_B) and anions

$({}^{\mathrm{VI}}R_{\mathrm{O}^{2-}}, {}^{\mathrm{VI}}R_{\mathrm{F}^{-}}, {}^{\mathrm{VI}}R_{\mathrm{Cl}^{-}})$ according to Shannon [4]. With this purpose, we determined the differences $R_{0A} = l_{0AO} - {}^{\mathrm{VI}}R_{\mathrm{O}^{2-}}$ $(l_{0AF} - {}^{\mathrm{VI}}R_{\mathrm{F}^{-}})$ and $R_{0B} = l_{0BO} - {}^{\mathrm{VI}}R_{\mathrm{O}^{2-}}$ $(l_{0BF} - {}^{\mathrm{VI}}R_{\mathrm{F}^{-}})$, regarded as the radii of the A and B cations corresponding to the average unstrained-bond lengths. It is ascertained that R_{0A} and R_{0B} are similar to the Shannon radii reported in [4] for a coordination number of six.

METHOD OF STUDY

A phase transition in a crystal from a distorted perovskite structure to the cubic structure, occurring at some temperature, is accompanied by relatively small changes in the crystal volume. Therefore, solving the problem stated in the first-order approximation, we can restrict our consideration to a cubic structure with the average parameter of a reduced cubic cell $a = (V/p)^{1/3}$, where V is the volume of the unit cell of the distorted structure and p is the number of formula units.

Let us consider the potential energy of interatomic interaction U for such a model crystal lattice ($T = 0$ K). In the two-body approximation, U is determined by the sum of the sublattice energies,

$$U(l_{AX}, l_{BX}) = U_A(l_{AX}) + U_B(l_{BX}), \tag{1}$$

which depend, respectively, on the distances in the pairs A–X (l_{AX}) and B–X (l_{BX}). For example, for ionic bonds, these components can be described by functions of the Born–Mayer potential type [6].

The minima of the functions $U_A(l_{AX})$ and $U_B(l_{BX})$ correspond to the equilibrium unstrained-bond lengths l_{0AX} and l_{0BX}. The strained-bond lengths l_{AX} and l_{BX} are expressed in terms of the average parameter a of the reduced cubic cell:

$$l_{BX} = l_{AX}/\sqrt{2} = \frac{a}{2}. \tag{2}$$

To estimate the interatomic interaction energy in the strained state, one can expand the components U_A and U_B in series, limiting the expansion to the second order of smallness:

$$\begin{aligned} U(l_{AX}, l_{BX}) &= U(l_{0AX}, l_{0BX}) \\ &+ \frac{C_A}{2}\left(\frac{a}{\sqrt{2}} - l_{0AX}\right)^2 + \frac{C_B}{2}\left(\frac{a}{2} - l_{0BX}\right)^2, \end{aligned} \tag{3}$$

where $C_A = \left(\dfrac{d^2U_A}{dl_{AX}^2}\right)_{l_{0,AX}}$ and $C_B = \left(\dfrac{d^2U_B}{dl_{BX}^2}\right)_{l_{0,BX}}$ are the rigidity constants of the A–X and B–X bonds, respectively.

The energy-minimum condition ($dU/da = 0$) yields the following expression for the average parameter a:

$$a = \frac{1}{1+2\eta}2l_{0BX} + \frac{2\eta}{1+2\eta}\sqrt{2}l_{0AX}, \tag{4}$$

where $\eta = C_A/C_B$ is a parameter depending on the character of the interatomic interaction. The quantities l_{0AX}, l_{0BX}, and η in (4) can be estimated from analysis of the average parameter of the reduced cell in homologous series of ABX_3 compounds. With this purpose, we will consider two types of such series. The homologous series of the first type (I) contains compounds with compositions differing only in the element B. A certain element A corresponds to each series of type I. The homologous series of the second type (II) contain compounds differing only in the element A and a certain element B corresponds to each series of type II.

Let us consider the differences $2l_{0BX} - a$ and $a - \sqrt{2}\,l_{0AX}$, which characterize a change in the average parameter of the reduced cell due to the bond strengthening for homologous series I and II, respectively. On the basis of (4), these differences can be written as

$$2l_{0BX} - a = \frac{4\eta}{1+2\eta}(l_{0BX} - l_{0AX}/\sqrt{2}), \tag{5}$$

$$a - \sqrt{2}l_{0AX} = \frac{2}{1+2\eta}(l_{0BX} - l_{0AX}/\sqrt{2}). \tag{6}$$

These relations describe the dependences of the differences $2l_{0BX} - a$ on l_{0BX} and $a - \sqrt{2}\,l_{0AX}$ on $l_{0AX}/\sqrt{2}$ for series I and II at fixed values of l_{0AX} in (5) and l_{0BX} in (6), respectively.

Since the spread of the ratio of the rigidity constants (3) for a number of compounds with a similar character of interatomic interaction is small, the parameter η for the representatives of the homologous series I or II, including the noted compounds, can be considered constant with some approximation. In this case, relations (5) and (6) demonstrate the linearity of the noted dependences for representatives of series I and II, respectively. Therefore, the slope $(\tan\gamma)$ of the observed straight line and the segment (l^0_{0BX}) intercept by this line on the abscissa axis determine, according to (5), the parameter η and the value of l_{0AX} for each homologous series I with a fixed element A:

$$\begin{aligned} \eta &= \frac{\tan\gamma}{4 - 2\tan\gamma}, \\ l_{0AX} &= \sqrt{2}l^0_{0BX}. \end{aligned} \tag{7}$$

Similarly, for each homologous series II:

$$\begin{aligned} \eta &= \frac{2 - |\tan\varepsilon|}{2|\tan\varepsilon|}, \\ l_{0BX} &= l^0_{0AX}/\sqrt{2}, \end{aligned} \tag{8}$$

where $l^0_{0AX}/\sqrt{2}$ is the segment intercept by the observed straight line on the abscissa axis (according to (6)) and $\tan\varepsilon$ is the slope of this line.

We present below the results of using this approach for determination of the average unstrained-bond lengths l_{0AX} and l_{0BX} and the corresponding cation radii for $A^+B^{2+}F_3$, $Cs^+B^{2+}Cl_3$, $A^+B^{5+}O_3$, $A^{2+}B^{4+}O_3$, and $A^{3+}B^{3+}O_3$ compounds.

HALIDE COMPOUNDS

The average parameter a of the reduced unit cell for halide perovskites was calculated from the structural data reported in [2]. Analysis of a for homologous series was performed in several stages, i.e., by the method of successive approximations.

First, it was assumed that the interatomic distances $B – X(l_{0BX})$ corresponding to unstrained bonds in perovskites are similar to those in the corresponding binary compounds BX_2, especially the ones in which the B^{2+} cation is in the octahedral coordination, as in perovskite. Since the values of the ionic radii found in [4] for a coordination number of six correspond, as a rule, to the interatomic distances in the noted binary compounds, the value of l_{0BX} was assumed to be equal to the sum of the above-mentioned ionic radii ($l_{0BX} = {}^{VI}R_{B^{2+}} + {}^{VI}R_{X^-}$) in the first stage (the superscript, as in [4], denotes the coordination number).

The values of l_{0BX} found in the first stage were used to plot the dependences of $2l_{0BX} – a$ on l_{0BX} in accordance with (5) for each homologous series I. Figure 1a shows the results obtained for several series of this type. As can be seen, despite some spread of the points, the dependence analyzed is, as a whole, linear for each homologous series. The spread of points is due to both possible spread of the parameter η for the compounds in the same series and an error in the choice of the values of l_{0BX}. It is noteworthy that, for the homologous series with Na, K, Rb, Cs, and NH_4, the approximating straight lines have almost the same slope. According to (5) and (7), this means that the values of η for these series are similar to each other. Due to this, the values of l_{0BX} can be refined by analyzing the dependence of $a - \sqrt{2}\, l_{0AX}$ on $l_{0AX}/\sqrt{2}$ (6), (8) (considering homologous series II). With this purpose, the values of l_{0AX} were estimated from segments intercept on the abscissa axis by the straight lines in Fig. 1a. Note that, due to the observed spread of points, some errors are possible in estimation of l_{0AX} in this stage of the analysis. However, since l_{0AX} enters both the left- and right-hand sides of Eq. (6), these errors only slightly affect the slopes of the dependences $a - \sqrt{2}\, l_{0AX}$ on $l_{0AX}/\sqrt{2}$ and, accordingly, the accuracy of estimating l_{0BX}.

The values of l_{0BX}, refined in the first stage, were used to perform the second refinement iteration. This iterative analysis revealed that the dependence of $2l_{0BX} – a$ on l_{0BX} for each homologous series I has a pronounced linear character (Fig. 1b): the points in the plots are fitted by straight lines within the error in determining the l_{0BX} values.

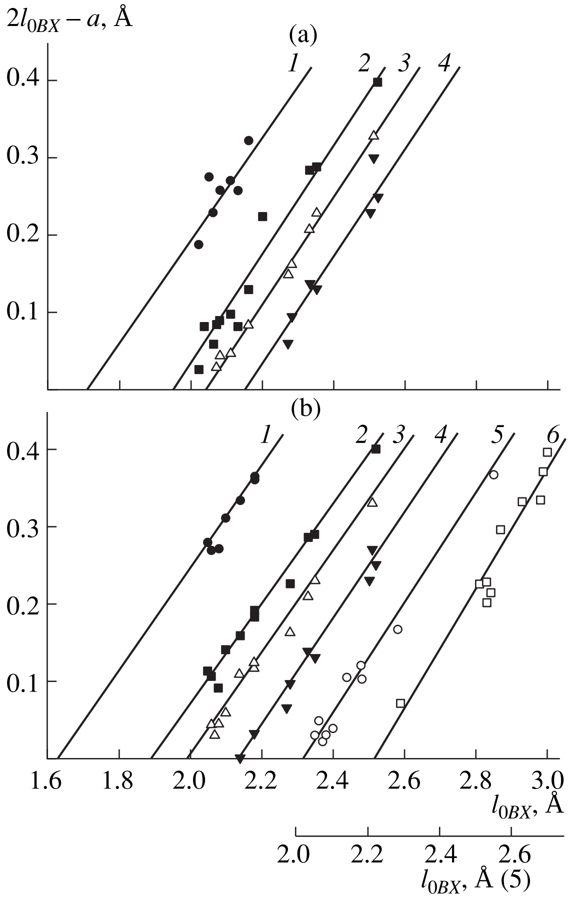

Fig. 1. Dependence of the change in the average unit-cell parameter on the length of unstrained $B–X$ bonds for the (*1*) $NaBF_3$, (*2*) KBF_3, (*3*) $RbBF_3$, (*4*) $CsBF_3$, (*5*) NH_4BF_3, and (*6*) $CsBCl_3$ perovskites. (a) One iteration and (b) two iterations.

The average values of the unstrained-bond lengths l_{0BX} and l_{0AX} and the parameter η obtained from the analysis are listed in Table 1. In most cases, the error in determining l_{0BX} and l_{0AX} was within 0.01 Å. For comparison, the interatomic distances $A–X$ and $B–X$ (L_{AX}, L_{BX}) in binary compounds of the AX and AX_2 types, respectively, are also listed in Table 1.

The found values of l_{0BX} and l_{0AX} were compared with the sums of the radii of the corresponding cations (R_A, R_B) and anions (${}^{VI}R_{F^-}$, ${}^{VI}R_{Cl^-}$) reported in [4]. With this purpose, we determined the differences $R_{0A} = l_{0AX} - {}^{VI}R_{X^-}$ and $R_{0B} = l_{0BX} - {}^{VI}R_{X^-}$, which can be considered the cation radii corresponding to the average unstrained-bond lengths. It was assumed that ${}^{VI}R_{F^-}$ =

Table 1. Average unstrained-bond lengths *l*, cation radii *R*, and rigidity constants η for $A^+B^{2+}F_3$ and $Cs^+B^{2+}Cl_3$ compounds

A–*X* bonds

homologous series II	l_{0AX}, Å	R_{0A^+}, Å	*AX** binary compounds: structure type (space group)	*AX** binary compounds: L_{AX}, Å	$^{XII}R_{A^+}$, Å [4]	$^{VI}R_{A^+}$, Å [4]	η	η_{calcd}
$NaBF_3$	2.31	1.12	NaCl ($O_h^5 - Fm\bar{3}m$)	2.31	1.53	1.16	0.23	0.26
KBF_3	2.67	1.48		2.67	1.78	1.52	0.25	0.27
$RbBF_3$	2.82	1.63		2.82	1.86	1.66	0.25	0.27
$CsBF_3$	3.01	1.82		3.01	2.02	1.81	0.24	0.27
NH_4BF_3	2.86	1.67	ZnS ($C_{6v}^4 - P6mc$)	2.68			0.25	
$AgBF_3$	2.56	1.37	($O_h^1 - Pm3m$)	2.55		1.29	0.25	
$TlBF_3$	2.87	1.68	($D_{4h}^{17} - I4/mmm$)	2.84	1.82	1.64	0.26	
$CsBCl_3$	3.56	1.88	($O_h^1 - Pm3m$)	3.57	2.02	1.81	0.32	

B–*X* bonds

homologous series I	l_{0BX}, Å	$R_{0B^{2+}}$, Å	BX_2^* binary compounds: structure type (space group)	BX_2^* binary compounds: L_{BX}, Å	$^{VI}R_{B^{2+}}$, Å [4]
$AMgF_3$	2.05	0.86	TiO_2, rutile ($D_{4h}^{14} - P4_2/mnm$)	2.05	0.86
$ANiF_3$	2.06	0.87		2.03	0.83
$AZnF_3$	2.07	0.88		2.04	0.88
$ACoF_3$	2.08	0.89		2.07	$0.89^{(HS)**}$
$AFeF_3$	2.14	0.95		2.10	$0.92^{(HS)}$
$AMnF_3$	2.18	0.99		2.12	$0.97^{(HS)}$
$ACrF_3$	2.18	0.99	($C_{2h}^2 - P2_1/m$)	2.13	$0.94^{(HS)}$
$ACuF_3$	2.10	0.91	CaF_2 ($O_h^5 - Fm\bar{3}m$)	2.34	0.87
$AAgF_3$	2.27	1.08		2.36	1.08
$ACdF_3$	2.28	1.09		2.34	1.08
$ACaF_3$	2.33	1.14		2.36	1.14
$AHgF_3$	2.35	1.16		2.40	1.16
$APbF_3$	2.52	1.33		2.58	1.33

* Here and in Tables 2–4, the lengths of corresponding interatomic distances *L* in binary compounds are given for comparison with unstrained bonds.

** High-spin state.

1.19 and $^{VI}R_{Cl^-}$ = 1.67 Å. These values, according to [4], are most similar to the physical sizes of ions in solids. Table 1 contains also the values of the cation radii accepted in [4] for coordination numbers of 12 and 6 (^{XII}R and ^{VI}R, respectively).

For compounds characterized by predominantly ionic bonds, the ratio of the rigidity constants was calculated based on the ionic crystal model (3), (4):

$$\eta_c = \frac{\left(\dfrac{d^2U_A}{dl_{AX}^2}\right)_{l_{0AX}}}{\left(\dfrac{d^2U_B}{dl_{BX}^2}\right)_{l_{0BX}}}. \qquad (9)$$

Table 2. Average unstrained-bond lengths *l*, cation radii *R*, and rigidity constants η for $A^+B^{2+}O_3$ compounds

A–O bonds

homologous series II	l_{0AO}, Å	R_{0A^+}, Å	A_2O binary compounds: structure type (space group)	A_2O binary compounds: L_{AO}, Å	$^{XII}R_{A^+}$, Å [4]	$^{VI}R_{A^+}$, Å [4]
Na*B*O$_3$	2.38	1.12	CaF_2 ($O_h^5 - Fm\bar{3}m$)	2.41	1.53	1.16
K*B*O$_3$	2.74	1.48		2.79	1.78	1.52
Rb*B*O$_3$	2.88	1.62		2.92	1.86	1.66
Cs*B*O$_3$	3.13	1.87	$CdCl_2$ ($D_{3d}^5 - R\bar{3}m$)	3.16	2.02	1.81

B–O bonds

homologous series I	l_{0BO}, Å	$R_{0B^{5+}}$, Å	B_2O_5 binary compounds: space group	B_2O_5 binary compounds: L_{BO}, Å	$^{VI}R_{B^{5+}}$, Å [4]	η
*A*NbO$_3$	2.03	0.77	$C_{2h}^6 - B2/b$	2.02	0.78	0.123
*A*TaO$_3$	2.01	0.75	$C_{2v} - C2mm$	1.97	0.78	0.136
*A*UO$_3$	2.23	0.97	$D_{2h}^5 - Pnma$	2.21	0.90	0.236
*A*PaO$_3$	2.27	1.01			0.92	0.248
*A*IO$_3$	2.42	1.16	$C_{2h}^5 - P2_1/c$	2.00	1.09	0.385

Within this model, U_A and U_B were represented by Born–Mayer functions and their second derivatives were calculated. The substitution of the calculated derivatives into (9), with regard to the equality $l_{0BX} = l_{0AX}/\sqrt{2}$, yields the following expression for fluorides:

$$\eta_c = \frac{(\alpha'_A + \alpha'_F)\left(\frac{l_{0AF}}{\rho_A} - 2\right)}{4(2\alpha'_B + \alpha'_F)\left(\frac{l_{0AF}}{\sqrt{2}\rho_B} - 2\right)}, \qquad (10)$$

where α'_A, α'_B, and α'_F are the reduced partial Madelung constants [6] for A^+, B^{2+}, and F^- ions, respectively. The parameters ρ_A and ρ_B in (10) were estimated using the corresponding values for binary compounds (fluorides of alkali and alkaline-earth elements).

The values of η found from the above analysis of the structural data are in satisfactory agreement (within a determination error) with the calculated values (Table 1).

As can be seen from Table 1, the lengths of the unstrained *A*–*X* bonds in ABF_3 and $CsBCl_3$ crystals almost coincide with the interatomic distances in the corresponding *AX* binary crystals with the NaCl-type structure despite the difference in the coordination numbers for the A^+ cation (12, 8, and 6 for the perovskite, CsCl, and NaCl structures, respectively). It is noteworthy that, for the NH_4BF_3 family, the length of the unstrained bond NH_4^+–F^- in the perovskite structure is much larger than the corresponding distance in NH_4F crystals. As a result, the values of the radii of A^+ cations (R_{0A^+}) corresponding to the average lengths of unstrained *A*–*X* bonds in perovskite structures are similar to the values taken in [4] for a coordination number of 6 ($^{VI}R_{A^+}$) and significantly smaller than the noted values for a coordination number of 12 ($^{XII}R_{A^+}$) (Table 1).

The relation between the lengths of unstrained *B*–*X* bonds (l_{0BX}) in perovskite structures and interatomic distances in BX_2 binary compounds (L_{BX}) depends on the structural type of the latter: $l_{0BX} \geq L_{BX}$ or $l_{0BX} < L_{BX}$ if a binary compound has a rutile (TiO_2) or fluorite (CaF_2) structure, respectively.

OXIDE COMPOUNDS

The unstrained-bond lengths (l_{0AO} and l_{0BO}) in $A^+B^{5+}O_3$, $A^{2+}B^{4+}O_3$, and $A^{3+}B^{3+}O_3$ oxide crystals were determined from the structural data reported in [1, 5]. Since the parameter η (4) for a group of the compounds $A^+B^{5+}O_3$ (*A* = Na, K, Rb, Cs; *B* = Nb, Ta, U, Pa, I) was found to be strongly dependent on the nature of the B^{5+} cation, the unstrained-bond lengths l_{0AO} were finally

Table 3. Average unstrained-bond lengths l, cation radii R, and rigidity constants η for $A^{2+}B^{4+}O_3$ compounds

A–O bonds

homologous series II	l_{0AO}, Å	$R_{0A^{2+}}$, Å	*A*O binary compounds		$^{XII}R_{A^{2+}}$, Å [4]	$^{VI}R_{A^{2+}}$, Å [4]
			structure type (space group)	L_{AO}, Å		
Cd*B*O$_3$	2.35	1.09	NCl ($O_h^5 - Fm\bar{3}m$)	2.35	1.45	1.09
Ca*B*O$_3$	2.40	1.14		2.40	1.48	1.14
Sr*B*O$_3$	2.58	1.32		2.58	1.58	1.32
Ba*B*O$_3$	2.78	1.52		2.77	1.75	1.49
Pb*B*O$_3$	2.76	1.50	SnO ($D_{4h}^7 - Pnmm$)	2.87	1.63	1.33

B–O bonds

homologous series I	l_{0BO}, Å	$R_{0B^{4+}}$, Å	*B*O$_2$ binary compounds		$^{VI}R_{B^{4+}}$, Å [4]	η
			structure type (space group)	L_{BO}, Å		
*A*GeO$_3$	1.94	0.68	($D_3^5 - P321$)	1.89	0.67	0.24
*A*CrO$_3$	1.96	0.70	TiO$_2$, rutile ($D_{4h}^{14} - P_{4_2}/mnm$)	1.91	0.69	0.25
*A*MnO$_3$	1.97	0.71		1.89	0.67	0.26
*A*TiO$_3$	2.03	0.77		1.96	0.75	0.28
*A*RuO$_3$	2.05	0.79		1.98	0.76	0.28
*A*MoO$_3$	2.05	0.79		2.01	0.79	0.20
*A*TcO$_3$	2.07	0.81			0.79	0.29
*A*SnO$_3$	2.11	0.85		2.05	0.83	0.25
*A*PbO$_3$	2.21	0.95		2.16		0.24
*A*ZrO$_3$	2.16	0.90	CaF$_2$ ($O_h^5 - Fm\bar{3}m$)	2.20	0.86	0.25
*A*HfO$_3$	2.13	0.87		2.22	0.85	0.21
*A*PuO$_3$	2.27	1.01		2.34	1.00	0.21
*A*UO$_3$	2.28	1.02		2.37	1.03	0.20

refined from the observed linear dependence of $\frac{1+2\eta}{4\eta}(2l_{0BO} - a)$ on l_{0BO} (5).

Tables 2–4 contain the obtained values of l_{0AO} and l_{0BO} for crystals of the noted compounds. For comparison, the average interatomic distances *A*–O (L_{AO}) and *B*–O (L_{BO}) for crystals of the corresponding binary compounds are also listed in Tables 2–4.

In some crystals of this group of binary compounds with a structure different from the simple cubic structure, the distance between the nearest ions (the bond lengths) significantly differ from each other. In these cases, their average value $\bar{L}$ was estimated from the condition of average energy per bond:

$$U = \frac{1}{m}\sum_j^m U_j, \qquad (11)$$

where m is the number of bonds and U_j is the energy of the jth bond. Taking into account that, in the general case, $U_j \sim 1/L^n$, it follows from (11) that

$$\bar{L} = \left(m/\sum_k 1/L_j^n\right)^{1/n}, \qquad (13)$$

where L_j is the length of the jth bond. In calculations of $\bar{L}$, the exponent n was assumed to be equal to 2.

The found values of l_{0AO} and l_{0BO} were used to determine the corresponding cation radii ($R_{O^{2+}}$ was assumed to be equal to 1.26 Å [4]), which were compared with the values of radii reported in [4] (Tables 2–4).

It can be seen from Tables 2–4 that the unstrained-bond lengths l_{0AO} in these compounds are similar to the values of interatomic distances L_{AO} in the correspond-

Table 4. Average unstrained-bond lengths *l*, cation radii *R*, and rigidity constants η for $A^{3+}B^{3+}O_3$ compounds

A–O bonds

homologous series I	l_{0AO}, Å	$R_{0A^{3+}}$, Å	A_2O_3 binary compound		$^{VI}R_{A^{3+}}$, Å [4]	η
			structure type (space group)	L_{AO}, Å		
Yb*B*O$_3$	2.26	1.00	Yb_2O_3 ($T_h^7 - Ia\bar{3}$)	2.25	1.01	0.27
Tu*B*O$_3$	2.28	1.02			1.02	0.27
Er*B*O$_3$	2.29	1.03	($T_h^7 - Ia\bar{3}$)	2.28	1.03	0.27
Y*B*O$_3$	2.30	1.04		2.29	1.04	0.26
Ho*B*O$_3$	2.30	1.04		2.29	1.04	0.27
Dy*B*O$_3$	2.32	1.06		2.30	1.05	0.28
Tb*B*O$_3$	2.32	1.06		2.32	1.06	0.24
Gd*B*O$_3$	2.34	1.08		2.33	1.08	0.24
Eu*B*O$_3$	2.35	1.09		2.34	1.09	0.25
Sm*B*O$_3$	2.36	1.10		2.36	1.10	0.25
Nd*B*O$_3$	2.39	1.13	Nd_2O_3 ($D_{3d}^3 - P\bar{3}m1$)	2.52	1.12	0.23
Pr*B*O$_3$	2.39	1.13		2.52	1.13	0.23
Ce*B*O$_3$	2.42	1.16		2.56	1.15	0.24
La*B*O$_3$	2.47	1.21		2.59	1.17	0.24
Bi*B*O$_3$	2.64	1.38	($T^3 - I_{23}$)	2.64	1.17	0.40
			($C_{2h} - P\bar{4}21c$)	2.40		

B–O bonds

homologous series I	l_{0BO}, Å	$R_{0B^{3+}}$, Å	B_2O_3 binary compounds		$^{VI}R_{B^{3+}}$, Å [4]
			structure type (space group)	L_{BO}, Å	
*A*AlO$_3$	1.97	0.71	Al_2O_3 ($D_{3d}^6 - R\bar{3}c$)	1.91	0.67
*A*CoO$_3$	1.99	0.73			0.75$^{(HS)*}$
*A*CrO$_3$	2.04	0.78	($D_{3d}^6 - R\bar{3}c$)	1.99	0.76
*A*GaO$_3$	2.05	0.79		1.95	0.76
*A*FeO$_3$	2.06	0.80		2.04	0.79$^{(HS)}$
*A*VO$_3$	2.07	0.81		2.02	0.78
*A*RhO$_3$	2.08	0.82		2.04	0.81
*A*TiO$_3$	2.07	0.81		2.05	0.81
*A*MnO$_3$	2.07	0.81	Yb_2O_3 ($T_h^7 - Ia\bar{3}$)	2.06	0.79$^{(HS)}$
*A*ScO$_3$	2.15	0.89		2.13	0.89
*A*InO$_3$	2.20	0.94		2.20	0.94
*A*TuO$_3$	2.28	1.02			1.02
*A*ErO$_3$	2.29	1.03	($T_h^7 - Ia\bar{3}$)	2.28	1.03
*A*YO$_3$	2.30	1.04		2.29	1.04
*A*HoO$_3$	2.30	1.04		2.29	1.04

* High-spin state.

ing binary compounds. The quantitative relationship between them depends on the structural type of the binary compounds. For example, for the $A^{2+}B^{4+}O_3$ (A = Cd, Ca, Sr, Ba) and $A^{3+}B^{3+}O_3$ (A are the rare-earth elements from Yb to Sm) compounds, the unstrained-bond lengths l_{0AO} coincide with the average values of interatomic distances L_{AO} in AO (NaCl type) and A_2O_3 (Yb_2O_3 (T_h^7 – $Ia\bar{3}$) type) binary compounds, respectively. In $A^+B^{5+}O_3$ (A = Na, K, Rb) and $A^{3+}B^{3+}O_3$ (A are the rare-earth elements from Nd to Ce or La), the values of l_{0AO} are somewhat smaller than the corresponding values of L_{AO} for A_2O (CaF_2 type) and A_2O_3 (D_{3d}^3 – $P\bar{3}_{m1}$)) binary compounds.

For oxide (as for halide) perovskite structures, the ionic radii of A cations corresponding to l_{0AO} close to the values taken in [4] for a coordination number of six.

The relationship between the lengths of unstrained bonds B–O (l_{0BO}) in oxide perovskite structures and interatomic distances L_{BO} in binary crystals has the same character as in the case of halide compounds. For binary crystals with rutile (TiO_2) or corundum (Al_2O_3) structures, $l_{0BO} \geq L_{BO}$ and, for compounds with fluorite (CaF_2) structure, $l_{0BO} < L_{BO}$.

In addition, we should note the following. Atoms of some elements (Tu, Er, Ho, Y) entering the crystal lattice of $A^{3+}B^{3+}O_3$ compounds, depending on the nature of the second cation, may occupy either B or A positions in the crystal. The data listed in Table 4 show that the lengths of unstrained cation–anion bonds for these elements and, hence, the corresponding radii are independent of the positions occupied by these elements in the crystal.

The character of the change in the ratio of the rigidity constants η for the series of perovskite-type crystals is of interest. It can be seen from Table 2 that, for the $A^+U^{5+}O_3$, $A^+Pa^{5+}O_3$, and $A^+I^{5+}O_3$ compounds, the parameter η is two to three times larger than for the Ta^{5+}- and Nb^{5+}-containing compounds. This fact indicates that the energy of B–O bonds in the compounds of this group is lower than, for example, in $A^+Nb^{5+}O_3$.

CONCLUSIONS

The obtained values of the lengths of unstrained A–X and B–X bonds in ABX_3 compounds with the perovskite structure are consistent to a certain extent with the interatomic distances in crystals of the corresponding binary compounds, both halide and oxide ones. The quantitative relationship between the bond lengths and interatomic distances depends on the nature of chemical elements entering the ABX_3 composition. For some compounds, these values almost coincide. It is noteworthy that the radii of A and B cations corresponding to the average unstrained-bond lengths are similar to the Shannon radii reported in [4] for a coordination number of six. Hence, the ionic radii from [4] can be used to estimate the unstrained-bond lengths in perovskite structures in the first-order approximation.

The quantitative estimation of l_{0AX} and l_{0BX} using the interatomic distances found for crystals of binary compounds requires taking into account the specific features of their crystal structure related to the character of interatomic interaction. In particular, one should bear in mind that many binary compounds can be crystallized into various polymorphs characterized by different interatomic distances and their average values (for example, Bi_2O_3 (Table 4)). BF_2, A_2O, and BO_2 compounds, depending on the nature of cations, may crystallize into either rutile (TiO_2) or fluorite (CaF_2) structures. The lengths of the unstrained A–X and B–X bonds in crystals with perovskite structure are smaller than the interatomic distances in fluorite-type binary crystals containing the corresponding elements but somewhat larger than the interatomic distances in rutile-type crystals.

Thus, the data obtained confirm that the chemical bonds in crystals with distorted perovskite structure are strained. The strengthening energy increases with increasing the difference $l_{0BX} - l_{0AX}/\sqrt{2}$, according to the observed increase in the degree of distortion of the crystal lattice. Investigation of the energy of strained bonds gives deeper insight into the nature and character of structural distortions and phase transitions in such crystals and facilitates solution of the problem of stability limits for most perovskite structures. Concerning the latter point, we should note that, for compounds with a relatively small radius of A cations (for example, Li^+), the perovskite structure is estimated to be energetically unfavorable due to the high strengthening energy (large difference $l_{0BX} - l_{0AX}/\sqrt{2}$), which is consistent with the absence of $LiBX_3$ compounds with perovskite structure. However, for the compounds with predominantly ionic bonds, for example, $LiBaF_3$, the structure of inverse perovskite is possible, in which A and B cations change positions with respect to each other and the bond-strengthening energy decreases.

REFERENCES

1. E. G. Fesenko, *Perovskite Family and Ferroelectricity* (Atomizdat, Moscow, 1972) [in Russian].
2. K. S. Aleksandrov, A. T. Anistratov, B. V. Beznosikov, and N. V. Fedoseeva, *Phase Transitions in Crystals of ABX_3 Halides* (Nauka, Novosibirsk, 1981) [in Russian].
3. V. P. Sakhnenko, E. G. Fesenko, A. T. Shuvaev, *et al.*, Kristallografiya **17**, 316 (1972) [Sov. Phys. Crystallogr. **17**, 268 (1972)].
4. R. D. Shannon, Acta Crystallogr., Sect. A: Cryst. Phys., Diffr., Theor. Gen. Crystallogr. **32**, 751 (1976).
5. Yu. N. Venevtsev, E. D. Politova, and S. A. Ivanov, *Ferroelectrics and Antiferroelectrics of the Barium Titanate Family* (Khimiya, Moscow, 1985) [in Russian].
6. V. S. Urusov, *Energetic Crystal Chemistry* (Nauka, Moscow, 1975) [in Russian].

Translated by Yu. Sin'kov

Crystallography Reports, Vol. 49, No. 5, 2004, pp. 741–746. Translated from Kristallografiya, Vol. 49, No. 5, 2004, pp. 829–834.

STRUCTURE OF INORGANIC COMPOUNDS

Crystal Structures of Double Cesium Zirconium and Barium Zirconium Orthophosphates

E. R. Gobechiya*, Yu. K. Kabalov*, V. I. Pet'kov, and M. V. Sukhanov****

** Moscow State University, Vorob'evy gory, Moscow, 119992 Russia*
e-mail: elgob@mail.ru
*** Nizhni Novgorod State University, pr. Gagarina 23, Nizhni Novgorod, 603600 Russia*

Received April 28, 2003

Abstract—Double cesium zirconium and barium zirconium orthophosphates with the compositions $CsZr_2(PO_4)_3$ and $Ba_{0.5}Zr_2(PO_4)_3$, respectively, were prepared by thermal treatment of stoichiometric gels. The samples were characterized by electron-probe microanalysis and powder X-ray diffraction analysis. The crystal structures of both phosphates were refined by the Rietveld method within the space groups $R\bar{3}c$ and $R\bar{3}$, respectively, with isotropic atomic displacement parameters for all atoms. *© 2004 MAIK "Nauka/Interperiodica".*

INTRODUCTION

The sodium dizirconium tris(phosphate) (NZP, $NaZr_2(PO_4)_3$) structural family [1] includes compounds with the general formula $M_x[L_2(TO_4)_3]$, where $0 \le x \le 4$, M is □ (vacancy), a cation, or a particular set of predominantly low-charge cations in oxidation states from +1 to +4, L is the key (structure-forming) octahedral cation in oxidation states from +1 to +5 with a predominantly covalent character of the metal–oxygen bond, and T is an anion-forming element with a tetrahedral arrangement of chemical bonds. The letters M, L, and T in the general formula not only denote a particular set of cations but also correspond to certain structural positions or groups of positions. The structural analogue of NZP is the natural mineral kosnarite $KZr_2(PO_4)_3$ (sp. gr. $R\bar{3}c$, $a = 8.687$ Å, $c = 23.877$ Å, $V = 1560.4$ Å^3, $Z = 6$ [2, 3]).

The distinguishing characteristic feature of the NZP structure is that the same crystallographic positions in this structure can accommodate elements, both small and large, in oxidation states from +1 to +5 with retention of the principal framework $\{[L_2(TO_4)_3]^{p-}\}_{3\infty}$. Frameworks in which L and T positions are occupied by cations in high oxidation states are more stable. For such framework compositions, a larger number of different compounds can be obtained. A decrease in the oxidation state of the framework cations is accompanied by a decrease in both the strength of chemical bonds and stability of the framework and a change in the structural motif.

It has been noted [4] that the high stability of rhombohedral framework structures, which are typical of phosphates of the NZP family and have the maximum possible number of positions occupied by cations, is related to the very close packing of octahedra and tetrahedra in the crystal space, as well as to the uniform distribution of cavities of different sizes suitable for both the smallest and largest alkali cations (Li^+ and Cs^+, respectively). Thirteen double orthophosphates with the general formulas $M^+[L_2^{4+}(PO_4)_3]$ and $M_{0.5}^{2+}[L_2^{4+}(PO_4)_3]$ belonging to the NZP structural type with a rhombohedral (R) unit cell have been structurally characterized (Table 1).

Negatively charged R frameworks are typical of the phosphates $ML_2^{4+}(PO_4)_3$ (M = Li, Na, K, Rb, Cs, Ag, or Tl; L^{4+} = Zr, Hf, Ti, or Ge) and $M_{0.5}L_2^{4+}(PO_4)_3$ (M = Ca, Sr, or Ba), as well as $M_3L_2^{3+}(PO_4)_3$ (for example, $Na_3Sc_2(PO_4)_3$). Large alkali and alkaline-earth cations occupy the cavities in the frameworks.

Rhombohedral structures of NZP-type phosphates are frameworks formed by L octahedra and PO_4 tetrahedra with the general formula $\{[L_2(PO_4)_3]^{p-}\}_{3\infty}$. A stable lantern-type fragment (Fig. 1) consists of two L octahedra linked by three bridging PO_4 tetrahedra around a circle and a small trigonal prismatic cavity, which is located between the octahedra and is cannot be occupied by cations. This fragment can be considered the characteristic component of the framework. These structure-forming components are arranged in columns extended along $\bar{3}$ axes. The adjacent analogous columns are linked to form the framework by sharing the terminal oxygen atoms of the PO_4 tetrahedra. Two vertices of these polyhedra are attached to the edges of the prisms, and the other two vertices are linked to the adjacent columns. The cavities in the framework are occu-

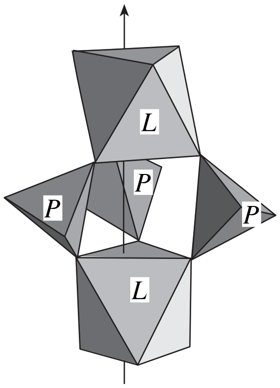

Fig. 1. Lantern-type fragment of the framework of the NZP structural type.

pied by low-valence cations, which neutralize the negative charge of the framework. The structural similarity of the frameworks consisting of *L* octahedra and PO_4 tetrahedra manifests itself in the comparability of the unit-cell parameters (Table 1).

The synthesis of new framework phosphates belonging to the NZP structural type, as well as detailed analysis of the geometric and topological features of the structures of new and known NZP-type phosphates aimed at revealing correlations between the crystal structures of these compounds and the practically valuable physicochemical properties, have attracted considerable attention in recent years [15, 16].

We studied the crystal structures of double cesium zirconium and barium zirconium orthophosphates by the Rietveld method. These compounds were structurally characterized for the first time. It should be noted that the unit-cell parameters and symmetry of the structures of these compounds were determined in [17–19] (where these compounds were synthesized and described). These characteristics are as follows: for $CsZr_2(PO_4)_3$ [17]—sp. gr. $R\bar{3}c$, $a = 8.62(6)$ Å, $c = 24.81(9)$ Å, $V = 1599$ Å^3, and $Z = 6$; and for $Ba_{0.5}Zr_2(PO_4)_3$ [18, 19]—sp. gr. $R\bar{3}$, $a = 8.638(1)$ Å, $c = 23.950(3)$ Å, $V = 1548$ Å^3, and $Z = 6$. The IR-spectroscopic study showed that $CsZr_2(PO_4)_3$ and $Ba_{0.5}Zr_2(PO_4)_3$ are functionally similar to phosphates $M^+Zr_2(PO_4)_3$ (M = Li, Na, K, or Rb) [20] and $M^{2+}_{0.5}Zr_2(PO_4)_3$ (M = Cd, Ca, Sr, or Ba) [18], respectively.

Phosphate $CsZr_2(PO_4)_3$, which contains the largest cation in the framework cavities, is of interest because it is a promising ultralow-thermal-expansion material [16] and is used as an active and selective catalyst for alcohol dehydration [21]. Phosphate $Ba_{0.5}Zr_2(PO_4)_3$ has a high melting point (>1973 K), is characterized by a small coefficient of thermal expansion [19], and forms solid solutions with other NZP compounds in a wide range, which makes it possible to predict compositions of ceramics with a controlled coefficient of thermal expansion, including ultralow-thermal-expansion ceramics. Such ceramics can withstand severe thermal loads. In addition, synthetic crystalline mineral-like single-phase matrix materials with the NZP structure can immobilize cesium radioisotopes (^{137}Cs, ^{134}Cs), barium radioisotopes (^{133}Ba), and other radionuclides present in nuclear wastes [22]. To understand the characteristic features of incorporation of radioisotopes and other toxic elements of wastes into the target NZP phase, it is necessary to know the structure of the latter, details of its crystal chemistry, and relationship with other NZP compounds.

Table 1. Double orthophosphates $M^+[L_2^{4+}(PO_4)_3]$ and $M_{0.5}^{2+}[L_2^{4+}(PO_4)_3]$ with *R* unit cells belonging to the NZP structural type

Phosphate	Space group	*a*, Å	*c*, Å	*V*, Å^3	Reference
$LiZr_2(PO_4)_3$	$R\bar{3}c$	8.847(1)	22.240(30)	1507.5	[5]
$NaZr_2(PO_4)_3$	$R\bar{3}c$	8.815(1)	22.746(7)	1530.7	[1]
$KZr_2(PO_4)_3$	$R\bar{3}c$	8.710(10)	23.890(20)	1569.6	[2]
$LiTi_2(PO_4)_3$	$R\bar{3}c$	8.51173(4)	20.8524(2)	1308.35	[6]
$NaTi_2(PO_4)_3$	$R\bar{3}c$	8.502(5)	21.833(9)	1366.7	[7]
$KTi_2(PO_4)_3$	$R\bar{3}c$	8.367(1)	23.074(3)	1398.9	[8]
$RbTi_2(PO_4)_3$	$R\bar{3}c$	8.290(1)	23.530(4)	1400.3	[9]
$LiGe_2(PO_4)_3$	$R\bar{3}c$	8.257(5)	20.470(30)	1213.9	[10]
$KGe_2(PO_4)_3$	$R\bar{3}$	8.007(1)	22.566(4)	1252.8	[11]
$Ca_{0.5}Zr_2(PO_4)_3$	$R\bar{3}$	8.7810(3)	22.675(1)	1514.1	[12]
$Ca_{0.5}Ti_2(PO_4)_3$	$R\bar{3}$	8.375(1)	22.062(2)	1340.2	[13]
$Sr_{0.5}Ti_2(PO_4)_3$	$R\bar{3}$	8.311(1)	22.667(2)	1356.0	[13]
$Ba_{0.5}Ti_2(PO_4)_3$	$R\bar{3}c$	8.3418(1)	23.0101(4)	1386.66	[14]

Table 2. Unit-cell parameters and results of the Rietveld refinement of the crystal structures of $CsZr_2(PO_4)_3$ and $Ba_{0.5}Zr_2(PO_4)_3$

Characteristic	$CsZr_2(PO_4)_3$	$Ba_{0.5}Zr_2(PO_4)_3$
a, Å	8.5758(2)	8.6468(6)
c, Å	24.9061(4)	23.9436(2)
V, Å^3	1586.30(4)	1550.35(1)
Space group, Z	$R\bar{3}c$, 6	$R\bar{3}$, 6
2θ-scan range, deg	20.00–110.00	12.00–139.98
Number of reflections	296	864
Number of refined parameters	25	35
R_{wp}	3.00	4.67
R_B	3.83	1.24
R_F	4.86	1.05
S	1.33	1.17

Note: $R_{wp} = [\Sigma w|I_{obs} - I_{calcd}|^2/\Sigma w I_{obs}^2]^{1/2}$; $R_B = \Sigma|I'_{obs} - I'_{calcd}/I'_{obs}$, where I'_{obs} and I'_{calcd} are the observed and calculated integrated intensities of Bragg reflections, respectively; and $R_F = \Sigma|F_{obs} - F_{calcd}|/F_{obs}$.

EXPERIMENTAL

$CsZr_2(PO_4)_3$ and $Ba_{0.5}Zr_2(PO_4)_3$ phosphates were prepared by the sol–gel method [23] using CsCl, $Ba(NO_3)_2$, $ZrOCl_2 \cdot 8H_2O$, and H_3PO_4 of reagent-grade purity as the starting compounds. An aqueous solution of cesium chloride or barium nitrate was added with stirring to a stoichiometric amount of an aqueous solution of zirconium oxychloride (the latter was dissolved in distilled water acidified with hydrochloric acid to prevent hydrolysis) at ~293 K. Then, a solution of orthophosphoric acid (a stoichiometric amount with respect to phosphate) was slowly added with stirring. The prepared gel was dried at 353 K and subjected to thermal treatment under aerobic conditions successively at 873, 1073, and 1273 K for at least 24 h in each step. After each stage of heating, the samples were dispersed to provide homogenization of the mixture. Finally, the samples were prepared as white polycrystalline powders.

The identification of compounds and further studies were carried out using a combination of physicochemical methods: electron-probe microanalysis, powder X-ray diffraction analysis, and X-ray structure analysis.

The chemical composition and homogeneity of the samples were examined on a Camebax electron microprobe equipped with a Link AN-10 000 energy-dispersive detector. The results demonstrated that the samples were homogeneous and their compositions were similar to the formulas $CsZr_2(PO_4)_3$ and $Ba_{0.5}Zr_2(PO_4)_3$.

Powder X-ray diffraction analysis was carried out on a DRON-3M diffractometer (filtered CuK_α radiation, scan rate 1 deg/min). A set of interplanar distances was compared with the data from the Powder Diffraction File (PDF2, nos. 34-0196 and 34-0095) maintained by the International Center for Diffraction Data (ICCD) [24].

X-ray diffraction spectra for the structure refinement were measured on an ADP-2 diffractometer (λ-CoK_α, Fe filter) with a 2θ-scan step of 0.02°; the exposure time at each point was 15 s. The refinement was carried out using the WYRIET program (version 3.3) [25]. The peak profiles were approximated by the Pearson VII function. The peak asymmetry was refined at $2\theta < 60°$. The ionic scattering curves were used for all elements. The crystal structures were refined with the gradual addition of parameters and continuous graphical modeling of the background until the R factors ceased to change.

The atomic coordinates in the space groups $R\bar{3}c$ [2] and $R\bar{3}$ [11] were used as the starting models for refinement of the $CsZr_2(PO_4)_3$ and $Ba_{0.5}Zr_2(PO_4)_3$ structures, respectively. Selected parameters of the X-ray-data collection and results of the structure refinement for cesium zirconium and barium zirconium orthophosphates are listed in Table 2. The experimental X-ray diffraction spectra of the compounds under study are shown in Figs. 2a and 2b. The atomic coordinates, isotropic thermal parameters, and occupancies of the cation positions are listed in Tables 3 and 4. The structure, calculated by the ATOMS program [26]), is shown in Fig. 3. The interatomic distances in the coordination polyhedra are in agreement with the typical values. In the $CsZr_2(PO_4)_3$ structure, the Zr–O and P–O bond lengths vary in the ranges 2.00(1)–2.16(1) and 1.52(1)–1.54(1) Å, respectively. In the $Ba_{0.5}Zr_2(PO_4)_3$ structure, the Zr(1)–O, Zr(2)–O, and P–O bond lengths vary in the ranges 1.961(8)–2.217(8), 2.020(7)–2.155(9), and 1.49(1)–1.59(1) Å, respectively.

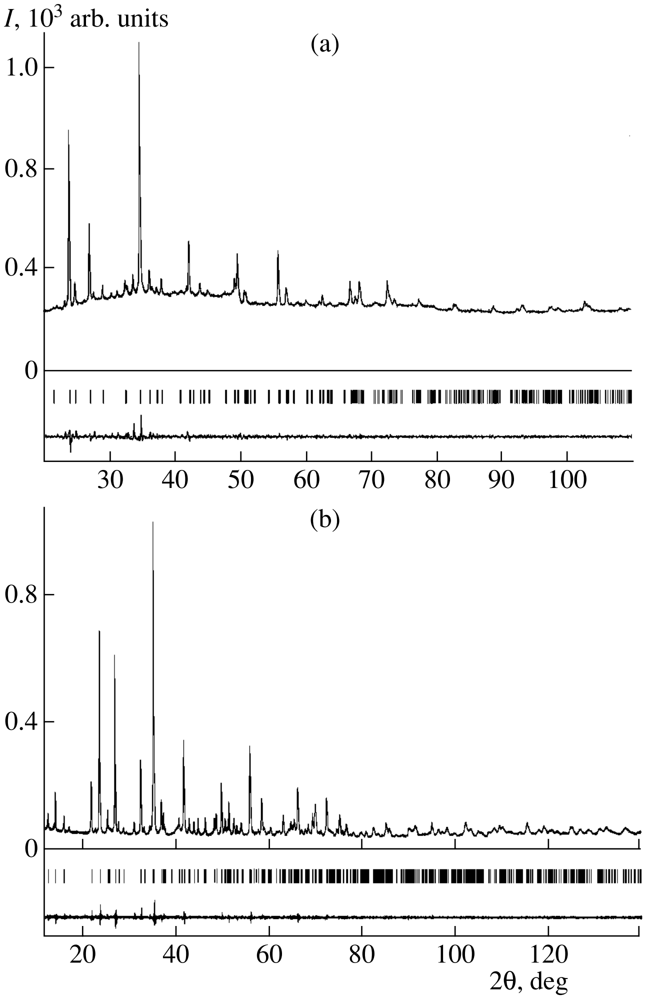

Fig. 2. Experimental X-ray diffraction spectra of (a) $CsZr_2(PO_4)_3$ and (b) $Ba_{0.5}Zr_2(PO_4)_3$. The vertical bars indicate the positions of the reflections of the theoretical X-ray pattern. The difference curve between the intensities of the experimental and theoretical spectra is at the bottom of the figure.

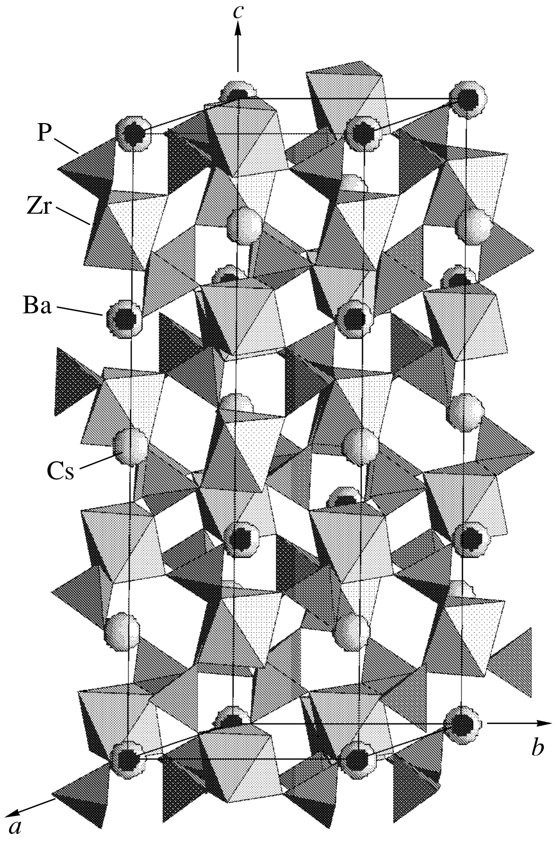

Fig. 3. Structure of double orthophosphates $CsZr_2(PO_4)_3$ (Cs atoms are shown as white balls) and $Ba_{0.5}Zr_2(PO_4)_3$ (Ba atoms are shown as black balls).

RESULTS AND DISCUSSION

The results of our study demonstrate that the crystal structures of $CsZr_2(PO_4)_3$ and $Ba_{0.5}Zr_2(PO_4)_3$ phosphates belong to the NZP structural type and are characterized by the presence of the complex anion radical $[Zr_2(PO_4)_3]$.

Therefore, the crystal structures of double cesium zirconium and barium zirconium orthophosphates can be described as a three-dimensional mixed framework formed by isolated Zr octahedra and PO_4 tetrahedra sharing vertices. Each Zr octahedron is linked to six PO_4 tetrahedra (Fig. 3). The extraframework octahedral

Table 3. Coordinates and equivalent atomic displacement parameters of the basis atoms in the structure of $CsZr_2(PO_4)_3$ phosphate

Atom	*x*	*y*	*z*	B_{iso}
Cs	0	0	0	0.6(2)
Zr	0	0	0.1546(2)	0.5(2)
P	−0.285(2)	0	0.25	0.9(4)
O(1)	0.306(2)	0.467(2)	0.2632(8)	1.4(6)
O(2)	0.167(2)	0.212(2)	0.1993(8)	0.9(6)

Table 4. Coordinates and equivalent atomic displacement parameters of the basis atoms in the structure of $Ba_{0.5}Zr_2(PO_4)_3$ phosphate

Atom	*x*	*y*	*z*	B_{iso}
Ba	0	0	0	2.2(1)
Zr(1)	0	0	0.1515(2)	0.11(2)
Zr(2)	0	0	0.6484(2)	0.14(8)
P	0.2926(2)	0.0076(1)	0.2527(5)	0.6(1)
O(1)	0.189(2)	0.003(2)	0.1973(8)	1.1(5)
O(2)	0.046(2)	−0.165(2)	0.6961(2)	2.0(5)
O(3)	0.183(2)	0.174(2)	0.0852(6)	0.3(2)
O(4)	−0.162(2)	−0.211(2)	0.5915(6)	2.0(6)

cavities are completely occupied by Cs atoms (the Cs–O distance is 2.89(1) Å) in the $CsZr_2(PO_4)_3$ structure and half-occupied by Ba atoms (the Ba–O distance is 2.56(9) Å) in the $Ba_{0.5}Zr_2(PO_4)_3$ structure. It should be noted that the frameworks of both structures are absolutely identical, in spite of the fact that they crystallize in different space groups ($R\bar{3}c$ and $R\bar{3}$). Since the c symmetry plane is absent in the crystal structure of $Ba_{0.5}Zr_2(PO_4)_3$, the identity of the frameworks is achieved through the doubling of the number of Zr and O atoms and displacement of the P atom from the special position 18*e* in the $CsZr_2(PO_4)_3$ structure to the general position in the $Ba_{0.5}Zr_2(PO_4)_3$ structure.

As can be seen from Fig. 4, the parameter a of the hexagonal unit cell in the series of the $MZr_2(PO_4)_3$ (M = Li, Na, K, Rb, or Cs) and $M_{0.5}Zr_2(PO_4)_3$ (M = Ca, Sr, or Ba) compounds decreases, the parameter c increases, and the unit-cell volume increases with increasing radius of the M cation. The unit-cell parameters for $RbZr_2(PO_4)_3$ and $Sr_{0.5}Zr_2(PO_4)_3$ were taken from the PDF2 database (nos. 44-0009 and 33-1360, respectively) [24]. This feature of the NZP structure is attributed to the fact that an increase in the size of the M cation leads to an increase in the volume of the extraframework cavity in the column between two surfaces of the adjacent ZrO_6 octahedra located along the c axis, thus increasing the parameter c. Simultaneously, the correlated rotation of the ZrO_6 octahedra and PO_4 tetrahedra that link the parallel columns occurs, resulting in a decrease in the distance between the columns and, consequently, a decrease in the parameter a. It should be noted that the unit-cell volume of Rb phosphate is similar to that of Cs phosphate. A small increase in the unit-cell volume in going from rubidium to cesium compound, apparently, indicates the upper limit of the radius of the alkali cation, which can be accommodated in the NZP structure.

Analysis of the interatomic distances in the structurally characterized NZP-type phosphates containing alkali and alkaline-earth elements [1, 2, 5, 12] shows that the distances between the framework cations and oxygen atoms (Zr–O and P–O) depend only slightly on the size of the M ion in the extraframework position. This is due to the fact that the chemical bonds in the framework are substantially stronger than the bonds with the ions occupying cavities in the structure.

The results of our study of the double orthophosphates $CsZr_2(PO_4)_3$ and $Ba_{0.5}Zr_2(PO_4)_3$ and comparison of these results with the above-mentioned data in the literature on the structure formation of framework phosphates of the $M_xZr_2(PO_4)_3$ family lead to the following conclusions:

Cesium zirconium and barium zirconium phosphates synthesized and characterized in this study supplement the series of known double zirconium orthophosphates $M_xZr_2(PO_4)_3$ with a framework structure, including those belonging to the NZP structural type (space groups $R\bar{3}c$ and $R\bar{3}$).

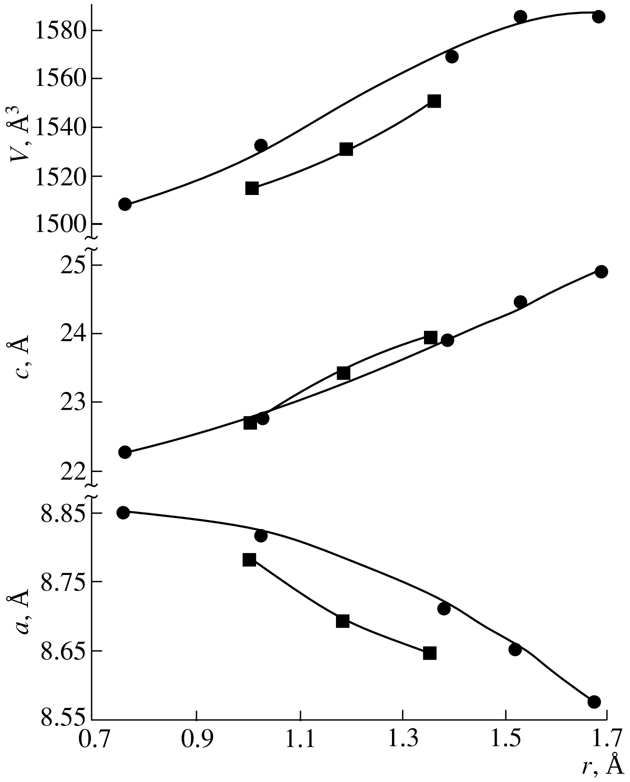

Fig. 4. Changes in the unit-cell parameters a and c and the unit-cell volume V depending on the radii of M cations for (●) $MZr_2(PO_4)_3$ (M = Li, Na, K, Rb, or Cs) and (■) $M_{0.5}Zr_2(PO_4)_3$ (M = Ca, Sr, or Ba) phosphates.

The structures of NZP-type phosphates containing Cs^+ and Ba^{2+} cations in the cavities of the framework have been studied for the first time.

The framework of NZP-type phosphates consists of relatively rigid octahedral–tetrahedral lantern-like fragments and can incorporate both small and large alkali and alkaline-earth cations in the extraframework positions.

The upper limits of the sizes of the compensating M cations in phosphates with the general formulas $M^+Zr_2(PO_4)_3$ and $M^{2+}_{0.5}Zr_2(PO_4)_3$ and the R unit cells are determined by the radii of the Cs^+ and Ba^{2+} cations (1.67 and 1.35 Å, respectively).

ACKNOWLEDGMENTS

This study was supported by the Russian Foundation for Basic Research (project nos. 03-05-64054, 02-03-32181, and 03-03-32538) and the program “Universities of Russia.”

REFERENCES

1. H. Y. Hong, Mater. Res. Bull. **11** (2), 173 (1976).
2. M. Sljukic, B. Matkovik, B. Prodic, and D. Anderson, Z. Kristallogr. **130**, 148 (1969).
3. M. E. Brownfield, E. E. Foord, S. J. Sutley, and T. Botinelly, Am. Mineral. **78**, 653 (1993).
4. V. I. Pet'kov, G. I. Dorokhova, and A. I. Orlova, Kristallografiya **46** (1), 76 (2001) [Crystallogr. Rep. **46**, 69 (2001)].
5. D. Petit, Ph. Colomban, G. Collin, and J. P. Boilot, Mater. Res. Bull. **21**, 365 (1986).
6. D. A. Woodcock and P. Lighfoot, J. Mater. Chem. **9**, 2907 (1999).
7. Yu. A. Ivanov, E. L. Belokoneva, Yu. K. Egorov-Tismenko, and N. V. Simonov, Dokl. Akad. Nauk SSSR **252**, 1122 (1980) [Sov. Phys. Dokl. **25**, 420 (1980)].
8. E. S. Lunezheva, B. A. Maksimov, and O. K. Mel'nikov, Kristallografiya **34** (5), 1119 (1989) [Sov. Phys. Crystallogr. **34**, 674 (1989)].
9. R. Duhlev, Acta Crystallogr., Sect. C: Cryst. Struct. Commun. **50**, 1525 (1994).
10. M. Alami, R. Brochu, J. L. Soubeyroux, *et al.*, J. Solid State Chem. **90**, 185 (1991).
11. R. Brochu, M. Louer, M. Alami, *et al.*, Mater. Res. Bull. **32**, 113 (1997).
12. J. Alamo and J. L. Rodrigo, Solid State Ionics **63–65**, 678 (1993).
13. S. Senbhagaraman, J. Mater. Chem. **3**, 309 (1993).
14. D. A. Woodcock, P. Lighfoot, and R. I. Smith, J. Mater. Chem. **9**, 2631 (1999).
15. J. Alamo, Solid State Ionics **63–65**, 547 (1993).
16. V. I. Pet'kov and A. I. Orlova, Neorg. Mater. **39** (11) (2003).
17. V. I. Pet'kov, A. I. Orlova, and O. V. Egor'kova, Zh. Strukt. Khim. **37**, 1104 (1996).
18. V. I. Pet'kov, V. S. Kurazhkovskaya, A. I. Orlova, and M. L. Spiridonova, Kristallografiya **47** (5), 802 (2002) [Crystallogr. Rep. **47**, 736 (2002)].
19. S. Y. Limaye, D. K. Agrawal, and H. A. McKinstry, J. Am. Ceram. Soc. C **70**, 232 (1987).
20. V. S. Kurazhkovskaya, A. I. Orlova, V. I. Pet'kov, *et al.*, Zh. Strukt. Khim. **41**, 74 (2000).
21. S. N. Ĭenealem, S. G. Gul'yanova, T. K. Chekhlova, *et al.*, in *Abstracts of I All-Russian Conference on Surface Chemistry and Nanotechnology* (St. Petersburg, 1999), p. 138.
22. B. E. Sheetz, D. K. Agrawal, E. Breval, and R. Roy, Waste Manage. Res. **14**, 489 (1994).
23. V. I. Pet'kov, A. I. Orlova, and D. A. Kapranov, Zh. Neorg. Khim. **43**, 1534 (1998).
24. *PCPDFWIN—a Windows Retrieval/Display Program for Accessing the ICDD PDF-2 Database* (JCPDS—International Center for Diffraction Data, 1998).
25. J. Schneider, in *Proceedings of International Workshop on the Rietveld Method* (Petten, 1989).
26. E. Dowty, *Atoms 3.2. A Computer Program for Displaying Atomic Structures* (Kingsport, 1995), TN 37663.

Translated by T. Safonova

Crystallography Reports, Vol. 49, No. 5, 2004, pp. 747–751. Translated from Kristallografiya, Vol. 49, No. 5, 2004, pp. 835–840.
Original Russian Text Copyright © 2004 by Zakharov, Troyanov, Kemnitz.

STRUCTURE OF INORGANIC COMPOUNDS

Synthesis and Crystal Structure of Rare Earth Selenates $Nd(HSeO_4)_3$, $Sm(HSeO_4)_3$, and $Nd_2(SeO_4)_3 \cdot 5H_2O$

M. A. Zakharov*, S. I. Troyanov*, and E. Kemnitz**
** Chemistry Department, Moscow State University, Vorob'evy gory, Moscow, 119992 Russia*
e-mail: max@struct.chem.msu.ru
*** Institute of Inorganic Chemistry, Humboldt University, Berlin, 12489 Germany*

Received March 18, 2003

Abstract—Single crystals of rare earth (RE) selenates of the compositions $Nd(HSeO_4)_3$, $Sm(HSeO_4)_3$, and $Nd_2(SeO_4)_3 \cdot 5H_2O$ are synthesized and studied by X-ray diffraction analysis at $T = 297$ and 180 K. It is established that Nd and Sm hydrogen selenates are isostructural to one another and to the corresponding hydrogen sulfates. Neodymium selenate pentahydrate is not isostructural to the analogous RE sulfates, although their structural motifs are similar. *© 2004 MAIK "Nauka/Interperiodica".*

INTRODUCTION

The crystal chemistry of rare earth elements is attracting ever growing attention because of its numerous aspects. The structures of RE compounds are often similar, although many structures also demonstrate fine and even principal differences. Relatively recently, the complete structural studies of lanthanide hydrogen sulfates described by the general formula $M(HSO_4)_3$ have been studied. This group of compounds consists of three structure types. The first type is built by compounds with M = La, Ce(III), Pr, and Nd that crystallize in the hexagonal sp. gr. $P6_3/m$ [1]. The system of hydrogen bonds in these structures consists of infinite columns along the z axis. The hydrogen atom is statistically disordered over two positions on the hydrogen bond. The neighboring layers of HSO_4 groups are related by the 6_3 axis. The second structure type is formed by compounds with M = Er (modification I) [2], Y [3], and Gd [4]. The third type is represented only by the Er compound of modification II [2]. The two latter types differ from one another (type I has an orthorhombic structure, sp. gr. $Pbca$, whereas type II has a monoclinic structure, sp. gr. $P2_1/n$; the numbers of the formula units are $Z = 8$ and 4, respectively). Although both compounds contain centrosymmetric hexamers $(HSO_4)_6$, their structures are different.

Selenates are studied to a lesser degree than sulfates. The structures of three selenates are known. These are $La(HSeO_4)_3$ [5], which is isostructural to the corresponding RE hydrogen sulfates of the first type; $M(HSeO_4)(SeO_4)$ with M = Gd [5] and Eu [6], which are isostructural and form their own structure type, in which the $HSeO_4$ and SeO_4 groups are bound into a dimer by an asymmetric hydrogen bond.

The structure of hydrates of RE sulfates has been studied in detail [7, 8]. They include tri-, tetra-, penta-, octa-, and nonahydrates. Among the hydrates of lanthanide selenates, only the structures of four compounds have been determined—$Pr_2(SeO_4)_3 \cdot 4H_2O$ [9], $Yb_2(SeO_4)_3 \cdot 8H_2O$ [10], $Sm_2(SeO_4)_3 \cdot 8H_2O$ [11], and $La_2(SeO_4)_3 \cdot 12H_2O$ [12].

The present study is aimed at the acquisition of detailed crystallochemical data on RE hydrogen selenates and the establishment of similar and different characteristics of RE hydrogen selenates and sulfates. Therefore, we synthesized and studied neodymium and samarium hydrogen selenates and neodymium selenate pentahydrate.

EXPERIMENTAL

$Nd(HSeO_4)_3$ and $Nd_2(SeO_4)_3 \cdot 5H_2O$ were obtained by dissolving Nd_2O_3 (reagent grade) in a 90% aqueous solution of selenic acid (analytical grade). The starting materials were taken in the molar ratio $Nd_2(SeO_4)_3 : H_2SeO_4$, i.e., proceeding from the stoichiometric ratio 1/3, we took selenic acid in a 1.5-fold excess. A large part of the oxide did not dissolve during mixing of the starting materials, therefore, we had to add a certain amount of water in order to completely dissolve the oxide. Pink prismatic crystals stable in air were grown during slow evaporation of the solution at 368 K. Then, they were isolated from the hot solution. As the subsequent X-ray study showed, the composition of the grown crystals corresponded to the formula $Nd_2(SeO_4)_3 \cdot 5H_2O$. In order to obtain neodymium hydrogen selenate, we continued evaporating the solution, first in air and then in a nitrogen atmosphere. Several days later, pink needlelike crystals were formed; their composition was determined by X-ray diffraction analysis as $(Nd(HSeO_4)_3$. Since the crystals grown were highly hygroscopic, they were studied in thin-walled capillaries.

Table 1. Crystallographic data, details of X-ray experiment and refinement of the structures of compounds **1–3**

Compound	$Nd(HSeO_4)_3$ (**1**)		$Sm(HSeO_4)_3$ (**2**)	$Nd_2(SeO_4)_3 \cdot 5H_2O$ (**3**)
Sp. gr.	$P6_3/m$		$P6_3/m$	$P2_1/c$
T, K	180(2)	293(2)	180(2)	180(2)
a, Å	9.561(1)	9.595(1)	9.522(1)	10.629(9)
b, Å	9.561(1)	9.595(1)	9.522(1)	13.98(1)
c, Å	6.058(1)	6.067(1)	6.011(1)	9.752(9)
β, deg	90		90	93.13(7)
V, Å^3	479.6(1)	483.7(1)	472.0(1)	1446(2)
Z	2		2	4
ρ_{calcd}, g/cm^3	3.990	3.956	4.097	3.294
θ_{max}, deg	30	31	30	26
$N_{obs.refl}/N_{indp.refl.}$	1877/513	3260/559	1838/504	4731/2808
N_{refl} with $I > 2\sigma(I)$	477	330	491	2199
N_{refl}/N_{param}	505/31	331/31	499/31	2631/210
Extinction coefficient	0.0051(8)	0.005(1)	0.0054(8)	0.0019(3)
R_1 ($I > 2\sigma(I)$)	0.031	0.025	0.026	0.049
wR_2 (F^2)	0.059	0.054	0.059	0.115
Residual electron density (min/max), e Å^{-3}	–1.95/2.41	–0.79/1.37	–1.761/1.086	–1.409/2.721

$Sm(HSeO_4)_3$ was synthesized using a similar ratio of Sm_2O_3 and H_2SeO_4 (reagent grade). After slow evaporation of the solution, first in air and then in the nitrogen atmosphere, we obtained colorless needlelike hygroscopic crystals and studied them also in capillaries.

The quality of the grown single crystals was checked in a polarization microscope. X-ray diffraction studies were performed at 180 K on a STADI-4 Stoe four-circle diffractometer with a point detector [13] (MoK_α radiation, $\lambda = 0.71073$ Å, graphite monochromator, ω scan). The main crystallographic characteristics and the experimental data obtained are listed in Table 1, and the interatomic distances in structures **1**, **2**, and **3**, in Table 2.

The absorption correction was introduced by empirical methods based on the data of a ψ-scan of several reflections. The coordinates of a heavy atom were determined by direct methods using the SHELXS97 program [14]. The remaining nonhydrogen atoms were determined from difference Fourier syntheses. The full matrix LS refinement was performed using the SHELXL97 complex [15] in the anisotropic approximation for all the nonhydrogen atoms. We failed to refine the coordinates of the hydrogen atoms. Since the structures had an elevated residual electron density caused by high anomalous scattering (fluorescence) of a selenium atom (Mo radiation) and also high absorption because of the presence of heavy Sm and Nd atoms, all the pronounced residual electron-density maxima were located in the vicinity of Se, Nd, or Sm atoms (≤1 Å). The figures were prepared using the DIAMOND program [16].

The data on the atomic coordinates and their thermal parameters for all the compounds are deposited in the database of inorganic structures (ICSD nos. 413487, 413488, 413489, and 413490 for structures **1** (studied at T = 297 and 180 K) and structures **2** and **3** studied at T = 180 K).

RESULTS AND DISCUSSION

Neodymium selenate pentahydrate was formed in a diluted solution of selenic acid (<90%), because lanthanide cations are strongly hydrated in solutions. The stability region of nonhydrated lanthanide hydrogen selenates is considerably shifted toward highly concentrated selenic acid solutions (>90%).

$M(HSeO_4)_3$, M = Nd (1), Sm (2). These compounds are isostructural to acid selenates and acid sulfates of the composition $M(HXO_4)_3$ studied earlier [1, 5], where M = La, Ce, Pr, Nd and X = S, Se (Fig. 1). M atoms in **1** and **2** are surrounded with O atoms forming tricapped triangular prisms with the M–O distances ranging within 2.469–2.487 Å (**1**) and 2.447–2.459 Å (**2**). The M–O bonds are formed by three O(1) and six O(2) ions from different nine selenate anions. The MO_9 polyhedra are bound by the selenate groups via O(2) atoms and form columns along the c axis. The SeO_4 tetrahedra connect the columns into a three-dimensional framework via the O(1) vertices. In this case, empty channels are formed with an axis that coincides with the 00z axis.

Table 2. Interatomic distances *d* (Å) in structures **1**–**3**

$Nd(HSeO_4)_3$ (**1**)* and $Sm(HSeO_4)_3$ (**2**)			$Nd_2(SeO_4)_3 \cdot 5H_2O$ (**3**)			
bond	*d* (**1**)	*d* (**2**)	bond	*d*	bond	*d*
M–O(1) × 3	2.469(5)	2.459(5)	Nd(1)–O(2)	2.581(9)	Se(2)–O(5)	1.625(9)
M–O(2) × 6	2.487(5)	2.447(4)	Nd(1)–O(3)	2.484(9)	Se(2)–O(6)	1.641(9)
Se–O(1)	1.611(5)	1.602(5)	Nd(1)–O(4)	2.392(9)	Se(2)–O(7)	1.641(9)
Se–O(2) × 2	1.604(5)	1.608(4)	Nd(1)–O(7)	2.400(9)	Se(2)–O(8)	1.635(9)
Se–O(3)	1.708(5)	1.705(5)	Nd(1)–O(9)	2.625(9)	Se(3)–O(9)	1.625(9)
O(3)…O(3') × 2	3.160(9)	3.163(9)	Nd(1)–O(12)	2.630(8)	Se(3)–O(10)	1.641(9)
O(3)…O(2') × 2	2.976(8)	2.973(8)	Nd(1)–O(12')	2.438(9)	Se(3)–O(11)	1.626(9)
			Nd(1)–O(22)	2.507(9)	Se(3)–O(12)	1.652(9)
			Nd(1)–O(23)	2.504(9)	O(20)···O(2)	2.86(1)
			Nd(2)–O(1)	2.421(9)	O(20)···O(9)	2.89(1)
			Nd(2)–O(5)	2.360(9)	O(20)···O(21)	2.80(1)
			Nd(2)–O(6)	2.435(9)	O(21)···O(24B)	2.85(3)
			Nd(2)–O(8)	2.418(9)	O(22)···O(8)	2.86(1)
			Nd(2)–O(10)	2.494(9)	O(22)···O(23)	2.90(1)
			Nd(2)–O(11)	2.371(9)	O(22)···O(24B)	2.85(3)
			Nd(2)–O(20)	2.644(9)	O(23)···O(2)	2.90(1)
			Nd(2)–O(21)	2.513(9)	O(23)···O(4)	2.96(1)
			Se(1)–O(1)	1.647(9)	O(23)···O(24A)	2.89(2)
			Se(1)–O(2)	1.653(8)	O(23)···O(24A)	2.94(2)
			Se(1)–O(3)	1.632(9)	O(24Ç)···O(7)	2.96(2)
			Se(1)–O(4)	1.644(9)	O(24Ç)···O(10)	2.82(2)

* *T* = 180 K.

The fourth vertex of the SeO_4 tetrahedron, O(3), is directed inside the empty channel (Fig. 1).

The tetrahedral $HSeO_4$ group is characterized by an elongated Se–O(3) distance equal to 1.708(5) Å in **1** and 1.705(5) Å in **2**; the remaining Se–O distances range within 1.604–1.611 Å in **1** and 1.602–1.608 Å in **2** and are characteristic of Se–OH bonds [5]. Analysis of the O···O distances and Se–O···O angles showed that the following distances may correspond to hydrogen bonds: O(3)···O(2') 2.976(8) Å in **1**, 2.973(8) Å in **2**, O(3)···O(3') 3.160(9) Å in **1**, and 3.163(9) Å in **2**, with electron-density maxima that could be ascribed to hydrogen atoms being corresponding to the positions of H atoms with a geometry characteristic of H-bonds. The first of these H-bonds connects the tetrahedra to the columns, and the second one, being considered individually, connects the tetrahedra to a trimer, whose plane is parallel to the (*xy*0) plane.The hydrogen bonds considered are somewhat different from those suggested in [1] for analogous sulfates. In [1], the existence of two hydrogen bonds was assumed. One of these bonds is formed by O(3) and O(2) atoms (~3.05 Å) and is similar to that suggested in our case, whereas the other (~3.5 Å) is formed by O(3) and O(3) atoms of the selenate tetrahedra located at different heights *z* (in our case, these tetrahedra are located at the same height). We believe that the latter of the H bonds suggested in [1] should not be taken into account because of a too

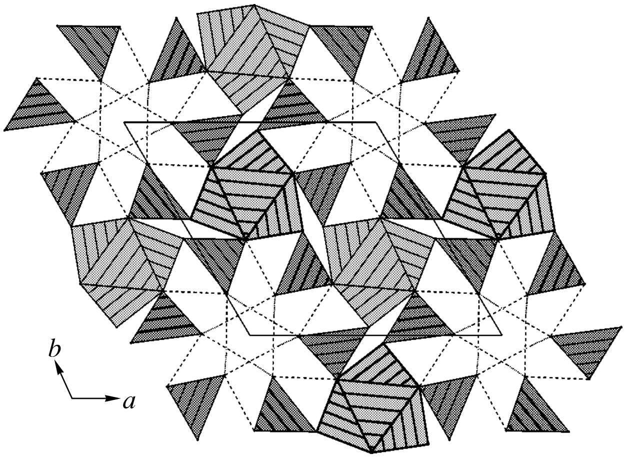

Fig. 1. Structure of $M(HSeO_4)_3$, *M* = Nd and Sm; projection along the *z* axis. A possible system of hydrogen bonds is indicated. One can see light MO_9 polyhedra and dark $HSeO_4$ polyhedra.

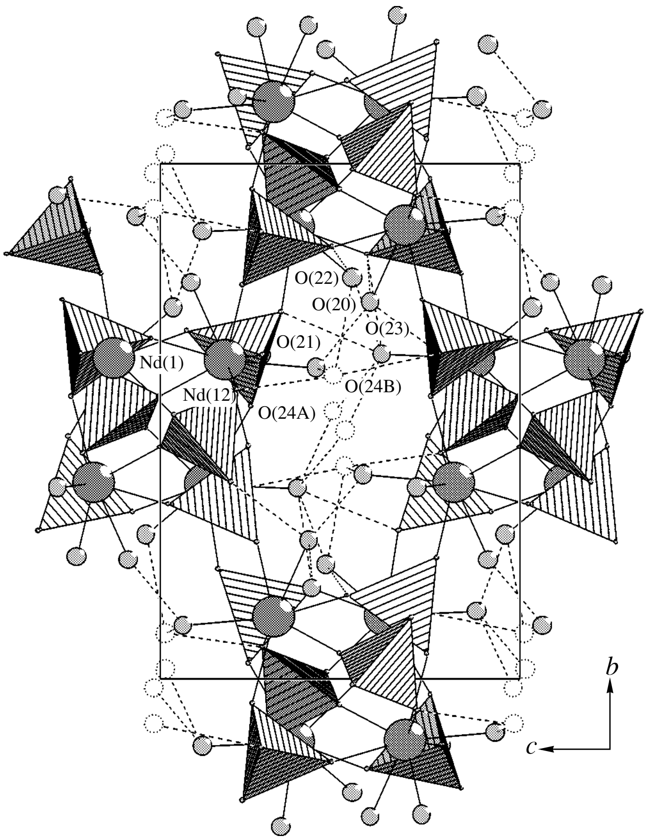

Fig. 2. Structure of a channel normal to the drawing plane and the systems of hydrogen bonds in the $Nd_2(SeO_4)_3 \cdot 5H_2O$ structure. White dashed circles indicate disordered water molecules.

large O···O distance. Also, we found some misprints in [1]: the O(1) atom forming a hydrogen bond with the O(3) lies at a too large distance from O(3) (>3.5 Å). It seems that, in actual fact, it is the O(2) atom. Moreover, the accuracy of the determination of the hydrogen bond angles O–H···O seems to be considerably overestimated. Considering the accuracy of the determination of the coordinates of hydrogen atoms (0.01–0.02 of the lattice parameter), we see that the error in the determination of the angle of a hydrogen bond cannot be 0.1° but should be larger by two orders of magnitude. However, these inconsistencies do not diminish the general importance of study [1]; moreover, these inconsistencies were removed in the following paper [5]. For RE hydrogen sulfates and, especially, for RE hydrogen selenates, the reliable localization of hydrogen atoms, and, hence, also the rigorous description of the system of hydrogen bonds, can be made only based on the neutron diffraction data.

It is also necessary to indicate that we calculated the structures of compounds **1** and **2** within the sp. gr. $P6_3$ with the ordered hydrogen atom. The refinement performed within this space group resulted in almost the same reliability factor R with a double number of parameters to be refined. However, the refinement of the structures was accompanied by strong correlations between the coordinates of those oxygen atoms that are related by the plane m in the sp. gr. $P6_3/m$. As a result, we have to return to the centrosymmetric sp. gr. $P6_3/m$ to provide stability of the refinement. Crystals **1** were also studied by X-ray diffraction analysis at room and lower temperatures with the use of several different sets of reflections (obtained for a complete reflection sphere and hemisphere); however, because of the correlation effects, we obtained no sufficient arguments in favor of a noncentrosymmetric structure of RE hydrogen selenates and sulfates. It seems that the decisive arguments may be obtained only by other independent methods, e.g., by second-harmonic generation.

$Nd_2(SeO_4)_3 \cdot 5H_2O$ (3). The independent part of the unit cell of this compound contains two Nd atoms and three SeO_4 groups. The Nd(1) atom is surrounded by nine O atoms forming a distorted tricapped trigonal prism with the Nd(1)–O distances ranging within 2.390–2.631 Å. The polyhedron of the Nd(2) atom with C.N. = 8 is a distorted square antiprism with the vertices occupied by O atoms and the Nd(2)–O distances ranging within 2.361–2.645 Å. Selenium atoms are surrounded by oxygen atoms forming a distorted tetrahedron with the Se–O distances ranging within 1.623(9)–1.654(9) Å, which correspond to the characteristic distances in a SeO_4^{2-} anion (see, e.g., [11]) in distinction from more pronounced differentiation of the distances in acid salts **1** and **2**.

The $[Nd(1)O_9]$ polyhedra share edges and form pairs. Each Nd(1) polyhedron shares vertices with three Se(1) tetrahedra (two of these tetrahedra are connected with both Nd(1) polyhedra of a pair) and one Se(2) tetrahedron and also shares an edge with a Se(3) tetrahedron. Thus, the $[Nd(1)O_9]_2$ dimer is connected to eight different SeO_4 groups. The $[Nd(2)O_8]$ antiprism shares vertices with six different SeO_4 tetrahedra. Four water molecules of the total five belong to NdO_x polyhedra. In turn, SeO_4 tetrahedra share Se(1) or Se(2) vertices or Se(3) edges with four different Nd polyhedra and, thus, form a three-dimensional framework (Fig. 2).

The structure has channels along the [100] direction. The fifth water molecule is located in these channels and is disordered over two positions with the occupancies 0.46(4) and 0.54(4) [O(24*A*)] and [O(24*B*)] and a distance between them of 1.16(3) Å. It should be emphasized that all the water molecules participating in the formation of Nd polyhedra are located inside the channels. Analysis of the O···O distances does not allow one to describe the system of hydrogen bonds adequately. Nevertheless, several systems of hydrogen bonds may be suggested. Each of the O(21) and O(24*A*) atoms participates in the formation of two hydrogen bonds O(21)···O(20) 2.80(1) Å, O(21)···O(24*B*) 2.85(3) Å, O(24*A*)···O(23) 2.89(2) Å, and O(24*A*)···O(23') 2.94(2) Å. Each of the O(22) and O(20) atoms may form three hydrogen bonds with the

O(8) [2.86(1) Å], O(23) [2.90(1) Å], O(24*B*) [2.85(3) Å], O(2) [2.86(1) Å], O(9) [2.89(1) Å], and O(21) [2.80(1) Å] atoms, respectively. The O(24*B*) atom may form four hydrogen bonds with the O(7), O(10), O(21), and O(22) atoms [2.96(2), 2.82(2), 2.85(3), and 2.85(3) Å, respectively]. The O(23) atom has five contacts with the O(2), O(4), O(22) and two O(24*A*) atoms [2.90(1), 2.96(1), 2.90(1), 2.89(12), and 2.94(2) Å, respectively]. It seems that the system of hydrogen bonds is somewhat disordered because some of the O atoms have several different possibilities for the formation of hydrogen bonds. Not going into the detailed consideration of the system of hydrogen bonds, we only indicate here its most important characteristic—all the hydrogen bonds are located inside the channels.

Among the RE sulfate and selenate hydrates, a pentahydrate structure was established only for the isostructural compounds $Nd_2(SO_4)_3 \cdot 5H_2O$ [17] and $Ce_2(SO_4)_3 \cdot 5H_2O$ [7]. Since both compounds are crystallized in the sp. gr. *C*2/*c*, they cannot be isostructural to compound *3*. However, the comparison of these structures with the structure of compound *3* shows that all the three compounds are characterized by the same structural motif. In sulfates and in compound *3*, the water molecule is located inside the channels and is disordered over two positions with the probabilities 0.5. Moreover, the unit cell parameters of these two compounds are also close: the a_{Se} parameter neodymium selenate (10.629 Å) is close to the c_S parameter of neodymium sulfate (10.262 Å); the b_{Se} parameter (13.98 Å) is close to the a_S parameter (15.702 Å), and the c_{Se} parameter (9.752 Å), to the b_S parameter (9.586 Å). The structural differences between the sulfate and selenate pentahydrates are reduced to the following. The selenate group is larger than the sulfate one, and the neodymium atom in selenate tends to surround itself with the equal number of anionic groups. As a result, the structure is distorted and loses the *C*-centering. This distortion is seen, e.g., from the environment of the neodymium atom: in sulfate, a crystallographically independent Nd is surrounded with nine oxygens, with the O(6) atom being bound to two metal atoms (there are two such oxygen atoms per two neodymium atoms), whereas in selenate, two independent neodymium atoms, Nd(1) and Nd(2), are surrounded with nine and eight oxygen atoms, respectively, of which only the O(12) atom coordinates two lanthanide atoms. This distortion also changes the channel structure, which results in a different location of the disordered water molecules inside the channel. Thus, the disordering vector (between two components of the disordered O atom) in sulfate is directed along the channel axis, whereas in selenate, this vector is almost normal to it.

It is not excluded that, in the structure of compound *3*, an increase in the temperature may result in a higher mobility of disordered water molecules up to their free motion along the columns, which, in turn, may give rise to higher ionic conductivity, because H_2O may serve as a carrier of ions (the so-called vehicle mechanism).

ACKNOWLEDGMENTS

M. Zakharov is grateful to the DAAD foundation for the financial support he received during his work in Humboldt University, Berlin, Germany.

REFERENCES

1. M. S. Wickleder, Z. Anorg. Allg. Chem. **624**, 1583 (1998).
2. M. S. Wickleder, Z. Anorg. Allg. Chem. **624**, 1347 (1998).
3. M. S. Wickleder, Z. Anorg. Allg. Chem. **625**, 1707 (1999).
4. H.-U. Hummel, P. Joerg, G. Pezzei, and A. Wolski, Z. Naturforsch. B **49**, 347 (1994).
5. I. Goehausen and M. S. Wickleder, Z. Anorg. Allg. Chem. **627**, 1115 (2001).
6. L. D. Iskhakova, S. M. Ovanisyan, and V. K. Trunov, Zh. Strukt. Khim. **32** (3), 30 (1991).
7. P. C. Junk, C. J. Kepert, B. W. Skelton, and A. H. White, Aust. J. Chem. **52**, 601 (1999).
8. M. S. Wickleder, Z. Anorg. Allg. Chem. **625**, 1548 (1999).
9. L. D. Iskhakova and L. G. Makarevich, Zh. Neorg. Khim. **41** (7), 1102 (1996).
10. L. Hiltunen and L. Niinistoe, Acta Crystallogr., Sect. C: Cryst. Struct. Commun. **5**, 567 (1976).
11. S. M. Ovanisyan, L. D. Iskhakova, and V. K. Trunov, Kristallografiya **33**, 69 (1988) [Sov. Phys. Crystallogr. **33**, 37 (1988)].
12. S. Karvinen and L. Niinistoe, Lanthanide Actinide Res. **1**, 169 (1986).
13. *STADI4 (Version 1.06) and XRED (Version 1.07)* (Stoe and Cie, Darmstadt, Germany, 1997).
14. G. M. Sheldrick, *SHELXS97. Program for the Solution of Crystal Structures* (Univ. of Göttingen, Germany, 1997).
15. G. M. Sheldrick, *SHELXL97. Program for the Refinement of Crystal Structures* (Univ. of Göttingen, Germany, 1997).
16. *DIAMOND. Visual Crystal Structure Information System. CRYSTAL IMPACT* (Bonn), Postfach 1251, D-53002.
17. L. O. Larsson, S. Linderbrandt, L. Niinistoe, and U. Skoglund, Suom. Kemistil. B **46**, 314 (1973).

Translated by L. Man

Crystallography Reports, Vol. 49, No. 5, 2004, pp. 752–757. Translated from Kristallografiya, Vol. 49, No. 5, 2004, pp. 841–846.
Original Russian Text Copyright © 2004 by Talipov, Ibragimov, Beketov, Praliev, Aripov.

STRUCTURE OF ORGANIC COMPOUNDS

Clathrates of Dianilinegossypol with Lower Acetate Ester Homologues: Structure, Isomorphism, and Morphotropic Transitions

S. A. Talipov[1], B. T. Ibragimov[1], K. M. Beketov[1, 2], K. D. Praliev[2], and T. F. Aripov[1]

[1] *Institute of Bioorganic Chemistry, Tashkent, Uzbekistan*
e-mail: root@ibc.tashkent.su
[2] *Bekturov Institute of Chemical Sciences, Academy of Sciences of Kazakhstan,*
ul. Krasina 106, Almaty, 480100 Kazakhstan

Received April 18, 2002

Abstract—The structure of dianilinegossypol clathrates is shown to be sensitive to size of the ester molecule included. The change in the guest component from methyl acetate to amyl acetate is accompanied by two morphotropic transitions in the acetic ester clathrate series and one transition into a nonsolvate dianilinegossypol form. *© 2004 MAIK "Nauka/Interperiodica".*

INTRODUCTION

Isomorphism has often been observed upon the formation of inclusion compounds in which the guest molecules replacing each other have a similar structure and geometry [1, 2]. Dianilinegossypol (DANG) [3–5] and guest molecules with a similar geometry also forms clathrates belonging to the same group of isostructural compounds [6–11]. In particular, dianilinegossypol forms the *A* group of isostructural clathrates with methyl acetate (MA), acetone [12], and methyl ethyl ketone. The *B* group contains complexes with ethyl acetate (EA) [13], propyl acetate, methyl propionate, ethyl propionate, and methyl butyrate. The complex with butyl acetate (BA) belongs to the *C* group (Table 1). Cavities formed by host molecules (*H*) can increase in size within certain limits to accommodate guest molecules (*G*). If the distortions fall beyond the permissible limits, the crystal structure of a dianilinegossypol clathrate undergoes a transformation: there occurs a morphotropic transition resulting in a new clathrate, whose cavities are suitable for accommodation of new guest molecules. The structure of the *B*-group clathrate with ethyl acetate was determined earlier in [13]. In the present work, we investigated the morphotropic transitions of dianilinegossypol clathrates with lower homologues of acetate esters and presented the results of

Table 1. Crystal data for the host–guest dianilinegossypol complexes

Group	*A*			*B*					*C*
Parameters	acetone	methyl acetate	methyl ethyl ketone	ethyl acetate	propyl acetate	methyl propionate	ethyl propionate	methyl butyrate	butyl acetate
a, Å	10.866(2)	11.076(3)	10.876(3)	18.025(3)	18.125(9)	18.331(9)	18.110(8)	18.283(6)	10.053(3)
b, Å	29.501(9)	29.418(9)	29.680(9)	10.840(3)	10.923(6)	10.676(2)	11.124(4)	10.875(4)	12.366(3)
c, Å	13.756(3)	13.550(4)	14.638(5)	25.021(3)	25.05(13)	25.600(8)	24.972(9)	25.338(8)	22.227(5)
				90	90	90	90	90	90.98(3)
β, deg	90	90	90	126.36(2)	126.14(6)	127.42(3)	126.12(3)	126.86(3)	100.93(3)
				90	90	90	90	90	115.05(4)
V, Å^3	4409	4415	4523	3937	4005	3978	4064	4030	2443
Space group	*Pccn*	*Pccn*	*Pccn*	$P2_1/c$	$P2_1/c$	$P2_1/c$	$P2_1/c$	$P2_1/c$	$P\bar{1}$
Host : guest ratio	1 : 2	1 : 2	1 : 2	1 : 1	1 : 1	1 : 1	1 : 1	1 : 1	1 : 2
Z	8	8	8	4	4	4	4	4	2
D_x, g/cm^3	1.18	1.19	1.19	1.27	1.28	1.18	1.28	1.27	1.19
Reference	[12]			[13]					

1063-7745/04/4905-0752$26.00 © 2004 MAIK "Nauka/Interperiodica"

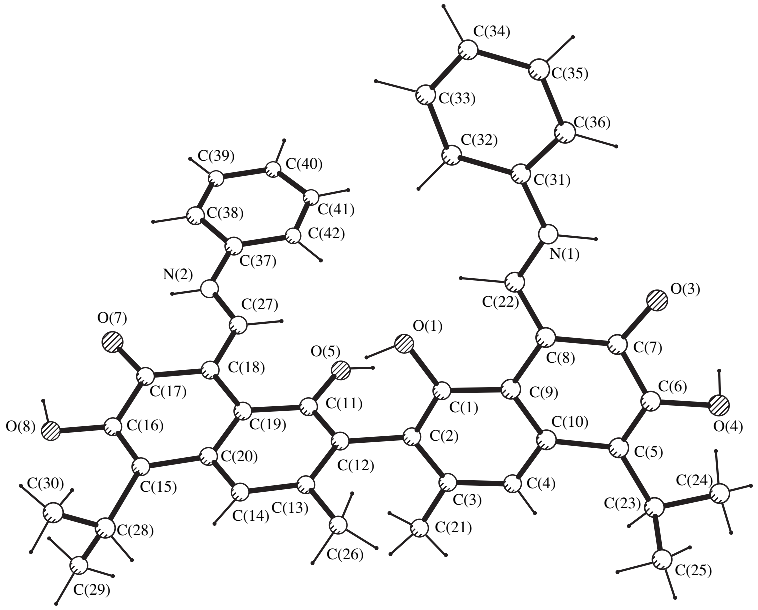

Fig. 1. Molecular structure of dianilinegossypol.

X-ray diffraction studies of dianilinegossypol clathrates with methyl acetate (DANG + MA, group *A*) and butyl acetate (DANG + BA, group *C*).

EXPERIMENTAL

The clathrates of dianilinegossypol to be studied were prepared by condensation reactions between gossypol and aniline in the corresponding solvents. For this purpose, aniline (0.005 ml) was added to a gossypol solution (approximately 100 mg of gossypol in 4–6 ml of a solvent). The solution obtained was allowed to stand in a thermostat at room temperature. The time required to form a crystal varied from several hours to several days.

Single crystals suitable for X-ray diffraction analysis were preliminarily chosen with the use of a microscope. Unstable crystals were sealed inside capillaries or coated with epoxy resin. The experiments were performed on a Syntex $P2_1$ automated four-circle diffractometer (CuK_α radiation, $\lambda = 1.542$ Å, graphite monochromator).

The experimental data were collected using the $\theta/2\theta$ scan technique up to the angle $2\theta_{\max} = 120°$. The scan speed varied within the range 4.8–11.2 deg/min. In the course of data collection, the crystal stability was checked every 100 reflections by measuring two control reflections.

After the weak reflections [$I < 2\sigma(I)$] were removed, 1147 and 3321 reflections remained out of 3059 and 5493 reflections collected for DANG + MA and DANG + BA, respectively. Both crystal structures were solved by direct methods. The structures were solved and refined with the SHELXS86 [14] and SHELXL93 [15] program packages, respectively. The hydrogen atoms were located from difference electron-density syntheses after several cycles of the refinement of the non-hydrogen atoms first in the isotropic approximation and then in the anisotropic approximation of the atomic displacements. The coordinates of the missing hydrogen atoms were calculated from the positional parameters of the relevant non-hydrogen atoms. The guest molecules in the DANG + MA structure are disordered over two positions with approximately equal occupancies. This provides an explanation for the relatively large discrepancy factor. The refinement procedures were terminated when further refinement did not result in a significant decrease in the *R* factor. After the final stages of the refinement of the positional and anisotropic thermal parameters, the discrepancy factors were $R = 0.098$ (DANG + MA) and 0.077 (DANG + BA). The coordinates of the non-hydrogen atoms are listed in Table 2. The molecular graphics were performed with the XP program included in the SHELXTL PLUS package [16].

RESULTS AND DISCUSSION

In the clathrates studied, the dianilinegossypol molecule has a quinoid tautomeric form (Fig. 1). The orientation of the isopropyl groups is the same in all the structures: the H(23) and H(28) isopropyl hydrogen atoms are directed toward the H(4) and H(14) atoms, respectively. Two types of intramolecular hydrogen bonds are characteristic of the molecule, namely, the N(1)–H···O(3) bond, which closes the C(7)–C(8)–C(22)–N(1)–H···O(3) six-membered ring, and the O(4)–H···O(3) bond, which closes the C(6)–C(7)–

Table 2. Atomic coordinates (×10^4) and equivalent thermal parameters (Å^2 × 10^3) in the structures of dianilinegossypol clathrates with methyl acetate and butyl acetate

Atoms	*x*/*a*	*y*/*b*	*z*/*c*	U_{eq}	Atoms	*x*/*a*	*y*/*b*	*z*/*c*	U_{eq}
Dianilinegossypol clathrates with methyl acetate					C(15)	2534(6)	1857(4)	4019(2)	54(2)
C(1)	1687(6)	6994(2)	5863(5)	44(2)	C(16)	1816(6)	1145(4)	4321(2)	62(2)
C(2)	2501(6)	7246(2)	6405(5)	48(2)	C(17)	1429(6)	384(4)	4020(2)	60(2)
C(3)	3325(6)	7008(2)	6991(5)	55(2)	C(18)	1767(5)	366(3)	3370(2)	47(1)
C(4)	3313(6)	6541(2)	7020(5)	63(2)	C(19)	2455(5)	1182(3)	3023(2)	43(1)
C(5)	2485(7)	5786(2)	6526(5)	63(2)	C(20)	2842(5)	1900(4)	3344(2)	46(1)
C(6)	1644(6)	5552(2)	6023(5)	58(2)	C(21)	1264(6)	4096(4)	1337(2)	75(2)
C(7)	738(7)	5775(2)	5399(5)	59(2)	C(22)	7583(6)	–231(4)	304(2)	48(1)
C(8)	740(5)	6252(2)	5312(5)	43(2)	C(23)	3067(6)	3504(4)	–986(2)	60(2)
C(9)	1627(5)	6517(2)	5866(4)	40(2)	C(24)	2305(6)	3078(4)	–1377(2)	77(2)
C(10)	2477(6)	6281(2)	6466(6)	61(2)	C(25)	3806(7)	4310(4)	–1386(2)	88(2)
C(11)	4202(7)	7271(2)	7657(6)	93(3)	C(26)	4518(6)	3629(4)	2040(2)	77(2)
C(12)	–146(6)	6434(2)	4678(5)	50(2)	C(27)	1434(6)	–449(4)	3113(2)	50(1)
C(13)	3446(10)	5522(3)	7122(10)	131(5)	C(28)	2963(7)	2605(4)	4365(2)	71(2)
C(14)	4222(8)	5221(4)	6455(11)	179(6)	C(29)	3778(7)	1922(5)	4908(2)	100(2)
C(15)	2895(11)	5248(3)	7970(7)	152(5)	C(30)	1628(7)	3699(4)	4563(2)	105(2)
C(16)	–1863(7)	6340(3)	3549(6)	71(2)	C(31)	10034(6)	–1801(4)	173(2)	51(2)
C(17)	–2214(6)	6789(3)	3501(6)	80(3)	C(32)	10511(6)	–1705(4)	695(2)	58(2)
C(18)	–3127(8)	6917(3)	2862(7)	100(3)	C(33)	11867(8)	–2500(5)	836(2)	72(2)
C(19)	–3683(8)	6601(4)	2292(8)	112(3)	C(34)	12722(7)	–3391(5)	474(3)	86(2)
C(20)	–3361(8)	6152(3)	2345(7)	115(4)	C(35)	12240(8)	–3453(6)	–47(3)	98(2)
C(21)	–2439(8)	6020(3)	2980(7)	99(3)	C(36)	10901(7)	–2688(5)	–196(2)	77(2)
O(1)	855(4)	7221(1)	5293(3)	66(2)	C(37)	485(6)	–2051(4)	3222(2)	56(2)
O(3)	–6(5)	5508(2)	4978(4)	80(2)	C(38)	869(7)	–2331(4)	2627(2)	79(2)
O(4)	1567(4)	5088(1)	6043(4)	82(2)	C(39)	523(8)	–3222(5)	2466(2)	100(2)
N(1)	–936(5)	6189(2)	4189(4)	58(2)	C(40)	–194(7)	–3821(5)	2889(3)	93(2)
C(1*A*)	4762(10)	6547(4)	4694(8)	117(9)	C(41)	–570(7)	–3531(5)	3481(2)	84(2)
C(2*A*)	3829(12)	6435(6)	3937(10)	131(7)	C(42)	–238(6)	–2648(4)	3651(2)	64(2)
C(3*A*)	6327(12)	6229(6)	5720(11)	146(9)	O(1)	5834(4)	506(3)	1351(1)	60(1)
O(1*A*)	4976(12)	6914(3)	5032(9)	119(5)	O(3)	7417(4)	–79(2)	–949(1)	58(1)
O(2*A*)	5385(11)	6183(3)	4988(9)	137(6)	O(4)	5518(4)	1683(3)	–1543(1)	60(1)
C(1*B*)	4988(12)	6636(5)	4901(9)	188(18)	O(5)	2334(4)	670(2)	2060(1)	57(1)
C(2*B*)	6023(16)	6694(8)	5590(14)	157(11)	O(7)	794(5)	–260(3)	4369(1)	91(1)
C(3*B*)	3932(18)	6078(6)	3929(14)	161(12)	O(8)	1406(5)	1097(4)	4944(1)	89(2)
O(1*B*)	4294(13)	6922(3)	4614(10)	95(5)	N(1)	8688(5)	–1011(3)	–13(2)	51(1)
O(2*B*)	4884(14)	6202(4)	4601(11)	142(8)	N(2)	810(5)	–1175(3)	3438(2)	58(1)
Dianilinegossypol clathrates with butyl acetate					C(43)	3355(7)	–228(5)	6474(2)	90(2)
C(1)	4826(6)	1414(4)	1034(2)	44(1)	C(44)	3727(6)	424(5)	6874(2)	71(2)
C(2)	3601(6)	2228(3)	1353(2)	46(1)	C(45)	4489(7)	2012(5)	6903(2)	86(2)
C(3)	2592(6)	3147(4)	1018(2)	53(2)	C(46)	5077(7)	2835(5)	6445(2)	91(2)
C(4)	2789(6)	3199(4)	385(2)	52(2)	C(47)	5413(8)	3663(6)	6778(3)	108(2)
C(5)	4137(5)	2476(3)	–614(2)	45(1)	O(9)	3649(5)	245(3)	7424(2)	99(2)
C(6)	5286(6)	1630(4)	–911(2)	47(1)	O(10)	4167(4)	1282(3)	6551(1)	81(1)
C(7)	6394(6)	653(4)	–608(2)	49(2)	C(48)	6122(9)	4441(6)	6341(3)	140(3)
C(8)	6355(6)	588(3)	45(2)	42(1)	C(49)	11133(8)	– 889(6)	–1799(3)	117(3)
C(9)	5076(5)	1456(3)	384(2)	41(1)	C(50)	11253(7)	–1976(6)	–2038(3)	86(2)
C(10)	3997(5)	2374(4)	56(2)	43(1)	C(51)	11558(8)	–2935(6)	–2918(3)	113(2)
C(11)	2739(5)	1334(3)	2375(2)	42(1)	C(52)	12081(8)	–2753(6)	–3601(3)	120(3)
C(12)	3397(5)	2100(3)	2044(2)	46(1)	C(53)	11939(10)	–3568(8)	–3952(4)	159(3)
C(13)	3783(6)	2789(4)	2372(2)	52(2)	O(11)	11077(7)	–2822(4)	–1727(2)	146(2)
C(14)	3502(6)	2679(4)	3002(2)	53(2)	O(12)	11508(5)	–1937(3)	–2648(2)	104(2)
					C(54)	12495(10)	–3372(8)	–4643(4)	191(4)

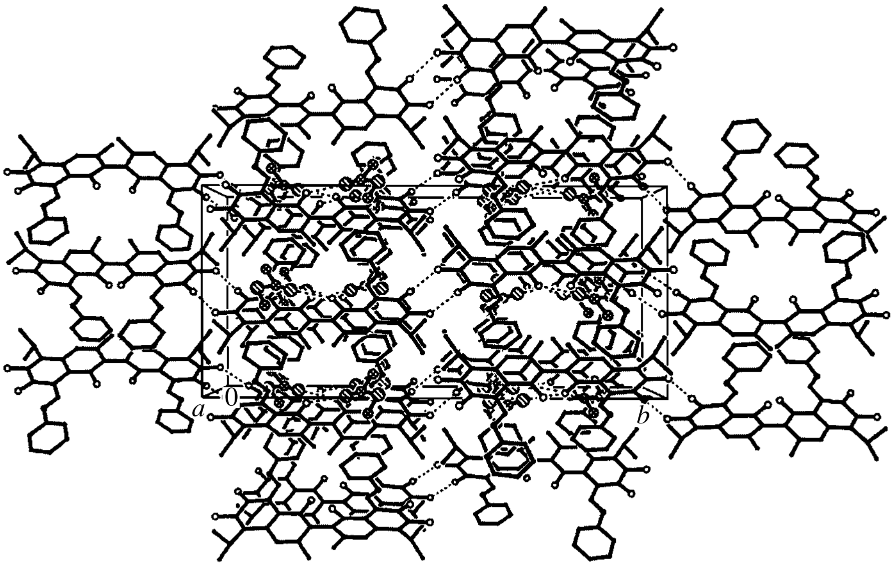

Fig. 2. Crystal structure of the DANG + MA clathrate.

O(3)···H–O(4) five-membered ring. Similar bonds are formed in the other half of the molecule (Fig. 1).

The dianilinegossypol molecule is conformationally mobile about the ordinary C(2)–C(12) bond between its two halves. The dihedral angle between the naphthyl rings in the clathrates and polymorphs of dianilinegossypol varies in the range 78°–97°. In addition, the aniline rings can form different dihedral angles with the naphthyl rings (4°–49°).

Investigations into the clathrate formation of dianilinegossypol with lower homologues of acetic esters have revealed that the structure of a clathrate strongly depends on geometric characteristics of the guest molecules included. Dianilinegossypol forms host–guest complexes with methyl acetate, ethyl acetate [13], propyl acetate, and butyl acetate, which belong to three different groups of isostructural clathrates. Dianilinegossypol precipitates in a nonsolvate crystal form from the amyl acetate medium. The crystallographic parameters of some isostructural host–guest complexes of dianilinegossypol are summarized in Table 1.

The 1 : 2 complex of dianilinegossypol with methyl acetate, which belongs to the *A* group of isostructural clathrates, crystallizes in space group *Pccn*. In these crystals, the host molecule retains its own symmetry [the twofold axis passes through the midpoint of the ordinary C(2)–C(12) bond] and the methyl acetate molecules occupy general positions (Fig. 2). In the structure of the DANG + MA complex, two of the six functional groups are involved in the host–guest hydrogen bonds. The dianilinegossypol molecules are linked by the centrosymmetric pairs of the O(4)–H···O(3) ($-x$, $1-y$, $1-z$) hydrogen bonds into infinite chains along the [011] direction. The packing of these chains in the crystal structure results in the formation of closed cavities accommodating methyl acetate molecules, which form the O(1)–H···O(*G*) hydrogen bonds (Fig. 2). Thus, the *A*-group complexes are cagelike clathrates (or cryptates) whose closed cavities include two guest molecules each.

Dianilinegossypol with the next two members of the series, namely, ethyl acetate (EA) and propyl acetate, form isostructural clathrates of the *B* group [13]. They are characterized by a 1 : 1 composition and belong to channel-like clathrates (tubulates). In the crystal structure of the DANG + EA tubulate, dianilinegossypol molecules are linked by two O(5)–H···O(3) ($1-x$, $-y$, $1-z$) hydrogen bonds into centrosymmetric dimers. The dimers, in turn, are linked by pairs of O(8)–H···O(7) ($-x$, $1-y$, $-z$) hydrogen bonds into two chains of infinite columns running along the [001] and [111] directions and intersecting at an angle of approximately 126°. The packing of these columns in the crystal results in the formation of channels stretched along the *y* axis. The ethyl acetate molecules are accommodated inside the channels and form the O(1)–H···O(*G*) hydrogen bonds (Fig. 3).

Butyl acetate with dianilinegossypol form the *C*-group tubulate, which is characterized by space group $P\bar{1}$ and has the composition DANG : BA = 1 : 2. The O(5)–H···O(3) ($1-x$, $-y$, $-z$) hydrogen bonds link dianilinegossypol molecules into typical centrosymmetric dimers [8], which, in turn, are linked by the O(8)–H···O(7) ($-x$, $-y$, $1-z$) hydrogen bonds into columns stretched along the [101] direction. These columns are packed in the crystal in such a way that channels are formed along the *y* axis. The channels accommodate two crystallographically independent butyl acetate molecules (Fig. 4), one of which forms the

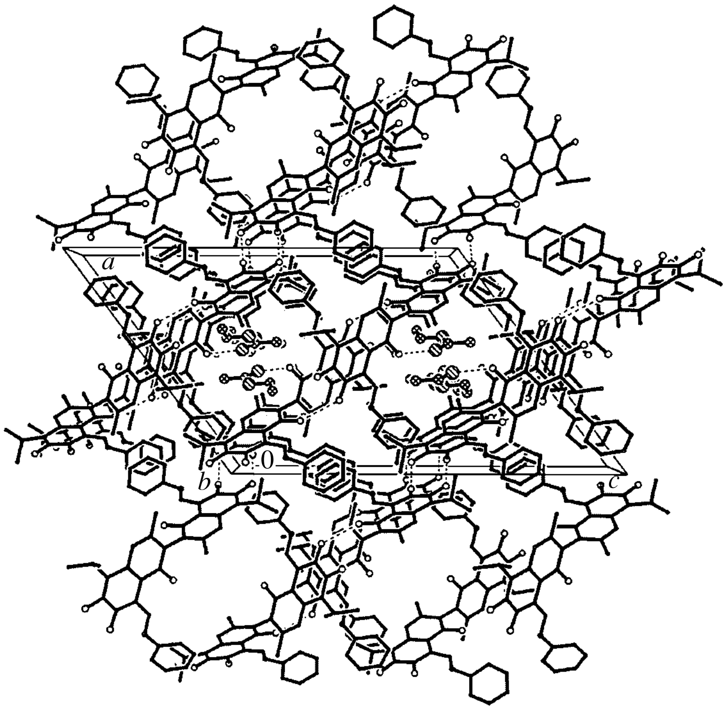

Fig. 3. Crystal structure of the DANG + EA clathrate.

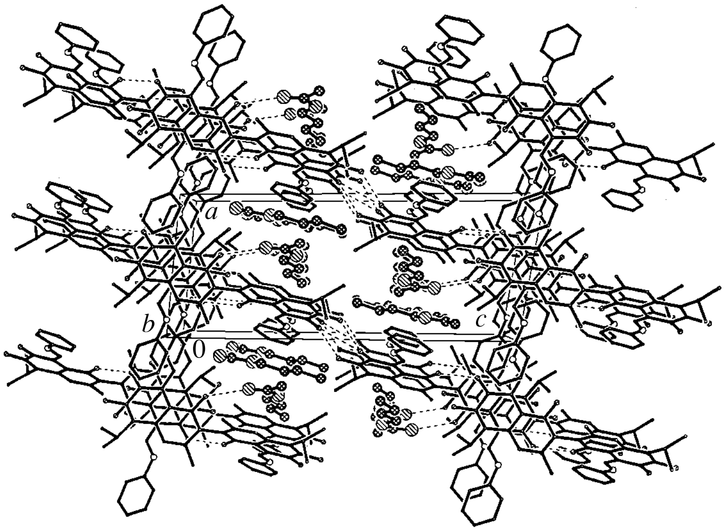

Fig. 4. Crystal structure of the DANG + BA clathrate.

O(1)–H···O(*G*) hydrogen bond with a dianilinegossypol molecule and the other of which is fixed in a channel only through van der Waals interactions.

The size of the amyl acetate molecule make the formation of an inclusion compound impossible. Thus, amyl acetate breaks off the series of guest molecules under consideration, which form host–guest complexes with dianilinegossypol. Dianilinegossypol precipitates in a nonsolvate form (the *P*1 polymorph) from an amyl acetate solution [17].

The main cause of the observed behavior of the dianilinegossypol clathrates studied is the ability of the dianilinegossypol molecule to form host–guest associates through the O(1)–H···O(*G*) hydrogen bond. According to the closest packing principle, the guest molecule in such an associate is coplanar to the naph-

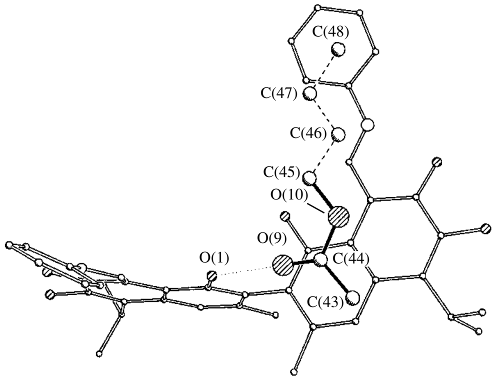

Fig. 5. Hydrogen bonding (dotted line) between the molecules of dianilinegossypol and methyl acetate (solid line) and between the molecules of dianilinegossypol and butyl acetate (dashed line).

thyl ring of the other half of the host molecule. In the DANG + MA clathrate, two guest molecules are bound through hydrogen bonds to each host molecule (the 1 : 2 associate). As the size of the guest molecule increases (when going from methyl acetate to ethyl acetate), the dianilinegossypol molecule associates with only one guest molecule (the 1 : 1 associate), which results in the breaking of molecular symmetry (twofold rotation axis). The O(5)–hydroxyl group, which is not involved in host–guest hydrogen bonds, participates in the formation of centrosymmetric dimers. The arrangement of guest molecules parallel to the naphthyl rings of the dianilinegossypol molecules and their gradual increase in length (Fig. 5) account for the fact that, first, isostructural clathrates are formed with methyl acetate, acetone, methyl ethyl ketone, and acetyl acetone (the *A* group) and, then, the *B*-group clathrates are formed with ethyl acetate, propyl acetate, methyl propionate, ethyl propionate, and methyl butyrate (Table 1). The size of the butyl acetate molecule is limiting for clathrate formation (the *C* group), because dianilinegossypol precipitates in the nonsolvate form from amyl acetate solutions.

Thus, in the homologous series of guest molecules, the following morphotropic transitions are observed when going from one member to another: group *A* (methyl acetate) → group *B* (ethyl acetate and propyl acetate) → group *C* (butyl acetate) → *P*1 polymorph. Going from ethyl acetate to propyl acetate provides the only example of isomorphic substitution in the *B* group. As the length of the ester molecules increases, the crystal symmetry lowers from orthorhombic (methyl acetate) to triclinic (butyl acetate) and the clathrate type changes from cryptate to tubulate.

ACKNOWLEDGMENTS

This study was supported in part by the US Civilian Research and Development Foundation for the Independent States of the Former Soviet Union (CRDF), grant no. ZC1-2451-TA-02.

REFERENCES

1. A. I. Kitaĭgorodskiĭ, *Organic Crystal Chemistry* (Akad. Nauk SSSR, Moscow, 1955).
2. A. I. Kitaĭgorodskiĭ, *Mixed Crystals* (Nauka, Moscow, 1983).
3. A. L. Markman and V. P. Rzhekhin, *Gossypol and Its Deriviatives* (Pishchevaya Promyshlennost’, Moscow, 1965).
4. R. Adams, T. A. Geismann, and J. D. Edwards, Chem. Rev. **60**, 555 (1960).
5. Ch. H. Boathner, in *Cottonseed and Cottonseed Products: Their Chemistry and Chemical Technology,* Ed. by A. E. Bailey (Interscience, New York, 1948), p. 213.
6. G. B. Nazarov, B. T. Ibragimov, and T. F. Aripov, Khim. Prir. Soedin. 661 (1998).
7. B. T. Ibragimov, G. B. Nazarov, and S. A. Talipov, Khim. Prir. Soedin. 666 (1988).
8. M. Gdaniec, B. T. Ibragimov, and S. A. Talipov, in *Comprehensive Supramolecular Chemistry,* Vol. 6: *Solid State. Supramolecular Chemistry: Crystal Engineering,* Ed. by D. D. MacNicol, E. Toda, and R. Bishop (Pergamon, Oxford, 1996), p. 117.
9. K. M. Beketov, B. T. Ibragimov, and S. A. Talipov, Khim. Farm. **1**, 16 (1996).
10. B. T. Ibragimov, K. M. Beketov, S. A. Talipov, and T. F. Aripov, J. Inclusion Phenom. **29**, 23 (1997).
11. K. M. Beketov, B. T. Ibragimov, and S. A. Talipov, Khim. Prir. Soedin. 58 (1994).
12. K. M. Beketov, B. T. Ibragimov, S. A. Talipov, and T. F. Aripov, J. Inclusion Phenom. **28**, 141 (1997).
13. K. M. Beketov, B. T. Ibragimov, S. A. Talipov, *et al.*, J. Inclusion Phenom. **27**, 105 (1997).
14. G. M. Sheldrick, Acta Crystallogr., Sect. A: Found. Crystallogr. **46**, 467 (1990).
15. G. M. Sheldrick, *SHELXL93: Program for the Refinement of Crystal Structures* (Univ. of Göttingen, Germany, 1993).
16. X. P. Siemens, *Molecular Graphics Program*, *Version 5.03* (Siemens Analytical X-ray Instruments Inst. Madison, Wisconsin, 1994).
17. K. M. Beketov, S. A. Talipov, B. T. Ibragimov, K. D. Praliev, and T. F. Aripov, Kristallografiya **48**, 691 (2003) [Crystallogr. Rep. **48**, 641 (2003)].

Translated by I. Polyakova

Crystallography Reports, Vol. 49, No. 5, 2004, pp. 758–766. Translated from Kristallografiya, Vol. 49, No. 5, 2004, pp. 847–854.
Original Russian Text Copyright © 2004 by Kuz'mina, Koval'chukova, Strashnova, Palkina, Zaĭtsev, Isaeva.

Physicochemical Properties of Solutions of Bis(2,3,5,6-Tetraoxo-4-Nitropyridinate) Dianions. Crystal Structures of Sodium 2,3,5,6-Tetraoxo-4-Nitropyridinate Trihydrate and Sodium Ammonium Bis(2,3,5,6-Tetraoxo-4-Nitropyridinate) Monohydrate

N. E. Kuz'mina*, O. V. Koval'chukova, S. B. Strashnova**, K. K. Palkina*,**
B. E. Zaĭtsev, and N. Yu. Isaeva****

** Kurnakov Institute of General and Inorganic Chemistry, Russian Academy of Sciences,*
Leninskiĭ pr. 31, Moscow, 119991 Russia

*** Peoples' Friendship University, ul. Miklukho-Maklaya 6, Moscow, 117198 Russia*

e-mail: okovalchukova@sci.pfu.edu.ru

Received October 7, 2002

Abstract—Ammonium 2,3,5,6-tetraoxo-4-nitropyridinate was shown to exist as stable dimers and act as a weak electrolyte in both a crystalline state and aqueous solutions. In a strongly alkaline medium, ammonium cations were successively replaced by sodium cations. The molecular and crystal structures of sodium 2,3,5,6-tetraoxo-4-nitropyridinate trihydrate and sodium ammonium bis(2,3,5,6-tetraoxo-4-nitropyridinate) monohydrate were established, and their spectroscopic characteristics were determined. *© 2004 MAIK "Nauka/Interperiodica".*

INTRODUCTION

Previously, we have described the unusual behavior of 2-amino-3-hydroxypyridine in an oxidative nitration reaction yielding the 2,3,5,6-tetraoxo-4-nitropyridinate anion [1]. This anion can be considered the first representative of a new class of compounds: tetraoxopyridines. The crystal structure of ammonium 2,3,5,6-tetraoxo-4-nitropyridinate (**I**) was determined in [2]. In the crystalline state, organic anions were shown to exist as stable head-to-tail dimers. In these dimers, intermolecular charge transfer occurs from the electron-donating fragment of one anion to the electron-withdrawing fragment of another anion.

This investigation is a continuation of our systematic studies of the 2,3,5,6-tetraoxo-4-nitropyridinate anion. With the aim of determining the forms of existence of this anion in solutions in different media, we studied the physicochemical properties of solutions of **I**, established the crystal structures of its sodium and mixed sodium ammonium salts, and determined their spectroscopic characteristics.

EXPERIMENTAL

Single crystals of sodium 2,3,5,6-tetraoxo-4-nitropyridinate trihydrate (**II**) and sodium ammonium bis(2,3,5,6-tetraoxo-4-nitropyridinate) monohydrate (**III**) were isolated from alkaline ethanolic solutions of **I**, which was synthesized according to a known procedure [3] at pH of 12.0 and 9.5, respectively.

The principal crystallographic parameters, details of X-ray data collection, and parameters of structure refinement of compounds **II** and **III** are listed in Table 1. The structures were solved by direct methods and refined by the full-matrix least-squares method with anisotropic thermal parameters for non-hydrogen atoms.

We ran into problems when trying to choose the space group of the crystal structure of **II**. Initially, we solved its structure in the space group $P2_1$. Analysis of the atomic coordinates revealed that certain atoms are symmetrically equivalent, which indicates that the crystal structure has the symmetry plane m. Therefore, the structure was then solved in the space group $P2_1/m$. A comparison of the reliability factors ($R = 0.077$ and 0.089, $R_w = 0.217$ and 0.242, *Goof* = 0.803 and 1.065 based on reflections with $I \geq 4\sigma$ for the space groups $P2_1/m$ and $P2_1$, respectively) led us to the conclusion that $P2_1/m$ is the true space group. In this group, the C–NO_2 and NH fragments of the organic anion and two water molecules involved in the coordination environment around the sodium atom are disordered relative to the symmetry plane m.

The disordered atoms were refined isotropically. The hydrogen atoms were not revealed from electron density maps. The conclusion that the ligand exists in

Table 1. Crystallographic characteristics, details of X-ray data collection, and parameters of structure refinement of compounds **II** and **III**

Parameter	**II**	**III**
Formula	$Na(C_5HN_2O_6) \cdot 3H_2O$	$NaNH_4(C_5HN_2O_6) \cdot 2H_2O$
Crystal system	Monoclinic	Monoclinic
Space group	$P2_1/m$	$P2_1/c$
Z	2	4
a, Å	6.227(3)	8.807(3)
b, Å	7.726(5)	18.595(10)
c, Å	10.262(5)	9.058(5)
β, deg	96.93(4)	90.33(4)
V, Å^3	490.1(5)	1483(1)
ρ_{calcd}, mg/m^3	1.776	1.92
F(000)	872	268
μ, mm^{-1}	0.208	0.204
Diffractometer	Enraf-Nonius CAD-4	Enraf-Nonius CAD-4
Radiation	MoK_α	MoK_α
θ_{max}	25	29
Number of independent reflections	1484	3025
Number of observed reflections with $I > 2\sigma(I)$	774	2297
R	0.077	0.039
R_w	0.217	0.103
Goof	0.803	0.959

Table 2. Atomic coordinates and isotropic thermal parameters for the structure of **II**

Atom	x	y	z	B_{eq}/B_{iso}
Na(1)	0.5338(4)	0.2500	0.5521(2)	3.08(6)
O(1)	0.3942(5)	0.0792(4)	0.3607(3)	3.37(6)
O(2)	0.2044(5)	0.0794(5)	–0.0884(3)	3.81(7)
O(3)*	0.2600(9)	–0.222(1)	0.2419(5)	4.1(1)
O(4)*	0.3070(9)	–0.239(3)	0.0416(5)	4.4(1)
O(5)*	0.8594(9)	0.1517(9)	0.4748(5)	3.2(1)
O(6)*	0.2057(9)	0.2023(8)	0.6349(5)	3.4(1)
O(7)	0.8551(9)	0.2500	0.2246(4)	4.6(1)
N(1)*	0.307(1)	0.409(1)	0.1352(9)	2.8(2)
N(2)*	0.2878(9)	–0.1429(9)	0.1411(6)	2.3(1)
C(1)	0.3491(6)	0.1510(6)	0.2563(4)	2.89(7)
C(2)*	0.291(2)	0.043(1)	0.1380(9)	2.4(2)
C(3)	0.2485(6)	0.1499(7)	0.0168(4)	3.36(8)
H(1)*	0.324	0.519	0.1340	

* The occupancies of the O(3), O(4), O(5), O(6), N(1), N(2), C(2), and H(1) atoms are 0.5.

Table 3. Atomic coordinates and isotropic thermal parameters for the structure of **III**

Atom	*x*	*y*	*z*	B_{eq}
Na(1)	–0.1977(1)	0.0234(1)	0.3220(1)	2.16(2)
O(1)	0.0939(2)	0.2779(1)	0.0470(2)	2.87(3)
O(2)	–0.1024(2)	0.3791(1)	–0.0296(2)	2.47(3)
O(3)	–0.4913(2)	0.2190(1)	0.1141(2)	3.04(3)
O(4)	–0.2797(2)	0.1269(1)	0.1845(2)	2.48(3)
O(5)	–0.3938(2)	0.4205(1)	–0.0146(2)	2.76(3)
O(6)	–0.5563(2)	0.3354(1)	–0.0360(3)	3.90(4)
O(7)	0.2276(2)	0.1449(1)	0.1624(3)	3.84(4)
O(8)	0.0082(2)	0.0513(1)	0.1701(2)	2.84(3)
O(9)	0.3852(2)	–0.1306(1)	0.1651(2)	2.85(3)
O(10)	0.5874(2)	–0.0270(1)	0.1909(2)	3.06(3)
O(11)	0.0972(2)	–0.1654(1)	0.1733(2)	2.96(3)
O(12)	–0.0720(2)	–0.0828(1)	0.1817(3)	3.96(4)
O(13)	–0.1978(2)	–0.0629(1)	0.5061(2)	3.02(3)
N(1)	–0.0899(2)	0.2036(1)	0.1292(2)	1.87(3)
N(2)	–0.4263(2)	0.3568(1)	–0.0100(2)	1.99(3)
N(3)	0.4109(2)	0.0600(1)	0.1731(2)	2.11(3)
N(4)	0.0619(2)	–0.1018(1)	0.1747(2)	2.05(3)
N(5)	0.6881(2)	–0.1994(1)	0.1726(2)	2.47(4)
C(1)	–0.0392(2)	0.2659(1)	0.0650(2)	1.85(3)
C(2)	–0.1567(2)	0.3227(1)	0.0160(2)	1.68(3)
C(3)	–0.3129(2)	0.3042(1)	0.0263(2)	1.70(3)
C(4)	–0.3615(2)	0.2385(1)	0.0892(2)	1.78(3)
C(5)	–0.2394(2)	0.1846(1)	0.1376(2)	1.69(3)
C(6)	0.2625(2)	0.0823(1)	0.1670(3)	2.15(4)
C(7)	0.1362(2)	0.0254(1)	0.1698(2)	1.85(3)
C(8)	0.1782(2)	–0.0481(1)	0.1711(2)	1.79(3)
C(9)	0.3341(2)	–0.0700(1)	0.1708(2)	1.88(3)
C(10)	0.4553(2)	–0.0102(1)	0.1802(2)	1.94(3)
H(1)	–0.027	0.170	0.160	
H(2)	0.478	0.095	0.181	
H(3)	–0.292	–0.089	0.517	
H(4)	–0.121	–0.102	0.518	
H(5)	0.773	–0.169	0.177	
H(6)	0.607	–0.169	0.177	
H(7)	0.677	–0.221	0.097	
H(8)	0.683	–0.221	0.237	

the anionic form rather than as an inner salt was made based on analysis of the composition of the reaction mixture and reaction conditions taking into account the neutrality of the system. The position of the hydrogen atom at the nitrogen atom of the heterocycle was calculated geometrically.

In the structure of compound **III**, the hydrogen atoms were located from a series of difference electron density maps and refined with fixed positional and thermal (B = 3.948 Å^2) parameters. Calculations were carried out with the use of the SHELXS86 [4] and SHELXL93 [5] program packages. The atomic coordinates and thermal parameters for the structures of **II** and **III** are listed in Tables 2 and 3, respectively. The bond lengths and bond angles in compounds **II** and **III** are listed in Tables 4 and 5, respectively. The parameters of the hydrogen bonds in the structure of **III** are given in Table 6.

The electronic absorption spectra of compounds **II** and **III** in aqueous and ethanolic solutions were recorded on a Specord UV-VIS spectrophotometer in the wavelength range 200–700 nm.

The degrees of dissociation were determined from the results of conductometric measurements of the electric conductivity. These measurements were carried out by the contact low-frequency method in a cell equipped with platinized electrodes according to a known procedure [6].

RESULTS AND DISCUSSION

Due to the ionic character of interactions in compound **I**, the latter should dissociate in polar solvents. In fact, compound **I** behaves as a weak binary electrolyte in aqueous solutions. At an infinite dilution, its degree of dissociation is 7.22%. At T = 293 K, the dissociation constant K of **I** is $(1.28 \pm 0.06) \times 10^{-4}$. Apparently, the behavior of compound **I** differs from that of inorganic ammonium salts because of the involvement of ammonium cations of **I** in strong hydrogen bonds with carbonyl groups of organic anions [2].

The cryoscopic determination of the molar weight of **I** in aqueous solutions at the calculated degree of dissociation gave M = 407–408 g/mol, which corresponds to the dimeric structure of the compound. Consequently, it can be assumed that dimers of **I** exist as stable species rather than decompose in solutions and only partially dissociate with elimination of ammonium cations.

The electronic absorption spectra of compound **I** are characterized by the presence of two main absorption bands at 41 170 and 28 500 cm^{-1}. These bands are broad and asymmetric, which is indicative of their complex character. The change in the pH of the medium from 2 to 12 only slightly changes the spectrum. However, the intensity of the long-wavelength band sharply increases (by approximately a factor of two) in a strongly alkaline medium (at pH > 12). Simultaneously, the band at

Table 4. Selected bond lengths and bond angles in the structure of **II**

Bond	*d*, Å	Angle	ω, deg
Na(1)–O(1)	2.438(3)	O(5)Na(1)O(1)	78.2(2)
Na(1)–O(1*a*)	2.438(3)	O(5)Na(1)O(1*a*)	98.0(2)
Na(1)–O(1*b*)	2.715(3)	O(5)Na(1)O(1*b*)	72.5(2)
Na(1)–O(1*c*)	2.715(3)	O(5)Na(1)O(1*c*)	107.1(2)
Na(1)–O(3*b*)	2.347(4)	O(5)Na(1)O(3*b*)	82.0(2)
Na(1)–O(5)	2.389(6)	O(6)Na(1)O(1)	97.8(2)
Na(1)–O(6)	2.335(6)	O(6)Na(1)O(1*a*)	88.0(2)
C(1)–C(1*a*)	1.531(7)	O(6)Na(1)O(1*b*)	98.3(2)
C(1)–C(2)	1.48(1)	O(6)Na(1)O(1*c*)	81.3(2)
C(1)–O(1)	1.209(5)	O(6)Na(1)O(3*b*)	95.4(2)
C(2)–C(3)	1.49(1)	O(5)Na(1)O(6)	170.5(2)
C(2)–N(2)	1.44(1)	Na(1)O(1)Na(1*a*)	102.3(1)
C(3)–C(3*a*)	1.547(8)	O(1)C(1)C(2)	118.5(5)
C(3)–O(2)	1.210(5)	O(1)C(1)C(1*a*)	117.3(4)
N(1)–C(1*a*)	1.32(1)	C(2)C(1)C(1*a*)	124.2(5)
N(1)–C(3*a*)	1.31(1)	N(2)C(2)C(1)	123.1(7)
N(1)–H(1)	0.86	N(2)C(2)C(3)	124.8(7)
N(2)–O(3)	1.232(9)	C(1)C(2)C(3)	112.1(7)
N(2)–O(4)	1.28(2)	O(2)C(3)C(2)	119.7(5)
		O(2)C(3)C(3*a*)	116.7(4)
		C(2)C(3)C(3*a*)	123.6(5)
		C(3)C(3*a*)O(2*a*)	116.6(6)
		N(1)C(3*a*)O(2*a*)	133.0(6)
		N(1)C(3*a*)C(3)	110.2(5)
		C(1*a*)N(1)C(3*a*)	139.0(8)
		C(1*a*)N(1)H(1)	110
		C(3*a*)N(1)H(1)	110
		N(1)C(1*a*)C(1)	110.4(5)
		N(1)C(1*a*)O(1*a*)	132.2(6)
		C(2)N(2)O(3)	121.2(7)
		C(2)N(2)O(4)	123.9(9)
		O(3)N(2)O(4)	114.9(9)

Table 5. Selected bond lengths and bond angles in the structure of **III**

Bond	*d*, Å	Angle	ω, deg	Bond	*d*, Å	Angle	ω, deg
Na(1)–O(2)	2.405(2)	Na(1)O(2)C(2)	125.9(2)	C(7)–C(8)	1.416(3)	C(6)N(3)C(10)	124.3(2)
Na(1)–O(4*a*)	2.402(2)	Na(1)O(4*a*)C(5*a*)	143.7(1)	C(8)–N(4)	1.431(3)	C(6)N(3)H(2)	114
Na(1)–O(5)	2.508(2)	Na(1)O(5)N(2)	125.9(1)	C(8)–C(9)	1.431(3)	C(10)N(3)H(2)	121
Na(1)–O(8*a*)	2.341(2)	Na(1)O(8*a*)C(7*a*)	129.0(2)	C(9)–O(9)	1.215(3)	N(3)C(6)O(7)	122.4(2)
Na(1)–O(10)	2.418(2)	Na(1)O(10)C(10)	133.6(2)	C(9)–C(10)	1.544(3)	N(3)C(6)C(7)	118.7(2)
Na(1)–O(12)	2.600(2)	Na(1)O(12*a*)N(4*a*)	130.7(1)	C(10)–O(10)	1.209(2)	O(7)C(6)C(7)	118.8(2)
Na(1)–O(13)	2.314(2)	Na(1)O(13)H(3)	115.4(2)	N(4)–O(11)	1.223(2)	C(6)C(7)O(8)	113.3(2)
N(1)–C(1)	1.372(3)	Na(1)O(13)H(4)	125.3(2)	N(4)–O(12)	1.232(2)	C(6)C(7)C(8)	118.4(2)
N(1)–C(5)	1.366(3)	C(1)N(1)C(5)	123.9(2)	N(5)–H(5)	0.94	O(8)C(7)C(8)	128.3(2)
N(1)–H(1)	0.88	C(1)N(1)H(1)	122	N(5)–H(6)	0.91	C(7)C(8)N(4)	119.1(2)
C(1)–O(1)	1.205(2)	C(5)N(1)H(1)	114	N(5)–H(7)	0.80	C(7)C(8)C(9)	121.6(2)
C(1)–C(2)	1.543(3)	N(1)C(1)O(1)	122.2(2)	N(5)–H(8)	0.71	N(4)C(8)O(9)	119.3(2)
C(2)–O(2)	1.226(3)	N(1)C(1)C(2)	118.8(2)			C(8)C(9)O(9)	128.3(2)
C(2)–C(3)	1.421(3)	O(1)C(1)C(2)	119.0(2)			C(8)C(9)C(10)	117.3(2)
C(3)–N(2)	1.436(3)	C(1)C(2)O(2)	114.9(2)			O(9)C(9)C(10)	114.5(2)
C(3)–C(4)	1.414(3)	C(1)C(2)C(3)	117.6(2)			N(3)C(10)C(9)	119.3(2)
C(4)–O(3)	1.222(2)	O(2)C(2)C(3)	127.6(2)			N(3)C(10)O(10)	121.8(2)
C(4)–C(5)	1.533(3)	C(2)C(3)N(2)	119.5(2)			C(9)C(10)O(10)	118.9(2)
C(5)–O(4)	1.207(3)	C(2)C(3)C(4)	122.1(2)			C(8)N(4)O(11)	119.5(2)
N(2)–O(5)	1.220(2)	N(2)C(3)C(4)	118.0(2)			C(8)N(4)O(12)	119.2(2)
N(2)–O(6)	1.234(2)	C(3)C(4)O(3)	128.1(2)			O(11)N(4)O(12)	121.4(2)
O(13)–H(3)	0.97	C(3)C(4)C(5)	117.8(2)			H(3)O(13)H(4)	102
O(13)–H(4)	0.998(2)	O(3)C(4)C(5)	114.0(2)			H(5)N(5)H(7)	116
N(3)–C(6)	1.373(3)	N(1)C(5)C(4)	119.3(2)			H(5)N(5)H(8)	110
N(3)–C(10)	1.363(3)	N(1)C(5)O(4)	122.3(2)			H(5)N(5)H(6)	106
N(3)–H(2)	0.89	C(4)C(5)O(4)	118.4(2)			H(6)N(5)H(7)	105
C(6)–O(7)	1.203(3)	C(3)N(2)O(5)	120.5(2)			H(6)N(5)H(8)	105
C(6)–C(7)	1.536(3)	C(3)N(2)O(6)	117.9(2)			H(7)N(5)H(8)	114
C(7)–O(8)	1.226(2)	O(5)N(2)O(6)	121.7(2)				

Table 6. Geometric parameters of hydrogen bonds in the structure of **III**

Bond *A*–H···*B*	Position of *B*	Distance, Å		∠*AHB*, deg
		A···*B*	H···*B*	
O(13)–H(4)···O(2)	–*x*; *y* – 0.5; 0.5 – *z*	2.862(2)	2.00	143
O(13)–H(3)···O(6)	–*x* – 1; *y* – 0.5; 0.5 – *z*	2.889(2)	1.94	164
N(5)–H(6)···O(9)	*x*; *y*; *z*	2.959(2)	2.09	161
N(5)–H(5)···O(12)	1 +*x*; *y*; *z*	3.028(3)	2.10	167

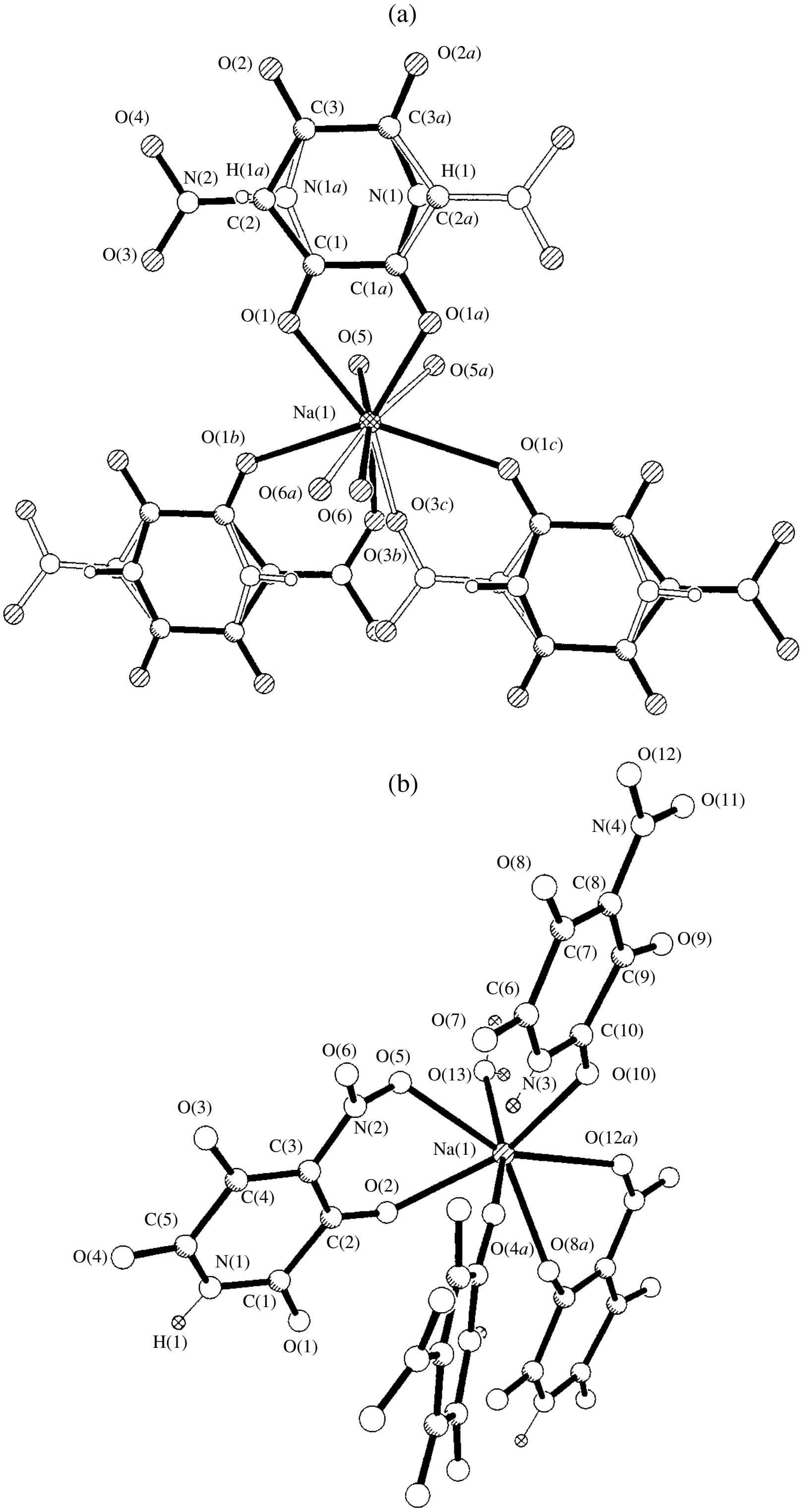

Fig. 1. Coordination modes of the sodium atoms in the structures of (a) **II** and (b) **III**.

41 170 cm^{-1} is bathochromically shifted to 36 500 cm^{-1}, and its intensity decreases. The observed changes in the spectrum are due to the fact that ammonium 2,3,5,6-tetraoxo-4-nitropyridinate is stable in acidic, neutral, and weakly alkaline media. However, this compound is transformed into sodium salt at pH > 12. This salt can be reversibly transformed into neutral form **IV** by subsequent titration. This process is described by the

following scheme:

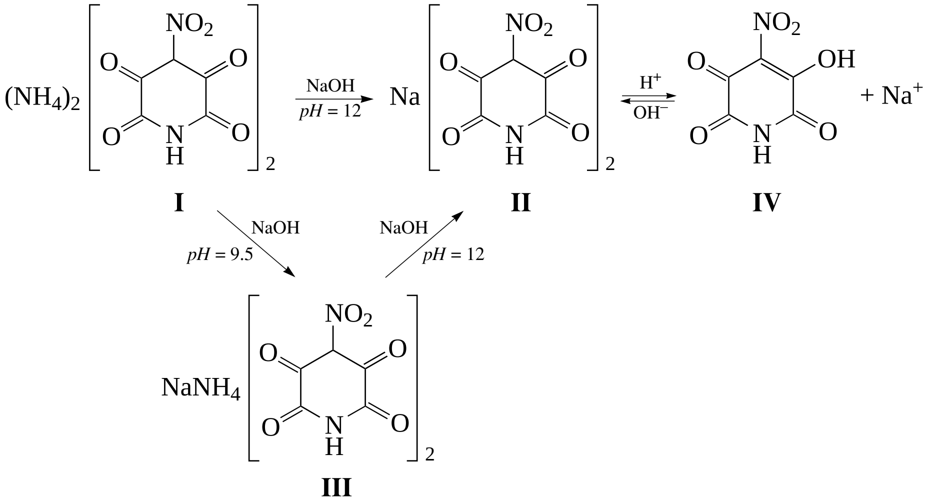

The spectrophotometrically determined acidic dissociation constant of **IV**, *pKa*, is 8.41 ± 0.36.

The gradual addition of alkali to a solution of compound **I** led to the replacement of one and two ammonium ions by sodium ions to give compounds **II** and **III**, respectively. These compounds were isolated as single crystals and studied by X-ray diffraction.

According to the results of X-ray diffraction analysis, the crystal structure of **II** is composed of polymeric neutral complexes $[Na^+(C_5HN_2O_6)^- \cdot 2H_2O]_n$ and water molecules of crystallization (sodium atoms and water molecules of crystallization occupy special positions in the symmetry plane *m*). In the crystal structure of **III**, the polymeric anion $[Na^+(C_5HN_2O_6)_2^- \cdot H_2O]_n$ and the ammonium cation are the structural units. In both structures, the coordination number of the sodium atom is 7. In the structure of **II**, the coordination environment around the sodium atom is formed by four carbonyl O atoms belonging to three 2,3,5,6-tetraoxo-4-nitropyridinate anions, the oxygen atom of the nitro group of one anion disordered relative to the plane *m*, and the oxygen atoms of two water molecules, which are also disordered over two positions with respect to the plane *m* (Fig. 1a). The NaO_7 coordination polyhedron can be described as a strongly distorted pentagonal bipyramid. The base of the bipyramid is formed by the oxygen atoms of the NO_2 and C=O groups (the average deviation of the oxygen and sodium atoms from the plane of the base is 0.07 Å). The axial positions are occupied by water molecules. The angle between the axial axis and the plane of the base is 90°.

In the structure of **III**, the coordination environment around the sodium atom is formed by two pairs of crystallographically independent 2,3,5,6-tetraoxo-4-nitropyridinate anions (*A* and *B*) and a water molecule (Fig. 1b). Two crystallographically independent organic anions *A* and *B* are coordinated to the sodium atom in a monodentate fashion (through the carbonyl oxygen atoms), whereas anions of another pair are coordinated to the sodium atom in a bidentate fashion (through the carbonyl oxygen atoms and oxygen atoms of the nitro groups). The NaO_7 coordination polyhedron can be described as a trigonal antiprism with one capped lateral face (O(12*a*) is in the cap position). The upper base of the antiprism is formed by the carbonyl O(4*a*) and O(10) atoms and the O(5) atom of the nitro group. The lower base is formed by the carbonyl O(2) and O(8*a*) atoms and the O(13) atom of the water molecule. The dihedral angle between the bases is 2.4°.

The organic anions in compounds **II** and **III** have similar structures. The tetraoxopyridinate fragments are nearly planar; the average deviations of the atoms from the mean planes are 0.018 Å in **II** and 0.033 and 0.045 Å (in independent anions *A* and *B*, respectively) in **III**. The imine and β-diketone fragments in the anions, like those in compound **I** [2], are bound by C–C single bonds (Tables 4 and 5). The involvement in the coordination to the sodium atom has only a slight effect on the bond lengths in the carbonyl groups of the tetraoxopyridinate anions. The C=O distances are similar to those found in the "free" 1,2,4,5-tetraoxo-3-nitropyridinate anion [2]. As in the latter anion, the C=O bonds in the β-diketone fragment in **II** and **III** are longer than those in the imine fragment, which is due to the difference in the degrees of conjugation in these fragments.

The presence of polymeric components is a common feature of the crystal structures of **II** and **III**. In the crystal of **II**, NaO_7 polyhedra are linked to each other by sharing edges to form infinite ribbons with composition $[Na^+(C_5HN_2O_6)^- \cdot 2H_2O]_n$ extended along the *Y* axis (Fig. 2a; for simplicity, the disorder of the structure is omitted). The oxygen atoms of the shared edges belong to carbonyl groups. The Na–O(C=O) distances are somewhat larger than all other Na–O distances. The organic anion cores and sodium atoms in the ribbon lie

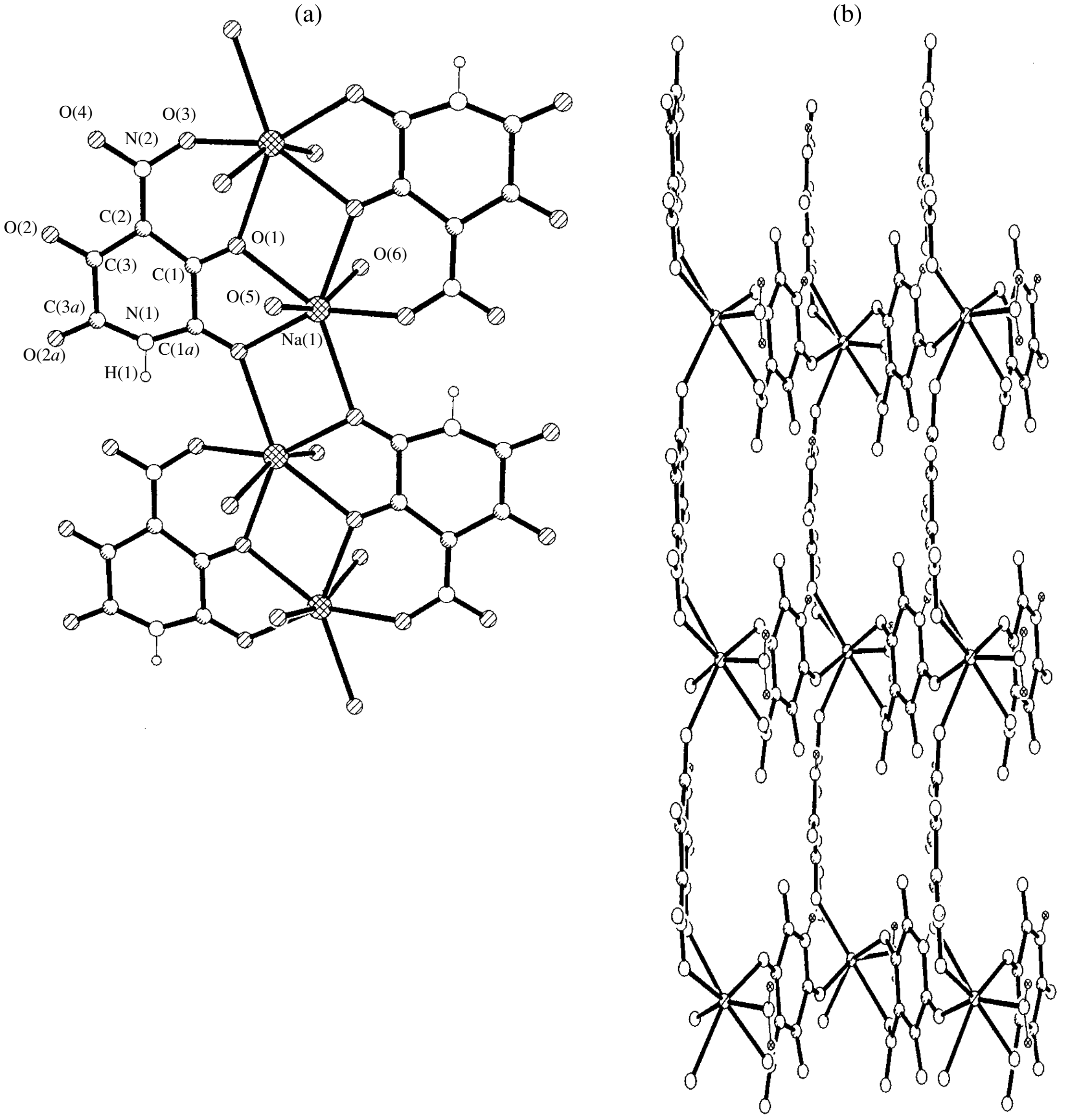

Fig. 2. Polymeric fragments in the structures of **II** and **III**. (a) The structure of the polymeric ribbon $[Na^+(C_5HN_2O_6)^- \cdot 2H_2O]_n$ projected along the *x* axis. (b) The structure of the polymeric layer $[Na^+(C_5HN_2O_6)_2^- \cdot H_2O]_n$ projected along the *y* axis.

approximately in the same plane (the average deviation of the atoms from the plane is 0.08 Å). The Na···Na distance in the ribbon is 4.017 Å. In the crystal, the polymeric ribbons form layers parallel to the *xy* plane. Water molecules of crystallization are located between these planes. The presence of short intermolecular O···O contacts is indicative of hydrogen bonding both between coordinated water molecules of adjacent ribbons in the layer (O(5)···O(6) is 2.58 Å) and between the water molecules incorporated in the layer and the "free" water molecules (O(5)···O(7) is 2.67 Å).

In the crystal of **III**, Na polyhedra do not share edges and corners and are linked through bridging anions in such a way that sodium atoms are linked to each other by anions of type *A* along the *z* axis and by anions of type *B* along the *x* axis to form a polymeric anionic layer $[Na^+(C_5HN_2O_6)_2^- \cdot H_2O]_n$ parallel to the *xz* plane (Fig. 2b). Each anion in the layer is coordinated to two sodium atoms differently (in monodentate and bidentate modes). The polymeric layers are linked in a three-dimensional framework by hydrogen bonds involving water molecules of one layer and carbonyl and nitro groups of anions *A* of another layer (Table 6). Ammonium cations are located between the polymeric anionic layers and form hydrogen bonds with organic anions *B* (Table 6).

The data on the crystal structures of **II** and **III** were deposited with the Cambridge Structural Database (refcodes CCDC 205 694 and 205 695, respectively).

REFERENCES

1. O. V. Koval’chukova, S. B. Strashnova, B. E. Zaĭtsev, *et al.*, Khim. Geterotsikl. Soedin., No. 12, 1690 (1999).
2. K. K. Palkina, N. E. Kuz’mina, O. V. Koval’chukova, *et al.*, Dokl. Akad. Nauk **370** (5), 631 (2000).
3. O. V. Koval’chukova, S. B. Strashnova, B. E. Zaĭtsev, *et al.*, RF Patent No. 2152386, Byull. Izobret., No. 19 (2000).
4. G. M. Sheldrick, *SHELXS86. Program for the Solution of Crystal Structures* (Univ. of Göttingen, Germany, 1986).
5. G. M. Sheldrick, *SHELXL93. Program for the Refinement of Crystal Structures* (Univ. of Göttingen, Germany, 1993).
6. T. A. Khudyakova and A. P. Kreshkov, *Theory and Practice of Conductometric and Chronoconductometric Analysis* (Khimiya, Moscow, 1976).

Translated by T. Safonova

Crystallography Reports, Vol. 49, No. 5, 2004, pp. 767–771. Translated from Kristallografiya, Vol. 49, No. 5, 2004, pp. 855–859.
Original Russian Text Copyright © 2004 by Polyakova, Mustyatsa, Zhizhin, Kuznetsov.

Structure of the Undecahydrodecaborate Anion $B_{10}H_{11}^{-}$. Crystal Structures of $[Ph_3PCH_2Naph]B_{10}H_{11}$ and $[Ph_3PEt]_2B_{10}H_{10}$

I. N. Polyakova, V. N. Mustyatsa, K. Yu. Zhizhin, and N. T. Kuznetsov

Kurnakov Institute of General and Inorganic Chemistry, Russian Academy of Sciences,
Leninskiĭ pr. 31, Moscow, 119991 Russia

e-mail: sokol@igic.ras.ru

Received February 28, 2003

Abstract—The crystal structures of $[Ph_3PCH_2Naph]B_{10}H_{11}$ (**I**) and $[Ph_3PEt]_2B_{10}H_{10}$ (**II**) are studied (110 K and room temperature, $R = 0.0673$ and 0.0609 for 4176 and 953 observed reflections in **I** and **II**, respectively). It is unambiguously determined that protonation of the $B_{10}H_{10}^{2-}$ anion proceeds at one of the faces of the apical belt and results mainly in a significant lengthening of the edges of the centered face [B_e–B_e, 1.948(4) Å; B_a–B_e, 1.770(5) Å and 1.787(5) Å]. *© 2004 MAIK “Nauka/Interperiodica”.*

INTRODUCTION

Since the 1970s, it has been repeatedly proposed that reactions of substitution in the *closo*-decaborate anion proceed through the formation of a protonated intermediate, that is, the $B_{10}H_{11}^{-}$ anion [1, 2]. Later [3, 4], some salts of the $B_{10}H_{11}^{-}$ anion were isolated and characterized by spectral methods. X-ray diffraction studies of the $[Ph_4P]B_{10}H_{11}$ and $[Ph_3PEt]B_{10}H_{11}$ salts at room temperature [5] revealed that the 11th proton is disordered over several positions, so that the resulting decaborate polyhedra are the sums of several polyhedra. Our attempt to “freeze” this proton in $[Ph_4P]B_{10}H_{11}$ failed: at 110 K, the crystal symmetry and site symmetry of the polyhedral anion did not change and the proton remained disordered. Upon cooling, $[Ph_3EtP]B_{10}H_{11}$ crystals undergo a phase transition, during which the polyhedral anions divide into two independent site systems [6]. In this case, however, the low-temperature X-ray diffraction experiment (at 110 K) also did not allow localization of the proton. Indirectly, based on the bond lengths, it was concluded that the proton is delocalized over two sites in both independent anions.

With the purpose of objectively determining the protonation site of the decaborate anion and the effect of the 11th proton on the geometric structure of the polyhedron, we synthesized the $[Ph_3PCH_2Naph]B_{10}H_{11}$ (**I**) salt and studied its crystal structure by X-ray diffraction at 110 K. This study was successful. We report its results along with the results of the X-ray diffraction study of the $[Ph_3PEt]_2B_{10}H_{10}$ (**II**) salt, which will allow us to compare the structure of the boron backbone in the protonated and nonprotonated decaborate anions.

EXPERIMENTAL

Compounds **I** and **II** were synthesized by the procedures described in [3, 4]. Crystals suitable for X-ray diffraction studies were obtained from acetonitrile solutions. The main crystal data and the characteristics of the experiment and refinement for compounds **I** and **II** are summarized in Table 1.

The diffraction experiment for crystal **I** was performed by the standard procedure [7] at $T = 110(2)$ K on a Bruker AXS SMART 100 diffractometer equipped with a CCD detector (λMo, graphite monochromator, ω scan mode). Correction for absorption was introduced semiempirically with the SADABS program [8].

The set of intensities $I(hkl)$ for crystal **II** was collected at room temperature on a CAD4 automated diffractometer (λMo, graphite monochromator, ω scan mode). Correction for absorption was not performed.

Structures **I** and **II** were solved by the direct method (SHELXS97 [9]). All the H atoms in structure **I** and the H atoms of the decaborate anion in structure **II** were located from difference Fourier syntheses. The positions of the H atoms of the Ph_3PEt^+ cation in structure **II** were calculated. In structure **I**, all the non-hydrogen atoms were refined in the anisotropic approximation and the H atoms were refined isotropically. In structure **II**, the B and P atoms were refined anisotropically, the C and H(B) atoms were refined isotropically, and H(C) atoms were treated as “riders” with thermal parameters

Table 1. Main crystal data and parameters of data collection and structure refinement for compounds **I** and **II**

Parameter	**I**	**II**
Empirical formula	$C_{29}H_{35}B_{10}P$	$C_{40}H_{50}B_{10}P_2$
M	522.64	700.84
Space group	$P2_1/c$	$C2/c$
a, Å	12.714(9)	19.117(4)
b, Å	9.643(7)	14.001(4)
c, Å	24.87(2)	17.785(4)
β, deg	101.477(9)	120.63(1)
V, Å^3	2988(4)	4096.3(5)
Z	4	4
ρ_{calcd}, g/cm^3	1.162	1.136
Crystal size, mm	0.10 × 0.20 × 0.60	0.12 × 0.24 × 0.30
μ_{Mo}, mm^{-1}	0.111	0.134
θ_{max}, deg	30	25
Number of reflections:		
measured	22252	3617
unique [R_{int}]	8504 [0.0640]	3499 [0.0547]
with $I > 2\sigma(I)$ (N_{obs})	4176	953
R_1, wR_2 for N_{obs}	0.0673, 0.1559	0.0609, 0.1618
GOOF	0.874	0.968
$\Delta\rho_{min}$ and $\Delta\rho_{max}$, e/Å^3	–0.376 and 0.519	–0.321 and 0.306

exceeding the thermal parameters of the corresponding C atoms by a factor of 1.2. The refinement was performed with the SHELXL97 program [10]. The coordinates and thermal parameters of atoms (excluding H atoms of the cations) are listed in Table 2.

RESULTS AND DISCUSSION

Crystals **I** are built of $Ph_3PNaphCH_2^+$ cations and undecahydrodecaborate anions $B_{10}H_{11}^-$, and crystals **II** consist of Ph_3EtP^+ cations and decahydro-*closo*-decaborate anions $B_{10}H_{10}^{2-}$. The structural units of **I** and **II** with the atomic numberings are shown in Figs. 1 and 2, respectively. In compound **II**, the crystallographic symmetry of the anions is C_2. The twofold rotation axis passes through the midpoints of the B(2)–B(2*A*) and B(4)–B(4*A*) equatorial edges.

The H(11*B*) atom is unambiguously localized in the structure. It centers asymmetrically the B(1)B(2)B(3) face of the apical belt, thus forming a longer bond [1.63(9) Å] with the B(2) atom as compared to the B(1) and B(3) atoms [1.11(9) and 1.24(9) Å, respectively]. Relatively large errors in determining the coordinates and the large isotropic parameter of thermal vibrations [$U = 0.24(4)$ A$_2$] even at a low temperature are apparently due to the high mobility of the H(11*B*) atom.

The nonprotonated $B_{10}H_{10}^{2-}$ anion in compound **II** has the normal shape of a bicapped Archimedean antiprism, in which edges of different types differ in length: the edges between the apical and equatorial vertices are the shortest, the edges between the equatorial vertices at the bases of the tetragonal pyramids are the longest, and the edges between the two bases of the tetragonal pyramids are intermediate in length. The corresponding B–B bond lengths lie in the ranges 1.66–1.68(1), 1.81–1.83(1), and 1.79–1.81(1) Å, respectively.

In the protonated $B_{10}H_{11}^-$ anion, the shape of the polyhedron is on the whole retained. The bases of the tetragonal pyramids forming the bicapped Archimedean antiprism remain planar, and the spacing between the basal planes remains unchanged (1.513 and 1.510 Å in $B_{10}H_{11}^-$ and $B_{10}H_{10}^{2-}$, respectively). No essential changes in the dihedral angles between the faces of the polyhedron take place, but some flattening of the B(1)B(4)B(5)B(8) and B(3)B(6)B(7)B(10) fragments is observed: the angles of folding along the B(4)–B(5) and B(6)–B(7) edges are 157.5° and 156.7°, respectively, whereas, in the $B_{10}H_{10}^{2-}$ anion, the angles of folding along the edges lying in the bases of the tetragonal pyramids fall in the range 153.0°–154.2°.

Addition of the proton to the $B_{10}H_{10}^{2-}$ anion results mainly in changes in the B–B bond lengths in the protonated tetragonal pyramid. The edges of the centered face lengthen to the greatest degree: B(2)–B(3), 1.948(4) Å; B(1)–B(3), 1.787(5) Å; and B(1)–B(2), 1.770(5) Å. The remaining edges lengthen to a lesser degree [B(1)–B(4), 1.745(5) Å; B(1)–B(5), 1.723(5) Å; B(3)–B(4), 1.846(5) Å; and B(4)–B(5), 1.872(5) Å], and the B(2)–B(5) bonds slightly shortens [1.786(5) Å]. In the other tetragonal pyramid, the two edges involving the B(6) atom, which is bound to the centered face, slightly lengthen: B(6)–B(7), 1.857(4) Å; and B(6)–B(10), 1.714(4) Å.

The nonuniform stretching of the polyhedral anion upon protonation results in a noticeable inequality of bond angles of the same type. The maximum difference between angles of the same type increases from 1.8° in $B_{10}H_{10}^{2-}$ to 6.0° in $B_{10}H_{11}^-$.

Table 2. Coordinates and parameters of thermal vibrations of atoms (U_{eq}/U_{iso}) in structures **I** and **II**

Atom	*x*	*y*	*z*	U_{eq}/U_{iso}, Å^2	Atom	*x*	*y*	*z*	U_{eq}/U_{iso}, Å^2
		I			H(2*B*)	0.447(2)	0.711(3)	0.433(1)	0.033(8)
P(1)	0.26071(5)	0.45136(7)	0.15214(2)	0.0208(2)	H(3*B*)	0.236(2)	0.669(3)	0.503(1)	0.032(7)
C(1)	0.2313(2)	0.3400(3)	0.20491(9)	0.0215(5)	H(4*B*)	0.105(3)	0.936(4)	0.427(1)	0.06(1)
C(2)	0.1532(2)	0.2380(3)	0.19118(10)	0.0324(6)	H(5*B*)	0.306(3)	0.977(4)	0.364(1)	0.05(1)
C(3)	0.1295(2)	0.1510(3)	0.23188(11)	0.0368(7)	H(6*B*)	0.285(2)	0.485(3)	0.423(1)	0.026(7)
C(4)	0.1811(2)	0.1675(3)	0.28548(10)	0.0296(6)	H(7*B*)	0.050(2)	0.641(3)	0.418(1)	0.036(8)
C(5)	0.2581(2)	0.2698(3)	0.29974(10)	0.0356(7)	H(8*B*)	0.096(3)	0.852(4)	0.316(1)	0.051(9)
C(6)	0.2829(2)	0.3560(3)	0.25964(10)	0.0335(6)	H(9*B*)	0.333(2)	0.698(3)	0.315(1)	0.044(9)
C(7)	0.2310(2)	0.3636(3)	0.08733(9)	0.0232(5)	H(10*B*)	0.117(2)	0.535(3)	0.318(1)	0.027(7)
C(8)	0.1290(2)	0.3780(3)	0.05413(10)	0.0307(6)	H(11*B*)	0.322(7)	0.781(9)	0.477(4)	0.24(4)
C(9)	0.1015(2)	0.3005(3)	0.00619(11)	0.0374(7)				**II**	
C(10)	0.1749(2)	0.2088(3)	−0.00869(11)	0.0365(7)	P(1)	0.1982(1)	0.9715(1)	0.0133(1)	0.0507(5)
C(11)	0.2767(2)	0.1956(3)	0.02424(11)	0.0370(7)	C(1)	0.2617(4)	0.9434(4)	−0.0304(4)	0.047(2)
C(12)	0.3047(2)	0.2719(3)	0.07221(10)	0.0314(6)	C(2)	0.3367(4)	0.9898(5)	0.0039(4)	0.068(2)
C(13)	0.1815(2)	0.6053(3)	0.14676(8)	0.0215(5)	C(3)	0.3878(4)	0.9661(5)	−0.0283(5)	0.076(2)
C(14)	0.1818(2)	0.6946(3)	0.10234(9)	0.0237(5)	C(4)	0.3627(5)	0.9020(5)	−0.0953(5)	0.078(2)
C(15)	0.1254(2)	0.8181(3)	0.09901(9)	0.0269(5)	C(5)	0.2894(4)	0.8596(5)	−0.1297(5)	0.078(2)
C(16)	0.0682(2)	0.8523(3)	0.13969(10)	0.0299(6)	C(6)	0.2380(4)	0.8792(5)	−0.0982(4)	0.067(2)
C(17)	0.0688(2)	0.7645(3)	0.18358(10)	0.0312(6)	C(7)	0.1007(4)	0.9194(5)	−0.0566(4)	0.055(2)
C(18)	0.1251(2)	0.6408(3)	0.18766(9)	0.0255(5)	C(8)	0.0364(4)	0.9735(5)	−0.1173(4)	0.060(2)
C(19)	0.4040(2)	0.4919(3)	0.17039(10)	0.0252(5)	C(9)	−0.0367(4)	0.9294(5)	−0.1763(5)	0.068(2)
C(20)	0.4386(2)	0.6150(3)	0.14148(9)	0.0224(5)	C(10)	−0.0450(4)	0.8338(5)	−0.1737(5)	0.076(2)
C(21)	0.4806(2)	0.5968(3)	0.09469(10)	0.0307(6)	C(11)	0.0180(4)	0.7786(6)	−0.1135(5)	0.086(2)
C(22)	0.5139(2)	0.7104(4)	0.06658(10)	0.0359(7)	C(12)	0.0917(4)	0.8218(5)	−0.0526(5)	0.076(2)
C(23)	0.5046(2)	0.8407(4)	0.08488(10)	0.0348(7)	C(13)	0.2392(4)	0.9253(4)	0.1212(4)	0.053(2)
C(24)	0.4639(2)	0.8656(3)	0.13338(10)	0.0288(6)	C(14)	0.3217(4)	0.9292(4)	0.1808(4)	0.062(2)
C(25)	0.4555(2)	1.0007(3)	0.15371(12)	0.0369(7)	C(15)	0.3513(4)	0.9045(5)	0.2676(5)	0.075(2)
C(26)	0.4129(2)	1.0244(3)	0.19932(13)	0.0383(7)	C(16)	0.2998(4)	0.8727(5)	0.2934(5)	0.076(2)
C(27)	0.3783(2)	0.9127(3)	0.22777(11)	0.0333(6)	C(17)	0.2192(4)	0.8694(5)	0.2367(5)	0.078(2)
C(28)	0.3884(2)	0.7808(3)	0.21027(9)	0.0257(5)	C(18)	0.1878(4)	0.8953(5)	0.1510(5)	0.071(2)
C(29)	0.4302(2)	0.7526(3)	0.16249(9)	0.0227(5)	C(19)	0.1922(4)	1.0979(4)	0.0179(4)	0.055(2)
B(1)	0.2998(3)	0.8760(4)	0.45190(14)	0.0354(7)	C(20)	0.1468(4)	1.1315(5)	0.0627(5)	0.083(2)
B(2)	0.3514(2)	0.7361(4)	0.41901(11)	0.0288(6)	B(1)	−0.0829(4)	0.2902(5)	−0.3631(5)	0.056(2)
B(3)	0.2382(3)	0.7134(4)	0.46080(12)	0.0332(7)	B(2)	−0.0538(4)	0.2057(6)	−0.2870(5)	0.051(2)
B(4)	0.1654(3)	0.8561(4)	0.41999(17)	0.0457(9)	B(3)	0.0136(4)	0.2544(5)	−0.3211(5)	0.050(2)
B(5)	0.2768(3)	0.8738(4)	0.38125(14)	0.0377(8)	B(4)	−0.0147(5)	0.3749(5)	−0.3065(5)	0.060(2)
B(6)	0.2568(2)	0.5943(3)	0.40688(11)	0.0268(6)	B(5)	−0.0821(4)	0.3248(5)	−0.2734(5)	0.055(2)
B(7)	0.1252(2)	0.6797(4)	0.40499(12)	0.0300(6)	H(1)	−0.127(3)	0.283(4)	−0.431(3)	0.05(2)
B(8)	0.1509(3)	0.7933(4)	0.35037(14)	0.0407(8)	H(2)	−0.093(3)	0.141(4)	−0.307(3)	0.05(2)
B(9)	0.2771(3)	0.7059(4)	0.35047(11)	0.0336(7)	H(3)	0.031(3)	0.229(3)	−0.364(3)	0.05(2)
B(10)	0.1618(2)	0.6193(4)	0.34827(11)	0.0310(7)	H(4)	−0.017(3)	0.444(3)	−0.338(3)	0.05(1)
H(1*B*)	0.341(3)	0.960(4)	0.478(2)	0.07(1)	H(5)	−0.141(3)	0.346(3)	−0.276(3)	0.04(1)

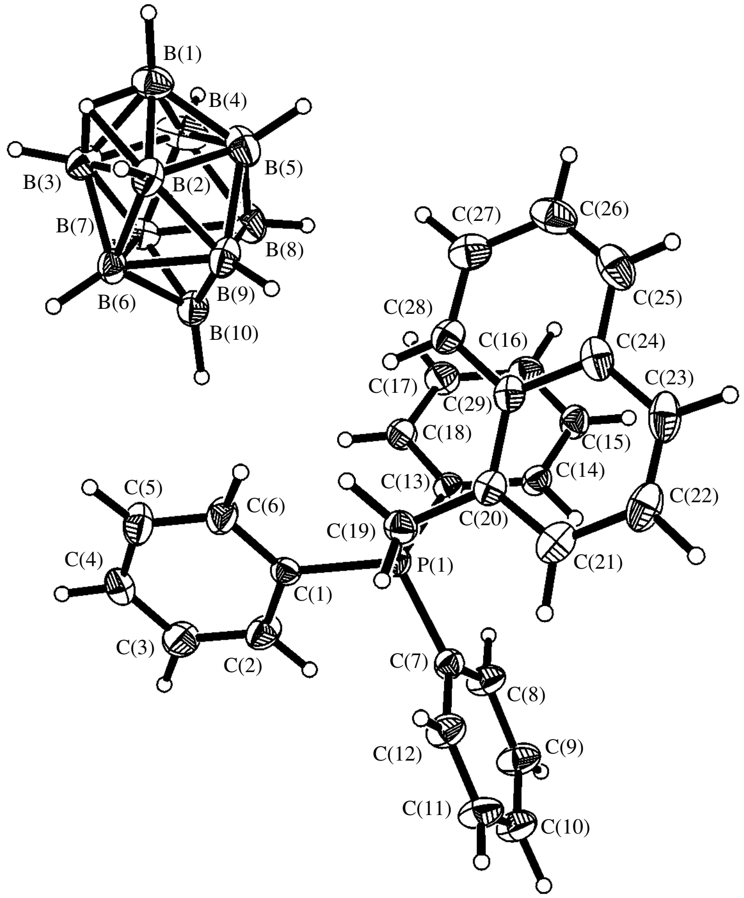

Fig. 1. Structures of the $B_{10}H_{11}^-$ anion and $[Ph_3PCH_2Naph]^+$ cation in crystal **I**.

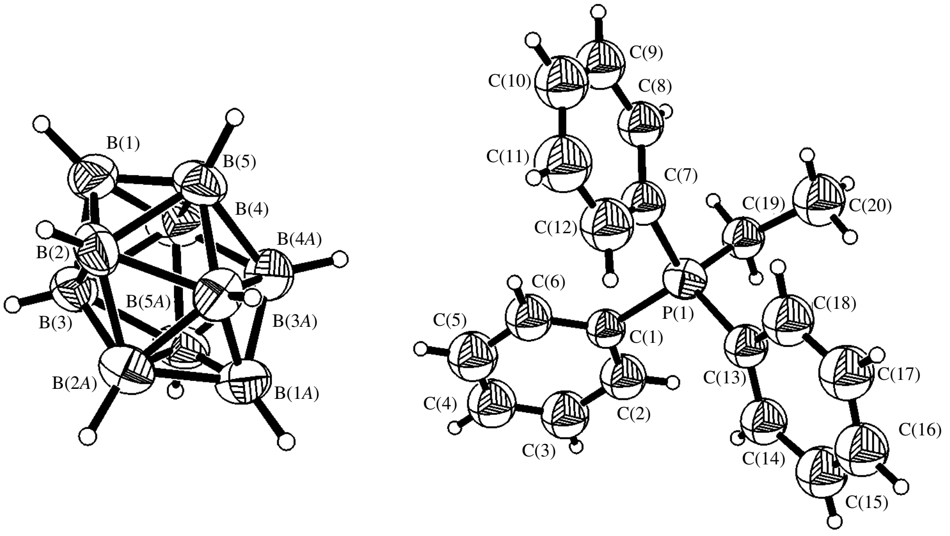

Fig. 2. Structures of the $B_{10}H_{10}^{2-}$ anion and $[Ph_3PEt]^+$ cation in crystal **II**.

The crystal data for compounds **I** and **II** are deposited in the Cambridge Structural Database (CCDC nos. 203740 and 203739, respectively).

ACKNOWLEDGMENTS

This study was performed within the State Program in Support of Leading Scientific Schools (NSh-1749.2003.3) and supported by the Russian Foundation for Basic Research (project nos. 02-03-32778 and 04-03-32874) and the Presidential grant (MK-3542.2004.3). We are also grateful to the Russian Foundation for Basic Research for support in the payment of the license for using the Cambridge Structural Database (project no. 02-07-90322) and to the Center of X-ray Structural Studies (Nesmeyanov Institute of Organoelement Compounds, Russian Academy of Sciences) for collecting one of the X-ray data sets (Russian Foundation for Basic Research, project no. 03-03-32214).

REFERENCES

1. P. A. Wegner, D. M. Adams, F. J. Callabretta, *et al.*, J. Am. Chem. Soc. **95** (22), 7513 (1973).
2. M. F. Hawthorne, I. J. Mavunkal, and C. B. Knobler, J. Am. Chem. Soc. **114** (11), 4427 (1992).
3. V. N. Mustyatsa, N. A. Votinova, K. A. Solntsev, and N. T. Kuznetsov, Dokl. Akad. Nauk SSSR **301** (6), 1396 (1988).
4. V. N. Mustyatsa, N. A. Votinova, L. V. Goeva, *et al.*, Koord. Khim. **27** (9), 662 (2001).
5. V. I. Ponomarev, K. A. Solntsev, V. N. Mustyatsa, and N. T. Kuznetsov, Koord. Khim. **17** (5), 640 (1991).
6. V. I. Ponomarev, K. A. Solntsev, V. N. Mustyatsa, *et al.*, Koord. Khim. **18** (4), 372 (1992).
7. *SMART (Control) and SAINT (Integration) Software: Version 5.0* (Bruker AXS, Madison, 1997).
8. G. M. Sheldrick, *SADABS: Program for Scaling and Correction of Area Detector Data* (Univ. of Göttingen, Germany, 1997).
9. G. M. Sheldrick, *SHELXS97: Program for the Solution of Crystal Structures* (Univ. of Göttingen, Germany, 1997).
10. G. M. Sheldrick, *SHELXL97: Program for the Refinement of Crystal Structures* (Univ. of Göttingen, Germany, 1997).

Translated by I. Polyakova

Crystallography Reports, Vol. 49, No. 5, 2004, pp. 772–778. Translated from Kristallografiya, Vol. 49, No. 5, 2004, pp. 860–866.
Original Russian Text Copyright © 2004 by Khrustalev, Antipin, Kosnikov, Antonovskiĭ.

Molecular and Crystal Structure of Diperoxides: X-ray Diffraction Studies of 2,5-Dimethyl-2,5-Dihydroperoxyhexane, 2,5-Dimethyl-2,5-Dihydroperoxyhex-3-ine, 2,5-Dimethyl-2,5-Di(*tert*-butylperoxy)hexane, and 1,4-Bis[2-(2-*tert*-butylperoxy)propyl]benzene

V. N. Khrustalev*, M. Yu. Antipin*, A. Yu. Kosnikov, and V. L. Antonovskiĭ[†]***

** Nesmeyanov Institute of Organoelement Compounds, Russian Academy of Sciences,*
ul. Vavilova 28, Moscow, 119991 Russia
e-mail: vkh@xray.ineos.ac.ru
*** Semenov Institute of Chemical Physics, Russian Academy of Sciences,*
ul. Kosygina 4, Moscow, 119991 Russia

Received February 7, 2003

Abstract—The crystal structures of two alkylhydrodiperoxides and two dialkyldiperoxides, namely, 2,5-dimethyl-2,5-dihydroperoxyhexane (**I**), 2,5-dimethyl-2,5-dihydroperoxyhex-3-ine (**II**), 2,5-dimethyl-2,5-di(*tert*-butylperoxy)hexane (**III**), and 1,4-bis[2-(2-*tert*-butylperoxy)propyl]benzene (**IV**), are studied by X-ray diffraction. The structures of **I**–**IV** are compared with previously studied structures of alkylhydroperoxides, dialkylhydroperoxides, and their S, Se, and Te analogues, such as bis(alkyl)disulfides, bis(alkyl)diselenides, and bis(alkyl)ditellurides. The factors responsible for the structure of compounds of this type are analyzed, and the specific structural features are discussed. *© 2004 MAIK “Nauka/Interperiodica”.*

INTRODUCTION

Owing to their high reactivity and structural variety, organic peroxides are of increased interest from both the theoretical and practical standpoints. Organic peroxides are widely used as strong oxidants and the main source of free radicals for initiating radical processes [1, 2]. Diperoxides are used for functionalizing and cross-linking of polymers [3, 4].

X-ray diffraction studies of organic peroxides are of obvious interest. However, it is clear that their instability and even explosion hazard under normal conditions give rise to experimental difficulties in the course of investigations. Moreover, many peroxides with small-sized molecules, which are of structural interest, have low melting temperatures (often below 0°C), which also significantly complicates X-ray diffraction studies of these compounds. In this respect, recent trends have been toward a growing contribution of theoretical methods to investigations of peroxides.

Our earlier X-ray diffraction studies [5, 6] and quantum-chemical calculations [7, 8] revealed that the molecular structure of organic peroxides is governed to a large degree by nonbonded interactions:

(1) mutual repulsion of lone electron pairs of oxygen atoms, which determines the *gauche* position of the substituents in the molecule;

(2) mutual repulsion of lone electron pairs and substituents at oxygen atoms, which determines the *trans* position of the substituents in the molecule;

(3) mutual repulsion of substituents at oxygen atoms;

(4) interaction between lone electron pairs and substituents at oxygen atoms, for example, $n_\pi \longrightarrow \sigma^*(C–X_g)$ (the anomeric effect [9]), which determines the *gauche* position of the substituents in the molecule; and

(5) interaction of the peroxide group with neighboring substituents, for example, $\sigma(C–X_t) \longrightarrow \sigma^*(O–O)$ (the *d*(*trans*) effect [10]).

In this work, we investigated the effect of all these factors and the effect of intramolecular and intermolecular hydrogen bonds on the structure of alkylhydroperoxides, dialkylperoxides, diperoxides, and their S, Se, and Te analogues. For this purpose, we used our X-ray diffraction data for four compounds, namely, 2,5-dimethyl-2,5-dihydroperoxyhexane (**I**), 2,5-dimethyl-2,5-dihydroperoxyhex-3-ine (**II**), 2,5-dimethyl-2,5-di(*tert*-butylperoxy)hexane (**III**), and 1,4-bis[2-(2-*tert*-butylperoxy)propyl]benzene (**IV**), and data from the Cambridge Structural Database [11].

[†] Deceased.

Table 1. Main crystal data and refinement parameters for compounds **I**–**IV**

Compound	**I**	**II**	**III**	**IV**
Empirical formula	$C_8H_{18}O_4$	$C_8H_{14}O_4$	$C_{16}H_{34}O_4$	$C_{20}H_{34}O_4$
Molecular weight	178.22	174.19	290.43	338.47
T, K	153	193	153	153
Crystal system	Monoclinic	Tetragonal	Monoclinic	Triclinic
Space group	$C2/c$	$P4_12_12$	$P2_1/n$	$P\bar{1}$
a, Å	14.201(2)	10.080(2)	5.665(3)	5.998(2)
b, Å	9.971(1)	10.080(2)	9.784(9)	5.997(2)
c, Å	9.493(1)	9.114(2)	16.88(2)	15.335(4)
α, deg	90	90	90	82.55(2)
β, deg	130.371(8)	90	94.75(4)	80.23(2)
γ, deg	90	90	90	67.36(2)
V, Å^3	1024.1(3)	926.0(3)	932(1)	500.5(5)
Z	4	4	2	1
d_{calcd}, g cm^{-3}	1.156	1.249	1.035	1.123
$F(000)$	392	376	324	186
μ, mm^{-1}	0.091	0.100	0.070	0.080
$2\theta_{\max}$, deg	90	75	54	60
Number of measured reflections	8470	4090	1714	2235
Number of unique reflections	3311	1787	1532	1813
Number of observed reflections with $I > 2\sigma(I)$	2505	1164	1240	1680
Number of refined parameters	95	83	159	177
R_1 ($I > 2\sigma(I)$)	0.0396	0.0361	0.049	0.034
wR_2 (all data)	0.1162	0.0991		
Rw ($I > 2\sigma(I)$)			0.036	0.031
GOOF	1.031	0.834	1.192	1.115

EXPERIMENTAL

Single crystals of purified compounds **I** (T_{melt} = 80°C), **II** (T_{melt} = 82°C), and **IV** (T_{melt} = 80°C) were grown by crystallization from melt. Compound **III** is a liquid at room temperature (T_{melt} = ~5°C); hence, a single crystal of **III** was grown in a Pyrex capillary (diameter, 0.6 mm; wall width, 0.03 mm) immediately at the diffractometer.

The unit cell parameters and intensities of reflections were measured on a Siemens P3 (compound **I**) or a Syntex P2_1 (compounds **II**–**IV**) automated four-circle diffractometers (λMoK_α, graphite monochromator, $\theta/2\theta$ scan mode). Main crystal data are summarized in Table 1. The structures of all the compounds were solved by direct methods with the SHELXS (for compounds **I**, **II**) or MULTAN (for compounds **III**, **IV**) program package. The non-hydrogen atoms were refined by the full-matrix (compounds **I**, **II**) or block-diagonal (compounds **III**, **IV**) least-squares procedures in the anisotropic approximation. Molecules of all the compounds occupy special positions C_i at the inversion center (compounds **I**, **III**, **IV**) or C_2 at the twofold axis (compound **II**). The hydrogen atoms in compounds **I** and **II** were located from difference Fourier syntheses (the hydrogen atom of the hydroxyl group in compound **I** is disordered statistically over two equally occupied positions), and the positions of the hydrogen atoms in compounds **III** and **IV** were calculated geometrically. All the hydrogen atoms were refined in the isotropic approximation. All the calculations were performed with the SHELXTL PLUS (Version 5.10) [12] (compounds **I**, **II**) or INEXTL [13] (compounds **III**, **IV**) program packages. The tables of atomic coordinates, bond lengths and angles, and anisotropic thermal parameters for compounds **I**–**IV** were deposited with the Cambridge Structural Database.

RESULTS AND DISCUSSION

The molecular structures of compounds **I**–**IV** are shown in Figs. 1–4, respectively, and the selected geometric parameters are listed in Tables 2 and 3. The geometric parameters of bis(alkyl)disulfides, bis(alkyl)dis-

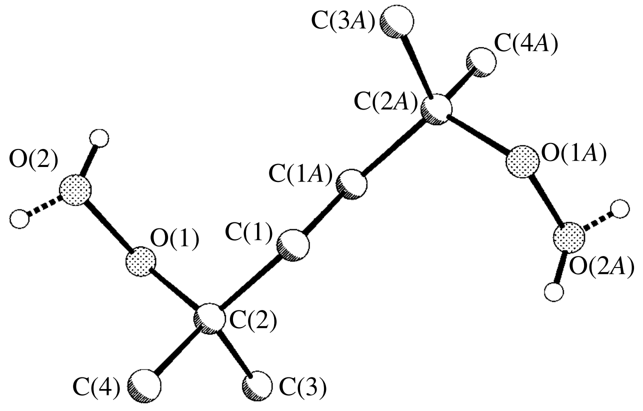

Fig. 1. Molecular structure of compound **I**. Dashed lines indicate the alternative positions of disordered hydrogen atoms of the hydroxyl groups.

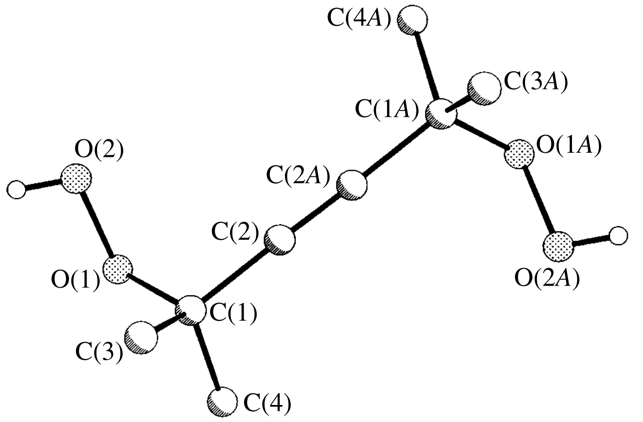

Fig. 2. Molecular structure of compound **II**.

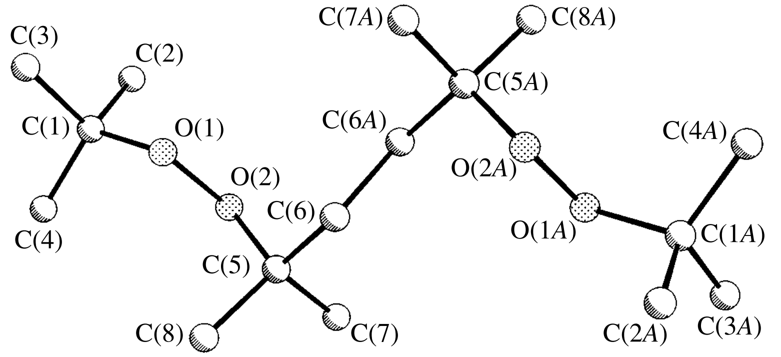

Fig. 3. Molecular structure of compound **III**.

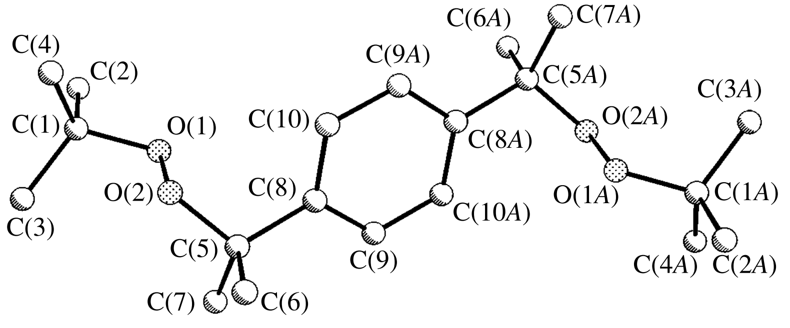

Fig. 4. Molecular structure of compound **IV**.

elenides, and bis(alkyl)ditellurides found in the Cambridge Structural Database are presented in Table 4 for comparison. The structures of compounds **I**–**IV** are discussed and compared with those of their alkylhydro and dialkyl analogues.

As follows from Tables 2 and 3, the O–O bond length of the peroxide fragment significantly exceeds the sum of the covalent radii of the oxygen atoms (1.32 Å [61]) and its values lie in a wide range (1.449–1.491 Å). The lengthening of the O–O bond is apparently due to strong repulsive interaction between the closely spaced lone electron pairs of the oxygen atoms. The wide range of O–O bond lengths can be explained by the additional effect of other (mainly, steric) intramolecular nonbonded interactions, which, in turn, further lengthen the O–O bond. These destabilizing interactions in peroxide molecules lead to a weakening of the O–O chemical bond and, as a consequence, the chemical instability of molecules. A different situation is observed for the S, Se, and Te analogues of dialkylp-

Table 2. Geometric parameters of alkylhydroperoxides

Compound	Bond lengths, Å		Angles, deg				Hydrogen bond type	Reference
	O–O	O–C	O–C–X_t	O–C–X_{g1}	O–C–X_{g2}	φ		
Me_3C–O–OH	1.472	1.463	101.5	109.3	109.6	100	OOH…OOH, chains	[14]
Ph_2MeC–O–OH	1.475	1.465	100.9	108.7	109.7	115	OOH…O(O)H, rings, cooperative	[15]
	1.478	1.456	100.7	108.9	110.2	104		
Ph_3C–O–OH	1.455	1.453	102.9	107.5	110.1	101	OOH…π	[16]
RH$_2$C–O–OH	1.465	1.439	102 (H)	103 (H)	114.6	112	OOH…O=C, chains	[17]
RMe_2C–O–OH	1.461	1.439	103.9	108.6	110.7	103	OOH…OH, chains, cooperative	[18]
RMe_2C–O–OH	1.472	1.448	101.9	109.9	112.2	91	OOH…OH, chains, intramolecular, cooperative	[19]
RPh_2C–O–OH	1.450	1.446	103.5	109.5	109.5	102	OOH…O = C, intramolecular	[20]
	1.463	1.450	103.3	109.1	109.3	115		
RPh_2C–O–OH	1.466	1.431	103.6	108.6	109.7	129	OOH…OH, intramolecular	[21]
[–RMe_2C–O–OH]$_2$ (**I**)	1.470(1)	1.454(1)	101.25(4)	110.48(4)	110.73(4)	118 –111*	OOH…O(O)H, chains, cooperative	This work
[–RMe_2C–O–OH]$_2$ (**II**)	1.449(1)	1.454(1)	102.32(9)	110.05(8)	110.83(8)	114	OOH…O(O)H, helices, cooperative	This work

Note: X_t and X_g are the substituents at the quaternary carbon atom that occupy the *trans* and *gauche* positions relative to the peroxide group, respectively.

* The torsion angle φ for the alternative position of the hydrogen atom.

Table 3. Geometric parameters of dialkylperoxides

Compound	Bond lengths, Å		Angles, deg				Reference
	O–O	O–C	O–C–X_t	O–C–X_{g1}	O–C–X_{g2}	φ	
[Me_3C–O–]$_2$	1.478	1.439	100.7	110.8	110.8	164.0	[10]
[$PhMe_2$C–O–]$_2$	1.486	1.442	102.0	110.1	110.3	180	[22]
[Ph_3C–O–]$_2$	1.480	1.461	99.5	109.9	110.5	180	[23]
	1.479	1.459	100.0	109.9	111.1	180	[24]
[RPh_2C–O–]$_2$	1.491	1.437	106.0	109.8	110.7	180	[25]
[(CH$_2$$Ph$)(OH)HC–O–]$_2$	1.479	1.413	105.4	99 (H)	110.7	153.8	[26]
		1.444	105.9	94 (H)	108.6		
[(C$_6$F$_5$NH)(C$_6$F$_5$)HC–O–]$_2$	1.462	1.358	103.6	114 (H)	127.7	164.1	[27]
[–RMe_2C–O–O–CMe_3]$_2$ (**III**)	1.463(2)	1.456(2)	99.8(2)	110.1(2)	111.7(2)	152.1	This work
		1.457(2)	100.6(2)	110.3(2)	111.5(2)		
[–RMe_2C–O–O–CMe_3]$_2$ (**IV**)	1.480(1)	1.443(1)	101.4(1)	110.1(1)	110.8(1)	152.6	This work
		1.443(1)	101.2(1)	110.3(1)	110.4(1)		

eroxides, namely, bis(alkyl)disulfides, bis(alkyl)diselenides, and bis(alkyl)ditellurides. The S–S, Se–Se, and Te–Te bonds (the average lengths are 2.034, 2.329, and 2.669 Å, respectively) are, on the contrary, slightly shorter than the sums of the covalent radii of the S, Se, and Te atoms (2.04, 2.34, and 2.74 Å, respectively [61]). Moreover, the longer the spacing between the lone electron pairs of the S, Se, or Te atoms, the more pronounced the shortening. The exception is provided by the compounds containing the most bulky [tris(trimethylsilyl)]methyl (SiMe_3)$_3$C substituents (Table 4 [52, 59]). It is interesting to note that strong electron-withdrawing substituents at the C_α quaternary carbon atom produce virtually no effect on the O–O, S–S, Se–Se, and Te–Te bond lengths.

Table 4. Geometric parameters of bis(alkyl)disulfides, bis(alkyl)diselenides, and bis(alkyl)ditellurides

Compound	Bond lengths, Å		Angles, deg				Reference
	S*–S*	S*–C	S*–C–X_t	S*–C–X_{g1}	S*–C–X_{g2}	φ	
[RH_2C–S–]$_2$, mean value	2.013–2.043 2.029	1.784–1.858 1.816	96 (H)–111 (H)	95 (H)–119 (H)	109.8–116.2	69.3–108.4 86.3	[28–48]
[RPr^iHC–S–]$_2$	2.034	1.834	108.4	108 (H)	110.3	85.2	[49]
[$RPhHC$–S–]$_2$	2.027	1.856	103.0	98 (H)	110.7	84.6	[50]
[RMe_2C–S–]$_2$	2.032	1.851, 1.858	102.0, 101.9	108.3, 109.0	109.5, 111.9	119.4	[51]
[Ph_3C–S–]$_2$	2.012	1.910, 1.952	101.1, 101.0	109.7, 108.6	109.9, 110.7	110.3	[52]
[CF_3–S–]$_2$	2.024	1.825, 1.824	107.0, 106.1	112.2, 112.5	113.2, 113.6	98.2	[53]
[(SO_2Me)Cl_2C–S–]$_2$	2.018	1.812, 1.820	103.3, 104.7	108.0, 109.1	115.7, 116.4	113.3	[54]
[($COOEt$)$_2ClC$–S–]$_2$	2.022	1.842, 1.849	108.4, 105.7	110.5, 110.9	112.7, 113.4	100.8	[55]
[($SiMe_3$)$_3C$–S–]$_2$	2.108	1.846	98.1	107.3	114.1	180	[52]
[(CH_2OPh)H_2C–Se–]$_2$	2.326	1.961, 1.963	108 (H), 109 (H)	108 (H), 109 (H)	116.8, 113.8	115.1	[56]
[Ph_2HC–Se–]$_2$	2.286	1.966	105.5	110 (H)	113.1	82.0	[57]
[Bu^t_2HC–Se–]$_2$	2.315	2.009, 2.012	106.3, 106.5	110 (H), 107 (H)	111.2, 110.9	112.1	[58]
[($SiMe_3$)$_3C$–Se–]$_2$	2.388	2.004	98.5	106.5	112.7	180	[59]
[CF_3–Te–]$_2$	2.669	2.176, 2.186	108.5, 109.8	113.4, 113.0	114.5, 113.1	88.3	[60]

* For diselenides and ditellurides, the S atom should be replaced by the Se and Te atoms, respectively.

In sterically unstrained peroxides, the most favorable molecular conformation is the *gauche* conformation due to the interaction between the lone electron pairs of the oxygen atoms. This can be readily illustrated with hydrogen peroxide (φ = 92°–112° [62–66]) and alkylhydroperoxides (φ = 91°–129°, Table 2). The different hydrogen bonds in these compounds (Table 2) do not substantially affect the molecular conformation. However, for peroxide molecules containing two alkyl substituents, the situation changes radically: repulsive interactions between the lone electron pairs of the oxygen atoms and their own substituents become dominant and lead to the *trans* conformation of these molecules (φ = 152.1°–180.0°, Table 3). It should be noted that the *trans* conformation of the peroxide molecules can also result from other intramolecular nonbonded interactions, which are often stronger than steric interactions, for example, intramolecular hydrogen bonds of the peroxide oxygen atoms with the hydroxyl group of the substituent at the neighboring oxygen atom (Table 3, [26]). Note also that, in bis(alkyl)disulfides and bis(alkyl)diselenides, the repulsive interactions between the lone electron pairs of the S and Se atoms and their own substituents prevail only in the case of very bulky substituents, such as [tris(trimethylsilyl)]methyl ($(SiMe_3)_3C$) substituents (Table 4). In the other compounds, the interaction responsible for the conformation of these molecules is the intramolecular mutual repulsion of the lone electron pairs of the S or Se atoms, which results in the *gauche* position of the substituents (φ = 69.3°–119.4°, Table 4). In ditelluride molecules, the repulsive interactions between the lone electron pairs of the Te atoms and their own substituents are apparently not able to affect the conformation significantly. In these compounds, the *trans* conformation of the molecules can be achieved only under other sufficiently strong intramolecular nonbonded interactions, for example, $Te\cdots N_{ar}$ (pyridyl) (φ = 180.0° [67]), $Te\cdots N_{sp^3}$ (amino group) (φ = 145.0° [68]), or Te··O (carbonyl group) (φ = 180.0° [69]).

An important specific feature of the structure of organic alkylperoxides is the deviation of the O–C–X_t bond angle (Tables 2–4) at the quaternary C_α atom from the ideal tetrahedral value of 109.5° (the *d* (distortion) effect [10]). The following two trends of this effect should be noted:

(i) the *d* effect decreases if the quaternary C_α atom bears strong electron-withdrawing substituents [26, 27, 53–55, 60] and

(ii) the *d* effect increases in molecules with *trans* conformation [10, 22–24, 52, 59, this work (**III**)].

Both trends agree well with the explanation of the nature of the *d* effect proposed in [10] [$\sigma(C–X_t) \longrightarrow \sigma^*(O–O)$ interaction].

Moreover, we revealed one more interesting specific structural feature of organic alkylperoxides containing the phenyl substituent at the quaternary C_α atom: the phenyl C_α substituent as a rule, occupies the sterically unfavorable *gauche* position [22, 32, 70, this work (**IV**)]. This fact can be explained only by the effect of a stronger intramolecular interaction. Possibly, it is the interaction between one of the lone electron pairs of an oxygen atom and the π system of the phenyl ring bound to the C substituent of the neighboring oxygen atom ($n \longrightarrow \pi$ interaction). The other phenyl substituent at the same C_α atom, as a rule, occupies the *trans* position [15, 20, 21, 25, 57], because a similar $n \longrightarrow \pi$ interaction with the second phenyl ring is sterically impossible.

Thus, based on the data of our own X-ray diffraction studies and the data taken from the Cambridge Structural Database, the general structural behavior of alkylhydroperoxides, dialkylperoxides, and diperoxides was described, the dependence of the structure of compounds of this type on different intramolecular and intermolecular nonbonded interactions was analyzed and the structural features of these compounds were discussed.

REFERENCES

1. V. L. Antonovskiĭ, *Organic Peroxide Initiators* (Khimiya, Moscow, 1972).
2. V. L. Antonovskiĭ, *Progress in Chemistry of Organic Peroxides* (TsNIITÉ Neftekhim, Moscow, 1992).
3. Z. N. Nudel'man, V. I. Myshkovskiĭ, and V. L. Antonovskiĭ, Kauch. Rezina, No. 3, 30 (1991).
4. V. L. Antonovskiĭ, Kinet. Katal. **44** (1), 62 (2003).
5. V. L. Antonovskiĭ, in *Organic and Organoelement Peroxides* (Nizhegor. Gos. Univ., Nizhni Novgorod, 1996), p. 1.
6. V. L. Antonovskiĭ and S. L. Khursan, *Physical Chemistry of Organic Peroxides* (Akademkniga, Moscow, 2003).
7. S. L. Khursan and V. L. Antonovskiĭ, Dokl. Akad. Nauk **382**, 657 (2002).
8. S. L. Khursan and V. L. Antonovskiĭ, Izv. Ross. Akad. Nauk, Ser. Khim., No. 6 (2003).
9. A. J. Kirby, *Anomeric Effect and Related Stereoelectronic Effects at Oxygen* (Springer, Berlin, 1983).
10. Yu. L. Slovokhotov, T. V. Timofeeva, M. Yu. Antipin, and Yu. T. Struchkov, J. Mol. Struct. **112**, 127 (1984).
11. F. H. Allen and O. Kennard, Chem. Design Autom. News **8** (1), 31 (1993); *Cambridge Crystallographic Database* (Cambridge, 2002).
12. G. M. Sheldrick, *SHELXTL PLUS: Version 5.10* (Bruker AXS, Madison, USA, 1997), WI-53719.
13. R. G. Gerr, A. I. Yanovskiĭ, and Yu. T. Struchkov, Kristallografiya **28** (5), 1029 (1983) [Sov. Phys. Crystallogr. **28**, 609 (1983)].
14. A. Yu. Kosnikov, V. L. Antonovskiĭ, S. V. Lindeman, *et al.*, Teor. Éksp. Khim. **25**, 81 (1989).
15. A. Yu. Kosnikov, V. L. Antonovskiĭ, S. V. Lindeman, *et al.*, Kristallografiya **34** (2), 360 (1989) [Sov. Phys. Crystallogr. **34**, 213 (1989)].
16. V. L. Antonovskiĭ, A. Yu. Kosnikov, N. A. Turovskiĭ, *et al.*, Izv. Akad. Nauk SSSR, Ser. Khim., No. 1, 68 (1990).
17. S. Hrycko, P. Morand, F. L. Lee, and E. J. Gabe, J. Org. Chem. **53**, 1515 (1988).
18. B. M. Howard, W. Fenical, J. Finer, *et al.*, J. Am. Chem. Soc. **99**, 6440 (1977).
19. H. Itokawa, E. Kishi, H. Morita, *et al.*, Chem. Lett. 2221 (1991).
20. Qian Chang-Yi, H. Nishino, K. Kurosawa, and J. D. Korp, J. Org. Chem. **58**, 4448 (1993).
21. M. Aoki and D. Seebach, Helv. Chim. Acta **84**, 187 (2001).
22. A. Yu. Kosnikov, V. L. Antonovskiĭ, N. A. Turovskiĭ, *et al.*, Izv. Akad. Nauk SSSR, Ser. Khim., No. 4, 791 (1988).
23. C. Glidewell, D. C. Liles, D. J. Walton, and G. M. Sheldrick, Acta Crystallogr., Sect. B: Struct. Crystallogr. Cryst. Chem. **35**, 500 (1979).
24. A. I. Yanovskiĭ, T. V. Timofeeva, N. G. Furmanova, *et al.*, Kristallografiya **26** (1), 203 (1981) [Sov. Phys. Crystallogr. **26**, 112 (1981)].
25. Huang Wen-Wei, H. Henry-Riyad, and T. T. Tidwell, J. Am. Chem. Soc. **121**, 3939 (1999).
26. A. Kobayashi, Y. Ikeda, K. Kubota, and Y. Ohashi, J. Agric. Food Chem. **41**, 1297 (1993).
27. G. G. Furin, A. O. Miller, Yu. V. Gatilov, *et al.*, J. Fluorine Chem. **28**, 23 (1985).
28. J. Donohue and J. P. Chesick, Acta Crystallogr., Sect. B: Struct. Crystallogr. Cryst. Chem. **31**, 986 (1975).
29. F. Bigoli, M. Lanfranchi, E. Leporati, *et al.*, Acta Crystallogr., Sect. B: Struct. Crystallogr. Cryst. Chem. **37**, 1258 (1981).
30. G. V. N. A. Rao, M. Seshasayee, G. Aravamudan, *et al.*, Acta Crystallogr., Sect. B: Struct. Crystallogr. Cryst. Chem. **38**, 2852 (1982).
31. M. Pierrot, A. Baldy, J. C. Maire, *et al.*, Acta Crystallogr., Sect. C: Cryst. Struct. Commun. **40**, 1931 (1984).
32. Zhigui Zhang and Fengshan Wang, Huaxue Tongbao (Chem. Bull.) 18 (1984).
33. C. P. Nash, M. M. Olmstead, B. Weiss-Lopez, *et al.*, J. Am. Chem. Soc. **107**, 7194 (1985).
34. M. Rajeswaran and R. Parthasarathy, Acta Crystallogr., Sect. C: Cryst. Struct. Commun. **41**, 726 (1985).
35. N. Galesic and A. Vlahov, Acta Crystallogr., Sect. C: Cryst. Struct. Commun. **43**, 2120 (1987).
36. K. A. Potekhin, A. V. Maleev, Yu. T. Struchkov, *et al.*, Dokl. Akad. Nauk SSSR **300**, 1135 (1988).
37. V. Nalini and G. R. Desiraju, Acta Crystallogr., Sect. C: Cryst. Struct. Commun. **45**, 1525 (1989).
38. P. A. Raj, S. D. Soni, N. Ramasubbu, *et al.*, Biopolymers **30**, 73 (1990).
39. M. Bolte, Acta Crystallogr., Sect. C: Cryst. Struct. Commun. **50**, 1368 (1994).
40. F. M. Menger, Y. Yamasaki, K. K. Catlin, and T. Nishimi, Angew. Chem. Int. Ed. Engl. **34**, 585 (1995).
41. B. Bartkowska and C. Kruger, Acta Crystallogr., Sect. C: Cryst. Struct. Commun. **53**, 1064 (1997).
42. D. E. Hibbs, M. B. Hursthouse, K. M. A. Malik, and M. North, Acta Crystallogr., Sect. C: Cryst. Struct. Commun. **53**, 1701 (1997).
43. A. Privett, T. Barclay, and W. Cordes, J. Chem. Cryst. **27**, 45 (1997).

44. D. F. Mullica, M. L. Trawick, P. W. N. Wu, and E. L. Sappenfield, J. Chem. Cryst. **28**, 761 (1998).
45. C. Jelsch and C. Didierjean, Acta Crystallogr., Sect. C: Cryst. Struct. Commun. **55**, 1538 (1999).
46. F. M. Menger and K. L. Caran, J. Am. Chem. Soc. **122**, 11679 (2000).
47. C. V. K. Sharma, G. A. Broker, G. J. Szulczewski, and R. D. Roger, Chem. Commun. 1023 (2000).
48. E. S. Lang, R. A. Burrow, A. L. Braga, *et al.*, Acta Crystallogr. E: Struct. Rep. Online **57**, 41 (2001).
49. J. C. Anderson, R. Cubbon, M. Harding, and D. S. James, Tetrahedron: Asymmetry **9**, 3461 (1998).
50. E. B. Klein and Z. Aizenshtat, J. Org. Chem. **58**, 6103 (1993).
51. L. G. Warner, T. Ottersen, and K. Seff, Acta Crystallogr., Sect. B: Struct. Crystallogr. Cryst. Chem. **30**, 1077 (1974).
52. M. Ostrowski, J. Jeske, P. G. Jones, and W.-W. Du Mont, Chem. Ber. **126**, 1355 (1993).
53. C. Meyer, D. Mootz, B. Back, and R. Minkwitz, Z. Naturforsch. Teil B **52**, 69 (1997).
54. J. S. Grossert, M. M. Bharadwaj, J. B. Faught, and A. Terzis, Can. J. Chem. **58**, 1106 (1980).
55. M. A. Hawata, A. M. El-Torgoman, S. M. El-Kousy, *et al.*, Eur. J. Org. Chem. 2583 (2000).
56. R. S. Laitinen, R. Oilunkaniemi, and M. Ahlgren, Z. Kristallogr. New Cryst. Struct. **216**, 55 (2001).
57. H. T. Palmer and R. A. Palmer, Acta Crystallogr., Sect. B: Struct. Crystallogr. Cryst. Chem. **25**, 1090 (1969).
58. T. G. Back and P. W. Godding, Can. J. Chem. **61**, 2749 (1983).
59. I. Wagner, W.-W. Du Mont, S. Pohl, and W. Saak, Chem. Ber. **123**, 2325 (1990).
60. W. Dukat, F. Gall, C. Meyer, *et al.*, Z. Anorg. Allg. Chem. **622**, 617 (1996).
61. *Lange's Handbook of Chemistry*, Ed. by J. A. Dean, 14th ed. (McGraw-Hill, New York, 1992).
62. C. J. Fritchie, Jr. and R. K. McMullan, Acta Crystallogr., Sect. B: Struct. Crystallogr. Cryst. Chem. **37**, 1086 (1981).
63. Hon Ping Kay and T. C. W. Mak, J. Cryst. Spectr. Res. **17**, 419 (1987).
64. M. A. Serra, B. K. Dorner, and M. E. Silver, Acta Crystallogr., Sect. C: Cryst. Struct. Commun. **48**, 1957 (1992).
65. I. Neda, T. Kaukorat, A. Fischer, *et al.*, J. Fluorine Chem. **69**, 35 (1994).
66. M. A. Cermak, M. Kvicalova, S. Sabata, *et al.*, Inorg. Chim. Acta **313**, 77 (2001).
67. T. Junk, K. J. Irgolic, and E. A. Meyers, Acta Crystallogr., Sect. C: Cryst. Struct. Commun. **49**, 975 (1993).
68. A. Edelmann, S. Brooker, N. Bertel, *et al.*, Z. Naturforsch. Teil B **47**, 305 (1992).
69. O. Niyomura, S. Kato, and S. Inagaki, J. Am. Chem. Soc. **122**, 2132 (2000).
70. E. John, J. A. Potenza, and H. J. Shugar, Acta Crystallogr., Sect. C: Cryst. Struct. Commun. **44**, 390 (1988).

Translated by I. Polyakova

Crystallography Reports, Vol. 49, No. 5, 2004, pp. 779–782. From Kristallografiya, Vol. 49, No. 5, 2004, pp. 867–870.

STRUCTURE OF ORGANIC COMPOUNDS

Molecular Structure of $[(C_5H_5)_2(C_5H_4CH_3)(C_4H_8O)Sm]$*

Taiqi Liu[1,2], Fuchen Ding[1], Jingli Li[1,3], and Qi Shen[2]

[1] *Peking Institute of Petrochemistry and Petrochemical Engineering, Peking, China*
e-mail: Liutaigi@bipt.edu.cn
[2] *Changchun Institute of Applied Chemistry, the Chinese Academy of Sciences, Changchun, 130022 China*
[3] *Changchun Land Administration Bureau, Changchun, 130021 China*

Received April 2, 2002; in final form, October 23, 2002

Abstract—The mixed tris-cyclopentadienyl tetrahydrofuranato samarium complex bis-(cyclopentadienyl) methylcyclopentadienyl tetrahydrofuranato samarium (I) was synthesized by reaction of $(C_5H_5)_2SmCl$ with methyl cyclopentadienyl sodium in THF. $[(C_5H_5)_2(C_5H_4CH_3)(C_4H_8O)Sm]$ (I) was characterized by elemental analyses—IR spectra and MS spectra. The structure of $[(C_5H_5)_2(C_5H_4CH_3)(C_4H_8O)Sm]$ (**I**), which has two slightly different independent molecules per asymmetric unit, has been elucidated through complete X-ray analysis. The crystals are monoclinic, with $a = 12.791(3)$ Å, $b = 10.467(2)$ Å, $c = 26.108(5)$ Å, $\beta = 98.22(2)°$, and space group Cc, $R = 0.0381$ for 2103 observed reflection with $I \geq 3\sigma(I)$. *© 2004 MAIK "Nauka/Interperiodica".*

INTRODUCTION

Tris-cyclopentadienyl lanthanide complexes were first reported by Birmingham and Wilkinson in 1956 [1]. X-ray structure study shows that the structures of trivalent lanthanide metallocenes, $(C_5H_5)_3Ln$ (Ln = lanthanide elements), are polymeric, involving μ–$\eta^5 : \eta^2$-C_5H_5 or μ-$\eta^5 : \eta^1$-C_5H_5 units, and $(CH_3C_5H_4)_3Ln$ are tetrameric complexes. However, the corresponding tetrahydrofuran coordinated lanthanide complexes, $(C_5H_5)_3Ln(THF)$ and $(CH_3C_5H_4)_3Ln(THF)$, are monomers [2–7]. Although a few mixed tris-cyclopentadienyl lanthanides have been reported [8–10], to our knowledge, little data on the structural information on mixed tris-cyclopentadienyl lanthanides has been reported up to now [10, 11]. We reported here the molecular structure of $[(C_5H_5)_2(C_5H_4CH_3)(C_4H_8O)Sm]$.

EXPERIMENTAL

Since the complexes described below are extremely air- and moisture-sensitive, all experiments were conducted under pure argon by Schlenk techniques. THF and hexane were distilled from sodium benzophenone ketyl. Complex Cp_2LnCl was prepared by the method of Dubeck [12]. Metal analysis was carried out by direct complexometric titration. The infrared spectrum was obtained as KBr pellets on a Digilab-FST-20E spectrometer. Mass spectrometric measurement was recorded on a VG-Quattro spectrometer by the EI^+ method at $T = 200°C$ and EV= 70 eV; the isotopes refer to ^{12}C, ^1H, ^{15}O, and ^{152}Sm. Carbon and hydrogen analyses were determined by use of combustion method.

Synthesis of compound $[(C_5H_5)_2(CH_3C_5H_4) \cdot (C_4H_8O)Sm]$ (**I**) : 10 mmol methylcyclopentadienyl

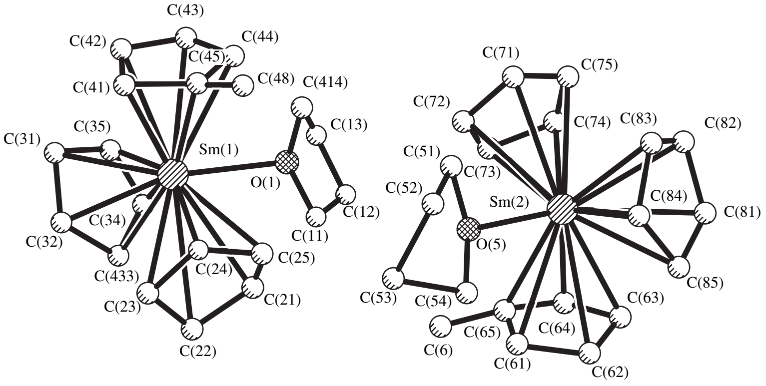

Fig. 1. Molecular of compound **I**.

---

* This article was submitted by the authors in English.

1063-7745/04/4905-0779$26.00 © 2004 MAIK "Nauka/Interperiodica"

Table 1. Crystal data of compound **I**

Formula	$[Sm(C_5H_5)_2(C_5H_4CH_3)(C_4H_8O)]$
Molecular weight	863.6
Space group	*Cc*
Cell constants	
a, Å	12.791(3)
b, Å	10.467(2)
c, Å	26.108(5)
β, deg	98.22(2)
V, Å^3	3455.6(2)
Z	4
D_x, M_g, m^{-3}	1.66
Radiation	MoK_α (0.71069 Å)
Reflections for lattice parameters	25
θ rang for lattice parameters	5.34–9.56
F(000)	1719.66
μ, cm^{-1}	34.43
Crystal color	yellow
Data collection	
Diffractometer	Nicolet R3 M/E
Scans	φ–2θ
Scan range 2θ, deg	5.75–53.57
H	0–15
K	0–12
L	–30–30
R_{int}	0.034
Measured reflections	3377
Independent reflections	3023
Reflections with $I \geq 3\sigma(I)$	2103
Standard reflections	2/100
Refinement	
R	0.0381
Rw	0.0377
S	1.41695
No. of parameters refined	387
Absolute structure parameter	0.00
(Δρ)min(e Å^3)	−0.605157
(Δρ)max(e Å^3)	1.7332

sodium in 30 ml THF was added to 10 mmol Cp_2SmCl in 100 ml THF in a tree-necked flask. The mixture was allowed to stir for 24 h at room temperature. The solid formed in the reaction was removed by filtering. The filtrate was concentrated, and 10 ml freshly distilled hexane was added; precipitated yellow crystals were obtained at –20°C after work up. Anal. Found: Sm, 35.0%, calcd. Sm, 34.9% IR, 3064m, 2956s, 2927s,

Table 2. Atomic coordinates (×10^4) and equivalent isotopic thermal parameters (Å × 10^3)

Atom	*x*	*y*	*z*	*U**
Sm(1)	−10156	7583(1)	−1506	52(1)
Sm(2)	−10776(1)	7426(1)	1440(1)	50(1)
O(1)	−10039(7)	5676(10)	−892(5)	63(3)
C(11)	−10860(15)	5051(19)	−672(9)	110(3)
C(12)	−10508(16)	3789(18)	−495(8)	99(3)
C(13)	−9491(16)	3567(16)	−689(10)	104(3)
C(14)	−9065(11)	5036(15)	−638(8)	67(3)
C(21)	−11919(13)	7653(17)	−997(8)	82(3)
C(22)	−12452(18)	7853(23)	−1493(10)	124(5)
C(23)	−11951(16)	8961(18)	−1641(9)	97(3)
C(24)	−11287(14)	9451(19)	−1170(9)	91(3)
C(25)	−11370(14)	8637(18)	−772(9)	88(3)
C(31)	−9774(13)	7127(16)	−2541(7)	74(3)
C(32)	−10896(13)	7086(15)	−2538(6)	60(3)
C(33)	−11463(17)	6217(16)	−2222(8)	93(3)
C(34)	−10605(15)	5427(19)	−2075(8)	83(3)
C(35)	−9673(16)	5981(20)	−2216(8)	115(3)
C(41)	−8835(12)	9590(18)	−1499(7)	70(3)
C(42)	−8244(13)	8557(16)	−1646(8)	87(3)
C(43)	−8033(10)	7741(18)	−1242(7)	76(3)
C(44)	−8353(11)	8286(16)	−801(7)	71(3)
C(45)	−8836(10)	9400(16)	−975(8)	66(3)
C(46)	−8943(30)	10217(29)	−609(12)	364(3)
O(5)	−11031(9)	9319(11)	833(5)	70(3)
C(51)	−10119(10)	10214(15)	810(8)	73(3)
C(52)	−10613(14)	11489(16)	726(9)	93(3)
C(53)	−11641(15)	11110(18)	375(8)	98(3)
C(54)	−11910(12)	10173(17)	789(8)	81(3)
C(61)	−12869(14)	7305(16)	1003(6)	93(3)
C(62)	−12929(19)	7088(20)	1485(8)	111(3)
C(63)	−12497(15)	5985(18)	1694(8)	87(3)
C(64)	−12272(13)	5400(15)	1244(7)	65(3)
C(65)	−12429(18)	6170(23)	819(8)	117(3)
C(66)	−12480(20)	6155(25)	268(8)	186(3)
C(71)	−8740(9)	7221(16)	1210(8)	84(3)
C(72)	−9399(17)	6772(19)	770(10)	100(3)
C(73)	−9813(16)	5555(18)	868(8)	91(3)
C(74)	−9379(13)	5403(13)	1407(7)	67(3)
C(75)	−8756(13)	6447(19)	1622(8)	84(3)
C(81)	−10840(12)	7922(15)	2427(7)	66(3)
C(82)	−9791(14)	7930(18)	2374(7)	77(3)
C(83)	−9825(14)	9188(16)	2186(7)	70(3)
C(84)	−10852(14)	9633(15)	2023(7)	72(3)
C(85)	−10593(17)	8912(19)	2226(8)	95(3)

* Equivalent isotropic *U* defined as one-third of the trace of the orthogonalized U_{ij} tensor.

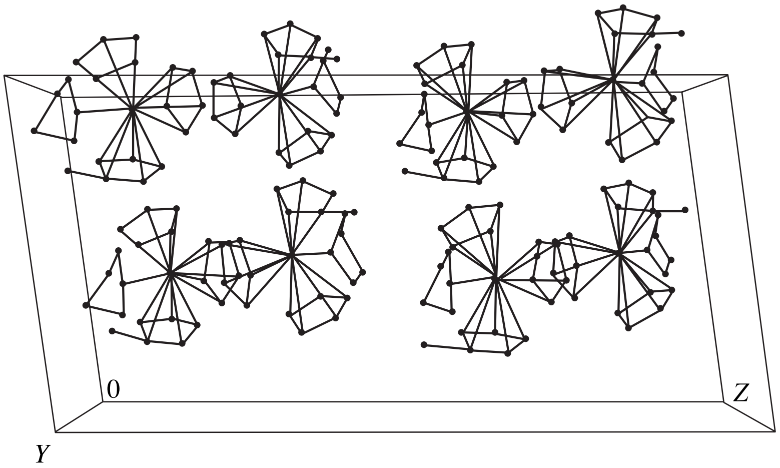

Fig. 2. Stereoscopic packing diagram of the complex **I**.

2856m, 1422m, 1376m, 1327w, 1258w, 1186w, 1086w, 1043w, 1012m, 855w, 809m, 764m, 666m, 561w. MS(*m*/*z*), 362, 297, 283, 217, 79, 66.

X-ray structure analysis: a yellow crystal with approximate dimensions of 0.31 × 0.38 × 0.56 mm was mounted in a thin-walled glass capillary under argon atmosphere and aligned on a Nicolet R_3 M/E four-circle diffractometer. Crystal data and experimental details are given in Table 1. The structure was solved by the heavy-atom method and refined by the block-diagonal least-squares method by the use of the SHELXTL program. The coordinates of hydrogen atoms were added according to a theoretical model. Atomic coordinates for nonhydrogen atoms and their equivalent thermal parameters are given in Table 2.

RESULTS AND DISCUSSION

The infrared spectra of compound **I** are similar to those of cyclopentadienyl ring coordinated samarium compounds [13–15] and have a C–H stretching frequency at 3064 cm^{-1} and intense bands at 1012 cm^{-1} (C–H bend parallel) and 764 cm^{-1} (C–H bend perpendicular). MS (m/e) of **I** at 362, 297, 283, 217, 79, 66 are fragmentations of $[(M–THF)H]^+$, $[M–Cp–THF]^+$, $[M–MeCp–THF]^+$, $[M–MeCp–Cp–THF]^+$, $[MeCp]^+$, $[CpH]^+$.

The molecular structure of compound **I**. Up to now, the molecular structure of mixed tris-cyclopentadienyl lanthanide complexes $(C_5Me_5)_2Sm(C_5H_5)$ and $(CH_3OCH_2CH_2Cp)Y(C_5H_5)_2$ has been determined by Evans [10] and Qian [11], respectively. However, the structure of **I** has never been reported.

From Fig. 1 and Fig. 2, we can see that the crystal structure of **I** consists of discrete molecules without short contacts. Although there are two crystallographically independent molecules in the asymmetric unit, they do not differ significantly in any respect and there are four pairs of molecules in the unit cell with the same crystallization energy [16]. Both molecules are comprised of a samarium atom residing in the center of a distorted tetrahedron formed by the centroides of the five-member rings and one oxygen atom; thus, the coordination number for Sm is 10, if the *Cp* ring is considered as occupying three coordination sites.

The average $Sm(1)–C(C_5H_5)$ bond length of I is 2.787(21) and 2.742(19) Å. The corresponding average distances of $Sm(2)–C(C_5H_5)$ are 2.777(18) and 2.754(19) Å. The average bond lengths of $Sm(1)–C(CH_3C_5H_4)$ and $Sm(2)–C(CH_3C_5H_4)$ are 2.748(16) and 2.808(20) Å, respectively. The average $Sm–C(CH_3C_5H_4)$ bond length in compound **I** is not obviously longer than that of $Sm–C(C_5H_5)$, as is that in the molecular structure of $(Me_5C_5)_2Sm(C_5H_5)$, and it is plausible that $CH_3C_5H_4$ is not as bulky as $(Me_5C_5)_2SmC_5H_5)$ [10]. The angles of $CH_3C_5H_4$(centroid)–Sm(1)–C_5H_5(centroid) in compound **I** are 122.0(1)° and 118.7(1)°, respectively. The corresponding data of $CH_3C_5H_4$(centroid)–Sm(2)–C_5H_5(centroid) are 118.4(1)° and 113.2(1)°. The angle C_5H_5(centroid)–Sm(1)–C_5H_5(centroid) is 112.9(1)° and C_5H_5(centroid)–Sm(2)–C_5H_5(centroid) is 119.9°. The angle of $CH_3C_5H_4$(centroid)–Sm–C_5H_5(centroid) is not obviously bigger than that of C_5H_5(centroid)–Sm–C_5H_5(centroid) in compound **I**. The distances of the central metal to the oxygen atom are 2.563 (Sm(1)–O(1)) and 2.523 Å (Sm(2)–O(5)), respectively.

SUPPLEMENTARY MATERIAL

Crystallographic data for the structural analysis has been deposited with the Cambridge Crystallographic Data Center (CCDC no. 171 249). Copies of this information may be obtained free of charge from: The Director, CCDC, 12 Union Road, Cambridge, CB2 1EZ, UK (fax: + 44-1223-336033; e-mail:

deposit@ccdc.cam.ac.UK or www: http://www.ccdc.cam.ac.uk).

ACKNOWLEDGMENTS

The work was supported by the National Science Foundation of China.

REFERENCES

1. J. M. Birmingham and G. Wilkinson, J. Am. Chem. Soc. **78**, 42 (1956).
2. S. D. Stults and R. A. Anderson, Organometallics **9**, 115 (1990).
3. Z. Xie, F. E. Nafa, and C. Qian, J. Organomet. Chem. **414**, C12 (1991).
4. Z. Wu, Z. Xu, X. You, *et al.*, Polyhedron **13**, 379 (1994).
5. Z. W. Ye, S. W. Wang, Y. F. Yu, *et al.*, Inorg. Chim. Acta **177**, 92 (1990).
6. W. Chen, G. Lin, J. Xia, *et al.*, J. Organomet. Chem. **467**, 75 (1994).
7. T. Liu, Crystallogr. Rep. **47** (3), 470 (2002).
8. C. Qian, Z. Xie, and Y. Huang, J. Organomet. Chem. **398**, 251 (1990).
9. C. Qian, C. Ye, H. Lu, *et al.*, J. Organomet. Chem. **247**, 161 (1983).
10. W. J. Evans and T. A. Ulibarri, J. Am. Chem. Soc. **109**, 4292 (1987).
11. C. Qian, B. Wang, and D. Deng, Polyhedron **12**, 2265 (1993).
12. R. E. Maginn, S. Manastyrskyj, and S. Dubeck, J. Am. Chem. Soc. **85**, 672 (1963).
13. G. W. Watt and E. W. Gillow, J. Am. Chem. Soc. **91**, 775 (1969).
14. L. Zhang, X. Zhou, R. Cai, and L. Weng, J. Organomet. Chem. **612**, 167 (2000).
15. C. Qian, Z. Xie, and Y. Huang, Inorg. Chim. Acta **139**, 195 (1987).
16. S. Wang, D. Kong, Z. Ye, *et al.*, J. Organomet. Chem. **496**, 37 (1995).

Crystallography Reports, Vol. 49, No. 5, 2004, pp. 783–787. Translated from Kristallografiya, Vol. 49, No. 5, 2004, pp. 871–875.
Original Russian Text Copyright © 2004 by Antsyshkina, Sadikov, Sergienko, Poznyak.

**STRUCTURE
OF ORGANIC COMPOUNDS**

Crystal Structure of the Mixed-Ligand Copper(II) Complex with *S*-Proline-*N*-Monoacetate Dianion and Imidazole [Cu(*Proma*)(*Im*)] · H_2O

A. S. Antsyshkina*, G. G. Sadikov*, V. S. Sergienko*, and A. L. Poznyak**

** Kurnakov Institute of General and Inorganic Chemistry, Russian Academy of Sciences,
Leninskiĭ pr. 31, Moscow, 119991 Russia*
e-mail: antas@igic.ras.ru
*** Institute of Molecular and Atomic Physics, Belarussian Academy of Sciences,
pr. F. Skoriny 70, Minsk, 220072 Belarus*

Received October 25, 2002

Abstract—The crystal structure of the [Cu(*Proma*)(*Im*)] · H_2O coordination compound (where *Proma*$^{2-}$ is an *S*-proline-*N*-monoacetate dianion and *Im* is imidazole) is studied by X-ray diffraction. The crystals are orthorhombic, $a = 8.286$ Å, $b = 8.546$ Å, $c = 17.309$ Å, $Z = 4$, and space group $P2_12_12_1$. The structural units of the crystal are the [Cu(*Proma*)(*Im*)] molecular complexes and crystallization water molecules. The square coordination of the Cu atom involves O atoms of two acetate groups (Cu–O, 1.958 and 1.955 Å) and N atoms of the *Proma* and *Im* ligands (Cu–N, 1.986 and 1.958 Å). The terminal O atoms of the neighboring complexes complete the Cu coordination polyhedron to a 4 + 1 + 1 square bipyramid (Cu–O, 2.578 and 2.783 Å) and form a framework structure. The hydrogen bonds involving oxygen atoms of the *Proma* ligand, water molecules, and an uncoordinated nitrogen atom of the *Im* ligand contribute to the strengthening of the framework. *© 2004 MAIK "Nauka/Interperiodica".*

INTRODUCTION

Earlier, the structures of [Cu(*Promp*)(H_2O)] [1], [Cu(*Promp*)(*Im*)] [2], and [Cu(*Proma*)(H_2O)] · $2H_2O$ [3] copper complexes (where H_2*Promp* and H_2*Proma* are *S*-proline-*N*-monopropionic and *S*-proline-*N*-monoacetic acids, respectively, and *Im* is imidazole) were determined in the course of systematic studies of aminopolycarboxylates. This paper reports on the results of an X-ray diffraction study of [Cu(*Proma*)(*Im*)] · H_2O (**I**), which is one more complex of this series. Moreover, the structure of complex **I** is compared with the structures of the aforementioned compounds.

EXPERIMENTAL

Synthesis. A solution of *S*-proline, acetic acid, and barium hydroxide in a 2 : 2 : 3 molar ratio was heated at 80°C for 1 h. The mixture was cooled and neutralized with sulfuric acid. Copper(II) sulfate (1 mole equivalent relative to proline) was added to the solution. The $BaSO_4$ precipitate was filtered off. The filtrate was applied to a Sephadex G-10 column to remove salts, and imidazole was added. Upon evaporation of the resultant solution at room temperature, crystals of **I** precipitated.

X-ray diffraction analysis. Crystals **I**, $C_{10}H_{15}CuN_3O_5$, are orthorhombic; $a = 8.286(2)$ Å, $b = 8.546(2)$ Å, $c = 17.309(4)$ Å, $V = 1225.7(4)$ Å^3, $M = 320.8$, $F(000) = 660$, $\rho_{calcd} = 1.738$ g/cm^3, $\mu_{Mo} = 1.803$ mm^{-1}, $Z = 4$, and space group $P2_12_12_1$.

The experimental data were obtained on an Enraf–Nonius CAD4 diffractometer (MoK_α radiation, graphite monochromator, $\theta/2\theta$ scan mode, $2\theta_{max} = 60°$).

The structure was solved by direct methods. The hydrogen atoms were located from difference Fourier syntheses. The least-squares refinement was performed using 1992 unique nonzero reflections. The non-hydro-

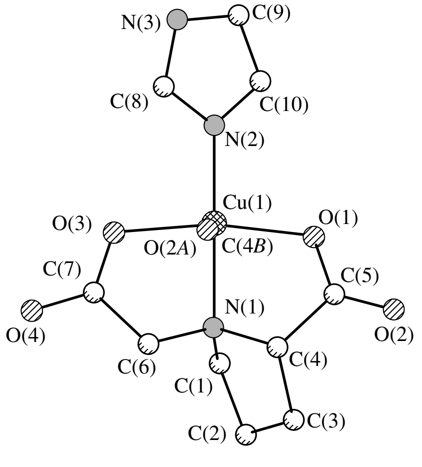

Fig. 1. Structure of molecular complex **I**.

1063-7745/04/4905-0783$26.00 © 2004 MAIK "Nauka/Interperiodica"

gen atoms were refined in the anisotropic approximation, and the hydrogen atoms were refined isotropically. The final discrepancy factors are as follows: R_1 = 0.0410, wR_2 = 0.1024 for 1892 reflections with $F_o \geq 4\sigma(F_o)$ and R_1 = 0.0431, wR_2 = 0.1042 for all 1992 reflections; *GOOF* = 0.976; 232 parameters refined; $\Delta\rho_{max}$ = 0.977 e/Å^3 and $\Delta\rho_{min}$ = –1.350 e/Å^3.

All the calculations were performed with the SHELXS86 [4] and SHELXL93 [5] program packages.

The atomic coordinates and thermal parameters are listed in Table 1.

Table 1. Atomic coordinates and thermal parameters U_{eq} or U_{iso}

Atom	x	y	z	U_{eq}/U_{iso}, Å^2
Cu(1)	0.02128(5)	0.36659(4)	0.37229(2)	0.0228(1)
N(1)	0.1687(3)	0.1874(3)	0.3534(1)	0.0190(4)
N(2)	–0.1300(3)	0.5364(3)	0.3952(2)	0.0250(5)
N(3)	–0.3581(4)	0.6637(4)	0.4032(2)	0.0316(6)
O(1)	0.1863(3)	0.4277(3)	0.4475(1)	0.0259(5)
O(2)	0.3871(4)	0.3306(4)	0.5170(2)	0.0511(9)
O(3)	–0.1223(3)	0.2630(3)	0.2987(2)	0.0276(5)
O(4)	–0.1459(3)	0.0404(3)	0.2339(2)	0.0345(6)
C(1)	0.2964(4)	0.2183(5)	0.2949(2)	0.0293(6)
C(2)	0.4277(5)	0.0982(6)	0.3128(3)	0.0405(9)
C(3)	0.4224(5)	0.0838(5)	0.4004(3)	0.0381(9)
C(4)	0.2623(4)	0.1602(3)	0.4251(2)	0.0218(5)
C(5)	0.2829(4)	0.3174(4)	0.4669(2)	0.0239(5)
C(6)	0.0619(4)	0.0577(4)	0.3296(2)	0.0257(6)
C(7)	–0.0786(3)	0.1238(4)	0.2827(2)	0.0227(5)
C(8)	–0.2889(4)	0.5270(4)	0.3859(2)	0.0281(6)
C(9)	–0.2398(5)	0.7674(4)	0.4234(3)	0.0338(7)
C(10)	–0.0987(4)	0.6868(4)	0.4190(3)	0.0323(7)
O(1*w*)	–0.6834(3)	0.6958(4)	0.3805(2)	0.0415(6)
H(11)	0.341(6)	0.304(7)	0.298(3)	0.03(1)
H(12)	0.259(7)	0.212(7)	0.241(4)	0.05(1)
H(21)	0.391(7)	–0.012(6)	0.293(3)	0.03(1)
H(22)	0.528(8)	0.150(8)	0.301(4)	0.06(2)
H(31)	0.502(6)	0.136(7)	0.416(4)	0.05(2)
H(32)	0.424(6)	–0.033(6)	0.417(3)	0.03(1)
H(41)	0.202(7)	0.095(7)	0.457(4)	0.04(1)
H(61)	0.029(6)	0.005(7)	0.375(3)	0.04(1)
H(62)	0.112(7)	–0.033(6)	0.302(3)	0.04(1)
H(81)	–0.345(5)	0.450(5)	0.363(3)	0.02(1)
H(91)	–0.273(8)	0.884(8)	0.430(5)	0.07(2)
H(101)	0.003(5)	0.719(5)	0.425(3)	0.03(1)
H(1*w*1)	–0.722(7)	0.610(7)	0.414(3)	0.04(1)
H(2*w*1)	–0.703(7)	0.636(7)	0.338(4)	0.05(2)
H(1N3)	–0.459(6)	0.684(5)	0.392(3)	0.02(1)

RESULTS AND DISCUSSION

The structural units of crystals **I** are the [Cu(*Proma*)(*Im*)] molecular complexes (Fig. 1) and crystallization water molecules. The coordination number of the Cu atom in the complex is 4 + 1 + 1, and the coordination polyhedron is a square bipyramid. The equatorial plane of the square bipyramid is occupied by two oxygen atoms of the acetate groups [Cu–O, 1.958(2) and 1.955(2) Å], the nitrogen atom of the pyrrolidine ring of the *Proma* ligand [Cu–N, 1.986(2) Å], and the nitrogen atom of the imidazole molecule [Cu–N, 1.958(2) Å] in the *trans* position to the nitrogen atom of the pyrrolidine ring. The axial positions are occupied by the terminal oxygen atoms of the acetate arms of the neighboring complexes, which form the elongated bonds Cu–O(4*B*) and Cu–O(2*A*) [2.578(2) and 2.783(2) Å, respectively] and the OCuO angle [177.8(1)°]. The coordination square of the central atom is almost planar, and the Cu(1) atom deviates from this plane toward the nearest axial vertex O(4*B*) by only 0.06 Å.

In the molecular complex, both acetate metallocycles adopt an envelope conformation: the N(1) atom deviates by 0.52 and 0.54 Å from the mean planes through the remaining atoms of each ring, which are coplanar to within 0.04 Å. The N(1)–C(1)–C(2)–C(3)–C(4) pyrrolidine ring has a slightly asymmetric *gauche* structure: the N(1) and C(1) atoms deviate from the plane of the remaining three atoms by 0.25 and –0.37 Å, respectively.

Upon coordination with the metal atom, the asymmetric C(4) atom of the *Proma* ligand retains an *S* absolute configuration and a new asymmetric center

Table 2. Geometric parameters of hydrogen bonds in structure **I**

A–H···*B* bond	Distances, Å			*AHB* angle, deg	Position of the *B* atom
	A···*B*	*A*–H	H···*B*		
O(*w*1)–H(1*w*1)···O(1)	2.786(4)	0.98(6)	1.83(6)	163(5)	*x* – 1, *y*, *z*
O(*w*1)–H(2*w*1)···O(4)	2.771(5)	0.91(7)	1.94(7)	150(6)	–*x* – 1, 0.5 + *y*, 0.5 – *z*
N(3)–H(1N3)···O(*w*1)	2.738(4)	0.87(5)	1.88(5)	169(4)	*x*, *y*, *z*

appears, namely, the N(1) atom with the opposite (*R*) absolute configuration.

Comparison of structure **I** with the structure of the related complexes shows that structural changes in the complexes of different composition do not touch the absolute configuration of the main asymmetric centers C(4) and N(1).

The replacement of the five-membered acetate ring by the six-membered propionate ring in [Cu(*Promp*)(*Im*)] (**II**) [2] does not substantially affect the structure of the complex as a whole. The most significant difference between these structures lies in the conformational change of the pyrrolidine ring due to the displacements of the C(7*A*) and C(6*A*) atoms in **II**

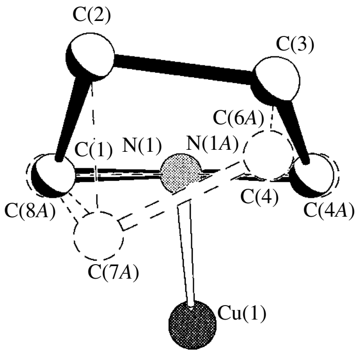

Fig. 2. Conformation of the pyrrolidine ring in structures **I** and **II** (dashes).

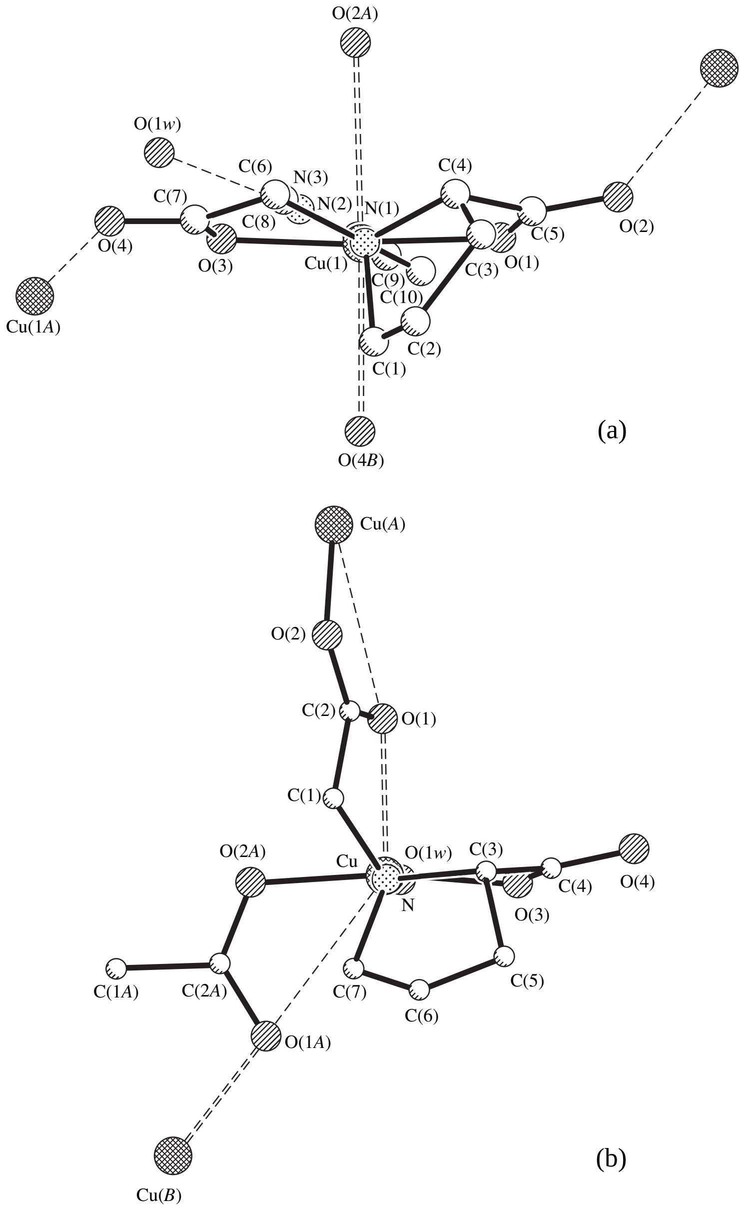

Fig. 3. Structural comparison of molecular complexes (a) **I** and (b) **III** (the designations and inverted atomic coordinates are taken from [3] for space group $P4_1$).

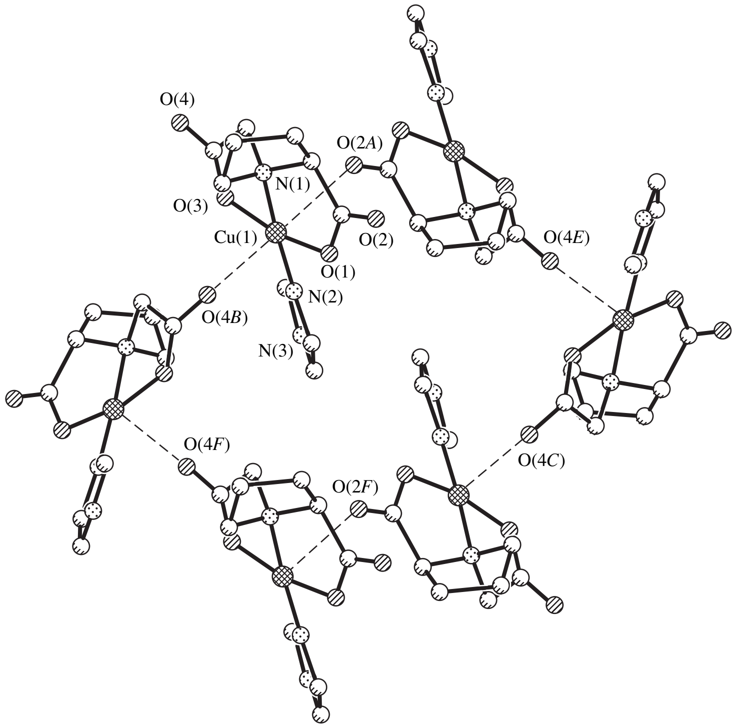

Fig. 4. Cyclic fragment involving six molecular complexes in framework structure **I**.

from the positions of the C(2) and C(3) atoms in **I** by 1.5 and 0.6 Å, respectively (Fig. 2). This circumstance, combined with the increased "tetrahedricity" of the basal square, leads to a transformation of the Cu coordination sphere into a semioctahedron and, consequently, results in the formation of a chain structure in crystal **II**, which differs from the framework structure in **I** (the *Promp* ligand retains a flattened structure).

The replacement of imidazole (the second ligand in the coordination sphere of **I**) by a water molecule brings about more significant changes in the structure of the complex. In the [Cu(*Proma*)(H_2O)] · $2H_2O$ compound (**III**) [3], the free acetate group is rotated through ~90° with respect to the rest of the *Proma* ligand; as a result, the initially flattened ligand becomes cornerlike in shape and occupies *cis* vertices in the Cu polyhedron (semioctahedron). The above structural transformation is illustrated in Fig. 3. In structure **III**, unlike structure **I**, the O(3) atom (Fig. 3a) occupies not an equatorial vertex but an axial vertex instead of the O(2*A*) atom. This position corresponds to O(1) in structure **III**, and the Cu–O(1) distance is 2.31 Å (Fig. 3b). The vacant position in the basal square of structure **III** is occupied by the terminal O(2*A*) atom of the acetate group of the neighboring complex (Fig. 3b). The O(1) atom acts as a pseudobridge [the Cu(*A*)–O(1) distance to the other copper atom is 2.90 Å]. This additionally strengthens the chain, which also represents a structural unit (supramolecular ensemble) of crystal **III**.

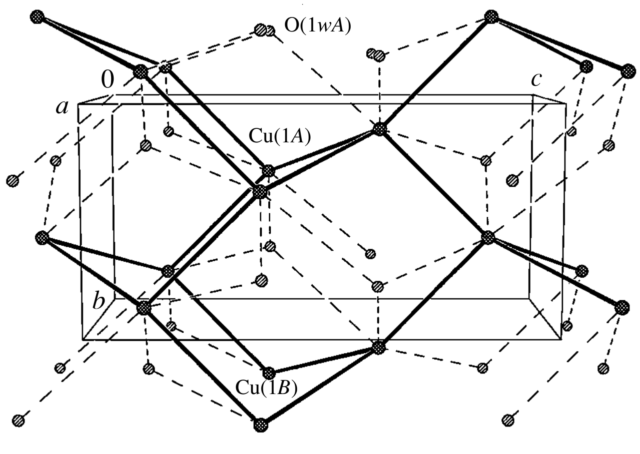

Fig. 5. Schematic drawing of the molecular packing of water and the copper framework in structure **I**.

The chain structure is revealed not only in compounds **II** and **III** but also in the [Cu(*Promp*)(H_2O)] complex (**IV**) [1]. The formation of chains in crystals **IV** is caused by the same factors. The *Promp* ligand fulfills a pentadentate chelating–bridging function. The ligand is cornerlike in shape and occupies three *cis* vertices in the coordination polyhedron (semioctahedron) of the Cu atom (two vertices of the basal square and the axial vertex); the two other basal vertices are occupied by the H_2O molecule and the "terminal" atom of the "chelate bridging" propionate group of the neighboring complex. The second oxygen atom of this group, namely, O(1), does not participate in the interaction [Cu···O(1), 2.86 Å] but shields the sixth potential coordination site in the metal polyhedron. In the case when the crystal structure is formed by the Cu atoms, which are characterized by a relatively low coordination capacity, and polydentate ligands (*Proma* in **III** and *Promp* in **IV**), the twofold 2_1 and fourfold 4_1 screw axes appeared to be the most suitable chain-forming translational crystallographic elements.

In crystal **I**, the situation is somewhat different. In the coordination six-vertex polyhedron (and not in a semioctahedron), two axial vertices are able to take part in the formation of chains. Actually, the terminal oxygen atoms of the acetate fragments of the *Proma* ligand act as bridges and link complexes into a framework formed by intersecting chains running in three directions. In structure **I**, there exist cyclic conjugated fragments involving six complexes (Fig. 4). The formation of the framework in crystal **I** is illustrated in Fig. 5, which shows the three-dimensional network of Cu atoms. Water molecules are located in voids of the framework and form hydrogen bonds O(*w*1)–H(1*w*1)···O(1) and O(*w*1)–H(2*w*1)···O(4) as proton donors and N(3)–H(1N3)···O(*w*1) as proton acceptors (Table 2), thus stabilizing the structure.

REFERENCES

1. A. B. Ilyukhin, L. M. Shkol'nikova, A. L. Poznyak, and S. S. Makarevich, Kristallografiya **36** (5), 1155 (1991) [Sov. Phys. Crystallogr. **36**, 653 (1991)].
2. I. F. Burshteĭn, A. L. Poznyak, and L. V. Stopolyanskaya, Zh. Neorg. Khim. **44** (8), 1251 (1999).
3. I. F. Burshteĭn, A. L. Poznyak, and L. V. Stopolyanskaya, Kristallografiya **45** (2), 259 (2000) [Crystallogr. Rep. **45**, 227 (2000)].
4. G. M. Sheldrick, Acta Crystallogr., Sect. A: Found. Crystallogr. **46**, 467 (1990).
5. G. M. Sheldrick, *SHELXL93: Program for the Refinement of Crystal Structures* (Univ. of Göttingen, Germany, 1993).

Translated by I. Polyakova

Crystallography Reports, Vol. 49, No. 5, 2004, pp. 788–791. Translated from Kristallografiya, Vol. 49, No. 5, 2004, pp. 876–879.
Original Russian Text Copyright © 2004 by Sergienko, Aleksandrov, Seĭfullina, Martsinko.

Synthesis and the Crystal and Molecular Structures of a Germanium(IV)–Copper(II) Heteronuclear Diethylenetriaminepentaacetate Complex, $[Cu(\mu\text{-H}Dtpa)_2\{Ge(OH)\}_2] \cdot 12H_2O$

V. S. Sergienko*, G. G. Aleksandrov*, I. I. Seĭfullina, and E. É. Martsinko****

** Kurnakov Institute of General and Inorganic Chemistry, Russian Academy of Sciences,*
Leninskiĭ pr. 31, Moscow, 119991 Russia

e-mail: aleks@igic.ras.ru

*** Odessa State University, ul. Petra Velikogo 2, Odessa, 27000 Ukraine*

Received March 4, 2003

Abstract—A procedure for synthesizing a mixed Cu–Ge complex with diethylenetriaminepentaacetic acid (H_5Dtpa) is worked out, the compound $[Cu\{Ge(OH)(HDtpa)\}_2] \cdot 12H_2O$ is synthesized, and its crystal structure is studied by X-ray diffraction. In the centrosymmetric trinuclear molecular complex, the octahedral coordination of the peripheral Ge atom involves three O and two N atoms of the $HDtpa^{4-}$ ligand and the O atom of the hydroxo ligand. The central Cu atom is coordinated by four O and two N atoms of two $HDtpa^{4-}$ ligands, which form a tetragonal bipyramid (4 + 2). The $HDtpa^{4-}$ ligand fulfills an octadentate hexachelate bridging function (3N, 5O). The molecular complexes and crystallization water molecules are linked by an extended hydrogen-bond network. © *2004 MAIK “Nauka/Interperiodica”.*

INTRODUCTION

In the course of systematic investigations into the complexation of germanium(IV) with various aminopolycarboxylic acids (such as nitrilotriacetic H_3Nta [1], ethylenediaminetetraacetic H_4Edta [2, 3], and diethylenetriaminepentaacetic H_5Dtpa [4] acids), we obtained chelate complexes of equimolar composition in which the $Ge(OH)^{3+}$ ion acts as a complexing agent. In these complexonates, H_4Edta and H_5Dtpa do not exhibit their maximum coordination capacity.

It was hypothesized that, owing to the free donor centers capable of forming bonds with other metals, these complexes can be used as initial reactants for the preparation of heteronuclear compounds. To the best of our knowledge, data on different-metal complexonates containing germanium are not available in the literature. In this work, we synthesized a germanium(IV)–copper(II) heteronuclear complex with H_5Dtpa (**I**) and performed an X-ray diffraction analysis of its crystal structure. Compound **I** has the structural formula $[Cu\{Ge(OH)(HDtpa)\}_2] \cdot nH_2O$ ($n \le 12$), which was determined in the X-ray diffraction study.

EXPERIMENTAL

Synthesis. Complex $[Ge(OH)(H_2Dtpa)] \cdot H_2O$, which was prepared according to the procedure described in [4], and copper(II) acetate were used as initial reactants for the synthesis of compound **I**. The reaction of $[Ge(OH)(H_2Dtpa)] \cdot H_2O$ with $Cu(CH_3COO)_2 \cdot H_2O$ in molar ratios ranging from 2 : 1 to 1 : 1 in an aqueous solution afforded crystals of compound **I**, which was identified using X-ray diffraction and chemical analyses. The elemental analysis was performed on a C,N,H-analyzer. The copper and germanium contents were determined by atomic emission spectroscopy with inductively coupled plasma on a Perkin-Elmer Optima 2000 DV spectrometer. The H_2O content was determined by thermogravimetry. Small single crystals of complex **I** suitable for X-ray diffraction analysis were obtained in the reaction system through slow evaporation (for ~2 months) of the solvent at room temperature.

X-ray diffraction analysis. Crystals **I** are monoclinic, $a = 7.497(1)$ Å, $b = 26.331(5)$ Å, $c = 11.946(2)$ Å, $\beta = 110.14(3)°$, $V = 2313.7(7)$ Å^3, $M = 1233.54$, $F(000) = 1272$, $\rho_{calcd} = 1.775$ g/cm^3, $\mu_{Mo} = 1.860$ cm^{-1}, $Z = 2$, and space group $P2_1/n$. The experimental set of intensities was obtained at room temperature on an Enraf–Nonius CAD4 diffractometer (λMoK_α, graphite monochromator, ω scan mode, $2\theta_{max} = 48°$). A total of 3344 reflections were measured, of which 3030 were unique reflections ($R_{int} = 0.129$; $0 < h < 6$, $0 < k < 30$, $-13 < l < 13$). No absorption correction was applied.

The structure was solved by direct methods (SHELXS97) [5]. The non-hydrogen atoms were refined by the least-squares procedure (on F^2) in the full-matrix anisotropic approximation (SHELXL97) [6]. The hydrogen atoms H(C) of the CH_2 groups, as well as H(O1) of the hydroxo ligand and H(O9) of an acetate group of the H*Dtpa*$^{4–}$ ligand, were calculated geometrically and included in the refinement at fixed positions (C–H, 0.97 Å; O–H, 0.82 Å). The thermal parameters U_{iso} of the H(C) and H(O) atoms were taken to be 1.2 and 1.5 times, respectively, larger than the U_{eq} values of the carbon and oxygen atoms to which they are attached.

The final results of the refinement are as follows: $R_1 = 0.0471$ and $wR_2 = 0.0943$ for 1328 reflections with $I > 2\sigma(I)$; $R_1 = 0.2202$ and $wR_2 = 0.1202$ for all reflections; and $GOOF = 1.001$. The values of $\Delta\rho_{\text{max}}$ and $\Delta\rho_{\text{min}}$ are 0.587 and –0.698 e Å^{-3}, respectively. The CIF file is deposited in the Cambridge Structural Database (CCDC no. 203897). The interatomic distances and bond angles are listed in Table 1.

RESULTS AND DISCUSSION

Our studies showed that only one compound, namely, **I**, is formed in the used range of molar ratios between the reactants. According to the elemental analysis, the composition of the compound synthesized corresponds to the empirical formula $C_{28}H_{40}CuGe_2N_6O_{22} \cdot 12H_2O$.

For **I** anal. calcd. (%): Cu, 5.17; Ge, 11.74; C, 27.16; N, 6.79; H, 5.17; H_2O, 17.46.

Found (%): Cu, 5.20; Ge, 11.80; C, 27.15; N, 6.80; H, 5.20; H_2O, 17.30.

Structural units of crystal **I** are centrosymmetric trinuclear molecular complexes [Cu{Ge(OH)(H*Dtpa*)}$_2$] (figure) and crystallization water molecules.

In the molecular complex, the coordination polyhedron of the central Cu atom is an elongated tetragonal bipyramid (4 + 2) with typical distortions caused by the Jahn–Teller effect. The Cu–O(H*Dtpa*) axial bonds are significantly longer than the analogous equatorial bonds [2.470(6) and 1.924(6) Å, respectively].The Cu–N(H*Dtpa*) bond length is 2.051(7) Å. The octahedral coordination of the peripheral Ge atom involves two N atoms and three O atoms of the H*Dtpa*$^{4–}$ ligand and the O(1) atom of the hydroxo ligand. The Ge–O(1) bond [1.760(6) Å] is considerably shorter than each of the three Ge–O(H*Dtpa*) bonds [1.889(6) ± 0.012 Å], which indicates an increased multiplicity of the former bond. The Ge–N(1) bond in the *trans* position with respect to the hydroxo ligand is slightly shorter (by 0.036 Å) than the Ge–N(2) bond in the *trans* position with respect to the O(H*Dtpa*) atom [2.072(7) and 2.108(7) Å, respectively]. The geometric parameters of the Ge polyhedron in structure **I** are comparable to those in other germanium(IV) complexes with mono-, di-, and triaminocarboxylates *L*, namely, [Ge(OH)(H*Dtpa*)] · H_2O (**II**) [4, 7], [Ge(OH)(*Nta*)(H_2O)] · $2H_2O$ (**III**) [1], and [Ge(OH)(H*Edta*)] · H_2O (**IV**) [2, 8].[1] In **II**, **III**, and **IV**, the bond lengths are, respectively, as follows: Ge–O(OH), 1.741(5), 1.762(3), and 1.768(5) Å; Ge–

Table 1. Bond lengths *d* (Å) and angles ω (deg) for compound **I**

Bond	*d*	Bond	*d*
Cu(1)–O(8)	2.474(6)	Cu(1)–O(10)	1.928(6)
Cu(1)–N(3)	2.057(7)	Ge(1)–O(1)	1.758(6)
Ge(1)–O(2)	1.887(6)	Ge(1)–O(4)	1.880(7)
Ge(1)–O(6)	1.902(6)	Ge(1)–N(1)	2.068(7)
Ge(1)–N(2)	2.110(7)	O(2)–C(2)	1.28(1)
O(3)–C(2)	1.23(1)	O(4)–C(4)	1.31(1)
O(5)–C(4)	1.20(1)	O(6)–C(8)	1.30(1)
O(7)–C(8)	1.21(1)	O(8)–C(12)	1.20(1)
O(9)–C(12)	1.33(1)	O(10)–C(13)	1.31(1)
O(11)–C(13)	1.23(1)	N(1)–C(3)	1.45(1)
N(3)–C(11)	1.45(1)	C(1)–C(2)	1.51(1)
C(3)–C(4)	1.50(2)	C(5)–C(6)	1.51(1)
C(7)–C(8)	1.48(1)	C(9)–C(10)	1.51(1)
C(11)–C(12)	1.51(1)	C(13)–C(14)	1.48(1)
Angle	ω	Angle	ω
O(8)Cu(1)O(10)	96.2(2)	O(8)Cu(1)N(3)	72.3(3)
O(10)Cu(1)N(3)	85.5(3)	O(1)Ge(1)O(2)	94.1(3)
O(1)Ge(1)O(4)	97.3(3)	O(1)Ge(1)O(6)	93.1(3)
O(1)Ge(1)N(1)	178.8(3)	O(1)Ge(1)N(2)	96.2(3)
O(2)Ge(1)O(4)	96.2(3)	O(2)Ge(1)O(6)	171.3(3)
O(2)Ge(1)N(1)	84.8(3)	O(2)Ge(1)N(2)	92.0(3)
O(4)Ge(1)O(6)	87.7(3)	O(4)Ge(1)N(1)	82.5(3)
O(4)Ge(1)N(2)	163.7(3)	O(6)Ge(1)N(1)	88.1(3)
O(6)Ge(1)N(2)	82.4(3)	N(1)Ge(1)N(2)	84.2(3)
Ge(1)O(2)C(2)	118.8(6)	Ge(1)O(4)C(4)	117.1(6)
Ge(1)O(6)C(8)	117.5(6)	Cu(1)O(8)C(12)	100.6(6)
Cu(1)O(10)C(13)	115.1(6)	Ge(1)N(1)C(3)	105.2(6)
Cu(1)N(3)C(11)	110.4(5)	O(2)C(2)O(3)	123.8(9)
O(2)C(2)C(1)	117.0(9)	O(3)C(2)C(1)	119.1(9)
N(1)C(3)C(4)	111.0(8)	O(4)C(4)O(5)	122(1)
O(4)C(4)C(3)	114.9(9)	O(5)C(4)C(3)	123(1)
O(6)C(8)O(7)	121.5(9)	O(6)C(8)C(7)	116.6(8)
O(7)C(8)C(7)	122.0(9)	N(3)C(11)C(12)	109.4(7)
O(8)C(12)O(9)	124.3(9)	O(8)C(12)C(11)	124.6(9)
O(9)C(12)C(11)	111.1(8)	O(10)C(13)O(11)	121.7(9)
O(10)C(13)C(14)	115.9(9)	O(11)C(13)C(14)	122.3(9)

---

[1] In [2], the formula of compound **IV** is wrongly given as [GeO(H_2*Edta*)] · H_2O.

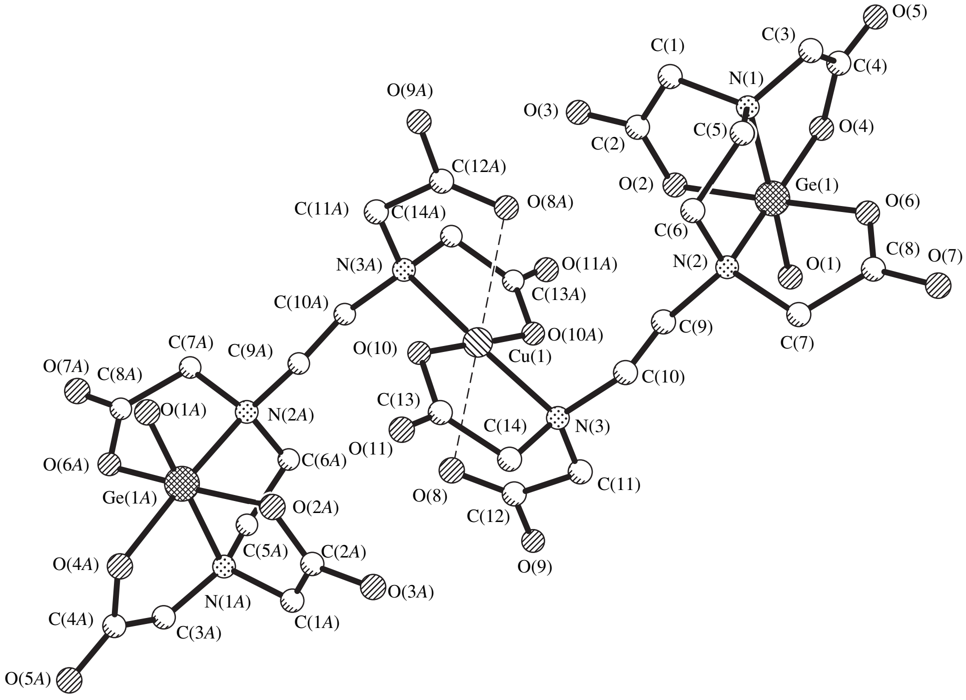

Structure of the molecular complex [Cu{Ge(OH)(μ-H*Dtpa*)}^{2}].

O(*L*), 1.895(6) ± 0.010, 1.890(3) ± 0.007, and 1.883(5) ± 0.009 Å; and Ge–N (*trans* to OH), 2.079(6), 2.084(3), and 2.081(5) Å.[2] The Ge–N [*trans* to O(*L*)] bond length is equal to 2.088(6) Å in **II** and 2.106(5) Å in **IV**. It is evident that, in structures **II** and **IV**, as in structure **I**, the Ge–N(*L*) bonds involving the nitrogen atom in the *trans* position with respect to the hydroxo ligand are slightly shorter (by 0.009 and 0.025 Å, respectively) than the Ge–N [*trans* to O(*L*)] bonds.

On the whole, neutral molecule **II** and the [Ge(OH)(H*Dtpa*)]$^-$ monoanionic fragment in **I** have very similar structures. In **I** and **II**, the polydentate ligand (triaminopolycarboxylate) coordinates the Ge atom in a pentadentate chelate manner (2N, 3O), thus closing four five-membered metallocycles, namely, the GeN_2C_2 ethylenediamine ring and three $GeNC_2O$ glycinate rings. When changing over from **II** to **I**, the only difference is observed in the deprotonation of the quaternized N(3) atom, which coordinates the Cu atom at an equatorial site. The Cu coordination also involves the O(10) and O(8) atoms (at the equatorial and axial sites, respectively) of two acetate arms, which are free of coordination in structure **II**.

Thus, the H*Dtpa*$^{4-}$ ligand in structure **I** coordinates the copper atom in a tridentate chelate manner (N, 2O), thus closing two glycinate rings. On the whole, the H*Dtpa*$^{4-}$ ligand in structure **I** fulfills an octadentate hexachelate bridging function (3N, 5O).

The hydrogen atoms in structure **I** could not be located experimentally. The position of the "acid" hydrogen atom of the H*Dtpa*$^{4-}$ ligand was determined from analyzing the O–C distances (with due regard for the function of the carboxyl groups) and the hydrogen-bond system (see below). In structure **I**, the C–O_t terminal bonds [1.21(1) ± 0.03 Å],[3] as a rule, are significantly shorter than the C–O_b bonds with "bridging" oxygen atoms that coordinate metal atoms [1.30(1) ± 0.02 Å]. The position of the acid H(O9) atom at the terminal O(9) atom is uniquely determined by the C(12)–O(9) distance [1.32(1) Å], which is considerably longer (on average, by 0.11 Å) than the remaining C–O_t distances. The C–O(H_2*Dtpa*) bond lengths in structure **II** [4] [C–O(OH), 1.31(1) Å; C–O_t, 1.23(1) ± 0.05 Å; C–O_b, 1.31(1) ± 0.01 Å] agree with the corresponding values in **I**.

As mentioned above, the octadentate (3N, 5O) chelate bridging H*Dtpa*$^{4-}$ ligand in structure **I** coordinates the Cu and Ge atoms, thus closing six five-membered metallocycles, namely, $\overline{\mathrm{CuN(3)C(14)C(13)O(10)}}$ (A), $\overline{\mathrm{CuN(3)C(11)C(12)O(8)}}$ (B), $\overline{\mathrm{GeN(1)C(1)C(2)O(2)}}$ (C), $\overline{\mathrm{GeN(1)C(3)C(4)O(4)}}$ (D), $\overline{\mathrm{GeN(2)C(7)C(8)O(6)}}$ (E), and $\overline{\mathrm{GeN(1)C(5)C(6)N(2)}}$ (F). Four of the five glycinate rings have an envelope conformation in which

---

[2] According to the data taken from [4] and [8] for **II** and **IV**, respectively.

[3] Among these bonds is the C(12)–O(8) bond [1.20(1) Å] with a "semicoordinated" oxygen atom at an axial site of the CuO_4N_2 polyhedron.

Table 2. Geometric parameters d (Å) of the O···Ointermolecular contacts shorter than 3.05 Å in structure **I**

A···B bond	d	Coordinates of the B atom
O(1w)···O(3)	2.92(1)	$x, y, 1 + z$
O(1w)···O(9)*	2.65(1)	$1 - x, -y, 1 - z$
O(1w)···O(11)	2.85(1)	$-x, -y, 1-z$
O(2w)···O(1)**	2.782(9)	x, y, z
O(2w)···O(10)	3.018(9)	$-x, -y, -z$
O(2w)···O(4w)	2.78(1)	x, y, z
O(3w)···O(3)	2.75(1)	x, y, z
O(3w)···O(5)	2.89(1)	$-0.5 + x, 0.5 - y, -0.51 + z$
O(3w)···O(5w)	2.60(2)	x, y, z
O(4w)···O(5)	2.92(2)	$0.5 + x, 0.5 - y, 0.5 + z$
O(4w)···O(5w)	2.71(3)	$x, y, 1 + z$
O(4w)···O(6w)	2.63(4)	$1 + x, y, z$
O(5w)···O(6w)	2.43(4)	$-x, -y, -z$

* The O(1w)···H(O9) contact is 1.83 Å, and the O(1w)H(O9)O(9) angle is 175°.

** The O(2w)···H(O1) contact is 1.99 Å, and the O(2w)H(O1)O(1) angle is 162°.

the N(3), Cu, N(1), and N(2) atoms in the A, B, D, and E rings deviate by 0.495, 1.204, 0.630, and 0.513 Å, respectively. The C glycinate ring is approximately planar (±0.017–0.040 Å). The F ethylenediamine ring has a typical asymmetric *gauche* conformation: the C(5) and C(6) atoms deviate from the plane of the Ge, N(1), and N(2) atoms by –0.517 and 0.144 Å, respectively. In the CuN_2O_4 polyhedron, the A/B dihedral angle is 75.8°. In the GeN_2O_4 polyhedron, the D glycinate ring lies approximately in the equatorial plane of the F ring (the D/F dihedral angle is 19.1°), whereas the C and E rings are approximately perpendicular to the F ring (C/F, 95.5°; E/F, 86.8°). Thus, two of the three glycinate rings in the Ge octahedron have an *R* conformation, and the third ring has a *G* conformation (according to the nomenclature by Poraĭ-Koshits and Polynova [9]).

The geometric parameters of hydrogen bonds in structure **I** are listed in Table 2. Each of the six independent water molecules forms from two to four O···O contacts with oxygen atoms of the neighboring water molecules and the [Cu{Ge(OH)(H*Dtpa*)}$_2$] molecular complexes. The O···O distances in the hydrogen bonds fall in the range 2.60–3.02 Å, with one exception (see below). Three of the four terminal O_t(H*Dtpa*) atoms and only one of the five O_b(H*Dtpa*) atoms, which coordinate the Ge and Cu atoms, are involved in O(H*Dtpa*)···O(H_2O) short contacts. The hydroxo ligand O(1)H(O1) and the protonated oxygen atom O(9) act as donors of almost linear hydrogen bonds. Their geometric parameters [O(1)···O(2w), 2.782(9) Å; H(O1)···O(2w), 1.99 Å; O(9)···O(1w), 2.65(1) Å; H(O9)···O(1w), 1.83 Å; and angles O(1)H(O1)O(2w), 162°; O(9)H(O9)O(1w), 175°] indicate that the acid hydrogen atoms in molecular complex **I** [in particular, the H(O9) atom at the O(9) atom] are positioned correctly.

The presence of six independent atoms [O(1w)–O(6w)] in structure **I** suggests that there are 12 crystallization water molecules per formula unit. However, large thermal parameters of the O(3w), O(4w), and O(5w) atoms and, especially, the O(6w) atom, as well as the O(5w)···O(6w) short contact [2.43(4) Å], do not rule out the possibility that some water molecules undergo positional disordering (partial occupation of the positions) and, consequently, that the number of H_2O molecules per formula unit can be less than 12.

CONCLUSIONS

Thus, the above investigation of structure **I** validated the hypothesis regarding the possible preparation of heteronuclear aminocarboxylates containing metal ions with different electronic structures (*p* and *d*) and radically different complex-forming abilities. The results of this study will be used in the development of methods for synthesizing new heteronuclear germanium aminocarboxylates.

REFERENCES

1. A. B. Ilyukhin, L. M. Shkol'nikova, I. I. Seĭfullina, *et al.*, Koord. Khim. **17** (6), 795 (1991).
2. I. I. Seĭfullina, T. P. Batalova, E. V. Kolchinskiĭ, and V. K. Bel'skiĭ, Koord. Khim. **16** (6), 773 (1990).
3. I. I. Seĭfullina, T. P. Batalova, and K. I. Popov, Koord. Khim. **17** (4), 452 (1991).
4. I. I. Seĭfullina, E. É. Martsinko, A. B. Ilyukhin, and V. S. Sergienko, Zh. Neorg. Khim. **43** (10), 1628 (1998).
5. G. M. Sheldrick, *SHELXS97: Program for the Solution of Crystal Structures* (Univ. of Göttingen, Germany, 1997).
6. G. M. Sheldrick, *SHELXL97: Program for the Refinement of Crystal Structures* (Univ. of Göttingen, Germany, 1997).
7. J. Zhu, T.-S. Huang, Y.-Q. Huang, *et al.*, Chin. J. Struct. Chem. (Jiegou Huaxue) **14** (1), 191 (1995).
8. T. Mizuta, T. Yoshida, and K. Miyoshi, Inorg. Chim. Acta **165** (1), 65 (1989).
9. M. A. Poraĭ-Koshits and T. N. Polynova, Koord. Khim. **10** (6), 725 (1984).

Translated by I. Polyakova

Crystallography Reports, Vol. 49, No. 5, 2004, pp. 792–797. Translated from Kristallografiya, Vol. 49, No. 5, 2004, pp. 880–885.
Original Russian Text Copyright © 2004 by Koval'chukova, Mordovina, Kuz'mina, Nikitin, Zaĭtsev, Strashnova, Palkina.

STRUCTURE OF ORGANIC COMPOUNDS

Crystal Structure and Spectral Characteristics of 2-Methyl-3-Chloro-9-Hydroxypyrido[1,2-*a*]pyrimidin-4-one and Bis(2-Methyl-3-Chloro-9-Hydroxypyrido[1,2-*a*]pyrimidin-4-onium) Perchlorate

O. V. Koval'chukova*, N. I. Mordovina*, N. E. Kuz'mina, S. V. Nikitin***, B. E. Zaĭtsev*, S. B. Strashnova*, and K. K. Palkina****

* *Peoples' Friendship University, ul. Miklukho-Maklaya 6, Moscow, 117197 Russia*
e-mail: okovalchukova@sci.pfu.edu.ru
** *Kurnakov Institute of General and Inorganic Chemistry, Russian Academy of Sciences, Leninskiĭ pr. 31, Moscow, 119991 Russia*
*** *Research Institute of Pharmacology, Russian Academy of Medical Sciences, Moscow, Russia*

Received March 3, 2003; in final form, March 1, 2004

Abstract—2-Methyl-3-chloro-9-hydroxypyrido[1,2-*a*]pyrimidin-4-one (**I**) and bis(2-methyl-3-chloro-9-hydroxypyrido[1,2-*a*]pyrimidin-4-onium) perchlorate (**Ia**) are synthesized and studied by X-ray diffraction and IR spectroscopy. It is shown that compound **I** exists in the molecular form in crystals and in the zwitterion form in solutions. The structural units of compound **Ia** are partially protonated centrosymmetric dimeric cations and perchlorate anions. The dimeric cation involves two molecules **I** in the zwitterion form. These molecules are linked together by a strong symmetric hydrogen bond formed with the participation of a proton located at the inversion center. The structures of a series of pyrido[1,2-*a*]pyrimidines are investigated and compared. It is demonstrated that the tautomeric equilibrium revealed in solutions of compounds of this class depends on the solvent type and pH of the medium. © *2004 MAIK "Nauka/Interperiodica".*

INTRODUCTION

Pyrido[1,2-*a*]pyrimidin-4-one derivatives are characterized by biological and pharmacological activity [1, 2]. A number of structural and spectroscopic investigations have been devoted to the specific features of the structure and properties of these compounds [3–6]. However, the aforementioned works dealt with pyridopyrimidines containing no hydroxyl groups. At the same time, it is known that compounds involving hydroxyl groups exhibit a wide variety of tautomeric, acid–base, and other properties. In our earlier works, we performed X-ray diffraction and spectroscopic studies of 2-methyl-9-hydroxypyrido[1,2-*a*]pyrimidin-4-one (**II**) [5], 2,4-dimethyl-9-hydroxypyrido[1,2-*a*]pyrimidinium perchlorate (**III**), and 2,4-dimethyl-3-chloro-9-hydroxypyrido[1,2-*a*]pyrimidinium perchlorate (**IV**) [6–8].

In this work, we continued our systematic investigations of pyrido[1,2-*a*]pyrimidin-4-one derivatives containing hydroxyl groups in the 9 position.

EXPERIMENTAL

2-Methyl-3-chloro-9-hydroxypyrido[1,2-*a*]pyrimidin-4-one, $C_9H_7ClN_2O_2$ (**I**), was synthesized according to the procedure described in [6]. Single crystals of compound **I** precipitated upon recrystallization from neutral ethanol solutions. Single crystals of $[C_{18}H_{15}Cl_2N_4O_4]^+ClO_4^-$ (**Ia**) were isolated from an ethanol solution in the presence of nickel perchlorate at pH = 5.5.

The X-ray diffraction analysis of compounds **I** and **Ia** was performed on an Enraf–Nonius CAD4 four-circle automated diffractometer (MoK_α radiation, graphite monochromator, ω scan mode, $\theta \le 30°$). The structures were solved by direct methods and refined using the full-matrix least-squares procedure in the anisotropic approximation for the non-hydrogen atoms. The hydrogen atoms were located from the electron-density difference synthesis and included in the refinement with fixed thermal and positional parameters. The calculations were performed on a Pentium PC with the SHELX93 program package [9]. The main crystal data, data collection, and refinement parameters for structures **I** and **Ia** are presented in Table 1. The coordinates and thermal parameters of the atoms are listed in Table 2.

The IR absorption spectra of crystals **I** and **Ia** (Nujol mulls, KBr pellets) and IR absorption spectra of solutions of compound **I** in CCl_4 for different degrees of dilution and with addition of polar solvents (dimethyl sulfoxide, dioxane) were recorded on a Specord-75IR spectrophotometer in the frequency range 4000–400 cm^{-1}.

RESULTS AND DISCUSSION

Depending on the conditions and pH of the medium, 2-methyl-3-chloro-9-hydroxypyrido[1,2-*a*]pyrimidin-4-one can exist in the molecular (*A*), zwitterion (*B*, *C*), or ionic forms:

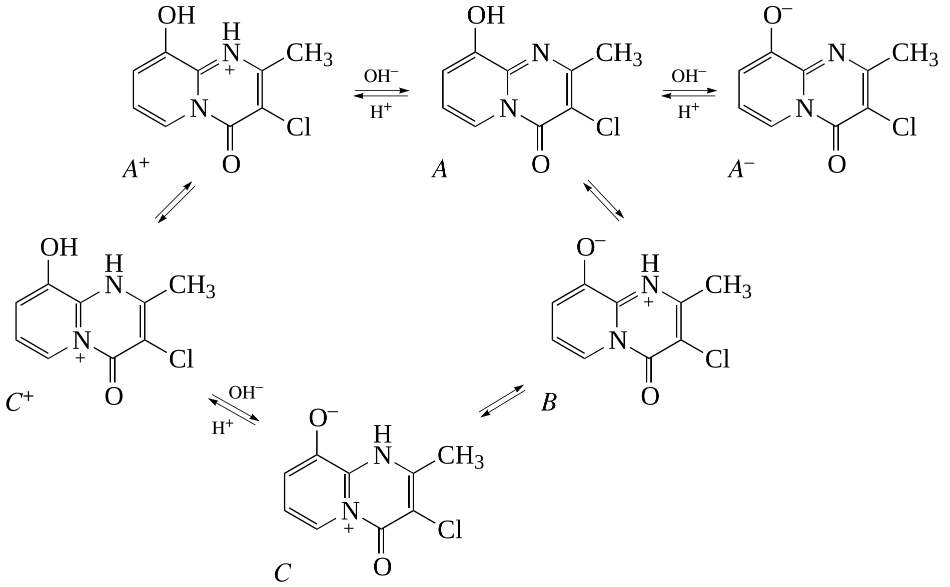

In the crystal, molecule **I** exists in the hydroxy form *A* (Fig. 1a). The molecule is nearly planar (the mean deviation of the non-hydrogen atoms from the plane is equal to 0.017 Å). The bonds involving the fusion nitrogen atom have a planar–trigonal orientation (the sum of the bond angles is equal to 359.9°). This orientation is in agreement with the X-ray diffraction data for molecules of 3-{2-[4-(4-benzoyl)piperidino]-ethyl}-2-methyl-4*H*-pyrido[1,2-*a*]pyrimidin-4-one (**V**) containing no hydroxyl group in the 9 position and pyridopyrimidinium cations **III** and **IV** (Table 3) [7, 8]. The sum of the bond angles in molecules of 6-methyl-3-caxboxyethyl-9-hydroxypyrido[1,2-*a*]pyrimidin-4-one (**VI**) is equal to 359.5° (Table 3) [10].

In molecule **I**, the N(2)–C(8) and N(2)–C(4) bond lengths (1.381 and 1.388 Å, respectively) are somewhat longer than the N(sp^2)–C(*ar*) bond length (1.336 Å) in the six-membered aromatic nitrogen-containing heterocycles. The elongation is maximum for the bond between the fusion nitrogen atom and the carbonyl carbon atom. In this case, the bond length (1.435 Å) is close to the length of the C(sp^3)–N(sp^3) single bond (1.469 Å). A similar nonequivalence of the bonds with the fusion nitrogen atom is observed for other pyrido[1,2-*a*]pyrimidin-4-ones, such as compounds **II**, **V**, and **VI** [4, 5, 10]. It should be noted that, in structures with hydrogenated pyridine rings, the N(2)–C bond with the carbonyl carbon atom is the shortest bond (1.385 Å) and the other two bonds involved in the formation of the perhydropyridine ring are considerably longer (1.490, 1.462 Å).

The C=O bond length in molecule **I** is equal to 1.229 Å. This is close to the bond length in molecule **VI**, which contains an ester group in the α position with respect to the carbonyl group [10].

The lengths of the N(1)–C(1) (1.354 Å) and N(1)–C(8) (1.309 Å) bonds with the cyclic nitrogen atom are typical of the majority of pyridopyrimidines [4, 5, 7, 10]. The C–OH (1.353 Å) bond is intermediate in

Table 1. Crystal data, data collection, and refinement parameters for structures **I** and **Ia**

Compound	**I**	**Ia**
Crystal system	Orthorhombic	Monoclinic
Space group	$P2_12_12_1$	$C2/c$
a, Å	5.053(3)	20.419(5)
b, Å	5.461(1)	6.286(3)
c, Å	31.65(1)	18.049(5)
β, deg	90	114.67(5)
V, Å^3	943.8(9)	2105(1)
ρ_{calcd}, g/cm^3	1.61	1.65
Z	4	4
μ_{Mo}, mm^{-1}	0.407	0.49
F(000)	472	1064.0
Number of unique reflections	1856	1773
Number of reflections with $I > 2\sigma(I)$	1559	1173
R, %	3.95	7.14
Rw, %	10.93	20.16
GOOF	1.14	0.905

Table 2. Atomic coordinates and thermal parameters B_{eq} (Å^2) for structures **I** and **Ia**

Atom	*x*	*y*	*z*	B_{eq}	Atom	*x*	*y*	*z*	B_{eq}
Structure **I**					Structure **Ia**				
Cl(1)	0.9040(2)	0.8067(1)	0.0415(0)	4.01(2)	Cl(1)	0.2390(1)	0.0529(3)	0.9175(1)	5.70(6)
O(1)	0.8792(4)	0.5156(3)	0.1208(0)	3.96(4)	Cl(2)	0.0000	0.1670(4)	0.7500	4.46(6)
O(2)	−0.0131(4)	1.1296(3)	0.1785(0)	3.67(3)	O(1)	0.2141(3)	0.2651(8)	0.7608(3)	5.2(1)
N(1)	0.3388(4)	1.0690(3)	0.1162(0)	2.95(3)	O(2)	0.0398(3)	−0.4491(8)	0.5736(3)	6.0(1)
N(2)	0.5289(4)	0.7241(3)	0.1505(0)	2.64(3)	O(3)*	0.0244(9)	0.005(2)	0.811(1)	6.9(4)
C(1)	0.5083(5)	1.0378(4)	0.0836(1)	2.88(4)	O(4)*	−0.0543(8)	0.275(1)	0.761(1)	8.0(4)
C(2)	0.6896(5)	0.8505(4)	0.0834(1)	2.85(4)	O(3*a*)*	0.056(1)	0.099(4)	0.830(2)	10.9(8)
C(3)	0.7178(5)	0.6826(4)	0.1175(1)	2.80(3)	O(4*a*)*	−0.021(2)	0.328(9)	0.791(1)	11.0(9)
C(4)	0.5345(5)	0.5707(4)	0.1855(1)	3.14(4)	N(1)	0.1167(3)	−0.2966(7)	0.7245(3)	3.7(1)
C(5)	0.3618(5)	0.6066(4)	0.2174(1)	3.24(4)	N(2)	0.1455(2)	0.0052(7)	0.6708(3)	3.40(9)
C(6)	0.1717(5)	0.7968(4)	0.2160(1)	3.11(4)	C(1)	0.1538(3)	−0.2322(9)	0.8032(4)	3.9(1)
C(7)	0.1660(5)	0.9469(4)	0.1821(1)	2.77(3)	C(2)	0.1891(3)	−0.044(1)	0.8187(4)	3.7(1)
C(8)	0.3512(4)	0.9153(3)	0.1479(1)	2.56(3)	C(3)	0.1863(3)	0.0930(9)	0.7534(4)	3.5(1)
C(9)	0.4843(7)	1.2167(5)	0.0479(1)	3.90(5)	C(4)	0.1424(4)	0.120(1)	0.6055(4)	4.9(1)
H(1)	0.691	0.442	0.187		C(5)	0.1076(4)	0.042(1)	0.5287(5)	5.8(2)
H(2)	0.365	0.502	0.241		C(6)	0.0701(4)	−0.154(1)	0.5111(4)	4.9(1)
H(3)	0.073	0.822	0.242		C(7)	0.0724(3)	−0.269(1)	0.5778(4)	4.1(1)
H(4)	0.461	1.139	0.020		C(8)	0.1111(3)	−0.1857(8)	0.6573(3)	3.3(1)
H(5)	0.369	1.318	0.058		C(9)	0.1534(5)	−0.377(1)	0.8681(4)	5.5(2)
H(6)	0.614	1.318	0.043		H(1)	0.095	−0.406	0.708	
H(7)	−0.016	1.181	0.154		H(2)	0.165	0.254	0.628	
					H(3)	0.107	0.082	0.481	
					H(4)	0.052	−0.204	0.470	
					H(5)	0.181	−0.318	0.921	
					H(6)	0.105	−0.399	0.861	
					H(7)	0.174	−0.511	0.863	
					H(8)	0.000	−0.500	0.500	

* The site occupancies of the O(3), O(4), O(3*a*), and O(4*a*) atoms are equal to 0.60, 0.60, 0.40, and 0.40, respectively.

length between the single C–O (1.47 Å) and double C=O (1.22 Å) bonds. This indicates a strong interaction of the hydroxyl group with the pyridopyrimidine ring.

Molecules **I** are joined together into chains by hydrogen bonds between the oxygen atoms of the carbonyl groups and the hydrogen atoms of the hydroxyl groups (Fig. 2a). The parameters of the O(2)–H(7)···O(1) hydrogen bond are as follows: the O···O distance is 2.84 Å, the H···O distance is 2.18 Å, and the OHO angle is 138.6°. The shortest distances between the adjacent chains [C(7)···C(3), 3.38 Å] and the adjacent layers [Cl(1)···Cl(1), 3.698 Å] are close to the sum of the van der Waals radii of the corresponding atoms.

The interaction of molecule **I** with nickel perchlorate in a water–ethanol solution at pH ~ 5 leads to the formation of partially protonated dimers (**Ia**). The specific feature of these dimers is that the cation is formed as a result of bonding of two molecules **I** by one proton (Fig. 1b).

According to the X-ray diffraction data, the structural units of compound **Ia** are the $[(C_9H_7ClN_2O_2)_2H]^+$ centrosymmetric dimeric cations and the ClO_4^- anions, which occupy special positions on the twofold axis. The dimeric cation involves two crystallographically equivalent molecules of 2-methyl-3-chloro-9-hydroxypyrido[1,2-*a*]pyrimidin-4-one in the zwitterion form. These molecules are linked together by the strong symmetric hydrogen bond O–H···O, which is formed with the participation of a proton located at the inversion center (Fig. 1b): the O(2)···O(2*a*) and H(8)···O(2) distances are equal to 2.550 and 1.28 Å, respectively, and the O(2)H(8)O(2*a*) angle is 180°.

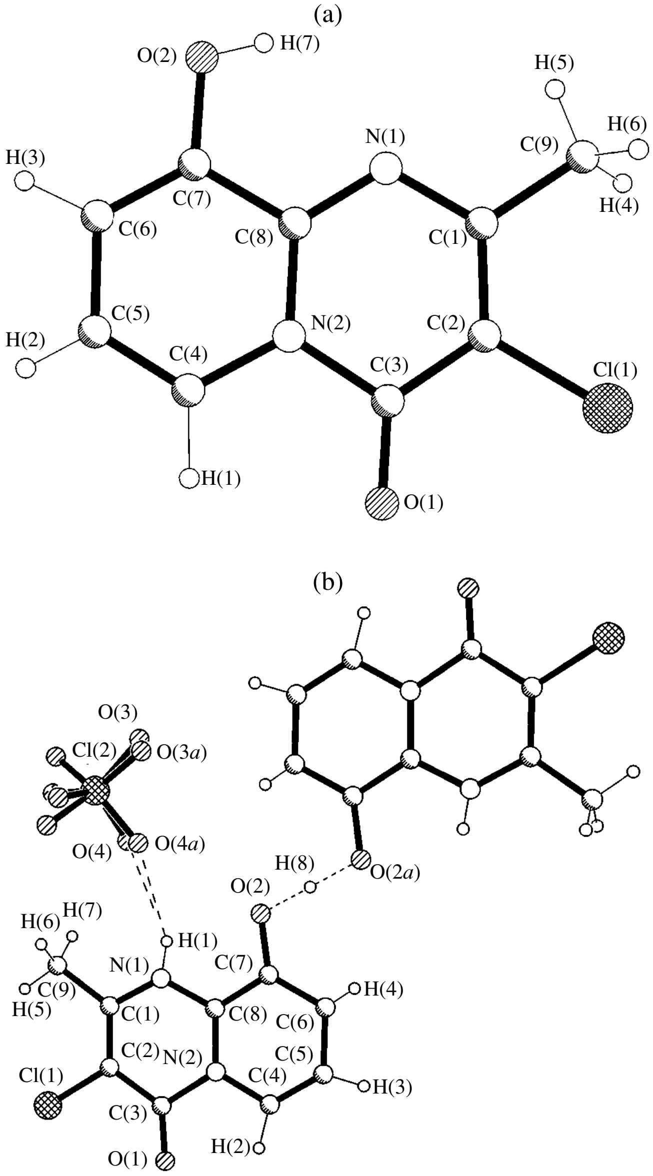

Fig. 1. Structures of (a) 2-methyl-3-chloro-9-hydroxypyrido[1,2-*a*]pyrimidin-4-one and (b) bis(2-methyl-3-chloro-9-hydroxypyrido[1,2-*a*]pyrimidin-4-onium) perchlorate.

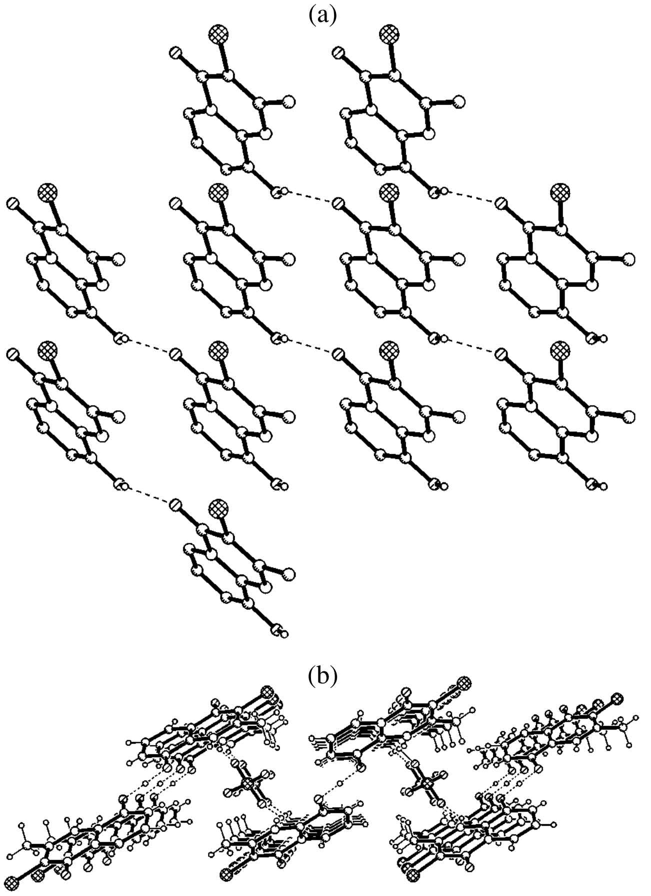

Fig. 2. Structure of layers in crystals **I** and **Ia**: (a) the projection of structure **I** along the *x* axis and (b) the projection of structure **Ia** along the *y* axis.

Similar dimeric cations are also formed in the structure of bis(8-hydroxy-2-quinolyl)amine hydroxide. The parameters of the hydrogen bond are as follows: the O···O distance is 2.437 Å, the H···O distance is 1.220 Å, and the OHO angle is 174.11° [11]. Moreover, Allen *et al.* [12] observed antipyrine dimers bonded by one proton.

In structure **Ia**, the zwitterion is almost planar (the mean deviation of the non-hydrogen atoms from the root-mean-square plane of the molecule is equal to 0.024 Å). The bonds of the nitrogen atoms of the bicyclic core have a planar–trigonal orientation: the sum of the bond angles at the N(1) and N(2) atom is equal to 360°. In general, the zwitterion structure is similar to the structure of molecule **I**. The main difference lies in the equalization of the bonds at the N(1) pyridine atom (1.363, 1.361 Å) and the shortening of the C(7)–O(2) hydroxyl bond (1.302 Å).

In the perchlorate anion, the oxygen atoms are disordered over two positions. The Cl–O bond lengths vary in the range from 1.38 to 1.48 Å, and the mean bond length (1.43 Å) is close to the standard value for perchlorate anions (1.414 Å).

Figure 2b shows the crystal structure of compound **Ia** (for clarity, the disorder of the perchlorate oxygen atoms is not shown). In the structure, the dimeric cations form columns that are aligned along the *y* axis and alternate with columns composed of perchlorate anions. The cations and anions of adjacent columns are joined together through the weak hydrogen bonds N–H···O formed with the participation of the pyrimidine nitrogen atom of the organic cation and the perchlorate oxygen atom: N(1)···O(4), 3.04 Å; H(1)···O(4), 2.32 Å; N(1)H(1)O(4), 147.7°; N(1)···O(4*a*), 3.01 Å; H(1)···O(4*a*), 2.24 Å; N(1)H(1)O(4*a*), 155.4°.

The spectral characteristics of compounds **I** and **Ia** are in agreement with the X-ray diffraction data. The IR

Table 3. Comparison of the structural characteristics for a number of pyrido[1,2-*a*]pyrimidine derivatives*

Compound	Sum of bond angles at the N_5 atom	Bond length, Å						
		N_5–C_4	N_5–C_6	C_5–C_{10}	N_1–C_2	N_1–C_{10}	C_4=O	C_9–R
I	359.9	1.435	1.388	1.381	1.354	1.309	1.229	1.353
Ia	360.0	1.478	1.362	1.360	1.363	1.361	1.203	1.302
II	360.0	1.447	1.388	1.375	1.359	1.321	1.321	1.355
III	359.9	1.393	1.378	1.380	1.303	1.334		1.352
IV	360	1.39	1.40	1.40	1.32	1.30		1.32
V	359.9	1.441	1.379	1.381	1.352	1.316	1.219	
VI	359.5	1.385	1.490	1.462	1.333	1.464	1.231	1.415

* The standard chemical numbering of atoms, which differs from the atomic numbering used for describing structures **I** and **Ia**, proceeds as follows:

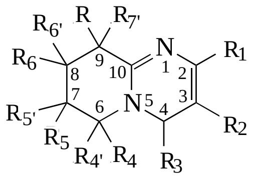

Appendix to Table 3

R_1	R_2	R_3	R_4/R'_4	R_5/R'_5	R_6/R'_6	R_7/R'_7	Compound
CH_3	Cl	O	–/H	–/H	–/H	–/OH	**I**
CH_3	Cl	O	–/H	–/H	–/H	O	**Ia**
CH_3	–	O	–/H	–/H	–/H	–/OH	**II**
CH_3	–	CH_3	–/H	–/H	–/H	–/OH	**III**
CH_3	Cl	CH_3	–/H	–/H	–/H	–/OH	**IV**
CH_3	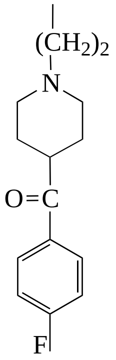	O	–/H	–/H	–/H	–/H	**V**
H	COOEt	O	H/CH_3	H/H	H/H	H/OH	**VI**

spectrum of crystal **I** contains a band associated with the stretching vibrations of the carbonyl group at the frequency ν(CO) = 1720 cm^{-1} and a broad band with the barycenter at 2750 cm^{-1} in the range of stretching vibrations of the hydroxyl and amino groups. The bands observed at the frequencies ν(C=O) and ν(O–H) are characteristic of neutral forms of compound **I**. The bands of medium intensity in the range 1605–1645 cm^{-1} can be assigned to the stretching vibrations of the C=N and C=C bonds.

In the IR spectrum of compound **I** in a CCl_4 solution, the ν(CO) frequency of the band associated with the stretching vibrations of the carbonyl group decreases to 1680 cm^{-1} and there appear two new bands, namely, a narrow band at a frequency of 3450 cm^{-1} against the background of the broad absorption band and a weak band at 3520 cm^{-1} in the range of vibrations of the OH and NH groups. The band at 3450 cm^{-1} is attributed to the stretching vibrations of the NH bond of the zwitterion form, whereas the band at 3520 cm^{-1} corresponds to the ν(OH) vibrations of the hydroxyl group of the molecular form. The broad band of the background is associated with the intermolecular hydrogen bonds. The dilution of the solution and addition of polar solvents (dimethyl sulfoxide, dioxane) leads to a decrease in the intensity of the band at a frequency of 3520 cm^{-1}. This can be explained by the increase in the concentration of the zwitterion form in the solution of compound **I**. Similar changes in the IR spectra of crystals and upon dissolution in CCl_4 were observed for 2-methyl-9-hydroxypyrido[1,2-*a*]pyrimidin-4-one (**II**) in our previous work [5].

The IR spectrum of crystal **Ia** exhibits a very intense band due to the stretching vibrations of the carbonyl group at the frequency $\nu(CO) = 1712$ cm^{-1}. A decrease in the frequency $\nu(CO)$ for compound **Ia** as compared to that for compound **I** is caused by the induction effect of the NH bond. In the region of stretching vibrations of the NH and OH groups, the IR spectrum contains a broad absorption band in the range 3600–2500 cm^{-1} with well-resolved maxima at frequencies of 3492 and 3214 cm^{-1}. According to the X-ray diffraction data, the band at a frequency of 3214 cm^{-1} should be assigned to the stretching vibrations of the N^+H bond of the zwitterion form. The broad absorption band observed in the range 3600–2500 cm^{-1} corresponds to the intermolecular hydrogen bonds. The band associated with the stretching antisymmetric vibrations of the perchlorate ions exhibit poorly resolved maxima at frequencies of 1158, 1128, and 1098 cm^{-1}. The splitting of the band of these vibrations suggests a nonequivalence of the Cl–O bonds in the ClO_4^- ion.

The data on the crystal structures have been deposited with the Cambridge Structural Database (CCDC, nos. 209071, 209072).

CONCLUSIONS

Thus, the analysis of the X-ray diffraction and IR spectroscopic data demonstrated that compound **I** exists in the molecular form in crystals and in the zwitterion form in solutions. The structure of compound **Ia** is formed by dimers consisting of molecules in the zwitterion form. These molecules are linked by a strong symmetric hydrogen bond with the participation of the proton.

REFERENCES

1. G. Horvath, I. Hermecz, A. Horvath, *et al.*, J. Heterocycl. Chem. **22**, 481 (1985).
2. C. L. Kaul and R. S. Grewal, Biochem. Pharmacol. **21**, 303 (1982).
3. A. Martin, A. I. Kiss, G. Horvath, and I. Hermecz, Acta Chim. Hung. **119**, 321 (1985).
4. N. M. Blaton, O. M. Peeters, and C. J. Ranter, Acta Crystallogr., Sect. C: Cryst. Struct. Commun. **51**, 533 (1995).
5. O. V. Koval'chukova, S. B. Strashnova, B. E. Zaĭtsev, *et al.*, Koord. Khim. **26** (8), 626 (2000).
6. M. I. Palomino, B. E. Zaĭtsev, S. B. Galiev, *et al.*, Khim. Geterotsikl. Soedin., No. 10, 1381 (1991).
7. O. V. Koval'chukova, S. B. Strashnova, B. E. Zaĭtsev, *et al.*, Koord. Khim. **26** (4), 310 (2000).
8. N. I. Mordovina, O. V. Koval'chukova, B. E. Zaĭtsev, *et al.*, Koord. Khim. **29** (12), 880 (2003).
9. G. M. Sheldrick, *SHELX93: Program for the Solution and Refinement of Crystal Structures* (Univ. of Göttingen, Germany, 1993).
10. K. Simon, L. Pusztay, M. Hanusz, *et al.*, Heterocycles **45** (11), 2175 (1997).
11. I. N. Polyakova, Z. A. Starikova, V. V. Parusnikov, *et al.*, Kristallografiya **28** (1), 96 (1983) [Sov. Phys. Crystallogr. **28**, 50 (1983)].
12. F. H. Allen, O. Kennard, and D. G. Watson, J. Chem. Soc., Perkin Trans. 2, Suppl. 1 (1987).

Translated by O. Borovik-Romanova

Crystallography Reports, Vol. 49, No. 5, 2004, pp. 798–806. Translated from Kristallografiya, Vol. 49, No. 5, 2004, pp. 886–894.
Original Russian Text Copyright © 2004 by Kuleshova, Averkiev, Gusev, Suponitskiĭ, Antipin.

STRUCTURE OF ORGANIC COMPOUNDS

Conformational Polymorphism of *N*-(4-Butoxyphenyl)-4-(4'-Nitrophenyl)-2-Thiazolamine

L. N. Kuleshova, B. B. Averkiev, D. V. Gusev, K. Yu. Suponitskiĭ, and M. Yu. Antipin
Nesmeyanov Institute of Organoelement Compounds, Russian Academy of Sciences,
ul. Vavilova 28, Moscow, 119991 Russia
e-mail: lukul@xrlab.ineos.ac.ru

Received March 13, 2003

Abstract—The molecular and crystal structures of three concomitant polymorphic modifications of *N*-(4-butoxyphenyl)-4-(4'-nitrophenyl)-2-thiazolamine are investigated by X-ray diffraction. These polymorphs are simultaneously formed upon recrystallization from toluene. It is established that different colors of the polymorphs are associated with the different conformations of the molecules in the crystal. The relative energy gain of the conformers and the energy of crystal packings are evaluated, and the possibility of occurring the structural phase transition between the polymorphic modifications is discussed. *© 2004 MAIK "Nauka/Interperiodica".*

INTRODUCTION

In recent years, polymorphism (the ability of a material to form different crystal structures) has been revealed in radically different classes of organic compounds, such as monoalcohols, polyalcohols, saturated and unsaturated acids, alkanes, aromatic π-conjugated systems, amino acids, etc. Investigation into polymorphic modifications, especially into the structural aspects of polymorphism, has become an efficient tool for designing organic materials with unique physical properties or biological activity. For example, research in the polymorphism of aromatic π-conjugated molecular systems is particularly important for the design of materials with a polar crystal structure providing nonlinear optical (and many other physical) properties. There are a number of pioneering works concerned with both the possible manifestation of polymorphism in particular classes of chromophore compounds [1–5] and the general structural features of centrosymmetric and noncentrosymmetric polymorphic modifications accumulated in the Cambridge Structural Database [6, 7].

Special interest has been expressed by researchers in crystalline organic systems with a large number of polymorphic modifications, because structural studies of these materials offer considerable possibilities for assessing the role played by intramolecular and intermolecular interactions in the formation of crystal packing. However, only a few such systems have been known to date. Among the 321 polymorphic organic molecular systems available in the Cambridge Structural Database (Version 1999), 291 systems involve two polymorphic modifications, 27 systems contain three modifications, and 3 systems include four modifications. Systems involving five or more modifications are not found at all. It is clear that these data do not reflect the real situation with respect to manifestation of the polymorphism in organic compounds, because structural analysis has most often been used only to determine the molecular structure without paying special attention to the search for possible polymorphic modifications. In the last few years, the use of polymorphism in crystal engineering has given impetus to a purposeful search for new polymorphic modifications, and, consequently, the number of works dealing with the design of possible polymorphs has increased significantly. In 2000, Lian *et al.* [8] described the hexamorphic system of 2-methyl-2-[(2-nitrophenyl)amino]-3-thiophenecarbo-nitrile. It was established that this compound has six polymorphic modifications, which differ in color and crystal habit. These modifications are characterized by different molecular conformations due to the rotation of the thiophene ring. Possibly, it is this difference in the color of the polymorphs that makes it possible to easily identify different modifications in the case of conformational polymorphism [9].

This paper reports on the results of X-ray diffraction investigation into the polymorphism of *N*-(4-butoxyphenyl)-4-(4'-nitrophenyl)-2-thiazolamine (**I**)

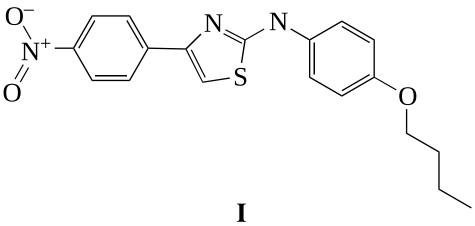

I

which was synthesized with the aim of searching for new classes of chromophores exhibiting nonlinear optical properties. Moreover, we performed an X-ray structural study of the acetamide derivative (**II**) of compound **I**:

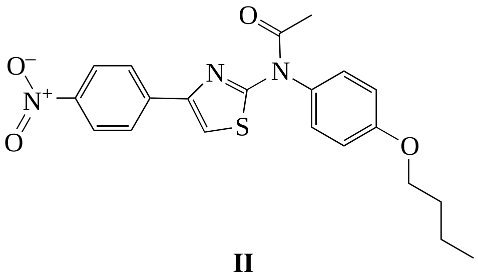

II

Molecule **I**, like molecules of 5-methyl-2-[(2-nitrophenyl)amino]-3-thiophenecarbonitrile, is conformationally flexible due to a weak conjugation of the lone electron pair of the nitrogen atom in the amino group with the adjacent aromatic rings of the molecule. In some sense, molecule **I** can be treated as an analogue of the 4-nitrophenylhydrazone derivatives belonging to the promising group of nonlinear optical compounds [10]. The crystallization of compound **I** from a toluene solution results in the formation of three concomitant polymorphic modifications, which differ in color and crystal habit. It should be noted that the polymorphic modifications of the 4-nitrophenylhydrazone derivatives described in our recent work [10] have different crystal habits but the same color. Furthermore, the conformation of the molecules in crystals remains virtually unchanged. The change in color of the polymorphs of 2-[(4'-butoxyphenyl)amino]-4-(4'-nitrophenyl)-1,3-thiazole is most likely associated with the variation in the molecular conformation in the crystal [11]. The other organic chromophore polymorphs that are different in color due to the different types of their crystal packing were described by Timofeeva *et al.* [12]. A number of other examples of concomitant (one-pot) polymorphism were considered by Bernstein *et al.* [13].

EXPERIMENTAL

Synthesis

Compound **I** was synthesized according to the following procedure. A reaction mixture consisting of a solution of bromomethane-4-nitroaldehyde (2 mmol) and 4-butoxy-arylthiourea (2 mmol) in dimethylformamide (5 ml) was boiled for 1 min and, then, was diluted with water (20 ml) and neutralized with 10% NH_4OH to pH = 8–10. The precipitate was filtered off, washed with water, and recrystallized from toluene. The yield was 62% (the melting temperature T_m = 146–148°C). Compound **II** was synthesized by boiling of a suspension of compound **I** in acetic anhydride (5 ml) for 10 min. Then, the prepared mixture was cooled, diluted with water (20 ml), and stirred for 4 h at room temperature. The precipitate was filtered off and dried. The yield was 91% (T_m = 130–132°C).

Crystallization

The recrystallization of compound **I** from toluene results in the formation of three crystalline modifications: aggregates of large-sized orange plates **Ia**, aggregates of small-sized pale yellow scales **Ib**, and single small-sized dark red orthorhombic prisms **Ic**. The crystals suitable for the X-ray diffraction analysis were prepared through recrystallization from solutions in isopropyl alcohol and acetonitrile. Bright red well-faceted plates of crystals **Ia** and pale yellow scale crystals **Ib** simultaneously precipitate from an isopropyl alcohol solution of compound **I**. Dark red orthorhombic prismatic crystals **Ic** (T_m = 151–153°C) precipitate from an acetonitrile solution of compound **I**. Our attempts to determine the melting temperature of crystalline modification **Ia** were not successful, because, upon heating to 80–85°C, these crystals undergo a phase transformation into modification **Ib** (T_m = 146–148°C) and their dark red color changes to pale yellow. Upon subsequent cooling, the crystals do not regain their original color. No visible fracture of the crystals is observed upon phase transformation. However, the repeated X-ray diffraction experiment revealed that, after the transition, the sample has a polycrystalline structure.

Pale yellow needle-shaped crystals of compound **II** were grown through slow evaporation from a butyl alcohol solution.

X-ray Diffraction Analysis

The unit cell parameters and the intensities of experimental reflections were measured on a Bruker SMART CCD 1000 automated diffractometer (MoK_α radiation, φ and θ scan modes). The crystal data, data collection, and refinement parameters for the studied structures are presented in Table 1. The structures were solved by direct methods and refined using the full-matrix least-squares procedure on F^2 in the anisotropic approximation for the non-hydrogen atoms. The hydrogen atoms were located from difference Fourier syntheses and refined in the isotropic approximation. All the calculations were performed with the SHELXTL PLUS (Version 5.10) program package [14]. The tables of the atomic coordinates, bond lengths, bond and torsion angles, and anisotropic thermal parameters have been deposited with the Cambridge Structural Database.

RESULTS AND DISCUSSION

The X-ray diffraction data for the polymorphic modifications of compound **I** and its acetamide derivative **II** are presented in Table 1. The general view of the molecules is given in Figs. 1 and 2. All the crystals are centrosymmetric. It was found that the crystal color depends on the molecular conformation in the crystal or, more precisely, on the degree of planarity of the conformer. The mean deviation δ of atoms from the root-mean-square plane through all the non-hydrogen atoms

Table 1. Crystal data, data collection, and refinement parameters for the studied structures

Compound	**Ia**	**Ib**	**Ic**	**II**
Empirical formula	$C_{19}H_{19}N_3O_3S$	$C_{19}H_{19}N_3O_3S$	$C_{19}H_{19}N_3O_3S$	$C_{21}H_{21}N_3O_4S$
Molecular weight	369.43	369.43	369.43	411.47
Crystal system	Monoclinic	Triclinic	Monoclinic	Monoclinic
Space group	$P2_1/c$	$P\bar{1}$	$P2_1/c$	$P2_1/c$
Z	4	2	8	4
a, Å	16.620(3)	6.990(3)	13.525(3)	12.534(4)
b, Å	5.529(1)	7.376(4)	24.135(5)	13.288(4)
c, Å	18.708(4)	17.131(8)	11.735(2)	12.295(4)
α, deg		91.50(1)		
β, deg	99.081(4)	91.74(1)	115.037(4)	99.368(7)
γ, deg		100.18(1)		
V, Å^3	1697.4(6)	868.5(7)	3471(1)	2020(1)
d_{calcd}, g/cm^3	1.446	1.413	1.414	1.353
$2\theta_{max}$, deg	60	60	56	56
Number of reflections measured	10773	10126	26181	14465
Number of unique reflections	4928	4996	8381	4869
R_{int}	0.0406	0.0340	0.1020	0.0406
Number of reflections with $I \geq 2\sigma(I)$	2654	2792	3434	2838
Number of parameters refined	311	311	621	346
$R[F^2 \geq 2\sigma(F^2)]$	0.0507	0.0497	0.0603	0.0505
$wR(F^2)$ for all reflections	0.1188	0.1115	0.1671	0.1203

of the molecule, except for the butoxy fragment, was used as an integrated measure of planarity. Conformer **Ic** with the maximum planarity (δ = 0.098, 0.121 Å for two independent molecules), nonplanar conformer **Ib** (δ = 0.327 Å), and flattened conformer **Ia** (δ = 0.193 Å) form dark red, pale yellow, and orange crystals, respectively. It is of interest to note that the color of crystals of 5-methyl-2-[(2-nitrophenyl)amino]-3-thiophenecarbonitrile is also associated with the molecular conformation. According to Lian [9], the different colors of polymorphic crystals can be explained by the fact that different conformers are characterized by different degrees of conjugation of the lone electron pair of the nitrogen atom in the amino group with the adjacent aromatic rings. The similarity in the behavior of these two polymorphic systems is most likely associated with the same nature of the conformational polymorphism: the conformational flexibility of both molecules is due to the small degree of conjugation of the lone electron pair of the nitrogen atom in the amino group with the adjacent aromatic rings.

Molecular Geometry

The selected geometric characteristics of the molecules are listed in Table 2. As follows from the data presented in this table and Figs. 1 and 2, the conformations of molecules **I** in the studied crystals differ substantially. It is possible to distinguish two main conformers with respect to the C(9)–N(3) bond, namely, the *cis* and *trans* conformers. In the *trans* conformers, which are observed in crystals **Ia** and **Ib**, the C(9)–N(2) bond of the thiazole fragment and the N(3)–C(10) bond are in the *s–trans* positions with respect to each other. The C(10)–N(3)–C(9)–N(2) torsion angles are equal to 162.3° and 178.2°, respectively. In this case, conformer **Ia** can be considered to be nearly planar (the *1–2* and *2–3* dihedral angles between the aromatic rings of the molecule are equal to 2.7° and 6.4°, respectively). At

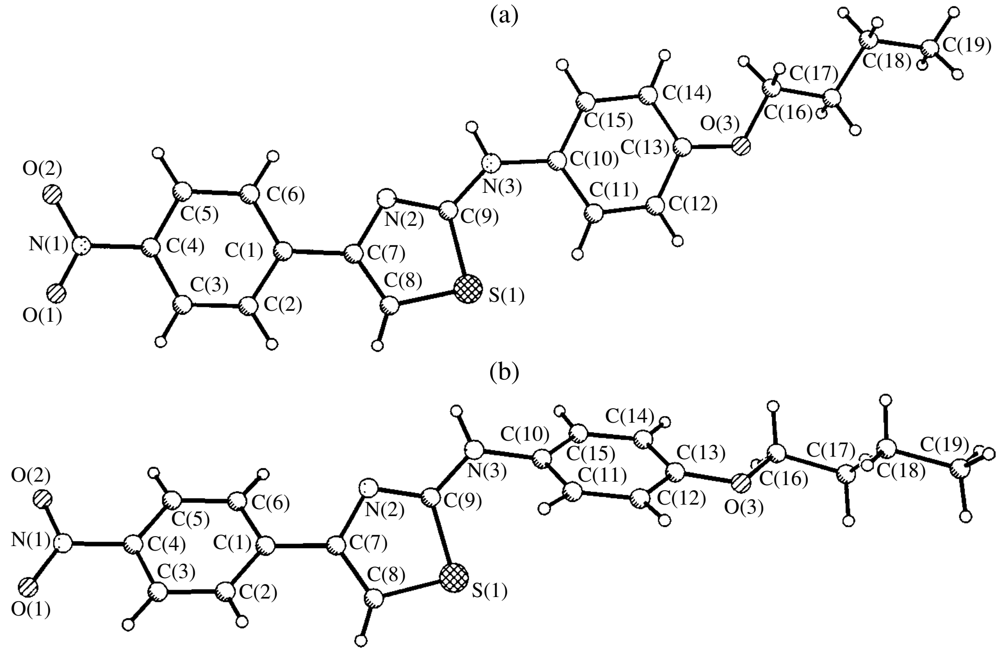

Fig. 1. A general view of the *trans* conformers of molecule **I** in crystalline modifications (a) **Ia** and (b) **Ib**.

the same time, conformer **Ib** significantly deviates from the planarity (the corresponding dihedral angles are equal to 38.3° and 57.2°, respectively). The planar conformation of molecule **Ia** should be stabilized by the CH···S intramolecular hydrogen bond (H···S, 2.437 Å; the sum of the van der Waals radii of the H and S atoms is 2.91 Å). However, the C(9)–N(3)–C(10) bond angle at the nitrogen atom of the amino group in crystal **Ia** is increased to 130.0°. Most probably, this increase is caused by the steric repulsion of the atoms of the thiazole and phenyl groups. Therefore, the combined effect of stabilization of the planar conformation due to the intramolecular hydrogen bond should be insignificant. In nonplanar *trans* conformer **Ib**, the H···S intramolecular distance is not shortened because of the rotation of the aromatic rings and corresponds to the normal van der Waals contact of the atoms. The C(9)–N(3)–C(10) bond angle is 124.6°, which is close to the value characteristic of trigonal nitrogen atoms.

In the *cis* conformers, which are observed in crystals **Ic** and **II** (Fig. 2), the C(9)–N(2) bond of the thiazole fragment and the N(3)–C(10) bond are in the *s*-*cis* positions with respect to the N(3)–C(9) bond. The C(10)–N(3)–C(9)–N(2) torsion angles are equal to 3.5° and –7.1° in two crystallographically independent molecules **Ic** and –5.6° in molecule **II**. Both of the independent molecules **Ic** are planar, and the difference in their geometric characteristics does not exceed the experimental error. The mean difference δ between the coordinates of the independent molecules (when their centers of gravity are brought into coincidence) is equal to 0.043 Å (Fig. 2c). The planar conformation of the *cis* conformer is stabilized by the CH···N intramolecular hydrogen bond (H···N, 2.224 and 2.327 Å in the independent molecules; the sum of the van der Waals radii of the H and N atoms is 2.74 Å). As in the *trans* conformer, the bond angle at the nitrogen atom of the amino group is increased to 128.8° and 129.0°. In the *cis* conformer of molecule **II**, in which the butoxyphenyl group is rotated by 86.1° with respect to the plane of the other part of the molecule, the corresponding angle is equal to 121.0°.

Despite the above differences in the geometry, the like bond lengths in the conformers are sufficiently conservative characteristics and have standard values within the limits of experimental error. What all the conformers have in common is that the C(9)–N(3) and N(3)–C(10) bonds joining the thiazole and butoxyphenyl rings with the amino group of the molecule are not equivalent. The C(9)–N(3) bonds (1.363 Å in **Ia**; 1.351 Å in **Ib**; 1.357, 1.358 Å in **Ic**; 1.409 Å in **II**) are regularly shorter than the N(3)–C(10) bonds (1.414 Å in **Ia**; 1.422 Å in **Ib**; 1.407 Å in **Ic**; 1.455 Å in **II**). Note that the C(9)–N(3) bond length virtually does not vary from conformer to conformer, whereas the N(3)–C(10) bond in the *trans* conformers (**Ia**, **Ib**) is considerably longer than that in the *cis* conformers (**Ic**).

From the foregoing, we can draw the conclusion that the lone electron pair of the nitrogen atom only partially participates in the conjugation with the adjacent aromatic thiazole rings and, apparently, is not conjugated with the butoxyphenyl fragment in conformers **Ia** and **Ib** and in molecule **II** (in which the conjugation occurs through the carbonyl group). At the same time, a similar, even if very weak, interaction is possible in con-

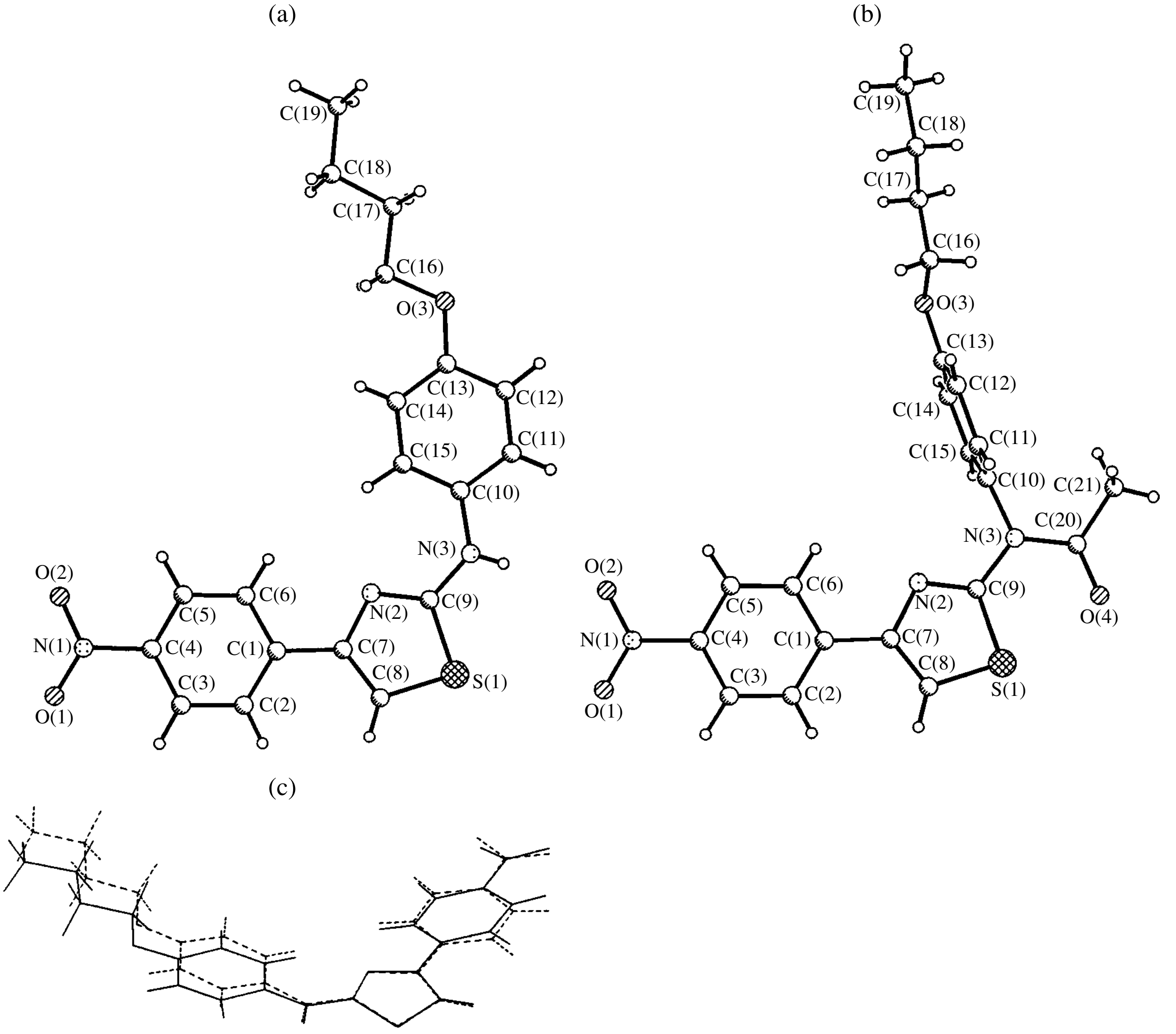

Fig. 2. A general view of the *cis* conformers of molecules in crystals (a) **Ic** and (b) **II** and (c) comparison of the geometries of the independent molecules in crystal **Ic**.

former **Ic**. This assumption is also confirmed by the bright color of crystals **Ic**.

Conformational Calculations

Since the polymorphs are simultaneously formed upon crystallization from the same growth solution, we can assume that either both conformers already exist in this solution or the conformation is stabilized under the crystal-field forces. As follows from the ^{1}H NMR spectrum of a solution of compound **I** in deuterated chloroform at room temperature, the solution contains only one conformer.

In order to evaluate the relative energy gain of the conformers formed in the crystals, we calculated their energies in the HF / 3-21G approximation according to the Gaussian94 software package [15]. The energy of *trans* conformer **Ic** was taken as zero energy. It was revealed that the relative energies of the conformers differ insignificantly and are as follows:

Ia $E = 2.4$ kcal/mol,

(ω_1[N(2)–C(9)–N(3)–C(10)] = 162.3°,

ω_2[C(9)–N(3)–C(10)–C(11)] = 18.1°),

Ib $E = 1.5$ kcal/mol ($\omega_1 = 178.2°$, $\omega_2 = -58.3°$),

Ic $E = 0$ kcal/mol ($\omega_1 = 3.5°$, $\omega_2 = -9.7°$),

I'c $E = 0.2$ kcal/mol ($\omega_1 = -7.1°$, $\omega_2 = -1.2°$).

We also calculated the conformational curves of rotation about the C(9)–N(3) and N(3)–C(10) bonds. The torsion angles ω_1 and ω_2 were varied in the range 0°–180° with a step of 30°. The barrier to rotation of the 4-nitrophenylthiazole group about the C(9)–N(3) bond (from the *cis* conformation to the *trans* conformation) (Fig. 3) appears to be rather high and is equal to

8.4 kcal/mol. The barriers to rotation of the butoxyphenyl fragment about the N(3)–C(10) bond are considerably lower: 2.7 kcal/mol for the *trans* conformer and 2.2 kcal/mol for the *cis* conformer (Fig. 3). These data confirm the inference that the C(9)–N(3) and N(3)–C(10) bonds are not equivalent. Moreover, it was found that a nonplanar geometry of the molecule is more favorable for the *trans* conformer (unlike the *cis* conformer) and that a broad flattened minimum corresponds to an angle of 90° (this angle is equal to 58.3° in molecule **Ib**). A difference of 0.5 kcal/mol between the barriers to rotation about the N(3)–C(10) bond in the *cis* and *trans* conformers is most likely associated with the fact that the H(11)···N(2) intramolecular contact in the *cis* conformer is somewhat more favorable than the H(11)···S(1) contact formed in the*trans* conformer.

Calculation of the Molecular Hyperpolarizability

The molecular hyperpolarizability β of *N*-(4-butoxyphenyl)-4-(4'-nitrophenyl)-2-thiazolamine was calculated according to the MOPAC program package [16] within the framework of the AM1 parametrization with the use of the experimental geometric parameters obtained for different polymorphs. The calculations demonstrated that the molecular hyperpolarizabilities β are virtually independent of the molecular geometry and are equal to 38 ± 1 cm^3/V^2 for molecule **Ia**, 39 ± 1 cm^3/V^2 for molecule **Ib**, 36.5 ± 0.3 cm^3/V^2 for molecule **Ic**, and 32.6 ± 0.3 cm^3/V^2 for molecule **II**. The differences lie within the limits of computational error, and the molecular hyperpolarizabilities are somewhat lower than those for hydrazones [10].

Molecular Packing

As was noted above, molecule **I** is a topological analogue of 4-nitrophenylhydrazone molecules whose crystal structure was discussed in our previous work [10]. Molecule **I** contains one reactive proton serving as a donor of hydrogen bonds and several competing atoms fulfilling the role of acceptors of hydrogen bonds. Therefore, it was reasonable to assume that systems of hydrogen bonds and structural fragments similar to those in hydrazones should be formed in crystals **I**. However, this assumption was only half justified: the systems of hydrogen bonds are predominantly similar to those in hydrazones, whereas the structural fragments are not similar due to the change in the molecular conformation. In particular, polymorph **Ia** involves λ contact typical of hydrazones [10]. This contact is formed by the intermolecular hydrogen bonds N(3)H(N3)···O(2) (N···O, 3.126 Å; H···O, 2.32 Å; the NHO angle is 155.0°) and C(15)H(15)···O(2) (C···O, 3.307 Å; H···O, 2.471 Å; the CHO angle is 145.5°). However, centrosymmetric dimers, rather than chiral λ chains, as is the case of hydrazones, are formed by this contact (Fig. 4a).

Table 2. Selected geometric parameters of molecules in the studied crystals

Parameter	**Ia**	**Ib**	**Ic**	**II**
Amino C–N–C, deg	130.0	124.6	128.8 129.0	121.0
HN–C (thiazole), Å	1.363	1.351	1.357 1.358	1.409
HN–C (phenyl), Å	1.414	1.422	1.407 1.407	1.455
Torsion angles, deg				
C(10)–N(3)–C(9)–S(1)	–20.0	–1.7	176.3 174.9	175.6
C(10)–N(3)–C(9)–N(2)	162.3	178.2	3.5 –7.1	–5.6
C(9)–N(3)–C(10)–C(11)	18.1	–58.3	–9.7 –1.2	97.9
N(3)–C(9)–S(1)–C(8)	–178.1	–179.2	179.3 177.7	178.8
Dihedral angles, * deg				
“1”–“2”	2.9	38.3	6.0 15.2	4.5
“2”–“3”	6.4	57.2	9.0 7.4	86.1
“1”–“3”	4.7	19.3	14.2 14.7	89.6
δ, ** Å	0.193	0.327	0.098 0.121	0.288

* “**1**,” “**2**,” and “**3**” are the planes of the nitrophenyl, thiazole, and O*Bu*-phenyl rings, respectively.

** The mean deviation from the root-mean-square plane through all the non-hydrogen atoms of the molecule, except for the O*Bu* fragment.

In crystals **Ib** with nonplanar molecules, the N(3)H(N3)···N(2) hydrogen bond (N···N, 2.960 Å; H···N, 2.07 Å; the NHN angle is 176.0°) contains the

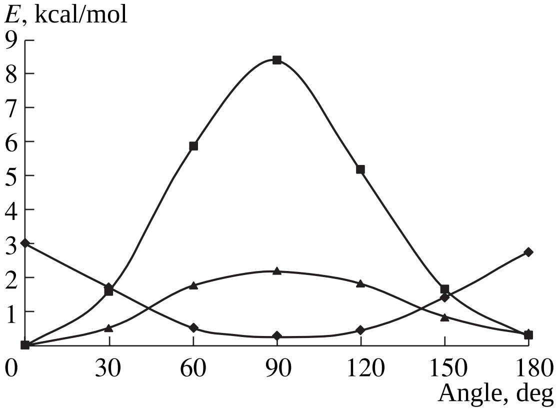

Fig. 3. Conformational curves of rotation (■) about the C(9)–N(3) bond (the ω_2 angle) from the *cis* conformation (0°) to the *trans* conformation (180°), (▲) about the N(3)–C(10) bond (the ω_1 angle) for the *cis* conformation, and (◆) about the N(3)–C(10) bond (the ω_1 angle) for the *trans* conformation.

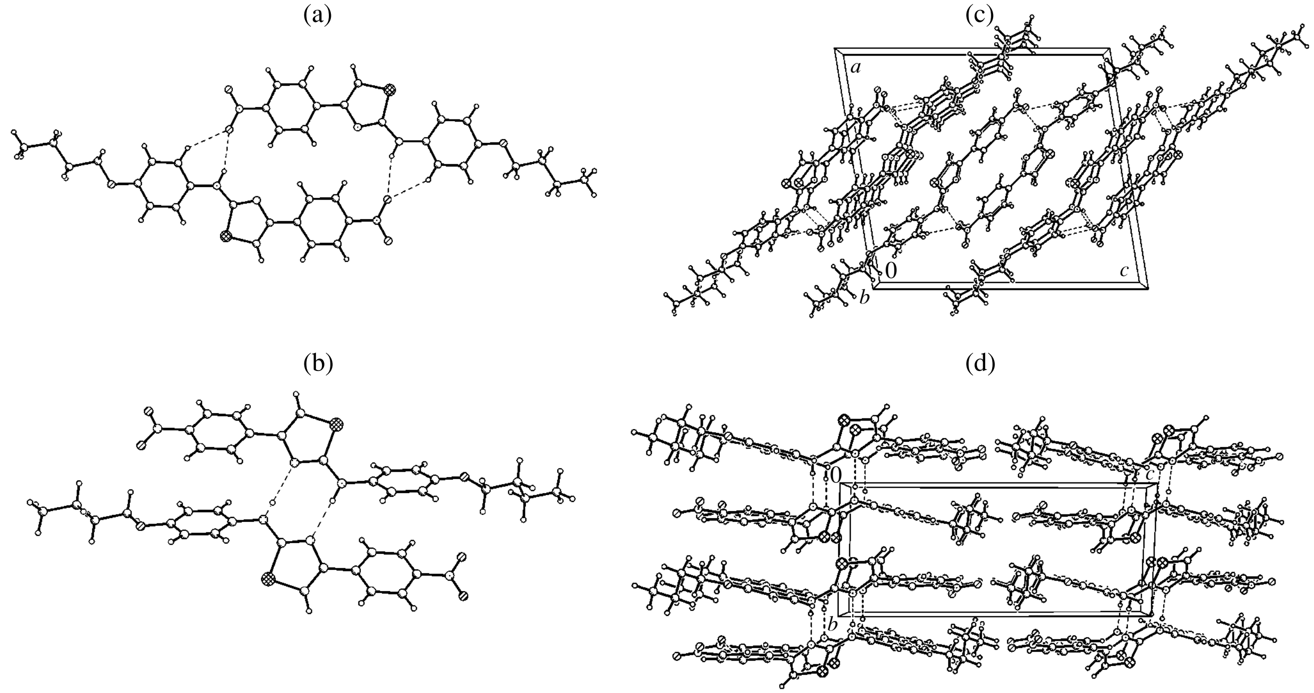

Fig. 4. Centrosymmetric dimers (a) **Ia** and (b) **Ib** and the molecular packing in crystal structures (c) **Ia** and (d) **Ib**.

nitrogen atom of the thiazole group and also forms the centrosymmetric dimer (Fig. 4b).

The crystal structures of both these polymorphs are built up from stacks of centrosymmetric dimers, which are parallel to the axis with the smallest unit cell parameter (Figs. 4c, 4d): the *b* axis in modification **Ia** and the *a* axis in modification **Ib**. In both modifications, the molecules make an angle with the stack axis. In polymorph **Ia**, the molecules in the stacks are superposed on each other so that the electron-donor thiazole ring is located above the electron-acceptor nitrophenyl group (Fig. 4). In this case, the interplanar distance *d* in the stacking contact turns out to be rather short and is equal to 3.26 Å. In polymorph **Ib**, owing to the nonplanar geometry, staking contacts are absent inside the stack, but the shortened C(2)H(2)···O(2) contact (C···O, 3.241 Å; H···O, 2.49 Å; the CHO angle is 141.7°) occurs between the molecules in the stack.

The homochiral molecular chains that are similar to the λ chains of hydrazones and are formed by the N(3)H(N3)···O(2) (N···O, 2.937 Å; H···O, 2.19 Å; the NHO angle is 164.6°) intermolecular hydrogen bonds between the independent molecules are observed only in polymorphic modification **Ic** (Fig. 5). It should be noted that, in this modification, the N(3)H(3)···O(2) intermolecular hydrogen bond is substantially shorter than the corresponding bond in structure **Ia**. The chains with different chiralities are linked into centrosymmetric layers (Fig. 5a) aligned parallel to the (101) diagonal plane with the formation of the crystal structure (Fig. 5b).

The analysis of crystal structure **Ic** revealed a set of pseudosymmetric operations that approximately transform the independent molecules into each other. These are two pseudocenters (with the coordinates [0.245, 0.878, 0.492], [0.755, 0.622, 0.508]); the rotation pseudoaxis 2, which is parallel to the crystallographic axis *b* and intersects the *ac* plane at the point [$x = 0.255$, $z = 0.258$]; and the glide-reflection pseudoplane *a*, which is aligned parallel to the *ac* plane. These operations indicate the possibility of forming a structure of higher symmetry [17]. This structure is determined by a hypothetical shift ($|\Delta r| = 1.1$ Å) of the pair of molecules related by the pseudoinversion operation, for example, from the point with the coordinates [0.755, 0.622, 0.508] to the nearest crystallographic point [0.75, 0.625, 0.5]: ($P2_1/c$, $Z' = 2$) + $\bar{1}$(0.75, 0.625, 0.5) $\longrightarrow$ ($C2/c$, $Z' = 1$).

Furthermore, we estimated the energies of crystal packing of polymorphs **Ia**–**Ic**. The calculations were performed with the SCORCRYST program package [18]. The calculated energies of the polymorphs are equal to 35.95 kcal/mol ($\rho = 1.446$ g/cm^3) for crystals **Ia**, 47.83 kcal/mol ($\rho = 1.413$ g/cm^3, $T_m = 146$–148°C) for crystals **Ib**, and 43.77 kcal/mol ($\rho = 1.414$ g/cm^3, $T_m = 151$–153°C) for crystals **Ic**. It is found that crystals **Ib** are characterized by the minimum energy of crystal packing. The calculated energies are in agreement with the occurrence of the aforementioned structural phase transition **Ia** $\longrightarrow$ **Ib** in the temperature range 80–85°C.

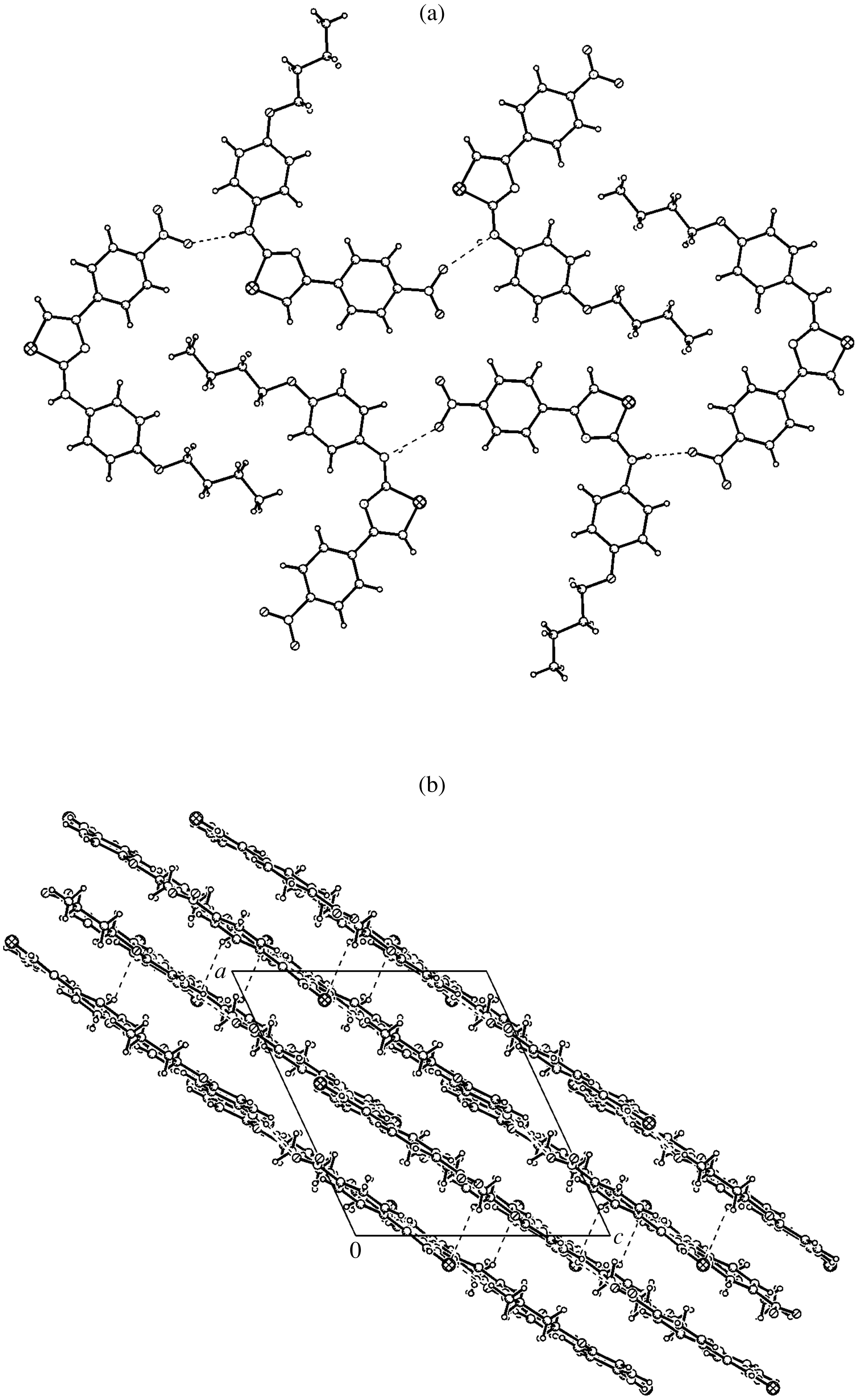

Fig. 5. (a) A layer formed by chiral chains and (b) the molecular packing in crystal **Ic**.

The acetamide derivative of compound **I** (compound **II**), like all the above polymorphs, crystallizes in a centrosymmetric space group. This fact, together with relatively low molecular hyperpolarizabilities β, excludes these compounds from further consideration in the search for potential nonlinear optical materials.

ACKNOWLEDGMENTS

We would like to thank the research group of Prof. Allinger (University of Georgia, Athens, United States) for providing an opportunity to use the required computer time for performing calculations with the Gaussian program package.

This work was supported by the Russian Foundation for Basic Research, project no. 03-03-32716a.

REFERENCES

1. C. Serbutoviez, C. Bossard, G. Knopfle, *et al.*, Chem. Mater. **7**, 1198 (1995).
2. I. Liakatas, M. S. Wong, V. Gramlich, *et al.*, Adv. Mater. **10** (10), 777 (1998).
3. F. Pan, C. Bossard, M. S. Wong, *et al.*, Chem. Mater. **9**, 1328 (1997).
4. S. R. Hall, P. V. Kolinsky, R. Jones, *et al.*, J. Cryst. Growth **79**, 745 (1986).
5. H. Kagawa, M. Sagawa, T. Hamada, *et al.*, Chem. Mater. **8**, 2622 (1996).
6. L. N. Kuleshova and M. Yu. Antipin, Kristallografiya **47** (2), 303 (2002) [Crystallogr. Rep. **47**, 268 (2002)].
7. L. N. Kuleshova and M. Yu. Antipin, Kristallografiya **48** (2), 289 (2003) [Crystallogr. Rep. **48**, 259 (2003)].
8. Lian Yu, G. A. Stephenson, C. A. Mitchel, *et al.*, J. Am. Chem. Soc. **122**, 585 (2000).
9. Lian Yu, J. Phys. Chem. A **106**, 544 (2002).
10. L. N. Kuleshova, M. Yu. Antipin, V. N. Khrustalev, *et al.*, Kristallografiya **48** (4), 645 (2003) [Crystallogr. Rep. **48**, 594 (2003)].
11. R. J. Davey, N. Blagden, G. D. Potts, and R. Docherty, J. Am. Chem. Soc. **119**, 1767 (1997).
12. T. V. Timofeeva, V. N. Nesterov, F. M. Dolgushin, *et al.*, Cryst. Eng., No. 3, 263 (2000).
13. J. Bernstein, R. J. Davey, and J.-O. Henk, Angew. Chem. Int. Ed. Engl. **38**, 3440 (1999).
14. G. M. Sheldrick, *SHELXTL: Version 5.10* (Bruker AXS, Madison, WI, 1997).
15. M. J. Frisch, G. W. Trucks, H. B. Schlegel, *et al.*, *Gaussian94, Revision E.2* (Gaussian Inc., Pittsburgh, PA, 1995).
16. *QCPE; MOPAC: Quantum Chemistry Program Exchange, Version 6* (1990).
17. L. N. Kuleshova, V. N. Khrustalev, and M. Yu. Antipin, Kristallografiya **45** (6), 1034 (2000) [Crystallogr. Rep. **45**, 953 (2000)].
18. J. Apostolakis, D. W. M. Hofmann, and T. Lengauer, Acta Crystallogr., Sect. A: Fundam. Crystallogr. **57**, 442 (2001).

Translated by O. Borovik-Romanova

Crystallography Reports, Vol. 49, No. 5, 2004, pp. 807–810. Translated from Kristallografiya, Vol. 49, No. 5, 2004, pp. 895–898.
Original Russian Text Copyright © 2004 by Malinovskiĭ, Bologa, Coropceanu, Gerbeleu.

Crystal and Molecular Structure of $[Co(DH)(o\text{-}phen)_2][BF_4]_2 \cdot 2H_2O$

S. T. Malinovskiĭ, O. A. Bologa, É. B. Coropceanu, and N. V. Gerbeleu
Institute of Chemistry, Academy of Sciences of Moldova, Academiei 3, Chisinau, MD-2028 Moldova
e-mail: coropceanu@mail.md

Received February 13, 2003

Abstract—The crystal structure of a new mixed-ligand complex $[Co(DH)(o\text{-}phen)_2][BF_4]_2 \cdot 2H_2O$ is determined by X-ray diffraction. The crystal is monoclinic, $a = 12.2081(11)$ Å, $b = 14.3474(9)$ Å, $c = 17.7393(16)$ Å, $\beta = 104.95(1)°$, and space group $P2_1/c$. The coordination octahedron of Co^{3+} is formed by two nitrogen atoms of the dimethylglyoxime molecule and four nitrogen atoms of *o*-phenanthroline molecules. The dimethylglyoxime molecule is singly deprotonated and acts as DH^-. The mean Co–N distances for dioxime and *o*-phenanthroline are 1.911 and 1.964 Å, respectively. The key role in the formation of the crystal structure is played by $[BF_4]^-$ outer-sphere anions and crystallization water molecules, which form an extended hydrogen-bond system. © *2004 MAIK "Nauka/Interperiodica".*

INTRODUCTION

The complex-forming ability of trivalent cobalt compounds containing dimethylglyoxime molecules has been studied in sufficient detail. It has been found that these compounds exhibit a remarkable ability to form complexes with a ratio Co : DH^- = 1 : 1 [1], 1 : 2 [2–5], or 1 : 3 [6] (where DH^- is the dimethylglyoxime residue $H_3C–C(NOH)–C(NO^-)–CH_3$) depending on the conditions of complex formation. Complexes with the ratio Co : DH^- = 1 : 2 can exist in the form of two geometric isomers for different pH values of the medium [4]. One of these isomers has an octahedral *trans* structure with nearly coplanar dimethylglyoxime residues, whereas the other isomer has a binuclear *cis*-dioximine structure in which metallocycles formed by coordinated dioxime molecules are arranged at an angle close to 90° [3, 4]. In the presence of HF, the reaction results in the formation of cobalt(III) trisdioximines (Co : DH^- = 1 : 3) [6]. It was shown earlier in [1, 7, 8] that, in addition to the coordinated dimethylglyoxime molecule, the complex can involve two other bidentate ligands, such as thiosemicarbazide, glycine, α,α'-dipyridyl, and *o*-phenanthroline. It was also established that the possibility of deprotonating a dimethylglyoxime molecule substantially depends on the type of bidentate ligand.

Investigations into the crystal structure of trivalent cobalt monodioximates (Co : DH^- = 1 : 1) with thiosemicarbazide [1] and *o*-phenanthroline [7] molecules revealed that, in the former case, protons are detached from both dioxime and thiosemicarbazide molecules depending on the pH of the medium, whereas in the latter case, only the dimethylglyoxime molecule is deprotonated. Different outer-sphere anions in structures determine both the specific features of the molecular packing in the crystal and the properties of the compound [9–11].

With the purpose of revealing the specific features of the formation of the crystal structure in the Co(III)–DH^{2-}–*o-phen* system in the presence of a $[BF_4]^-$ counterion, we undertook an X-ray diffraction study of the compound $[Co(DH)(o\text{-}phen)_2][BF_4]_2 \cdot 2H_2O$ (**I**).

EXPERIMENTAL

Single crystals **I** were prepared according to the following procedure. Dimethylglyoxime (0.12 g, 0.001 mol) in methanol (30 ml) and *o*-phenanthroline (0.4 g, 0.002 mol) in methanol (30 ml) were added to a solution of $Co(BF_4)_2 \cdot 6H_2O$ (0.34 g, 0.001 mol) in water (30 ml). The solution obtained was heated in a graphite crucible on a water bath at 50°C for ~10 min in air. Upon slow cooling of the dark brown solution, dark brown prismatic crystals precipitated. The yield was ~35%. The compound is readily soluble in alcohol.

For $C_{28}H_{27}CoF_8N_6O_4B_2$ anal. calcd. (%): Co, 7.92; C, 45.19; H, 3.66; N, 11.29.

Found (%): Co, 7.52; C, 44.98; H, 3.45; N, 11.05.

The X-ray diffraction experiment was performed on an STOE IPDS automated diffractometer. The main crystal data are presented in Table 1. The structure was solved and refined with the SHELXS97 and SHELXL97 program packages [12]. The final R factor is 0.050. The crystal chemical data for structure **I** have

Table 1. Crystal data, data collection, and refinement parameters for structure **I**

Empirical formula	$C_{28}H_{27}CoF_8N_6O_4B_2$
Molecular weight	744.11
T, K	223(2)
Wavelength, Å	0.71073
Crystal system, space group	Monoclinic, $P2_1/c$
a, Å	12.2081(11)
b, Å	14.3474(9)
c, Å	17.7393(16)
β, deg	104.95(1)
V, $Å^3$	3001.9(4)
Z	4
ρ_{calcd}, g/cm^3	1.520
F(000)	1380
Crystal size, mm	0.40 × 0.35 × 0.35
Absorption coefficient, mm^{-1}	0.662
θ range, deg	3.24–25.89
Index range	$-13 \le h \le 15$, $-17 \le k \le 17$, $-21 \le l \le 21$
Number of reflections measured	22025
Number of unique reflections	5774
Number of reflections observed	3274 [$R_{int} = 0.1050$]
Number of parameters refined	508
Goodness-of-fit on F^2 (*S*)	0.799
Final *R* factors [$I > \sigma(I)$]	$R_1 = 0.0500$, $wR_2 = 0.1188$
R factors (for all reflections)	$R_1 = 0.0951$, $wR_2 = 0.1336$

been deposited with the Cambridge Structural Database (deposit no. 213282).

RESULTS AND DISCUSSION

The crystal is built of $[Co(DH)(o\text{-}phen)_2]^{+2}$ cationic complexes, $[BF_4]^-$ outer-sphere anions, and two crystallization water molecules (Fig. 1). The octahedral coordination of the cobalt atom involves six nitrogen atoms from three ligands that close three five-membered metallocycles: one ring is formed by the dimethylglyoxime molecule, and the two other rings are formed by *o-phen* molecules.

The structure of the cationic complex as a whole is similar to that of the compound studied earlier in [7]. The octahedron around the central atom is distorted. The chelate angles at the cobalt atom vary in the range 83.4°–89.1°. Note that the Co–N bonds in the phenanthroline ligands located in *trans* positions with respect to the dimethylglyoxime residue are elongated. The mean $(Co–N)_{DH^-}$ and $(Co–N)_{o\text{-}phen}$ distances are 1.911 and 1.964 Å, respectively. All the dihedral angles between the rms planes through the dimethylglyoxime and *o*-phenanthroline ligands differ from the ideal value (90°) and fall in the range 83.9°–85.7°. The dioxime molecule is partially deprotonated and acts as a DH^- monoanion. The proton is localized at the oxygen atom of the oxime group at the O(1)–H(1) distance of 0.829 Å. The O(1) and O(2) atoms of the oxime groups deviate from the plane of the metallocycle by 0.11 and 0.02 Å, respectively. The significant deviation of the O(1) atom from the rms plane of the dimethylglyoxime metallocycle is apparently due to the proton attached to the oxygen atom of the oxime group involved in the intermolecular hydrogen bond. The *o-phen* molecules are not exactly planar: the atomic deviations from the rms planes vary between –0.137 and 0.093 Å, which agrees well with the results obtained in [7, 13, 14]. Comparison of the N···N interatomic distances in *o-phen* molecules (2.622 and 2.623 Å; this work) with those in the uncoordinated (2.767 Å [9]) and coordinated (2.620 and 2.608 Å [7]) molecules suggests that significant changes in these distances upon coordination are due to not only the for-

Table 2. Hydrogen-bond system in structure **I**

D–H	*d*(*D*–H)	*d*(H…*A*)	*DHA* angle, deg	*d*(*D*…*A*)	*A*
O(1)–H(1)	0.827	1.784	176.48	2.610	O(1*w*)
O(1*w*)–H(1*w*1)	0.883	1.845	166.31	2.711	O(2*w*) [*x*, –*y* + 1/2, *z* – 1/2]
O(1*w*)–H(2*w*1)	0.904	1.920	165.14	2.804	F(3) [–*x* + 1, –*y* + 1, –*z* +1]
O(2*w*)–H(1*w*2)	0.926	2.038	151.58	2.887	F(1)
O(2*w*)–H(1*w*2)	0.926	2.452	142.99	3.240	F(2)
O(2*w*)–H(2*w*2)	0.917	1.919	150.26	2.754	F(8) [*x* – 1, *y*, *z*]

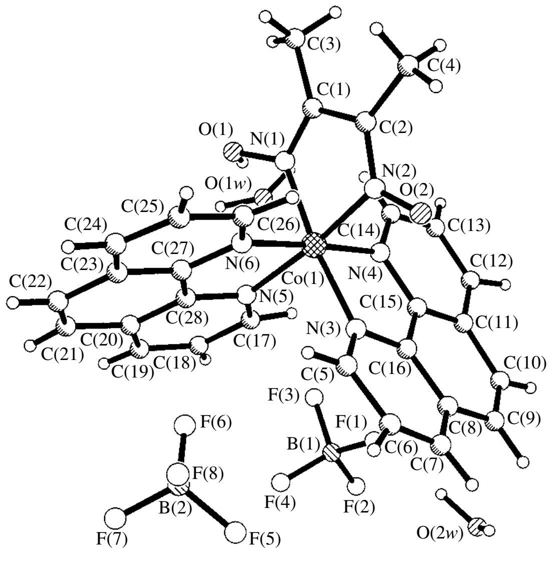

Fig. 1. Structure of complex **I**.

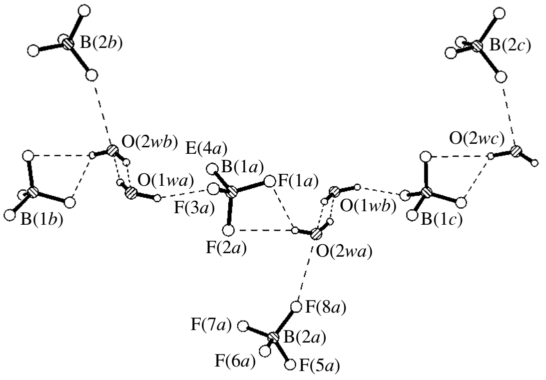

Fig. 2. A fragment of the hydrogen-bond system in structure **I**.

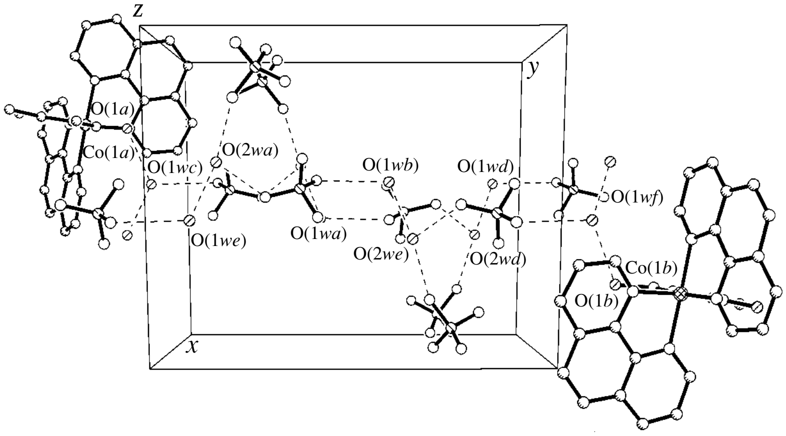

Fig. 3. A fragment of crystal structure **I**.

mation of closed metallocycles, as was noted in [7], but also the effect of the outer-sphere anions involved in different hydrogen-bond systems in the crystal structures under investigation.

In $[BF_4]^-$ outer-sphere anions, the B–F distances and F–B–F angles vary in the ranges 1.307–1.399 Å and 108.7°–114.6°, respectively, and differ from the ideal values. This can be explained by the fact that the fluorine atoms participate in the formation of an extended hydrogen-bond system involving two molecules of crystallization water in the outer sphere. The hydrogen bonding disturbs the favorable energy state of the $[BF_4]^-$ anion. Note that, in the crystal structure, a strong "tandem" hydrogen bond is formed between two crystallization water molecules, O(1*w*) and O(2*w*), which act as both a donor and an acceptor together (Fig. 2). A fragment of the crystal structure (parallel to the *x*0*y* plane) is shown in Fig. 3. The main parameters of the hydrogen bonds are listed in Table 2. Within the notation of the Bernstein graph sets [15], the bond between two water molecules can be described as $R_2^2(4)$ and the hydrogen bond between the O(2*w*) water molecule and two fluorine atoms, F(1) and F(2), can be described as $R_1^2(4)$.

The results obtained in this study and in [1, 7, 8] allowed us to conclude that, upon the formation of a cobalt complex, the compatibility of bidentate ligands (*AA*), such as thiosemicarbazide, glycine, α,α'-dipyridyl, and *o*-phenanthroline, is higher than that of dimethylglyoxime. As a consequence, all the trischelates studied are characterized by the ratio $DH^- : AA = 1 : 2$.

ACKNOWLEDGMENTS

We are grateful to Prof. Helen Stoeckli-Evans (Neuchätel University, Switzerland) for her aid in the data collection.

REFERENCES

1. S. T. Malinovskiĭ, Yu. A. Simonov, A. V. Ablov, *et al.*, Dokl. Akad. Nauk SSSR **232**, 326 (1977).
2. A. A. Dvorkin, Yu. A. Simonov, and T. I. Malinovskiĭ, in *Crystal Chemistry of Inorganic Compounds* (Shtiintsa, Kishinev, 1976), p. 3.
3. A. V. Ablov, Yu. A. Simonov, S. T. Malinovskiĭ, *et al.*, Dokl. Akad. Nauk SSSR **221**, 605 (1975).
4. Yu. Simonov, T. I. Malinovsky, A. V. Ablov, and S. T. Malinovsky, in *Abstracts of IV European Crystallographic Meeting* (Oxford, 1977), p. 181.
5. S. T. Malinovsky, E. B. Coropceanu, and O. A. Bologa, in *Proceedings of the 14th Conference on Physical Methods in Coordination and Supramolecular Chemistry* (2002), p. 142.
6. Yu. A. Simonov, O. A. Bologa, A. A. Dvorkin, *et al.*, Koord. Khim. **20**, 106 (1994).
7. M. M. Botoshanskiĭ, N. F. Krasnova, Yu. A. Simonov, *et al.*, Zh. Strukt. Khim. **20**, 1052 (1979).
8. A. V. Ablov, N. M. Samus’, and O. A. Bologa, Zh. Neorg. Khim. **8**, 860 (1963).
9. A. A. Desyatnik, N. V. Gerbeleu, E. B. Coropcheanu, *et al.*, Koord. Khim. **28**, 144 (2002).
10. S. T. Malinovskiĭ, E. B. Coropcheanu, O. A. Bologa, *et al.*, Koord. Khim. **28**, 370 (2002).
11. S. T. Malinovskiĭ, E. B. Coropcheanu, V. E. Zavodnik, *et al.*, Kristallografiya **47**, 58 (2002) [Crystallogr. Rep. **47**, 51 (2002)].
12. G. M. Sheldrick, *SHELXS97: Program for the Solution of Crystal Structures; SHELXL97: Program for the Refinement of Crystal Structures* (Univ. of Göttingen, Germany, 1997).
13. S. R. Hall, D. L. Kepert, C. L. Raston, and A. H. White, Aust. J. Chem. **30**, 1955 (1977).
14. T. W. Hambley, C. L. Raston, and A. H. White, Aust. J. Chem. **30**, 1965 (1977).
15. J. Bernstein, R. E. Davis, L. Shimoni, and N. L. Chang, Angew. Chem. Int. Ed. Engl. **34**, 1555 (1995).

Translated by I. Polyakova

Crystallography Reports, Vol. 49, No. 5, 2004, pp. 811–815. Translated from Kristallografiya, Vol. 49, No. 5, 2004, pp. 899–904.
Original Russian Text Copyright © 2004 by Karachinov.

Microtip Roughness of Erosion-Induced Disturbed Layers in Silicon Carbide Crystals

V. A. Karachinov
Novgorod State University, Bol'shaya Sankt-Peterburgskaya ul. 41, Velikiĭ Novgorod, 173003 Russia
e-mail: tel@novsu.ac.ru

Received April 4, 2003; in final form, January 29, 2004

Abstract—The defect structure of a disturbed layer formed in the process of erosion cutting of bulk silicon carbide crystals has been studied experimentally. The characteristic features revealed are discussed in terms of the erosion-front interaction with growth defects and of the partial electrical volume breakdown in SiC. © *2004 MAIK "Nauka/Interperiodica".*

INTRODUCTION

Today, the main method of producing silicon carbide substrates is cutting of single-crystal silicon carbide ingots with the subsequent grinding and polishing of the cuts obtained [1, 2]. The intense and durable action of a cutting instrument (diamond disk or abrasive wire) on the SiC surface gives rise not only to considerable wastes of material but also to the formation of a deep disturbed layer [2, 3].

Crystalline SiC substrates with low resistivity and a diameter exceeding 30 mm may be obtained by the method of erosion cutting with a wire electrode [4]. Despite the well-known disadvantages of this method, it excludes the direct mechanical action of the electrode and allows one to select an appropriate mode of SiC treatment—that of a liquid phase, explosive evaporation, or shock fracture [5, 6]. At the same time, preliminary studies showed that the main factor that does not allow one to obtain sufficiently thin substrates is the thickness of the disturbed layer. The nature and structure of the disturbed layer and its relation to the electrical and technological parameters of the erosion process and the growth defects inherited from the SiC crystal have been studied insufficiently.

Below, we report the results of experimental studies of an erosion-induced disturbed layer formed during the preparation of SiC films.

EXPERIMENTAL

Bulk silicon carbide single crystals were cut into ~300–500-μm-thick plates by the method of erosion cutting on industrial setups [4, 7]. The profiled electrode was prepared from DKRPM KTL63 brass wire with a diameter d = 100 μm. The technological processes were conducted in tap water. We studied bulk SiC (polytype 6H) single crystals with a diameter D = 20–50 mm and length 10 mm with the concentration of uncompensated donors $N_d - N_a \simeq 5 \times 10^{17}$–$3 \times 10^{18}$ cm^{-3}.[1] Crystals were grown in the [0001] direction. The disturbed layer was studied on a slanting wedge and cleavage using layer-by-layer chemical etching of SiC in the KOH melt and its local decoration with copper from a porous electrode [8]. The disturbed layers were also studied with the aid of chemical and X-ray fluorescence analysis [9]. We used a television metallographic microscope and computer image processing, a BS-340 scanning electron microscope in the mode of secondary electron emission, and also an ED2000 device for X-ray fluorescence analysis.

RESULTS AND DISCUSSION

Our studies showed that cutting of SiC ingots at admissibly high rates (Fig. 1) results in the formation of a structurally inhomogeneous disturbed layer. The properties of this layer are determined by the number and kind of defects in the initial crystal and can considerably vary within the substrate, e.g., in the transition from the substrate center to its periphery. In particular, we observed local regions with inverted polarity of the (0001) face, second-phase inclusions, twins, etc.

Thermal calculations performed by the methods suggested elsewhere [10] showed that the depth of a heated SiC layer at a discharge pulse duration of about 3–4 μs is about ~60–80 μm (with no allowance made for evaporation).

Consider the main characteristics of the disturbed layer caused by the inherited defects and the experimental conditions.

Structure of a disturbed layer. Figure 2 shows the morphology of the disturbed-layer profile after SiC etching in the KOH melt. One can see that the crystal surface of both the (0001)C and (0001)Si faces has a

---

[1] The SiC ingots were grown in the laboratory headed by Yu.M. Tairov.

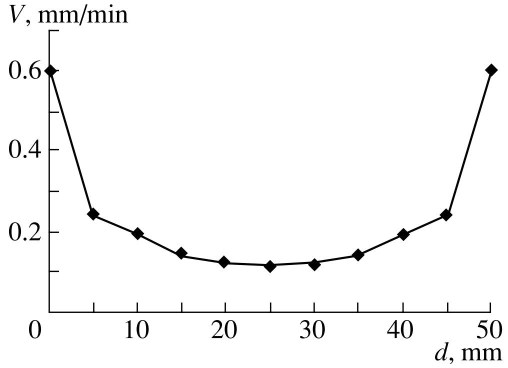

Fig. 1. Average experimental cutting rate as a function of the diameter of a SiC ingot.

~30–40-μm-thick layer with high defect concentration. With an increase of the distance from the substrate surface, the defect density decreases, so that one observes only some discrete sites. It should be noted that the disturbed-layer thickness on the (0001)C surface is usually higher than on the (0001)Si face. This is consistent with the results obtained in studies of the mechanical nature of a disturbed layer in a SiC crystal [3].

The analysis of the experimental data obtained by the method of a slanting wedge and layer-by-layer chemical etching allowed us to establish the structure of the disturbed layer. As is seen from Fig. 3, the disturbed layer has four zones with well developed phase boundaries. These are (*1*) the zone of adsorption of the working-liquid elements and products of the chemical reactions; (*2*) the zone of deposition of the electrode material; (*3*) the zone of SiC recrystallization; and (*4*) the porous zone. The first two zones are the conventional zones observed in the erosion treatment of various materials [10].[2] Their existence of these zones in SiC is confirmed by the chemical and X-ray fluorescence analysis of the disturbed layer. We established the presence of copper and zinc from the brass electrode and also of iron and several oxides. Thus, according to X-ray fluorescence analysis, the copper and zinc concentrations in SiC crystals subjected to the erosion treatment considerably exceed the initial concentration of these elements and, on the average, are 5.0–6.5% Cu and ~3.5–3.8% Zn. Zones (*1*) and (*2*) play the part of a masque of the lower zones and "conceal" the true microrelief of the disturbed layer.

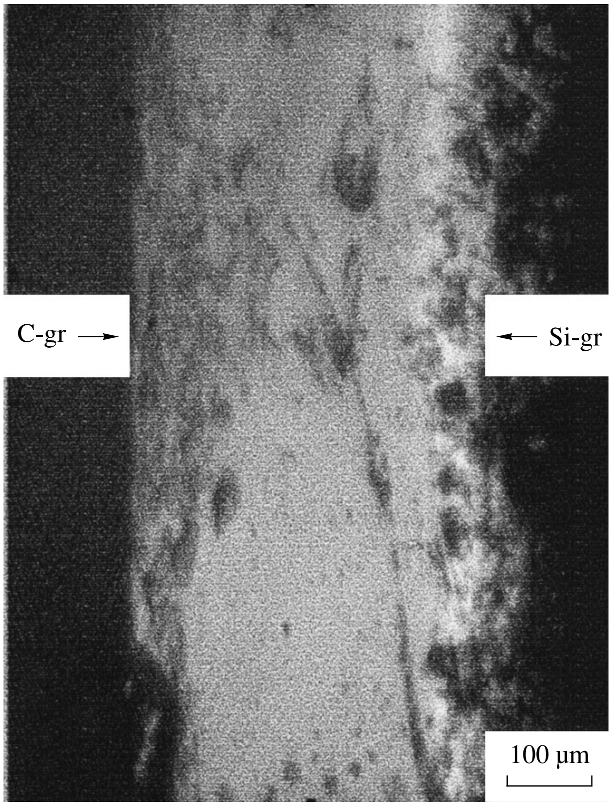

Fig. 2. Surface morphology of the disturbed layer after chemical etching of a SiC crystal in the KOH melt. t_{etch} = 500°C. The $(10\bar{1}0)$ cleavage.

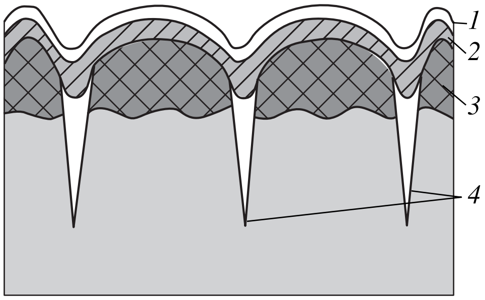

Fig. 3. Structure of the erosion-induced disturbed layer (model).

The recrystallization zone is the most structurally developed zone, which includes the regions of the SiC crystal in which the processes of evaporation, growth, brittle fracture, and plastic deformation proceed under the action of pulsed thermal, electric, and sonic loads. The thickness of this zone range within ~10–20 μm depending on the pulse energy. This zone, together with zones (*1*) and (*2*), determines the external roughness of the disturbed layer. The thermodynamically nonequilibrium conditions of this zone formation (hot layer–cold substrate) provide accumulation and relaxation of thermoelastic stresses, which weaken chemical bonds in SiC. This manifested itself, e.g., in the fact that the transverse cleavage of the substrate with a disturbed layer was accompanied by the formation of a relatively smooth step along the internal boundary of the recrystallization zone. The processes determining the defect structure of the zone were established from the analysis of etch figures.

---

[2] Analysis was performed at the analytical center of the *Akron* research and production center.

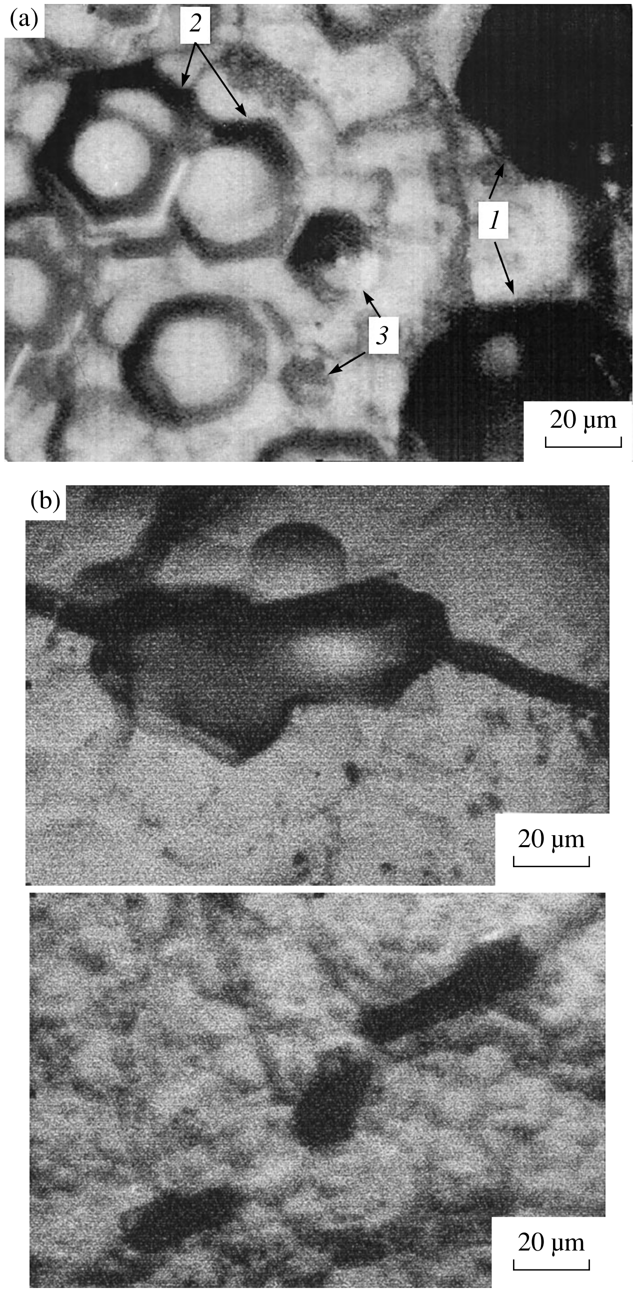

Fig. 4. Etch figures of the disturbed layer. Recrystallization zone, (0001)Si face. (a) Large pits (*1*), (*2*) pits with flat bottoms, (*3*) pyramidal pits; (b) pits of irregular shape and elongated hexagonal pits.

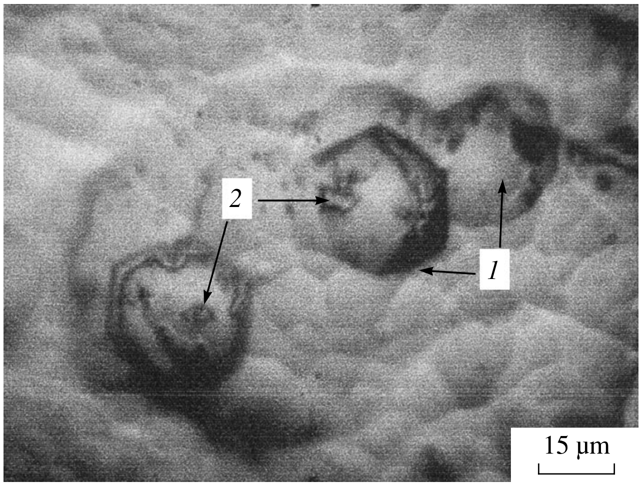

Fig. 5. Evolution of hexagonal etch pits with flat bottoms, (0001)Si face. (*1*) Disappearing holes and (*2*) their traces close to the bottoms.

Etch figures. As is seen from Fig. 4a, etching of a disturbed layer in the KOH melt gives rise to the formation of etch figures on the (0001)Si face whose main parameters are indicated in the table. It is possible to unambiguously state that hexagonal etch pits of the conic type are associated with dislocations in SiC, whereas deep large hexagonal pits (dark ones), with negative dislocations of the growth nature and pores (channels of volume breakdown of SiC) arising in the process of erosion [11]. The nature of other etch pits was determined from the consideration of the evolution of these defects in the course of long chemical etching of the disturbed layer. The hexagonal pits with flat bottoms are formed as a result of regeneration of erosion pits in the KOH melt. As is seen from Fig. 5, each disappearing hole leaves a trace in the form of a single conic hole or a group of holes having different depths close to the bottom; later, they become faceted. The elongated hexagonal or irregular pits (Fig. 4b) have finite depths. They seem to be associated with the inclusions of the second phase—carbon (graphite)—formed during growth of SiC crystals [12]. The substrate surface is highly saturated with these pits.

It should be indicated that during the etching process, the (0001)C face is covered with holes due to second-phase inclusions and also with regular conic hills.

Relaxation processes. Our experiments showed that the main cause of the formation of specific defects in the recrystallization zone is deformation arising during the interaction of the erosion front with the inherited defects of the SiC crystal. Thus, brittle fracture of SiC in the form of long (exceeding 10 mm) cracks localized in the recrystallization zone is induced by stress relaxation during cutting-off of the second-phase inclusions or pores by the erosion front. This process is illustrated by Fig. 6a. As a rule, the fracture system propagates along the $(10\bar{1}0)$ cleavages. The propagating erosion front “scatters” the cracks over the substrate surface so that their lines close at the macrodefects of the disturbed layer. In this case, almost all the known mechanisms of crack propagation and interaction work [13].

We observed for the first time the individual regions of plastic deformation in the disturbed layer. At the etching patterns of SiC, these regions are seen as disordered accumulations of hexagonal etch pits and also the chains of the etch pits along the $\langle 11\bar{2}0\rangle$ direction

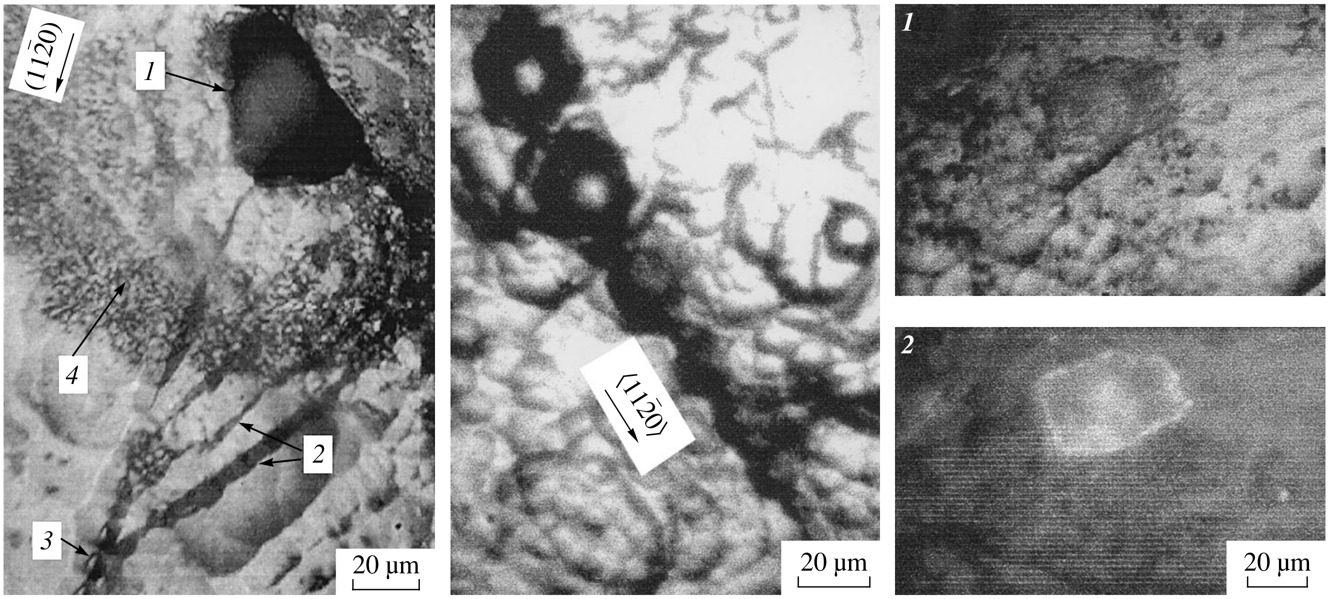

(a) (b) (c)

Fig. 6. Relaxation of thermoelastic stresses in the disturbed layer. (0001)Si face. (a) Brittle fracture: (*1*) macrodefect, (*2*) "stream-like" cracks, (*3*) main crack, (*4*) halo; (b) plastic deformation; (c) visualized stressed regions of the disturbed layer: images in (*1*) conventional and (*2*) polarized light.

(Fig. 6b). Taking into account that these etch figures are obtained within the same etching time, one may conclude that the dislocations associated with these figures have different Burgers vectors [14]. It is important that, within the disturbed layer, we also observed in the polarized light regions with elevated thermoelastic stresses (Fig. 6c).

Porous zone. To observe the disturbed layer inside the crystal simultaneously on the Si and C faces, we prepared special microprisms from the SiC substrate. The optical studies showed that the disturbed layer possesses a well developed internal roughness, which is represented by a quasi-regular system of conic pores or microtips oriented at a certain angle to the substrate surface. This system was observed on both Si- and C-faces (Fig. 7). The average pore density ranged within $N_p = 10^1$–10^3 cm^{-2} and the pore length within ~5–70 μm depending on the erosion mode. At the same time, we also observed a certain scatter in the analogous estimates for polar faces. The elevated values of the parameters were usually observed in the disturbed layer on the carbon face. The propensity of a carbon face to form pores was observed earlier in the study of the kinetics of conventional thermal evaporation of SiC [15].

The formation of conic pores should be associated with the partial volume electric breakdown of SiC arising at the probing-pulse amplitudes higher than 100 V [11]. In fact, under conditions of electrical erosion, SiC behaves as a poor dielectric.

Additional experimental studies of this phenomenon in the mode of single discharges showed that a conic pore acts as a Knudsen cell, which may result in the specific face morphology (Fig. 7c).

Thus, the disturbed layer induced by erosion in SiC crystals has an inhomogeneous structure. The interaction of the erosion front with the inherited growth defects in the SiC crystal generates a new system of

Etch pits in the recrystallization zone of the disturbed layer in SiC

Shape	Point symmetry group	Typical dimension	Average density, cm^{-2}
Large hexagonal pits	6 *mmm*	Diameter 60–70 μm	10^1–10^3
Hexagonal pits with flat bottoms	6 *mmm*	Diameter 30–40 μm	$>10^6$
Hexagonal conic (pyramidal) pits	6 *mmm*	Diameter 20–25 μm	Some discrete sites 10^3–10^4
Hexagonal pits elongated in the [11$\bar{2}$0] direction	2 *mm*	Length ~20 μm, width ~10 μm	10^5–10^7
Faceted pits of irregular shape	–	Length ~30–60 μm, width ~10–30 μm	$\leq 10^3$

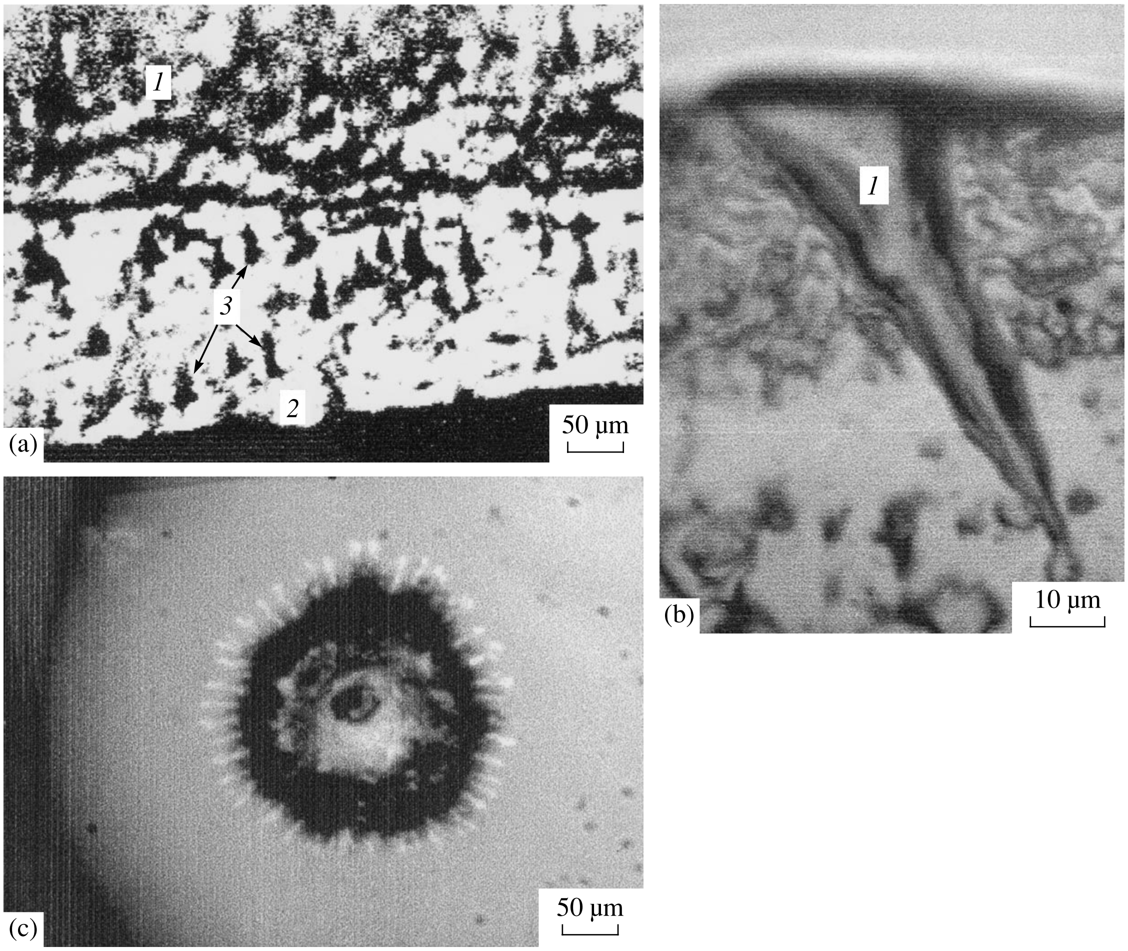

Fig. 7. Effects of partial volume breakdown in SiC. (a) Porous zone of the disturbed layer: (*1*) (0001)Si face, (*2*) (0001)C face, (*3*) conic pores; (b) profile of a conic pore: (*1*) solidified melt; (c) surface morphology in the vicinity of a conic pore.

defects localized in the recrystallization zone of the disturbed layer.

The disturbed layer possesses not only the external microroughness but also the internal microtip roughness associated with partial electric breakdown in the SiC crystal.

REFERENCES

1. N. S. Sudarshan and I. I. Khlebnikov, in *Abstracts of IV International Seminar on Silicon Carbide and Related Materials* (Novgorod, 2002), p. 82.
2. A. O. Okunev, Candidate's Dissertation in Physics and Mathematics (Novgorod State Univ., Novgorod, 1999).
3. N. I. Dolotov, B. I. Levchuk, V. V. Makarov, *et al.*, Fiz. Khim. Obrab. Mater., No. 4, 69 (1986).
4. V. A. Karachinov, RF Patent No. 2,202,135 (April 10, 2003).
5. V. A. Karachinov, RF Patent No. 2,189,664 (September 20, 2002).
6. O. A. Ageev, N. A. Kovalev, and A. L. Vasilenko, Fizika (Baku), No. 4, 16 (2000).
7. O. G. Bazhenov and V. A. Karachinov, Pis'ma Zh. Tekh. Fiz. **22** (21), 26 (1996) [Tech. Phys. Lett. **22**, 875 (1996)].
8. V. A. Karachinov, Pis'ma Zh. Tekh. Fiz. **28** (10), 83 (2002) [Tech. Phys. Lett. **28**, 439 (2002)].
9. *Preparative Methods in Solid State Chemistry*, Ed. by P. Hagenmuller (Academic, New York, 1972; Mir, Moscow, 1976).
10. N. K. Foteev, *Technology of Electro-Erosion Treatment* (Mashinostroenie, Moscow, 1980) [in Russian].
11. V. A. Karachinov, Zh. Tekh. Fiz. **72** (4), 60 (2002) [Tech. Phys. **47**, 432 (2002)].
12. P. A. Ivanov and V. E. Chelnokov, Fiz. Tekh. Poluprovodn. (St. Petersburg) **29** (11), 1921 (1995) [Semiconductors **29**, 1003 (1995)].
13. L. A. Shuvalov, A. A. Urusovskaya, I. S. Zheludev, *et al.*, in *Modern Crystallography*, Vol. 4: *Physical Properties of Crystals*, Ed. by B. K. Vaĭnshteĭn, A. A. Chernov, and L. A. Shuvalov (Nauka, Moscow, 1981; Springer, Berlin, 1988).
14. S. Amelinckx and G. Struname, J. Appl. Phys. **35** (12), 3618 (1964).
15. V. F. Tsvetkov, Izv. Leningr. Élektrotekh. Inst., No. 338, 3 (1984).

Translated by L. Man

Crystallography Reports, Vol. 49, No. 5, 2004, pp. 816–819. Translated from Kristallografiya, Vol. 49, No. 5, 2004, pp. 905–908.
Original Russian Text Copyright © 2004 by Sarafanov.

Mechanism of Spatial Ordering of Dislocations during Plastic Deformation of Crystals[1]

G. F. Sarafanov
Nizhni Novgorod State Pedagogical Institute, GSP-37, ul. Ulyanova 1, Nizhni Novgorod, 603950 Russia
e-mail: sarafanov@sinn.ru

Received January 31, 2003

Abstract—Mechanisms of spatial ordering of dislocations during plastic deformation of crystals are considered. The system of evolution equations, which take into account the effects of elastic and correlated interactions of screw dislocations, is derived. The study is performed with due regard for the dynamics of spatial fluctuations of the dislocation density. *© 2004 MAIK "Nauka/Interperiodica".*

Usually, analysis of the general laws governing the behavior of nonequilibrium systems and processes of their structural rearrangements is based on the theory of dissipative structures [1, 2]. Historically, the basic model that describes the formation of such structures is the system of reaction–diffusion equations, which, in the region of instability, is reduced to the universal class of the Swift–Hohenberg equations [2, 3]. A similar scheme of analysis of the self-organization phenomena in an ensemble of dislocations was applied to the formation of inhomogeneous dislocation structures, e.g., in [4–7].

Despite the existence of a wide spectrum of possible solutions, this class of equations has certain limitations in description of dislocation structures. First, it is well known [8, 9] that the cellular dislocation structures observed experimentally can hardly be identified with rigorously periodic formations. One may rather consider the quasi-crystallinity and turbulence of dislocation structures [8]. However, such solutions cannot be obtained within the framework of the Swift–Hohenberg equations [3]. Second, the formation of the structures on the basis of the reaction-diffusion models is associated with the development of a Turing instability, which may arise only in the presence of several (at least two) components in the system [7, 10]. The latter circumstance imposes rather rigid requirements on the dislocation kinetics, which decreases the probability of homogeneous-state layering by the generation-recombination mechanism.

Thus, one has to establish the range of applicability of the reaction-diffusion models to the description of the evolution of a dislocation ensemble and to consider alternative mechanisms of formation of instability in the homogeneous dislocation distribution.

At a developed state of plastic deformation, when the dislocation density is rather high, the diffusion interactions of the system components become a too rough approximation and, therefore, one has also to take into account inelastic interactions of dislocations and fluctuation dynamics. The existence of the charge characteristic of dislocations (Burgers vector) gives rise to the occurrence of certain phenomena in the dislocation ensemble that are characteristic of the system of charged particles [11, 12]. Screening of the long-range field results in efficient (correlation) attraction of the particles generating this field and layering of the homogeneous state [13, 14]. The mechanisms of formation of inhomogeneous dislocation structures were studied in [15] on the basis of the system of equations suggested earlier, which describe the dynamics of a dislocation ensemble with a physically set correlation flow of defects [14]. It is shown that, with the attainment of the critical nonequilibrium conditions in a local volume corresponding to the correlation instability, the dissipative structures of various types are spontaneously formed in the system.

Below, we suggest a consistent derivation of a system of evolution equations that take into account the effects of elastic and correlation interactions of screw dislocations. The consideration takes into account the dynamics of spatial fluctuations of the dislocation density, which allows us to substantiate the correlation flow of defects considered in [14].

The initial system [14] is a set of self-consistent equations for an ensemble of screw dislocations and is averaged on the scale L_0 selected proceeding from the condition $\bar{r} < L_0 < R_c$ ($\bar{r}$ is the average dislocation distance between dislocations and R_c is the curvature radius of dislocation lines). If the fluctuation scale is on the order of L_0 or exceeds this scale, one has to take into account also higher-order moments.

---

[1] This work was submitted to the symposium "Phase Transformations in Solid Solutions and Alloys" (OMA, Sochi, Russia, 2002).

To understand the role of such fluctuations, we use the method of moments in the approximation of the second correlation functions [16]. We represent the dislocation density in the form $\rho^a(\mathbf{r}, t) = \rho_a(\mathbf{r}, t) + \delta\rho_a(\mathbf{r}, t)$, where $\rho_a(\mathbf{r}, t)$ and $\delta\rho_a(\mathbf{r}, t)$ are the average dislocation density and the fluctuation of this density, respectively. Now, substitute this sum into the initial system and separate the scales under the assumption that the characteristic space and time scales (L_c and T_c) of the $\rho_a(\mathbf{r}, t)$ variations considerably exceed the scales of the fluctuation variations (r_c and τ_c). Then, the system of evolution equations for the average quantities acquires the form

$$\frac{\partial\rho_a}{\partial t} + \operatorname{div}\rho_a\mathbf{v}_a = F_a(\{\rho_a\}) - \operatorname{div}\langle\delta\rho_a\delta\mathbf{v}_a\rangle, \qquad (1)$$

$$\begin{aligned} \mathbf{v}_a(\mathbf{r}, t) &= \mathbf{V}_a + \hat{M}^a\mathbf{f}_a(\mathbf{r}, t), \\ \operatorname{div}\mathbf{f}_a(\mathbf{r}, t) &= Gb^a\sum_a b^a\rho_a(\mathbf{r}, t), \end{aligned} \qquad (2)$$

where $\mathbf{v}_a(\mathbf{r}, t)$ is the average velocity of the dislocation glide; $\mathbf{V}_a$ is the constant component of the dislocation velocity (drift velocity) determined by the flow stress σ_{ext} in the glide plane ($V_a = M_{\parallel}^a b_a\sigma_{\text{ext}}$); $\mathbf{f}_a$ is the force acting on the unit length of a dislocation from the side of the system of dislocation charges; $\hat{M}^a$ is the dislocation-mobility tensor with the nonzero diagonal components $M_{\parallel}^a$ and $M_{\perp}^a$ characterizing the dislocation mobility in the glide plane and in the plane of the transverse glide, respectively (usually, $M_{\parallel}^a \gg M_{\perp}^a$ [17]); and a is the index, which allows one to distinguish the dislocations from the directions of their Burgers vectors $\mathbf{b}_a$ with respect to $\mathbf{l}$ ($\mathbf{l}$ is the unit vector tangential to the dislocation line). In an ensemble of screw dislocations ($\mathbf{b}_a \parallel \mathbf{l}$), the Burgers vector of a dislocation may take two values $b_a = z_a b = \pm b$ ($z_a = \pm 1$) and, therefore, b_a plays the role of the dislocation charge, whereas the subscript a characterizes the type of the dislocation with a certain charge sign, G is the shear modulus, and $\mathbf{r} = (x, y)$ is a two-dimensional radius-vector ($\mathbf{r} \perp \mathbf{l}$). Considering the nonlinear functions F_a, which characterize the generation–recombination processes, we ignored the fluctuations of the dislocation density, which is quite justified if the system does not undergo nonequilibrium phase transitions induced by these processes [1].

The above system of equations is not closed, because it has the term $\operatorname{div}\mathbf{J}_a^{\text{corr}} = \operatorname{div}\langle\delta\rho_a\delta\mathbf{v}_a\rangle$, determined by fluctuations. Because the fluctuations are assumed to be small, the corresponding equations for fluctuations may be represented in the linearized form using the approximation of the local stationary state,

$$\left(\frac{\partial}{\partial t} + \mathbf{V}_a\nabla\right)\delta\rho_a + \frac{1}{2\tau}\sum_a\delta\rho_a = -\rho_a\nabla\delta\mathbf{v}_a, \qquad (3)$$

$$\delta\mathbf{v}_a(\mathbf{r}) = -\hat{M}^a\sum_c\int\delta\rho_c(\mathbf{r}')\frac{\partial W_{ac}(|\mathbf{r}-\mathbf{r}'|)}{\partial\mathbf{r}}d\mathbf{r}'. \qquad (4)$$

Here ,$W_{ac}(\mathbf{r}) = (Gb_ab_c/2\pi)\ln(r_0/r)$ is the energy of interaction between two dislocations with the dislocation charges b_a and b_c (r is the distance between the dislocations, $r_0 \sim b$ is the radius of the dislocation core [17]), and τ is the time of relaxation to the quasi-stationary state $\rho_a(\mathbf{r}, t)$ (when analyzing the fluctuation dynamics in this state, we assume that the dependence on coordinates and time is parametrically set). The form of the terms in Eq. (3) is related to the problem symmetry with respect to the dislocation sign and the fulfillment of the condition $\sum_a b_aF_a = 0$. This reflects the conservation of the Burgers vector in dislocation reactions and dislocation multiplication [17]. Moreover, we also assume that system (3), (4) satisfies the condition of quasi-neutrality $\sum_a b_a\rho_a = 0$.

With due regard for Eq. (4), the dislocation flow $\mathbf{J}_a^{\text{corr}} = \langle\delta\rho_a\delta\mathbf{v}_a\rangle$ takes the form

$$\begin{aligned} \mathbf{J}_a^{\text{corr}}(\mathbf{r}, t) &= -\hat{M}^a\sum_c\int\langle\delta\rho_a(\mathbf{r}, t)\delta\rho_c(\mathbf{r}', t)\rangle \\ &\times\frac{\partial W_{ac}(|\mathbf{r}'-\mathbf{r}|)}{\partial\mathbf{r}}d\mathbf{r}' \end{aligned} \qquad (5)$$

and has the sense of the correlation flow, because it is provided with the correlation of fluctuations. Thus, the problem of dislocation density reduces to the calculation of the correlator in Eq. (5), which may be represented in the form [16]

$$\begin{aligned} &\langle\delta\rho_a(\mathbf{r}, t)\delta\rho_c(\mathbf{r}', t)\rangle \\ &= \rho_a(\mathbf{r}, t)\rho_c(\mathbf{r}', t)g_{ac}(\mathbf{r}, \mathbf{r}') + \delta_{ac}\rho_a(\mathbf{r}', t)\delta(\mathbf{r}-\mathbf{r}'). \end{aligned} \qquad (6)$$

Here, $g_{ac}(\mathbf{r}, \mathbf{r}') = g_{ac}(\mathbf{r}-\mathbf{r}')$ is a two-particle correlation function to be determined (in the approximation of the local stationary state, it depends only on the difference in the coordinates), $\delta(\mathbf{r})$ is the delta function, and δ_{ac} is the Kronecker symbol.

In a similar way, one may also represent a fluctuation $\delta\rho_a(\mathbf{r}, t)$ as a sum form of two terms [16], $\delta\rho_a = \delta\rho_a^{\text{ind}} + \delta\rho_a^{\text{sou}}$, which determine the fluctuations induced by the elastic field and the dislocations that induced this field.

For convenience, introduce the variables $\rho = \sum_a\rho_a = \rho_+ + \rho_-$ and $I = \sum_a b_a\rho_a/b = (\rho_+ - \rho_-)$ to characterize the total density of dislocations and their charge. Thus, we have for $\delta\rho^{\text{sou}}$ and δI^{sou}

$$\begin{gathered}\frac{\partial}{\partial t}\delta\rho^{\text{sou}} + (\mathbf{V}\nabla)\delta I^{\text{sou}} + \frac{1}{\tau}\delta\rho^{\text{sou}} = 0,\\ \frac{\partial}{\partial t}\delta I^{\text{sou}} + (\mathbf{V}\nabla)\delta\rho^{\text{sou}} = 0.\end{gathered} \tag{7}$$

Since we consider the problem against the background of the quasi-stationary state and, in fact, deal with large-scale kinetic fluctuations, it is natural to assume that $\tau \ll \tau_c$. Under this assumption, Eq. (7) yields a homogeneous equation for I^{sou}, whence follows the equation for a two-time correlator,

$$\left[\frac{\partial}{\partial t} + \tau(\mathbf{V}\nabla)^2\right]\langle\delta I\delta I^{\text{sou}}\rangle_{\mathbf{r}-\mathbf{r}',\,t-t'} = 0. \tag{8}$$

Decomposing $\langle\delta I\delta I^{\text{sou}}\rangle_{\mathbf{r}-\mathbf{r}',\,t-t'}$ into the Fourier integral with due regard for Eqs. (6) and (8), we arrive at the equation for the spectral density,

$$\langle\delta I\delta I^{\text{sou}}\rangle_{\omega,\mathbf{k}} = \frac{2\rho(\mathbf{r}')\tau(\mathbf{kV})^2}{\omega^2 + \tau^2(\mathbf{kV})^4}. \tag{9}$$

Now, determine the form of the spectral density $\langle\delta I\delta I\rangle_{\mathbf{k}}$. Knowing this form, we may determine the expression for $g_{ac}(\mathbf{r}, \mathbf{r}')$. In the adiabatic approximation ($\tau \ll \tau_c$), Eq. (3) yields the system of equations for fluctuations δI and δI^{sou}. Passing to the Fourier components, we finally obtain

$$\left[1 + \frac{\tau(\mathbf{kV})^2\mathbf{k}^2 r_d^{-2}}{i\omega + \tau(\mathbf{kV})^2}\right]\delta I_{\omega,\mathbf{k}} = \delta I^{\text{sou}}_{\omega,\mathbf{k}}. \tag{10}$$

Here, $r_d = \sqrt{T_{\text{ext}}/Gb^2\rho(\mathbf{r})}$ is the screening radius of the fields of elastic dislocations introduced in [14] and T_{ext} is the deformation energy.

Using Eqs. (9) and (10), we may determine the spatial–temporal spectral density of fluctuations, whence

$$\begin{aligned}\langle\delta I\delta I\rangle_{\mathbf{k}} &= \frac{1}{2\pi}\int\limits_{-\infty}^{\infty}\frac{2\rho(\mathbf{r}')\tau(\mathbf{kV})^2 d\omega}{\omega^2 + \tau^2(\mathbf{kV})^4(1 + \mathbf{k}^{-2}r_d^{-2})^2}\\ &= \rho(\mathbf{r}') - \frac{Gb^2\rho(\mathbf{r})\rho(\mathbf{r}')}{T_{\text{ext}}(\mathbf{k}^2 + r_d^{-2})}.\end{aligned} \tag{11}$$

Using Eq. (11), we finally obtain

$$\begin{aligned}g_{ac}(\mathbf{r}, \mathbf{r}') &= -\frac{Gb_a b_c}{(2\pi)^2 T_{\text{ext}}}\int\frac{\exp - i\mathbf{kr}}{\mathbf{k}^2 + r_d^{-2}}d\mathbf{k}\\ &= -\frac{Gb_a b_c}{2\pi T_{\text{ext}}}K_0(r/r_d).\end{aligned} \tag{12}$$

Here, $K_0(r/r_d)$ is the Macdonald function of the zeroth order and $r = |\mathbf{r} - \mathbf{r}'|$ is the interdislocation distance.

Thus, the form of correlation function (12) coincides with the expression based on physical considerations in [14] and provides the correlation of dislocations spaced by the distance $r_c = r_d$. With due regard for the dislocation characteristics and the two-dimensionality of the problem, this function is analogous to the correlation function of charged plasma particles [16].

The correlation interaction provides efficient attraction of dislocations irrespective of the sense of their Burgers vectors [14]. This interaction results in the appearance of an additional correlation flow (5) in the system of evolution equations, which, in the case of a weak inhomogeneity ($r_d \ll L_c$), is reduced to

$$\mathbf{J}_a^{\text{corr}}(\mathbf{r}) \simeq \hat{M}\rho_a(\mathbf{r})(A_1 + \Delta A_2 + \dots)\nabla\rho(\mathbf{r}), \tag{13}$$

where $\rho(\mathbf{r}) = \sum_a \rho_a(\mathbf{r})$ is the total dislocation density, $A_1 = Gb^2/4\pi\rho_0$, and $A_2 = Gb^2 r_d^2/8\pi\rho_0$.

Flow (13) is the Cahn–Hilliard flow [18] well known in the theory of phase layering in order–disorder-type systems. Substituting Eq. (13) into Eq. (1), we obtain the system of evolution equations (1), (2) in the form

$$\frac{\partial\rho_a}{\partial t} + \operatorname{div}(\mathbf{J}_a + \mathbf{J}_a^{\text{corr}}) = F_a(\{\rho_a\}), \tag{14}$$

$$\mathbf{J}_a(\mathbf{r}, t) = \rho_a(\mathbf{r}, t)\mathbf{V}_a + \rho_a(\mathbf{r}, t)\hat{M}^a\mathbf{f}_a(\mathbf{r}, t), \tag{15}$$

$$\mathbf{J}_a^{\text{corr}}(\mathbf{r}, t) = \hat{M}\rho_a(\mathbf{r}, t)(A_1 + \Delta A_2)\nabla\sum_c\rho_c(\mathbf{r}, t), \tag{16}$$

$$\operatorname{div}\mathbf{f}_a(\mathbf{r}, t) = Gb_a\sum_a b_a\rho_a(\mathbf{r}, t). \tag{17}$$

This system of equations is the generalization of well-known models for nonlinear nonequilibrium media [1, 2]. Here, the flow $\mathbf{J}_a$ determines the dislocation flow in the approximation of the medium field.

The theoretical studies of the laws of formation of inhomogeneous dislocation structures performed within the framework of system (14)–(17) and the isotropic model for dislocations of one type [15] showed that, at the initial stages of plastic deformation and the dislocation density lower than a certain critical value,

$$\rho_0 < \rho_c = \frac{8\pi}{(\sqrt{3} - 1)^2 b^2}\left(\frac{kT}{\Gamma G}\right)^2, \tag{18}$$

the dislocation distribution is homogeneous (Γ is the activation volume and T is the temperature). With an increase in deformation at $\rho_0 \geq \rho_c$, the system acquires a correlation instability, which is accompanied by nucleation of the crystal and quasi-crystal structures at the total and excessive dislocation densities. The critical ρ_c value corresponds to a dislocation density of the order of 10^9 cm^{-2}, which is also confirmed by the experimental data [8, 9].

The correlation mechanism of homogeneous-state layering considered above, as well as the generation–recombination mechanism, corresponds to the stage of plastic deformation at which slightly misoriented dislocation structures are formed. The description of the structures with a pronounced misorientation (striated, fragmented, or fine-grained) is a more complex problem that may be solved only with the invocation of new concepts, e.g., disclinations [19, 20]. As is well known [20], in fact, disclinations are equilibrium dislocation formations appearing as a result of spontaneous rearrangements in a dislocation ensemble. Nucleation of disclinations is usually associated with a rotational instability whose mechanism is induced by layering of dislocation charges. We believe that this layering is induced by the correlation instability accompanied by formation of the dynamic dissipative structure for the total and excessive dislocation density [21]. The elements of the dissipative structure serve as nuclei for the subsequent formation of the equilibrium disclination fragments. The corresponding phase transition is the transition to equilibrium structures and may take place only under essentially nonequilibrium conditions. The description of this transition requires further detailed studies.

ACKNOWLEDGMENTS

This study was supported by the Russian Foundation for Basic Research, project no. 02-02-16526.

REFERENCES

1. G. Nicolis and I. Prigogine, *Self-Organization in Non-Equilibrium Systems* (Wiley, New York, 1977; Mir, Moscow, 1979).
2. H. Haken, *Synergetics* (Springer, Berlin, 1978; Mir, Moscow, 1980).
3. M. I. Rabinovich and A. B. Ezerskiĭ, *Dynamical Theory of Shape Formation* (Yanus-K, Moscow, 1998) [in Russian].
4. D. Walgraef and E. C. Aifantis, Int. J. Eng. Sci. **23**, 1351 (1985).
5. E. C. Aifantis, Mater. Sci. Eng. **81**, 563 (1986).
6. G. A. Malygin, Fiz. Tverd. Tela (St. Petersburg) **37** (1), 3 (1995) [Phys. Solid State **37**, 1 (1995)].
7. S. N. Nagornykh and G. F. Sarafanov, Metallofizika (Kiev) **16** (5), 67 (1992).
8. V. I. Trefilov, V. F. Moiseev, É. P. Pechkovskiĭ, *et al.*, *Deformation Strengthening and Failure of Polycrystalline Materials* (Naukova Dumka, Kiev, 1987) [in Russian].
9. N. A. Koneva and É. V. Kozlov, Izv. Vyssh. Uchebn. Zaved., Fiz., No. 2, 87 (1990).
10. G. F. Sarafanov, Fiz. Met. Metalloved., No. 3, 46 (1998).
11. D. L. Holt, J. Appl. Phys. **41**, 3197 (1970).
12. Sh. Kh. Khannanov, Fiz. Met. Metalloved., No. 10, 34 (1992).
13. Sh. Kh. Khannanov, Fiz. Met. Metalloved., No. 2, 31 (1994).
14. G. F. Sarafanov, Fiz. Tverd. Tela (St. Petersburg) **39** (9), 1575 (1997) [Phys. Solid State **39**, 1403 (1997)].
15. G. F. Sarafanov, Fiz. Tverd. Tela (St. Petersburg) **43** (6), 1041 (2001) [Phys. Solid State **43**, 1077 (2001)].
16. Yu. L. Klimontovich, *Statistical Physics* (Nauka, Moscow, 1982; Harwood Academic, New York, 1986).
17. J. P. Hirth and J. Lothe, *Theory of Dislocations* (McGraw-Hill, New York, 1967; Atomizdat, Moscow, 1972).
18. J. W. Cahn, Acta Metall. **14**, 1685 (1966).
19. V. V. Rybin, *High Plastic Deformations and Fracture of Metals* (Metallurgiya, Moscow, 1986) [in Russian].
20. V. A. Likhachev and R. Yu. Khaĭrov, *Introduction to Disclination Theory* (Leningr. Gos. Univ., Leningrad, 1975) [in Russian].
21. V. I. Vladimirov and A. E. Romanov, *Disclinations in Crystals* (Nauka, Leningrad, 1986) [in Russian].

Translated by L. Man

Crystallography Reports, Vol. 49, No. 5, 2004, pp. 820–827. Translated from Kristallografiya, Vol. 49, No. 5, 2004, pp. 909–916.
Original Russian Text Copyright © 2004 by Reznichenko, Shilkina, Gagarina, Yuzyuk, Razumovskaya, Kozinkin.

REAL STRUCTURE OF CRYSTALS

Crystallographic Shear in Niobium Oxides of Different Compositions

L. A. Reznichenko, L. A. Shilkina, E. S. Gagarina, Yu. I. Yuzyuk,
O. N. Razumovskaya, and A. V. Kozinkin
Institute of Physics, Rostov State University, pr. Stachki 194, Rostov-on-Don, 344104 Russia
e-mail: alex@ip.rsu.ru

Received March 4, 2003

Abstract—Defect structures related to crystallographic displacement are revealed in niobium oxides of different composition (Nb_2O_5, $NaNbO_3$, and solid solutions based on $NaNbO_3$) by X-ray powder diffraction, X-ray fluorescence spectroscopy, and Raman scattering. It is suggested that lattice shear in $NaNbO_3$ and $NaNbO_3$-based solid solutions lead to the block structure of crystals. The effect of the thermodynamic history of objects under study on the formation of a defect structure of this type is demonstrated. *© 2004 MAIK “Nauka/Interperiodica”.*

INTRODUCTION

It was suggested by us in [1, 2] that crystallographic shear planes exist in Ti-containing complex oxides with perovskite structure. Shear planes are formed due to the annihilation of anion vacancies, which arise due to the tendency of titanium to change its valence easily. This work continues the studies performed in [3]; it is devoted to complex oxides and their solid solutions containing niobium, which, like titanium, belongs to transition metals with unstable electronic structure and tends to change its oxidation state easily: $5^+ \longleftrightarrow 4^+$.

The crystal structure of binary and some ternary niobium oxides is very similar to the structure of ReO_3 (composed of ReO_6 octahedra with shared vertices) since it also contains two sets of almost orthogonal shear planes, which, extending through the entire crystal, partition it into blocks [4]. When blocks become jointed, unoccupied octahedral and tetrahedral positions arise in the lattice. The degree of filling of these positions may affect significantly the macroscopic properties of the crystals. Such block structures were found, for example, in Nb_2O_5–TiO_2, Nb_2O_5–WO_3, and GeO_2–$9Nb_2O_5$ systems [5]. It is known [6] that blocks are formed in a Nb–O system of any composition subjected to a long-term annealing. Various block structures can be observed for the same composition. For example, Nb_2O_5 exists in 14 different polymorphic modifications, 10 of which have a block structure. The most stable one is the high-temperature polymorph Nb_2O_5 (α phase), which is the main raw component of Nb-containing oxides.

OBJECTS OF STUDY AND METHODS OF PREPARATION AND INVESTIGATION OF SAMPLES

We investigated samples of Nb_2O_5, $NaNbO_3$, and some binary solid solutions $(1-x)NaNbO_{3-x}$CII (CII is the second component: $LiNbO_3$, $PbTiO_3$, or $KNbO_3$) with a low concentration x in the range of the orthorhombic phase with the following parameters of perovskite cell: $a = c > b$. The samples under study were either ceramics (obtained by a conventional ceramic technology (C_{CCT}) or hot pressing (C_{HP}) [7]) or single crystals grown by mass crystallization (SC_{MC}) from flux using $NaBO_2$ as a solvent [8]. To prepare the ceramic samples, we used chemically pure Na_2CO_3 and Li_2CO_3 as starting reagents; high-purity PbO and TiO_2; and Nb_2O_5, either high-purity or of the Nbo-Pt grade. In the latter case, some commercially produced sets of Nb_2O_5 with different concentrations of anionic impurity (fluorine) were used [9]. The CII concentration x was varied, as well as the temperature and pressure of the ceramics synthesis (T_{synth} = 1070–1490 K and P = 0–40 MPa, respectively). Samples of $NaNbO_3$ containing no ferroelectric Q phase (which is often present in this compound) were chosen [10, 11].

The structure of the samples was studied by X-ray powder diffraction using DRON-3 and ADP diffractometers (FeK_α radiation; Mn filter; FeK_β radiation; Bragg–Brentano geometry). Ground objects were investigated, which allowed us to eliminate the influence of surface effects, stresses, and textures arising during the ceramics fabrication and the single-crystal growth. Raman spectra were excited by polarized radiation of an argon laser (5145 Å). Measurements were performed in the 180°-reflection geometry and a signal was measured by a Jobin Yvon T64000 triple spectrom-

1063-7745/04/4905-0820$26.00

eter equipped with a CCD detector. The electronic structure of $Na_{0.9}Pb_{0.1}Nb_{0.9}Ti_{0.1}O_3$ was measured by X-ray fluorescence spectroscopy: TiK_{β_5} spectra were recorded using a DRS-2M long-wavelength spectrograph (BKhV-7Cr X-ray tube). A quartz plate with a $(13\bar{4}0)$ surface plane, bent with a radius of 500 mm, was used as a crystal analyzer. TiK_{β_5} spectra were obtained by measuring the intensity for the second-order reflection from the $(10\bar{1}0)$ plane located at an angle of 14° to the surface, with a resolution of 0.7 eV.

RESULTS AND DISCUSSION

α-Nb_2O_5. Commercially produced Nb_2O_5 is almost always multiphase and contains, as a rule, two or three polymorphs, the type and content of which are not regulated by the existing standards and, as a result, are not reproduced from set to set. Generally, the most stable high-temperature phase, α-Nb_2O_5, has the lowest concentration. X-ray diffraction patterns obtained for different sets of Nb_2O_5 with different grades of purity have the following specific features: diffuse scattering is concentrated around main diffraction reflections and manifests itself in diffuse wings or satellites; in the range of large scattering angles θ, the diffuse scattering intensity increases and the profiles of the main lines are strongly broadened and almost merge with the background. In general, the X-ray diffraction patterns indicate the presence of extended defects in Nb_2O_5 (Figs. 1a, 1b).

To stabilize the phase state of Nb_2O_5, we subjected it to a thermal treatment (according to the technique described in [12]) at temperatures in the range 1390–1440 K (depending on the grade of Nb_2O_5 and the set it was taken from). As a result of this treatment, transition from the hetero- to the single-phase (α-Nb_2O_5) state occurred. The X-ray diffraction pattern of the thermally treated α-Nb_2O_5 shows satellites of equal intensity near the $90\bar{3}$ reflection (Fig. 1c), which become most pronounced when annealed ceramics Nb_2O_5 is subjected to hot pressing (at $P = 40$ MPa) (Fig. 1d). These satellites are located asymmetrically with respect to the main maximum. The modulation wavelengths (periods) λ[1] calculated from the positions of c^- and c^+ satellites for some α-Nb_2O_5 samples of different grades, with different impurity compositions, and taken from different sets, are listed in Table 1. It can be easily seen that λ decreases with increasing the concentration of impurities in Nb_2O_5 in going from high-purity samples to commercial-grade (Nbo-Pt) ones and, within the same set, to the sample with the highest concentration of anionic impurities (fluorine) (Table 1, sample 5). The reason for this may be as follows. The α-Nb_2O_5 phase consists of blocks with sizes of 3 × 4 and 3 × 5 octahedra, formed by repetitive $(20\bar{9})$ and (601) shear planes [5]. As is well known [5], Wadsley defects (irregular shear planes, i.e., boundaries between structural elements with blocks of different sizes or orientations) may exist in block structures. These defects, violating

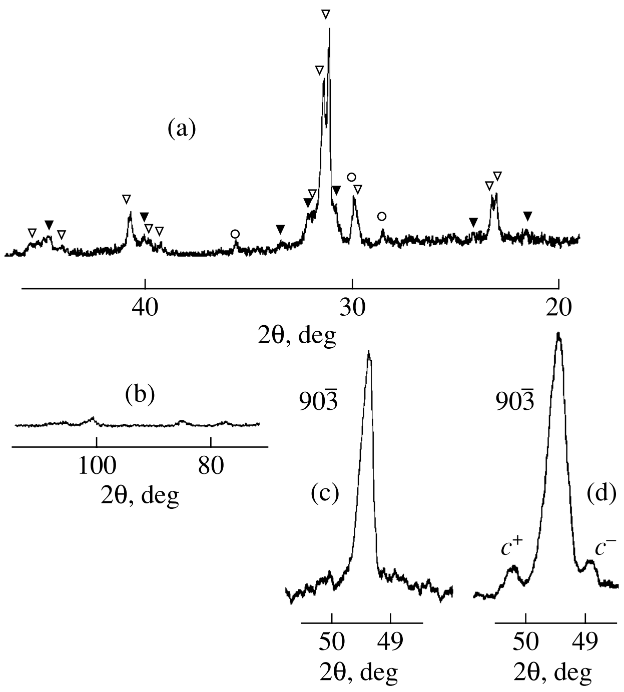

Fig. 1. Fragments of the X-ray diffraction patterns (FeK_α radiation) of the initial Nb_2O_5 compound (a, b) (open triangles, filled triangles, and open circles denote η-Nb_2O_5, α-Nb_2O_5, and L-Nb_2O_5 phases, respectively) and α-Nb_2O_5 samples obtained from the initial Nb_2O_5 by annealing at 1430 K for 2 h (c) with subsequent hot pressing (P = 400 kgf/cm^2, T = 1470 K, 1 h) (d).

Table 1. Modulation wavelengths in the $[90\bar{3}]$ direction for α-Nb_2O_5 samples of different purity grades, taken from different sets

Nb_2O_5 set			λ, Å	
sample no.	serial number	Nb_2O_5 grade	c^- satellite	c^+ satellite
1		Chemically pure	270	200
2		Chemically pure	260	190
3	70	Nbo-Pt	240	180
4	51	Nbo-Pt	240	180
5	47	Nbo-Pt	220	170

---

[1] The measuring method does not make it possible to determine unambiguously the positions of diffuse maxima in the reciprocal space. Therefore, the reported values of λ may differ from the real modulation wavelength in the $[90\bar{3}]$ direction; nevertheless, they give some information on the character of its change in the lattice.

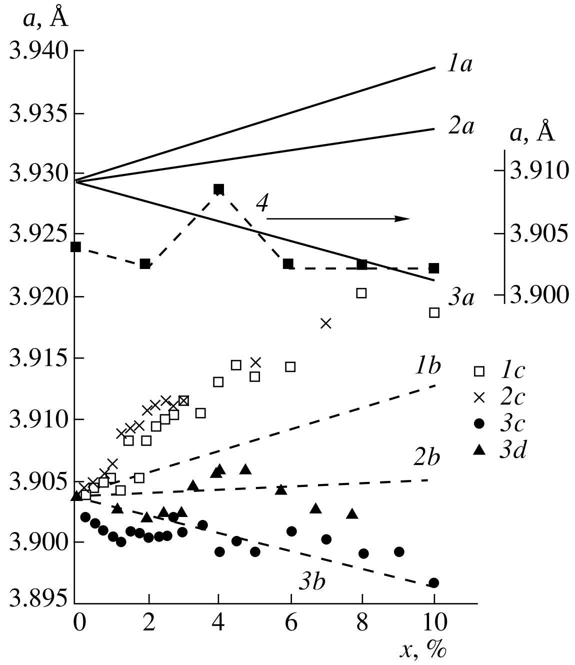

Fig. 2. Concentration dependences of the calculated (y = (a) 0 and (b) 0.04) and experimental values of the average parameter of the perovskite cell for (*1*) $(1 - x)NaNbO_3 - xKNbO_3$, (*2*) $(1 - x)NaNbO_3 - xPbTiO_3$, (*3*) $(1 - x)NaNbO_3$ –– $xLiNbO_3$ (C_{CCT} (c) and SC_{MC} (d)), and (*4*) $Na_{1-x}NbO_{3-x/2}$ solid solutions.

the long-range order in the structure, have a tendency to ordering, which results in the occurrence of diffuse maxima. An increase in the amount of impurities leads to an increase in the density of defects and, accordingly, reduces the value of λ.

$NaNbO_3$ and solid solutions on its basis. The perovskite structure with the general formula ABO_3, as well as Nb_2O_5, can be considered as a derivative from the ReO_3 structure, which, in fact, is the limiting case of perovskites with vacancies in A positions [5, 13]. In perovskites, cubooctahedral voids in the oxygen framework are occupied by large cations with radii R_A ranging from 1.00 to 1.69 Å [13]. Taking into account this circumstance, the formation of the $NaNbO_3$ structure can be regarded as filling of cubooctahedral voids in the α-Nb_2O_5 lattice by Na cations with simultaneous building up the anion sublattice. As a result, a block structure can be inherited by $NaNbO_3$ but with other sizes of blocks and type of their connection. We report below the data indicating the presence of defects of this type in $NaNbO_3$ and a number of solid solutions on its basis.

Table 2. Experimental values of the average parameter of the perovskite cell for $NaNbO_3$ samples synthesized at different temperatures

$\bar{a}_{\text{exper}}$, Å	Synthesis temperature, K	Ratio of the intensities of maximum reflections of the impurity phase and $NaNbO_3$, I_{imp}/I_{110}
3.9050	1070	0.06 – $Na_2Nb_4O_{11}$
3.9047	1220	0.02 – $Na_2Nb_4O_{11}$
3.9044	1420	0.01 – $NaNb_3O_8$
3.9033	1470	<0.01 – $NaNb_3O_8$
3.9035	1490	–

The calculated ($\bar{a}_{\text{calcd}}$) and experimental ($\bar{a}_{\text{exper}}$) average values of the perovskite cell parameters ($\bar{a} = \sqrt[3]{V}$, V is the perovskite-cell volume) for $NaNbO_3$ samples prepared under different conditions were compared. The calculation was performed by the formula [14]

$$\bar{a}_{\text{calcd}} = \frac{\sqrt{2}n_A L_{AO} + 2n_B L_{BO}}{n_A + n_B}, \qquad (1)$$

where L_{AO} and L_{BO} are the lengths of unstrained A–O and B–O bonds, respectively, and n_A and n_B are the valences of A and B cations, respectively. When, according to Belov and Bokii [15], the bond lengths are assumed to be the sums of the ionic radii, $\bar{a}_{\text{calcd}}$ = 3.946 Å. If one uses the value of L_{BO} = 2.01 Å (which is derived from the values of $\bar{a}_{\text{exper}}$ for a large number of perovskite oxides [13] and, thus, is the averaged Nb–O bond length), $\bar{a}_{\text{calcd}}$ = 3.9293 Å. In our calculations, the value of L_{NbO} = 2.01 Å was used. Analysis of the data in the literature and our investigations showed that, in $NaNbO_3$ and the solid solutions considered here [3, 7, 8, 16] (Fig. 2), $\bar{a}_{\text{exper}}$ is much smaller than $\bar{a}_{\text{calcd}}$ and depend strongly on the method of fabrication of the samples under study (Tables 2, 3). The largest of the reported values of $\bar{a}_{\text{exper}(NaNbO_3)}$ is 3.909 Å [17] and the smallest value is 3.900 Å [3]. This indicates that the structure is not ideal. The deviation from ideality can be explained as follows.

In comparison with classical shear structures, in perovskites, simultaneously with the elimination of oxygen vacancies, strictly the same number of A positions are eliminated [18] (Fig. 3). As a result, the composition of sodium niobate corresponds to the formula $Na_{1-y}NbO_{3-y/2}$ (where y is the structural nonstoichiometry, i.e., deficit of A positions) rather than to the formula ABO_3. The value of y can be estimated by adding to formula (1) a multiplier $(1 - y)$ before the first term in the numerator and assuming its value to be equal to $\bar{a}_{\text{exper}}$. Depending on $\bar{a}_{\text{exper}}$, which ranges from 3.900 to 3.909 Å, the corresponding calculated values of y range from 0.079 to 0.035. The value of y = 0.044 corresponds to the most frequently used value of $\bar{a}_{\text{exper}}$ = 3.9035 Å [19].

Obviously, the presence of defects in the form of shear planes indicates that the stoichiometric composition of the blend used in the solid-phase synthesis contains an excess amount of Na with respect to the structure obtained, which is equal to y. The Raman scattering spectra of $(1 - x)NaNbO_3 - xPbTiO_3$ solid solutions (Fig. 4) confirm the deficit of A positions in the structure obtained. The two observed low-frequency peaks at 60 and 74 cm^{-1} are due, according to the data of [20], to vibrations of Na^{+1} ions with respect to NbO_6 octahedra. These peaks correspond to two different positions of Na ions (Na(1) and Na(2)) in the $NaNbO_3$ structure in the antiferroelectric phase [19]. At the transition to the ferroelectric phase, the period along the b axis decreases two times. Since the configurations of the nearest environment of Na(1) and Na(2) ions are very similar in this phase [21], the corresponding doublet transforms into a single line. In the range $0.05 \le x \le 0.20$, with an increase in the content of $PbTiO_3$, the frequency of the ν_x peak shifts according to the simple mass relation:

$$(\nu_{x'}/\nu_{x''})^2 = \{(1-x'')m_{Na} + x''m_{Pb}\}/\{(1-x')m_{Na} + x'm_{Pb}\}. \tag{2}$$

However, the doublet of peaks at 60 and 74 cm^{-1} almost does not shift when $x < 0.05$, although, due to the difference in the Pb and Na masses ($m_{Pb} = 207$, $m_{Na} = 23$), such a shift should be pronounced in the vibrational spectrum even at small values of x. Thus, the substitution of sodium with lead begins only at a certain concentration in the range $0.0275 \le x \le 0.05$. This is confirmed by the X-ray diffraction data reported in [16]. According to these data, when x increases from 0 to $\simeq 0.044$, an increase in $\bar{a}_{exper}$ is observed, which is much more rapid than it should be in the case of substitution of Na with Pb (Fig. 3). In [16], this range of x is related to the formation of an interstitial solid solution. In this case, not only Na^+ are interstitial ions (as was ascertained in [3, 22, 23]), but also some fraction of Ti^{4+} ions (which occupy vacant tetrahedral voids) and Pb^{4+} ions that are always present in real crystals of lead titanate and solid solutions on its basis [23]. Irregular octahedra may also contain Pb^{2+} ions with a radius exceeding that of Na^+ ions (1.26 and 0.98 Å, respectively). The dumbbell-shaped electron shell of Pb^{2+} ions allows them to occupy extended oxygen octahedra along shear planes [22, 23]. Only beginning with $x > y$, when the excess sodium is removed from the blend and unoccupied A positions arise, are substitutional solid solutions formed.

Table 3. Values of $\bar{a}_{exper}$ for $NaNbO_3$ and the $Na_{0.875}Li_{0.125}NbO_3$ solid solution synthesized at different hot-pressing pressures

$\bar{a}_{exper}$, Å		Hot-pressing pressure P, MPa
$Na_{0.875}Li_{0.125}NbO_3$	$NaNbO_3$	
3.900	3.904	0
3.897	3.903	5
3.896	3.903	10
3.894	3.902	20
3.891	3.901	40

The structure nonstoichiometry of $NaNbO_3$ exceeds that of titanates of alkaline-earth metals, cadmium, and lead ($y \sim 0.025$) [1, 2]. An excess of sodium leads to the formation of impurity phases during synthesis of $NaNbO_3$ (predominantly, $Na_2Nb_4O_{11}$, $NaNb_3O_8$, and $NaNb_7O_5F$ compositions) [15]. An increase in T_{synth} and P upon hot pressing reduces the content of impurity phases (which indicates the dissolution of the excess sodium in the initial structure). The simultaneous decrease in $\bar{a}_{exper}$ (Tables 2, 3) indicates that some fraction of Na ions are located in irregular tetrahedral voids expected to be at joints between blocks. The ionic radius of Na^+ is rather small (0.98 Å) and, thus, Na^+ ions may occupy tetrahedral sites, as, for example, in Na_2O [24]. The occupation of tetrahedral sites leads to

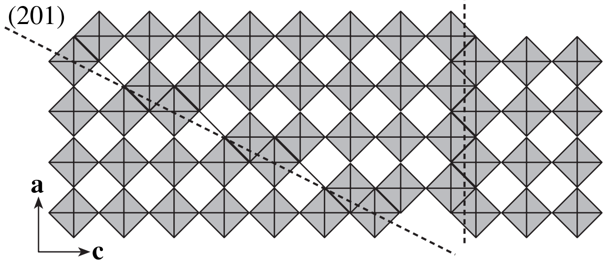

Fig. 3. Crystallographic shear planes (201) and (001) in the structures of the ReO_3 and perovskite ABO_3 types in the (010) section. Hatched squares are BO_6 octahedra, and unhatched squares are either unoccupied (ReO_3) or occupied (A for ABO_3) cubooctahedral positions.

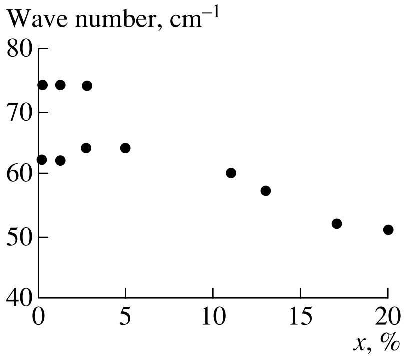

Fig. 4. Concentration dependences of the low-frequency modes in the Raman scattering spectra of the system of $(1 - x)NaNbO_3 - xPbTiO_3$ solid solutions at $x \le 0.2$.

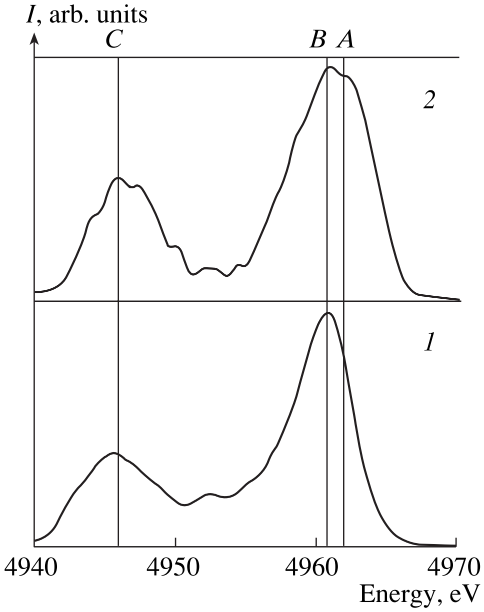

Fig. 5. TiK_{β_5} spectra of the (*1*) standard compound $PbTiO_3$ and (*2*) $Na_{0.9}Pb_{0.1}Nb_{0.9}Ti_{0.1}O_3$ solid solution.

a decrease in $\bar{a}_{exper}$, since the volume of an occupied void in the oxygen framework is smaller than that of an unoccupied one due to the attractive forces acting between oppositely charged ions, while the radius of cations with a coordination number of 4 is smaller than that of cations with a coordination number of 12 in cubooctahedral positions. The decrease in $\bar{a}_{exper}$ for $(1 - x)NaNbO_3 - xLiNbO_3$ solid solutions with $x < 0.01$ is related to the incorporation of lithium into tetrahedral voids [16]. The increase in $\bar{a}_{exper}$ (Fig. 2) for nonstoichiometric $Na_{1-x}NbO_{3-x/2}$ (x = 0.04) [25] to 3.909 Å—the maximum value reported for $NaNbO_3$ in [17]—is in favor of the above conclusions.

The existence of tetrahedral unoccupied positions, which are not characteristic of an ideal ABO_3 structure, has been proved by studying $Na_{0.9}Pb_{0.1}Nb_{0.9}Ti_{0.1}O_3$ solid solutions by X-ray fluorescence spectroscopy. Figure 5 shows the TiK_{β_5} spectra of the solid solution under consideration and the standard compound $PbTiO_3$. It is known [26] that the atomic orbitals or molecular orbitals of environmental ligands coordinated with respect to a metal atom manifest themselves in the TiK_{β_5} spectra. The TiK_{β_5} spectrum of the solid solution under study has the same shape and energy position as the spectra of titanium oxides with the oxidation state of titanium about +4. As can be seen from Fig. 5, two main components (*B* and *C*) manifest themselves in the spectrum of the solid solution, as well as in the standard spectrum. The components *B* and *C* correspond to the interaction of valence *p* orbitals of Ti atoms with 2*p* and 2*s* orbitals of oxygen atoms, respectively. The main distinction observed in the spectrum of the solid solution under study is the distinct manifestation of the component *A*, which is absent in the standard spectrum. It is well known that the high-energy component *A*, which coincides with the peak of the TiK_{β_5} spectrum of metallic Ti, manifests itself in the TiK_{β_5} spectra only in the presence of the metal–metal (Ti–Ti) bond, as, for example, in the rutile (TiO_2) structure or when the environmental symmetry of the Ti atom is reduced (in this case, mixing of *p* and *d* orbitals at one center of the Ti atom becomes possible). The fact that the solid solution under study contains no impurities of metallic Ti and TiO_2 suggests that Ti atoms in this com-

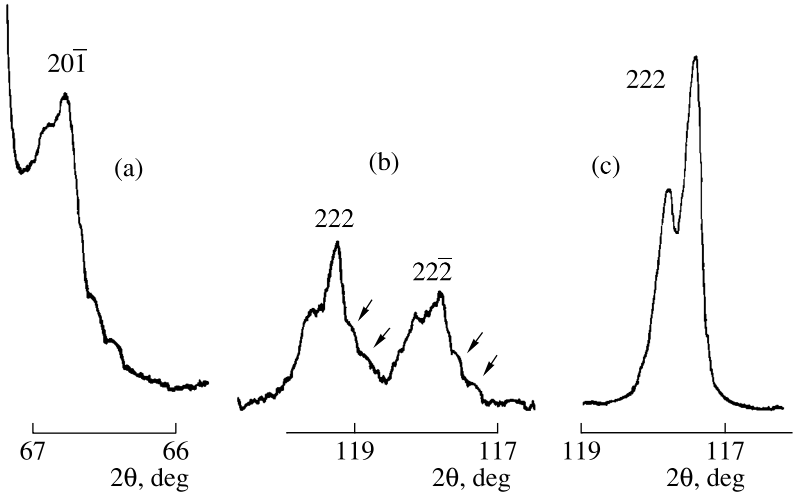

Fig. 6. Diffraction reflections (FeK_α radiation) (a) $20\bar{1}$ and (b) $22\bar{2}$ for $NaNbO_3$ and (c) 222 for the $Na_{0.74}Pb_{0.26}Nb_{0.74}Ti_{0.26}O_3$ solid solution; diffuse maxima are marked by arrows.

Table 4. Parameters of the block structure for $NaNbO_3$ and solid solutions on its basis calculated from the positions of the satellites and main reflections $10\bar{1}$

Sample no.	Sample (composition and method of fabrication)	Satellite	$10\bar{1}$			
			λ, Å	N_{cell}	D, Å	D/λ
1	$Na_{0.98}Li_{0.02}NbO_3$ (SC_{MC})	c_1	58	10.5	~250	~4
2	$Na_{0.9}Li_{0.1}NbO_3$ + 4 mol% Li_2O ($C_{HP} \cdot T_{HP}$ = 1400 K, P = 20 MPa, τ = 1 h)	c_2	75	13.5	~140	~2
3	$Na_{0.9}Li_{0.1}NbO_3$ + 6 mol% Li_2O ($C_{HP} \cdot T_{HP}$ = 1420 K, P = 20 MPa, τ = 1 h)	c_1	56	10.5	~230	~4
4	$Na_{0.98}K_{0.02}NbO_3$ ($C_{HP} \cdot T_{HP}$ = 1450 K, P = 20 MPa, ρ = 1 h)	c_2	84	15	~160	~2
5	$NaNbO_3$ ($C_{HP} \cdot T_{HP}$ = 1470 K, τ = 2 h)	c_1	59	10.5	~185	~3
		c_3	117	21	~220	~2
6	$NaNbO_3$ ($C_{HP} \cdot T_{HP}$ = 1490 K, τ = 2 h)	c_1	56	10	~445	~8
		c_2	80	14	~240	~3
		c_3	117	21	~240	~2

pound are mainly in a tetrahedral rather than octahedral environment.

The diffuse scattering observed in $NaNbO_3$ at room temperature is attributed to the structural disorder along the perovskite axes, but the mechanisms of this phenomenon are still unclear [27, 28]. It is noted that the diffuse scattering along the a^* (c^*) and b^* axes has a different nature. The scattering along the b^* axis is attributed to the violation of the alternation of displacements of Nb atoms perpendicular to the b axis [10, 27]. Obviously, the presence of crystallographic-shear defects caused by the relaxation of stresses in nearby regions should lead to static displacements of atoms only in the direction perpendicular to the shear planes, which would manifest itself in effects of diffuse scattering (Figs. 6a, 6b). In addition, the violation of the regular alternation of atoms caused by crystallographic shear, along with the effects of displacements, will result in asymmetry of diffuse X-ray scattering with respect to the averaged-lattice sites, as can be seen well in the X-ray diffraction patterns of barium, cadmium, and lead titanates [1]. However, the broadening of structural maxima in $NaNbO_3$ is symmetric, which can be related to the mutual compensation of the contributions of O and Na atoms to the diffuse scattering due to both opposite signs of their displacements and the equality of their scattering abilities ($f_{Na^+} \sim f_{O^{2-}}$). Thus, we can estimate the amplitude of atomic displacements u in the [hkl] direction in the approximation of one-dimensional (1D) modulation by the formula [29]:

$$I_{sat}/I_{main}^{hkl} = u^2N^2\pi^2/d_{hkl}^2, \tag{3}$$

where I_{sat} and I_{main} are the intensities of a satellite and the main reflection, respectively; d_{hkl} is the interplane distance, which is modulated sinusoidally in the direct lattice; and N is the number of a site from the corresponding reciprocal-lattice row. The obtained values of u for the $[10\bar{1}]$, $[30\bar{1}]$, and $[20\bar{1}]$[2] directions are 0.140, 0.145, and 0.155 Å, respectively, which is in good agreement with the corresponding displacements of Nb atoms [19] from ideal positions in the perovskite cell. Thus, the diffuse scattering near the structural maxima $h0l$ is determined mainly by displacements of Nb atoms. It is noteworthy that no significant broadening of X-ray reflections is observed for the $Na_{1-x}Pb_xNb_{1-x}Ti_xO_3$ (x = 0.26) solid solution (Fig. 6c). Taking into consideration the coincidence of the parameters $\bar{a}_{exper}$ and $\bar{a}_{calcd}$ for this solid solution, we believe that the density of defects related to crystallographic shear planes is very small [16]. Therefore, we may suggest that the diffuse scattering observed in $NaNbO_3$ is due to crystallographic shear defects. Since Nb atoms are displaced in the $[20\bar{1}]$ direction in $NaNbO_3$ and the 1D modulation occurs in the same direction, the shear planes in $NaNbO_3$ are, apparently, planes of the {201} type, which form blocks with mutually perpendicular boundaries. In this case, the double maxima of diffuse scattering observed on the main-reflection wings (Figs. 6a, 6b) may correspond to either nonquadratic blocks or blocks of different sizes.

Along with the diffuse maxima on the line wings, we observed maxima before the $10\bar{1}$, 110, 101 multiplet [3, 11]. According to the data obtained by studying various samples, these satellites do not always manifest themselves as one, two, or (very seldom) three diffuse maxima and cannot be attributed to any of the known

---

[2] The indices of the planes and directions used here correspond to the perovskite axes a, b, and c.

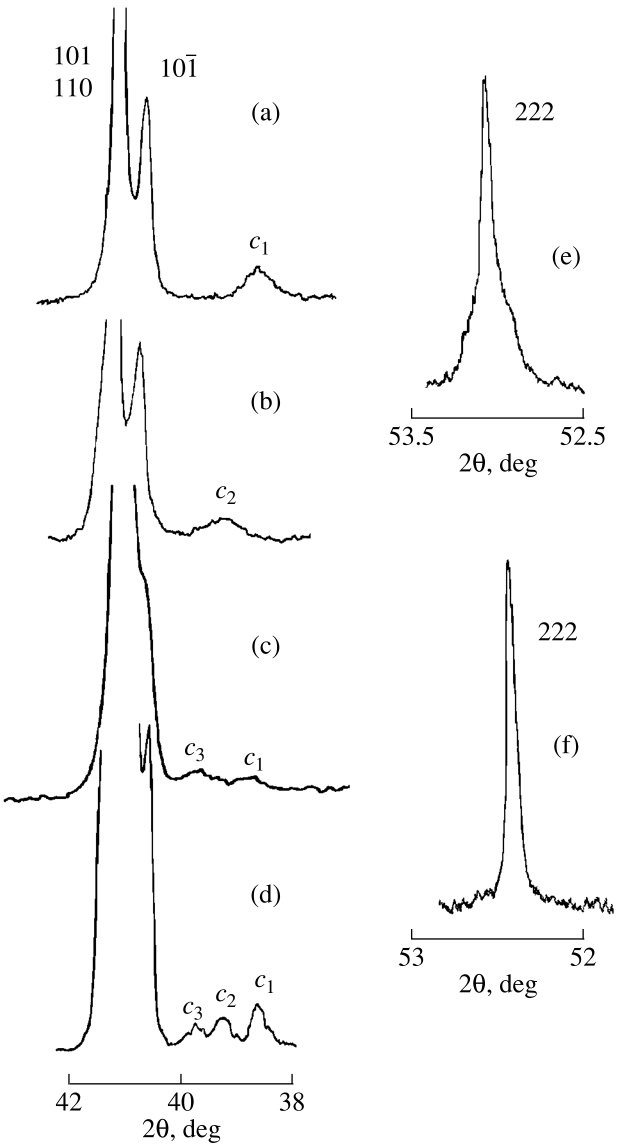

Fig. 7. Fragments of the X-ray diffraction patterns of different $NaNbO_3$ and $Na_{1-x}Li_xNbO_3$ samples (a–d): samples (a) 1, (b) 2, (c) 5, and (d) 6 (see Table 4; FeK_α radiation); diffraction reflections 200 for the cubic phase: (e) ground $NaNbO_3$ single crystals at 950 K, and (f) $Na_{0.74}Pb_{0.26}Nb_{0.74}Ti_{0.26}O_3$ ceramics at 450 K (FeK_β radiation).

impurities that may be present in the samples. Figure 7a shows the corresponding fragments of X-ray diffraction patterns for a number of investigated objects. Table 4 contains values of λ with respect to main reflection $10\bar{1}$, $N_{cell} = \lambda/2d_{10\bar{1}}$, and λ/*D*, where *D* is the size of the coherent-scattering regions calculated from the width of the diffuse maxima. As can be seen from Table 4, there are three characteristic values of λ for samples with different compositions obtained by different methods. Almost all the samples show the c_1 maximum with λ ~ 56–59 Å. This maximum is identified as $6/5.0.\bar{3}/5$, which corresponds to the planes parallel to $(20\bar{1})$. The indices of the other diffuse maxima are as follows: $\bar{6}/5.1/2.2/5$ (c_2) and $6/5.1/4.3/5$ (c_3). The multiplicity of the indices *h*, *l* 1/5 can be related to the block structure of α-Nb_2O_5, the unit cell of which contains blocks of five octahedra. The available X-ray diffraction data do not make it possible to interpret unambiguously the diffuse scattering observed. Nevertheless, we can suggest that it is due to either the short-range order caused by displacements in the structure or the formation of clusters with ordered blocks in the matrix structure. The introduction of CII, apparently, increases the volume of the regions of disordered structure, since the satellites $c_1 - c_3$ are observed more often for solid solutions with compositions similar to $NaNbO_3$ than for the pure compound.

High-temperature investigations showed that the diffuse maxima both before the multiplet $10\bar{1}$, 110, 101 [11] and in the vicinity of the line wings are retained up to the cubic phase. Figures 7e and 7f show the profiles of the diffraction reflections 200 for $NaNbO_3$ and $Na_{0.74}Pb_{0.26}Nb_{0.74}Ti_{0.26}O_3$ in the cubic phase. In the latter compound, as was mentioned above, the density of crystallographic shear defects is very small (close to zero). This additionally confirms the relationship between the observed diffuse scattering and the quasi-regular defect structure and indicates the stable character of the latter.

CONCLUSIONS

Thus, the structures containing BO_6 octahedra with shared vertices, in which *B* ions have a variable valence, are characterized by crystallographic shear defects, which are responsible for the conservation of the highly ordered structure in anion-deficient oxides. The experimental results are reported, which indicate the presence of defects of such a kind in the $NaNbO_3$ compound and a number of solid solutions on its basis. The obtained experimental data—the decrease in the volume with respect to the ideal structure ($\bar{a}_{exper} < \bar{a}_{calcd}$), good agreement between the calculated and experimentally evaluated structural nonstoichiometry, the presence of tetrahedral voids in the close-packed perovskite structure, the diffuse-scattering effects, and the observed dependences of these effects and the value of $\bar{a}_{exper}$ on the method and conditions of sample preparation—indicate the presence of extended defects (crystallographic shear planes and blocks) in the crystals under consideration.

ACKNOWLEDGMENTS

This study was supported in part by the Russian Foundation for Basic Research, project no. 02-02-17781.

REFERENCES

1. L. A. Reznichenko, L. A. Shilkina, S. V. Titov, and O. N. Razumovskaya, in *Proceedings and Abstracts of International Symposium on Ordering in Minerals and Alloys, OMA-2000* (Rostov-on-Don, 2000), p. 127.
2. L. A. Reznichenko, L. A. Shilkina, S. V. Titov, and O. N. Razumovskaya, Kristallografiya **48** (3), 421 (2003) [Crystallogr. Rep. **48**, 377 (2003)].
3. L. A. Reznichenko, L. A. Shilkina, S. V. Titov, *et al.*, in *Proceedings and Abstracts of International Symposium on Ordering in Minerals and Alloys, OMA-2000* (Rostov-on-Don, 2000), p. 111.
4. J. S. Anderson, B. Collen, U. Knylenstiren, and A. Magneli, Acta Chem. Scand. **11**, 1641 (1957).
5. C. N. R. Rao and J. Gopalakrishnan, *New Directions in Solid State Chemistry* (Cambridge Univ. Press, Cambridge, 1986; Nauka, Novosibirsk, 1990).
6. Yu. D. Tret'yakov, *Chemistry of Nonstoichiometric Oxides* (Mosk. Gos. Univ., Moscow, 1974) [in Russian].
7. L. A. Reznichenko and L. A. Shilkina, Izv. Akad. Nauk SSSR, Ser. Fiz. **39** (5), 1118 (1975).
8. E. S. Gagarina, L. A. Shilkina, L. A. Reznichenko, *et al.*, Izv. Ross. Akad. Nauk, Ser. Fiz. **65** (6), 780 (2001).
9. L. A. Reznichenko, O. N. Razumovskaya, L. A. Shilkina, *et al.*, Izv. Akad. Nauk SSSR, Neorg. Mater. **24** (10), 1708 (1988).
10. I. Lefkowitz, K. Lukaszewiecz, and H. D. Megaw, Acta Crystallogr. **20**, 670 (1966).
11. L. A. Reznichenko, L. A. Shilkina, E. S. Gagarina, *et al.*, Kristallografiya **48** (3), 493 (2003) [Crystallogr. Rep. **48**, 448 (2003)].
12. E. M. Kuznetsova, L. A. Reznichenko, O. N. Razumovskaya, and L. A. Shilkina, Pis'ma Zh. Tekh. Fiz. **27** (5), 36 (2001) [Tech. Phys. Lett. **27**, 189 (2001)].
13. E. G. Fesenko, *Perovskite Family and Ferroelectricity* (Atomizdat, Moscow, 1972) [in Russian].
14. V. P. Sakhnenko, E. G. Fesenko, A. T. Shuvaev, *et al.*, Kristallografiya **17** (2), 316 (1972) [Sov. Phys. Crystallogr. **17**, 268 (1972)].
15. G. B. Bokiĭ, *Introduction to Crystal Chemistry* (Mosk. Gos. Univ., Moscow, 1954) [in Russian].
16. L. A. Reznichenko, L. A. Shilkina, O. N. Razumovskaya, *et al.*, Izv. Ross. Akad. Nauk, Neorg. Mater. **39** (2), 187 (2003).
17. E. A. Wood, Acta Crystallogr. **4**, 353 (1951).
18. A. G. Petrenko and V. V. Prisedskiĭ, *Structure Defects in Ferroelectrics* (Uchebno-Metod. Kab. Vyssh. Obraz., Kiev, 1989) [in Russian].
19. A. C. Sakowski-Cowley, K. Lukaszewiecz, and H. D. Megaw, Acta Crystallogr., Sect. B: Struct. Crystallogr. Cryst. Chem. **25**, 851 (1969).
20. Z. X. Shen, X. B. Wang, M. H. Kuok, and S. H. Tang, J. Raman Spectrosc. **29**, 379 (1998).
21. V. A. Shuvaeva, M. Yu. Antipin, S. V. Lindeman, *et al.*, Ferroelectrics **141**, 307 (1993).
22. S. V. Titov, L. A. Shilkina, O. N. Razumovskaya, *et al.*, in *Proceedings and Abstracts of International Symposium on Ordering in Minerals and Alloys*, *OMA-2000* (Rostov-on-Don, 2000), p. 167.
23. S. V. Titov, L. A. Shilkina, O. N. Razumovskaya, *et al.*, Izv. Ross. Akad. Nauk, Neorg. Mater. **37** (7), 849 (2001).
24. I. Naray-Szabo, *Kristalykemia* (Akademia Kiado, Budapest, 1969).
25. L. A. Reznichenko, O. N. Razumovskaya, L. A. Shilkina, *et al.*, Zh. Tekh. Fiz. **72** (3), 43 (2002) [Tech. Phys. **47**, 325 (2002)].
26. V. I. Nefedov, É. Z. Kurmaev, M. A. Poraĭ-Koshits, *et al.*, Zh. Strukt. Khim., No. 4, 637 (1972).
27. C. N. W. Darlington, Ferroelectrics **3**, 9 (1971).
28. F. Denoyer, R. Comes, and M. Lambert, Acta Crystallogr., Sect. B: Struct. Crystallogr. Cryst. Chem. **27**, 414 (1971).
29. A. Guinier, *Théorie et Technique de la Radiocristallographie* (Dunod, Paris, 1956; Fizmatgiz, Moscow, 1961).

Translated by Yu. Sin'kov

Crystallography Reports, Vol. 49, No. 5, 2004, pp. 828–831. Translated from Kristallografiya, Vol. 49, No. 5, 2004, pp. 917–920.
Original Russian Text Copyright © 2004 by Nepochatenko.

Comparative Analysis of Two Methods of Calculation of the Orientation of Domain Walls in Ferroelastics

V. A. Nepochatenko

Bila Tserkva State Agrarian University, Sobornaya pl. 8/1, Bila Tserkva, Kiev oblast, 09117 Ukraine

e-mail: aaa@btsau.kiev.ua

Received January 27, 2003

Abstract—Two types of domain-wall equations are analyzed: the equations derived by the Sapriel method and the equations obtained by interface matching of the thermal-expansion tensor. It is shown that, for *W*-type domain walls, these methods yield the same equations. For *W*'-type domain walls, the equations obtained by different methods coincide for proper ferroelastics and differ for improper ferroelastics. © *2004 MAIK "Nauka/Interperiodica".*

INTRODUCTION

The method proposed by Sapriel [1] is considered a basic and well-recognized method for deriving the domain-wall equations for ferroelastic materials. It is based on the matching of the spontaneous-strain tensor at the interface between different orientation states. Sapriel demonstrated that two types of domain walls are possible: *W* and *W*' [1]. The *W*' orientation depends on the components of a spontaneous-strain tensor, whereas the *W* orientation corresponds to the symmetry plane for the paraelastic phase.

However, this method cannot be used for determining the orientation of domain walls in crystals containing no regions of paraelastic phase. Application of this method to improper ferroelastics is also problematic, since spontaneous strain is not an order parameter for these crystals.

Along with the Sapriel method [1], another approach was proposed [2, 3], which is based on the matching of the thermal-expansion tensor at a domain wall. This method implies that the material remains continuous when its temperature varies. This method is not related to the order parameter of the phase transition and can be used for any domains differing in the strain tensor with respect to the chosen frame of reference.

In this context, it is of interest to analyze the domain-wall equations derived by the two above methods by examples of proper and improper ferroelastics. Since the determination of the domain-wall equations for crystals without the paraelastic phase is a challenge for the theory, we will use the method reported in [2] to find the domain-wall equations without introducing the parameters and symmetry characteristics of the paraelastic phase and then analyze the obtained equations. As model objects, we chose pure ferroelastics [4] $Pb_3(PO_4)_2$ and $BiVO_2$.

DOMAIN-WALL EQUATIONS FOR THE IMPROPER FERROELASTIC $Pb_3(PO_4)_2$ IN THE REFERENCE FRAME CORRESPONDING TO THE β-PHASE

Lead orthophosphate $Pb_3(PO_4)_2$ is the most thoroughly studied pure improper ferroelastic and exhibits a first-order phase transition to the $\bar{3}mF2/m$ phase [5]. Three orientation states and two types of domain walls, *W* and *W*', are formed in the ferroelastic α-phase [6, 7]. The orientation of domain walls corresponds to the symmetry elements (lost at the phase transition) of the paraelastic β-phase: the *W* type corresponds to the symmetry plane, and *W*' type corresponds to the twofold axis. An increase in a spontaneous strain is accompanied by changes in the orientation of crystallographic axes in a multidomain crystal. At 20°C, the angles between monoclinic axes *b* in adjacent domains separated by *W*- and *W*'-type walls are equal to 58° ± 1° and 118° ± 1°, respectively [8].

Let us choose the following orthogonal frame of reference: the X_1 axis is parallel to the *c* axis, the X_2 axis is parallel to the *b* axis, and the X_3 axis makes angle $\varphi = \beta - 90°$ with the *a* axis. We denote by C_1, C_2, and C_3 different orientation states. Let X_{0i} be the coordinate axes in the β-phase. The orientation state C_2 is obtained from the state C_1 by rotating the latter by an angle of 120° around the X_3 axis.

Let us consider the equations for domain walls separating the C_1 and C_2 states in the frame of reference of C_1. In this frame of reference, the spontaneous-strain tensor has the form [9]

$$S_1 = \begin{pmatrix} -a & 0 & c \\ & a & 0 \\ & & 0 \end{pmatrix}, \quad (1)$$

where $a = -0.5(e_{11} - e_{22})$, $c = e_{13}$.

According to [1], we have the following domain-wall equations:

$$X_{01} - \frac{\sqrt{3}}{3}X_{02} = 0, \tag{2}$$

$$X_{01} + \sqrt{3}X_{02} - \frac{2c}{a}X_{03} = 0, \tag{3}$$

where a and c are the components of the spontaneous-strain tensor.

Let us use the second method. In the β-phase, we choose a vector $\mathbf{r}_0$ in the frame of reference corresponding to C_1. In going to the α-phase, this vector transforms into $\mathbf{r}_1$. The thermal-expansion tensor has the form

$$T = \begin{pmatrix} e_{11} & 0 & e_{13} \\ & e_{22} & 0 \\ & & e_{33} \end{pmatrix}. \tag{4}$$

Hence, the components of the vector $\mathbf{r}_1$ can be derived from the equations

$$\begin{aligned} X_1 &= (1 + e_{11})X_{01} + e_{13}X_{03}, \\ X_2 &= (1 + e_{22})X_{02}, \\ X_3 &= e_{13}X_{01} + (1 + e_{33})X_{03}. \end{aligned} \tag{5}$$

In the β-phase, let us pass to the frame of reference corresponding to C_2 as a result of rotation of C_1 around the X_{03} axis by an angle α. In the new frame of reference, we find the components of the vector $\mathbf{r}_0$ from the equations

$$X'_{0i} = c_{ij}X_{0j}, \tag{6}$$

where c_{ij} is the transformation matrix. In this frame of reference, we find the components of $\mathbf{r}_1$ similar to (5),

$$\begin{aligned} X'_1 &= (1 + e_{11})(X_{01}\cos\alpha + X_{02}\sin\alpha) + e_{13}X_{03}, \\ X'_2 &= (1 + e_{22})(-X_{01}\sin\alpha + X_{02}\cos\alpha), \\ X'_3 &= e_{13}(X_{01}\cos\alpha + X_{02}\sin\alpha) + (1 + e_{33})X_{03}. \end{aligned} \tag{7}$$

The vector $\mathbf{r}_1$ has the same length in different frames of reference. As a result, we have

$$\begin{aligned} X_{01}^2 - X_{02}^2 + 2X_{01}X_{02}A_{12} + 2X_{01}X_{03}A_{13} \\ + 2X_{02}X_{03}A_{23} = 0, \end{aligned} \tag{8}$$

where

$$A_{12} = -\cot\alpha, \quad A_{13} = m/(1 + \cos\alpha),$$

$$A_{23} = -m/\sin\alpha, \; m = \frac{e_{13}(2 + e_{11} + e_{33})}{(1 + e_{11})^2 - (1 + e_{22})^2 + e_{13}^2}.$$

Under the condition

$$\det|A_{ij}| = 0, \tag{9}$$

Equation (8) corresponds to the domain-wall equations

$$X_{01} + BX_{02} = 0, \tag{10}$$

$$X_{01} + NX_{02} + KX_{03} = 0, \tag{11}$$

where $B = \sin\alpha/(\cos\alpha - 1)$, $N = (1 - \cos\alpha)/\sin\alpha$, and $K = 2m/(\cos\alpha + 1)$.

Substituting α = 120° into Eqs. (10) and (11), we obtain the domain-wall equations for $Pb_3(PO_4)_2$:

$$X_{01} - \frac{\sqrt{3}}{3}X_{02} = 0, \tag{12}$$

$$X_{01} + \sqrt{3}X_{02} + 4mX_{03} = 0. \tag{13}$$

We can see that Eqs. (2) and (12) for W coincide, whereas Eqs. (3) and (13) for W' are different. The angle that the W' wall makes with the $X_{01}0X_{02}$ plane depends on all components of the thermal-expansion tensor, and this is not consistent with Eq. (3). The coefficient $4m$ in Eq. (13) can be written in the form

$$4m = \frac{4e_{13}(2 + e_{11} + e_{33})}{2(e_{11} - e_{22}) + e_{11}^2 - e_{22}^2 + e_{13}^2} \approx -\frac{2c}{a}, \tag{14}$$

where $c = e_{13}$ and $a = -0.5(e_{11} - e_{22})$. It is obvious that the difference between Eqs. (3) and (13) for W' is mainly due to the small second-order terms.

DOMAIN-WALL EQUATIONS FOR $Pb_3(PO_4)_2$ IN THE REFERENCE FRAME CORRESPONDING TO THE α-PHASE

In the α-phase, we choose the frame of reference corresponding to the C_1 state. From the experimental data of [8], we can determine (for a temperature of 20°C) the matrices of transformation to the C_2 frame of reference for W- and W'-type domain walls [10]:

$$\begin{gathered} C'_{ij} = \begin{pmatrix} -0.4693 & 0.883 & 0 \\ -0.883 & -0.4693 & 0 \\ 0 & 0 & 1 \end{pmatrix}, \\ C_{ij} = \begin{pmatrix} -0.5316 & 0.847 & 0.0195 \\ -0.847 & -0.5319 & 0.0108 \\ 0.0195 & -0.0108 & 0.99975 \end{pmatrix}. \end{gathered} \tag{15}$$

For two temperatures (t_1 = 20°C and t_2 = 150°C), we will determine the thermal-expansion tensor from the α-phase lattice constants [11]:

$$e_{ij} = \begin{pmatrix} -0.0093 & 0 & 0.0036 \\ & 0.015 & 0 \\ & & -0.0039 \end{pmatrix}. \qquad (16)$$

Substituting the values of C'_{ij} and e_{ij} into Eqs. (6)–(11), we derive the following equations:

$$X_1 - 0.6X_2 = 0, \qquad (17)$$

$$X_1 + 1.664X_2 - 0.54X_3 = 0. \qquad (18)$$

Similarly, for the C_{ij} matrix, we obtain

$$X_1 - 0.5518X_2 - 0.0126X_3 = 0, \qquad (19)$$

$$X_1 + 1.836X_2 - 0.618X_3 = 0. \qquad (20)$$

Equations (18) and (19) correspond to experimentally observed equilibrium domain walls of the *W* and *W*' types. Equations (17) and (20) describe the orientation of the domain walls with an accuracy of about 2°. We define them as a special solution to Eq. (8) in the frame of reference corresponding to the ferroelastic phase.

DOMAIN-WALL EQUATIONS FOR THE PROPER FERROELASTIC $BiVO_4$ IN THE REFERENCE FRAME CORRESPONDING TO THE β-PHASE

Bismuth vanadate $BiVO_2$ is a pure proper ferroelastic, which exhibits a second-order phase transition $4/mF2/m$ from the tetragonal β-phase to the monoclinic α-phase [12, 13]. Two orientation states (C_1, C_2) and two domain walls of the *W*' type may exist in the ferroelastic phase [1, 14]. The orientation of the domain walls is not determined by the symmetry elements of the high-temperature phase.

Let us choose the following orthogonal frame of reference: the X_1 axis is parallel to the *a* axis, the X_3 axis is parallel to the *c* axis, and the X_2 axis makes angle $\varphi = \gamma - 90°$ with the *b* axis. We denote by X_{0i} the corresponding coordinate axes in the β-phase. We will find the domain-wall equations in the frame of reference corresponding to C_1. In this frame of reference, the spontaneous-strain tensor has the form

$$S_1 = \begin{pmatrix} -a & b & 0 \\ & a & 0 \\ & & 0 \end{pmatrix}, \qquad (21)$$

where $a = -0.5(e_{11} - e_{22})$ and $b = e_{12}$. According to [1], we obtain the following domain-wall equations:

$$X_{01} - PX_{02} = 0, \qquad (22)$$

$$X_{01} + \frac{1}{P}X_{02} = 0, \qquad (23)$$

where $P = \dfrac{b + \sqrt{a^2 + b^2}}{a}$ and *a* and *b* are the components of the tensor S_1.

Using the method based on the interface matching of the thermal-expansion tensor, we derive the following equations:

$$X_{01} - KX_{02} = 0, \qquad (24)$$

$$X_{01} + \frac{1}{K}X_{02} = 0, \qquad (25)$$

where $K = -(2e_{12} + \sqrt{4e_{12}^2 + (e_{11} - e_{22})^2}\,)^2)/(e_{11} - e_{22})$. One can show that the coefficients *K* and *P* have the same values. Hence, for *W*'-type domain walls, Eqs. (22) and (24) coincide with each other, as well as Eqs. (23) and (25).

DISCUSSION AND CONCLUSIONS

The analysis performed shows that the equations for the *W*'-type domain walls derived by the two calculation methods coincide for a proper ferroelastic and differ for an improper ferroelastic. The equations for the latter case depend on all components of the thermal-expansion tensor for the crystal. Therefore, in addition to a small difference in orientations, their temperature dependence differs from that reported in [1]. Note that this difference is related mainly to the contribution of the squared components of the thermal-expansion tensor of the crystal.

The equations for the *W*-type domain walls are completely determined by the symmetry elements of the paraelastic phase and do not depend on either the spontaneous-strain tensor or the thermal-expansion tensor of a crystal. When finding the domain-wall equations in the frame of reference corresponding to the ferroelastic phase, one should take into account that singular solutions characterized by certain errors can arise in this case. Therefore, it is undesirable to find equations for the *W*'-type domain walls in improper ferroelastics by the Sapriel method because, in this case, the equations do not meet the conditions of matching for the components of the thermal-expansion tensor and such domain walls cannot be considered equilibrium ones.

ACKNOWLEDGMENTS

I am grateful to S.A. Minyukov for valuable comments.

REFERENCES

1. J. Sapriel, Phys. Rev. B **12** (11), 5128 (1975).

2. V. A. Nepochatenko, Kristallografiya **47** (3), 514 (2002) [Crystallogr. Rep. **47**, 467 (2002)].
3. V. A. Nepochatenko, in *Abstracts of Scientific and Practical Conference* (Belaya Tserkov’, 1994), p. 90.
4. L. A. Shuvalov, Izv. Akad. Nauk SSSR, Ser. Fiz. **43** (8), 1554 (1979).
5. V. Keppler, Z. Kristallogr. **132**, 228 (1970).
6. L. H. Brixner, P. E. Bierstedt, W. F. Jaep, and J. R. Barkley, Mater. Res. Bull. **8**, 497 (1973).
7. E. F. Dudnik, E. V. Sinyakov, V. V. Gene, and S. V. Vagin, Fiz. Tverd. Tela (Leningrad) **17**, 1212 (1975) [Sov. Phys. Solid State **17**, 1212 (1975)].
8. M. Chabin, J. P. Ildefonse, and F. Gilletta, Ferroelectrics **13**, 333 (1976).
9. J. C. Toledano, L. Pateau, J. Primot, *et al.*, Mater. Res. Bull. **10**, 103 (1975).
10. V. A. Nepochatenko, Kristallografiya **48** (2), 324 (2003) [Crystallogr. Rep. **48**, 290 (2003)].
11. C. Joffren, J. P. Benoit, L. Deschamps, and M. Lambert, J. Phys. (Paris) **38** (2), 205 (1977).
12. A. W. Sleight and H. Y. Chen, Mater. Res. Bull. **14** (12), 1571 (1979).
13. W. J. F. David, A. Glazer, and A. W. Hewat, Phase Transit. **1** (4), 155 (1979).
14. C. Manolikas and S. Amelinckx, Phys. Status Solidi A **60**, 167 (1980).

Translated by K. Kugel

Crystallography Reports, Vol. 49, No. 5, 2004, pp. 832–842. Translated from Kristallografiya, Vol. 49, No. 5, 2004, pp. 921–931.
Original Russian Text Copyright © 2004 by Korotkov, Shuvalov.

LATTICE DYNAMICS AND PHASE TRANSITIONS

Transitions to the Relaxor and Dipole-Glass States in Mixed Crystals of the Potassium Dihydrogen Phosphate Family

L. N. Korotkov* and L. A. Shuvalov**
** Voronezh State Technical University, Moskovskiĭ pr. 14, Voronezh, 394026 Russia*
*** Shubnikov Institute of Crystallography, Russian Academy of Sciences,*
Leninskiĭ pr. 59, Moscow, 119333 Russia
e-mail: l_korotkov@mail.ru

Received July 8, 2003

Abstract—Regularities of the formation of the relaxor and dipole-glass states in the systems of mixed ferroelectric–antiferroelectric crystals of the potassium dihydrogen phosphate family are discussed. The problems related to the crystal structure, lattice dynamics, and relaxation processes in dipole glasses and relaxors implemented in systems of this type are considered. *© 2004 MAIK "Nauka/Interperiodica".*

1. INTRODUCTION

In recent years, ferroelectrics with a strongly diffuse phase transition (relaxors) and dipole glasses have attracted much attention from researchers. These compounds are typical paraelectrics in the high-temperature phase; however, below the temperature of the transition to the relaxor or dipole-glass state, they demonstrate properties universal for glassy systems, including canonical glasses [1, 2].

At the transition to the dipole-glass state, freezing of some oscillation modes of atoms of one or several sublattices occurs, which is responsible for the random orientation of the relevant electric dipole moments. The main reason for the glassy state is the presence of either random alternating dipole–dipole interactions in the system or sources of random fields, due to which transitions to the dipole-glass state occur instead of ferroelectric or antiferroelectric phase transitions.

A much larger number of hypotheses has been proposed to explain the spread of the ferroelectric phase transition and the transition to the relaxor state, which is observed predominantly in compounds of the oxygen-octahedron type [3–5]. At the same time, relaxor ferroelectrics and dipole glasses have much in common. This was discovered in the course of investigation of various systems demonstrating glass-like behavior. The common feature of all these systems is the violation of order in the atomic arrangement, at least, in one of the crystal sublattices. Mixed ferroelectric–antiferroelectric crystals of the potassium dihydrogen phosphate (KDP) family are a typical example of such systems.

2. PARENT COMPOUNDS

The parent compounds of the systems under consideration are of the general formula $M^*H_2^*R^*O_4$, where M^* is K, Rb, Cs, or NH_4; R^* is P or As; and H* is H or D. At room temperature, these crystals have a tetragonal crystal structure of the $\bar{4}2m$ $\bar{1}$ $\bar{4}2d$ class [3]. In the compounds in which $M^* \neq NH_4^*$, a decrease in temperature results in the ferroelectric phase transition; below the Curie point T_C, the symmetry is reduced to the orthorhombic symmetry of the $mm2$, $Fdd2$ class.

The phase transition is due to the ordering of protons in the net of hydrogen O–H···O bonds, which are dynamically disordered above T_C [3, 6]. The protons are ordered in such a way that two of them are located at either the top or bottom part of each R^*O_4 tetrahedron. This leads to a displacement of M^* and R^* cations along the tetragonal axis *c* of the crystal and occurrence of spontaneous polarization, the vector of which is parallel to the *c* axis. The oxygen–proton configurations formed below T_C correspond to the antiferroelectric ordering of dipole moments in the *ab* plane, which is perpendicular to the polar axis. Thus, the phase transition in KDP can be considered ferroelectric and antiferroelectric simultaneously [7].

In antiferroelectric compounds $NH_4H_2PO_4$ and $NH_4H_2AsO_4$ and their deuterated analogs, below the phase transition point T_N, the crystal structure becomes an orthorhombic one of the 222, $P2_12_12_1$ class. In the low-temperature phase [6], four protonic (lateral) configurations of H_2PO_4 are predominantly implemented. Two pairs of antiparallel dipole moments lying in the *ab* plane correspond to these configurations.

All the crystals of the KH_2PO_4 group are characterized by a strong isotopic effect, which manifests itself in an almost twofold increase in the phase-transition temperature and an increase in the spontaneous polarization as a result of substitution of hydrogen by deuterium.

3. T–x PHASE DIAGRAMS OF $K_{1-x}(NH_4)_xH_2PO_4$ SYSTEMS

The T–x phase diagram of the $K_{1-x}(NH_4)_xH_2PO_4$ (KADP–x%) system, plotted on the basis of the results of [8–12], is shown in Fig. 1. In the compounds in which the ammonium concentration $x \le x_F$ ($x_A < x < 1$), transitions to the ferroelectric (antiferroelectric) phase occur. In the intermediate concentration range ($x_F < x < x_A$), the dipole-glass state is implemented. Its formation begins in the vicinity of T^*. However, the temperature of the transition to the glassy state T_g depends on the observation time. In the limit of static measurements, it corresponds to the Vogel–Fulcher temperature T_0.

The T–x phase diagrams of protonated systems $Rb_{1-x}(NH_4)_xH_2PO_4$ (RADP–x%) [13], $Rb_{1-x}(NH_4)_xH_2AsO_4$ (RADA–x%) [14, 15], $Cs_{1-x}(NH_4)_xH_2AsO_4$ [16] and deuterated systems $Rb_{1-x}(ND_4)_xD_2PO_4$ (DRADP–x%) [17, 18] and $Rb_{1-x}(ND_4)D_2AsO_4$ (DRADA–x%) [19, 20] are, generally, similar.

At the same time, the T–x diagrams of arsenate systems (in this case, the phase-transition temperatures for parent compounds differ by a factor of 1.5–2 ($T_C < T_N$)) are significantly asymmetric: the concentration range corresponding to the ferroelectric phase is much narrower than the range in which the antiferroelectric phase exists. The transition temperatures T_C and T_N in the parent compounds of phosphate systems differ only insignificantly, and their T–x diagrams are more symmetric.

Substitution of hydrogen by deuterium leads to a strong increase in T_C, T_N, and T_0 and, in addition, expands the ranges of concentrations x corresponding to the ordered ferroelectric and antiferroelectric phases. Along with this, transitions from the ordered phases to the mixed ones have been revealed in deuterated systems at temperatures far below T_C (T_N) (ferroelectric–dipole-glass and antiferroelectric–dipole-glass phases, respectively). Concerning protonated compounds, transitions to the mixed ferroelectric–dipole-glass state have been revealed only in the RADA [15] and KADA [21] arsenate systems and a transition to the mixed antiferroelectric–dipole-glass state has been revealed in the RADP system [1].

In pseudospin models [22, 23], the isotopic effect is explained by the decrease in the tunneling probability of particles in deuterated crystals. Apparently, the destruction of the long-range ferroelectric or antiferroelectric order near x_F and x_A in KADP and RADP systems is mainly due to the tunnel effect. In deuterated systems, transitions to ordered phases are suppressed predominantly by strong alternating fluctuations of the dipole–dipole interaction energy.

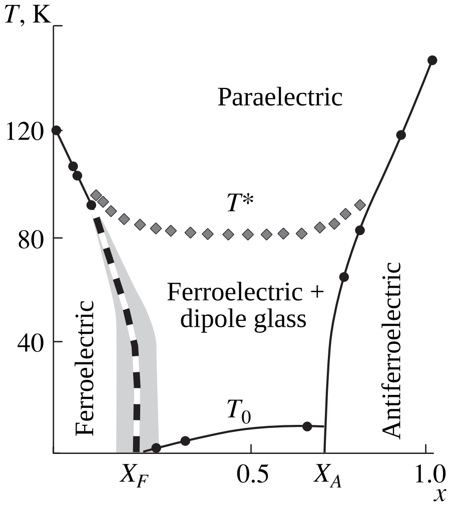

Fig. 1. T–x phase diagram of the $K_{1-x}(NH_4)_xH_2PO_4$ system [8–12].

4. LATTICE STRUCTURE AND DYNAMICS

The crystal structure of the low-temperature phases of mixed crystals with the ammonium concentration $x < x_F$ and $x_A < x < 1$ is similar to that observed for the corresponding parent compounds [24].

Compounds with the ammonium concentration in the intermediate range ($x_F < x \le x_A$) retain the symmetry of the paraelectric phase up to liquid helium temperature. However, below T^* (Fig. 1), local lattice distortions arise, which are responsible for the increase in the diffuse X-ray scattering intensity in the vicinity of the (h, 0, –2) reciprocal-space line (Fig. 2) [25]. Spatial fluctuations in the ab plane begin to evolve below $T^* \sim 100$ K and reach saturation at about 30 K. They have a dynamic character near T^* but become static at low temperatures [25]. The lattice strains arising under these conditions are related to a cluster structure with a correlation length of ~20 Å, which is antecedent to the transition to the dipole-glass state [24–30] at T_g. Analysis of the ^{87}Rb NMR spectra of DRADP crystals showed that the short-range order in the clusters can be described as an antiferroelectric or pseudoantiferroelectric one [17, 31, 32].

In the DRADP compounds in which the ammonium concentration somewhat exceeds x_F, inclusions of a polar phase were found [17, 32]. Similar results were obtained by X-ray analysis of RADP crystals with the ammonium concentration close to x_F [28, 29]. The Bragg peaks due to the ferroelectric phase are weak but

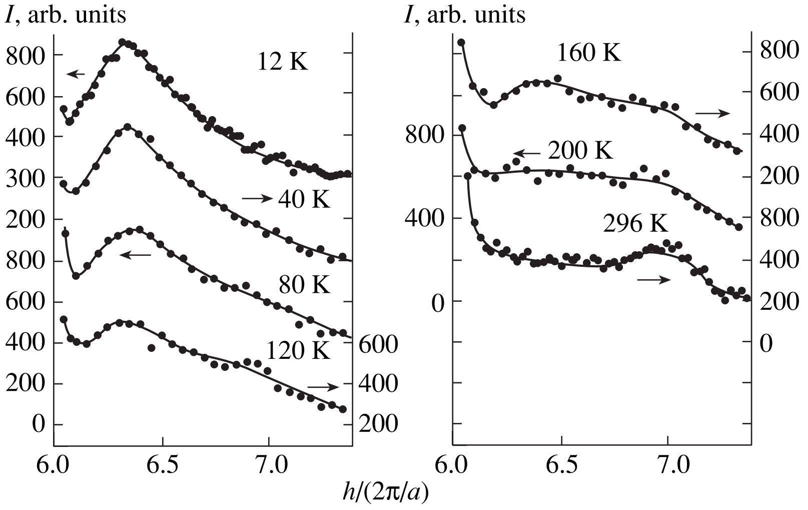

Fig. 2. Dependences of X-ray scattering intensity I on wave vector h in the vicinity of the (h 0 –2) line for an RADP-49 mixed crystal at different temperatures [25].

not broadened. This indicates that the volume of the ferroelectric phase in the dipole-glass matrix is small, whereas the polar regions are fairly large in size. Their total volume in crystals with $x > x_F$ rapidly decreases with an increase in the ammonium concentration. Even at a small excess of x over x_F, the ferroelectric phase has not been observed in X-ray studies [24].

Formation of the cluster structure in the vicinity of T^* is also observed for the ferroelectric and antiferroelectric compositions with x close to x_F and x_A, respectively [24, 28–32]. Figure 3 shows the temperature dependences of the intensity of the diffuse X-ray scattering related to the dipole-glass state and the scattering from the ferroelectric-phase regions in an RADP-20 mixed crystal ($x \sim x_F$) [28]. The lattice distortions characteristic of the dipole-glass state are maximum in the vicinity of the ferroelectric phase transition, which is observed at the temperature T_C^c upon cooling the crystal. With a further decrease in temperature, the distortions decrease with increasing the polar-phase volume. In some temperature range, a mixed dipole-glass–ferroelectric state exists. Upon heating from low temperatures to the temperature $T_C^h > T_C^c$, the ferroelectric phase remains stable, due to which the range of existence of the mixed state narrows (the temperature hysteresis of the ferroelectric phase transition $\Delta T_C = T_C^h - T_C^c \sim 10$ K).

In antiferroelectric compositions with an ammonium concentration similar to x_A, coexistence of the short-range dipole-glass and long-range antiferroelectric orders has been revealed. With a decrease in the ammonium concentration, the total volume and the size of the antiferroelectric-phase regions gradually decrease. In mixed crystals with $x \le x_A$, the antiferroelectric phase is present in the form of small clusters ~100 Å in size [24].

Study of the lattice dynamics by Raman [33–35] and neutron [24, 26, 36] scattering mainly deals with the analysis of temperature dependences of the frequencies of internal modes ν_1 and ν_2 of the PO_4 tetrahedron (which are sensitive to the proton ordering) and the librational mode of NH_4.

For the RADP [33] and KADP [34, 35] systems, a deviation of the temperature dependence of the frequency of the ν_2 mode from the "normal" dependence has been found below $T^* \sim 100$ K. This deviation becomes saturated at about 30 K (Fig. 4). The librational mode of NH_4 at room temperature is strongly damped and diffuse. Upon cooling, this mode narrows

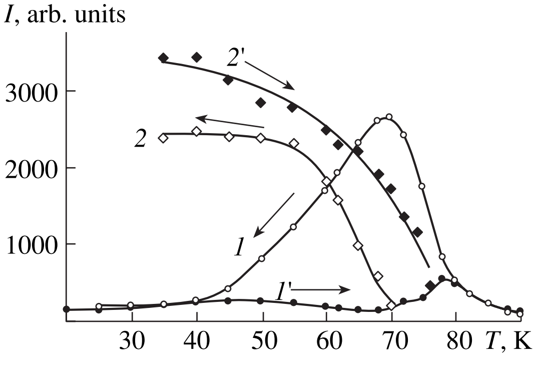

Fig. 3. Dependences of the intensity of X-ray scattering due to the dipole-glass structure with a short-range order (*1*, *1'*) and the ordered orthorhombic phase (*2*, *2'*) measured during cooling (*1*, *2*) and heating (*1'*, *2'*) of an RADP-20 mixed crystal [28].

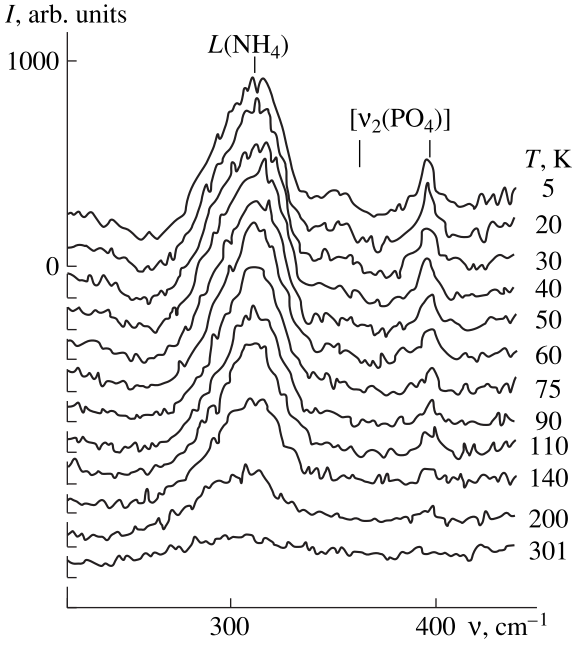

Fig. 4. Raman spectra of an RADP-35 crystal at different temperatures. The librational mode of NH_4 and two internal modes of the PO_4 phosphate group [33] are marked by lines.

and the corresponding spectral maximum becomes pronounced near T^*.

The formation of the pronounced line of the librational mode is due to the freezing of the hopping motion of ammonium groups, which occurs according to the Arrhenius law [35, 36]. The localization of ammonium ions at one of the noncentrosymmetric sites leads to a specific strain of the crystal lattice and the formation of a cluster structure. Comparison of the $\nu_1(A_1)$ librations of $(NH_4)^+$ ions (Fig. 5) in the antiferroelectric phase of a KADP-74 crystal and in the dipole-glass phase of a KADP-32 crystal [35] showed their identity. This confirms that the short-range order of the cluster structure is similar to the antiferroelectric order.

The dielectric spectroscopy of RADP-50 crystals [37] revealed dispersion ε in the frequency range 10–100 cm^{-1}, which is related, as in parent compounds, to the dynamics of protons in the O–H···O bonds. The high- and low-frequency regions of the background behave differently: the former disappears at low temperatures, while the latter almost does not change. This fact suggests the existence of two independent mechanisms of polarization: the high-frequency intracluster dynamics and the low-frequency dynamics of cluster boundaries. The latter, being charged due to the violation of ordering and the formation of Takagi defects $(HPO_4)^-$–$(H_3PO_4)^+$, interact with the acoustic vibrational branch, forming a microscopic piezoelectric resonance mode. The estimates of the correlation length (~15 Å) are in good agreement with the results of X-ray and neutron measurements.

Thus, it can be seen that, in KADP crystals, with the exception of parent compounds, the appearance of a short-range order cluster structure due to the freezing of hopping motion of ammonium groups is antecedent to the transitions to the ferroelectric and antiferroelectric phases or the dipole-glass state.

The substitution of hydrogen by deuterium leads to a shift of the frequencies of all the modes that are sensitive to the motion of protons [38]. In this case, all the

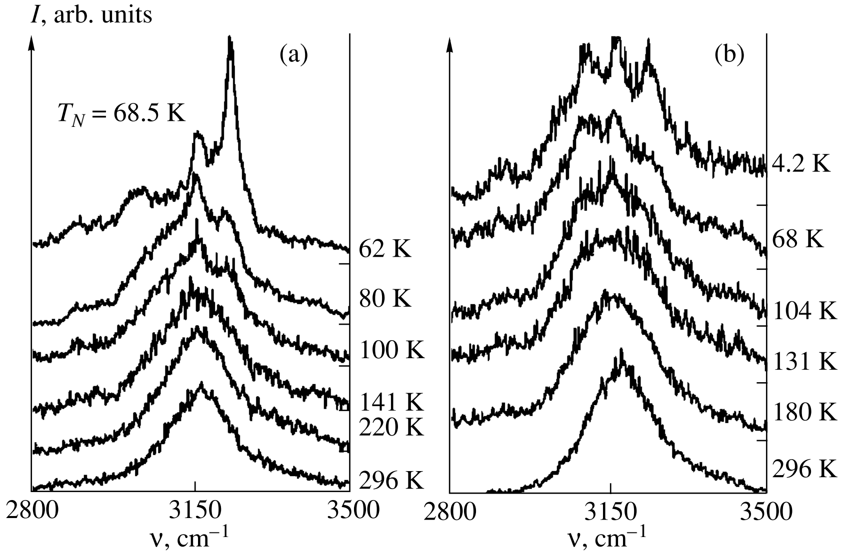

Fig. 5. Raman spectra of (a) KADP-74 and (b) KADP-32 crystals measured in the $x(zz)y$ geometry at different temperatures in the vicinity of the internal mode $\nu_1(A_1)$ of ammonium ions [35].

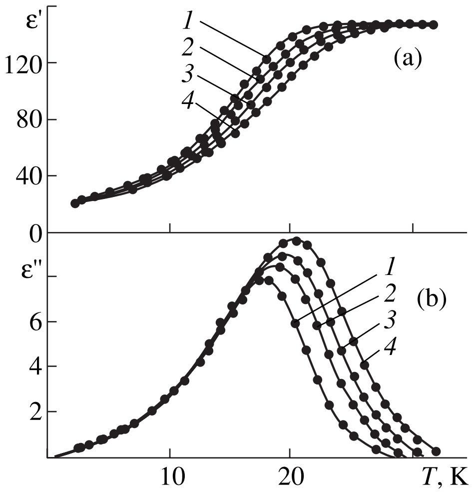

Fig. 6. Temperature dependences of (a) ε'_{33} and (b) ε''_{33} for an RADP-35 crystal measured at frequencies of (*1*) 100, (*2*) 1064, (*3*) 10640, and (*4*) 33700 Hz [39].

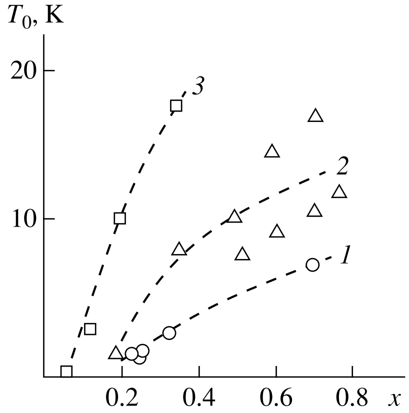

Fig. 7. Dependences of the Vogel–Fulcher temperature T_0 on ammonium concentration for (*1*) KADP, (*2*) RADP, and (*3*) RADA mixed crystals [11].

features of the lattice-vibration spectrum are shifted to higher temperatures by about 100 K.

5. DIELECTRIC RELAXATION AT THE TRANSITION TO THE DIPOLE-GLASS STATE

The dispersion of the real and imaginary components of the complex permittivity $\varepsilon^* = \varepsilon' - i\varepsilon''$, which is observed in dipole glasses in a wide range of frequencies f (Fig. 6), can be described taking into account the distribution of the relaxation times $g(\ln\tau)$ [39, 40]:

$$\varepsilon^* = (\varepsilon_s - \varepsilon_\infty)\int_{-\infty}^{\infty}\frac{g(\ln\tau)}{1 - i\omega\tau}d\ln\tau + \varepsilon_\infty, \qquad (1)$$

where $\omega = 2\pi f$ and ε_s and ε_∞ are the values of ε' at $\omega \longrightarrow 0$ and $\omega \longrightarrow \infty$, respectively.

The form of the function $g(\ln\tau)$ is determined by the distribution of the potential barriers $f(U)$, which is similar to uniform for protonated systems [39, 40]. As follows from the data of the dielectric [39–41], IR [37, 38], ultrasonic [42], hypersonic [43], and Brillouin [44, 45] spectroscopies, the distribution $f(U)$ in the vicinity of T_g is, apparently, temperature-independent.

A decrease in temperature leads to a strong extension of the relaxation-time spectrum, in which the longest time τ increases according to the empirical Vogel–Fulcher relation [1, 39, 40]:

$$\tau = \tau_0\exp[U/k(T - T_0)]. \qquad (2)$$

Here, time τ_0 is the reciprocal of the frequency of attempts to overcome the potential barrier U, k is the Boltzmann constant, and T_0 is the Vogel–Fulcher temperature. In the case of an RADP-35 crystal, expressions (1) and (2) adequately describe the dielectric-relaxation rate in an extremely wide frequency range from 10^{-4} to 10^{12} Hz [13].

The value of T_0 depends on ammonium concentration x and phase-transition temperatures T_C and T_N in the parent compounds (Fig. 7). A correlation exists between T_0 and the ratio of the mean-square deviation of the dipole–dipole interaction energy to the tunneling frequency of protons [11].

As in the case of parent compounds, a strong isotopic effect is observed in dipole glasses, which leads to the following changes for DRADP [40, 41, 46, 47] and DRADA [48, 49] deuterated crystals: the Vogel–Fulcher temperature increases by approximately a factor of three, the distribution function $f(U)$ significantly narrows, and the average value of the potential barrier increases. Temperature T_0 only weakly depends on the composition for intermediate ammonium concentrations. At low and high ammonium concentrations, T_0 rapidly decreases, asymptotically tending to zero as $x \longrightarrow 0$ and $x \longrightarrow 1$.

6. POLARIZATION IRREVERSIBILITY AND THE LONG-TERM RELAXATION

One of the effects characteristic of dipole glasses is the irreversibility of their polarization and permittivity below the temperature of the transition to the glass-like state. Polarization irreversibility was observed for dipole glasses of both protonated RADP [50] and KADP [51] systems and deuterated DRADP [52] and DRADA [53, 54] systems.

During the experiment, a sample was first cooled in the absence of a field from room temperature to some minimum temperature $T_{\min} < T_g$. At $T = T_{\min}$, measuring field E was switched on, and, upon heating, polarization

P was measured (the zero-field-cooled (ZFC) mode). At temperatures much higher than T_g, the heating was stopped and, without switching off the field, the crystal was cooled again to temperature $T_{\min}$ (the field-cooled (FC) mode). The results of the measurements are shown in Fig. 8 [54] in the form of temperature dependences of the permittivities $\varepsilon_{\mathrm{ZFC}}$ and $\varepsilon_{\mathrm{FC}}$ calculated by the formula $\varepsilon = P/(\varepsilon_0 E)$ (where ε_0 is the permittivity of vacuum).

The curves $\varepsilon_{\mathrm{FC}}(T)$ and $\varepsilon_{\mathrm{ZFC}}(T)$ coincide at $T > T_g$ but diverge at temperatures below T_g. The remanent polarization P_r, observed during heating a sample that was cooled previously in the presence of a field vanishes near T_g. The experimental results indicate the nonergodicity of the dipole-glass state, which is characterized by long-term processes of polarization relaxation.

The time dependences of the polarization for both protonated [50] and deuterated [55] dipole glasses, as for spin glasses [56], are adequately approximated by the expression $P \sim t^{-\alpha(T)}$, where α is the temperature-dependent parameter.

The time dependences of the X-ray scattering intensity observed below T_g during the structural relaxation under the action of a bias electric field $E_=$ in RADP-22 ($x \sim x_F$) mixed crystals [29] have a similar shape. The relaxation is accompanied by a decrease in the components of scattering intensity related to the dipole-glass phase and polar regions, in which the polarization vector is directed opposite to the field $E_=$. At the same time, the intensity of scattering from the polar-phase regions oriented along the field increases.

It can be seen from the above observations that processes of relaxation in dipole glasses of different systems are typical of compounds with a hierarchical structure of the potential profile, which is inherent in glassy systems [1, 2, 56]. Taking into account the specific features of the structure of dipole glasses, it can be suggested [57] that the long-term relaxation of polarization after switching on (off) the field $E_=$ is due to the diffusion of Takagi defects $(HPO_4)^-$ and $(H_3PO_4)^+$, which results from the motion of protons (deuterons) in hydrogen O–H···O bonds. It is the dynamics of “oxygen” protons in these bonds that is responsible for the relaxation processes in KADP-type dipole glasses.

The motion of oxygen protons is not frozen completely even at temperatures much below T_0. This was shown by recent investigations of the spectra of two-dimensional exchange nuclear magnetic resonance for a DRADA crystal [58, 59]. The rate of the deuteron motion at low temperatures has an athermal character. Hence, even deuterated crystals of the KADP type are quantum glasses.

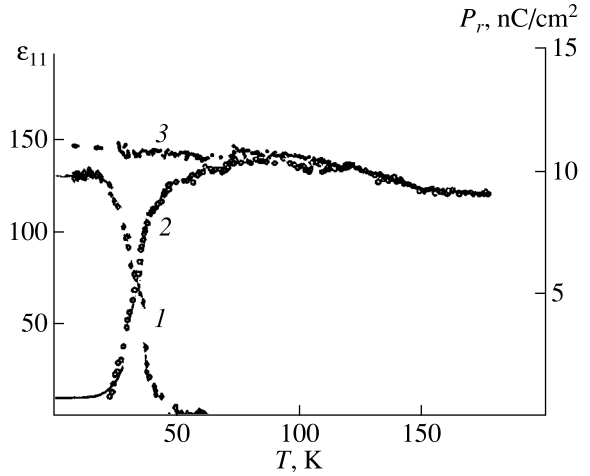

Fig. 8. Temperature dependences of the remanent polarization P_r (*1*) and the permittivities $\varepsilon_{\mathrm{ZFC}}$ (*2*) and $\varepsilon_{\mathrm{FC}}$ (*3*) for a DRADA-28 crystal [54].

7. SPREAD OF THE FERROELECTRIC PHASE TRANSITION

An expected spread of ferroelectric (antiferroelectric) phase transitions in KADP mixed crystals with an increase (decrease) in the ammonium concentration has been revealed experimentally. To estimate the degree of the phase-transition spread quantitatively, it is convenient to use the spread parameter σ, which can be easily determined from the temperature dependence of ε. In the model suggested in [3], in which a diffuse phase transition is considered as a set of local transitions with different T_C, the parameter σ has the meaning of a mean-square deviation of a local Curie temperature.

The inset of Fig. 9, along with the dependence $\sigma(x)$ plotted for ferroelectric compositions of the KADP system [60], shows the estimates of σ made by us based on the measurements of the dielectric response in RADP [28, 61], RADA [62], and KADA [21] crystals. For the same ammonium concentration, the values of σ for all the compounds are approximately the same. This means that the phase-transition spread in these systems occurs via identical mechanisms.

According to the model suggested in [3], for ferroelectric and antiferroelectric KADP compositions with concentrations x and $1 - x$, respectively, one would expect approximately the same values of σ provided that $x = 1 - x$. In fact, the ferroelectric transitions are more diffuse than the antiferroelectric ones [60, 63]. This is due to the interaction of polar regions with chaotic crystal fields induced by local lattice distortions

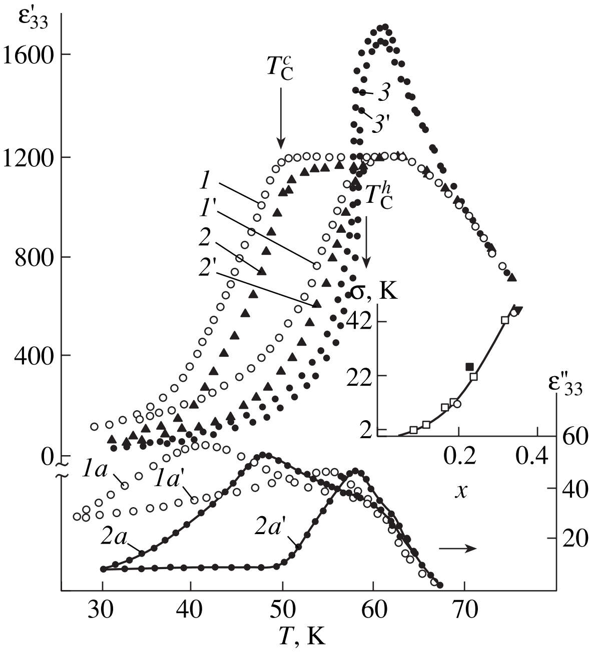

Fig. 9. Temperature dependences of ε'_{33} (*1–3*, *1'–3'*) and ε''_{33} (*1a*, *2a*, *1a'*, *2a'*) measured during cooling (*1–3*, *1a*, *2a*) and heating (*1'–3'*), *1a'*, *2a'*) of a KADP-19 crystal at $E_= = 0$ (*1*, *1'*, *1a*, *1a'*), 2 (*2*, *2'*, *2a*, *2a'*), and 6 (*3*, *3'*) kV/cm [12]. The inset shows the parameter σ as a function of ammonium concentration for KADP (□), KADA(■), RADP (●), and RADA (▲) mixed crystals [60].

(see Section 3). Application of a bias field $E_=$ partially compensates for the effect of random fields, which makes a ferroelectric transition more distinct and shifts it to much higher temperatures (Fig. 9) [60].

The dependence $T_m(E_=)$, where T_m is the temperature corresponding to the maximum value of ε'_{33} is anomalous (see inset to Fig. 10). In contrast to canonical ferroelectrics, for which $T_m(E_=) \sim E^\beta$ (where $\beta = 1$ and 2/3 for first- and second-order phase transitions, respectively [6]), the shift of the peak value of ε'_{33} is insignificant at fields $E_=$ lower than some critical value E_{cr}. When $E_= > E_{cr}$, T_m rapidly increases. Such dependences $T_m(E_=)$ are characteristic of ferroelectrics containing random-field defects [64].

8. DIELECTRIC NONLINEARITY

Nonlinear susceptibility of magnetic systems is the property that is most sensitive to the transition to the spin-glass state. Its behavior is critical near T_g [56]. One might expect a radical difference in the character of nonlinear response near the transitions to the ferroelectric, relaxor, and dipole-glass states [65].

The temperature dependences of the nonlinear permittivity $\Delta\varepsilon = [\varepsilon'_{33}(E_=) - \varepsilon'_{33}(E_= = 0)]/\varepsilon'_{33}(E_= = 0)$ are shown in Fig. 10 [66]. For nominally pure KH_2PO_4, a sharp asymmetric minimum of Δε is observed in the vicinity of T_C. An increase in the field $E_=$ leads to an increase and some shift of this anomalous feature to lower temperatures, which indicates the dominant contribution of the domain mechanism to the dielectric nonlinearity below T_C.

For crystals with higher ammonium concentration (KADP-12 and KADP-19), at temperatures much lower than T_C, the bias field is responsible for the decrease in the dielectric response ($\Delta\varepsilon < 0$), as in the case of KH_2PO_4 crystals. However, in the vicinity of T_C,

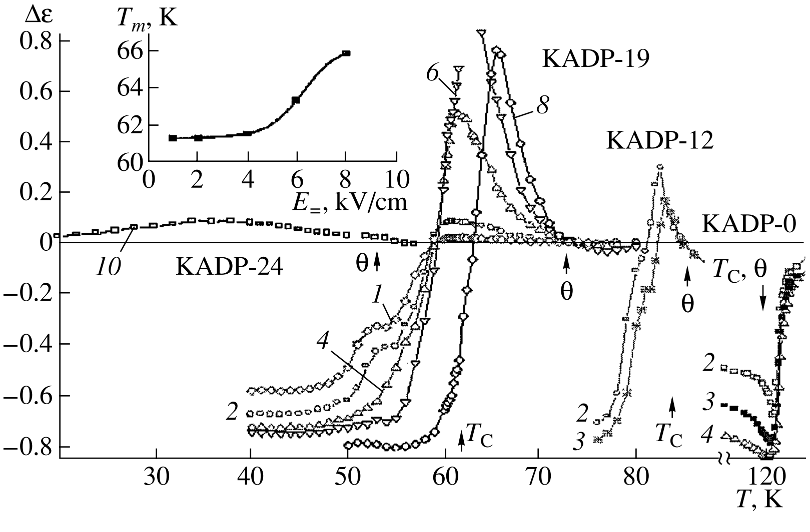

Fig. 10. Temperature dependences of Δε. Numbers at the curves indicate the values of the bias field $E_=$ (kV/cm). The Curie–Weiss temperature θ and phase-transition temperature T_C are indicated by arrows [66]. The inset shows the dependence $T_m(E_=)$ for a KADP-19 crystal.

$\Delta\varepsilon$ increases significantly and the nonlinear permittivity changes its sign. For all the values of the field strength $E_=$ used in the experiment, $\Delta\varepsilon > 0$ in the temperature range θ–T_C (θ is the Curie–Weiss temperature). At $T > \theta$, the sign of $\Delta\varepsilon$ changes again (becomes negative).

For the glass composition of KADP-24, the field $E_=$, at which the change in ε'_{33} becomes noticeable, is significantly higher than that for KADP-12 and KADP-19 and $\Delta\varepsilon \geq 0$ at all temperatures below θ. For crystals with $x \geq 0.32$, the effect of an electric field on the dielectric response has not been revealed experimentally.

The dependences $\Delta\varepsilon(T)$ obtained for the KADP-12, KADP-19, and KADP-24 compositions are consistent with the random-field model [65]. According to [65], $\Delta\varepsilon < 0$ for ferroelectric and paraelectric phases. At the same time, $\Delta\varepsilon > 0$ when a mixed ferroelectric–dipole-glass (relaxor) state is implemented. It can be seen from Fig. 10 that the mixed-state range is extended quite naturally with an increase in the concentration of NH_4. For KADP-24 crystals, this range is extended to the lowest temperatures.

KADP-24 crystals exhibit a number of features typical of relaxor ferroelectrics: the peak of ε'_{33} is rounded and its position depends on frequency (Fig. 11), the dependence $\varepsilon'_{33}(T)$ in a wide temperature range above T_m does not obey the Curie–Weiss law [60], the symmetry of the paraelectric phase remains upon cooling up to liquid helium temperature [67], and an external electric field induces a polar state below T_m (note that the dielectric-hysteresis loops $P(E)$, as for most relaxor ferroelectrics [3], are not saturated (see inset to Fig. 11) [12]).

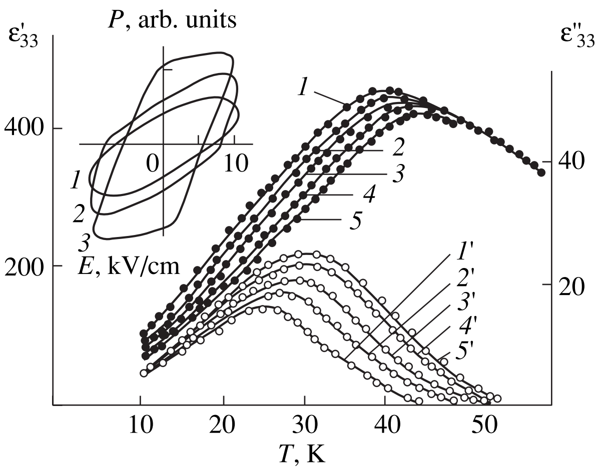

Fig. 11. Temperature dependences of ε'_{33} (*1–5*) and ε''_{33} (*1'–5'*) measured for a KADP-24 crystal heated at frequencies of 0.02 (*1*, *1'*), 0.075 (*2*, *2'*), 1 (*3*, *3'*), 10 (*4*, *4'*), and 50 (*5*, *5'*) kHz [51]. The inset shows the dielectric-hysteresis loops $P(E)$ observed at T = 31 K at frequencies of 0.5 (*1*), 0.1 (*2*), and 0.02 (*3*) Hz [12].

9. DIELECTRIC RELAXATION IN FERROELECTRIC COMPOSITIONS

Relaxation of permittivity, which is due to the motion of domain boundaries, always occurs in the ferroelectric phase, but it is most pronounced near T_C, where maxima of ε'_{33} and ε''_{33} are observed. The positions of the maxima of ε'_{33} and ε''_{33} only weakly depend on the measuring-field frequency due to the strong temperature dependence of the activation energy of the motion of domain boundaries in the vicinity of T_C [3, 6].

In crystals with a concentration of NH_4 close to x_F, for example, in KADP-19 ($x_F \simeq 0.20$), the maxima of ε'_{33} and ε''_{33} are combinations of two anomalies (Figs. 9, 12). In thermal-cycling measurements, the positions of the high-temperature anomalies of ε'_{33} and ε''_{33} do not change. The low-temperature anomalies, observed during cooling the sample, are shifted to lower temperatures. Their positions approximately correspond to the temperature above which a fast decrease in the remanent polarization occurs and waists arise on the dielectric-hysteresis loops $P(E)$ [68]. Therefore, it is reasonable to attribute the low-temperature anomalies of ε'_{33} and ε''_{33} to the ferroelectric-phase transition at T_C^c (T_C^h) upon cooling (heating) a crystal, as in the case of RADP-20 crystals (Fig. 3). The high-temperature anomalies are related to the dielectric relaxation in the mixed ferroelectric–dipole-glass state.

The mechanisms of relaxation in the ferroelectric–dipole-glass state have not been adequately studied. However, based on the general considerations and the structural data [28, 29], the relaxation processes in this state should be attributed predominantly to thermal reorientations of the polar regions, fluctuations of their volume, and the motion of domain boundaries. These processes are long-term ones that lead to the irreversibility of the temperature dependences of polarization [69, 70] and give grounds to identify the intermediate mixed state as a nonergodic one.

The single-domainization of the sample structure by the field $E_=$ suppresses the domain contribution to the dielectric response. As a result, the peak of ε''_{33} (Fig. 9, curves *1a'*, *2a'*), which is due to the polarization relaxation in the mixed state, becomes pronounced. The width of this peak, as well as the width of the $\Delta\varepsilon$ anomaly, can be used to estimate the temperature range of existence of the intermediate ferroelectric–dipole-glass state (the region of existence of this state is hatched in the T–x phase diagram in Fig. 1).

The range of existence of the mixed state depends on the preliminary thermal treatment of the material. Upon cooling from the paraelectric phase, due to the

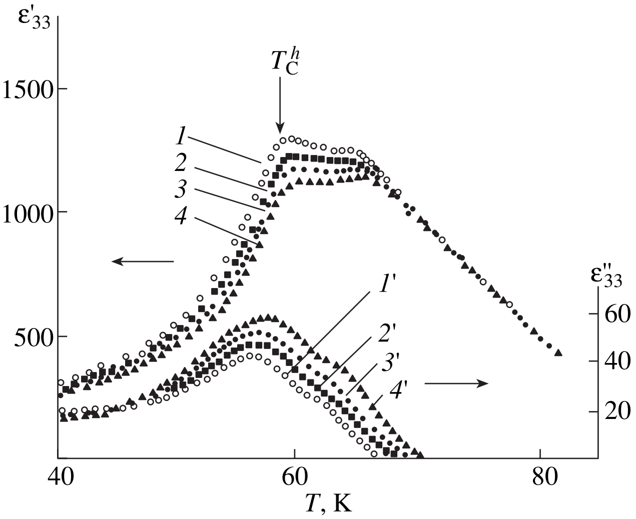

Fig. 12. Temperature dependences of ε'_{33} (*1–4*) and ε''_{33} (*1'–4'*) measured for a KADP-19 crystal heated at frequencies of 0.175 (*1, 1'*), 1 (*2, 2'*), 10 (*3, 3'*), and 50 (*4, 4'*) kHz [70].

delay of the ferroelectric transition, the temperature range of existence of this state exceeds that for the case of heating from the polar phase. The temperature hysteresis of T_C is accompanied by the hysteresis of some physical properties, including permittivity ε'_{33} (Fig. 9). The value of hysteresis in the crystals with the ammonium concentration $x \sim x_F$ significantly exceeds the range of coexistence of metastable phases at the first-order phase transition in canonical ferroelectrics.

In isothermal measurements in the temperature range $\Delta T_C \sim T_C^h - T_C^c$, relaxation of ε'_{33} is observed [69], which indicates instability of the state occurring in the range of thermal hysteresis of ε'_{33}.

The external field $E_=$ homogenizes a crystal, which leads to the formation of a pronounced peak of ε'_{33} and a decrease in the thermal hysteresis of the permittivity (Fig. 9) [12, 54]. However, the induced ferroelectric phase is unstable above T_C^c. It decays in several stages after the field is switched off [71]. The first stage is related to the decrease in the total polarization of the crystal and the internal field. When the latter becomes lower than some critical field, an avalanche-like decay of the macroscopic polar state begins, accompanied by precipitation of randomly oriented polar regions in the nonpolar matrix.

In the range of existence of the mixed state of KADP-19 ($x \le x_E$) crystals, the permittivity is characterized by strong dispersion (Fig. 12). With an increase in frequency, the peaks of ε'_{33} and ε''_{33} shift to higher temperatures. Average relaxation time τ of the low-temperature relaxation process is described by the Arrhenius law taking into account the temperature dependence of the activation energy $U \simeq U_0 + w(T_0^* - T)$ [70]:

$$\tau = \{\tau_0 \exp(-w/k)\}\exp[(U_0 + wT_0^*)/kT]. \qquad (3)$$

For the samples with ammonium concentration x somewhat higher than x_F (for example, KADP-24), the temperature dependence of τ, determined from the frequency shift of the ε''_{33} peak (Fig. 11), obeys law (3), as in the previous case [70]. However, in this case, the dependence $U(T)$ is weaker than for KADP-19.

Note that the relaxation processes in KADP-19 and KADP-24 crystals are not related directly to the slowing of proton oscillations along O–H···O bonds. Investigations of the transverse permittivity, which is sensitive to proton dynamics, have not revealed any characteristic dispersion of ε'_{11}, which would indicate the freezing of the proton motion in KADP crystals with $x \le 0.25$ [8, 72].

In contrast to KADP and RADP crystals, for RADA compounds [73] and DRADA [19, 73] and DRADP [18, 19] deuterated compounds with a low ammonium concentration ($x < x_F$), relaxation of ε'_{11} is observed below T_C, which initiates freezing of the proton (deuteron) motion along hydrogen O–H···O bonds and the transition to the dipole-glass state (see the review on the problem of coexistence of the ferroelectric and dipole-glass phases [73]). In KADP and RADP crystals with similar compositions, the transition to the dipole-glass state does not occur, due to the strong effect of proton tunneling [11].

Thus, in ferroelectric crystals with an ammonium concentration close to x_F, an intermediate glass-like state is formed in some temperature range above T_C, which is characterized by the long-term processes of dielectric relaxation related to the motion of polar regions and domain boundaries. The activation energy of the relaxation processes increases with decreasing temperature, while the dependence $U(T)$ becomes weaker with increasing the concentration x. In the case of crystals with ammonium concentrations in the range corresponding to the glass-like state, the distribution of the activation energies becomes almost independent of temperature.

ACKNOWLEDGMENTS

This study was supported by the program "Support of Leading Scientific Schools" (grant no. NSh-1514.2003.2), and the Russian Foundation for Basic Research (project nos. 02-02-16267 and 02-02-17330).

REFERENCES

1. U. T. Hochli, K. Knorr, and A. Loidl, Adv. Phys. **39**, 405 (1990).
2. A. Feltz, *Amorphe und Glasartige Anorganische Festkörper* (Akademie, Berlin, 1983; Mir, Moscow, 1986).
3. G. A. Smolenskiĭ, V. A. Bokov, V. A. Isupov, N. N. Kraĭnik, R. E. Pasynkov, and M. S. Shur, *Ferroelectrics and Antiferroelectrics* (Nauka, Leningrad, 1971) [in Russian].
4. A. A. Bokov, Ferroelectrics **131**, 49 (1992).
5. M. D. Glinchuk and R. Farhi, J. Phys.: Condens. Matter **8**, 6985 (1996).
6. M. Lines and A. Glass, *Principles and Applications of Ferroelectrics and Related Materials* (Oxford Univ. Press, Oxford, 1977; Mir, Moscow, 1981).
7. S. Havlin, E. Litov, and E. A. Ueling, Phys. Rev. B **9** (3), 1024 (1974).
8. Y. Ono, T. Hikita, and T. Ikeda, J. Phys. Soc. Jpn. **56** (2), 577 (1987).
9. S. A. Gridnev, L. N. Korotkov, S. P. Rogova, *et al.*, Ferroelectr. Lett. Sect. **13** (3), 67 (1991).
10. Oh. J. Kwon and J.-J. Kim, Phys. Rev. B **48** (9), 6639 (1993).
11. T. N. Korotkova, L. N. Korotkov, L. A. Shuvalov, and R. M. Fedosyuk, Kristallografiya **41** (3), 505 (1996) [Crystallogr. Rep. **41**, 477 (1996)].
12. S. A. Gridnev, L. N. Korotkov, L. A. Shuvalov, and R. M. Fedosyuk, Ferroelectrics **175**, 107 (1996).
13. E. Courtens, Ferroelectrics **72**, 229 (1987).
14. Z. Trybula, J. Stankowski, L. Szczepanska, *et al.*, Physica B (Amsterdam) **153**, 143 (1988).
15. Z. Trybula, V. H. Schmidt, and J. E. Drumheller, Phys. Rev. B **43**, 1287 (1991).
16. T. K. Song, S. E. Moon, K. H. Noh, *et al.*, Phys. Rev. B **50**, 6637 (1994).
17. N. Korner, Ch. Pfammatter, and R. Kind, Phys. Rev. Lett. **70**, 1283 (1993).
18. Z. Kutnjak, R. Pirc, A. Levstic, *et al.*, Phys. Rev. B **50**, 12421 (1994).
19. A. Levstic, Z. Rutnjak, C. Filipic, and R. Pirc, Ferroelectrics **167**, 17 (1995).
20. J. P. DeLooze, B. Campbell, G. Mac, *et al.*, Physica B (Amsterdam) **162**, 1 (1990).
21. Z. Trybula, S. Los, C. S. Tu, and V. H. Schmidt, J. Phys.: Condens. Matter **7**, 947 (1995).
22. V. L. Aksenov, M. Bobeth, and N. M. Plakida, J. Phys. C **18**, L519 (1985).
23. R. Pirc, B. Tadic, and R. Blinc, Phys. Rev. B **36**, 8607 (1987).
24. E. Courtens, R. A. Cowley, and H. Grimm, Ferroelectrics **78**, 275 (1988).
25. E. Courtens, T. E. Rosenbaum, S. E. Nagler, and P. M. Horn, Phys. Rev. B **29**, 515 (1984).
26. A. V. Belushkin, Kristallografiya **42** (3), 549 (1997) [Crystallogr. Rep. **42**, 501 (1997)].
27. R. A. Cowley, T. Ryant, and E. Courtens, J. Phys. C **18**, 2793 (1985).
28. S. Amin, R. A. Cowley, and E. Courtens, Z. Phys. B **67**, 229 (1987).
29. S. Amin, Z. Phys. B: Condens. Matter **74**, 113 (1989).
30. S. Hayase, T. Futurama, H. Sakashita, and H. Terauchi, J. Phys. Soc. Jpn. **54** (2), 812 (1985).
31. N. Korner and R. Kind, Phys. Rev. B **49** (9), 5918 (1994).
32. R. Kind, N. Korner, Th. Koenig, and Ch. Jetziner, J. Korean Phys. Soc. **32**, S799 (1998).
33. E. Courtens and H. Vogt, Z. Phys. B **62**, 143 (1986).
34. Yu. A. Popkov, A. V. Van'kevich, L. A. Shuvalov, and R. M. Fedosyuk, Fiz. Nizk. Temp. **19** (2), 195 (1993) [Low Temp. Phys. **19**, 138 (1993)].
35. A. V. Van'kevich, Yu. A. Popkov, and I. Taranova, Fiz. Nizk. Temp. **27** (1), 80 (2001) [Low Temp. Phys. **27**, 61 (2001)].
36. A. V. Belushkin, C. J. Carlie, and L. A. Shuvalov, Europhys. Lett. **22**, 701 (1993).
37. A. A. Volkov, G. B. Kozlov, S. P. Lebedev, *et al.*, Zh. Éksp. Teor. Fiz. **101**, 248 (1992) [Sov. Phys. JETP **74**, 133 (1992)].
38. J. Petzelt, S. Kamba, and I. Gregora, Phase Transit. **63**, 107 (1997).
39. E. Courtens, Phys. Rev. Lett. **52** (1), 69 (1984).
40. E. Courtens, Phys. Rev. B **33** (4), 2975 (1986).
41. P. He, K. Deguchi, M. Hirokane, and E. Nakamura, J. Phys. Soc. Jpn. **59** (5), 1835 (1990).
42. E. Sandvold, T. Lagreid, and E. Courtens, Phys. Scr. **38**, 732 (1988).
43. E. Courtens, F. Huard, and R. Vacher, Phys. Rev. Lett. **55** (7), 722 (1985).
44. E. Courtens and R. Vacher, Phys. Rev. B **35** (13), 7271 (1987).
45. E. Courtens, R. Vacher, and Y. Dagorn, Phys. Rev. B **33** (11), 7625 (1986).
46. P. He, J. Phys. Soc. Jpn. **60** (1), 2143 (1991).
47. Z. Kutnjak, R. Pirc, A. Levstik, *et al.*, Phys. Rev. B **50**, 12421 (1994).
48. Z. Kutnjak, A. Levstik, C. Filipic, *et al.*, J. Phys.: Condens. Matter **3**, 91 (1991).
49. F. L. Howell, N. J. Pinto, and V. H. Schmidt, Phys. Rev. B **46**, 13762 (1992).
50. I. N. Geĭfman, I. V. Kozlova, R. M. Fedosyuk, and L. A. Shuvalov, Kristallografiya **35** (1), 104 (1990) [Sov. Phys. Crystallogr. **35**, 62 (1990)].
51. S. A. Gridnev, L. N. Korotkov, and L. A. Shuvalov, Ferroelectrics **167**, 99 (1995).
52. I.-H. Ko, Y.-S. Choi, and J.-J. Kim, Ferroelectrics **240**, 257 (2000).
53. A. Levstic, C. Filipic, Z. Kutnjuk, *et al.*, Phys. Rev. Lett. **66**, 2368 (1991).
54. N. J. Pinto, K. Ravindran, and V. H. Schmidt, Phys. Rev. B **48**, 3090 (1993).
55. K. Hwan and S. Kwun, J. Korean Phys. Soc. **32**, S824 (1998).
56. K. Binder and A. P. Young, Rev. Mod. Phys. **58**, 801 (1986).
57. V. H. Schmidt, J. Mol. Struct. **177**, 257 (1988).
58. J. Dolinsek, B. Zalar, and R. Blinc, Phys. Rev. B **50** (2), 805 (1994).

59. R. Blinc, R. Pirc, B. Tadic, *et al.*, Kristallografiya **44** (2), 209 (1999) [Crystallogr. Rep. **44**, 177 (1999)].
60. L. N. Korotkov, S. A. Gridnev, and R. M. Fedosyuk, Kristallografiya **44** (5), 881 (1999) [Crystallogr. Rep. **44**, 821 (1999)].
61. E. Courtens, J. Phys. Lett. **43**, L199 (1983).
62. Z. Trybula, V. H. Schmidt, J. Drumheller, *et al.*, Phys. Rev. B **40**, 5289 (1989).
63. L. N. Korotkov and T. N. Korotkova, Solid State Commun. **115**, 453 (2000).
64. S. N. Dorogovtsev, Fiz. Tverd. Tela (Leningrad) **24** (6), 1661 (1982) [Sov. Phys. Solid State **24**, 948 (1982)].
65. M. D. Glinchuk and V. A. Stephanovich, J. Phys.: Condens. Matter **10**, 11081 (1998).
66. L. N. Korotkov, Phys. Status Solidi B **222** (2), R1 (2000).
67. Y. Ono, N. Yamada, and T. Hikita, J. Phys. Soc. Jpn. **60** (8), 2673 (1991).
68. S. A. Gridnev, L. N. Korotkov, L. A. Shuvalov, and R. M. Fedosyuk, Kristallografiya **41** (5), 891 (1996) [Crystallogr. Rep. **41**, 848 (1996)].
69. S. A. Gridnev, L. N. Korotkov, and L. A. Shuvalov, Ferroelectrics **144**, 157 (1993).
70. L. N. Korotkov and L. A. Shuvalov, Ferroelectrics **285**, 67 (2003).
71. L. N. Korotkov, A. P. Kotov, L. A. Shuvalov, and R. M. Fedosyuk, Izv. Ross. Akad. Nauk, Ser. Fiz. **61** (2), 238 (1997).
72. L. N. Korotkov, Fiz. Tverd. Tela (St. Petersburg) **43** (6), 1076 (2001) [Phys. Solid State **43**, 1112 (2001)].
73. V. H. Schmidt, Z. Trybula, N. J. Pinto, and S. M. Shapiro, Phase Transit. **67**, 499 (1998).

Translated by Yu. Sin'kov

Crystallography Reports, Vol. 49, No. 5, 2004, pp. 843–846. Translated from Kristallografiya, Vol. 49, No. 5, 2004, pp. 932–935.
Original Russian Text Copyright © 2004 by Popov, Popova.

PHYSICAL PROPERTIES OF CRYSTALS

Theoretical Calculation of Optical Properties of Crystals with Statistical Distribution of Atoms over Crystallographic Positions Based on the Model of Point Dipoles

D. Yu. Popov* and O. A. Popova**

* *Institute of Chemistry, Far-East Division, Russian Academy of Sciences, Vladivostok, Russia*
e-mail: popov@ich.dvo.ru
** *Far-East Geological Institute, Far-East Division, Russian Academy of Sciences, Vladivostok, Russia*

Received June 3, 2003

Abstract—Principal refractive indices and orientations of indicatrices of eleven minerals characterized by the statistical distribution of some ions over the crystallographic positions spaced by forbidden distances are calculated theoretically on the basis of the model of point dipoles. The calculated optical signs of the minerals of the medium crystallographic systems and the orientation of the indicatrices of the orthorhombic and monoclinic minerals agree with the experimentally determined values. *© 2004 MAIK "Nauka/Interperiodica".*

A considerable number of studies dedicated to the theoretical calculation of the parameters of the optical indicatrix in crystals and determination of atomic polarizabilities have been performed based on the model of point dipoles [1–9]. For further studies along this direction, one has to extend the model of point dipoles to the case of the statistical distribution of atoms over the crystallographic positions spaced from one another by forbidden distances. Below, we describe such a study.

In terms of the model of point dipoles, the atoms in a crystal are considered as dipoles with dimensions negligible in comparison with interatomic distances. In this approximation, the local electric field due to a light wave in the k position of the unit cell has the form [10]

$$\mathbf{F}(k) = \mathbf{E} + 4\pi\sum_{k'} L(kk')\mathbf{P}(k')/v, \qquad (1)$$

where $\mathbf{E}$ is the macroscopic field, $\mathbf{P}(k')$ is the dipole moment in the position k', v is the unit-cell volume, and $L(kk')$ is the Lorentz tensor dependent on the structure geometry.

The dipole moment at the position k' is related to the local electric field $\mathbf{F}(k')$ in this position by the equation

$$\mathbf{P}(k') = \alpha(k')\mathbf{F}(k'), \qquad (2)$$

where $\alpha(k')$ is polarizability. The total dipole moment of the unit cell is

$$\mathbf{P} = \sum_{k} \alpha(k)\mathbf{F}(k). \qquad (3)$$

Substituting Eq. (2) into Eq. (1), we arrive at the system of linear equations with respect to the components of vectors $\mathbf{F}$. Solving this system and substituting the vectors $\mathbf{F}$ thus obtained into Eq. (3), one obtains the tensor relating the total dipole moment of the unit cell to the vector of the macroscopic field. Dividing the components of this tensor into the unit-cell volume, we obtain the dielectric susceptibility tensor and then pass to the permittivity tensor.

In the case of the statistical distribution of atoms over the unit-cell positions, the calculation of the permittivity tensor is somewhat more complicated. The reasons are that, first, the polarizabilities of the atoms in Eqs. (2) and (3) should be multiplied by the corresponding occupancy factors. Second, the location of an atom in a certain position does not signify that other positions located at forbidden distances from this atom are empty. Therefore, one has to subtract the fields whose values are equal to the fields of dipoles in the empty positions k' from the local field given by Eq. (1),

$$\mathbf{F}'(kk') = \frac{3(\mathbf{P}(k')\mathbf{R}(kk'))\mathbf{R}(kk')}{R(kk')^5} - \frac{\mathbf{P}(k')}{R(kk')^3}, \qquad (4)$$

where $\mathbf{R}(kk')$ is the vector with the origin in the position k' and the end, in the position k; and $R(kk')$ is the magnitude of the vector $\mathbf{R}(kk')$.

Using the above approach, we calculated theoretically the optical properties of a number of minerals (Table 1) with the statistical distribution of some ions over the crystallographic positions. Each of these ions may be located in one of several positions spaced by different distances from one another. The types of statistically distributed ions, the number of positions located at the forbidden distances from one another, and the minimum (D_{min}) and maximum (D_{max}) distances between the positions are indicated in Table 2. When performing the calculations, we used as ion

Table 1. Minerals for which the optical properties were calculated

Mineral	Composition	Structure determination	
		R factor	reference
Sugilite	$Na_2KFe_{1.66}Al_{0.34}Li_3Si_{12}O_{30}$	0.017	[11]
Plumbogummite	$PbAl_3(P_{0.95}As_{0.05}O_4)_2(OH)_5H_2O$	0.037	[12]
Osumilite	$(K_{0.78}Na_{0.22})(Mg_{0.92}Fe_{0.92}Mn_{0.16})(Al_{2.63}Fe_{0.37})(Si_{10.2}Al_{1.8})O_{30}(H_2O)$	0.066	[13]
Hinsdalite	$PbAl_3(P_{0.69}S_{0.31}O_4)_2((OH)_{5.62}(H_2O)_{0.38})$	0.030	[12]
Milarite	$KNa_{0.19}Ca_2(Al_{0.81}Be_{2.19}Si_{12}O_{30})(H_2O)_{0.67}$	0.029	[14]
Rhomboclase	$(H_5O_2)Fe(SO_4)_2(H_2O)_2$	0.030	[15]
Kersutite	$(Na_{0.53}K_{0.41})Ca_{2.06}(Mg_{3.01}Fe_{1.07}Mn_{0.01}Ti_{0.52}\ Al_{0.34})(Si_{5.87}Al_{2.13})O_{22}(O\ H)_2$	0.056	[16]
Edenite	$K_{0.33}Na_{1.22}Ca_{1.65}Sr_{0.01}Mg_{3.74}Fe_{0.85}Mn_{0.04}\ Ti_{0.16}Si_{6.94}Al_{1.06}O_{22}F_2$	0.029	[17]
Hastingsite	$Na_{0.8}K_{0.2}Ca_2Mg_{0.55}Fe_{4.45}Al_{1.68}Si_{6.32}O_{23}(O\ H)$	0.057	[18]
Pargasite (I)	$(Na_{0.79}K_{0.02})(Na_{0.05}Ca_{1.76}Fe_{0.19})(Mg_{3.42}Fe_{0.63}Al_{0.93}Ti_{0.02})(Si_{6.2}Al_{1.8})O_{22}(O\ H)_2$	0.026	[19]
Pargasite (II)	$(Na_{0.91}K_{0.01})(Ca_{1.77}Na_{0.03}Mg_{0.07}Fe_{0.13})(Mg_{3.73}Fe_{0.31}Al_{0.93}Cr_{0.03})Si_{6.12}Al_{1.88}O_{22}F_{0.04}(OH)_{1.96}$	0.016	[20]

Table 2. Character of statistical distribution of ions

Mineral	Position	D_{min}, D_{max}, Å	Types of ions
Sugilite	2	0.375, 0.375	Na^+
Plumbogummite	6	0.288, 0.576	Pb^{2+}
Osumilite	6	1.037, 2.074	O^{2-}
Hinsdalite	6	0.219, 0.439	Pb^{2+}
Milarite	2	0.174, 0.174	Ca^{2+}
	2	1.119, 1.119	Na^+, O^{2-}
Rhomboclase	2	0.720, 0.720	O^{2-}
Kersutite	2	0.745, 0.745	Na^+, K^+
Edenite	3	0.573, 1.145	Na^+, K^+
Hastingsite	4	0.589, 0.892	Na^+, K^+
Pargasite (I)	4	0.586, 0.970	Na^+, K^+
	2	0.366, 0.366	Na^+, Ca^{2+}, Fe^{2+}
Pargasite (II)	5	0.301, 1.108	Na^+, K^+
	2	0.375, 0.375	Na^+, Ca^{2+}, Fe^{2+}, Mg^{2+}

Table 3. Calculated optical properties of minerals of medium systems

Mineral	N_o, N_e	N_g-N_p	Optical sign
Sugilite	1.667 (1.610) 1.666 (1.607)	0.001 (0.003)	– (–)
Plumbo-gummite	1.942 (1.653–1.680) 1.964 (1.675–1.698)	0.022 (0.018–0.022)	+ (+)
Osumilite	1.636 (1.540–1.546) 1.641 (1.546–1.550)	0.005 (0.004–0.006)	+ (+)
Hinsdalite	1.932 (1.688) 1.965 (1.697)	0.033 (0.009)	+ (+)
Milarite	1.627 (1.553) 1.622 (1.549)	0.005 (0.004)	– (–)

Note: Experimental values are indicated in parentheses.

polarizabilities the values of the ion refraction of the respective chemical elements [21, 22].

The computations were performed using the specially designed program AnRef3. The input data were the parameters of an elementary parallelepiped, coordinates of all the atoms of the unit cell, and atomic polarizabilities. The Lorentz tensor was calculated by the method described in [10]. If the permittivity tensor thus calculated is nondiagonal, then it is reduced to the principal axes and the principal refractive indices are calculated, which are equal to square roots of the diagonal components.

The calculated optical properties of minerals crystallizing in the medium systems are indicated in Table 3, and those of the orthorhombic mineral rhomboclase and five monoclinic amphiboles, in Table 4. The experimental values for the line D (λ_D = 589 μm) were borrowed from the following sources: for the minerals of medium systems, from [23]; for rhomboclase, from [24]; and for amphiboles, from [25].

One can see the considerable deviations of the calculated principal refractive indices from the experimentally determined values, which is explained by the considerable effect of ion polarizabilities on these values. The calculation of the exact values of polarizabilities is rather difficult, because the ion polarizabilities depend on various factors of which the most important is the bond polarity. The presence of the covalent component results in higher values of atomic polarizabilities in

Table 4. Calculated optical properties of orthorhombic and monoclinic minerals

Mineral	N_g, N_m, N_p	N_g-N_p	Optical sign, 2*V*, deg	∠(*a* N_g), deg
Rhomboclase	1.647 (1.635) 1.599 (1.550) 1.572 (1.533)	0.076 (0.102)	+ (+) 76 (27)	
Kersutite	1.680 (1.700–1.772) 1.649 (1.690–1.741) 1.648 (1.670–1.689)	0.032 (0.019–0.083)	+ (–) 23 (66–82)	123 (86–105)
Edenite	1.685 (1.632–1.730) 1.677 (1.618–1.714) 1.668 (1.615–1.705)	0.017 (0.014–0.026)	– (–, +) 84 (27–95)*	132 (71–92)
Hastingsite	1.735 (1.730) 1.735 (1.729) 1.695 (1.702)	0.040 (0.028)	– (–) 8 (10)	115 (93)
Pargasite (I)	1.714 (1.635) 1.700 (1.618) 1.687 (1.613)	0.026 (0.022)	+ (+) 87 (60)	123 (79)
Pargasite (II)	1.709 (1.635) 1.695 (1.618) 1.685 (1.613)	0.025 (0.022)	+ (+) 83 (60)	123 (79)

Note: The experimental values are indicated in parentheses.
* –2*V*.

comparison with the polarizabilities of ionic bonds [21, 22]. Since chemical bonding varies for various compounds, the atomic polarizabilities in the crystals of the studied minerals differ from the refraction used in the calculations, which explains the scatter between the calculated and experimentally determined refractive indices. The allowance made for the nature of chemical bonding in atomic polarizabilities is associated with considerable difficulties, but we are interested mainly in the theoretical calculation not of the absolute values of the refractive indices, but of the parameters which characterize the anisotropy of optical properties. The characteristics of anisotropy of optical properties may be calculated with a high accuracy, because optical anisotropy depends mainly on the geometry of the crystal structure, whereas the effect of ionic polarizability on the anisotropy of optical properties is much weaker. This was shown by the calculations of the indicatrix orientation for monoclinic and triclinic minerals [6–8].

A number of parameters that characterize the anisotropy of optical properties showed a good accordance between the calculated and experimental values. The optical sign of all the minerals that belong to the medium systems coincided with the experimentally determined sign. The calculated principal birefringence considerably differs from the experimentally determined one only in the mineral hinsdalite. The calculated orientation of the indicatrix with respect to the crystallographic axes in the orthorhombic mineral orthoclase turned out to be correct.

The monoclinic amphiboles studied have similar structural motifs and close unit-cell parameters. The orientations of their indicatrices are also close. In the crystals of all the minerals, the N_m axis coincides with the twofold symmetry axis, which is consistent with the calculated data. The indicatrix axis N_g in the symmetry plane *m* deviates from the positive direction of the axis *a* toward the positive direction of the *c* axis by the angle ranging within 71°–105°. The analogous calculated angles have somewhat higher values ranging within 115°–132°; in other words, the calculations gave the directions of the N_g axis deviating from the experimental axes for quite large angles. The deviation of analogous angles in kersutite and hastingsite are considerably less than 45°, i.e., the calculated N_g direction is closer to the true N_g direction than to the true N_p direction. In both varieties of pargasite, this angle is close to 45°. In edenite, the deviation of the calculated N_g direction from the true one is difficult to determine because of the lack of rigorous experimental data. We may only state that this deviation ranges within 40°–61°.

In addition to the above discrepancies, one has also to indicate that the calculated and experimentally measured optical signs for kersutite are different and that the calculated angle 2*V* for orthoclase considerably differs from the true value. The discrepancies between the calculated and true parameters are explained by the limited applicability of the approximation used to the interpretation of the optical properties of crystals [4]. One of the most important explanations of this limitation is the use of the isotropic ionic polarizabilities in the calculations. It is established that anisotropy of atomic polarizabilities due to directionality of the ionic–covalent and metal bonds considerably affects the optical anisotropy [26, 27]. The second important reason for the limited applicability of the above approximation is the assumption that the dipoles are located at the centers of ions. The center of gravity of the outer orbitals strongly affecting the ion polarizabilities does not necessarily coincide with the center of an ion whose position was determined in an X-ray diffraction experiment.

REFERENCES

1. D. Pohl, Acta Crystallogr., Sect. A: Cryst. Phys., Diffr., Theor. Gen. Crystallogr. **34**, 574 (1978).
2. D. Pohl, J. C. Eck, and K. H. Klaska, Acta Crystallogr., Sect. A: Cryst. Phys., Diffr., Theor. Gen. Crystallogr. **34**, 1027 (1978).
3. J. Granzin, Neues Jahrb. Mineral. Monatsh. **11**, 491 (1988).
4. D. Pohl and R. Rath, Acta Crystallogr., Sect. A: Cryst. Phys., Diffr., Theor. Gen. Crystallogr. **35**, 694 (1979).
5. G. A. Lager, Th. Armbruster, and D. Pohl, Phys. Chem. Miner. **14**, 177 (1987).
6. R. N. Abbott, Am. Mineral. **78**, 952 (1993).
7. R. N. Abbott, Can. Mineral. **32**, 909 (1994).
8. R. N. Abbott, Can. Mineral. **34**, 595 (1996).
9. T. Arlt and Th. Armbruster, Eur. J. Mineral. **9**, 953 (1997).
10. P. G. Cummins, D. A. Dunmur, R. W. Munn, and R. J. Newham, Acta Crystallogr., Sect. A: Cryst. Phys., Diffr., Theor. Gen. Crystallogr. **32**, 847 (1976).
11. T. Armbruster and R. Oberhaensli, Am. Mineral. **73**, 595 (1988).
12. U. Kolitsch, E. R. T. Tiekink, P. G. Slade, *et al.*, Eur. J. Mineral. **11**, 513 (1999).
13. G. E. Brown and G. V. Gibbs, Am. Mineral. **54**, 101 (1969).
14. F. C. Hawthorne, M. Kimata, P. Cerny, *et al.*, Am. Mineral. **76**, 1836 (1991).
15. K. Mereiter, TMPM Tschermaks Mineral. Petrogr. Mitt. **21**, 216 (1974).
16. F. Pechar, H. Fuess, and W. Joswig, Neues Jahrb. Mineral. Monatsh. **3**, 137 (1989).
17. R. K. Rastsvetaeva, D. Yu. Pushcharovskiĭ, and B. E. Borutskiĭ, Kristallografiya **40** (1), 33 (1995) [Crystallogr. Rep. **40**, 27 (1995)].
18. K. Makino and K. Tomita, Am. Mineral. **74**, 1097 (1989).
19. F. C. Hawthorne, R. Oberti, and N. Sardone, Can. Mineral. **34**, 577 (1996).
20. R. Oberti, F. C. Hawthorne, L. Ungaretti, and E. Cannillo, Can. Mineral. **33**, 867 (1995).
21. S. S. Batsanov, *Structural Refractometry* (Vysshaya Shkola, Moscow, 1976) [in Russian].
22. S. S. Batsanov, *Structural Chemistry: Facts and Dependencies* (Dialog MGU, Moscow, 2000) [in Russian].
23. M. Fleischer, R. E. Wilcox, and J. J. Matzko, *Microscopic Determination of the Nonopaque Minerals* (US Gov. Print. Office, Washington, DC, 1984; Nedra, Leningrad, 1987), US Geol. Survey Bull., No. 1627.
24. A. N. Winchell and H. Winchell, *The Microscopical Characters of Artificial Inorganic Solid Substances: Optical Properties of Artificial Minerals*, 3rd ed. (Academic, New York, 1964; Mir, Moscow, 1967).
25. W. A. Deer, R. A. Howie, and J. Zussman, *Rock-Forming Minerals*, Vol. 2: *Chain Silicates* (Longmans, London, 1963; Mir, Moscow, 1965).
26. S. S. Batsanov and I. A. Poroshina, Zap. Vsesoyuz. Mineral. O–va **108** (1), 74 (1979).
27. I. A. Poroshina and S. S. Batsanov, Byul. Mosk. O. Ispyt. Prir. Otd. Geol. **63** (3), 104 (1988).

Translated by L. Man

Crystallography Reports, Vol. 49, No. 5, 2004, pp. 847–850. Translated from Kristallografiya, Vol. 49, No. 5, 2004, pp. 936–940.
Original Russian Text Copyright © 2004 by Veremeĭchik, Galiulin.

PHYSICAL PROPERTIES OF CRYSTALS

Electrons of *l* Shells of Free Atoms As a Regular System of Points on a Sphere: I. Modeling by Polyhedra

T. F. Veremeĭchik and R. V. Galiulin

Shubnikov Institute of Crystallography, Russian Academy of Sciences,
Leninskiĭ pr. 59, Moscow, 119333 Russia
e-mail: vtam@ns.crys.ras.ru

Received February 19, 2004

Abstract—Electron *l* shells of free atoms have been modeled on the basis of regular and semiregular polyhedra by determining stable systems of identical Coulomb particles with an increase in their number. It is shown that such stable systems correspond to the location of the maxima of electron density at the vertices of inversion-center polyhedra forming a sequence in which the first polyhedron has two vertices and the number of vertices in each subsequent polyhedron exceeds the number of vertices in the previous one by four. The electron *s*, *p*, *d*, and *f* shells are modeled by a dumbbell and trigonal, pentagonal, and heptagonal antiprisms, respectively. Thus, in addition to the quantum-mechanical properties, *l* shells should have the symmetry properties of these antiprisms. It is believed that consideration of the noncrystallographic (for the three-dimensional Euclidean space) fivefold and sevenfold symmetries of *d* and *f* shells of free atoms will make it possible to obtain a unified explanation for a number of phenomena in crystal structures and other ordered media. *© 2004 MAIK "Nauka/Interperiodica".*

INTRODUCTION

The assumption that atoms have a shell structure was made by E.S. Fedorov, the author of the classical derivation of 230 structural crystallographic groups (the 150th anniversary of Fedorov's birth was celebrated on December 23, 2003). He wrote in a manuscript dated 1880 that "small bodies forming an atom are not closely packed but, like planets, are located at a significant distance from each other" and "the system can be sufficiently stable not with an arbitrary number of such small bodies" [1]. It is possible that it is this prediction of Fedorov (based exclusively on the extension of the spatial representation of complex multicomponent systems to atoms) in which the concept of the shell structure of atoms was suggested for the first time (as in the case of many other of Fedorov's ideas).

Electron *nl* shells, which are equivalent with respect to radial and azimuthal parameters—the principal quantum number *n* and the angular momentum *l*, respectively, correspond to the solutions of the Schrödinger equation for particles in a centrally symmetric field. The projections of momentum *l* onto the *z* axis are integers (in $\hbar$ units): $m_l = \pm l, \pm l - 1, \ldots 0$. The electron spin has orientations $m_s = \pm 1/2$. The maximum number of electrons in the *l* shell, in accordance with the Pauli exclusion principle, is limited by the value of *N*, which, obviously, is determined by the number of the values of m_l and m_s, so that $N = 2(2l + 1)$. For the *s*, *p*, *d*, and *f* shells, which are characterized by *l* equal to 0, 1, 2, and 3, respectively, *N* is equal to 2, 6, 10, and 14.

The shell model of a free atom, expressed in terms of the quantum-mechanical numbers *n*, *l*, m_l, and m_s, made it possible to explain their properties, primarily the spectroscopic ones. However, it is obvious that a closed system of *N* equivalent interacting particles should also have certain spatial symmetry properties. In this study, we report the results of investigations of the electron *l* shells in the context of Fedorov's ideas (i.e., as regular systems of points) and possible manifestations of their spatial symmetry.

CONSTRUCTION OF STABLE ELECTRON SYSTEMS

Let us determine the stable states of electrons on a sphere. Only the vertices of (i) Platonic and Archimedean bodies and (ii) prisms and antiprisms forming two infinite series correspond to stable positions of equivalent interacting particles on a sphere [2, 3] (Fig. 1). The vertices of these regular and semiregular polyhedra are equivalent, and they all have an even number of vertices. This means that equivalent particles can be in a stable state on a sphere only when their number is even. Obviously, a dumbbell should be added to the polyhedra shown in Fig. 1, since two particles form the simplest stable system.

Let us add two more particles to this simplest stable system. A tetrahedron—a polyhedron without an inversion center—corresponds to stable positions of four particles. Adding two more particles provides correspondence to a polyhedron with an inversion center (octahedron). Thus, adding two (four) particles to the simplest stable system leads to a polyhedron without (with) an inversion center, respectively.

A closed system of *N* equivalent interacting particles in the stable state is a regular system. Hence, its potential energy should be minimum [2–5]. Note that an inversion operation generally results in larger dis-

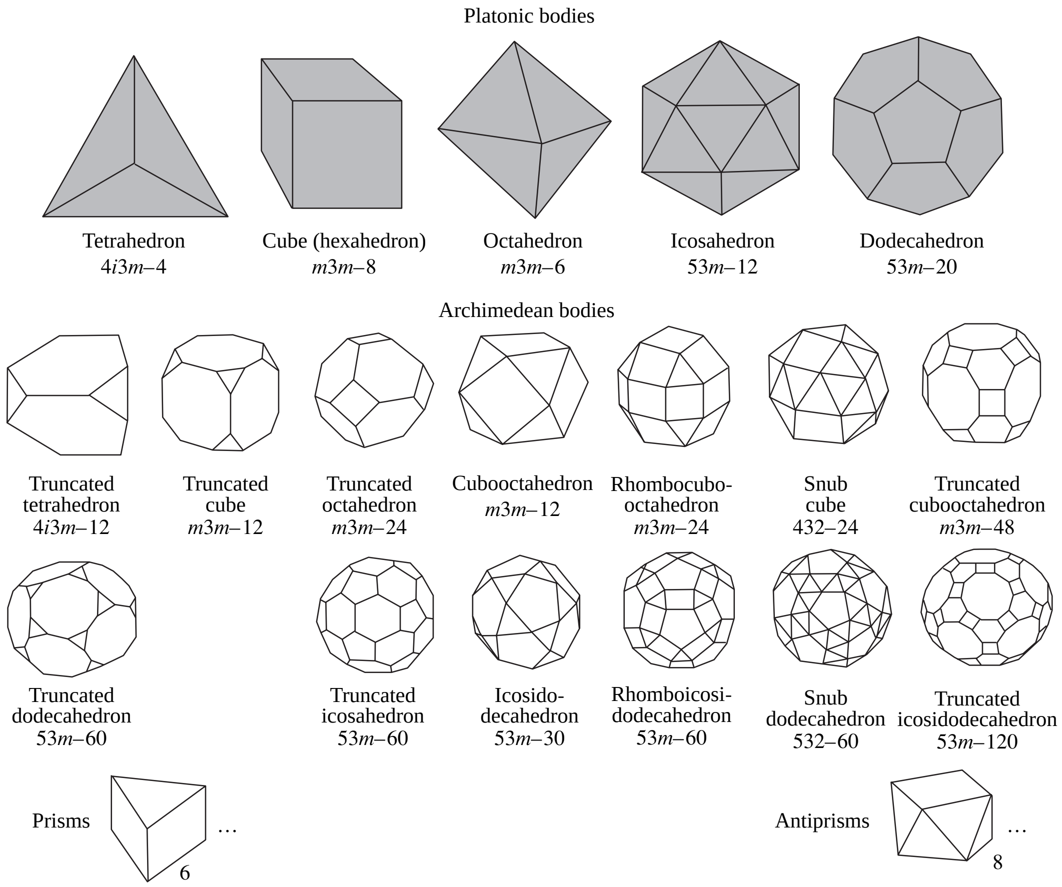

Fig. 1. Regular and semiregular polyhedra, the vertices of which correspond to the stable positions of identical interacting particles on a sphere. Symmetry and number of vertices are indicated for each polyhedron.

tances between the points than a reflection in a plane or rotation around a twofold axis. For identically charged Coulomb particles, this means that the inversion center corresponds to the lowest potential energy of the system of particles. This statement is in agreement with the well-known experimental fact: about 98% of molecular systems correspond to structures in which two orientations of a molecule are linked by an inversion center [6]. This fact accounts also for the following: the inversion operation makes it possible to introduce a characteristic related to the orientation of an individual particle in space. The necessity of the inversion operation follows also from the spherical symmetry of the problem.

Thus, minima of the energy of a system of identical Coulomb particles are obtained periodically. The first stable system consists of two particles; the number of particles in each subsequent system exceeds the number of particles in the previous one by four. The polyhedra modeling these stable systems should have inversion centers and be distinguished by four vertices. From all the polyhedra shown in Fig. 1, only a series of antiprisms with the following sequence of numbers of vertices: 2, 6, 10, 14, … satisfies these requirements. Therefore, the stable systems of 2, 6, 10, and 14 particles are modeled by a dumbbell (one-dimensional (1D) antiprism) and trigonal, pentagonal, and heptagonal antiprisms, respectively (Fig. 2). These antiprisms, as follows from the previous section, model the *s*, *p*, *d*, and *f* electron shells of free atoms, respectively [4, 7–9].

l SHELLS IN THE ELECTRON LAYER OF A FREE ATOM

Since an energy minimum can be obtained only in regular systems, we can state that the equivalence of the *l*-shell electrons postulated by quantum mechanics results from the minimization of the potential energy by implementation of regularity in a certain electron layer. In other words, the *l*-shell electrons become equivalent because the ensemble they form tends to acquire the lowest possible energy. The subsequent (l + 1) shell is formed with an increase in the number of electrons due to the violation of the stability of the *l* shell in the following way: the potential gradient (by analogy with the other regular system of points—crystal structure [10])—affects the additional electrons until they form their own regular system. The stability of the (l + 1) shell can be obtained by adding only four electrons.

The regularity of a system of particles forming an *l* shell also manifests itself in the radial reproducibility of each type of the *l* shell: 2*s* and 2*p* shells; 3*s*, 3*p*, and 3*d* shells; 4*s*, 4*p*, 4*d*, and 4*f* shells; and so on are imple-

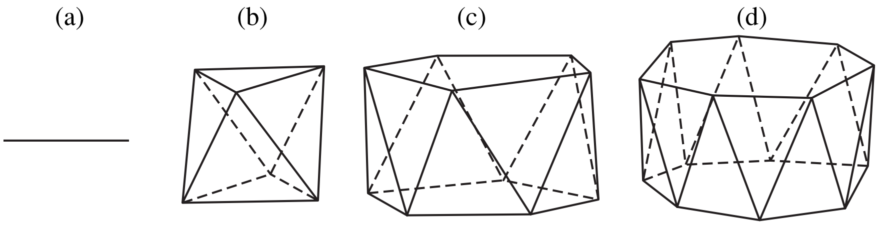

Fig. 2. Antiprisms, the vertices of which correspond to the maxima of the electron-density probability for the (a) *s*, (b) *p*, (c) *d*, and (d) *f* shells.

mented at $n = 2, 3, 4$, and so on. As is well known, such multiply periodic systems result from the central symmetry of the potential, but the reproducibility [11, 12] or similarity [5] in these periods of each *l* shell accounts for the regularity in one of the internal composite parts of a multicomponent system. According to Feynman, if the arrangement of particles in some region corresponds to the deepest potential minimum, there exist another region where the arrangement of particles is the same [11].

RESULTS AND DISCUSSION

The electron *l* shells of free atoms can be constructed by regarding them only as equilibrium closed systems of equivalent Coulomb particles. Within this approach, *l* shells are modeled by polyhedra, the vertices of which are equivalent on a sphere. Since the vertices can be associated (as in [3]) with the maxima of the electron-density probability and are indistinguishable (which corresponds to the indistinguishability of identical particles and the uncertainty principle), the crystallographic model proposed is consistent with the quantum-mechanical model of the *l* shells of an atom. For example, the number of different combinations that can be obtained from the electrons of an $l^{N'}$ shell, where $N' < N$ over N positions is $k = N!/N'!(N - N')!$; it corresponds to the total statistical weight of the levels of the $l^{N'}$ shell. Moreover, the noted relationship between the inversion operation and the deepest energy minimum of the system under consideration leads naturally to the concepts of spin and indistinguishability of identical quantum particles, since it is the inversion of the coordinate system that is equivalent to the permutation of two such particles [13].

Some other parallels with the quantum-mechanical characteristics lie in that different values of m_l can be attributed to the vertices of each base of the antiprisms corresponding to the *s*, *p*, *d*, and *f* shells and different values of m_s can be attributed to each base (Fig. 3). Thus, in a completely filled *l* shell (l^N shell), the orbital and spin momenta are compensated: $\Sigma_i^N m_l = 0$ and $\Sigma_i^N m_s = 0$, which corresponds to the only ${}^1S$ term of the l^N shell in the theory of an atom. All the terms of the $l^{N'}$ shell can be obtained by combining certain vertices.

Thus, electrons with the same spins form regular simplexes with odd numbers of vertices. When these simplexes are combined by the inversion center, they form octahedra in odd-dimensional (1D, three-dimensional (3D), five-dimensional (5D), and seven-dimensional (7D)) spaces.

Note that the entire polyhedron [7] should be associated with not only the filled shell, but also with the N' electrons of this shell, since the number of electrons on this shell different from N forms an unstable system. For example, any system with an odd number of electrons is unstable since there are no regular or semiregular polyhedra with an odd number of vertices. In the case of the $l^{N'}$ shell, the requirement of equality of distances between equivalent particles leads to different in magnitude (in contrast to the l^N shell) but nonzero for any of N vertices electron-density probability.

Thus, one should expect that, in addition to the well-known quantum-mechanical properties, the *s*, *p*, *d*, and *f* shells of free atoms should have certain geometric symmetry properties.

The well-known filling of the two-dimensional space with different polyhedra (Fig. 4) demonstrates that it is impossible to fill, without gaps, the 3D Euclidean space with polyhedra having five-, seven-, and higherfold axes. Obviously, pentagonal and heptagonal antiprisms can fill, without gaps, the spaces of higher orders (5D and 7D spaces, respectively). In other words, the dumbbell and trigonal antiprisms modeling the *s* and *p* shells coincide with the regular polyhedra (octahedra of the one-dimensional and 3D spaces,

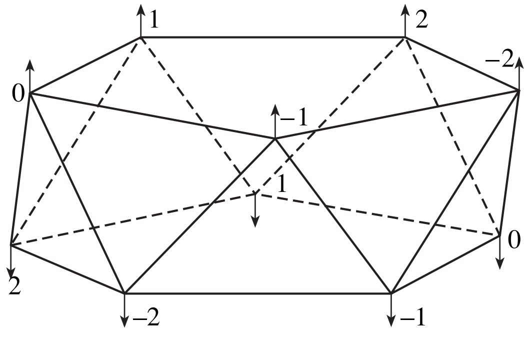

Fig. 3. Pentagonal antiprism, the vertices of which correspond to the maxima of the electron-density probability for the *d* shell. Numbers and arrows indicate the values of *ml* (projections of the orbital momentum *l* on the *z* axis) and the spin orientations, respectively.

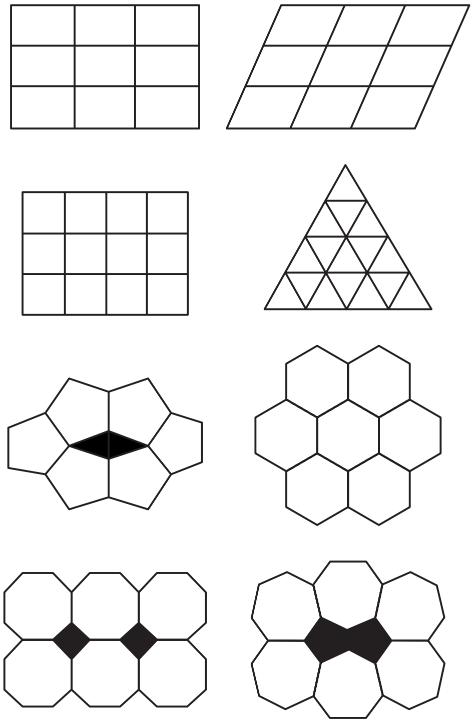

Fig. 4. Filling of a plane by regular polyhedra of different symmetry [14].

respectively), whereas the antiprisms modeling the *d* and *f* shells coincide with octahedra only in the 5D and 7D spaces. Their representations in the 3D space are only projections of the octahedra of the spaces of higher dimensions onto the 3D space.

Thus, in spaces with other geometries (for example, the spherical or Lobachevsky spaces) or spaces of other dimensions [15], atoms with *d* and *f* shells, characterized by axes that are multiples of the five- and sevenfold axes, can form a crystal structure, while, in the 3D Euclidean space, only atoms with *s* and *p* shells have this property.

In this context, the periodic table of elements can be divided into two groups: the chemical elements that contain only *s* and *p* shells and can be inserted without distortion into a 3D crystal structure and the elements that contain *d* and *f* shells and cannot be inserted into a 3D crystal structure without distortion.

Obviously, the tendency of the *d* and *f* shells to implement their own (noncrystallographic) symmetry always competes with the tendency of a crystal to implement the translational symmetry. The result depends on many factors, in particular, the crystal-field potential and the degree of mixing between different types of *l* shells in a free atom and between *l* shells and electron shells of ligands upon formation of a chemical bond. However, there is a wide range of phenomena in crystals and other ordered media, which, in our opinion, find a unified explanation as a manifestation of the particular symmetry of *d* and *f* shells of free atoms shown in this study.

We should note that *l* shells (including *s*, *p*, *d*, and *f* shells), which are well-known from the theory of atomic spectra, correspond to relatively small values of the principal quantum number *n*. Large values of *n* are realized in Rydberg atoms [16–18], the electron shells and hybridizations of which are also modeled by vertices of the polyhedra shown in Fig. 1. If the number of electrons in a shell exceeds 120, such shells can only be modeled by infinite series of either antiprisms or prisms. Such Rydberg atoms of corresponding sizes can fill the space vacuum.

REFERENCES

1. S. A. Shchukarev and R. B. Dobrotin, Kristallografiya, No. 3, 85 (1955).
2. R. V. Galiulin, Usp. Fiz. Nauk **172** (2), 229 (2002) [Phys. Usp. **45**, 221 (2002)].
3. L. A. Aslanov, *Structure of Atoms, Molecules, Crystals* (Mosk. Gos. Univ., Moscow, 1985) [in Russian].
4. R. V. Galiulin, Kristallografiya **48** (6), 965 (2003) [Crystallogr. Rep. **48**, 899 (2003)].
5. É. N. Elissev, *Physicochemical Modeling* (Nauka, Leningrad, 1975) [in Russian].
6. P. M. Zorkiĭ and O. N. Zorkaya, Zh. Strukt. Khim. **39** (1), 126 (1998).
7. T. F. Veremeĭchik and R. V. Galiulin, *Crystallogenesis and Mineral* (S.-Peterb. Gos. Univ., St. Petersburg, 2001), p. 409.
8. T. F. Veremeĭchik and R. V. Galiulin, in *Proceedings of VI International Conference on Crystals: Growth, Properties, Structure, and Application* (Aleksandrov, 2003), p. 201.
9. T. F. Veremeĭchik and R. V. Galiulin, in *Proceedings of International Conference Dedicated to the 150th Anniversary of E. S. Fedorov* (Gornyĭ Inst., St. Petersburg, 2003), p. 12.
10. T. F. Veremeĭchik and R. V. Galiulin, Neorg. Mater. **38** (9), 1110 (2002).
11. R. P. Feynman, R. B. Leighton, and M. Sands, *The Feynman Lectures on Physics* (Addison-Wesley, Reading, Mass., 1966; Mir, Moscow, 1977), Vol. 7.
12. B. N. Delone, N. P. Dolbilin, M. I. Shtogrin, and R. V. Galiulin, Dokl. Akad. Nauk SSSR **227** (1), 19 (1976) [Sov. Math. Dokl. **17**, 319 (1976)].
13. L. D. Landau and E. M. Lifshitz, *Course of Theoretical Physics*, Vol. 3: *Quantum Mechanics: Non-Relativistic Theory*, 3rd ed. (Nauka, Moscow, 1974; Pergamon, New York, 1977).
14. M. P. Shaskol'skaya, *Crystallography* (Vysshaya Shkola, Moscow, 1976) [in Russian].
15. R. V. Galiulin, Zh. Vychisl. Mat. Mat. Fiz. **43** (6), 791 (2003).
16. N. B. Delone, Soros Educational Journal, No. 4, 64 (1998).
17. J. Neukamner, H. Rinenberg, K. Vitzke, *et al.*, Phys. Rev. Lett. **59**, 26 (1987).
18. M. M. Frey, S. B. Hill, K. A. Smith, *et al.*, Phys. Rev. Lett. **75** (5), 810 (1995).

Translated by Yu. Sin'kov

Crystallography Reports, Vol. 49, No. 5, 2004, pp. 851–854. Translated from Kristallografiya, Vol. 49, No. 5, 2004, pp. 941–944.
Original Russian Text Copyright © 2004 by Aleksandrov, Sel'skaya.

**SURFACE,
THIN FILMS**

Growth and Real Structure of Diamond Films Synthesized on Polycrystalline Tungsten Substrates

V. D. Aleksandrov and I. V. Sel'skaya

Donbass State Academy of Civil Engineering and Architecture, Makeevka, Ukraine

e-mail: yugov@donace.dn.ua

Received June 26, 2002

Abstract—X-ray diffraction studies of diamond films obtained by chemical transport reactions at the concentrations of 2% methane and 98% hydrogen under pressures of 10.7 and 21.3 kPa showed that they are textured. The character of the texture depends on the substrate temperature. The films have $\langle 110\rangle$, $\langle 311\rangle$, or double $\langle 110\rangle + \langle 311\rangle$ textures. It is established that the dependence of the growth rate of diamond films on the substrate temperature has maxima. The diamond films are finely dispersed and are characterized by pronounced microdeformations and high dislocation densities. The temperature dependence of the growth rate correlates with the parameters of the real structure of the films. *© 2004 MAIK "Nauka/Interperiodica".*

INTRODUCTION

One of the problems of the material science of diamond is growth of diamond films with preset properties. The real structure of synthetic diamond films determines most of their properties [1–3]. An important role is also played by the parameters of their synthesis—pressure, temperature, and gas concentration [4–7]. The appropriately chosen conditions of film synthesis allow one to control the growth process and obtain materials with a preset structure. Therefore, the problems of diagnostics of a real structure of diamond films are of great importance for the technology of their synthesis and the subsequent use of the grown films. Synthesis of diamond films is performed on both native and foreign substrates practically by all the methods known in thin-film technology [8].

The present study was aimed at the study of the effect of vapor pressure and substrate temperature on growth rate and real structure of diamond films grown on polycrystalline tungsten substrates.

EXPERIMENTAL

Synthesis of crystalline diamond films was performed by the method of chemical transport reactions [9] in the graphite–hydrogen–methane system under pressures lower than atmospheric. The activator was a graphite rod heated to 2323 K. The temperature of the graphite rod was measured by a Promin' optical pyrometer. The temperature of the substrates on a cooled substrate holder was maintained constant during the whole process and was T_s = 973, 1013, 1033, 1053, 1068, 1113, 1173, and 1373 K. The substrate temperature was measured by a thermocouple. The preliminarily ground tungsten substrates were polished and chemically purified by 1-h boiling in hydrochloric acid. No seeding diamond powders were used. Thickness d of the films thus grown was determined from the increment in their weight on a VKLT-500-M scale with an error of about 5%. The growth rate was calculated from the known film thickness and the synthesis time. Taking into account the difficulties in performing experiments on film synthesis under various conditions, the calculations were performed by measurements for three films obtained under the same growth conditions in order to increase the reliability of the main growth parameters and growth rates determined. Altogether, 33 films with a thickness exceeding 8 μm were synthesized.

The formation of a texture in the films, the average size of the mosaic blocks $\langle D\rangle$, the value of microdeformation $\sqrt{\langle E^2\rangle}$, and the dislocation density γ in crystallites were determined by the X-ray diffraction method (DRON-4-07 diffractometer, characteristic CuK_α radiation). Diamond films on tungsten substrates with the dimensions $(8 \times 10 \times 1) \times 10^{-3}$ were studied at room temperature. The fine structure was analyzed by the method of approximation of the profiles of X-ray interference lines [10, 11]. The dislocation density was determined by the method suggested in [12].

RESULTS

Consider the results obtained on the growth rates for the diamond films (Fig. 1) obtained under vapor pres-

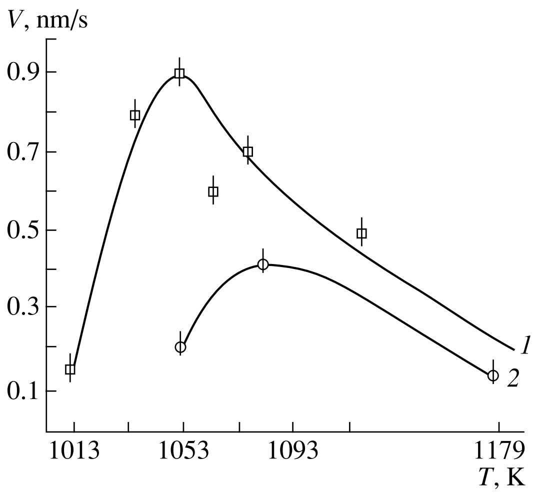

Fig. 1. Growth rate V of diamond films as a function of substrate temperature T_s at the component concentrations 2% CH_4 and 98% H_2 under the vapor pressures (*1*) 10.7 and (*2*) 21.3 kPa.

sures $p = 10.7$ and 21.3 kPa, the component concentrations 2% CH_4 and 98% H_2 at different substrate temperatures T_s. The studies shows that at $p = 10.7$ kPa and $T_s = 1013$ K, the growth rate is rather low, $V \sim 0.1$ nm/s (Fig. 1, curve *1*). With an increase of the substrate temperature up to 1033 K, the growth rate of diamond films increases to 0.80 nm/s, and at $T_s = 1053$ K, it attains the maximum value ~0.9 nm/s. At the substrate temperatures 1068, 1083, and 1113 K, the growth rate decreases and is equal to 0.58, 0.65, and 0.58 nm/s, respectively. It is seen from curve *1* that at $T_s < 1013$, the growth rate of diamond films tends to zero; at $T_s > 1053$, the growth rate decreases. At $T_s = 973$ and 1373 K, no diamond films are formed at all.

With an increase of the vapor pressure of CH_2 and H_2 in the growth chamber up to 21.3 kPa and the constant concentration of methane and hydrogen (2 and 98%) at the substrate temperature 1053 K, the growth rate is relatively low (Fig. 1, curve *2*). With an increase of the substrate temperature up to 1083 K, the growth rate of the film increases up to 0.42 nm/s. With a further increase of T_s up to 1173 K, the growth rate decreases down to 0.14 nm/s. It is seen from curve *2* that, with the approach of the substrate temperature to 1033 K and at $T_s \longrightarrow 1273$ K, the growth rate of the diamond film tends to zero.

Structural characteristics of diamond films grown under the vapor pressure 10.7 kPa and the component concentration 2% CH_4 + 90% H_2

T_s, K	⟨D⟩, µm	$\sqrt{\langle E^2\rangle}$, $\times 10^{-3}$	γ, $\times 10^{14}$ m^{-2}
1013	0.010	0.085	5.47
1033	0.052	0.49	6.29
1053	0.097	1.11	7.5
1068	0.026	0.99	24.93
1083	0.036	1.34	24.37
1113	0.029	0.60	13.55

As is seen from Fig. 1, the temperature dependences of the growth rate of diamond films at the pressures 10.7 and 21.3 kPa are the curves with a maximum. Under higher vapor pressures, the growth rates decrease and the curve $V = f(T_s)$ is displaced toward higher temperatures. This indicates that diamond films obtained under these growth conditions show the classical dependence of the growth rate on temperature [13, 14].

X-ray diffraction studies of the real structure of diamond films synthesized under 10.7 kPa showed that the film structure depends on the substrate temperature. The films grown at the substrate temperatures 1013 and 1113 K have a texture with the texture axis ⟨110⟩. In other words, small diamond crystallites grow in the films with the (110) planes being parallel to the tungsten substrate. In the diamond films obtained at the substrate temperatures 1033 and 1053, the small crystallites grow with random orientations. At the substrate temperature 1068 K, the films have a weak texture with the ⟨311⟩ axis, and at the substrate temperature 1083 K, the films are characterized by the double ⟨110⟩ + ⟨311⟩ texture.

When analyzing the experimental parameters of the real structure of diamond films, ⟨D⟩, $\sqrt{\langle E^2\rangle}$, and γ, as functions of the substrate temperature, we considered films with equal thicknesses obtained under the same conditions (see table). The thickness of these films was ⟨d⟩ = 8.2 ± 0.3 µm, and the dependence of ⟨D⟩, $\sqrt{\langle E^2\rangle}$, and γ on the substrate temperature for these films had the form of curves with the maximum (Fig. 2). As is seen from Fig. 2, the maximum dimensions of the mosaic blocks is observed at $T_s = 1053$ K; the maximum microdeformation, at $T_s = 1083$ K; and the maximum dislocation density, at $T_s = 1068$ K. Comparing these curves with the temperature dependence of the growth rate of these films (Fig. 1, curve *1*), we see their good correlation.

The films obtained under the vapor pressure 21.3 kPa and the substrate temperature 1083 K are characterized by a double texture, ⟨110⟩ + ⟨311⟩. At the temperature 1173 K, the films have a pronounced texture with the ⟨110⟩ axis. These films are finely dispersed, with the dimension ⟨D⟩ being equal to 0.017 and 0.029 µm, respectively. The films are also characterized by high microdeformations $\sqrt{\langle E^2\rangle}$ of crystallites (~1.72×10^{-3} and 1.4×10^{-3}) and high dislocation densities γ (66.25×10^{14} and 31.61×10^{14} m^{-2}).

DISCUSSION

Correlation of the temperature dependences of growth rate with parameters $\langle D\rangle$, $\sqrt{\langle E^2\rangle}$, and γ of the real structure of diamond films indicates that the same structural elements are responsible for nucleation of a new phase and the formation of the real structure of the films [13]. In synthesis of diamond films in the activated graphite–hydrogen–methane system under different conditions, the formation of carbon fractions and hydrocarbons with different molecular weights is also possible. These fractions, which consist mainly of C_n molecules, may have the form of branched clusters—structural units for formation of diamonds, chains for formation of carbines, closed rings for formation of graphite, etc. With change of the temperature, these structural elements may have different concentrations. In the vicinity of the optimum $T_s^{\max}$ temperatures at which the growth rate and the defect concentration in diamond crystals have maximum values (Figs. 1, 2), short molecules of the indicated types may prevail and promote the formation of a large number of crystallization centers of diamond and, at the same time, also of defects, e.g., at the expense of rings (structural units of another allotropic modification of carbon—graphite) incorporated into the diamond structure. In this case, dislocations are generated by stresses due to the concentration gradient $\Delta C/\Delta x$ [15] and impurities may be nanoinclusions of the graphite phase. At relatively low T_s values, the rate of crystallite growth is lower than at the optimum T_s temperature, because of a low kinetic energy of the molecules. In this case, their structure has a lower number of defects, because the molecular fractions of another configuration may be pushed away by the growth front. At relatively high T_s (exceeding $>T_s^{\max}$), the molecules are very active and, therefore, are only rarely attached to the crystallization front of crystallites, which, in turn, would reduce the growth rate and the number of defects in the films.

Another explanation of defect formation, in particular, of dislocations, in diamond crystals may be thermal stresses [16] arising during film synthesis because of the temperature gradient between the substrate–film system and the heating graphite rod. The inhomogeneous temperature distribution results in nonuniform variation of the lattice parameter in various portions of the crystal and, thus, in the appearance of tensile and compressive stresses giving rise to the formation of dislocations, whose density may be calculated by the formula $\gamma = \alpha\Delta T/b\Delta x$, where α is the thermal expansion coefficient, $\Delta T \sim 1000$ K is the temperature gradient, b is the Burgers vector, and Δx is the substrate–activator distance equal to ~2×10^{-3} m [16]. The competing processes of crystal growth and relaxation of possible stresses may result in both higher and lower defect concentration. It is difficult to control the above factors that promote defect formation, because the parameters necessary for their calculations are technological parameters and may hardly be controlled during synthesis of diamond films.

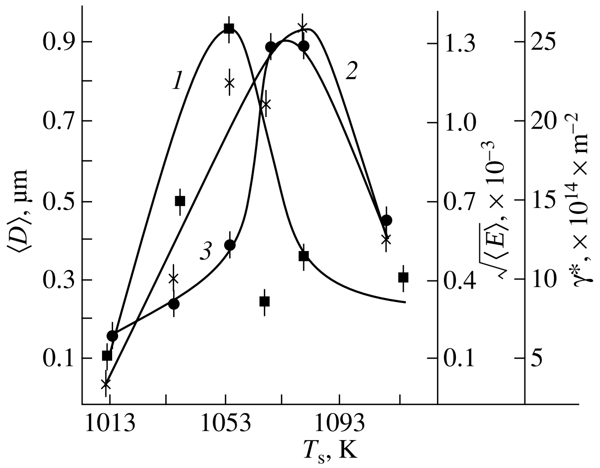

Fig. 2. Parameters of the real structure of diamond films as functions of substrate temperature T_s under the vapor pressure 10.7 kPa. (*1*) Size of mosaic blocks $\langle D\rangle$, (*2*) microdeformation $\sqrt{\langle E^2\rangle}$, and (*3*) dislocation density γ.

REFERENCES

1. *The Properties of Natural and Synthetic Diamond*, Ed. by J. E. Field (Academic, New York, 1992).
2. V. D. Andreev, Yu. I. Sozin, V. A. Semenovich, *et al.*, Sverkhtverd. Mater., No. 6, 19 (1987).
3. B. D. Deryagin, B. V. Spitsyn, A. V. Aleksenko, *et al.*, Dokl. Akad. Nauk SSSR **213** (5), 1059 (1973) [Sov. Phys. Dokl. **18**, 822 (1973)].
4. V. D. Aleksandrov, N. E. Malinovskaya, I. V. Sel'skaya, and O. V. Aleksandrova, Vestn. DGASA, Ser.: Kompoz. Mater. Stroit., Nos. 2 (22), 139 (2000).
5. I. V. Sel'skaya and P. I. Ignatenko, Materialovedenie, Nos. 7 (52), 41 (2001).
6. I. V. Sel'skaya, in *Proceedings of 5th International Symposium on Diamond Films and Films of Related Materials* (Kharkov, 2002), p. 20.
7. V. D. Aleksandrov and I. V. Sel'skaya, Poverkhnost, No. 12, 38 (2001).
8. B. V. Spitsyn and A. E. Aleksenko, in *Proceedings of 5th International Symposium on Diamond Films and Films of Related Materials* (Kharkov, 2002), p. 122.

9. B. V. Spitsyn, Tekh. Sredstv Svyazi, Ser: Tekhnol. Proizvod. Oborud., No. 4, 71 (1997).
10. V. I. Iveronova and G. P. Revkevich, *Theory of X-ray Scattering* (Mosk. Gos. Univ., Moscow, 1978) [in Russian].
11. P. I. Ignatenko and N. P. Ivanitsyn, *X-ray Diffraction Analysis of Real Crystals* (Donets. Gos. Univ., Donetsk, 2000) [in Russian].
12. A. A. Shul’zhenko, V. N. Tovstogan, V. A. Shishkin, *et al.*, in *Effect of High Pressures on the Structure and Properties of Superhard Materials* (ISM Ukr. SSR, Kiev, 1982), p. 8.
13. V. D. Aleksandrov, Doctoral Dissertation in Chemistry (Donetsk, 1992).
14. B. Wunderlich, *Macromolecular Physics*, Vol. 2: *Crystal Nucleation, Growth, and Annealing* (Academic, New York, 1976; Mir, Moscow, 1983).
15. W. A. Tiller, in *The Art and Science of Growing Crystals*, Ed. by J. J. Gilman (Wiley, New York, 1963; Metallurgizdat, Moscow, 1968).
16. E. Billing, in *Silicon*, Ed. by D. A. Petrov (Mir, Moscow, 1960), p. 131.

Translated by L. Man

Crystallography Reports, Vol. 49, No. 5, 2004, pp. 855–857. Translated from Kristallografiya, Vol. 49, No. 5, 2004, pp. 945–947.

Flux Crystallization of Trigonal $GdFe_3(BO_3)_4$ Competing with the Crystallization of α-Fe_2O_3[1]

L. N. Bezmaternykh, S. A. Kharlamova, and V. L. Temerov

Kirenskiĭ Institute of Physics, Siberian Division, Russian Academy of Sciences,
Akademgorodok, Krasnoyarsk, 660036 Russia

e-mail: bezm@iph.krasn.ru

Received February 26, 2003

Abstract—The formation of trigonal $GdFe_3(BO_3)_4$ crystals in the $Bi_2Mo_3O_{12}$–B_2O_3–Li_2MoO_4–Gd_2O_3–Fe_2O_3 system was studied. The flux compositions for which $GdFe_3(BO_3)_4$ is the high-temperature phase with a wide range of crystallization were determined. The features of nucleation of these crystals and their growth near the phase boundary with α-Fe_2O_3 were analyzed. The growth of $GdFe_3(BO_3)_4$ single crystals involving preliminary nonequilibrium crystallization of α-Fe_2O_3 is described. *© 2004 MAIK “Nauka/Interperiodica”.*

INTRODUCTION

The most important results in the growth, characterization, and applications of rare-earth borate single-crystals Re(Al, Fe, Ga, Sc)$_3$(BO$_3$)$_4$ with a huntite structure were attained for $GdAl_3(BO_3)_4 : Nd^{3+}$ [1–3] and several rare-earth scandium borates doped with Nd^{3+}, Er^{3+}, and Yb^{3+} ions [4]. $GdAl_3(BO_3)_4 : Nd^{3+}$ crystals of up to 30 mm in size were grown from flux based on the $K_2Mo_3O_{10}$–B_2O_3 system, whereas crystals of rare-earth scandium borates of a larger size were grown from melt by the Czochralski method. Study of the optical spectra, lasing characteristics, and nonlinear optical properties of these materials has shown that they are one of the most appropriate media for diode-pumped self-frequency-doubling lasers.

At the same time, the present state of the art in methods for growing single crystals of other compounds with a huntite structure [1–4] severely limits the possibility of making a comprehensive study of the elastic, piezoelectric, and optical properties of these crystals and, hence, carrying out the corresponding applied research and development.

In this study, in order to develop techniques for growing $GdFe_{3-x}Ga_x(BO_3)_4$ single crystals, we analyze, in the first stage, the formation of trigonal $GdFe_3(BO_3)_4$ crystals in fluxes containing, along with crystal-forming oxides, bismuth trimolybdate and lithium molybdate. Particular attention is given to the nonequilibrium effects at the boundary of the crystallization region of α-Fe_2O_3 (hematite). The growth conditions for $GdFe_3(BO_3)_4$ single crystals involving the preliminary nonequilibrium crystallization of α-Fe_2O_3 are described.

FLUXES BASED ON THE $Bi_2Mo_3O_{12}$–B_2O_3–Li_2MoO_4 SYSTEM

First, we studied the phase formation in the fluxes

$$(100 - n)\ \text{wt}\ \%\ (Bi_2Mo_3O_{12} + aB_2O_3 + bGd_2O_3) + n\ \text{wt}\ \%\ GdFe_3(BO_3)_4 \quad (1)$$

in the ranges $0.5 \le a \le 3$, $0.2 \le b \le 0.8$, $10 \le n \le 30$, and $850 \le t \le 1050$°C. It was found that, at certain values of parameters a, b, and n, trigonal $GdFe_3(BO_3)_4$ is a high-temperature phase and the saturation temperature does not exceed 1000°C. For example, at $a = 2$, $b = 0.6$, and $n = 25$, $GdFe_3(BO_3)_4$, being a high-temperature phase, crystallizes in the temperature range from 980 to 860°C. The concentration dependence of the saturation temperature for a flux with these values of a and b is shown in Fig. 1. Then, it was determined that, with a time of observation from 20 to 24 h, the width of the metastable zone is about 20°C. These crystallization parameters and the stability of properties at working temperatures up to 1050°C in the dissolution stage of the flux under study are, at least, not inferior to those known from the data in the literature.

The density of this flux, although slightly lower, is close to that of $GdFe_3(BO_3)_4$ single crystals. Therefore, crystals spontaneously nucleated at the flux surface should grow, being kept at the surface by surface ten-

---

[1] This study was presented at the National Conference on Crystal Growth (NCCG-2002, Moscow).

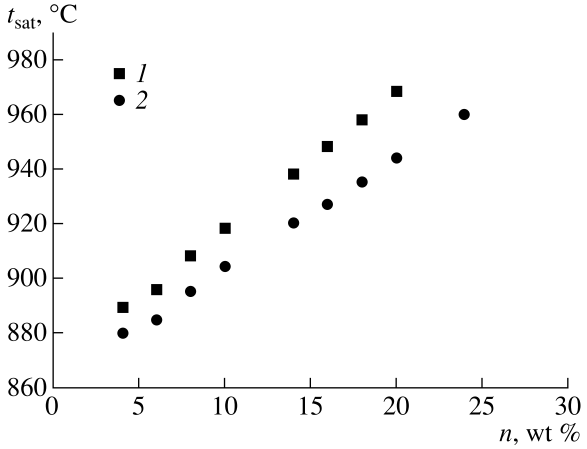

Fig. 1. Concentration dependences of the saturation temperatures for (*1*) $(100 - n)$ wt % $(Bi_2Mo_3O_{12} + 2B_2O_3 + 0.6Gd_2O_3) + n$ wt % $GdFe_3(BO_3)_4$ and (*2*) $(100 - n)$ wt % $(Bi_2Mo_3O_{12} + 3.84\ B_2O_3 + 0.75\ Gd_3O_3 + 0.96\ Li_2MoO_4) +$ n wt % $GdFe_3(BO_3)_4$ fluxes.

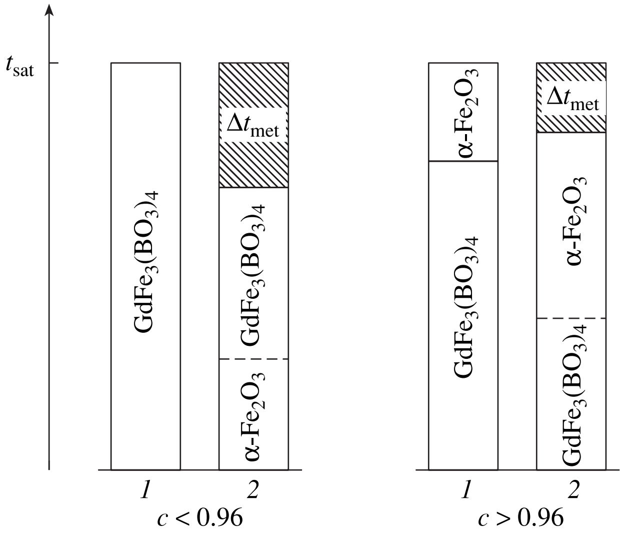

Fig. 2. Temperature sequences of the crystallizing phases in the 74 wt % $(Bi_2Mo_3O_{12} + 3.84B_2O_3 + 0.75Gd_3O_3 +$ $cLi_2MoO_4)$ + 26 wt % $GdFe_3(BO_3)_4$ flux for the growth of $GdFe_3(BO_3)_4$ single crystals at (*1*) under nearly equilibrium conditions and (*2*) at the spontaneous nucleation; Δt_{met} is the width of the metastability range.

sion forces. Naturally, this factor is undesirable for controlled crystallization.

Hence, in the second stage, we studied the formation of $GdFe_3(BO_3)_4$ crystals in the fluxes

$$(100 - n) \text{ wt \% } (Bi_2Mo_3O_{12} + aB_2O_3 + bGd_2O_3 + cLi_2MoO_4) + n \text{ wt \% } GdFe_3(BO_3)_4. \quad (2)$$

It turned out that, at certain values of parameters a, b, c, and n, $GdFe_3(BO_3)_4$ is a high-temperature phase with a wide range of crystallization. For a flux with $a = 3.84$, $b = 0.75$, and $c = 0.96$, the concentration dependence of the saturation temperature is also shown in Fig. 1. For this flux, the saturation temperature $t_{sat} = 980$°C corresponds to $n = 30$ and the slope of the curve $t_{sat}(n)$ is somewhat smaller. Here, the width of the metastable zone is also about 20°C. However, the flux density is significantly lower due to the greater amount of B_2O_3 and the addition of Li_2MoO_4. The viscosity of this flux is lower as well. It is this flux that seems to be most appropriate for controlled crystallization of gadolinium–iron borate.

NONEQUILIBRIUM EFFECTS. CHOICE OF CRYSTALLIZATION CONDITIONS

Depending on the values of a and b, there is a limiting value of c_0 for fluxes of type (2) above which hematite becomes a high-temperature equilibrium phase. At $a = 3.84$ and $b = 0.75$, this effect was observed at $c > 0.96$ (Fig. 2). Near this limiting content of Li_2MoO_4, the temperature sequence of the two adjacent phases $GdFe_3(BO_3)_4$ and α-Fe_2O_3 significantly deviates from equilibrium at spontaneous nucleation. The equilibrium phase sequence was determined using test crystals upon slow cooling (at a rate of about 1 K/h) of fluxes with a small mass. In experiments with spontaneous nucleation, a platinum test seed was dipped into a homogenized flux at $t > t_{sat}$ and, then, the temperature was lowered to a given value at a rate of 100–150 K/h. After 5–7 h, the test seed was taken out to evaluate the crystal formation on it. At $c < 0.96$, hematite is not a high-temperature equilibrium phase and, therefore, arises only upon deep supercooling. At $c > 0.96$, hematite is a high-temperature equilibrium phase only in a narrow temperature range and remains in the form of a single phase down to deep supercooling.

In view of this, it is reasonable to use a flux with $c < 0.96$ under conventional seed-growth conditions. At $c > 0.96$, $GdFe_3(BO_3)_4$ single crystals can be grown using preliminary spontaneous crystallization into hematite structure. In this case, one might expect higher growth rates for high-quality $GdFe_3(BO_3)_4$ single crystals as long as their growth is additionally fed by dissolving nonequilibrium hematite.

CONCLUSIONS

Trigonal $GdFe_3(BO_3)_4$ is a high-temperature phase in fluxes based on the $Bi_2Mo_3O_{12}$–B_2O_3–Li_2MoO_4 system. This compound crystallizes in a wide temperature range when the B_2O_3 and Gd_2O_3 contents are much larger than the corresponding stoichiometric values.

At spontaneous nucleation of crystals in the vicinity of the boundary with the hematite phase, the sequence of phases significantly deviates from the equilibrium one (the effect of disequilibrium).

We proposed conditions for growing $GdFe_3(BO_3)_4$ single crystals with preliminary nonequilibrium crystallization into a hematite structure. The macroscopic magnetic characteristics of the grown single crystals were studied, and a low-temperature spin-reorientation transition was revealed [5].

ACKNOWLEDGMENTS

This study was supported in part by Program 9 of the Russian Academy of Sciences and the Russian Foundation for Basic Research (project no. 03-02-16286).

REFERENCES

1. N. I. Leonyuk, E. V. Koporulina, S. N. Barilo, *et al.*, J. Cryst. Growth **191** (1–2), 135 (1998).
2. Chaoyang Tu, H. Yichuan, Q. Minwang, *et al.*, J. Cryst. Growth **206** (3), 249 (1999).
3. E. V. Koporulina, N. I. Leonyuk, A. V. Mokhov, *et al.*, J. Cryst. Growth **211** (1–4), 491 (2000).
4. S. T. Durmanov, O. V. Kuzmin, G. M. Kuzmicheva, *et al.*, Opt. Mater. **18** (2), 243 (2001).
5. A. D. Balaev, L. N. Bezmaternykh, S. A. Kharlamova, *et al.*, J. Magn. Magn. Mater. **258–259**, 532 (2003).

Translated by K. Kugel

Crystallography Reports, Vol. 49, No. 5, 2004, pp. 858–862. Translated from Kristallografiya, Vol. 49, No. 5, 2004, pp. 948–952.
Original Russian Text Copyright © 2004 by Malyshev, Gab.

Initial Stages of Nucleation of Carbide Phases in Oxide Melts

V. V. Malyshev and A. I. Gab
National Technical University of Ukraine, pr. Pobedy 37, Kiev 56, 03056 Ukraine
e-mail: victor_malyshev@mail.ru

Received January 31, 2002

Abstract—The initial stages of nucleation of Mo_2C and W_2C crystals in the tungstate–molybdate–carbonate melts of the known compositions on Ag, Au, Cu, Pt, and Ni substrates are studied by the method of electrodeposition depending on the electrocrystallization conditions—temperature, deposition time, initial current pulse, and current density. © *2004 MAIK “Nauka/Interperiodica”.*

INTRODUCTION

Usually, Mo_2C and W_2C coatings are applied onto nonoriented metal substrates by electrolysis of Na_2WO_4-based oxide melts [1, 2]. However, in many instances, it is necessary to obtain continuous cathode deposits with preset properties (structure, orientation, and crystallite size). Therefore, an important role in electrolysis is played by the initial stages of crystal nucleation. In [3–5], the results of such a study for electrodeposited Mo and W are presented. The initial stages of nucleation of Mo and W carbides have not been studied as yet. The only known investigation was performed for platinum and glassy carbon electrodes [6]. The present work was undertaken with the aim to investigate the initial stages of nucleation of the crystals of carbide phases in oxide melts on various substrates under different conditions of electrodeposition.

EXPERIMENTAL METHODS

We studied the initial stages of crystal nucleation by the electrochemical methods used in the study of phase formation with simultaneous investigation of the microstructure of the substrate surface and electrolysis products. The experimental setup consisted of a resistance furnace with a crucible, a complex of apparatus for measuring galvanostatic switch (potential–time) curves, which are, in fact, the dependences of the electrode potential on time after the action of the initial current pulse (i_{pulse}) for the time τ_{pulse}, and equipment for the microstructural studies based on an MBS-9 microscope. The measurements were performed in a three-electrode cell. The anode, a platinum crucible, simultaneously served as a melt container; the working electrode was the end electrode (prepared from different metals) with a diameter ranging within 0.5–1.0 nm fused in quartz glass. The reference electrode consisted of pressed Mo_2C and W_2C strips on a platinum current lead. After being washed with distilled water, the deposits were studied on a DRON-4 X-ray diffractometer and in a Stereoscan S-4 scanning electron microscope. The grain size was averaged over 50–100 grains. The surface morphology of the layers was determined in a Camebax scanning electron microscope.

RESULTS AND DISCUSSION

In [7], we showed that carbide electrodes in tungstate–molybdate–carbonate melts of certain compositions have equilibrium electrode potentials. These results were also confirmed by the study of the reaction kinetics in electrodeposition of carbide coatings onto solid electrodes. As is seen from the switching curves in Fig. 1, the deposition of carbide onto a solid foreign substrate at the switched-on current is characterized by three important features: the shift of the potential to the electronegative region (point *A*), the shift of the potential to the electropositive region up to the attainment of a certain value (stationary state); and the equilibrium value of the potential of the deposited compound after switching-off of the current (point *B*). The dependence of the electrode potential is shown in Fig. 1 with respect to the equilibrium potential E_{eq} taken to be zero (the right-hand scale of ordinates η) and with respect to the reference platinum–oxygen electrode (the left-hand scale of ordinates E). The difference between the electrode potentials at points *A* and *B* corresponds to the crystallization overvoltage (η_{cr}).

It is established that the first crystals start growing immediately after the appearance of the peak on the switching curves. The repeated switching-on of the current within a short period of time (5–10 s) does not give rise to peak formation. These facts indicate that the crystallization overvoltage is associated with three-dimensional nucleation. Based on the experimental results, we evaluated the crystallization overvoltage due to a considerable energy loss for component nucleation at the first moments of synthesis. These energy

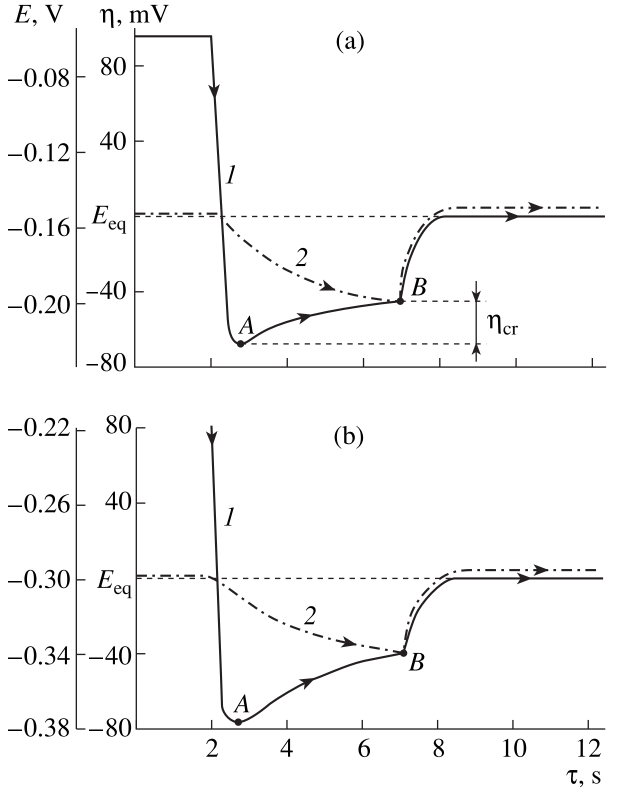

Fig. 1. Switching curves at electrocrystallization of (a) Mo_2C and (b) W_2C on the electrodes prepared from (*1*) Ag, (a, curve *2*) Mo_2C and (b, curve *2*) $W_2C(2)$; T = 1073 K; cathode area 7.5×10^{-3} cm^2. (a) Na_2WO_4 melt—1 mol % MoO_3 at 7.5 atm. CO_2, i_{pulse} = 0.75 mA; τ_{pulse} = 5 s. (b) Na_2WO_4—1.5 mol % WO_3 melt under a pressure of 10 atm CO_2, i_{pulse} = 1.0 mA, τ_{pulse} = 5 s.

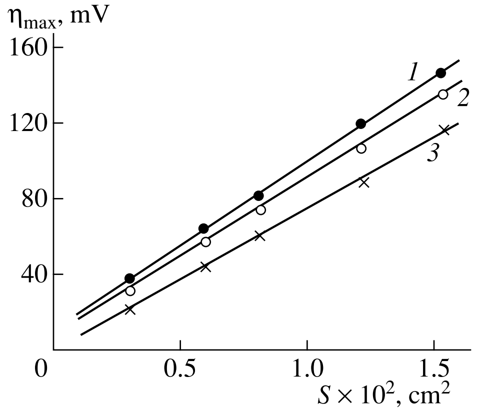

Fig. 2. Influence of the electrode area on the value of η_{max} during electrodeposition of W_2C (T = 1173 K, i = 0.1 A/cm^2) onto various electrodes: (*1*) Ag, (*2*) Au, (*3*) Cu.

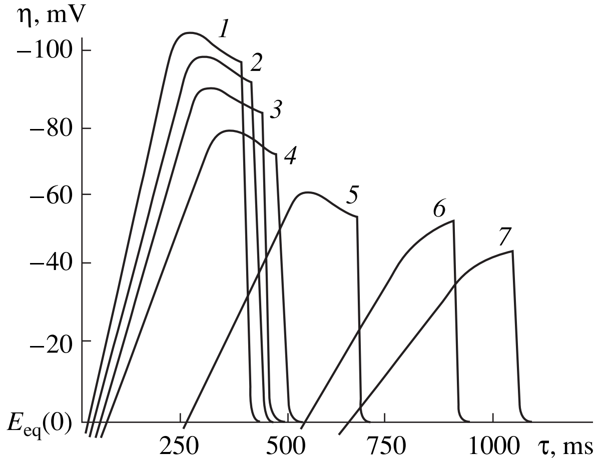

Fig. 3. Switching curves at Mo_2C electrocrystallization on a Pt electrode at various melt temperatures (S_{cr} = 7.5×10^{-3} cm^2, i_{pulse} = 0.75 mA and T equal to (*1*) 1023, (*2*) 1053, (*3*) 1083, (*4*) 1103, (*5*) 1123, (*6*) 1173, (*7*) 1223 K.

losses at the Ag electrodes in the temperature range 973–1023 K attain the values of 8–40 mV. The carbide deposition onto the substrates prepared from the same solid materials was not accompanied by crystallization overvoltage (Fig. 1). Crystallization overvoltage took place only at low overvoltage values at metals characterized by high exchange current (Fig. 2). Under these conditions, the stage of surface diffusion does limit the rate of the process at the electrode. With an increase of the rate of carbide deposition, the number of crystallization centers increases, which reduces deceleration caused by surface diffusion. As a result, higher overvoltages seem to change the limiting stage so that the process rate is determined either by the rate of electron transfer or by the rate of diffusion from the melt volume.

An increase in the melt temperature may complicate the crystallization process because of the interaction between the deposited components and the material matrix (Fig. 3). For metals forming alloys with the deposited components, crystallization overvoltage is observed for a surface oxide film (Fig. 4). After mechanical treatment of the surfaces of the working electrodes, they were electrochemically polished with simultaneous control of the substrate state in a microscope. The time of electrical polishing was determined with allowance made for the dissolution time of the Beilby layer [8].

A typical switching curve corresponding to carbide electrodeposition onto the native substrate over wide temperature and current-density ranges (973–1173 K, (i = 0.02–0.40 A/cm^2) indicates the absence of any hindrances to crystallization and any passivating films on the surface (Fig. 5). To determine the degree of the substrate inertness, we studied the overvoltage maximum and the time of its formation during electrocrystallization of Mo_2C under galvanostatic conditions on the Mo, Ti, Ni, Ag, Cu, Pt, and Mo_2C substrates. The choice of

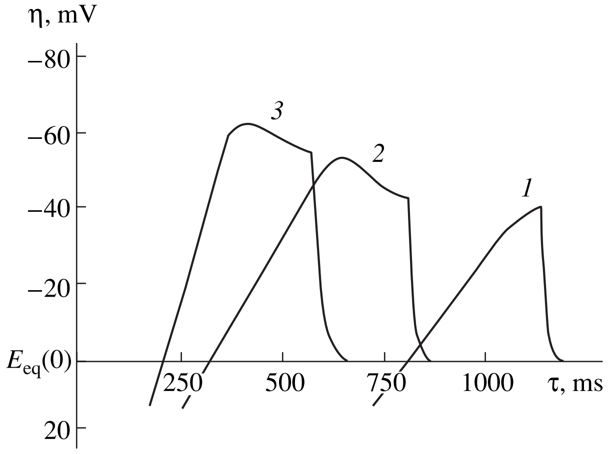

Fig. 4. Switching curves at W_2C electrocrystallization on Ni electrodes (*1*) without oxide film and (*2, 3*) with an oxide film. Oxidation time of Ni in air at $T = 1273$ K is (*2*) 15 and (*3*) 30 min.

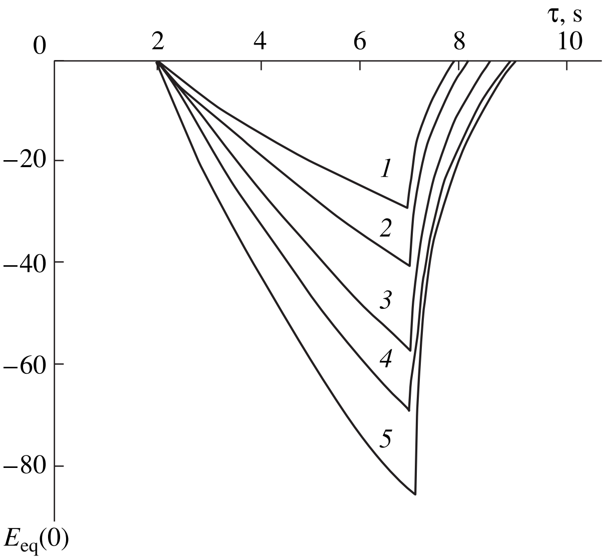

Fig. 5. Switching curves at Mo_2C electrocrystallization on the native substrate ($S_{cr} = 7.5 \times 10^{-3}$ cm^2, $\tau_{pulse} = 5$ s) from the Na_2WO_4—5 mol % MoO_3—10 mol % Li_2CO_3 at the following values of *T*, K and i_{pulse}, mA: (*1*) 973, 0.37; (*2*) 1173, 0.75; (*3*) 1073, 0.75; (*4*) 973, 0.75; (*5*) 973, 2.25.

the material of the working electrode was made with due regard for its metallochemical properties [9] and phase diagrams of binary metal systems with the Mo and C components [10]. Figure 6 shows the switching curves obtained at $T = 1173$ K and the current density $i = 0.14$ A/cm^2, which reflect the initial stages of Mo_2C electrocrystallization on various substrates.

It is characteristic that the height of the overvoltage maximum for the above metals is proportional to the reciprocal time of their formation. This seems to be associated with the penetration of the part of the deposited components into the substrate bulk due to solid-phase diffusion, which allowed us to qualitatively characterize the degree of inertness of the substrate material. Thus, crystallization overvoltage η_{max} on the Ni substrate is observed only at certain current-density values. On a Pt substrate, one observes noticeable depolarization with two pronounced waves that seem to correspond to the formation of alloys with different compositions.

An increase in the melt temperature usually activates the cathode surface, increases the rate of mutual diffusion of the deposited components of the synthesized material and the substrate, and also intensifies the reactions of their chemical interaction. We showed experimentally that Mo_2C electrodeposition at temperatures above 1173 K, even in the case of an inert Ag substrate, is accompanied by depolarization due to alloy formation. Measurements performed over the wide temperature range (973–1123 K) indicate a regular change of the initial stages of Mo_2C electrocrystallization on the substrate with an increase in temperature. Figure 7 shows switching curves, which reflect the process of nucleation of a new phase at different temperatures of the process. Curves *1–3* clearly demonstrate a decrease in the energy of formation of critical nuclei, as well as an increase in the time necessary for the attainment of the desirable supersaturation with adatoms at the moment of new-phase formation. An increase in the temperature up to 1173 K removes the crystallization hindrances at the moment of formation of stable aggregates of a new phase. A further increase in the temperature results in the fixation of obvious depolarization processes.

Figure 8 shows the dependence of the potential of the Ag electrode during electrodeposition of Mo_2C. It is seen that the crystallization overvoltage increases with an increase in the current density. According to [5], if the decelerated stage is the stage of primary formation of three-dimensional nuclei, then the following relationship should be fulfilled:

$$\log\tau = A + (k/\eta^2),$$

where τ is the time of formation of three-dimensional nuclei, *A* and *k* are the constants dependent on the material of the electrode, and η is the crystallization overvoltage. In actual fact, the experimental points in the $\log\tau - 1/\eta^2$ coordinates (Fig. 9) fit the straight lines at different melt temperatures. The further deposit growth proceeds by the layer-by-layer mechanism.

Studying electrodeposition of carbides onto different single-crystal substrates, we observed a structural mismatch. The heteroepitaxial Mo_2C and W_2C layers on the single-crystal Mo and W substrates of various orientations were deposited from the Na_2WO_4–$MoO_3(WO_3)$–CO_2 melts at $T = 1123$ K and $i = (0.5$–

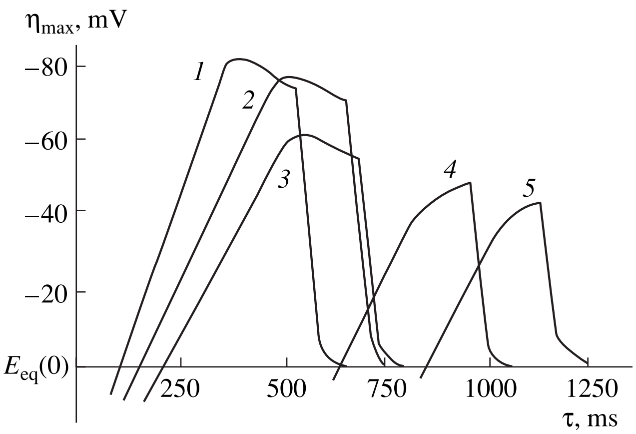

Fig. 6. Switching curves at W_2C crystallization onto the substrates prepared from different materials (S_{cr} = 7.5 × 10^{-3} cm^2, i_{pulse} = 0.75 mA, T = 1173 K; (*1*) Ag, (*2*) Au, (*3*) Cu, (*4*) Pt, (*5*) Ni.

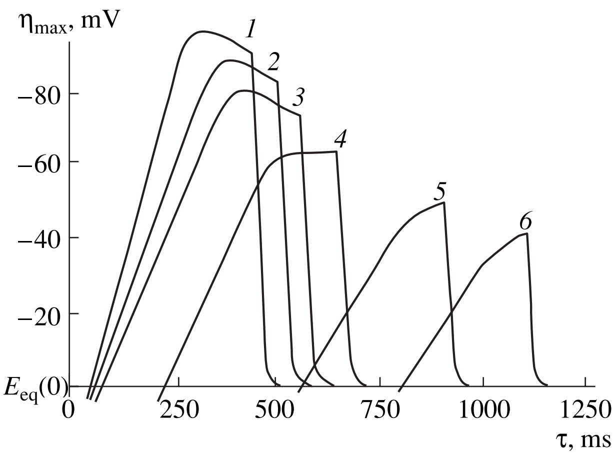

Fig. 7. Switching curves at Mo_2C electrocrystallization on Ag electrode at different temperatures (S_{cr} = 7.5 × 10^{-3} cm^2, i_{pulse} = 0.75 mA). T = (*1*) 1073, (*2*) 1123, (*3*) 1173, (*4*) 1223, (*5*) 1273, (*6*) 1323 K.

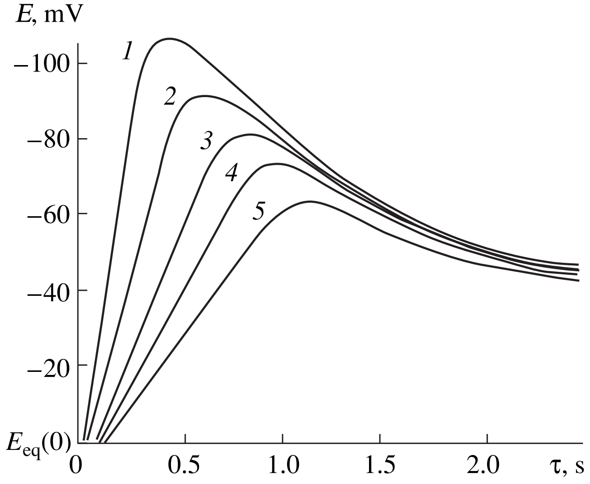

Fig. 8. Potential of Ag electrode as a function of time at W_2C electrodeposition from the melt Na_2WO_4—1.5 mol % WO_3 under 10 atm CO_2 at 1073 K (S_{cr} = 7.5 × 10^{-3} cm^2, i_{pulse} = 1.9 mA) at different current densities i: (*1*) 0.20; (*2*) 0.15; (*3*) 0.10; (*4*) 0.07; (*5*) 0.03 A/cm^2.

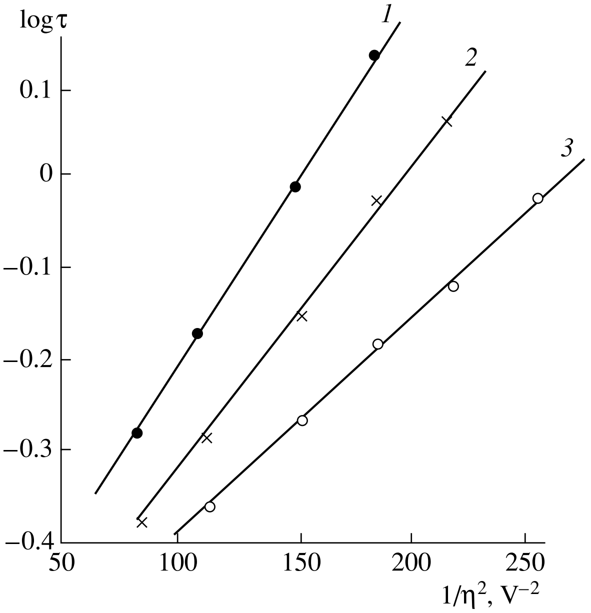

Fig. 9. Dependence of log τ on $1/\eta^2$ at W_2C electrodeposition from the melt Na_2WO_4—1.5 mol% WO_3 under a pressure of 10 atm CO_2 on the Ag electrode at T: (*1*) 1023; (*2*) 1073; (*3*) 1173 K.

1.0) × 10^3 A/m^2. Under conditions of electrolysis onto the Mo substrates with the {100}, {111}, and {112} orientations and W substrates with the {112} orientations, we obtained the layers with one and two preferable orientations. Carbides are crystallized on these substrates in the form of hexagonal plates differently oriented with respect to the substrates. The main faceting face is the basis {001} plane. The orientational relationships determined in the process of X-ray diffraction analysis are

$$(2023)Mo_2C \parallel (100)Mo,$$

$$(1011)Mo_2C \parallel (100)Mo,$$

$$(1120)[0001]Mo_2C \parallel (111)[112]Mo,$$

$$(1122)Mo_2C \parallel (112)Mo,$$

$$(1013)W_2C \parallel (112)W.$$

CONCLUSIONS

Thus, the experimental study of the initial stages of Mo_2C electrocrystallization from the tungstate–molybdate–carbonate melts with the electrodes prepared from various materials over a wide temperature range allows us to put forward the following concepts of nucleation. Thus, using the inert substrates at $T < 1073–1173$ K, we observed considerable crystallization hindrances associated with the formation of three-dimensional nuclei. An increase in the electrolysis temperature facilitates diffusion of atoms of the components into the substrate, which results in a decrease of the crystallization overvoltage. Simultaneously, a transition from the three- to two-dimensional nucleation is observed and, in some instances, to depolarization phenomena due to solid-phase saturation of the boundary layers of the electrode with the components (molybdenum and carbon) and the formation of an alloy with the material of the electrode.

REFERENCES

1. V. V. Malyshev and V. I. Shapoval, Fiz.-Khim. Mekh. Mater. **34**, 63 (1998).
2. V. I. Shapoval, V. V. Malyshev, A. A. Tishchenko, and Kh. B. Kushkhov, Zh. Prikl. Khim. (St. Petersburg) **73**, 567 (2000).
3. A. N. Baraboshkin, K. A. Kaliev, T. B. Ksenofontova, and K. P. Tarasova, Tr. Inst. Élektrokhim. Ural. Nauchn. Tsentr. Akad. Nauk SSSR, No. 15, 74 (1970).
4. K. A. Kaliev, A. G. Aksent'ev, and A. N. Baraboshkin, Tr. Inst. Élektrokhim. Ural. Nauchn. Tsentr. Akad. Nauk SSSR, No. 28, 47 (1979).
5. A. N. Baraboshkin, *Electrochemical Crystallization of Metals from Melted Salts* (Nauka, Moscow, 1976) [in Russian].
6. V. A. Polishchuk, Kh. B. Kushkhov, and V. I. Shapoval, Élektrokhimiya **26**, 305 (1990).
7. V. V. Malyshev and V. I. Shapoval, in *Abstracts of X Russian Conference on Structure and Properties of Metal and Slag Melts* (Yekaterinburg, 2001), p. 26.
8. Yu. P. Pshenichnikov, *Establishment of Thin Structure of Metals* (Nauka, Moscow, 1974) [in Russian].
9. N. A. Bogomolova, *Practical Metallography* (Vysshaya Shkola, Moscow, 1982) [in Russian].
10. W. B. Pearson, *Crystal Chemistry and Physics of Metals and Alloys* (Wiley, New York, 1972; Mir, Moscow, 1977).

Translated by L. Man

Crystallography Reports, Vol. 49, No. 5, 2004, pp. 863–870. Translated from Kristallografiya, Vol. 49, No. 5, 2004, pp. 953–960.
Original Russian Text Copyright © 2004 by Andrushevskiĭ, Shchedrin, Simonov.

CRYSTALLOGRAPHIC SOFTWARE

Algorithms for Solving Atomic Structures of Nanodimensional Clusters in Single Crystals Based on X-ray and Neutron Diffuse Scattering Data

N. M. Andrushevskiĭ, B. M. Shchedrin*, and V. I. Simonov**
** Faculty of Computational Mathematics and Cybernetics, Moscow State University,*
Vorob'evy gory, Moscow, 119992 Russia
e-mail: nandrush@cs.msu.su
*** Shubnikov Institute of Crystallography, Russian Academy of Sciences,*
Leninskiĭ pr. 59, Moscow, 119333 Russia

Received April 2, 2004

Abstract—New algorithms for solving the atomic structure of equivalent nanodimensional clusters of the same orientations randomly distributed over the initial single crystal (crystal matrix) have been suggested. A cluster is a compact group of substitutional, interstitial or other atoms displaced from their positions in the crystal matrix. The structure is solved based on X-ray or neutron diffuse scattering data obtained from such objects. The use of the mathematical apparatus of Fourier transformations of finite functions showed that the appropriate sampling of the intensities of continuous diffuse scattering allows one to synthesize multiperiodic difference Patterson functions that reveal the systems of the interatomic vectors of an individual cluster. The suggested algorithms are tested on a model one-dimensional structure. *© 2004 MAIK "Nauka/Interperiodica".*

INTRODUCTION

At present, crystalline compounds whose ideal spatial structure is distorted by nanodimensional inclusions possessing their own atomic structures are attracting ever increasing attention from numerous researchers. Thus, atoms located in quantum dots form a stable spatial structure, and the atomic groups thus formed are distributed over the initial semiconductor crystalline films. Another example is formed by fluorite phases of the composition $(M^{+2}_{1-x}TR^{+3}_{x})F_{2+x}$ doped with rare earth atoms, whose clusters most often have the composition $(M, TR)_4F_{26}$ or $(M, TR)_6F_{36}$ with linear dimensions on the order of several nanometers. It should be noted that even the substitution (or incorporation) of only one atom gives rise to noticeable displacements of the surrounding atoms of the initial crystal structure (crystal matrix). The precision X-ray methods and electron microscopy methods with atomic resolution showed that the perturbations caused by an incorporated atom attenuate at distances of the order of 1–2 nm. The spectral methods, which are more sensitive to the electronic structure, allow one to record structure distortions at larger distances. Therefore, a point defect and the displaced (relaxed) atoms of the nearest environment form a cluster whose effective dimensions are measured in nanometers. The existence of nanodimensional clusters and the changes in the electronic structure in the vicinity of each cluster considerably influence the physical properties of crystals. Thus, the presence of clusters in fluorite structures may change the ionic conductivity with respect to fluoride ions by several orders of magnitude. The determination of the spatial structure of nanodimensional clusters distributed over the crystal matrix at the atomic level is an urgent problem in modern structural crystallography.

There are numerous publications to this effect in authoritative scientific journals [1–4]. As a rule, these publications consider the determination of the nanoparticle shape from the respective X-ray diffuse scattering data. The methods described in these publications are usually associated with the determination of phase relationships for the experimentally measured diffuse-scattering intensities. Our approach to the solution of the atomic structure of equivalent nanodimensional clusters of the same orientation in the crystal matrix is associated with synthesis of an analogue of the Patterson function of interatomic vectors from the diffuse scattering data [5].

Contrary to the case of ideal crystals with the characteristic Bragg diffraction maxima, the crystals with clusters show a continuous distribution of X-ray or neutron diffraction intensities over the whole diffraction space. In this case, it is possible to ignore thermal diffuse scattering (which may be suppressed at low temperatures or may be taken into account by well known methods) and scattering from defects having no structural organization (the interblock material in mosaic crystals, etc.). The experimental record of diffuse scattering increases the volume of useful information by several orders of magnitude in comparison with the information provided by a discrete set of Bragg reflections. The interpretation of such data is considerably complicated because the diffuse-scattering intensity distribution depends on the atomic structure of clusters and their distribution and orientation in the crystal matrix. The development of efficient algorithms for interpretation of diffuse scattering is an individual problem different from the problems considered by classical diffraction analysis.

Below, we suggest and discuss numerical algorithms for the determination of the atomic structure of nanodimensional clusters in crystals. The algorithms for solving the formulated problem are based on the following assumptions. Let a crystal matrix have nanodimensional inclusions in the form of clusters possessing the same atomic structure. The equivalent orientation of these particles is predetermined by the structure of the crystal matrix. A cluster consists of several adjacent unit cells with interstitial, substitutional or relaxed atoms of the crystal matrix considerably displaced from their positions. In other words, the cluster dimension is multiple to the unit-cell dimension of the crystal matrix. Beyond the cluster, the ideal structure of the initial crystal is preserved. The distances between the clusters exceed their linear dimensions. Only under this condition, the interatomic vectors within one cluster would be spatially separated from the interatomic vectors between clusters. The latter statement is very important and considerably simplifies the determination of the atomic structure of a cluster from the corresponding function of its interatomic vectors.

Structure analysis of crystals with nanodimensional inclusions by the diffraction methods requires the use of mathematical apparatus with due regard of the finite dimensions of scattering objects. This apparatus is based on the theory of Fourier transformations of finite functions. The mathematical theory of such transformations was developed long ago and is widely used for solving various physical problems [6–9]. The application of the mathematical apparatus of finite functions to our problem allows us to synthesize multiperiodic difference Patterson functions and localize the vector systems of interatomic distances of a cluster. These functions allow us to solve the atomic structures of individual clusters. The development of the algorithms suggested in this study is based on the specific features of the Fourier analysis of finite functions and is considered in brief below.

SPECIFIC FEATURES OF FOURIER TRANSFORMATION OF FINITE FUNCTIONS

For clearer presentation and simplicity, consider the functions of one variable. Of course, the main results obtained may readily be extended to the three-dimensional case. Let $\rho(x)$ (and its square) be integrable continuous functions with a compact support L, i.e., $\rho(x) \equiv 0$ for all $|x| > L/2$. These functions are called finite. The most important characteristic of the Fourier transformation of finite functions is the relation between the coefficients of their expansions into trigonometric Fourier series and the integral Fourier transform.

The expression

$$F(q) = \int_{-L/2}^{L/2} \rho(x)\exp(-i2\pi qx)dx \tag{1}$$

is the Fourier transform of a finite function. Based on a number of theorems known in the theory of analytical functions of a complex variable, it was established that the Fourier transform $F(q)$ is always infinite [9]. In other words, there exist no finite functions possessing a finite Fourier transform. Now, expand the finite function $\rho(x)$ into a Fourier series in the basis functions $\exp\left(i2\pi\frac{k}{L}x\right)$ with the common period $T = L$, i.e.,

$$\rho(x) = \sum_{k=-\infty}^{\infty} C_k(L)\exp\left(i2\pi\frac{k}{L}x\right), \tag{2}$$

where the coefficients $C_k(L)$ are obtained from the equations

$$C_k(L) = \frac{1}{L}\int_{-L/2}^{L/2} \rho(x)\exp\left(-i2\pi\frac{k}{L}x\right)dx. \tag{3}$$

Equations (1) and (3) yield the proportionality relation $C_k(L) = \frac{1}{L}F(k\Delta q)$, where $\Delta q = 1/L$. Thus, in order to reconstruct the finite function $\rho(x)$, it is sufficient to synthesize the Fourier series

$$\rho(x, L) = \frac{1}{L}\sum_{k=-\infty}^{\infty} F\left(k\frac{1}{L}\right)\exp\left(i2\pi\frac{k}{L}x\right) \tag{4}$$

from the uniform discrete sampling of the $F\left(k\frac{1}{L}\right)$ values. Since, for all x and $x_n = x + nL$, n is an arbitrary integer, the following equation is valid: $\exp\left(i2\pi\frac{k}{L}(x+nL)\right) = \exp\left(i2\pi\frac{k}{L}x\right)$. Then, $\rho(x_n, L) = \rho(x, L)$. Thus, series (4) not only reproduces the function $\rho(x)$ at the interval L, but also continues it periodically with the period $T = L$. The sampling with a step $\Delta q = 1/L$ has the optimum density, and the synthesis of the functions with the optimum step is called a *saturated* synthesis.

It follows from the above stated facts that the Fourier transformation of finite functions is characterized by excessive information in terms of the problem of the reconstruction of the function from its Fourier transform, i.e., instead of calculating the integral

$$\rho(x) = \int_{-\infty}^{\infty} F(q)\exp(i2\pi qx)dq, \tag{5}$$

we have to sum up series (4) with the optimum discrete sampling of $F\left(k\frac{1}{L}\right)$ values. The reconstruction accuracy depends only on the number of terms (series termination) in this summation. Therefore, it is more favorable to perform the summation of the Fourier series with the optimum sampling of $F(q)$ values. The excessive information contained in the Fourier transformation of the finite function also manifests itself in the existence of the well-known Whittaker–Kotelnikov–Shannon interpolation formula [6–8], according to which the $F(q)$ value at any point may be calculated from the value of the optimum sampling $F\left(k\frac{1}{L}\right)$.

The Fourier series synthesized based on a denser sampling of $F(k\Delta q)$ values, where $\Delta q = 1/L(1 + \lambda)$ and $\lambda > 0$,

$$\rho(x, L(1+\lambda)) = \frac{1}{L(1+\lambda)}\sum_{k=-\infty}^{\infty} F\left(k\frac{1}{L(1+\lambda)}\right)\exp\left(i2\pi\frac{k}{L(1+\lambda)}x\right), \tag{6}$$

allow us to reconstruct the periodic function with the period $T = L(1 + \lambda)$. The $\rho(x, L(1 + \lambda))$ function coincides with $\rho(x)$ for all $|x| \le L/2$, and, in the intervals $(-L(1 + \lambda)/2, -L/2)$ and $(L/2, L(1 + \lambda)/2)$, the function identically goes to zero. In other words, using Fourier series (6), one may synthesize an infinite number of copies of the initial finite function $\rho(x)$ separated by the windows of zero values, with the window width being λL. The formation of windows of zero values becomes clear from the following consideration. Let us calculate the Fourier coefficients in an enlarged region $[-L(1 + \lambda)/2, L(1 + \lambda)/2]$ from the basis functions $\exp\left(-i\frac{2\pi}{L(1+\lambda)}kx\right)$ with the common period $T = L(1 + \lambda)$. Then, when calculating the coefficients $C_k(L(1 + \lambda))$, we also integrate the peripheral regions of the zero values of the function. At the same time, these coefficients coincide with the values of $\frac{1}{L(1+\lambda)}F\left(k\frac{1}{L(1+\lambda)}\right)$. As a result, the function synthesized with the use of these coefficients would acquire windows of zero values.

With an increase in λ (a decrease in the sampling step), the basis copy $\rho(x)$ remains intact, whereas the width of the windows of zero values increases. Moreover, if $\lambda \longrightarrow \infty$, the window width tends to infinity, $\lambda L \longrightarrow \infty$, which corresponds to integral representation (5) of the initial finite function. The synthesis of functions with the step $\Delta q = 1/L(1 + \lambda)$, $\lambda > 0$ is called *supersaturated*. If we posses high-resolution data, such syntheses may be used for evaluating the error of the function approximation by a finite Fourier series from the oscillations in the region of zero windows. These oscillations depend only on the Fourier series termination.

Quite different effects arise with an increase in the sampling step (*unsaturated sampling*). Let $\Delta q = 1/L(1 - \lambda)$, $0 < \lambda < 1$. Then, the Fourier series

$$\rho(x, L(1-\lambda)) = \frac{1}{L(1-\lambda)}\sum_{k=-\infty}^{\infty} F\left(k\frac{1}{L(1-\lambda)}\right)\exp\left(i2\pi\frac{k}{L(1-\lambda)}x\right) \tag{7}$$

also gives rise to a periodicity but with a different period, $L(1 - \lambda)$. Since $L(1 - \lambda) < L$, the function to be synthesized differs from the initial one. At $0 < \lambda < 2/3$, the distortions are caused by the cross superposition of the left-hand wing of the initial function onto the right-hand wing and vice versa, whereas, at $2/3 < \lambda < 1$, the superpositions are more complicated [10].

The most interesting effect is the n-tuple superposition. We calculate the Fourier coefficient $C_k(L/n)$ of the initial finite function $\rho(x)$ with the substrate $[-L/2, L/2]$ over the basis trigonometric functions $\exp\left(-i2\pi\frac{nk}{L}x\right)$ with the common period $T = L/n$, where $n > 1$ is a fixed integer. Then, the coefficients $C_k(L/n)$, being the results of the integration of the functions $\rho(x)\exp\left(-i2\pi\frac{nk}{L}x\right)$ over the region $[-L/2, L/2]$, would identically coincide with the Fourier coefficients $D_k(L/n)$ of the function $\hat{\rho}(x)$ obtained as a result of the superposition of n parts of the initial functions within the interval $[-L/2n, L/2n]$. At the same time, the coefficients $C_k(L/n)$ coincide with the $\frac{n}{L}F(k\Delta q)$ values (where $\Delta q = n/L$). Therefore series (7) is the superposition function $\hat{\rho}(x)$ with the period $T = 4/n$. Thus, with an n-tuple increase in the optimum-sampling step, an effect of the n-tuple superposition is observed. For arbitrary finite functions, the effect of the superposition, including the n-tuple superposition, results in the negative phenomenon of the dramatic change of the initial function [10]. However, for the functions of the special class, the effect of the n-tuple superposition results only in the proportional increase in the values of the initial function, i.e., has a multiplicative character. The electron-density distributions in single crystals with a finite number of the translational repetitions of electron-density of one unit cell belong to this class of functions,

$$\rho(x) = \sum_{m=1}^{N} \rho_1(x-m), \tag{8}$$

where $\rho_1(x) \geq 0$ is the electron-density distribution in one unit cell and $N = nl$ is the number of unit cells in the single crystal. Hereafter, we use the relative spatial coordinates conventional in the structure analysis, i.e., the coordinates x in the relative units of the unit-cell parameters and, therefore, also the coordinates q in the reciprocal space in the relative units of the reciprocal unit-cell parameters. These functions are reconstructed with the optimum discretization step $\Delta q = 1/N$. However, at $F(k\Delta q)$ sampling with the step $\Delta q = n/N = 1/l$, the function synthesized with the aid of the Fourier series has the period $T = l$ and is the result of n-tuple superposition of the identical electron-density portions having the length of l unit-cells, i.e.,

$$\hat{\rho}(x) = n\sum_{j=1}^{l} \rho_1(x-j). \tag{9}$$

Thus, for finite distributions with a finite number of translations, the effect of n-tuple superposition results only in a proportional increase in the initial-function values. This is valid only if $N/n = l$ is an integer. It should also be indicated that if $N = nl + r$ and $0 < r < l$, the distortions are caused only by the superposition of a certain part of the electron-density portion of length equal to r unit cells. Since diffraction intensities for single crystals are recorded only at the integral points of the reciprocal space (Bragg points), the only possible sampling step is $\Delta q = N/N = 1$ and, therefore, the functions to be synthesized are 1-periodic functions. In this case, the effect of the N-tuple superposition introduces no distortions to the electron-density distribution within one unit cell. The algorithms for interpreting diffuse scattering from crystals with clusters allow one to control the selection of the discretization step more flexibly. Thus, if the cluster dimension equals $l \geq 1$ unit cells, then it is expedient to compare the periodic Patterson functions with the multiple periods $T = kl$, where $k = 2, 4$. Therefore, with this aim, one has to use sampling of $I(q) = |F(q)|^2$ values with the step of $\Delta q = 1/kl$.

MULTIPLY PERIODIC DIFFERENCE PATTERSON SYNTHESES

The direct calculation of the autocorrelation (Patterson) function of a finite one-dimensional distribution $\rho(x)$ set in the region $[0, N]$, reduces to the calculation of the parametric set of integrals,

$$P(x) = \int_{\max(x,0)}^{\min(x+N,N)} \rho(u)\rho(u+x)du. \tag{10}$$

Obviously, $P(x)$ is defined within the interval $[-N, N]$ and is an even function. It follows from Eq. (10) that, in finite single-crystal distribution (8), we obtain at the integral points $x = n$ the Patterson function $P(n) = (N - |n|)\int_0^1 \rho_1^2(u)du = (N - |n|)P_1(0)$, where $P_1(x)$ is the autocorrelation function of the electron density within one unit cell. The $P(x)$ distribution is a symmetric cascade of $2N$-similar distributions which tend to zero according to the linear law

$$P(x) = \sum_{n=-N}^{N} w(x)P_1(x-n), \tag{11}$$

with the weight function $w(x) = N - |x|$, $|x| \leq N$. Since the support of $P_1(x)$ is defined within the interval $[-1, 1]$, then each unit cell should unavoidably have the peaks due to the interaction with the atoms of the neighboring cells.

For the complete reconstruction of the autocorrelation function of electron density of a crystal of finite dimensions with the aid of its Fourier transform $|F(q)|^2$, one has to use the optimum sampling step $\Delta q = 1/2N$. If an isometric crystalline sample used in the diffraction experiment consists of $N \sim 10^{18}$ unit cells, then the optimum discretization step equals $\Delta q \sim 10^{-6}$ along each coordinate direction of the reciprocal space. In reality, the experimental measurements are usually performed at a considerably lower resolution and, therefore, the superposition effects are unavoidable.

Now, consider the effect produced by multiple superpositions. First of all, consider the case $n = 2N$, i.e., $\Delta q = 1$. Then, since the weight function $w(x)$ at $2N$-tuple superposition is linear, we arrive at the 1-periodic Patterson function, $P(x, 1) = N^2\hat{P}_1(x, 1)$, where $\hat{P}_1(x, 1)$ differs from $P_1(x)$ in that each unit cell has genetical peaks due to interactions with the atoms of the neighboring unit cells. This hinders the localization on the Patterson function of the unique image of the atomic structure, i.e., the interpretation of the corresponding vector system.

It is expedient to compare the syntheses of the autocorrelation functions at the sampling steps $\Delta q = 1/2l$ and $\Delta q = 1/4l$. It follows from Eq. (11) that, for a single crystal with a very large number of unit cells, one may write the relationship

$$P(x, 2l) = 2P(x, 4l), \tag{12}$$

which is valid with a high degree of accuracy and plays an important role in the algorithm for interpreting diffuse scattering from crystals with clusters. Consider the

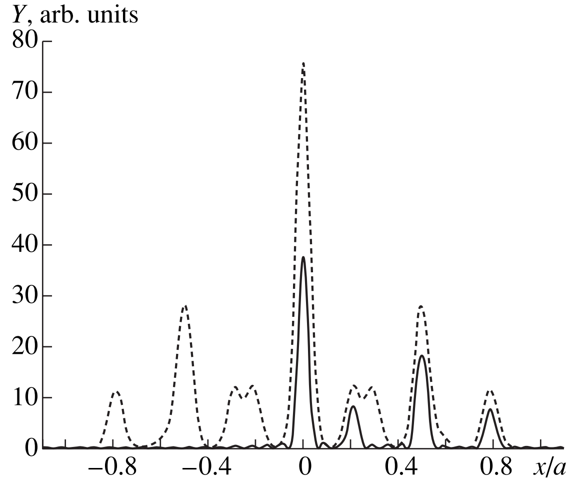

Fig. 1. Electron-density distribution for a group of atoms—Y, O, K, and O—on a 10-Å-long segment (solid line) and the autocorrelation function of this distribution (dashed line).

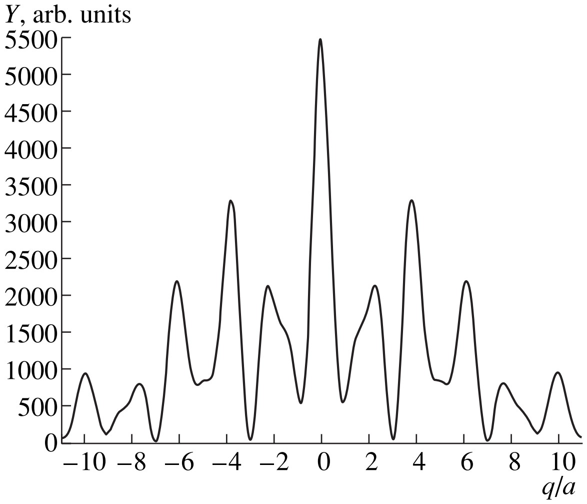

Fig. 2. X-ray scattering intensity from the atomic group shown in Fig. 1.

electron density of a crystal with clusters,

$$\rho(x) = \rho_1(x) + \rho_2(x) = \sum_{n \in I_1} \rho_{\text{mat}}(x-n) + \sum_{m \in I_2} \rho_{\text{clast}}(x-m),$$

which consists of $N = N_1 + N_2$ unit cells, where N_1 is the number of the unit cells in an ideal crystal matrix, $N_2 = lN_{\text{clast}}$ is the total number of the unit cells occupied by clusters, N_{clast} is the number of clusters, l is the cluster dimensions, $\rho_{\text{mat}}(x)$ is the electron-density distribution in one unit cell of the crystal, $\rho_{\text{clast}}(x)$ is the electron-density distribution in a cluster, I_1 is the set of the coordinates of the unit cells of the crystal matrix, and I_2 is the set of cluster coordinates.

Let $F_{\text{mat}}(q)$ and $F_{\text{clast}}(q)$ be the Fourier images of the electron density of the crystal matrix and the electron density of the set of clusters, respectively. Then, the intensity $I(q)$ of diffuse scattering consists of three terms,

$$I(q) = |F_{\text{mat}}(q)|^2 + [F_{\text{mat}}(q)F^*_{\text{clast}}(q) + F^*_{\text{mat}}(q)F_{\text{clast}}(q)] + |F_{\text{clast}}(q)|^2.$$

Here, an asterisk indicates complex-conjugated quantity. These terms are the Fourier transforms of the autocorrelation function $P_{\text{mat}}(x)$ of the electron density of the crystal matrix, the cross correlation function $P_{\text{cross}}(x)$ between the electron densities of the matrix crystal and the set of clusters, and the autocorrelation function $P_{\text{clast}}(x)$ of the clusters. If the number of the unit cells in the crystal is very large and $lN_{\text{clast}}/N \ll 1$, then the following relationships are valid for the synthesized Patterson functions with the sampling of the $I\left(k\frac{1}{2l}\right)$ and $I\left(k\frac{1}{4l}\right)$ values:

$$\begin{aligned} P_{\text{mat}}(x, 2l) &\approx 2P_{\text{mat}}(x, 4l), \\ P_{\text{cross}}(x, 2l) &\approx 2P_{\text{cross}}(x, 4l), \\ P_{\text{clast}}(x, 2l) &> 2P_{\text{clast}}(x, 4l). \end{aligned} \tag{13}$$

The latter inequality is provided by the fact that, at random cluster distribution, the superposition of the autocorrelation functions on the synthesized functions occurs more often within the interval with the dimension $2l$ and not in the interval with the dimension $4l$. It follows from (13) that, at the difference Patterson synthesis,

$$\begin{aligned} R(x) &= P(x, 2l) - 2P(x, 4l) \\ &\approx K[P_{\text{clast}}(x, 2l) - 2P_{\text{clast}}(x, 4l)], \end{aligned} \tag{14}$$

the autocorrelation function of one cluster is seen in the region $|x| \le 2l$. For clusters containing interstitial or substitutional heavy atoms, the difference synthesis reveals the images of the cluster structure in these atoms.

It should be emphasized that the difference syntheses of the integral multiply periodic syntheses of the autocorrelation distributions are more representative because they clearly reveal the vector system of interatomic distances. This imposes some requirements on the appropriate choice of diffuse-scattering intensities at a discrete network. Naturally, *a priori* knowledge of the cluster dimension facilitates the procedure for the purposeful search for a solution.

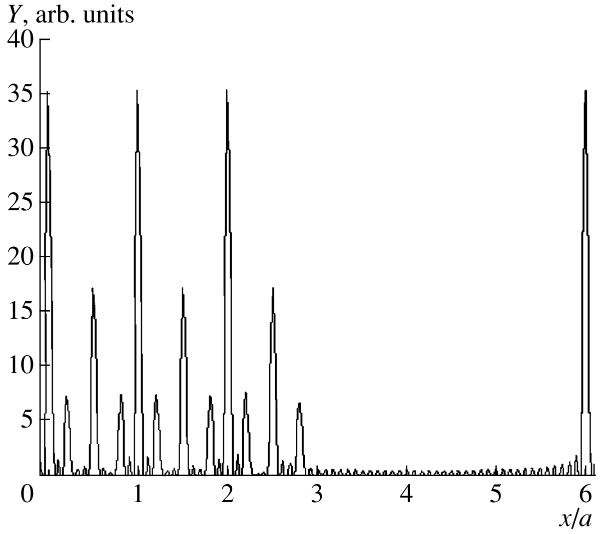

Fig. 3. Electron density of a triple group of atoms shown in Fig. 1 and restored from its Fourier transform with double density of the optimum sampling.

ALGORITHM TEST ON ONE-DIMENSIONAL MODELS

For a clearer and simpler representation of the specific features of the Fourier transformation of finite functions, consider the arrangement of four atoms within the linear segment a = 1 nm (10 Å), namely, Y (x = 0.00), O (x = 0.2), K (x = 0.5), and O (x = 0.8). The atomic coordinates are indicated in parentheses in the relative units of the segment length. The electron-density distribution of this "nanoparticle" is shown by the solid line in Fig. 1. The autocorrelation function (function of interatomic vectors) of this atomic group is centrosymmetric and occupies a segment of a length of 2 nm (dashed line in Fig. 1). The intensity of X-ray scattering from this particle is shown in Fig. 2 in the range of the reciprocal-lattice vector q from –10/a to +10/a. Beyond this interval, the scattering intensity rapidly decreases.

Above, when considering the specific features of the Fourier transformations of the finite functions, we restored the functions from their Fourier transforms with the saturated, unsaturated, and supersaturated discrete samplings. For practice, the supersaturated sampling is very interesting, because its values allow one not only to restore the function, but also to estimate the effect of the corresponding Fourier-series termination. As a characteristic example, consider a "minicrystal" obtained by translational tripling of the initial nanoparticle. The crystal dimension is only 3 nm. The Fourier transform $F(q)$ of the electron density of this crystal and the scattering intensity $|F(q)|^2$ are continuous functions. To restore the electron density of the crystal with the dimension 3a, it is sufficient to synthesize the Fourier series with the use of a discrete set of $F(k\Delta q)$ values, where $\Delta q = 1/3a$ is the optimum sampling step. Figure 3 shows the restoration of the electron-density distribution of this nanocrystal with double density of the sam-

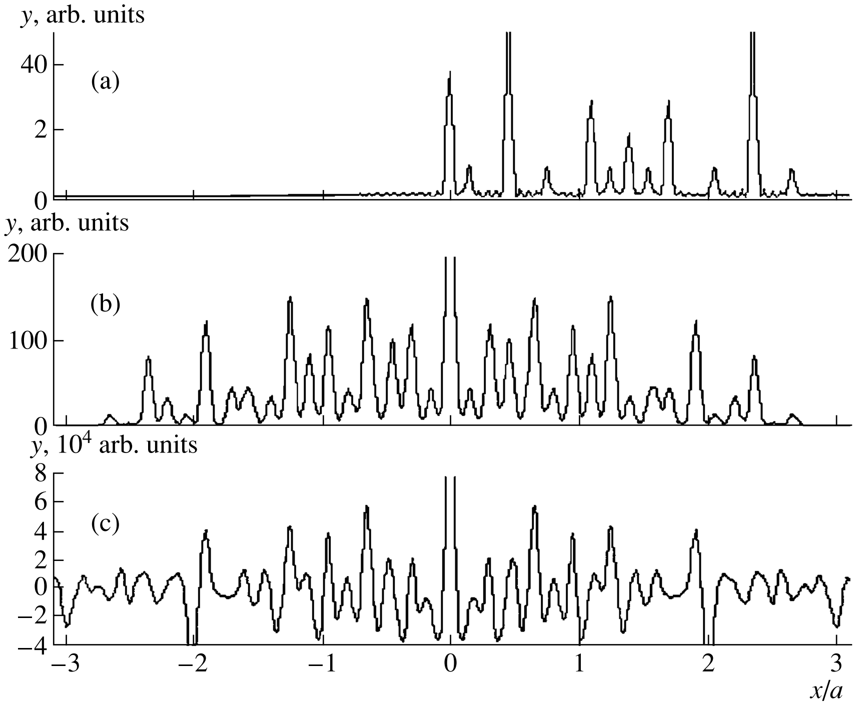

Fig. 4. (a) Electron density of a cluster occupying three unit cells and consisting of Y, O, Ba, O, Zn, O, K, O, Zn, O, Ba, and O atoms. (b) Patterson function of this cluster; (c) difference synthesis of multiply periodic Patterson functions.

pling, i.e., $\Delta q = 1/6a$. In this case, the crystal structure is completely restored within the interval $3a$, which is followed by the interval $3a$ of the zero electron-density values. The use of the Fourier series instead of the Fourier integral resulted in the formation of a periodicity with the period $T = 6a$. It is seen from Fig. 3 that the accepted series termination does not introduce considerable distortions into the electron density of the crystal under consideration.

The efficiency of the algorithms for analysis of the diffuse-scattering intensities from crystals with clusters is illustrated by the following model. A crystal matrix with the period $a = 10$ Å is constructed by multiple translation of an initial nanoparticle consisting of four atoms. This crystal includes clusters having the same structure. A cluster with the dimension 30 Å or, in relative units, $l = 3$ unit cells, consists of 12 atoms: Y($x = 0.00$), O($x = 0.15$), Ba($x = 0.45$), O($x = 0.75$), Zn($x = 1.10$), O($x = 1.25$), K($x = 1.40$), O($x = 1.55$), Zn($x = 1.70$), O($x = 2.05$), Ba($x = 2.35$), and O($x = 2.65$). The atomic coordinates in the relative units are indicated in parentheses. This cluster is obtained by replacement of two K atoms by Ba atoms and two Y atoms by Zn atoms in three successive unit cells of the single crystal with the structure of the basic nanoparticle. All the remaining atoms became noticeably displaced from their positions in the nanoparticle. The electron-density distribution in the cluster and the corresponding autocorrelation function are shown in Figs. 4a and 4b.

The diffuse-scattering intensity was calculated for a crystal with the dimension $N = 1020$ unit cells, of which 102 unit cells occupied 34 clusters. The basic nanoparticles are located in 918 unit cells of the crystal matrix. The clusters were randomly distributed. The distances between the clusters ranged within 3–15 unit cells. Since the number of electrons in a cluster is $M_c = 278$ and the number of electrons in three unit cells of the crystal matrix is $M_m = 222$, the total number of electrons in all the clusters amounts to 12% of the total number of electrons in the crystal. Such a large number of irregularly distributed clusters provides a level of diffuse-scattering intensities sufficient for measurement. The intensity $|F(q)|^2$ was calculated in the region $|q/a| \leq 10$ with the step $\Delta q = 1/4l = 1/12a$. The choice of the discretization step was based on *a priori* information on the cluster dimension $l = 3a$. These data were used to synthesize multiply periodic Patterson functions with the periods $T_1 = 6a$ and $T_2 = 12a$. Then, their difference function was calculated (Fig. 4c). The contrast of the Patterson syntheses was enhanced by the optimum-sharpening method [11].

Comparing the Patterson function of one cluster (Fig. 4b) with the difference synthesis of the multiply periodic Patterson functions (Fig. 4c), we see that the difference function allows one to localize all the vectors between the heavy atoms of the cluster. The suggested approach has one important characteristic. It allows one to localize those interatomic vectors in a cluster whose lengths exceed the unit-cell dimensions in the crystal matrix.

CONCLUSIONS

The approach to the determination of the atomic structure of nanodimensional inclusions possessing a certain structure and orientation in the crystal matrix is based on the use of X-ray or neutron diffuse-scattering data. A crystal with an ideal structure allows one to measure only discrete Bragg reflections. Diffuse scattering is observed if the regular structure of the crystal is distorted or if the dimensions of the scattering objects are considerably reduced. In the present study, we analyzed diffuse scattering from nanodimensional clusters present in the crystal. The analysis of such inclusions was performed with the aid of the mathematical apparatus of the Fourier transformations of finite functions. It turns out that, in this case, the resolution with which the experimental measurements of the continuous diffuse-scattering distribution are made is of great importance. As in the case of Bragg reflections, in the case of diffuse scattering, we measure only the intensities, whereas there is no information on the phases. The atomic structure of the object can be established from the intensity data by only two methods—either by solving the phase problem or by synthesizing and interpreting the function of interatomic vectors.

In the present study, we formulated the problem of construction of an analogue of the Patterson function that would allow one to single out the interatomic vectors of only one cluster. It is shown that this problem may be solved based on the multiply periodic difference Patterson syntheses. The efficiency of the corresponding algorithms is demonstrated on one-dimensional models. The extension of the results obtained to a real three-dimensional crystal gives rise to no considerable difficulties, but requires an enormous number of experimental diffuse-scattering measurements in the three-dimensional space and powerful computers for subsequent interpretation of the data obtained.

The above algorithms were considered in the one-dimensional variant in order to simplify the consideration and make it clearer. It should be indicated that the use of the number of unit cells of a finite crystal in the mathematical expressions is rather formal. In the final analysis, the knowledge of the real number of the unit cells is not necessary, because the knowledge of the linear cluster dimensions is sufficient for the correct use of the discrete values of diffuse-scattering intensities. In the absence of the necessary information on the cluster dimensions, it may be established by trial and error.

The practical efficiency of the suggested approach depends on the solution of two problems. The first one is the collection of the experimental data at a necessary resolution. The second one is the determination of the structure from the distribution of interatomic vectors, conventional for the Patterson methods.

ACKNOWLEDGMENTS

This study was supported by the program for Leading Scientific Schools, project no. NSh-1642.2003.5.

REFERENCES

1. J. Miao, P. Charalambons, J. Kirz, and D. Sayre, Nature **400**, 342 (1999).
2. J. Miao, T. Ishikawa, B. Johnson, *et al.*, Phys. Rev. Lett. **89** (8), 088303 (2002).
3. J. C. H. Spence, J. S. Wu, C. Giacovazzo, *et al.*, Acta Crystallogr., Sect. A: Fundam. Crystallogr. **59**, 255 (2003).
4. I. A. Vartanyants and I. K. Robinson, J. Synchrotron Radiat. **10**, 409 (2003).
5. N. M. Andrushevskiĭ, B. M. Shchedrin, L. F. Malakhova, and V. I. Simonov, Kristallografiya **47** (3), 518 (2002) [Crystallogr. Rep. **47**, 471 (2002)].
6. J. M. Whittaker, Proc. Math. Soc. Edinburg **1**, 169 (1929).
7. V. A. Kotel'nikov, in *Proceedings of I All-Union Meeting on Problems in Technical Reconstruction of the Communication* (Vsesoyuz. Énerg. Komitet, Moscow, 1933).
8. C. Shannon, *Papers on the Information Theory and Cybernetics* (Inostrannaya Literatura, Moscow, 1963).
9. Ya. I. Khurgin and V. P. Yakovlev, *Finite Functions in Physics and Engineering* (Nauka, Moscow, 1971) [in Russian].
10. I. Daubechies, *Ten Lectures on Wavelets* (Society for Industrial and Applied Mathematics, Philadelphia, 1992; RKhD, Moscow, 2001).
11. N. M. Andrushevskiĭ, N. P. Zhidkov, and B. M. Shchedrin, Dokl. Akad. Nauk SSSR **261** (3), 616 (1981) [Sov. Phys. Dokl. **26**, 1022 (1981)].

Translated by L. Man

Crystallography Reports, Vol. 49, No. 5, 2004, pp. 871–877. Translated from Kristallografiya, Vol. 49, No. 5, 2004, pp. 961–968.

CRYSTALLOGRAPHIC SOFTWARE

A Program Set for Direct Calculation of Vibrational States of Crystal Structures in a Molecular Approach

L. A. Gribov and V. A. Dement'ev

Institute of Geochemistry and Analytical Chemistry, Russian Academy of Sciences,
ul. Kosygina 19, Moscow, 119991 Russia
e-mail: dementiev@geokhi.ru

Received April 8, 2003

Abstract—A Crystal program set intended for calculation of vibrational states of finite arbitrary crystal structures on a personal computer and an MVS-1000 supercomputer is described. Examples of calculated frequency histograms for models of different sizes are reported. © *2004 MAIK "Nauka/Interperiodica".*

INTRODUCTION

Information on the entire spectrum of vibrational frequencies of crystals serves as a basis for theoretical constructions in many fields of knowledge related to physical and chemical properties of materials. In particular, all thermodynamic functions of crystals are calculated based on their vibrational spectra. The calculation of the vibrational spectrum of a crystal is always a difficult and cumbersome problem. It is always solved in a particular approximation. The most popular approach is the infinite crystal approximation, in which the use of the translational symmetry of a crystal makes it possible to obtain analytical expressions for the cutoff frequencies of normal waves in the crystal. However, this approximation cannot be used in all cases. Its significant drawback is the complete loss of information on the surface vibrational states, whereas many important applications of crystal chemistry require knowledge of the phenomena occurring on the surface of a vibrating crystal or crystallite. For example, the growth dynamics and the morphology of polycrystalline formations are determined in many respects by the distribution of the vibrational energy between the surface and volume vibrations of initial and intermediate crystallites forming the final aggregate. These factors also determine the behavior of domains during phase transformations. Finally, the problems of the theory of ultrathin crystal films and crystalline nanoparticles require exact calculation of the entire vibrational spectrum for these objects. In this case, the infinite-crystal approximation is quite useless, because it gives no information on the shape and sizes of the object under study. Thus, the theory of crystal vibrations encounters an urgent problem of modeling the vibrational states of real crystal objects of certain shapes and sizes, containing dislocations and characterized by other specific features.

In this study, we propose a method for calculating vibrational spectra of crystallites of arbitrary shape and size, which can be easily extended to crystallites containing defects of any type. The basic concept of the method is the representation of a crystallite as a supermolecule. Of course, this representation can also be referred to as a molecular approach. However, we will try to show that the limitations imposed on this approach are much less strict than for other known approximations.

The choice of a method for theoretical analysis of a complex chemical object depends on many factors. Some of them determine the strategy of developing the method; others must be taken into account in elaborating computational procedures implementing the tactics for planned studying of the object. Our experience shows that the most successful and long-lived methods are the ones that maximally take into account the decisive strategical factors, which allows one to choose the optimal tactics based on promising informational technologies.

One of the most important factors for theoretical analysis is the optimal choice of a physical model of a complex chemical object. A physical model can be considered ideal if it can be used for a wide class of objects under study and makes it possible to increase easily the complexity and dimension of objects of the chosen type. In our opinion, the best model for describing vibrations in crystals is the model of a supermolecule in which vibrations are set in the so-called natural vibrational coordinates [1, 2]. The following considerations speak in favor of this model.

Infinite crystal structures can be exhaustively described by the Cartesian coordinates of atoms in the unit cell and the translation vectors. Therefore, theoreticians, quite naturally, have tended to describe the vibrational motions of atoms in an infinite crystal in Cartesian coordinates taking into account its translational symmetry. This approach very seriously limits the possibility of applying the infinite-crystal approximation to a wide class of crystal structures and also narrows the range of problems arising in spectrochemical investigations. First of all, the force parameters of the model have no translational invariance in the Cartesian coordinates. This circumstance excludes the possibility of applying the force parameters obtained previously by studying fragments of a crystal or related chemical structures to the model of the crystal under consideration. At the same time, the application of the parameters determined by solving inverse spectroscopic problems for simpler objects to the solution of direct problems for more complex objects is the main line of research aimed at accumulating material spectrochemical constants. One can easily see that the description of vibrations in crystals in the Cartesian coordinates isolates the spectrochemistry of crystals from the entire set of spectrochemical studies. This is especially pronounced in the case of molecular crystals, the nature of which facilitates the separation of vibrational motions into local and intermolecular vibrations. When the motions are described in Cartesian coordinates, such a separation into intramolecular and intermolecular vibrations is highly impeded. In addition, it is impossible to use the force constants found previously by studying the molecules entering the unit cell of a molecular crystal. Thus, a new system of force constants should be sought, which strongly reduces the research efficiency.

In contrast to this approach, the description of motions in a crystal in natural vibrational coordinates accepted in the theory of vibrational spectra of polyatomic molecules makes it possible to pass, in investigations, from molecules to crystals and thus continue the unified process of spectrochemical study of matter. Our experience in studying the homologous series of organic compounds [3–6] shows that the force constants of polyatomic functional groups can be successfully transferred from one compound to another along with these groups. This circumstance allows one to use a relatively limited set of conventional molecular models when investigating spectra of an immense number of organic compounds containing fragments of these models. The above considerations refer also (though to a lesser extent) to electro-optical parameters, knowledge of which is necessary for calculating band intensities in IR spectroscopy. It can be assumed with confidence that, when natural vibrational coordinates are used in studying molecular crystals, the models approved by solving inverse problems can be fully used, i.e., built in the unit cell of a crystal along with all the set of their force and geometric parameters. Then, there will remain only one thing to do: to introduce the vibrational coordinates describing intermolecular bonds. In the case of a real crystal, this approach can also be efficient if one investigates, previously, a small cluster, solves the inverse spectral problem for it, and then applies the found force constants to the extended model of the crystal.

Another serious restriction imposed by the use of Cartesian coordinates concerns the study of anharmonic motions in molecules and crystals. The vibrational anharmonicity is an essentially nonlinear effect, which should be described in curvilinear generalized coordinates [7]. The natural vibrational coordinates are most convenient for description of both harmonic and anharmonic motions of a molecular model. In this case, the form of the vibrational Hamiltonian in the harmonic approximation is significantly simplified, since all the matrix elements become constant, whereas, in the anharmonic approximation, they are functions of generalized coordinates. However, it is important that, as our experience shows, the use of natural vibrational coordinates in the anharmonic approximation also makes it possible to simplify the analysis of vibrations, since one can select the vibrations with anharmonicity that can be neglected and exclude them from a solution to the anharmonic problem. This concept was verified by an example of vibrations in complex compounds and we can assume with confidence that analysis of anharmonic vibrations in molecular crystals can be performed carrying out the same procedures if natural vibrational coordinates are introduced into the model of a crystal. Therefore, the use of an adequate coordinate system in description of crystals leads directly to investigation of anharmonicity effects, which contribute to many properties of crystals, for example, thermal expansion.

We mentioned above the advantages of using natural vibrational coordinates in the analysis of molecular vibrations. We should note again the clarity of this approach and the relevant simplicity of interpreting the results obtained. However, application of this approach to complex molecular and crystal structures always gives rise to a large number of extra (dependent) coordinates. As a rule, it is impossible to introduce initially only independent coordinates, if for no other reason than the symmetry considerations. Therefore, a special algorithm excluding this dependence is required. It was shown in [1, 2] that this problem can be solved in the general form if rectangular rather than square (generally accepted in theoretical mechanics) matrices are used in the necessary coordinate transformations. Physically, this means a transition from the initial coordinates to their independent linear combinations. We will demonstrate below how this procedure works in the case of crystals.

STAGES OF PROGRAM CONSTRUCTION OF A CRYSTAL MODEL IN NATURAL VIBRATIONAL COORDINATES

We propose the following sequence of operations to construct a crystal model and the corresponding algorithms in the form of a new program set (Crystal program set).

For a real crystal, the Cartesian coordinates of atoms and the geometric parameters of the unit cell are generally known from the X-ray diffraction data. These data are input into the special program Crystall.m, which is written in the MatLab programming system. The input data for the program are the Cartesian coordinates and chemical symbols of all atoms forming the cell and one of the three translation vectors. The program translates each atom of the unit cell in a specified direction at a specified distance, tracing the overlapping of newly formed atoms at the unit-cell faces. Overlapped (extra) atoms are rejected. Thus, a column containing two unit cells is obtained. This process can be repeated any number of times, specifying a multiple value of the translation vector for the new model. As a result, a one-dimensional (1D) crystalline chain is formed. In the same way, a spatial model of a crystal filament can be obtained. Such nanofilaments have already been obtained experimentally, and their properties are being studied.

Furthermore, the thus obtained 1D structure is translated in the second crystallographic direction. As a result, a model of a two-dimensional (2D) ultrathin crystal film is obtained. Such films are of much interest for nanotechnology. Then, the obtained 2D model can be translated in the third direction to obtain a model of a crystallite of any shape and size. In contrast to the infinite-crystal model, this model has a clearly pronounced surface, to which films with another structure can be added, which is necessary for modeling surface reactions and catalytic phenomena.

For a molecular crystal, the procedure of constructing a model is even simpler if there are ready models of the molecules forming the crystal unit cell. Such models are formed by the LEV program set [8] and stored in its databank. These models should be imported into the JoinFragments program, which combines fragments of the models into the new model and orients properly the imported models with respect to each other. As a result, a researcher automatically obtains the Cartesian coordinates of all atoms forming the unit cell. Then, the coordinates and symbols of all atoms in the thus obtained model of the unit cell of the future crystal are input into the Crystall.m program and translated as noted above.

When the construction of the crystallite structure is finished, the program analyzes the distances between the atoms, finds pairs of atoms with minimum distances, and makes necessary marks for these pairs in the adjacency matrix. Thus, a correspondence with possible valence bonds between atoms in the crystal is established. At the output, the program creates a text file. The numbers of atoms and valence bonds in the crystal model are written in the file; then, the Cartesian coordinates and the chemical symbol of each atom are written; and, finally, the upper triangle of the adjacency matrix is written. This file structure corresponds to the format of files with the .CT extension into which the information on the spatial structures of molecules is input/output by the well-known chemical-modulating system ChemOffice [9]. A researcher, if needed, can use the possibilities of ChemOffice to construct a required crystal model and write it in an external file in the .CT format. These intermediate results will be identical. However, the program proposed here makes it possible to increase significantly the research efficiency, since it carries out all the operations related to the unit-cell translation and formation of the system of valence bonds in a model.

Using the possibilities of our system of visual molecular modeling—LevInfinite—the Cartesian coordinate of all atoms of the crystal model derived can be imported into the CreateVibrModel program along with the adjacency matrix from the file with the .CT extension. Based on this information, the CreateVibrModel program constructs a visual model of a crystallite with a ready system of vibrational coordinates of the valence-bond stretching type. Then, if necessary, the program automatically forms the system of coordinates of variations in all bond angles of the crystal model.

In the next stage, the FcEOPs program from the LevInfinite system should be used. This program creates a system of force constants for the crystal model. In the first stage, the program forms a system of equivalent vibrational coordinates and characteristic force constants. Those coordinates are considered equivalent, describe identical sets of atoms, and have the same geometric characteristics. Inertia tensors of the groups of atoms used in the description of each vibrational coordinate are taken as the geometric characteristics. The tensors are reduced to the principal axes, which makes it possible to use only three numbers for comparing the geometry of atomic groups, independent of their position in space as a unified system. The system of characteristic signs for the pairs of interacting vibrational coordinates is formed in the same way. For long-range interactions, the force constants are not introduced. As a result, the force field of a highly extended crystal model can be described by a relatively small number of characteristic force constants.

The second operation carried out by the FcEOPs program is the input of characteristic force constants. This can be done either in a dialog mode or automatically (in this case, the program imports the characteristic constants from any previously prepared molecular or crystal model containing fragments of the new model).

Thus, a researcher can rapidly model a great variety of crystal structures (crystallites, nanofilms, nanofilaments, polymer filaments and grids, and so on) using the same visual technique on a personal computer. Moreover, the initial information on crystal structures can be used in any accessible form. This information may include published X-ray diffraction data, data from computer banks on molecular and crystal structures, and ready molecular models from computer banks of standard vibrational models.

CALCULATION OF THE VIBRATIONAL SPECTRUM FOR A FINITE CRYSTAL MODEL

The description of vibrational motions in a crystal model using natural vibrational coordinates implies the choice of computational procedures for determining the entire vibrational spectrum of the model. We have an extensive library of approved original algorithms for calculating vibrational spectra of polyatomic molecules [2, 3]. The only thing to do is to adapt them to specific features of crystal models and make sure that they are capable of solving problems of much higher dimensions.

In this case, there is a danger that is absent in the description of vibrational motions in the Cartesian coordinates. It was noted above that the natural vibrational coordinates chosen with regard to the valence bonds and bond angles in a molecule are almost always interrelated by complex dependences. In a crystal model, the number of such dependences can be very large. Our program, CreateVibrModel, automatically introduces all possible coordinates of the bond-angle variation type. Therefore, at minimum, one vibrational coordinate arises for each atom. In principle, one can do without this coordinate, since it is related by a simple linear dependence to other angles at this atom. In some cases, the bond-stretching coordinates are sufficient to describe the entire dynamics of vibrations in a crystal. However, in the general case, such coordinates should not be excluded and the dependences between the vibrational coordinates should not be rejected for two reasons. The first reason is related to the symmetry of the model under consideration. As a rule, crystal models have high symmetry, and taking into account this symmetry facilitates significantly the solution of a problem and interpretation of the results obtained. If we exclude one of the angles at each atom, the symmetry of the system of vibrational coordinates will be lower than the symmetry of the atomic system. This circumstance will impede significantly the operation of the programs that automatically search for symmetry and take it into account. The second reason is the occurrence of numerous cycles in the crystal model, due to which the bond-stretching coordinates and the variations in the bond angles turn out to be related by numerous and very complex linear dependences. To select and exclude the extra coordinates under such conditions, even in molecular models, are very difficult (and almost impossible in intricate cases) tasks.

In our algorithms and programs intended for modeling vibrations of polyatomic molecules, the problem of taking into account and excluding the dependence between the vibrational coordinates is solved in a different way [1, 2]. First, the vibrational Hamiltonian is written in dependent coordinates. Hence, it can be easily reduced to a block form using symmetry transformations. In each block of such a Hamiltonian, rows and columns may be related by linear dependences corresponding to the dependences between the vibrational coordinates. Diagonalization of the kinematic part of the Hamiltonian leads to the occurrence of zero eigenvalues. Their number is equal to the number of linear dependences between the vibrational coordinates. We reject the zero eigenvalues and the corresponding eigenvectors. The dynamic part of the Hamiltonian is reduced to new independent vibrational coordinates (linear combinations of the initial coordinates) using the obtained system of eigenvalues and eigenvectors. The corresponding transformation involves rectangular matrices, which leads to a lower dimension of the Hamiltonian matrix. Diagonalization of the transformed dynamic part of the Hamiltonian yields frequencies and modes of the model vibrations. The vibrational modes are described in the initial system of dependent vibrational coordinates, which significantly facilitates interpretation of the results obtained. In addition, the vibrational modes are transformed into Cartesian displacements of atoms, which makes it possible to obtain a visual animation picture of model vibrations.

Note that all the above-described computational procedures are carried out with limited machine and algorithmical accuracy. Hence, the dependences between the vibrational coordinates are also inaccurate to some extent. As a result, diagonalization of the Hamiltonian yields some small values rather than exact zeros; these values should be recognized and selected using a discriminator. The experience with molecular models containing up to a hundred atoms showed that the programs proposed solve this problem successfully. However, we were not sure that our algorithms and programs aimed at taking into account and excluding dependences between vibrational coordinates can be successfully applied to a crystal model in the molecular approach. To clarify this question, we performed special computational experiments. The results showed that, in the case of crystal models containing hundreds of atoms, our programs can also be successfully used to find the vibrational frequencies and modes, exclude zero vibrations, and cut off extra frequencies. An appropriate example will be given below.

One question is left, which is related to the high dimension of the vibrational problem as applied to crystals. This difficulty can be overcome using a modern computational tool—an MVS-1000 supercomputer. We took into account that crystal models of arbitrary sizes have high symmetry if their sizes in all three translational directions are multiples of the lengths of the translation vectors. This condition is specified in the proposed method of constructing a crystal model. For symmetric models, our algorithms provide for an automatic search of the symmetry group of a model and transformation of the Hamiltonian to a block form using the obtained symmetry matrix. The Hamiltonian blocks can be diagonalized independently of each other either successively on a personal computer or simultaneously on an MVS-1000 supercomputer.

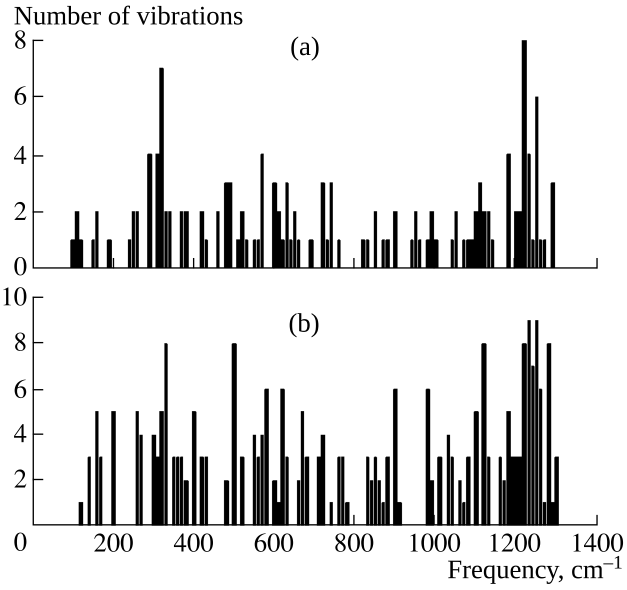

Fig. 1. Frequency histograms of the density of vibrations for models of a diamond crystal with sizes of (a) 2 × 2 × 1 and (b) 2 × 2 × 2 unit cells. The correlation coefficient is 0.3351. The "crystal saturation" does not manifest itself.

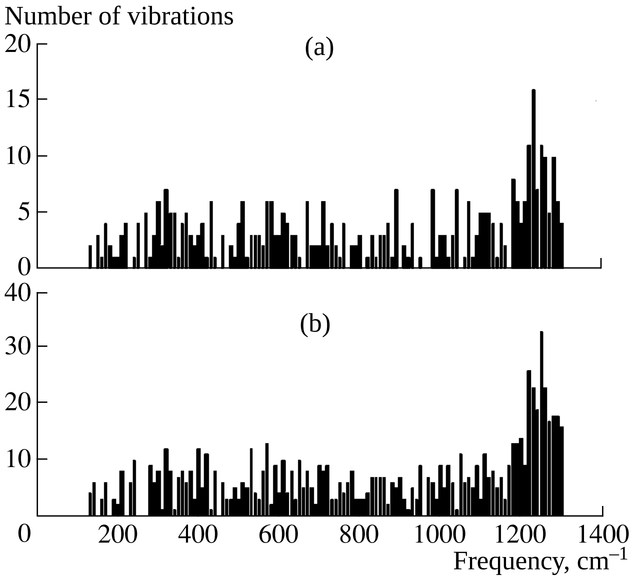

Fig. 2. Frequency histograms of the density of vibrations for models of a diamond crystal with sizes of (a) 3 × 2 × 2 and (b) 3 × 3 × 3 unit cells. The correlation coefficient is 0.5897. The similarity of the histograms increases.

We developed two variants of programs based on identical computational procedures. The first variant is intended for calculating vibrational frequencies and modes for a crystal model on an MVS-1000 supercomputer in the parallel regime. The input data are the parameters of the atomic system and the system of vibrational coordinates in the crystal model, the system of characteristic force constants, and the symmetry transformation matrix. These data are obtained on a personal computer using the above-described procedures. Then, they are transferred to a supercomputer and serve as input data for our programs. The computational program uses the parameters of atoms, vibrational coordinates, and characteristic force constants to form the elements of the Hamiltonian matrix and, using the symmetry matrix, transform the Hamiltonian directly to the block form. The thus obtained Hamiltonian blocks are diagonalized. As a result, the vibrational frequencies and modes are obtained, as well as the displacements of atoms during vibrations. The number of processors involved is equal to the number of symmetry blocks. The results obtained are transferred again to a personal computer to be visualized. A personal computer is also used to calculate various functions of the vibrational spectrum of the crystal, in particular, histograms of distribution of vibrational frequencies over spectral intervals (see Figs. 1–3).

The second variant is intended for a personal computer. If a modeled crystal is small, all the noted procedures are performed on a personal computer in a successive regime.

Let us consider an example of modeling a crystal. To verify the normal operation of the programs proposed, we chose a diamond crystal. In particular, a model of a crystallite 4 × 3 × 3 unit cells in size was constructed. The model contains 361 atoms and is described by 567 bond stretchings and 1484 bond-angle variations. The total number of vibrational coordinates is 2060, and the number of symmetry blocks is 6. This model yields 1073 normal vibrations in the calculated vibrational spectrum. Almost 1000 dependences between the vibrational coordinates were successfully recognized and taken into account. Four vibrations were lost in the calculation, since atomic groups that do not enter cycles are present on the crystallite surface. For such groups, three-dimensional vibrational coordinates should be introduced to describe internal torsional vibrations. However, we did not introduce these coordinates deliberately and accepted a loss of only four degrees of freedom from 1077 in exchange for model simplicity. This loss is unlikely to affect the accuracy of calculation of any functions of the vibrational spectrum obtained.

To check the accuracy of the method proposed, we performed calculations both on an MVS-1000 supercomputer and on a personal computer. The histograms of calculated frequencies coincide for both cases, which gives grounds to consider both variants of programs operating with similarly good accuracy despite the significant difference in the computational platforms. The frequency histogram has pronounced features of an outlined band structure, which indicates the adequacy of the proposed method for modeling vibrational states of crystal structures.

Note that the method and programs proposed can be easily extended to crystals containing defects and dislocations. If some atoms are regularly replaced in a regu-

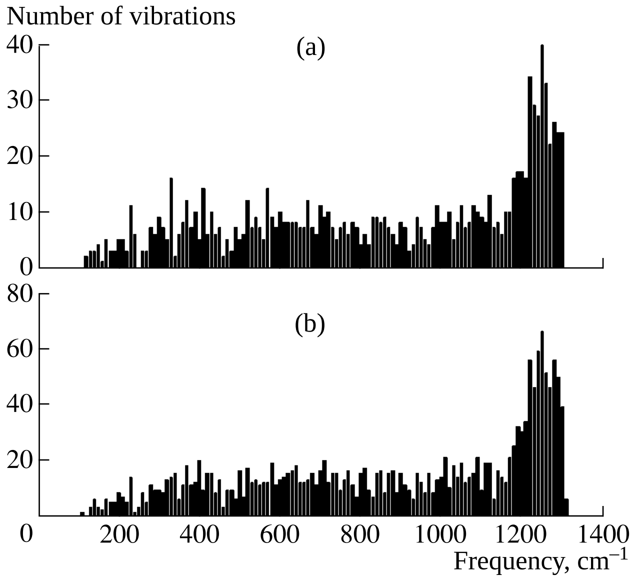

Fig. 3. Frequency histograms of the density of vibrations for the models of a diamond crystal with sizes of (a) 4 × 3 × 3 and (b) 4 × 4 × 4 unit cells. The correlation coefficient for the histograms is 0.9116. The tendency to the crystal saturation is pronounced.

lar crystal (as in a regular solid solution), one should prepare in advance the information on the Cartesian coordinates of all types of atoms in the unit cell and then carry out modeling and calculations according to the above scheme.

If impurity atoms are randomly located in a crystalline solid solution, one should first construct a model of a regular crystal without impurities and then, using the CreateVibrModel program, replace some atoms randomly on the basis of the known impurity concentration. In this case, of course, the symmetry of the model will be lost and the calculations should be performed on an MVS-1000 supercomputer, setting for the program the single-processor mode of operations with a single Hamiltonian block. In this case, the program remains the same but the calculation time increases significantly.

If it is required to describe a dislocation of any type, a model without a dislocation should be constructed first and, then, a program displacement should be set in the MatLab system for the atoms located in the specified spatial region. In this case, the model, most likely, will also lose its symmetry.

If defects in a crystal should be described, the CreateVibrModel program can be used to set an operation of eliminating atoms with certain numbers in the regular entire model of the crystal. In this case, the valence bonds and other vibrational coordinates referring to the noted atoms are eliminated automatically.

The above brief list of the properties of the proposed program set demonstrates that it is quite universal and convenient for carrying out crystallochemical investigations.

CONCLUSIONS

Let us consider the second histogram shown in Fig. 3. It was obtained using the above-described program set for the model of a diamond crystal 4 × 4 × 4 unit cells in size. The model contains 617 atoms and is described by 1024 bond stretchings and 2712 bond-angle variations. The total number of vibrational coordinates is 3736. The number of symmetry blocks is 10. This model contains 1837 normal vibrations in its calculated vibrational spectrum. The total computation-time consumption for this model was 47 min.

Visual comparison of the two histograms shown in Fig. 3 suggests that, in going from the model with a size of 4 × 3 × 3 unit cells to the model with a size of 4 × 4 × 4 unit cells, the general character of the frequency spectrum changes very little. The similarity of two spectral distributions can be estimated impartially using the correlation coefficient, which is equal to 0.9116 for these two models. For comparison, we calculated the correlation coefficient for the histograms obtained for the models with sizes of 3 × 2 × 2 and 3 × 3 × 3 unit cells (Fig. 2). In this case, the correlation coefficient is 0.5897. Thus, with an increase in the size of a crystal model, the physical transition to infinity occurs very rapidly (i.e., the character of the spectrum becomes independent of the crystallite size). This also holds true for the specific thermodynamic functions. Further increase in the crystal-model size loses its physical meaning. Thus, we can conclude that the molecular approach developed in this study for calculating the entire spectrum of a crystal makes it possible to estimate correctly the thermodynamic properties of a crystal using models of moderate size. Such models with simple unit cells can be processed on personal computers. For models with complex unit cells, a supercomputer with a small number of processors operating simultaneously can be used.

At the same time, visual comparison of the histograms in Fig. 3 shows that the spectra differ in details. Such a sensitivity of the calculated spectra to the model size allows one to solve intricate problems, in which the shape of nanocrystallites should be taken into account. In this case, the molecular approach ensures success, since it does not use any computational simplifications. Harmonicity of vibrations in crystals is the only physical assumption adopted here. In other respects, the problem of vibrational states in crystallites is solved exactly.

ACKNOWLEDGMENTS

This study was supported by the Russian Foundation for Basic Research, project no. 01-07-90042.

REFERENCES

1. M. V. Vol'kenshteĭn, L. A. Gribov, M. A. El'yashevich, and B. I. Stepanov, *Molecular Vibrations* (Nauka, Moscow, 1972) [in Russian].
2. L. A. Gribov and V. A. Dement'ev, *Calculation Methods and Algorithms in the Theory of Vibrational Spectra of Molecules* (Nauka, Moscow, 1982) [in Russian].
3. L. A. Gribov and V. A. Dement'ev, *Computer Modeling of Vibrational Spectra of Complex Compounds* (Fizmatlit, Moscow, 1989) [in Russian].
4. L. A. Gribov, V. A. Dement'ev, and A. T. Todorovskiĭ, *Interpretation of Vibrational Spectra of Alkanes, Alkenes, and Benzene Derivatives* (Nauka, Moscow, 1986) [in Russian].
5. L. A. Gribov, V. A. Dement'ev, and O. V. Novoselova, *Interpretation of Vibrational Spectra of Hydrocarbons with Isolated and Conjugated Bonds* (Nauka, Moscow, 1987) [in Russian].
6. M. E. Élyashberg, Yu. Z. Karasev, V. A. Dement'ev, and L. A. Gribov, *Interpretation of Vibrational Spectra of Hydrocarbons—Cyclohexane and Cyclopentane Derivatives* (Nauka, Moscow, 1988) [in Russian].
7. L. A. Gribov and A. I. Pavlyuchko, *Variation Methods for Solving Anharmonic Problems in the Theory of Vibrational Spectra of Molecules* (Nauka, Moscow, 1998) [in Russian].
8. *LEV. Light-Handed Elucidation of Vibrations, Description of the Program and User Manual* (Inlan, Moscow, 1995).
9. *ChemOffice. CambridgeSoft World Wide Web Page* (1999), http://www.camsoft.com

Translated by Yu. Sin'kov

Crystallography Reports, Vol. 49, No. 5, 2004, pp. 878–879. Translated from Kristallografiya, Vol. 49, No. 5, 2004, pp. 969–970.
Original Russian Text Copyright © 2004 by the Editorial Board.

Evgeniĭ Invievich Givargizov (on the Occasion of His 70th Birthday)

On August 1, 2004, Doctor of Physical–Mathematical Sciences Professor Evgeniĭ Invievich Givargizov, one of the most prominent experts in growth of semiconductor films and whiskers, will celebrate his 70th birthday.

Givargizov was born in the village of Urmiya in Krasnodar oblast, Russia on August 1, 1934. He graduated from a high school in the city of Armavir with a gold medal and entered the Physics Faculty of the Moscow State University, from which he graduated with distinction in 1958. Since this time, his life has been closely linked with the Shubnikov Institute of Crystallography of the Russian Academy of Sciences.

Givargizov became a post-graduate student of Professor N.N. Sheftal and started studying the growth mechanism of epitaxial semiconductor films by chemical reactions from the vapor phase. At that time, it was a novel method, which, finally, led to the developemnt of microelectronics. The first publication to this effect was written by Prof. Sheftal in 1957. Givargizov was the first in this country to defend a Candidate's dissertation on epitaxial growth of thin films (1965).

Immediately after the defense of the Candidate's dissertation, Givargizov started studying a new problem—growth of semiconductor whiskers. He worked with a number of diverse semiconductor materials and deeply penetrated into the growth mechanism, morphology, and real structure of whiskers. In his doctoral dissertations defended in 1975, Givargizov considered an important technological aspect of growth of whiskers and elaborated the method of controlled growth of oriented regular systems of semiconductor whiskers. This predetermined the widespread use of whiskers for various practical applications.

In 1978, Givargizov headed the Sector of Crystallization from the Vapor Phase, and, in 1982, after the reorganization of the sector into a laboratory, became the head of this laboratory.

Givargizov, a prominent scientist and a man of talent, who developed the technology of growth of whiskers and the method of preparing nanometer tips based on them, could not pass by such fields of physics as field emission and field-emission and field-ion microscopy. Together with his colleagues and the Special Design Bureau of the Institute of Crystallography, he managed to create a unique apparatus for studying semiconductors by field-emission and field-ion microscopy. Soon, the first publications in this area appeared.

In the 1990s, Givargizov focused his attention on field emission from single- and multiwhisker silicon systems and their possible use as light sources and elements of field-emission displays. The emphasis was on the improvement of the mechanical, thermal, and field-emission properties of silicon cold cathodes prepared from whiskers with diamond coatings (in cooperation with laboratories of electron diffraction and electron microscopy). Together with the Research Institute of Nuclear Physics of Moscow State University (E.S. Mashkova and V.A. Molchanov), Givargizov performed a series of studies on sharpening of the diamond coatings of silicon whiskers. These studies proved an important role of diamond coatings in improvement of the field-emission properties of silicon cathodes and resulted in the design of the first prototype of an autonomic field-emission source of light.

In parallel with the study of whiskers and their field-emission properties, Givargizov also developed another important field—growth of single-crystal semiconductor films on nonoriented substrates by the method of artificial epitaxy (graphoepitaxy). The idea of growing single-crystal films on the substrate with an artificial relief was first formulated and, then, experimentally confirmed by Sheftal in 1972. The subsequent studies performed under Givargizov's guidance allowed the authors to obtain for the first time large-area single-crystal silicon films on nonorienting substrates, which was of great importance for microelectronics.

Givargizov and the scientists of the laboratory of proteins managed to obtain for the first time single-crystal films of catalase, canavalin, and lysozyme by the method of artificial epitaxy (1990). These were pioneering works, which were further developed as a part of the space program, in which the Institute of Crystallography is an active participant.

At present, the laboratory headed by Givargizov is engaged in studies of the most urgent problem for both fundamental science and practical applications in microelectronics, which are directed to the creation of regular oriented systems of nanowires with efficient photo- and electroluminescence at room temperature. The practical importance of such systems for microelectronics is the optical transmission of a signal between the electronic components of integrated circuits, which would considerably increase their operation speed. In fact, the creation of such systems would signify a transition from classical microelectronics to optoelectronics. Studies in this direction are actively performed everywhere in the world, but the approach to the solution of this problem suggested by Givargizov is quite original.

Givargizov is the author of more than 250 publications, including 4 monographs on growth of whiskers and artificial epitaxy (2 monographs were ordered by foreign publishers and are written in English).

Givargizov is a member of the editorial boards of the international journals *Progress in Crystal Growth and Characterization of Materials* and *Materials Innovations*.

He also continues to edit the series *Crystal Growth* (volumes 11–22), the first ten volumes of which were edited by Sheftal.

Givargizov is an industrious and hard-working person, who is not afraid any difficulties. He works systematically and, which is of great importance, always obtains reliable and important results. On the other hand, he is a modest, kind, and responsive person, ready to help everybody by doing everything possible–or even impossible.

The editorial board of *Kristallografiya*, colleagues, and friends congratulate Evgeniĭ Invievich on his 70th birthday and wish him good health and many years of creative work.

Translated by L. Man

Crystallography Reports, Vol. 49, No. 5, 2004, pp. 880–881. Translated from Kristallografiya, Vol. 49, No. 5, 2004, pp. 971–972.

JUBILEES

Dmitriĭ Yur'evich Pushcharovskiĭ (on the Occasion of His 60th Birthday)

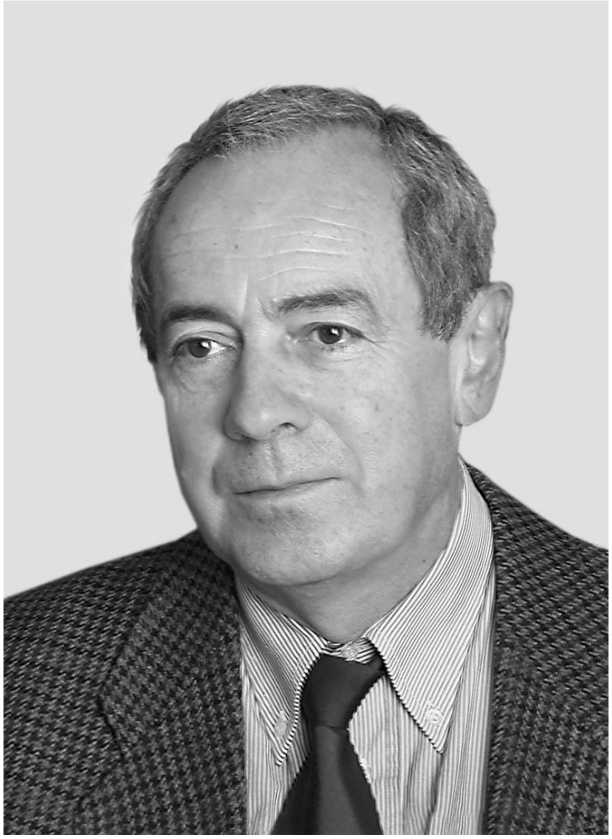

On May 16, 2004, Corresponding Member of the Russian Academy of Sciences Professor Dmitriĭ Yur'evich Pushcharovskiĭ celebrated his 60th birthday. Dean of the Geology Faculty of Moscow State University, head of the Department of X-ray Diffraction Analysis, and an Honorary Scientist of the Russian Federation, Pushcharovskiĭ is one of the best-known representatives of the scientific school founded by Professor N.V. Belov. Developing the traditions of this school, Pushcharovskiĭ heads the Project on Structural Crystallography of the Presidential Program for the Support of Leading Scientific Schools. Many of Belov's students and followers working at the Shubnikov Institute of Crystallography of the Russian Academy of Sciences and at the Crystallography and Crystal Chemistry Departments of the Geology Faculty of Moscow and Nizhni Novgorod State Universities are taking an active part in the fulfillment of this project.

Pushcharovskiĭ was born in Moscow in 1944 in a family of graduates from Moscow State University. His father, Academician Yuriĭ Mikhaĭlovich Pushcharovskiĭ, finished the Great Patriotic War (1941–1945) as a lieutenant in the air force and, then, worked for 60 years at the Geological Institute of the Russian Academy of Sciences. His mother, Faina Arkad'evna Pushcharovskaya, was a candidate of biological sciences, worked for many years at the Institute of Psychiatry of the Russian Academy of Medical Sciences, and received recognition as an expert in the electroencephalography of the brain.

In 1961, Pushcharovskiĭ graduated from high school with a silver medal and entered the Geology Faculty of Moscow State University, from which he graduated with distinction in 1967 and received a diploma as a geologist–geochemist. Then, he became a postgraduate at the Department of Crystallography and Crystal Chemistry of the Geology Faculty of Moscow State University, where he was guided by Professor Belov. Since 1969, he has worked at this department first as a junior scientist and, finally, as a professor.

Pushcharovskiĭ created several special courses for students, such as X-ray Diffraction Analysis of Minerals, X-ray Diffraction Analysis, and Structure and Properties of Crystals, in which he managed to describe in detail various physical phenomena that accompany the processes of X-ray scattering and diffraction in crystals without using a sophisticated mathematical apparatus. Another characteristic feature of these courses is a detailed consideration of the concepts underlying the first experimental studies that formed the basis of modern X-ray diffraction analysis of crystals. This material is necessary for understanding the logistics of the development of the structural studies and is always accepted by students and experts in this field with great enthusiasm. Pushcharovskiĭ also developed new programs for practical and laboratory work for these courses and included in these works the most advanced approaches used in the crystal chemistry of minerals (the acquisition of diffraction data with the use of synchrotron radiation and position-sensitive detectors, the methods of full-profile analysis, the study of phenomena that considerably complicate diffraction analysis, and the latest complexes of computer programs). In 2001, Pushcharovskiĭ was awarded the Lomonosov prize for his pedagogical activity.

Pushcharovskiĭ has a broad scientific scope, erudition, and a deep logical and consistent understanding not only of the physical foundations of the structure of matter, but also a clear understanding of the structure of the universe. This is associated, to a large extent, with his work in a number of laboratories and research centers all over the world, such as Geneva University (1973–1974), the State University of New York (1980), Australian National University (1990), the University Ouro-Preto in Brazil (1994), and the Universities of Pisa and Turin (1999–2003), where he worked in cooperation with such well-known crystallographers as E. Parthé, Ch. Prewitt, B. Hyde, G. Ferraris, S. Merlino, and many others.

The main area of Pushcharovskiĭ’s scientific interests includes structural mineralogy, crystal chemistry, and structural crystallography. He has performed complete structural studies of more than 80 minerals and synthetic compounds and established 40 new structure types, which formed the basis for the discovery of 19 new mineralogical species, development of new classifications of silicates, sulfates, phosphates, and germanates, and establishment of the structural principles of the most important rock-forming silicates and related mineralogical groups. Many of the crystal structures solved by Pushcharovskiĭ are among the most complex mineral species known today. The experiments performed by Pushcharovskiĭ with the use of synchrotron radiation are unique and open a new epoch in the physics and chemistry of minerals. Pushcharovskiĭ is a coauthor of a series of studies on the tectonics of deep-seated geosphere, which was awarded the main prize of the Maik/Nauka publishers in 2000.

Pushcharovskiĭ’s enormous pedagogical practice and great skill in delivering lectures are well known beyond the walls of Moscow State University. His excellent knowledge of English and French has allowed him to present papers and deliver lectures in 25 universities all over the world. He has taught large courses in Cuba (1987), India (1991), Italy (1992), Brazil (1994), and China (2000). As an invited speaker, he made presentations at the International NATO School on Modern Perspectives in Inorganic Crystal Chemistry (Erice, Italy, 1992). Since 1997, he has been repeatedly awarded the title of Soros Professor and is a winner of the competition Moscow Grants. In 1998, Pushcharovskiĭ led the symposium “Teaching of Crystallography” in Prague within the framework of the European Crystallography Meeting. He supervised two Doctoral and six Candidate’s dissertations. In recent years, students of the Geology Faculty have defended about 40 Bachelor’s and Master’s works supervised by Pushcharovskiĭ. He has also guided the probation work of experts from various institutes of the Russian Academy of Sciences and universities in Italy, Algeria, and Azerbaijan. In 1997–2001, Pushcharovskiĭ participated in seven regional teacher’s conferences in Moscow, Smolensk, Cherkessk, Yaroslavl, Nal’chik, Dubna, and Tambov, where he delivered lectures on modern problems of mineralogy and crystallography.

Pushcharovskiĭ is the author of more than 350 scientific publications, including a textbook and seven monographs. These are *X-ray Diffraction of Minerals* (2001), *Structure and Properties of Crystals* (1982), *Structure Types of Minerals* (1990), *Structural Mineralogy of Silicates and Their Synthetic Analogues* (1986), *Crystal Chemistry of Sulfates* (1989), and others. These editions are used not only at the Geology Faculty, but also at the Faculty of Materials Sciences and the Chemistry and Physics Faculties of Moscow State University.

Pushcharovskiĭ’s works are well-known abroad. Swiss mineralogists named a mineral after him—pushcharovskite—a new natural copper arsenate discovered in 1996. In 1997–1998, Pushcharovskiĭ coordinated a Russian–Swiss project and in 1999–2001, he led a joint Russian–Chinese project. Since 2004, he has led a joint Russian–Austrian project. In all these joint projects, an active part is played by postgraduates, magisters, and students of Moscow State University.

Pushcharovskiĭ made an important contribution to the development of the history and methodology of crystal chemistry; he wrote a number of publications concerning the scientific heritage of Belov, Goldschmidt, Werner, and other well-known geochemists, and also a series of popular articles for the *Soros Educational Journal* and the journal *Priroda*.

Pushcharovskiĭ is also engaged in intense and diverse scientific–organizational work. He is a member of the National Committee of Russian Crystallographers, the vice-chairman of the National Committee of Russian Geologists, the chairman of the Commission of Classification of Minerals of the International Mineralogical Association (IMA), and the Scientific Secretary of the Commission on Inorganic and Mineral Structures of the International Union of Crystallography. Pushcharovskiĭ is the editor- in-chief of the journal *Vestnik MGU*, *Series Geology*, and a member of the editorial boards of the journals *Kristallografiya* (Crystallography Reports) and the *European Journal of Mineralogy.* He is also a member of the Program Committee of the 20th International Congress of Crystallography, 2005.

The editorial board of *Kristallografiya* wishes Dmitriĭ Yur’evich Pushcharovskiĭ good health and many years of successful creative work for the prosperity of the Russian Science.

Translated by L. Man

Crystallography Reports, Vol. 49, No. 5, 2004, pp. 882–883. Translated from Kristallografiya, Vol. 49, No. 5, 2004, pp. 973–974.
Original Russian Text Copyright © 2004 by the Editorial Board.

MEMORIAL DATA

On the Occasion of the 100th Birthday of Nikolaĭ Alekseevich Brilliantov

Nikolaĭ Alekseevich Brilliantov, doctor of technical sciences and associate professor of the Chair of Low Temperatures of the Faculty of Physics of Moscow State University, was born on February 26, 1904, in Velikiĭ Novgorod into the family of a military doctor.

After leaving school, he worked for a year as a fitter in mechanical shops. From 1922 to 1924, Brilliantov was a student at the Faculty of Physics and Mathematics of the Leningrad Polytechnical Institute. Since his second course, he worked at the laboratory of I.V. Obreimov. First, he worked as a laboratory assistant and then performed the duties of an engineering physicist. This cooperation with Obreimov grew into friendship for life. In 1924, six students (A.I. Shal’nikov, V.S. Gorskiĭ, B.M. Gokhberg, N.A. Brilliantov, A.N. Arsen’eva, and N.S. Usatova) from among those attending a seminar of V.Ya. Frenkel were, even before graduating, taken to work at the Physicotechnical Institute.

In 1929, Obreimov’s laboratory was transferred to Kharkov, and Brilliantov became a research worker at the Ukraine Institute of Physics and Technology, where domestic physicists were prepared at that time. His colleagues were young, talented, and, to a great extent, mischievous and merry people. The hostel they lived in was referred to as the Rock Whale. In those hard and hungry years, their life was full of ideas and jokes. Brilliantov’s colleagues wrote about this period in their memoirs. Ten years of work under the supervision of Obreimov were a good school of experimental physics for Brilliantov. The ability to work with his own hands in any field and at any time was very important for him and he did his best to pass this ability to his students (including his son). He was always on friendly terms with workers in mechanical shops.

In 1931, Brilliantov was appointed the head of the Advice Bureau at the Institute of Physics and Technology, which served Kharkov industrial works.

Brilliantov was fond of sports and went in for ski mountaineering. In 1936, he took part, along with Yu.N. Ryabinin and V. Fomin, in the first winter militarized expedition to Elborus. All the participants of the expedition descended from the mountain on skis.

Simultaneously with scientific research, Brilliantov was engaged in pedagogical activity for 23 years. In 1931–1934, he was the head of the Chair of Physics of the evening division of the Kharkov Institute of Chemical Technology. He taught students at the special X-ray diffraction laboratory at the Faculty of Physics and Mathematics of Kharkov State University (1934–1937).

In 1938, on the recommendation of Obreimov, Brilliantov was sent to Moscow to the Institute of Physical Problems organized by P.L. Kapitza. Brilliantov was among the first five researchers involved in the foundation of the Institute of Physical Problems. Kapitza wrote: “I have three physicists–experimenters on the staff—Strelkov, Shal’nikov, and Brilliantov.”

In 1938, Brilliantov was awarded the degree of Candidate of Physics and Mathematics for the entire set of his studies (without defending a Candidate’s dissertation).

At the Institute of Physical Problems, as well as at the Ukraine Institute of Physics and Technology, much attention was paid to training of young staff. Thus, most researchers working at the institute lectured on the fundamentals of physics and trained young experts in the things they worked on.

In 1939, Brilliantov was involved in the organization of the Chair of Low Temperatures at the Faculty of Physics of Moscow State University, organized and carried out special practical studies in physics of low temperatures, took part in writing methodical guidelines for these studies (along with Strelkov), and gave a special course on low-temperature technology.

During the Great Patriotic War, Brilliantov was in evacuation, where he worked, theoretically and experimentally, on demagnetization of sea ships. The results obtained by him saved many lives of our sailors.

In 1944, Brilliantov became an associate professor of the Chair of Low Temperatures at the Faculty of Physics of Moscow State University and, in 1950, he was awarded the degree of a senior researcher in experimental physics. In 1955, he defended his Doctoral dissertation in technical sciences and was awarded the degree of Doctor of Technical Sciences.

In 1953, according to a government decree, Brilliantov was appointed the head of a laboratory at the enterprise referred to as Post Office Box 3394. The subject of the studies performed there has remained secret up till now.

In 1956, Brilliantov moved to the Institute of Crystallography as a deputy chief for research.

The range of scientific interests of Brilliantov was fairly wide. However, his first publication was devoted to crystallography. He also worked actively in the fields of chromatography and physics of low temperatures; he studied the liquefaction of oxygen, helium, and nitrogen. Many of his investigations were secret, and we do not know their subject. Brilliantov had several inventor's certificates.

The Brilliantov' contribution to domestic science and industry was highly estimated by the government: he was awarded by two Badges of Honour (in 1945 and 1954) and Medals for Distinction in Labor (1943), Labor Valor during the Great Patriotic War 1941–1945 (1945), and Labor Valor (1956).

As fate willed it, Brilliantov moved to the town of his youth—Leningrad—in 1966, where he worked as a head of a laboratory and a consultant.

Brilliantov died on March 24, 1984, in Moscow.

Many brilliant people work in science, revealing or verifying new laws and phenomena. However, the implementation, confirmation, and verification of new concepts are often impossible without the help of devoted colleagues and assistants.

Brilliantov was devoted to science and his friends. He did not desert his friends even in the hard years of the repressions, and, in the period of rehabilitation, was among those who ardently defended the innocence of the employees of the Ukraine Institute of Physics and Technology who had been subjected to repression (he was one of the authors of the paper published in the journal *Zvezda* in defense of people subjected to repression).

Brilliantov was a very responsive man and a kind and exacting father and grandfather.

Translated by Yu. Sin'kov

Crystallography Reports, Vol. 49, No. 5, 2004, pp. 884–885. Translated from Kristallografiya, Vol. 49, No. 5, 2004, pp. 975–976.
Original Russian Text Copyright © 2004 by the Editorial Board.

OBITUARIES

Oleg Pavlovich Aleshko-Ozhevsky
(July 3, 1934–January 25, 2004)

Oleg Pavlovich Aleshko-Ozhevsky, a leading researcher at the Institute of Crystallography of the Russian Academy of Sciences, died suddenly on January 25, 2004. All those who knew this charming, beautiful, and responsive human being felt the loss deeply.

Aleshko-Ozhevsky was born on July 3, 1934, in Kiev. After graduating from the Moscow Engineering Physics Institute in 1958, he was appointed to the enterprise referred to as Post Office Box 3100, where he dealt with the physics and technology of nuclear reactors until 1962. In 1962, he went to work at the Institute of Crystallography of the Academy of Sciences of the Soviet Union. In 1963, Aleshko-Ozhevsky began to work fruitfully in the sector of neutron diffraction analysis. He advanced the methods for studying magnetoelectrics and developed corresponding equipment. He has grown more than 30 types of crystals, mainly hexagonal ferrites. He was the first in the Soviet Union to design a setup using a beam of monochromatic polarized neutrons. He discovered (along with I.I. Yamzin) noncollinear magnetic domain structures, in particular, conical ferromagnetic domain spirals in scandium-substituted ferrites. In 1969, he defended his Candidate’s dissertation based on his productive research in this field.

Later, after moving into the sector of real structure of crystals, Aleshko-Ozhevsky was engaged in work on synchrotron-radiation sources. Soon he became a leader in this new field of experimental research. After a short time, he developed a method of synchrotron topography and designed a diffraction apparatus (advanced for that time) equipped with a system of visualization of X-ray images of objects under study. In 1981, at the International Conference on Synchrotron Radiation (Novosibirsk), Aleshko-Ozhevsky demonstrated—for the first time in the world—a real-time film showing the regularities of the dynamics of a ferroelectric phase transition and repolarization of domains in

1063-7745/04/4905-0884$26.00 © 2004 MAIK “Nauka/Interperiodica”

the immediate vicinity of the phase-transition point. In the course of further laborious studies, he revealed a transition layered structure arising in DKDP crystals at a step first-order phase transition.

In 1986, Aleshko-Ozhevsky went, quite naturally, to work at the laboratory of X-ray optics and synchrotron radiation and actively participated in the development of experimental equipment based on synchrotron sources. He developed a method of time-resolved X-ray topography on the basis of modulated X-ray beams, including a method of stroboscopic synchrotron topography, and studied the interaction of X-rays with crystals subjected to ultrasonic vibrations. In 1993, he defended his Doctoral dissertation titled “Dynamic X-ray Topography as Applied to Ferro- and Piezoelectric Phenomena.”

Aleshko-Ozhevsky is the author of more than 70 publications in domestic and foreign scientific journals and more than 50 reports at conferences. His studies were awarded seven times at competitions organized at the Institute of Crystallography. He was deeply engaged in pedagogical work: three Candidate’s dissertations and several graduation theses were defended under his supervision.

Never limiting himself to scientific research alone, Aleshko-Ozhevsky was deeply involved in the public life of the Institute of Crystallography. He was continuously the chairman of the BRIZ (Committee on Inventions and Rationalization Proposals) and the head of the hunting community of the Institute of Crystallography and was twice elected a member of the local trade union committee.

Those who were privileged enough to know Aleshko-Ozhevsky will remember him as an open, charming, and benevolent man, who was always ready to help other people in word and deed. His cheerfulness and sense of humor created a friendly atmosphere around him, brought good spirits to other people, and inspired them with optimism and faith in their potential.

Translated by Yu. Sin’kov

Crystallography Reports, Vol. 49, No. 5, 2004, p. 886.

ERRATA

Errata: “Indicators of the Magnetic State in the Charge Distributions of MnO, CoO, and NiO. II: Para- and Antiferromagnetism of CoO” [*Crystallogr. Rep.* 49, 357 (2004)]

J.-P. Vidal, G. Vidal-Valat, and K. Kurki-Suonio

1. The title of the article should read:

Indications of the Magnetic State in the Charge Distributions of MnO, CoO, and NiO. II: Para- and Antiferromagnetism of CoO

2. The web address on p. 360, right column, and on p. 368, figure caption, should read:

http://bus.cines.fr/vidaljp/mag3D

3. The letter B in Fig. 4 (Contd.) on p. 367, for (100) on the O^{2-} map should be in the $\langle 110 \rangle$ direction.

1063-7745/04/4905-0886$26.00 © 2004 MAIK “Nauka/Interperiodica”